Springer Series in Optical Sciences 226

Minhaeng Cho *Editor*

Coherent Multidimensional Spectroscopy

Springer

Springer Series in Optical Sciences

Volume 226

Springer Series in Optical Sciences is led by Editor-in-Chief William T. Rhodes, Florida Atlantic University, USA, and provides an expanding selection of research monographs in all major areas of optics:

– lasers and quantum optics
– ultrafast phenomena
– optical spectroscopy techniques
– optoelectronics
– information optics
– applied laser technology
– industrial applications and
– other topics of contemporary interest.

With this broad coverage of topics the series is useful to research scientists and engineers who need up-to-date reference books.

More information about this series at http://www.springer.com/series/624

Minhaeng Cho
Editor

Coherent Multidimensional Spectroscopy

Springer

Editor
Minhaeng Cho
Department of Chemistry
Korea University
Seoul, Korea (Republic of)

ISSN 0342-4111 ISSN 1556-1534 (electronic)
Springer Series in Optical Sciences
ISBN 978-981-13-9752-3 ISBN 978-981-13-9753-0 (eBook)
https://doi.org/10.1007/978-981-13-9753-0

This Springer imprint is published by the registered company Springer Nature Singapore Pte Ltd.
The registered company address is: 152 Beach Road, #21-01/04 Gateway East, Singapore 189721, Singapore

Preface

Coherence generally describes the statistical similarity of fields such as sound waves, electromagnetic fields, and quantum wave packets at two points in space and/or time. If a chosen pair of waves have a constant relative phase, they are said to be coherent and can produce an interference pattern with finite visibility. The two waves in perfect coherence are not distinguishable due to the complementarity theorem relating distinguishability to visibility. In ultrafast optical and vibrational spectroscopy, ultrashort pulses that have become readily available over the past two decades can be used to generate coherent wave packets of vibrational/electronic motions of molecules in condensed phases. Over a sufficiently short time, the coherent oscillation of the wave packets consisting of charged particles maintains in phase for all the chromophores interacted with each pulse and an electromagnetic field with the same frequency can be generated from the material. However, on a longer time scale, the relative phases of electromagnetic field-driven wave packet oscillations of chromophores become uncorrelated due to different and rapid chromophore-solvent dynamics that are intrinsically chaotic and indeterministic in the time domain. This loss of coherence in oscillating wave packets of chromophores in condensed phases has been referred to as a dephasing process. Conventional one-dimensional spectroscopy whose signal is plotted with respect to the frequency of applied electromagnetic field provides direct information on the rate of dephasing because it is partially related to the width of measured spectrum as well as on the average electronic/vibrational transition frequency that is averaged over the ensemble of chromophores.

Over the past two decades, sources of ultrafast THz, IR, near-IR, visible, UV, and X-ray pulses have become readily available, and they have been used to develop a variety of time-resolved vibrational/electronic spectroscopic techniques. One of the natural extensions of the general pump–probe, doorway–window, or excitation–detection-type spectroscopy is multidimensional spectroscopy utilizing multiple coherent laser pulses. The coherent nature of incident pulsed electromagnetic fields is transferred to chromophores via radiation–matter interactions, and their electronic/vibrational wave packets oscillate in phase over a time period set by the dephasing constant. Unlike conventional one-dimensional spectroscopy,

multidimensional spectroscopy involves more than one coherent oscillation of electronic, vibrational, or vibronic wave packets that are separated in the time domain. To measure the amplitude and relative phase of coherent quantum molecular waves, they are subjected to interfere with an additional pulsed electromagnetic field that serves as the reference wave. This phase-and-amplitude measurement of nonlinear optical/vibrational spectroscopic signal electric field enables quantitative characterization of nonlinear responses of molecules against multiple laser pulses, which can be theoretically formulated in terms of multi-point time-correlation functions. Indeed, the time correlations between multiple time-separated quantum mechanical events on an ensemble of chromophores in condensed phases provide invaluable information about molecular dynamics such as electronic and vibrational relaxation processes, chemical reaction dynamics, conformational transitions in biological molecules, exciton dynamics in natural light-harvesting proteins and semiconductors, protein structural dynamics, and ultrafast solvation dynamics in solutions, to name a few.

Due to the clear advantages of coherent multidimensional spectroscopy over conventional approaches, this research field is rapidly expanding. Combining multiple laser pulses whose frequencies are quite different, e.g., IR and visible pulses, one can explore multidimensional frequency space that could not be reached with conventional multidimensional vibrational or electronic spectroscopy utilizing multiple IR or visible pulses not both. The marriage of ultrafast multidimensional spectroscopy with microscopy is one of the most exciting developments in molecular microspectroscopy experiments, which would be of great use to study not just temporal correlations between vibrational and electronic wave packets of chromophores in condensed phases but also spatial correlations between them in coupled chromophore systems within and beyond the diffraction limit. Another new direction of coherent multidimensional spectroscopy that we have witnessed over the past few years is to use more than one coherent, ultrafast lasers that are phase-locked with one another to a reference atomic clock frequency in the radio frequency domain. This will enable wide dynamic range of measurements of multidimensional spectroscopic signals without using mechanical time-scanning devices. Multidimensional X-ray spectroscopy is still in its infancy but holds a promise ultimately to allow one to elucidate electron correlation and dynamics of molecular systems in the sub-femtosecond time domain.

This book presents the latest advances in the coherent multidimensional spectroscopy techniques and applications. I am much obliged to all the contributors who are at the forefront of this and related research fields. Also, I owe special thanks to my colleagues, the production editor, and staff of Springer Nature for their help and encouragement.

Seoul, Korea (Republic of) Minhaeng Cho

Contents

Editor and Contributors

About the Editor

Minhaeng Cho is the Director of the IBS Center for Molecular Spectroscopy and Dynamics, established in December 2014 and Professor of Chemistry at Korea University, Seoul, Korea. He grew up in Seoul, where he attended the public schools. He received his B.S. and M.S. from Seoul National University in 1987 and 1989, respectively, before studying in USA, where he received his Ph.D. in 1993 from the University of Chicago. He returned to Korea in 1996 as an Assistant Professor at the Korea University after a 2-year post-doctoral research experience at MIT, Cambridge, USA. He became a Full Professor at the Korea University in 2003 before his directorship with IBS in 2014. IBS Center for Molecular Spectroscopy and Dynamics (CMSD), located in the Seoul campus of Korea University, emphasizes developments of novel time- and space-resolved spectroscopy techniques and their applications to chemically reactive and biologically important systems. CMSD uses ultrashort duration pulses of light to generate stroboscopic movies of the molecular motions that lead to the chemical, biological, and physical transformations of condensed matter. The researchers in CMSD use a broad range of radiation sources to measure the dynamics of electronic and vibrational degrees of freedom in a wide range of systems, perform quantum chemical and molecular mechanical computations of dynamic systems in condensed phases, and develop novel linear and nonlinear optical imaging and microscopy technologies to monitor time evolution of chemically and biologically reactive systems in real time. He is a member of Korean Academy of Science and Technology (KAST) and received numerous awards given by American Chemical Society, National Science Foundation in Korea, KAST, Kyung-Am Science Foundation, and National Academy of Science in Korea.

Contributors

E. A. Arsenault Department of Chemistry, University of California Berkeley, Berkeley, USA;
Molecular Biophysics and Integrated Bioimaging Division, Lawrence Berkeley National Laboratory, Berkeley, CA, USA

Mischa Bonn Department of Molecular Spectroscopy, Max Planck Institute for Polymer Research, Mainz, Germany

Minhaeng Cho Center for Molecular Spectroscopy and Dynamics, Institute for Basic Science (IBS), Seoul, Republic of Korea;
Department of Chemistry, Korea University, Seoul, Republic of Korea

Lev Chuntonov Technion – Israel Institute of Technology, Haifa, Israel

Jeffrey A. Cina Department of Chemistry and Biochemistry and Oregon Center for Optical, Molecular and Quantum Science, University of Oregon, Eugene, OR, USA

Bar Cohn Technion – Israel Institute of Technology, Haifa, Israel

Steven T. Cundiff Department of Physics, University of Michigan, Ann Arbor, MI, USA

Peter A. Eckert Department of Chemistry, University of Michigan, Ann Arbor, MI, USA;
Oak Ridge National Laboratory, Oak Ridge, TN, USA

Thomas Elsaesser Max-Born-Institute, Berlin, Germany

Benjamin P. Fingerhut Max-Born-Institute, Berlin, Germany

Graham R. Fleming Department of Chemistry, University of California Berkeley, Berkeley, USA;
Molecular Biophysics and Integrated Bioimaging Division, Lawrence Berkeley National Laboratory, Berkeley, CA, USA

Maksim Grechko Department of Molecular Spectroscopy, Max Planck Institute for Polymer Research, Mainz, Germany

Elad Harel Department of Chemistry, Northwestern University, Illinois, USA

Masahiro Higashi Department of Chemistry, Biology and Marine Science, University of the Ryukyus, Nishihara, Okinawa, Japan;
Department of Molecular Engineering, Kyoto University, Kyoto, Japan

Ken-ichi Inoue Molecular Spectroscopy Laboratory, RIKEN, Saitama, Japan;
Department of Chemistry, Graduate School of Science, Tohoku University, Sendai, Japan

Alexis J. Kiessling Department of Chemistry and Biochemistry and Oregon Center for Optical, Molecular and Quantum Science, University of Oregon, Eugene, OR, USA

JunWoo Kim Center for Molecular Spectroscopy and Dynamics, Institute for Basic Science (IBS), Seoul, Republic of Korea

Amber T. Krummel Department of Chemistry, Colorado State University, Colorado, USA

Kevin J. Kubarych Department of Chemistry, University of Michigan, Ann Arbor, MI, USA

Nicholas H. C. Lewis James Franck Institute, The University of Chicago, Chicago, IL, USA

Bachana Lomsadze Department of Physics, University of Michigan, Ann Arbor, MI, USA;
Department of Physics, Santa Clara University, Santa Clara, CA, USA

Bradley M. Luther Department of Chemistry, Colorado State University, Colorado, USA

Robert T. Mackin Department of Chemistry, Tulane University, New Orleans, USA

Satoshi Nihonyanagi Molecular Spectroscopy Laboratory, RIKEN, Saitama, Japan;
Ultrafast Spectroscopy Research Team, RIKEN Center for Advanced Photonics (RAP), Saitama, Japan

Kaoru Ohta Molecular Photoscience Research Center, Kobe University, Nada, Kobe, Japan;
Graduate School of Science, Kobe University, Nada, Kobe, Japan

Masaki Okuda Molecular Photoscience Research Center, Kobe University, Nada, Kobe, Japan

Sabine Oldemeyer Department of Chemistry, University of California Berkeley, Berkeley, USA;
Molecular Biophysics and Integrated Bioimaging Division, Lawrence Berkeley National Laboratory, Berkeley, CA, USA

Hanju Rhee Korea Basic Science Institute, Seoul, Republic of Korea

Igor V. Rubtsov Department of Chemistry, Tulane University, New Orleans, USA

Shinji Saito Department of Theoretical and Computational Molecular Science, Institute for Molecular Science, Myodaiji, Okazaki, Aichi, Japan

Tahei Tahara Molecular Spectroscopy Laboratory, RIKEN, Saitama, Japan;
Ultrafast Spectroscopy Research Team, RIKEN Center for Advanced Photonics (RAP), Saitama, Japan

Howe-Siang Tan Division of Chemistry and Biological Chemistry, School of Physical and Mathematical Sciences, Nanyang Technological University, Singapore, Singapore

Clara A. Tibbetts Department of Chemistry, Colorado State University, Colorado, USA

Keisuke Tominaga Molecular Photoscience Research Center, Kobe University, Nada, Kobe, Japan;
Graduate School of Science, Kobe University, Nada, Kobe, Japan

Laura Vietze Department of Molecular Spectroscopy, Max Planck Institute for Polymer Research, Mainz, Germany

John C. Wright Department of Chemistry, University of Wisconsin, Madison, WI, USA

Eric C. Wu Department of Chemistry, University of California Berkeley, Berkeley, USA;
Molecular Biophysics and Integrated Bioimaging Division, Lawrence Berkeley National Laboratory, Berkeley, CA, USA

Chapter 1
Introduction to Coherent Multidimensional Spectroscopy

Minhaeng Cho

Abstract Coherent multidimensional spectroscopy is a state-of-the-art technique with applications in a variety of subjects, such as chemistry, molecular physics, biochemistry, biophysics, and materials science. Due to dramatic advances in ultrafast laser technologies, a diverse range of coherent multidimensional spectroscopic methods utilizing combinations of THz, infrared, visible, UV, and X-ray radiation sources have been developed and used to study the real-time dynamics of small molecules in solutions, proteins and nucleic acids in condensed phases and membranes, single and multiple exciton states in functional materials like semiconductors, quantum dots, and solar cells, photo-excited states in light-harvesting complexes, ions in battery electrolytes, electronic and conformational changes in charge or proton transfer systems, and excess electrons and protons in water and biological systems. In this chapter, we introduce the theory behind coherent multidimensional spectroscopy and a summary of recent experiments.

1.1 Introduction

A spectrometer is a device that measures radiation intensity as a function of electromagnetic field frequency or wavelength, and it has become indispensable in modern-day chemical and biological research. A variety of spectroscopic techniques have been developed to study the interaction between matter and electromagnetic waves, in particular investigating the spectra or distribution of the quantum eigenstates of molecules and materials in the frequency domain and their population evolution and coherent vibrational/electronic oscillatory motion in the time domain.

On a microscopic level, a number of fundamental molecular processes of interest occur over a broad dynamic range of timescales, from femtoseconds (10^{-15} s) to

M. Cho (✉)
Center for Molecular Spectroscopy and Dynamics, Institute for Basic Science (IBS), Seoul 02841, Republic of Korea
e-mail: mcho@korea.ac.kr

Department of Chemistry, Korea University, Seoul 02841, Republic of Korea

M. Cho (ed.), *Coherent Multidimensional Spectroscopy*,
Springer Series in Optical Sciences 226,
https://doi.org/10.1007/978-981-13-9753-0_1

nanoseconds (10^{-9} s) and even microseconds [1, 2]. For example, electrons transfer from an electron-donating group to an electron-accepting group in femtoseconds to nanoseconds, depending on the distance between them. In addition, energy transfer and migration processes in light-harvesting protein complexes after photoexcitation have a broad distribution of kinetic rate constants on a picosecond timescale. Similarly, in aqueous solutions, water molecular reorientation takes place on a picosecond timescale, and H-bonding network dynamics are subpicosecond processes that can be slowed down when hydrophobic molecules are nearby. Dihedral rotations about single chemical bonds are another important elementary process involved in a variety of conformational transitions of flexible polyatomic molecules and proteins. The internal rotation of a small molecule about a carbon-carbon bond in solution, which represents a barrier-crossing process, takes tens of picoseconds, which is clearly dependent on the potential energy barrier along the reaction coordinate connecting the two conformer states [3]. Small solvent molecules in solution around electronic chromophore molecules (e.g., dyes) can reorganize themselves on a subpicosecond to several picosecond timescale when the chromophore is electronically excited by an impulsive light pulse [4, 5].

To understand the molecular processes taking place on femtosecond to nanosecond timescales in chemistry, physics, and biology, ultrafast nonlinear spectroscopy is a powerful experimental technique that has been used extensively [1, 2, 6–8]. For example, Ti:Sapphire oscillator and amplifier systems are commercially available, producing pulses with a duration in the tens of femtoseconds and a few mJ of energy per pulse. Femtosecond pulses in the frequency range from UV-vis to mid-IR and THz can be readily generated by various optical processes using nonlinear crystals. Therefore, multiple time-separated coherent laser pulses whose amplitudes and relative phases can be precisely controlled have been used to electronically or vibrationally perturb molecular systems under investigation. These field-matter interactions put the systems into superposition states, where each of them can be described as a linear combination of molecular eigenstates. The non-stationary states evolve over time, and the randomly fluctuating solute-solvent interactions in solution allow the systems to relax to a new thermal equilibrium state. These transitions and relaxations can be monitored with a probe pulse using other field-matter interactions.

Naturally, a variety of ultrafast nonlinear spectroscopic techniques have been used to investigate the structure and dynamics of molecular systems. For instance, in the pump-probe spectroscopy of chromophores in condensed phases, a strong pump pulse coherently excites many molecules, and a time-delayed probe pulse is used to monitor the collective relaxation of the non-equilibrium molecular systems as a function of delay time. Because the probe absorption spectrum is recorded at a given waiting time using dispersive optics and an array detector, the measured signals are time and frequency-resolved pump-probe spectra that are plotted against probe frequency.

To extend pump-probe spectroscopy to two-dimensional (2D) measurement methods, it is necessary to include an additional control variable in the time or frequency domain. Over the past two decades, many attempts have been made to develop 2D electronic, vibrational, and electronic-vibrational hybrid spectroscopic techniques

that can be used to study the congested dynamic information of molecular systems that cannot be extracted from one-dimensional spectra. This involves disentangling the complex nonlinear response functions and susceptibilities of materials or molecules of interest into two-dimensional (excitation and emission) frequency space. A natural extension of widely used 2D spectroscopy is to add more time-delayed pulses or frequency-scanning schemes with one or more phase-stabilized coherent lasers to develop novel coherent multidimensional spectroscopy (CMS) [7, 8].

Of the many possible *N*-dimensional spectroscopic techniques, two-dimensional (2D) optical and/or IR spectroscopy, which can be regarded as an ultrafast optical analog of 2D nuclear magnetic resonance (2D NMR), is one of the most widely used. Including the emissive field-matter interaction that produces the signal electric field under detection, four-wave-mixing (4WM) 2D spectroscopy involves four field-matter interactions, which are separated in time by three time intervals, denoted as τ, T, and t, where the incident pulses are assumed to be Dirac delta function-like. Thus, the measured signal can be expressed as $S(t, T, \tau)$. The 2D spectrum $S(\omega_t, T, \omega_\tau)$, which is obtained from the double Fourier transformation of $S(t, T, \tau)$ with respect to τ and t, provides information on the electronically/vibrationally resonant transitions of molecules by pump fields at waiting time (T) zero and those by a probe field at a later waiting time. By monitoring the 2D spectra at different waiting times, dynamic information on the system can be extracted. Time-dependent diagonal peak intensities are determined by the survival probabilities of the excited states with regard to population and orientation, whereas the time dependence of off-diagonal peak intensities is associated with the conditional probability of finding the state in resonance with a probe field at time T when the initial state at time zero was in resonance with a pump field. Therefore, 2D electronic/vibrational spectroscopy is capable of time-resolving the molecular dynamics of the relaxation of excited states and state-to-state transitions between molecular quantum states.

Two-dimensional electronic spectroscopy (2D ES) is based on the electronic transition of molecular systems of interest induced by their interactions with femtosecond UV or visible pulses [7]. Often, the UV-vis absorption spectra of chromophores in condensed phases are broad and featureless due to ultrafast electronic dephasing and large inhomogeneous line-broadening. Interestingly, photon echo spectroscopy has been shown to be useful for selectively measuring the pure dephasing rate and spectral diffusion. In addition, if chromophores are electronically coupled to produce delocalized exciton states, 2D ES can be used to measure the electronic coupling strength between chromophores, as well as exciton annihilation, migration, and coherence transfer in coupled multi-chromophore systems. One of the most successful uses of 2D ES is in the investigation of photosynthetic light-harvesting complexes and exciton dynamics in semiconductors, where the relaxation, energy transfer, and coherent and incoherent evolution of created single and multiple exciton states have been of great interest.

Two-dimensional infrared (2D IR) spectroscopy utilizing multiple IR pulses has been widely used to analyze the structure and dynamics of molecular systems and to probe the chemical exchange and conformational transition processes of complicated

molecular systems in real time [8]. The IR absorption bandwidth of a given normal mode is typically much narrower than that of a broadband mid-IR pulse (>250 cm^{-1}), so the entire band shape and intensity can be monitored with 2D IR spectroscopy. Because vibrational frequency, intensity, and line shape are strongly affected by the local environment and chemical structure, small IR probes that can be easily incorporated into biomolecules and reactive species are excellent reporters for the structure and dynamics of systems under study [9, 10]. For example, femtosecond IR pulses are used to excite various fundamental vibrational modes of molecules in the wavelength range of 2.5–7 μm (mid-IR range), such as −OH, −NH, −CH, −CD, −CN, −SCN, $-N_3$, and −C=O. Because each individual mid-IR photon has an energy that is almost one order of magnitude smaller than that of UV or visible photons, photochemical damage is not a serious issue even though multiple IR excitation-dissipation processes cause an increase in local temperature. To broaden the probe spectral window, a plasma-generated continuum IR pulse has been used to obtain a 2D IR spectrum that covers the entire mid-IR frequency range.

For coupled multi-oscillator systems, vibrational frequency and dynamics are strongly affected by vibrational couplings between local modes through space via intermolecular interactions and/or through bonds via anharmonicities on the multidimensional potential energy surface. However, because the linear vibrational spectrum is mainly determined by harmonic properties such as fundamental transition frequency and the 0–1 transition dipole moment, it is difficult to quantitatively extract weak features like the vibrational coupling constants and potential anharmonic coefficients of coupled oscillators from the linear vibrational spectra. In contrast, coherent multidimensional vibrational spectroscopic methods have been found to be exceptionally useful for estimating vibrational coupling constants by analyzing cross peaks in 2D IR spectra [7, 8]. The changes in the line shapes and intensities of the cross peaks provide crucial information on structural dynamics involving time-dependent changes in the spatial proximity and relative orientation of vibrational chromophores.

Although 2D IR spectroscopy that employs three incident IR laser pulses is one of the most widely used forms of coherent multidimensional vibrational spectroscopy, variations of this method have also been developed for specific purposes. Examples include surface-specific 2D sum-frequency-generation spectroscopy, 2D Raman and terahertz spectroscopy, and 2D IR-IR-visible spectroscopy. (See the other chapters in this book for more details on these.)

In parallel with the advances in experimental techniques, extensive theoretical and computational research on coherent 2D electronic/vibrational spectroscopy has been carried out over the years. Theory and computation can provide valuable insights into the microscopic origin of 2D spectroscopic features, aid in the interpretation of experimental spectra, predict spectra for new systems, and, in some cases, even suggest potentially useful novel nonlinear spectroscopy techniques [11]. Two-dimensional spectroscopic observables are completely determined by the nonlinear response functions of a system. This response function theory provides a framework for the description of the 2D spectroscopy in general, and explicit expressions are available for a number of important model systems [6]. In accordance with the theory, the molecular response to multiple incident light pulses can be decomposed into quan-

tum transition pathways with different time evolution patterns. In 2D spectroscopy, these nonlinear electronic/vibrational transition pathways can be selectively measured, thus microscopic information on the system itself and the influence of the environment can be extracted [7]. For more realistic systems composed of multiple chromophores, the Frenkel exciton model provides an adequate description. The nonlinear response functions derived from this model reflect the delocalization of quantum states due to inter-chromophore couplings, i.e., resonance effects, and the fluctuation in transition frequencies due to chromophore-solvent interactions, i.e., dephasing and rephasing phenomena. The individual components of these nonlinear response functions can be calculated separately using electronic structure calculation methods and molecular dynamics (MD) simulation methods. The former approaches provide information on the transition energies, electronic couplings, and involved transition dipole strengths, whereas the latter approaches are useful for taking into account solute-solvent interaction-induced dephasing and line-broadening effects. An alternative approach is also available for numerically simulating 2D vibrational spectra of complex systems, which is based on the classical limit of the nonlinear vibrational response function and utilizes MD simulations with hybrid quantum mechanical/molecular mechanical (QM/MM) force fields.

In this chapter, a brief historical account of coherent 2D spectroscopy will be presented in Sect. 2. Following this, a general theoretical framework and numerical calculation methods for coherent 2D spectroscopy will be presented and discussed in Sect. 3. Critical experimental techniques that have been developed over the past decade will then be briefly discussed in Sect. 4. Finally, Sect. 5 will summarize the various perspectives on coherent multidimensional spectroscopy experimentation and theory and offer concluding remarks.

1.2 A Brief Account of the Early Developments in Coherent Two-Dimensional Spectroscopy

Coherent 2D spectroscopy has rapidly developed over the past two decades, emerging as one of the most widely used nonlinear spectroscopic techniques. Older reports alluded to the possibility of using multiple laser pulses to realize coherent 2D optical spectroscopy. However, the experimental feasibility of this idea was only demonstrated after lasers that were capable of generating ultrashort pulses had been developed. Today, two of the most popular techniques are 2D electronic spectroscopy and 2D IR spectroscopy. They are an extension of three-pulse stimulated photon echoes, where three time-delayed pulses are used to create third-order material polarization in the sample, which then acts as a radiation source. Weiner, De Silvestri, and Ippen experimentally demonstrated three-pulse scattering spectroscopy [12], which was later found to be of use for analyzing chromophore-solvent dynamics in condensed phases. In addition, a few interesting theoretical studies on the principles underlying

photon echo phenomena arising from chromophores with a heterogeneous distribution of transition frequencies have been reported.

Before the development of spectral interferometric detection, 4WM spectroscopy experiments were performed by measuring the generated third-order (in electric fields) signal field intensity $|\mathbf{E}_s(\mathbf{r}, t)|^2$, i.e., homodyne detection. Because the phase information of the signal field is lost in this case, it was not possible to obtain the complex 2D electronic response from optical chromophores in condensed phases. However, the inhomogeneous distribution of the transition frequencies of chromophores in solution and its time-dependent change could be successfully investigated using photon echo peak shift (PEPS) measurements. As shown by Cho and Fleming, the PEPS signal with respect to waiting time T is directly related to the transition frequency-frequency correlation function and spectral diffusion process [5]. The Fleming research group showed that PEPS measurement is an exceptionally useful method for studying ultrafast chromophore-solvent dynamics. As an extension of this optical photon echo technique into the IR frequency domain, vibrational photon echo measurements, which are an IR analog of the optical photon echo, were experimentally demonstrated by the Fayer research group in 1993, who used IR pulses from a free-electron laser [13].

Theoretically, Tanimura and Mukamel in 1993 proposed fifth-order 2D Raman scattering spectroscopy, which allows the analysis of intermolecular vibrational rephasing phenomena from Raman-active molecules whose intermolecular vibrational frequencies are inhomogeneously distributed in liquids [14]. The fifth-order Raman response function, which represents the nonlinear correlation of polarizabilities at different times, depends on two time variables, which is why it was referred to as the 2D time-domain Raman response function. Later, Tominaga, Yoshihara, Fleming, Tokmakoff, Blank, Dwayne-Miller and many others attempted to measure fifth-order Raman signals from neat liquids such as CS_2. However, undesired cascading contributions to the detected signal (i.e., two third-order rather than truly fifth-order) are often dominant, as shown by Blank, Fleming, and coworkers [15, 16]. Because the direct fifth-order Raman signal becomes large and dominant as the field frequencies approach electronic transition frequencies, the resonant version of fifth-order Raman scattering spectroscopy theoretically proposed by Cho in 1998 could be of use in investigating 2D Raman responses from chromophores in condensed phases [17].

Independently, Cho and Fleming in 1994 theoretically demonstrated that fifth-order three-pulse scattering spectroscopy probing correlations of electronic transition frequencies at two different times could be useful when investigating the inhomogeneous line-broadening effect on the optical spectrum of chromophores in condensed phases [18]. In contrast to traditional integrated intensity photon echo spectroscopy, which probes one electronic coherence evolution, fifth-order three-pulse scattering spectroscopy can be considered fifth-order 2D electronic spectroscopy that is capable of measuring time-dependent changes in optical transition frequencies. However, due to limitations in controlling the center frequencies of multiple pulses, only degenerate fifth-order three-pulse scattering experiments were performed.

After array detectors in the visible and IR frequency domains became available, heterodyne-detected 2D spectroscopic techniques were developed. Once a generated nonlinear signal electric field is allowed to interfere with an added local oscillator field, a spectral interferogram can be obtained using a monochromator (e.g., a grating) and an array detector. Spectral interferometric detection has been particularly useful in developing coherent multidimensional spectroscopy (CMS) because it enables the simultaneous characterization of the phase and amplitude of a generated 4WM signal electric field. Jonas and coworkers in 1998 showed that the spectral interferometric detection of three-pulse scattering or a photon echo signal field is experimentally feasible [19]. In 2D IR spectroscopy, Hamm, Lim, and Hochstrasser used a frequency-tunable IR pump-probe spectroscopic method to obtain the reconstructed 2D amide I IR spectra of polypeptides in solution, where amide I vibration is mainly carbonyl stretch mode of an amide group or a peptide bond [20]. In their study, a narrowband IR pump pulse was used to selectively excite resonant oscillators, and the transient probe absorption spectrum was then measured. Scanning the pump frequency, they obtained a series of time- and probe frequency-resolved pump-probe spectra, which were used to construct time-resolved 2D IR spectra. Later, 2D IR photon echo experiments were performed by Zanni, Hochstrasser, and coworkers and Tokmakoff and coworkers to determine the solution structure of small oligopeptides.

In parallel with experimental studies using 2D IR spectroscopy, there have been efforts to numerically simulate the 2D vibrational spectra of a variety of molecular systems. Two-dimensional vibrational spectroscopy can be used to achieve both ultrafast time resolution and high spectral resolution. Therefore, this method provides rich information on molecular systems, such as homogeneous (anti-diagonal) and inhomogeneous (diagonal) spectral broadening, vibrational anharmonicity, spectral diffusion, vibrational mode-mode coupling strength, and their time-dependent changes [7, 8].

Although the 2D IR and 2D ES methods, which are based on heterodyne-detected three-pulse scattering geometry, have been found to be useful, the center frequencies of the pulses used were the same, i.e., degenerate. To study a wider range of vibrational dynamics and intramolecular vibrational relaxations, two-color 2D vibrational spectroscopic techniques have since been developed. Theoretically, Park and Cho proposed a new class of non-degenerate 4WM 2D vibrational spectroscopy that requires both IR and visible pulses [21]. Two IR pulses could be used to create two consecutive vibrational coherences or super-position state evolutions. An incident visible pulse, whose frequency is electronically non-resonant, puts the molecular system into a state of electronic coherence. This third-order polarization radiates an IR-IR-vis sum or a difference frequency field that provides information on the 2D vibrational responses of electronically ground-state molecules. The Wright research group experimentally demonstrated that an IR-IR-vis difference frequency generation scheme can be used to measure the cross peak between the C-C stretch and C-N stretch of acetonitrile, which results from both the mechanical and electronic anharmonic couplings between the two modes [22].

In the present section, a brief account of the early developments in coherent 2D spectroscopy in the 1990s was presented. It should be emphasized that this account

is far from complete, so readers are strongly recommended to read the representative review articles cited in this chapter and other chapters in this book.

1.3 Theoretical Description and Numerical Simulation Methods

In general, spectroscopic measurement involves both excitation and detection. In 2D spectroscopy, the molecular system of interest interacts with three coherent laser pulses and the generated signal field is then detected and presented with respect to the excitation and detection frequencies [7]. In each of the four field-matter interaction events, a quantum transition takes place between the eigenstates of the system. Depending on both the configuration of the optical laser pulses, including the frequency, direction of propagation (i.e., wave vector), and beam polarization, and the detection method employed, different quantum transition pathways can occasionally be selectively measured.

One of the most widely used methods for theoretically describing various nonlinear spectroscopic observables is to use the formalism of the nonlinear response function [6], which naturally emerges from the application of quantum mechanical time-dependent perturbation theory to the molecular system in the presence of perturbative light-matter interactions during the preparation step. In this section, I sketch the theoretical analysis in a stepwise manner and present key results that are particularly relevant to coherent 2D spectroscopy, though the formal theory can easily be generalized to describe other CMS measurement methods.

1.3.1 Third-Order Response Functions

In coherent 2D spectroscopy, the molecular system interacts with the incident electric field and, in the electric dipole approximation, the interaction Hamiltonian can be written as

$$H_{\text{int}}(\mathbf{r}, t) = -\hat{\boldsymbol{\mu}} \cdot \mathbf{E}(\mathbf{r}, t), \tag{1.1}$$

where $\hat{\boldsymbol{\mu}}$ is the electric dipole operator and $\mathbf{E}(\mathbf{r}, t)$ is the superposition of the three X-ray, UV-visible, IR, or THz pulses (depending on the specific experiment), which are generally denoted as $\mathbf{E}_1$, $\mathbf{E}_2$, and $\mathbf{E}_3$. The approximate Hamiltonian of the composite system is the sum of the molecular or material Hamiltonian H_0 in the absence of radiation and the field-matter interaction Hamiltonian $H_{\text{int}}(\mathbf{r}, \text{t})$. The system evolves over time according to the quantum Liouville equation for the density operator $\rho(\mathbf{r}, t)$ of the system, where $\rho(\mathbf{r}, t)$ is the state vector in the Liouville space, as follows:

$$\frac{\partial \rho(\mathbf{r},t)}{\partial t} = -\frac{i}{\hbar}[H_0 + H_{\text{int}}(\mathbf{r},t), \rho(\mathbf{r},t)] \tag{1.2}$$

The solution to this equation provides information about any physical observable $A(\mathbf{r}, t)$ of the system through the expectation value of $\text{Tr}[\hat{A}\rho(\mathbf{r}, t)]$. Here, Tr denotes the trace of the matrix and $\hat{A}$ is the operator associated with the observable A. Diagonal element ρ_{aa} of the density matrix represents the probability that the system is in state a, or the *population* of the system in state a. Off-diagonal element ρ_{ab} of the density matrix, which is related to the *coherence* or distinguishability of the two quantum states, gives rise to the temporal oscillation of the aforementioned probability with the frequency $\omega \approx \omega_{ab} = (E_a - E_b)/\hbar$ determined by the energy difference of the two eigenstates a and b.

Treating $H_{\text{int}}(\mathbf{r}, t)$ as a perturbation to the system described by the molecular Hamiltonian H_0, (1.2) can be solved by applying time-dependent perturbation theory. The solution is expressed as a power series expansion of $\rho(\mathbf{r}, t)$ with respect to the perturbation energy, the zeroth-order term of which is the equilibrium density operator for the unperturbed system $\rho^{(0)}(t) = \rho_{eq}$. The nth-order term $\rho^{(n)}(\mathbf{r}, t)$ contains n factors of $H_{\text{int}}(\mathbf{r}, t)$ and is given by [6].

$$\rho^{(n)}(\mathbf{r},t) = \left(-\frac{i}{\hbar}\right)^n \int_{t_0}^{t} \mathrm{d}\tau_n \int_{t_0}^{\tau_n} \mathrm{d}\tau_{n-1} \cdots \int_{t_0}^{\tau_2} \mathrm{d}\tau_1 G_0(t-\tau_n) L_{\text{int}}(\tau_n)$$
$$G_0(\tau_n - \tau_{n-1}) L_{\text{int}}(\tau_{n-1}) \cdots G_0(\tau_2 - \tau_1) L_{\text{int}}(\tau_1) G_0(\tau_1 - t_0)\rho(t_0) \tag{1.3}$$

where $G_0(t) = \exp(-iL_0 t/\hbar)$ is the time-evolution operator in the absence of radiation. The Liouville operators are defined as $L_a A = [H_a, A]$ for $a = 0$ or int. According to (1.3), the system initially defined by $\rho(t_0)$ evolves freely without perturbation for $\tau_1 - t_0$ as given by $G_0(\tau_1 - t_0)$ and then interacts with the radiation at time τ_1 as given by $L_{\text{int}}(\tau_1)$. This propagation-interaction sequence is repeated n times until the final field-matter interaction at τ_n, as given by $L_{\text{int}}(\tau_n)$. Finally, the system evolves freely until observation time t for $t - \tau_n$ according to $G_0(t - \tau_n)$. The multiple integrals over $\tau_1, \ldots, \tau_n$ account for all possible interaction times under the time ordering condition $t_0 \le \tau_1 \le \ldots \le \tau_n \le t$.

Each term of the power series expansion of $\rho(\mathbf{r}, t)$ in (1.3) gives rise to the corresponding nth-order polarization $\mathbf{P}^{(n)}(\mathbf{r}, t) = \text{Tr}\left[\hat{\boldsymbol{\mu}}\rho^{(n)}(\mathbf{r}, t)\right]$ in the system as follows:

$$\mathbf{P}^{(n)}(\mathbf{r},t) = \int_0^{\infty} \mathrm{d}t_n \ldots \int_0^{\infty} \mathrm{d}t_1 \mathbf{R}^{(n)}(t_n, \ldots, t_1) \vdots \mathbf{E}(\mathbf{r}, t - t_n) \ldots \mathbf{E}(\mathbf{r}, t - t_n \ldots - t_1) .. \tag{1.4}$$

The nth-order response function is formally given by

$$\mathbf{R}^{(n)}(t_n, \ldots, t_1) = \left(\frac{i}{\hbar}\right)^n \theta(t_n) \cdots \theta(t_1) < \boldsymbol{\mu}(t_n + \cdots + t_1)[\boldsymbol{\mu}(t_{n-1} + \cdots + t_1), [\cdots [\boldsymbol{\mu}(t_1), [\boldsymbol{\mu}(0), \rho_{\text{eq}}]] \cdots]] > \tag{1.5}$$

where $\hat{\boldsymbol{\mu}}(t) = \exp(i H_0 t / \hbar)\hat{\boldsymbol{\mu}} \exp(-i H_0 t / \hbar)$ is the dipole operator in the interaction picture and the angular bracket in (1.5) denotes the trace of a matrix. The linear response can be obtained by setting $n = 1$ in (1.5). The 2D spectroscopy signal is determined by the third-order polarization $\mathbf{P}^{(3)}(\mathbf{r}, t)$ and the third-order response function $\mathbf{R}^{(3)}(t_3, t_2, t_1)$ [23]. Here, the latter is a fourth-rank tensor. Note that the time variables t_1, …, t_{n-1} in (1.4) and (1.5) are the time intervals between consecutive field-matter interactions related to τ_1, …, τ_n in (1.3) as $t_m = \tau_{m+1} - \tau_m$ ($1 \leq m \leq n - 1$), while $t_n = t - \tau_n$ is the time elapsed after the last field-matter interaction. Therefore, t_1, …, t_n are all positive and the response function must vanish if any of its time arguments t_m ($m = 1 \ldots n$) are negative in accordance with the causality principle, as imposed by the Heaviside step function s $\theta(t)$ in (1.5). In addition, $\mathbf{R}^{(n)}$ is a real function because $\mathbf{P}^{(n)}(\mathbf{r}, t)$ and $\mathbf{E}(\mathbf{r}, t)$ in (1.4) are both real quantities, though individual terms comprising $\mathbf{R}^{(n)}$ are complex in general and represent different quantum transition pathways.

The signal electric field $\mathrm{E}_S^{(n)}(\mathbf{r}, t)$ detected in nth-order nonlinear spectroscopy is obtained by solving Maxwell's equation where the material nonlinear polarization $\mathbf{P}^{(n)}(\mathbf{r}, t)$ acts as a radiation source. After making the simplifying assumptions that (i) the generated signal field is only weakly absorbed by the medium, (ii) the temporal envelopes of the polarization and signal fields vary slowly in time compared to the optical period, (iii) the signal field envelope spatially varies slowly compared to its wavelength, and (iv) the frequency dispersion of the medium refractive index is weak, the approximate solution can be obtained as [6, 7].

$$\mathbf{E}_S^{(n)}(t) \propto \frac{i\omega_s}{n(\omega_s)} \mathbf{P}_S^{(n)}(t). \tag{1.6}$$

Here, $n(\omega)$ is the refractive index of the medium and $\mathbf{P}_S^{(n)}(t)$ is the polarization component propagating with wave vector $\mathbf{k}_S$ and frequency ω_S, which represent one of the combinations $\pm\mathbf{k}_1 \pm \mathbf{k}_2 \cdots \pm \mathbf{k}_n$ and $\pm\omega_1 \pm \omega_2 \cdots \pm \omega_n$, respectively. These components make up the total nth-order polarization as

$$\mathbf{P}^{(n)}(\mathbf{r}, t) = \sum_l \mathbf{P}_l^{(n)}(t) \exp(i\mathbf{k}_l \cdot \mathbf{r} - i\omega_l t). \tag{1.7}$$

By appropriately changing the location of the detector, individual components of the polarization with different wave vectors can be selectively measured.

1.3.2 Nonlinear Response Function Components

Two-dimensional vibrational spectroscopy usually induces transitions up to the second vibrational excited state. Therefore, a three-level system with eigenstates $|g\rangle$, $|e\rangle$, and $|f\rangle$ is a useful model for the nonlinear response function relevant to coherent 2D spectroscopy. Because the third-order response function vanishes for a harmonic oscillator (i.e., a molecular vibration or an electronic Lorentz oscillator), the model system must represent an anharmonic oscillator where the fundamental transition frequency ω_{eg} differs from ω_{fe}.

The evaluation of a realistic response function critically depends on an accurate description of the system-bath interaction, which is essentially responsible for dephasing, relaxation, spectral diffusion, and population and coherence transfers. To highlight the structure of the response function, I consider a simple model where a single three-level chromophore interacts with the environment according to the following Hamiltonian:

$$H_0 = \sum_{m=g,e,f} \left[\hbar\omega_m + V_m(\mathbf{q}) + H_{\mathrm{B}}(\mathbf{q})\right]|m\rangle\langle m|, \tag{1.8}$$

where $\hbar\omega_m$ is the energy of the mth state in the absence of a bath. $V_m(\mathbf{q})$ is the chromophore-bath interaction energy of the state, where $\mathbf{q}$ represents the bath coordinates. In (1.8), $H_B(\mathbf{q})$ is the energy of the bath. The off-diagonal elements of the chromophore-bath interaction are assumed to be negligible for the sake of simplicity. Using this Hamiltonian, the three nested commutators in the response function in (1.5) can be expanded as the sum of eight terms:

$$\mathbf{R}^{(3)}(t_3, t_2, t_1) = \left(\frac{i}{\hbar}\right)^3 \theta(t_3)\theta(t_2)\theta(t_1) \sum_{i=1}^{4} [\mathbf{R}_i(t_3, t_2, t_1) - (\text{c.c.})], \tag{1.9}$$

where c.c. denotes the complex conjugate and the fourth-rank tensor components $\mathbf{R}_i(t_3, t_2, t_1)$ are given by

$$\begin{aligned}
\mathbf{R}_1(t_3, t_2, t_1) &= \boldsymbol{\mu}_{ge}\boldsymbol{\mu}_{eg}\boldsymbol{\mu}_{ge}\boldsymbol{\mu}_{eg} \exp\left[i(-\bar{\omega}_{eg}t_3 - \bar{\omega}_{eg}t_1)\right] F_1^{gege}(t_3, t_2, t_1) \\
&\quad + \boldsymbol{\mu}_{ge}\boldsymbol{\mu}_{ef}\boldsymbol{\mu}_{fe}\boldsymbol{\mu}_{eg} \exp\left[i(\bar{\omega}_{fe}t_3 - \bar{\omega}_{eg}t_1)\right] F_1^{gefe}(t_3, t_2, t_1) \\
\mathbf{R}_2(t_3, t_2, t_1) &= \boldsymbol{\mu}_{ge}\boldsymbol{\mu}_{eg}\boldsymbol{\mu}_{ge}\boldsymbol{\mu}_{eg} \exp\left[i(-\bar{\omega}_{eg}t_3 + \bar{\omega}_{eg}t_1)\right] F_2^{gege}(t_3, t_2, t_1) \\
&\quad + \boldsymbol{\mu}_{ge}\boldsymbol{\mu}_{ef}\boldsymbol{\mu}_{fe}\boldsymbol{\mu}_{eg} \exp\left[i(\bar{\omega}_{fe}t_3 + \bar{\omega}_{eg}t_1)\right] F_2^{gefe}(t_3, t_2, t_1) \\
\mathbf{R}_3(t_3, t_2, t_1) &= \boldsymbol{\mu}_{ge}\boldsymbol{\mu}_{eg}\boldsymbol{\mu}_{ge}\boldsymbol{\mu}_{eg} \exp\left[i(-\bar{\omega}_{eg}t_3 + \bar{\omega}_{eg}t_1)\right] F_3^{gege}(t_3, t_2, t_1) \\
&\quad + \boldsymbol{\mu}_{ge}\boldsymbol{\mu}_{ef}\boldsymbol{\mu}_{fe}\boldsymbol{\mu}_{eg} \exp\left[i(\bar{\omega}_{fe}t_3 + \bar{\omega}_{fg}t_2 + \bar{\omega}_{eg}t_1)\right] F_3^{gefe}(t_3, t_2, t_1) \\
\mathbf{R}_4(t_3, t_2, t_1) &= \boldsymbol{\mu}_{ge}\boldsymbol{\mu}_{eg}\boldsymbol{\mu}_{ge}\boldsymbol{\mu}_{eg} \exp\left[i(-\bar{\omega}_{eg}t_3 - \bar{\omega}_{eg}t_1)\right] F_4^{gege}(t_3, t_2, t_1) \\
&\quad + \boldsymbol{\mu}_{ge}\boldsymbol{\mu}_{ef}\boldsymbol{\mu}_{fe}\boldsymbol{\mu}_{eg} \exp\left[i(-\bar{\omega}_{eg}t_3 - \bar{\omega}_{fg}t_2 - \bar{\omega}_{eg}t_1)\right] F_4^{gefe}(t_3, t_2, t_1)
\end{aligned} \tag{1.10}$$

Here, it is assumed that the system is initially in the ground state g. In (1.10), $\boldsymbol{\mu}_{ab}$ is the transition dipole moment between states a and b, which is often assumed to be independent of the bath coordinates (i.e., the Condon approximation). In (1.10), the energy gap averaged over bath degrees of freedom is defined as $\hbar\bar{\omega}_{ab} = \hbar(\omega_a - \omega_b) + < V_a(\mathbf{q}) - V_b(\mathbf{q}) >_B$. $F_n^{gabc}(t_3, t_2, t_1)$ is the line shape function expressed in terms of the time-ordered exponentials of the fluctuations in the system-bath interactions, $U_m(\mathbf{q}) = V_m(\mathbf{q}) - < V_m(\mathbf{q}) >_B$. The total response function is composed of multiple quantum transition pathways represented by individual $\mathbf{R}_i$, each of which is the product of three factors determining the transition strength (i.e., the products of transition moments), the transition frequency (i.e., coherence oscillation), and the line shape function ($F_{1\text{–}4}$). To facilitate the computation of $F_n^{gabc}(t_3, t_2, t_1)$, the time-ordered exponential operators can be approximated by normal exponential functions containing the difference potential energies $U_{ab}(\mathbf{q}) = U_a(\mathbf{q}) - U_b(\mathbf{q})$. Alternatively, the nonlinear line shape function can be approximately described by invoking second-order cumulant expansion technique, which becomes exact when the fluctuation of the transition frequency obeys Gaussian statistics [7, 11]. Because detailed theoretical expressions of line shape functions can be found in other review articles and books [6–8, 23], I will not present them here.

The general formulation for multi-level systems has been reported and provides an excellent framework for interpreting experimental results and for understanding the effect of chromophore-solvent interaction dynamics on the diagonal and off-diagonal peak shapes in 2D spectra. For instance, a distinction between homogenous and inhomogeneous line broadening can be achieved by analyzing the extent of the diagonal elongation of a given diagonal peak. Furthermore, time-dependent 2D peak shape analysis of both diagonal and cross peaks provides critical information on the timescale of solvent dynamics affecting transition frequency fluctuations and on the correlation or anticorrelation of the solvent-induced frequency fluctuations of the two associated states, respectively.

1.3.3 Classical Approximation to 2D Vibrational Response Functions

Although the nonlinear response function formalism is exact, fully quantum mechanical simulations of 2D peak shape functions remain difficult and impractical for systems with many degrees of freedom. Thus, applicable and efficient methods based on the classical mechanical description of molecular vibrations have been developed and used to calculate 2D vibrational response functions for coupled oscillator systems [24].

One of these is to use trajectories of equilibrium MD simulations with classical approximations of the vibrational response functions. First, the classical mechanical response functions are derived using the relationship between the quantum mechanical commutator and the Poisson bracket, i.e., $(i\hbar)^{-1}[X, Y] = \{X, Y\}_{\mathrm{PB}}$,

where X and Y are physical variables and the Poisson bracket is expressed as $\{X, Y\}_{\mathrm{PB}} = (\partial X/\partial \mathbf{q})(\partial Y/\partial \mathbf{p}) - (\partial X/\partial \mathbf{p})(\partial Y/\partial \mathbf{q})$. For instance, the classical linear response function of a physical quantity A to a perturbation B is given as $(1/k_B T)\langle B'(0)A(t)\rangle$, where B' is the time derivative of B. The above relationship between the quantum mechanical commutator and the classical mechanical Poisson bracket can be applied to derive the classical nonlinear response function [25]. For 4WM-based 2D vibrational spectroscopy, the corresponding classical third-order response function that is related to 2D IR spectroscopy is expressed as

$$\begin{aligned} R^{(3)}(t_1, t_2, t_3) &= \beta\langle\{\{\mu(t_1 + t_2 + t_3), \mu(t_1 + t_2)\}_{\mathrm{PB}}, \mu(t_1)\}_{\mathrm{PB}}\mu'(0)\rangle \\ &= -\beta\langle\{\mu(t_1 + t_2 + t_3), \mu(t_1 + t_2)\}_{\mathrm{PB}}(\beta\mu'(t_1)\mu'(0) - \{\mu(t_1), \mu'(0)\}_{\mathrm{PB}})\rangle \end{aligned} \tag{1.11}$$

Here, the Poisson brackets of the physical variables at two different times, e.g., $\{\mu(t), \mu(t')\}_{\mathrm{PB}}$, are calculated using equilibrium MD trajectories. This involves the calculation of the stability matrix representing the transformation of the phase space along the trajectory. Using this method, Jeon and Cho investigated 2D IR spectra, employing a quantum mechanical/molecular mechanical (QM/MM) simulation method for an accurate description of the intramolecular vibrations of the solute molecules (deuterated *N*-methylacetamide [d-NMA] and HOD) [24]. They were able to calculate the 2D IR spectra of the OD stretch of HOD molecules in water and demonstrated that various 2D IR spectroscopic features can be successfully reproduced by this classical approach to calculate the 2D IR spectra.

However, because this approach requires stability matrix calculations, it is computationally expensive and suffers from numerical instability, which makes it difficult to calculate nonlinear response functions accurately. Another approach that has been developed to overcome this problem utilizes the simulation of non-equilibrium MD trajectories. In this case, nonlinear vibrational response functions are evaluated by considering external field-matter interactions directly, in a similar way to real experiments performed with pulsed electromagnetic fields. In other words, instead of using equilibrium MD trajectories, the nonlinear vibrational responses can be calculated by directly taking into consideration radiation-molecule interaction by means of carrying out a number of independent non-equilibrium MD simulations. For instance, the linear response function can be approximately calculated using [26].

$$R^{(1)}(t) = \lim_{\varepsilon \to 0} \frac{1}{\varepsilon}\{\langle A(t)\rangle_{B(0)} - \langle A\rangle\}, \tag{1.12}$$

where ε is the perturbation parameter. Here, the first term is the expectation value of $A(t)$ on the perturbed trajectory determined by the Hamiltonian $H_0 - \varepsilon B\delta(t)$, where B is, for example, $\mu(\mathbf{r}) \cdot \mathbf{E}(\mathbf{r}, t)$. The second term $\langle A\rangle$ is the expectation value of A on the trajectory in the absence of perturbation. In this non-equilibrium finite-field method, the third-order response function for 2D vibrational spectroscopy is expressed as

$$R^{(3)}(t_1,t_2,t_3)=\lim_{\varepsilon\to 0}\frac{1}{\varepsilon^3}\big\{\langle\mu(t_1+t_2+t_3)\rangle_{E(0),E(t_1),E(t_1+t_2)}-\langle\mu(t_1+t_2+t_3)\rangle_{E(0),E(t_1)}$$
$$-\langle\mu(t_1+t_2+t_3)\rangle_{E(0),E(t_1+t_2)}-\langle\mu(t_1+t_2+t_3)\rangle_{E(t_1),E(t_1+t_2)}$$
$$+\langle\mu(t_1+t_2+t_3)\rangle_{E(0)}+\langle\mu(t_1+t_2+t_3)\rangle_{E(t_1)}$$
$$+\langle\mu(t_1+t_2+t_3)\rangle_{E(t_1+t_2)}-\langle\mu(t_1+t_2+t_3)\rangle\big\}. \tag{1.13}$$

Jansen and coworkers have further developed an efficient method using positive and negative electric fields [27].

Although non-equilibrium MD simulation methods do not require the direct calculation of a cumbersome stability matrix, it is still expensive computationally because a number of non-equilibrium trajectories need to be obtained to accurately calculate the nonlinear vibrational response functions. To save computational time, the Tanimura research group developed an efficient method that combines the equilibrium MD simulation and non-equilibrium finite perturbation methods [28].

The third-order vibrational response functions obtained from equilibrium and/or non-equilibrium MD simulations in principle allow any third-order vibrational spectra to be predicted. However, despite these recent developments in computational spectroscopy, it is still computationally demanding to calculate the third-order response functions of complicated systems in solution. Furthermore, the fundamental validity of the classical approximations used previously has been re-investigated by several groups and it has been found that classical nonlinear response functions are not stable for integrable systems and systems without dissipation. Sakurai and Tanimura examined the quantum effects on the IR and 2D IR spectra of a Morse oscillator interacting with a collection of harmonic bath oscillators [29]. They showed that the classical 2D IR spectra represent a good approximation of the quantum 2D IR spectra when the system is largely modulated by the bath via a strong system-bath coupling or when the bath modulation is fast even in a weak system-bath coupling regime. Recently, this issue was investigated again by Reppert and Brumer, who showed that the classical 2D IR spectra of a Morse oscillator mimicking amide I mode can reproduce most of the qualitative features of the quantum 2D IR spectra very well [30]. From these studies, it is clear that the validity of the classical approximation when calculating linear and nonlinear IR spectra depends on system-bath coupling.

Although classical nonlinear spectral simulations have been shown to reproduce spectra derived via quantum mechanical calculations reasonably well when system vibrations are largely modulated by the bath, there remain intrinsic differences with regards to the quantum mechanical description of vibrational transitions. In fact, real vibrational spectra are described as transitions from one vibrational level to another in quantum mechanics, whereas they are obtained from the fluctuation of dipole moments in classical mechanics. Furthermore, the anharmonic frequency shift observed in 2D IR spectra is determined by information about the entire potential energy function. In contrast, no discrete vibrational quantum states are considered in any approaches based on classical mechanics. Trajectories in a classical mechanical regime are determined by local information on coordinates and momenta. Consequently, the anharmonic shift corresponding to the frequency difference between

the positive and negative peaks in classical 2D IR spectra arises from the difference between the curvatures of the trajectories perturbed by one and multiple electric fields. Therefore, the anharmonic shifts found in the 2D IR spectra obtained with classical approaches are small compared to those in the experimental or quantum mechanically calculated 2D IR spectra [25].

The other important quantity determining each nonlinear vibrational response function component is the transition dipole moment. In quantum mechanics, spectral intensity is related to the transition dipole moments between vibrational levels, whereas classical mechanically calculated spectra are determined by the dipole moments induced by vibrational and conformational changes. Therefore, it is absolutely crucial to model highly accurate potential function and transition (dipole, polarizability, etc.) moments to correctly simulate nonlinear vibrational response functions and corresponding spectra. Of course, fully quantum mechanical MD simulation methods exist, but the calculation of quantum mechanical nonlinear response functions that include all of the effects of the surrounding thermal bath remain challenging and impractical, despite the dramatic advances in computer technology and algorithms. Therefore, other semiclassical approach es like semiclassical initial value representation, centroid MD, and ring-polymer MD, which have been used to calculate the linear spectroscopic properties of molecules in condensed phases, should be employed in the calculation of various coherent 2D vibrational spectra in the near future.

1.3.4 Numerical Integration of the Vibrational Schrödinger Equation

Instead of considering the fluctuation in system-bath interaction-induced frequency and the change in transition dipoles over time using MD simulations, the fluctuating vibrational frequency and the transition dipole of the oscillator of interest in condensed phases can be described using theoretical models. The task remaining is then to solve the time-dependent vibrational Schrödinger equation. This approach has been referred to as the Numerical Integration of the Schrödinger Equation (NISE) theory [31]. In this case, each oscillator is treated as a weakly anharmonic oscillator with three vibrational levels that are coupled to bath degrees of freedom. The latter is taken into account through their time-dependent modulation of the parameters of the quantum oscillator, such as the harmonic frequency and transition dipole. For coupled multi-oscillator systems interacting with external electric fields, the corresponding time-dependent Hamiltonian can be written as

$$H(t) = \sum_{n}^{N} \hbar\omega_n(t) a_n^{\dagger} a_n + \sum_{n,m}^{N} J_{nm}(t) a_n^{\dagger} a_m - \frac{1}{2} \sum_{n}^{N} \Delta_n(t) a_n^{\dagger} a_n^{\dagger} a_n a_n$$

$$+\sum_{n}^{N}\mathbf{E}(t)\cdot\boldsymbol{\mu}_n(t)\left(a_n^{\dagger}+a_n\right)+\sum_{n}^{N}\mathbf{E}(t)\cdot\boldsymbol{\alpha}_n(t)\cdot\mathbf{E}(t)\left(a_n^{\dagger}+a_n\right) \quad (1.14)$$

Here, $a_n^{\dagger}$ and a_n are the creation and annihilation operators of the nth oscillator considered quantum mechanically. The individual local modes are characterized by their frequency $\omega_n(t)$, transition dipole $\boldsymbol{\mu}_n(t)$, transition polarizability $\boldsymbol{\alpha}_n(t)$, and anharmonicity $\Delta_n(t)$. Any pair of local modes can be mixed by their mutual couplings $J_{nm}(t)$. In this approach, the time dependence of these parameters strictly arises from the coupling of each individual oscillator with bath degrees of freedom. The last two terms in (1.14) account for the interaction of the oscillating dipoles and molecular polarizabilities with the applied electric field(s) $\mathbf{E}(t)$, respectively, depending on the specific experimental configuration.

Determining the fluctuating frequencies, transition moments, and coupling constants in the above time-dependent Hamiltonian depends on the system under consideration. Once there exist quantitatively reliable models for these parameters, approximate time-evolution operator approaches can be used to calculate the response functions. The key step is to divide the propagation time into sufficiently short time intervals so that the Hamiltonian during these intervals can be considered time-independent. The solution for the time-dependent Schrödinger equation for each short time interval can then be easily obtained. Successive applications of the finite-difference time-evolution operator s for neighboring time-intervals enable the time-dependent vibrational wavefunction of the coupled multi-oscillator systems to be calculated.

The success of this NISE approach relies on the accuracy of the computed parameters needed to construct the time-dependent Schrödinger equation. The vibrational frequency and transition moment of a given oscillator depends on the local environment and is determined by the intermolecular interaction potential and the vibrational anharmonicity of the multidimensional intramolecular vibrational potential. For instance, an early attempt to calculate the solute-solvent interaction-induced shift of vibrational frequency was based on the assumption that the solute-solvent interaction is dictated by electrostatic interactions. The vibrational frequency shift of an oscillator was assumed to be dependent on the solvent electric potential, electric field, or sometimes the electric field gradient on specific sites of the solute molecule. These vibrational frequency mappings have allowed the frequency trajectories of the coupled oscillators to be obtained from equilibrium MD trajectories. However, recently it has been shown that the vibrational solvatochromic frequency shift is determined by not just electrostatic interactions but also dispersive interaction, short-range Pauli repulsion, polarization, and even multipole-multipole interactions [32].

The anharmonicity of a given molecular vibration also depends on its interaction with the solvent molecules. For multi-oscillator systems, the vibrational coupling constant between any pair of local modes should be accurately calculated to describe the delocalized nature of the vibrational modes. One of the most popular models is the transition-dipole coupling model, which is based on the assumption that the two oscillators interact with each other through electric dipole-dipole interactions. So

far, this form of semiempirical mapping has been found to be exceptionally useful, achieving a chemical accuracy within a few wavenumbers, something which cannot be achieved using current classical or even ab initio MD simulation methods.

The quantum-classical methods discussed here have a number of crucial advantages. One of the commonly used methods that incorporates second-order cumulant approximation or another method that requires an assumption that the coupled bath degrees of freedom are harmonic oscillators cannot account for intermolecular interaction-induced effects properly. On the other hand, the quantum-classical methods take them correctly. Nevertheless, the quantum-classical methods still have clear limitations. The time-dependent Hamiltonian for NISE does not allow for the relaxations between the different excitation manifolds. Furthermore, while these quantum-classical methods are able to account for the effect that the bath exerts on the system, the feedback of the system to the bath when in an excited state is unable to be considered. As a consequence, the method cannot reproduce the correct thermalization in quantum systems, which results in artifacts at low temperatures. Another inherent difficulty of NISE is that the quantum mechanical oscillators need to be well defined and localized. If the nature of an oscillator changes over time (e.g., H-bond vibrations and delocalized intermolecular modes), it is not possible to treat them quantum mechanically.

As mentioned in this section, despite the prolonged efforts to develop approximate theory and computational methods, clear limitations in the accurate calculation of the coherent multidimensional spectra of molecules in condensed phases exist. The next section will now switch focus to experimental techniques and their underlying principles.

1.4 Experimental Methods

1.4.1 Femtosecond Laser Light Sources

Owing to the recent developments in high-power Ti:Sapphire lasers, stable femtosecond pulses in the 750–900 nm wavelength range have been used in a variety of ultrafast spectroscopic studies. Ti:Sapphire laser systems that produce pulses centered at 800 nm of ~50 fs in duration and a pulse energy of a few mJ are commercially available. The 800-nm pulses can then be used to generate femtosecond pulses in the visible (400–700 nm), near IR (1.2–2.4 μm), mid-IR (2.5–7.0 μm), and even THz (10–30 μm) frequency ranges by employing various nonlinear optical techniques with appropriate nonlinear crystals, such as optical parametric amplification (OPA), second and higher harmonic generation, sum frequency generation, and difference frequency generation. Thus, the generated femtosecond pulses have been used to carry out various forms of time-resolved spectroscopic research. More recently, 100-kHz repetition rate lasers and optical frequency comb lasers with repetition frequencies in the hundreds of MHz have been added to the list of radiation sources for

coherent 2D spectroscopy experiments. In fact, two or more phase-stabilized optical frequency comb lasers, with each producing a train of phase-stabilized pulses with well-defined and constant repetition and carrier-envelop-offset frequencies, can be used to construct double- and multiple-comb spectrometers. A review article written by Kim et al. will be of interest for understanding state-of-the-art theories and experiments regarding dual-comb-based nonlinear spectroscopy (see the chapter 16 written by Kim and Cho in this book too) [33]. They present an extensive discussion of the advantages and limitations of this technique compared to conventional time-resolved spectroscopic methods using a single mode-locked laser with beam splitters and translational stages.

1.4.2 Interferometry

In spectroscopy and microscopy, various interferometric approaches to measuring the phase and amplitude of an unknown field by having it interfere with a reference field have been adopted. One of the most popular techniques used in nonlinear spectroscopy is Mach-Zehnder (MZ) interferometry (Fig. 1.1a). A single pulse from a coherent radiation source (e.g., a laser) is split into two daughter pulses that propagate along two different paths. The two beams are then combined by a beam combiner placed before a photon detector. Now, suppose one of the two path lengths is changed intentionally. As long as the two beams remain coherent with each other, the recorded intensity at the detector will exhibit an interference fringe with respect to the difference in the path lengths. Let us denote the waves in the upper and lower paths as ψ_u and ψ_l, respectively, and the incident wave as ψ_0. For the sake of simplicity, it is assumed that the incident beam is split into two by a 50:50 beam splitter that is fabricated from a lossless material. The wave arriving at the detector is given by

$$\psi = \psi_u + \psi_l = (1/\sqrt{2})\psi_0(e^{i\phi_u} + e^{i\phi_l}), \tag{1.15}$$

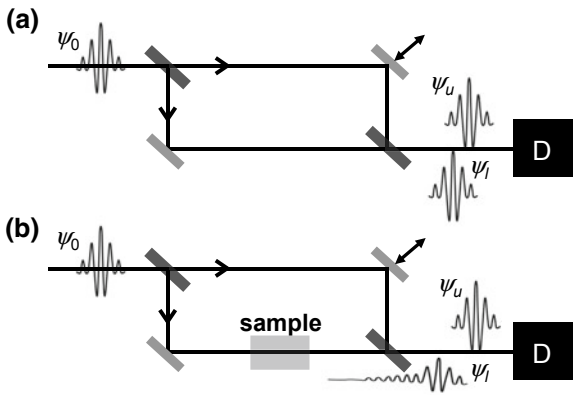

Fig. 1.1 Mach-Zehnder interferometry for spectroscopy. **a** The incoming wave is divided in two by a beam splitter. The two waves pass through the upper and lower paths and then interfere to produce a fringe of varying path length differences. **b** The wave on the lower path is modified by the complex susceptibility of the optical sample, which changes the interference pattern

where ϕ_u (ϕ_l) is the phase acquired by the upper (lower) beam. The detected intensity of the total wave is

$$|\psi|^2 = |\psi_0|^2\{1 + \cos(\phi_u - \phi_l)\}. \tag{1.16}$$

The phase difference $\phi_u - \phi_l$ is primarily determined by the difference in path length and it determines the fringe spacing. The sinusoidal term in (1.16) represents the coherence or distinguishability of the two waves. From the complementarity relation $D^2 + V^2 = 1$ for a single particle, distinguishability (D) is related to the visibility (V) of the fringe, where the former is a particle characteristic and the latter a wave characteristic. Thus, any finite visibility in the interference pattern indicates that the particle path is not completely distinguishable, i.e., $|D| < 1$. Now, suppose that there exist media on one or both of the two paths that can induce random phase fluctuations, $\varphi_m(t)$, in the two waves, i.e., $\psi_m = (1/\sqrt{2})\psi_0 e^{i\phi_m + i\varphi_m(t)}$ for $m = l$ and u. The interference term will then vanish when it is averaged over the broad and randomly fluctuating phases. This is known as the dephasing process, which is measurable with MZ interferometry.

Now, let us consider the case where a real optical sample that resonantly interacts with the incident beam is placed on the lower beam path (Fig. 1.1b). Due to the absorptive and dispersive properties of the sample, the wave passing through the lower path is modified and can be written as $\psi_l = (1/\sqrt{2})\psi_0 e^{-\kappa_l + i\eta_l + i\phi_l}$, where κ_l is the attenuation factor (α extinction coefficient) due to the resonant absorption of the radiation by chromophores in the sample and η_l is the phase shift due to the dispersion (α refractive index) of the sample. These two factors, κ_l and η_l, are related to the imaginary and real parts of the linear susceptibility of the sample, respectively. The measured signal in this case is

$$|\psi_s|^2 = (1/2)|\psi_0|^2\{1 + e^{-2\kappa_l} + 2e^{-\kappa_l}\cos(\phi_u - \phi_l - \eta_l)\}. \tag{1.17}$$

In principle, by comparing this interference pattern with that produced without an optical sample (or, more specifically, chromophores in the solution), quantitative information about the real and imaginary parts of the linear susceptibility of chromophores can be extracted.

Heterodyne-detected coherent 2D spectroscopic measurement [19, 34] is also based on MZ interferometry (Fig. 1.2). Instead of placing a sample cell containing molecules of interest on the lower beam path, the optical setup shown in the lower box in Fig. 1.2 is employed there. The pulse incident into the 4WM setup is split into three pulses, the relative delay times of which are controlled by two mechanical delay devices. The three pulses interact with the optical sample of interest, which then generates a third-order signal field propagating along the phase-matching direction. This signal field interferes with the reference beam traveling along the upper path, which closes the MZ interferometry circuit. In this form of coherent 2D spectroscopy, the output wave from the lower path can be generalized as

$$\psi_l = (1/\sqrt{2})\psi_0 e^{-\kappa_l(t,T,\tau) + i\eta_l(t,T,\tau) + i\phi_l}, \tag{1.18}$$

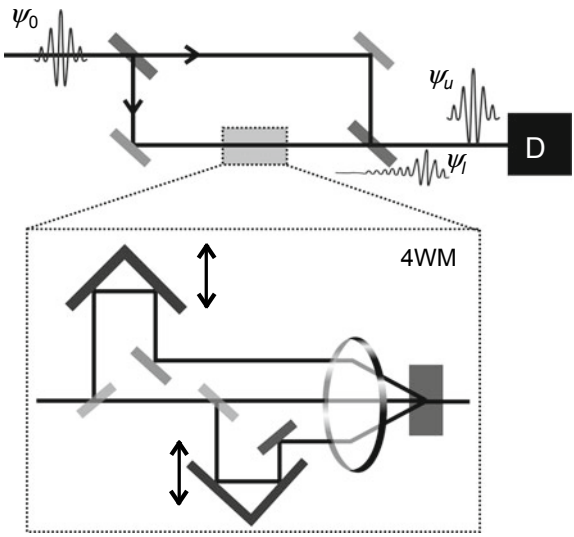

Fig. 1.2 Modified MZ interferometry. The experimental setup for 4WM scattering is placed on the lower beam path. The generated third-order signal electric field, which results from the desired phase-matching condition, is combined with the local oscillator (i.e., reference) field passing through the upper path. The interference pattern is recorded using a monochromator and array detector pair or a single detector depending on the experimental configuration

where $\kappa_l(t, T, \tau)$ and $\eta_l(t, T, \tau)$ represent the attenuation (extinction) factor and the phase shift factor, respectively. Note that they depend on the two pulse-to-pulse delay times τ and T and are related to the imaginary and real parts of the third-order response susceptibility. The wave passing along the lower path interferes with the wave from the upper path, and the interference term is selectively measured by the detector (D). Depending on the specific experimental configuration, the spectral interferogram in the frequency domain or the temporal interferogram in the time domain can be measured. In conventional 2D spectroscopy with laser pulses (Fig. 1.2), the time delay between the local oscillator field and the signal field is usually fixed. Using a monochromator and array detector, the spectral interferogram is measured experimentally, which provides information on the phase and amplitude of the third-order 2D spectroscopic signal field.

Recently, dual frequency comb spectroscopy has been shown to be useful in measuring the nonlinear electronic response functions of atomic (Rb) vapor or chromophores in condensed phases [35, 36]. Because the down conversion factor, which is determined by the ratio of the mean repetition frequency and the difference in repetition frequency between the two comb lasers is in the order of 10^6–10^8, it is possible to use a single detector to monitor ultrafast molecular response and relaxation processes with microsecond timescale detectors [37, 38]. Thus, for multiple frequency comb spectroscopy, the time-domain interferogram is recorded with a single detector and its Fourier transformation provides direct information about the spectrum of the sample with respect to the probe frequency. Although the underlying interferometry in dual and even multiple frequency comb spectroscopic techniques is more similar to Michelson interferometry than to MZ interferometry, the underlying principles are the same in the sense that the linear or nonlinear optical signal field

is characterized by analyzing the interference patterns produced by the interference between the signal field and the local oscillator (i.e., reference) field.

1.4.3 2D Electronic and Vibrational Spectroscopy

Two-dimensional electronic and vibrational spectroscopy that utilizes multiple laser pulses whose frequencies cover a broad range from THz, UV, to X-ray can be considered a time-domain 4WM process. The first three femtosecond pulses propagate along a non-collinear beam geometry. The pulse-to-pulse time intervals are controlled by changing the relative optical path lengths with motorized translational stages or dispersive materials such as a pair of wedged glasses. In coherent 2D spectroscopy, the molecular system evolves on different density matrix elements. The coherence evolution time τ is almost identical to the delay time between the first and second pulses when they are assumed to be ultrashort compared to the molecular relaxation processes. The waiting time T is the time interval between the second and third pulses, and the detection time t is the time between the third pulse and the emitted signal. Initially, the chromophores in condensed phases are in the thermal equilibrium state. The first $\mathbf{E}_1$ field-matter interaction creates a coherence state between the ground and excited states, i.e., the superposition of the ground and excited states. The second interaction with the $\mathbf{E}_2$ pulse puts the molecular system back to a population in either an excited or ground state. When there are multiple vibrational states or electronically delocalized exciton states that can be excited by spectrally broadband pulses, the state vector during T will demonstrate an oscillating pattern, i.e., quantum beats. The third pulse $\mathbf{E}_3$ shifts the molecular system to another coherence and it evolves for t. If the initial excitation frequency is different from the emission frequency due to changes in the local environment or the chemical structure of the chromophores during the waiting time, quantitative information about these processes can be extracted by analyzing the changes in both the diagonal and cross-peak shapes and intensities.

Various nonlinear response function components can usually be conveniently classified into non-rephasing $\mathbf{R}^{(3)}_{\mathrm{NR}}(\tau, T, t)$ and rephasing $\mathbf{R}^{(3)}_{\mathrm{R}}(\tau, T, t)$ transition pathways. In experiments, the non-rephasing and rephasing signals can be selectively measured by changing the time sequence of the first three pulses.

The emitted signal electric field is thus a function of the two delay times τ and T, i.e., $\mathbf{E}_{\mathrm{s}}(t, T, \tau)$. To measure the phase and amplitude of this signal electric field, a successful strategy is to have it interfere with an additional reference field, i.e., local oscillator field $\mathbf{E}_{\mathrm{LO}}(\mathbf{k}_{\mathrm{LO}})$, and to measure and analyze the spectral interferogram (Fig. 1.3). This detection technique is known as heterodyned detection because the spectral distribution of the local oscillator can differ from that of the third-order signal electric field. Because the spectral components of the total electric field are measured using an array detector combined with a monochromator, the measured spectrum is given by

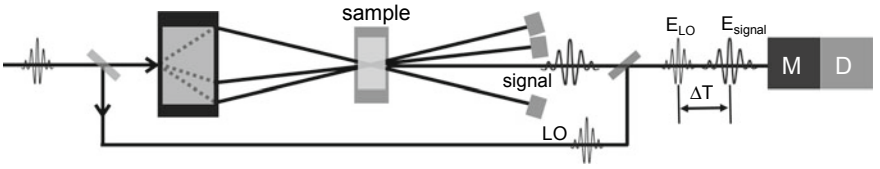

Fig. 1.3 Coherent 2D spectroscopy based on the measurement of a spectral interferogram. Delay stages in the first black box are used to control the relative time intervals between pulses. M = monochromator. D = detector

$$S(\omega_t, T, \tau) = |\mathbf{E}_{\mathrm{s}}(\omega_t, T, \tau) + \mathbf{E}_{\mathrm{LO}}(\omega_t)|^2 = |\mathbf{E}_{\mathrm{LO}}(\omega_t)|^2 + |\mathbf{E}_{\mathrm{s}}(\omega_t, T, \tau)|^2 + 2\mathrm{Re}[\mathbf{E}_s^*(\omega_t, T, \tau) \cdot \mathbf{E}_{\mathrm{LO}}(\omega_t)] \tag{1.19}$$

where ω_t is the Fourier frequency conjugated with detection time t. In (1.19), $|\mathbf{E}_{\mathrm{LO}}(\omega_t)|^2$ contributes to the measured spectral interferogram as a constant independent from the two delay times τ and T so that it can be removed from the measured intensity. The signal field intensity, which is often referred to as the homodyne signal, $|\mathbf{E}_{\mathrm{s}}(\omega_t, T, \tau)|^2$, is negligibly small compared to the last interference term because of the inequality $|\mathbf{E}_{\mathrm{LO}}(\omega_t)| \gg |\mathbf{E}_{\mathrm{s}}(\omega_t, T, \tau)|$. Thus, the measured heterodyne-detected signal that is needed to obtain the 2D spectrum is

$$S_{het}(\omega_t, T, \tau) \propto 2\mathrm{Re}[\mathbf{E}_s^*(\omega_t, T, \tau) \cdot \mathbf{E}_{\mathrm{LO}}(\omega_t)]. \tag{1.20}$$

To retrieve the complex signal electric field, i.e., both the real and imaginary parts of the signal field, from the spectral interferogram, it should first be Fourier transformed to the time domain data. The positive time component of the time-domain signal is only taken into consideration for the subsequent inverse Fourier transformation back to the frequency (ω_t) domain. Thus, the obtained spectrum is a function of τ, T, and ω_t, which is denoted as $\bar{S}_{\mathrm{het}}(\omega_t, T, \tau)$. Finally, the Fourier transformation of $\bar{S}_{\mathrm{het}}(\omega_t, T, \tau)$ with respect to τ produces the 2D spectrum $S_{2\mathrm{D}}(\omega_t, T, \omega_\tau)$. The absorptive component of the signal is measured when the signal is in phase with that of the LO field, whereas the dispersive component is obtained when the signal is 90° out of phase with respect to the LO. In practice, the dispersive and absorptive components of the heterodyned signal can be obtained using phase cycling methods such as the dual phase scan method.

To obtain purely absorptive 2D spectra, the non-rephasing and rephasing signals are measured independently using two different pulse time sequences at a fixed waiting time T. These signals are Fourier transformed with respect to t and τ and are added together to obtain the absorptive 2D spectrum:

$$S_{\mathrm{abs}}(\omega_t, T, \omega_\tau) = S_{\mathrm{NR}}(\omega_t, T, \omega_\tau) + S_{\mathrm{R}}(\omega_t, T, \omega_\tau). \tag{1.21}$$

In experiments, the time resolution is determined by the duration of the incident pulses, whereas the spectral resolution is determined by (1) the characteristics of the

monochromator (e.g., the grating and focal length), (2) the pixel size of the CCD or IR array detector, and (3) the scanning range of the delay time τ between the first and second pulses.

The measured 2D spectra are then displayed with respect to the excitation (pump) frequency ω_τ and the emission (probe) frequency ω_t for varying waiting times T. The horizontal axis labeled as ω_τ provides information on the molecular transition frequencies of an ensemble of chromophores, whereas the peak positions along the vertical probe frequency (ω_t) axis provide information on the quantum states involved in the created superposition state of the system after the waiting time T. Thus, coherent 2D spectroscopy is composed of photon-labeling (i.e., writing), waiting, and photon-detecting (i.e., reading) steps. A molecule labeled (i.e., excited) by the first two field-matter interactions spontaneously undergoes a variety of relaxations, transitions, or reactions, which essentially result in the change in the transition frequency of the labeled molecule. The 2D optical spectrum can therefore be considered a 2D frequency correlation map between the initial and final frequencies or states, which provides quantitative information on the dynamics of molecules.

The overall experimental layout shown in Fig. 1.3 is also similar to the Mach-Zehnder interferometer. Usually, the local oscillator field does not need to pass through the optical sample. In practice, the amplitude ratio of $|\mathbf{E}_s|/|\mathbf{E}_{LO}|$ is deliberately varied to optimize the signal-to-noise ratio. One of the most difficult issues in measuring the 2D spectrum is to keep the relative phases of the pulses stable and constant throughout the experimental time. The relative phase of the signal field with respect to that of the LO (reference) field is determined by the relative phases of incident pulses:

$$\phi = \phi_{LO} - \phi_s = \phi_{LO} - (\phi_{\mathbf{E}_1} - \phi_{\mathbf{E}_2} + \phi_{\mathbf{E}_3}) = (\phi_{LO} - \phi_{\mathbf{E}_3}) - (\phi_{\mathbf{E}_1} - \phi_{\mathbf{E}_2}). \quad (1.22)$$

Here, the phase differences $\phi_{\mathbf{E}_1} - \phi_{\mathbf{E}_2}$ and $\phi_{LO} - \phi_{\mathbf{E}_3}$ fluctuate in time because the time delays between $\mathbf{E}_1$ and $\mathbf{E}_2$ and between $\mathbf{E}_3$ and $\mathbf{E}_{LO}$, respectively, fluctuate. Usually, it is quite challenging to precisely control the relative phase between the signal and LO fields. The heterodyne-detected signal inevitably consists of both absorptive and dispersive contributions. Thus, to extract the purely absorptive spectra from the measured spectral interferograms, the relative time delay errors between the incident pulses and the chirps on the incident pulses need to be numerically corrected afterward. This numerical procedure is often referred to as *phasing*. The most successful and widely used method is based on the pump-probe projection theorem. This theorem holds that the integrated spectrum of $S_{2D}(\omega_t, T, \omega_\tau)$ over frequency ω_τ should, in principle, be identical to the pump-probe spectrum with respect to the probe frequency ω_t. Therefore, the phase factor by which the complex 2D spectrum is multiplied should be adjusted to ensure the 2D spectrum projected onto the ω_t-axis better matches the pump-probe spectrum, thus completing phasing correction.

1.4.4 Phasing

As emphasized above, the important step for successful heterodyne-detected 2D spectroscopy is to measure the amplitude and phase of the signal field $\mathbf{E}_s$ with respect to the local oscillator field $\mathbf{E}_{LO}$. The period of electromagnetic waves in the UV-visible range is just a few femtoseconds per cycle, so it is difficult to accurately and repeatedly measure the absorptive component of the third-order signals with fixed relative phases. Suppose that the phases of incident pulses vary in time due to fluctuations in the incident beam paths. The relative phase $\phi(t)$ can be written as the sum of the time-averaged constant phase angle ϕ_0 and the fluctuating component $\delta\phi_f(t)$ as $\phi(t) = \phi_0 - \delta\phi_f(t)$. If the relative phase between the signal and LO fields varies randomly over the timescale of the experimental data collection, the measured signal that represents the average of the fluctuating phases would be distorted or even vanish depending on the amplitude of the phase fluctuation.

To stabilize the relative phase, an active phase-locking scheme has been developed using an additional interferometer to monitor the phase errors. A feedback loop is then implemented to control the position of each individual optic component on the incident beam path. Another approach is to use diffractive optics for passive phase-locking. A diffractive optical element acts like a beam splitter. If two beams propagating along different directions are focused onto the diffractive optical element, each beam is split into two ($\pm$) first-order beams. The waiting time T is controlled before the diffractive optics, but the other delay times are scanned with a pair of sliding glass wedges. Thus, the four generated beams are reflected by the same optical element, e.g., mirrors, and are focused onto the sample. Therefore, the phase noise of the incident beams cancels out. This passive phase-locking technique based on diffractive optics can be easily implemented within a coherent 2D spectrometer without requiring additional interferometer or feedback electronics. A 2D optical spectrometer based on diffractive optics is compact and has been found to be more effective for 2D electronic spectroscopy in the visible frequency domain.

1.4.5 Frequency-Scanning 2D Pump-Probe Spectroscopy

Unlike coherent 2D spectroscopy that utilizes three pulses with different propagation directions, coherent 2D spectroscopy based on a pump-probe geometry has a relatively simple experimental configuration. Typical pump-probe spectroscopy is performed with two pulses propagating non-collinearly. The pump beam $\mathbf{E}_{pu}(\mathbf{k}_{pu})$ with frequency ω_τ excites only those chromophores that are resonant with the ω_τ field. After a finite delay time of T, the probe beam $\mathbf{E}_{pr}(\mathbf{k}_{pr})$ is used to monitor the relaxation processes of those excited molecules. In this case, the pump-pump-probe electric field-matter interactions create the corresponding third-order polarization $\mathbf{P}^{(3)}(t)$, which in turn generates the pump-probe signal electric field $\mathbf{E}^{(3)}(t)$, whose wave vector is $\mathbf{k}_s = -\mathbf{k}_{pu} + \mathbf{k}_{pu} + \mathbf{k}_{pr}$. This pump-probe signal field propagates

along the same direction as the probe beam, and the spectrum of the interference between the signal and probe fields is measured with a monochromator and an array detector. Because no additional local oscillator (reference) field is used to detect the amplitude and phase of the pump-probe signal field, there is no need to precisely control the relative phase. This is why it is known as self-heterodyne detection spectroscopy. Note that the pump-probe signal field is naturally in phase with the probe beam, which allows the absorptive component of the 2D spectrum to be measured.

This pump-probe scheme has been used to obtain 2D spectra by scanning the pump frequency. The excitation frequency ω_τ of the pump can be selected using, for example, a Fabry-Pérot interferometer. To obtain the 2D spectrum $S_{\mathrm{PP}}(\omega_t, T, \omega_\tau)$, the excitation frequency ω_τ needs to be scanned over the molecular transition band. The frequency resolution is therefore determined by the spectral bandwidth of the frequency-selected pump beam. The temporal resolution of frequency-scanning 2D pump-probe spectroscopy is determined by the convolution of the frequency-selected pump beam and the probe beam at the sample position. The narrow spectral bandwidth of the pump beam unfortunately generates a 2D spectrum with poor time resolution. In other words, there is a trade off between the temporal resolution and the spectral resolution. Therefore, this frequency-scanning 2D pump-probe measurement method has been used to study molecular systems with relatively slow relaxation processes and chemical or biological reactions.

1.4.6 Time-Scanning 2D Pump-Probe Spectroscopy

Unlike frequency-scanning 2D pump-probe spectroscopy, time-scanning 2D pump-probe spectroscopy utilizes three broadband femtosecond pulses in the pump-probe geometry. In contrast to the three-pulse scattering geometry (Fig. 1.3), the first two incident pulses ($\mathbf{E}_{\mathrm{pu1}}$ and $\mathbf{E}_{\mathrm{pu2}}$), which are separated by τ in time, propagate collinearly along the direction set by the same wave vector $\mathbf{k}_{\mathrm{pu}}$. The pump 1/pump 2/probe interactions with the chromophores generate the pump-probe signal field along the probe direction due to the phase-matching condition of $\mathbf{k}_{\mathrm{s}} = -\mathbf{k}_{\mathrm{pu}} + \mathbf{k}_{\mathrm{pu}} + \mathbf{k}_{\mathrm{pr}} = \mathbf{k}_{\mathrm{pr}}$. The generated signal electric field $\mathbf{E}^{(3)}(t)$ interferes with the probe field itself and the spectrum of this interference term is measured using a monochromator and an array detector (Fig. 1.4). In contrast to pump frequency-scanning 2D pump-probe spectroscopy, temporal interferograms are collected with respect to τ at detection frequencies (ω_t). Therefore, additional Fourier transformation of the τ-dependent data provides additional frequency information for the nonlinear response function along the ω_τ axis. One of the advantages of this form of spectroscopy is that the absorptive 2D spectra can be obtained without sacrificing the temporal resolution. However, the desired 2D signal is measured together with the stronger pump-probe signals originating from the pump 2/pump 2/probe interactions with the chromophores, thus the noise inherently present in the two-beam pump-probe signals contributes to the pump 1/pump 2/probe 2D signal. These strong two-beam pump-probe signals act like an additional time-dependent local oscillator field, which

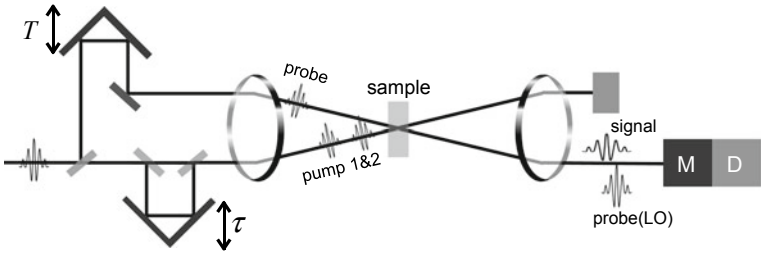

Fig. 1.4 Schematic representation of time-scanning 2D pump-probe spectroscopy. The time delay between pump 1 and pump 2 is controlled with a translational stage (or sometimes two sliding wedged glasses). The probe field is delayed from pump 2 by waiting time T. The generated third-order pump-probe signal field interferes with the probe beam itself. The spectrum of the interference signal is measured by a monochromator (M) and an array detector (D)

causes the spectral distortion of the 2D signal. Furthermore, this time-scanning 2D pump-probe method still requires phasing correction to obtain the 2D spectrum, even though the number of phasing parameters is reduced. The timing error between $\mathbf{E}_{\mathrm{pu1}}$ and $\mathbf{E}_{\mathrm{pu2}}$ and the unbalanced chirp also give rise to the spectral distortion of the measured 2D spectrum. In real experiments, the two beams $\mathbf{E}_1$ and $\mathbf{E}_2$ are usually combined by a 50:50 beam combiner, which means that a loss of almost 50% in the intensity of each beam is unavoidable. To overcome some of these problems, pulse-shaping technology has thus been employed.

1.4.7 2D Spectroscopy with a Pulse Shaper

With the development of pulse-shaping technology, it has become possible to carry out coherent 2D pump-probe spectroscopy experiments with commercially available pulse shapers. In principle, this approach is similar to time-scanning 2D pump-probe spectroscopy because a pair of collinearly propagating pump pulses are used to excite molecules and a time-delayed probe pulse is used to monitor the relaxation processes of the excited molecules in condensed phases. Here, it is the pulse shaper that generates the pair of femtosecond pump pulses that are temporally separated in time by τ (Fig. 1.5). The underlying principle of a pulse shaper is well-known. Suppose that an incident pulse electric field $E_{\mathrm{in}}(t)$ has the spectral distribution $E_{\mathrm{in}}(\omega)$. To obtain time-separated twin pulses, the pulse shaper modulates the spectral distribution of the incident beam, which is achieved with the use of a mask in the frequency domain, producing the shaped spectral pulse electric field $E_{\mathrm{out}}(\omega)$ as $E_{\mathrm{out}}(\omega) = M(\omega)E_{\mathrm{in}}(\omega)$. Here, the spectrum of the acousto-optic modulator (AOM) is in general given by $M(\omega) = A(\omega)\exp[i\varphi(\omega)]$, where the spectral amplitude of the mask is denoted as $A(\omega)$ and its spectral phase is $\varphi(\omega)$. The time profile of the generated electric field $E_{\mathrm{out}}(t)$ is given by the inverse Fourier transformation of the output field spectrum $E_{\mathrm{out}}(\omega)$. In principle, the phase and chirp of the shaped pulse or pulses can

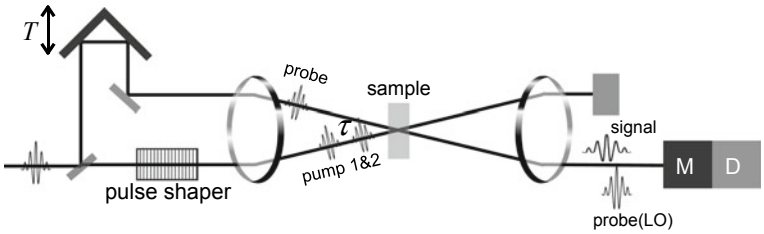

Fig. 1.5 2D pump-probe spectroscopy with a pulse shaper. A pair of twin pump pulses that are separated by τ in time are generated by a pulse shaper on the lower path. The time (T) delayed probe is used to generate the third-order pump-probe signal field and to produce the interference signal detected by the monochromator and the array detector

be controlled by changing the mask spectrum. To generate a pair of femtosecond pulses with a time delay of τ using the acousto-optic modulator, the static acoustic wave needs to be electronically generated so that the mask spectrum is given by $M(\omega) = \cos(\omega\tau/2)\exp[i\omega\tau/2]$. The time delay between the two pulses is inversely proportional to the fringe spacing (wavelength) of the acoustic wave created by the AOM. The maximum time delay is therefore limited by the resolution of the AOM. In addition to the time delay between the two pulses, the relative phase and chirp of the generated pulses can also be controlled using the pulse shaper. Essentially, the throughput of the pulse shaper is determined by the efficiency of the grating as well as the AOM. Often, a significant loss in the intensity of the input beam when it passes through the pulse shaper cannot be avoided.

In this form of 2D pump-probe spectroscopy, the pulse shaper can modulate the relative phase between the pump 1 and pump 2 pulses, i.e., $\Delta\phi = \phi_{E_1} - \phi_{E_2} = 0$ and $\Delta\phi = \pi$, and the absorptive 2D spectrum can be directly obtained by the phase-cycling method. A pulse shaper with a laser system operating at a repetition rate of 1 kHz can produce 500 data points per second. Therefore, a complete 2D spectrum at fixed waiting time T can be collected within a few seconds. However, a drawback of this method is that it cannot control the polarization states of the three beams, which limits its use in exploring all fourth-rank tensor properties of the nonlinear response function of molecules in condensed phases.

Over the past decade, a variety of coherent 2D spectroscopic techniques have been developed and demonstrated. Using a two-dimensional array detector (CCD) working in the visible frequency domain, it has been shown that single-shot 2D electronic and IR spectroscopic measurements are feasible [39, 40]. Using combined spherical and cylindrical lenses, the different spectral components of a broadband pulse can be encoded onto different positions of the sample in space and different pixels on a 2D array detector are used to record the different spectral components of coherent 2D signals. Another possibility is using a wedge-shaped material to induce a pump-to-pulse time delay gradient along the wedge axis. This approach is advantageous because neither a mechanical translational stage nor a pair of sliding wedged glasses is needed to control the time delay between the pulses. Nevertheless, the principles behind these techniques do not differ from those discussed above.

1.5 Perspectives and Concluding Remarks

1.5.1 Coherent Multidimensional Spectroscopy with Mixed IR and Visible Beams

Nonlinear IR (e.g., near-IR, mid-IR, far-IR, and THz) spectroscopy provides critical information on molecular structure and dynamics because vibrational properties are highly sensitive to chemical structure and intermolecular interactions. Although the theory and experimental feasibility of mixed IR-vis 4WM spectroscopy was proposed in 1998 and demonstrated in 1999, only recently have fully time-resolved mixed IR-vis 4WM experiments been performed. They are an IR-optical analogue of heteronuclear 2D NMR because there are two different kinds of oscillating charged particles that are resonant with external fields: electrons and nuclei. Because mixed IR-vis 2D spectroscopy can be used in the analysis of vibration-electronic coupling, it is especially useful for investigating electronic transition-induced changes in molecular structures and the long-lived electronic states or vibrational coherences of photo-excited molecules during chemical reactions.

Another important development in CMS is fluorescence-detected coherent 2D electronic or vibrational spectroscopy [41]. Instead of measuring third-order signal electric fields using spectral interferometric detection, the population of excited state molecules can be measured by detecting the fluorescence intensity after the molecular system interacts with a sequence of optical or IR pulses whose relative phases are accurately controlled. This form of fluorescence-detected 2D spectroscopy can be extended to coherent 2D microspectroscopy by combining it with a microscope system.

1.5.2 Coherent Multidimensional Spectroscopy with More Than One Phase-Stabilized Mode-Locked Laser

Most CMS techniques developed and used over the past two decades use a single mode-locked laser. Although it produces a train of femtosecond pulses, each CMS signal field is generated by considering one pulse at a time. More specifically, a single laser pulse is split into two or more pulses and their relative delay times are controlled with mechanical delay devices (Fig. 1.6a). The generated daughter pulses thus originate from the same mother pulse, meaning they should remain coherent. However, in practice, this is not always the case because the beam paths fluctuate due to the environmental vibrations of optical mounts and chaotic air flow, which results in the decoherence of pulsed electric fields. However, as long as this noise is actively or passively controlled, each individual signal measurement is performed with one pulse from the laser at a time. The 2D spectrum is thus the average of the signals obtained from many thousands of laser pulses.

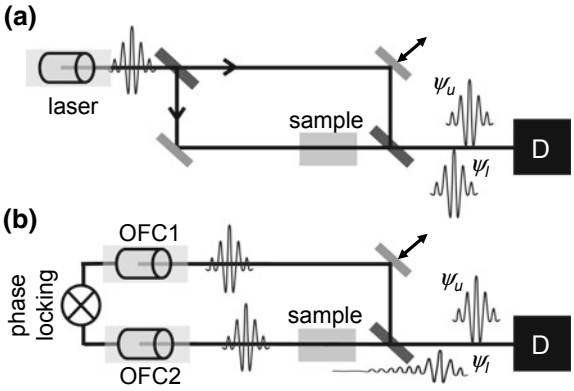

Fig. 1.6 **a** Conventional interferometric measurement of a sample's linear or nonlinear optical response signal field. Here, only one mode-locked laser producing a train of femtosecond pulses is used. **b** Schematic representation of dual optical frequency comb (OFC) spectroscopy. The two frequency comb lasers are phased-locked with each other using one standard atomic clock radio frequency. Any pair of pulses from the two OFC lasers will thus have a fixed phase relationship, which means that the pulsed fields are coherent. The upper wave from OFC1 is used as the reference field, which is then allowed to interfere with the sample's generated linear or nonlinear optical response signal field. By deliberately making the two repetition frequencies differ slightly from each other, automatic time scanning can be achieved, and the down-converted temporal interferogram can be measured with a single detector

Very recently, an interesting development in CMS has been reported, in which more than one mode-locked laser is used, where the phase-stabilized ultrafast laser is referred to as an optical frequency comb, which generates a train of pulses with highly stable repetition and carrier-envelop-offset frequencies. To understand how this differs from more conventional Ti:Sapphire lasers, it should be noted that the optical phase of a pulse from an ordinary 1 kHz Ti:Sapphire laser has no correlation with that of another pulse separated by 1 ms. On the other hand, there is a fixed phase relationship between any pair of pulses within the train of pulses from a highly stabilized frequency comb laser. This long-term coherence among the pulses is a key feature of the frequency comb. If two frequency comb lasers are stabilized simultaneously with respect to one standard frequency, e.g., a GPS-disciplined Rb atomic clock, the two trains of pulses from the two comb lasers will have a precisely defined phase relationship. Therefore, these two radiation sources together can be used to carry out coherent nonlinear spectroscopic measurements (Fig. 1.6b). This can be viewed as Young's double slit interference, where the coherent waves from the two slits that will combine to produce an interference fringe pattern are replaced with two phase-stabilized comb lasers. Due to the fixed phase relationship between any pair of pulses from the two frequency comb lasers, the two waves are coherent with each other. One of the two trains of pulses can be used as the reference (i.e., local oscillator) field, whereas the other linearly or nonlinearly interacts with molecular systems. The signal field from the latter then interferes with the reference field to produce a time-

domain interferogram. Its Fourier transformation provides information about the spectrum of molecular quantum eigenstates. Therefore, CMS signals can be obtained with a single detector [42]. It is anticipated that a variety of CMS techniques will be developed by combining optical frequency comb and IR frequency comb lasers in the future.

1.5.3 Nonlinear Microspectroscopy

A natural extension of nonlinear optical spectroscopy is to combine it with a microscope to develop novel microspectroscopy techniques. One of the most successful label-free imaging techniques is coherent Raman scattering microscopy. Since the first experimental demonstration of coherent anti-Stokes Raman scattering microscopy, a number of papers have reported a variety of coherent nonlinear optical or vibrational microspectroscopy techniques. For 2D electronic microspectroscopy, the detection of the fluorescence emitted by chromophores that are excited by multiple femtosecond laser pulses can be used, where the coherent 2D spectroscopic signal is selectively measured using phase-cycling techniques.

To achieve coherent 2D IR microspectroscopy, reflective objective lenses or upconversion techniques can be used to measure the 2D IR response with detectors in the visible frequency range.

1.5.4 Computational Spectroscopy

A number of computational methods for calculating 2D vibrational spectra have been developed and demonstrated to be of exceptional use in simulating and interpreting experimental results. In addition to pairwise couplings, diagonal and off-diagonal potential anharmonicities, and mode-mode frequency correlation, more information about multiple oscillator systems can be obtained from higher-order CMS methods generating multidimensional spectra. For example, 3D infrared spectroscopy has been explored experimentally and simulated based on classical or semiclassical methods. Nevertheless, it is still difficult to fully interpret these 2D spectra because of the increased number of couplings and the higher dimensionality of the relevant potential energy surface.

In the numerical integration of the Schrödinger equation method, an essential step is the modeling and parameterization of the multi-chromophore Hamiltonian from the electronic structure calculations of their static structures. In contrast, the classical mechanical approach relies on an accurate description of molecular vibrational properties in the context of classical dynamics. This often requires the use of sophisticated molecular mechanics potential models or quantum mechanical potential. In this regard, recently proposed ab initio theories of vibrational solvatochromism and direct QM/MM or full ab initio MD simulations of vibrational spectra can be fruitfully adapted for either approach to improve their efficiency and accuracy.

Two-dimensional vibrational spectra can be calculated using the exact hierarchical equation of motion (HEOM) approach. It should be noted, however, that this HEOM approach is based on the assumption that the spectral density description of the bath is valid and accurate. This means that the bath is modeled as a collection of independent harmonic oscillators, i.e., the Caldeira-Leggett quantum dissipative bath model, and the spectral distribution of solute-solvent coupling constants is well-known. Under this assumption, the quantum correlation between the system and the bath can be accounted for. However, this method scales rather unfavorably, limiting its application to relatively small systems even though a number of approximations have been developed to improve its efficiency. Another limitation is that the method requires the parameterization of the spectral density.

1.5.5 Summary

In this chapter, I have presented a brief introduction to the fundamental theory, computational methods, and experimental techniques that have been used to describe or measure a variety of coherent multidimensional spectroscopic signals. Theoretically, the formalism of the nonlinear response function has been developed to describe various CMS methods. For nonlinear vibrational spectroscopy, one of the widely used theoretical approaches is based on the approximation that the associated quantum mechanical nonlinear vibrational response function can be evaluated using the MD simulation trajectories of either equilibrium or non-equilibrium systems. Another popular method of choice is to solve the time-dependent vibrational Schrödinger equation of coupled oscillators where their frequencies, coupling constants, and anharmonicities, which fluctuate in time due to the system-bath interactions, can be obtained with independent computational methods and theoretical models. Experimentally, over the past decade, a variety of 2D vibrational and/or electronic spectroscopic techniques that utilize femtosecond IR, THz, and/or UV-visible pulses have been developed and used to study molecular structure and dynamics, protein conformation and folding-unfolding processes, large-scale delocalized modes in condensed phases, and ultrafast reaction dynamics during chemical and biological reactions. We have recently witnessed novel forms of coherent multidimensional spectroscopy, such as multiple frequency comb spectroscopy and nonlinear optical and vibrational microspectroscopy. There is no doubt that the theory and experimentation in coherent multidimensional spectroscopy and microspectroscopy will pave the way for the development of novel time and space resolved spectroscopy and microscopy tools that are useful for understanding the underlying principles, mechanisms, and functions of novel materials and synthetic and biological molecules in condensed phases.

Acknowledgements This work was supported by IBS-R023-D1.

References

1. G.R. Fleming, *Chemical Applications of Ultrafast Spectroscopy*. (Oxford University Press, 1986)
2. A.H. Zewail, Femtochemistry: atomic-scale dynamics of the chemical bond using ultrafast lasers (Nobel Lecture). Angew. Chem. Int. Ed. **39**, 2586–2631 (2000). https://doi.org/10.1002/3527600183.ch1
3. J. Zheng, K. Kwak, J. Xie, M.D. Fayer, Ultrafast carbon-carbon single-bond rotational isomerization in room-temperature solution. Science **313**, 1951–1955 (2006). https://doi.org/10.1126/science.1132178
4. M. Maroncelli, J. Macinnis, G.R. Fleming, Polar solvent dynamics and electron-transfer reactions. Science **243**, 1674–1681 (1989). https://doi.org/10.1126/science.243.4899.1674
5. G.R. Fleming, M. Cho, Chromophore-solvent dynamics. Annu. Rev. Phys. Chem. **47**, 109–134 (1996). https://doi.org/10.1146/annurev.physchem.47.1.109
6. S. Mukamel, *Principles of Nonlinear Optical Spectroscopy*. (Oxford University Press, 1995)
7. M. Cho, *Two-Dimensional Optical Spectroscopy*. (CRC Press, 2009)
8. P. Hamm, M. Zanni, *Concepts and Methods of 2D Infrared Spectroscopy*. (Cambridge University Press, 2011)
9. H. Kim, M. Cho, Infrared probes for studying the structure and dynamics of biomolecules. Chem. Rev. **113**, 5817–5847 (2013). https://doi.org/10.1021/cr3005185
10. J. Ma, I.M. Pazos, W. Zhang, R.M. Culik, F. Gai, Site-specific infrared probes of proteins. Annu. Rev. Phys. Chem. **66**, 357–377 (2015). https://doi.org/10.1146/annurev-physchem-040214-121802
11. M. Cho, Coherent two-dimensional optical spectroscopy. Chem. Rev. **108**, 1331–1418 (2008). https://doi.org/10.1021/Cr078377b
12. A.M. Weiner, S. De Silvestri, E.P. Ippen, Three-pulse scattering for femtosecond dephasing studies: theory and experiment. J. Opt. Soc. Am. B **2**, 654–662 (1985). https://doi.org/10.1364/JOSAB.2.000654
13. D. Zimdars et al., Picosecond infrared vibrational photon echoes in a liquid and glass using a free electron laser. Phys. Rev. Lett. **70**, 2718–2721 (1993). https://doi.org/10.1103/PhysRevLett.70.2718
14. Y. Tanimura, S. Mukamel, Two-dimensional femtosecond vibrational spectroscopy of liquids. J. Chem. Phys. **99**, 9496–9511 (1993). https://doi.org/10.1063/1.465484
15. D.A. Blank, L.J. Kaufman, G.R. Fleming, Fifth-order two-dimensional Raman spectra of CS2 are dominated by third-order cascades. J. Chem. Phys. **111**, 3105–3114 (1999). https://doi.org/10.1063/1.479591
16. M. Cho et al., Intrinsic cascading contributions to the fifth- and seventh-order electronically off-resonant Raman spectroscopies. J. Chem. Phys. **112**, 2082–2094 (2000). https://doi.org/10.1063/1.480777
17. M. Cho, On the resonant coherent two-dimensional Raman scattering. J. Chem. Phys. **109**, 5327–5337 (1998). https://doi.org/10.1063/1.477151
18. M. Cho, G.R. Fleming, Fifth-order three-pulse scattering spectroscopy: can we separate homogeneous and inhomogeneous contributions to optical spectra? J. Phys. Chem. **98**, 3478–3485 (1994). https://doi.org/10.1021/j100064a033
19. J.D. Hybl, A.W. Albrecht, S.M. Gallagher Faeder, D.M. Jonas, Two-dimensional electronic spectroscopy. Chem. Phys. Lett. **297**, 307–313 (1998). https://doi.org/10.1016/S0009-2614(98)01140-3
20. P. Hamm, M. Lim, R.M. Hochstrasser, Structure of the amide I band of peptides measured by femtosecond nonlinear-infrared spectroscopy. J. Phys. Chem. B **102**, 6123–6138 (1998). https://doi.org/10.1021/jp9813286
21. K. Park, M. Cho, Time- and frequency-resolved coherent two-dimensional IR spectroscopy: Its complementary relationship with the coherent two-dimensional Raman scattering spectroscopy. J. Chem. Phys. **109**, 10559–10569 (1998). https://doi.org/10.1063/1.477756

22. W. Zhao, J.C. Wright, Spectral simplification in vibrational spectroscopy using doubly vibrationally enhanced infrared four wave mixing. J. Am. Chem. Soc. **121**, 10994–10998 (1999). https://doi.org/10.1021/ja9926414
23. S. Mukamel, Multidimensional femtosecond correlation spectroscopies of electronic and vibrational excitations. Annu. Rev. Phys. Chem. **51**, 691–729 (2000)
24. T.L.C. Jansen, S. Saito, J. Jeon, M. Cho, Theory of two-dimensional vibrational spectroscopy. J. Chem. Phys. **150**, 100901 (2019). https://doi.org/10.1063/1.5083966
25. S. Mukamel, V. Khidekel, V. Chernyak, Classical chaos and fluctuation-dissipation relations for nonlinear response. Phys. Rev. E **53**, R1–R4 (1996). https://doi.org/10.1103/PhysRevE.53.R1
26. S. Mukamel, J.B. Maddox, All-forward semiclassical simulations of nonlinear response functions. J. Chem. Phys. **121**, 36–43 (2004). https://doi.org/10.1063/1.1756582
27. T.I.C. Jansen, K. Duppen, J.G. Snijders, Close collisions in the two-dimensional Raman response of liquid carbon disulfide. Phys. Rev. B **67**, 134206 (2003). https://doi.org/10.1103/physrevb.67.134206
28. T. Hasegawa, Y. Tanimura, Calculating fifth-order Raman signals for various molecular liquids by equilibrium and nonequilibrium hybrid molecular dynamics simulation algorithms. J. Chem. Phys. **125**, 074512 (2006). https://doi.org/10.1063/1.2217947
29. A. Sakurai, Y. Tanimura, Does $\hbar$ play a role in multidimensional spectroscopy? reduced hierarchy equations of motion approach to molecular vibrations. J. Phys. Chem. A **115**, 4009–4022 (2011). https://doi.org/10.1021/jp1095618
30. M. Reppert, P. Brumer, Classical coherent two-dimensional vibrational spectroscopy. J. Chem. Phys. **148**, 064101 (2018). https://doi.org/10.1063/1.5017985
31. T.I.C. Jansen, J. Knoester, Nonadiabatic effects in the two-Dimensional infrared spectra of peptides: application to alanine dipeptide. J. Phys. Chem. B **110**, 22910–22916. https://doi.org/10.1021/jp064795t (2006)
32. B. Błasiak, C.H. Londergan, L.J. Webb, M. Cho, Vibrational probes: From small molecule solvatochromism theory and experiments to applications in complex systems. Acc. Chem. Res. **50**, 968–976 (2017). https://doi.org/10.1021/acs.accounts.7b00002
33. J. Kim, J. Jeon, T.H. Yoon, M. Cho, Dual frequency-comb spectroscopy of chromophores in condensed phases. Chem. Phys. **520**, 122–137 (2019). https://doi.org/10.1016/j.chemphys.2018.12.012
34. M.C. Asplund, M.T. Zanni, R.M. Hochstrasser, Two-dimensional infrared spectroscopy of peptides by phase-controlled femtosecond vibrational photon echoes. Proc. Natl. Acad. Sci. **97**, 8219–8224 (2000). https://doi.org/10.1073/pnas.140227997
35. B. Lomsadze, S.T. Cundiff, Frequency combs enable rapid and high-resolution multidimensional coherent spectroscopy. Science **357**, 1389–1391 (2017). https://doi.org/10.1126/science.aao1090
36. J. Kim, T.H. Yoon, M. Cho, Interferometric measurement of transient absorption and refraction spectra with dual frequency comb. J. Phys. Chem. B **122**, 9775–9785 (2018). https://doi.org/10.1021/acs.jpcb.8b09262
37. I. Coddington, N. Newbury, W. Swann, Dual-comb spectroscopy. Optica **3**, 414–426 (2016). https://doi.org/10.1364/optica.3.000414
38. T. Ideguchi, A. Poisson, G. Guelachvili, N. Picqué, T.W. Hänsch, Adaptive real-time dual-comb spectroscopy. Nat. Commun. **5**, 3375 (2014). https://doi.org/10.1038/ncomms4375
39. M.F. DeCamp, L.P. DeFlores, K.C. Jones, A. Tokmakoff, Single-shot two-dimensional infrared spectroscopy. Opt. Express **15**, 233–241 (2007). https://doi.org/10.1364/OE.15.000233
40. E. Harel, A.F. Fidler, G.S. Engel, Real-time mapping of electronic structure with single-shot two-dimensional electronic spectroscopy. Proc. Natl. Acad. Sci. **107**, 16444–16447 (2010). https://doi.org/10.1073/pnas.1007579107

41. P.F. Tekavec, G.A. Lott, A.H. Marcus, Fluorescence-detected two-dimensional electronic coherence spectroscopy by acousto-optic phase modulation. J. Chem. Phys. **127**, 214307 (2007). https://doi.org/10.1063/1.2800560
42. J. Kim, B. Cho, T.H. Yoon, M. Cho, Dual-frequency comb transient absorption: Broad dynamic range measurement of femtosecond to nanosecond relaxation processes. J. Phys. Chem. Lett. **9**, 1866–1871 (2018). https://doi.org/10.1021/acs.jpclett.8b00886

Chapter 2
Two-Dimensional Electronic Vibrational Spectroscopy

Graham R. Fleming, Nicholas H. C. Lewis, E. A. Arsenault, Eric C. Wu and Sabine Oldemeyer

Abstract Two-dimensional infrared and electronic spectroscopies have reached considerable levels of maturity as articles elsewhere in this volume demonstrate. Two-dimensional electronic-vibrational (2DEV) spectroscopy.

2.1 Introduction

Two-dimensional infrared and electronic spectroscopies have reached considerable levels of maturity as articles elsewhere in this volume demonstrate. Two-dimensional electronic-vibrational (2DEV) spectroscopy brings together some of the advantages of both the degenerate spectroscopies, but also contains new information not readily obtainable from other time-resolved spectroscopies. 2DEV spectroscopy can be viewed as a kind of extreme cross peak spectroscopy (see Fig. 2.1) where the very large frequency difference between the visible and infrared pulses precludes the convenient use of phase matching techniques to isolate the signal of interest. This brings in the need to utilize phase cycling detection methods so that the experiment can be performed in the pump-probe geometry.

2.2 The Information Content of 2DEV Spectroscopy

2DEV spectroscopy contains a wide variety of different types of information, some of which appear to be unique to the method. The fundamental aspect of 2DEV spectra

G. R. Fleming (✉) · E. A. Arsenault · E. C. Wu · S. Oldemeyer
Department of Chemistry, University of California Berkeley, Berkeley, USA
e-mail: grfleming@lbl.gov

Molecular Biophysics and Integrated Bioimaging Division, Lawrence Berkeley National Laboratory, Berkeley, CA 94720, USA

N. H. C. Lewis
James Franck Institute, The University of Chicago, Chicago, IL 60637, USA

M. Cho (ed.), *Coherent Multidimensional Spectroscopy*,
Springer Series in Optical Sciences 226,
https://doi.org/10.1007/978-981-13-9753-0_2

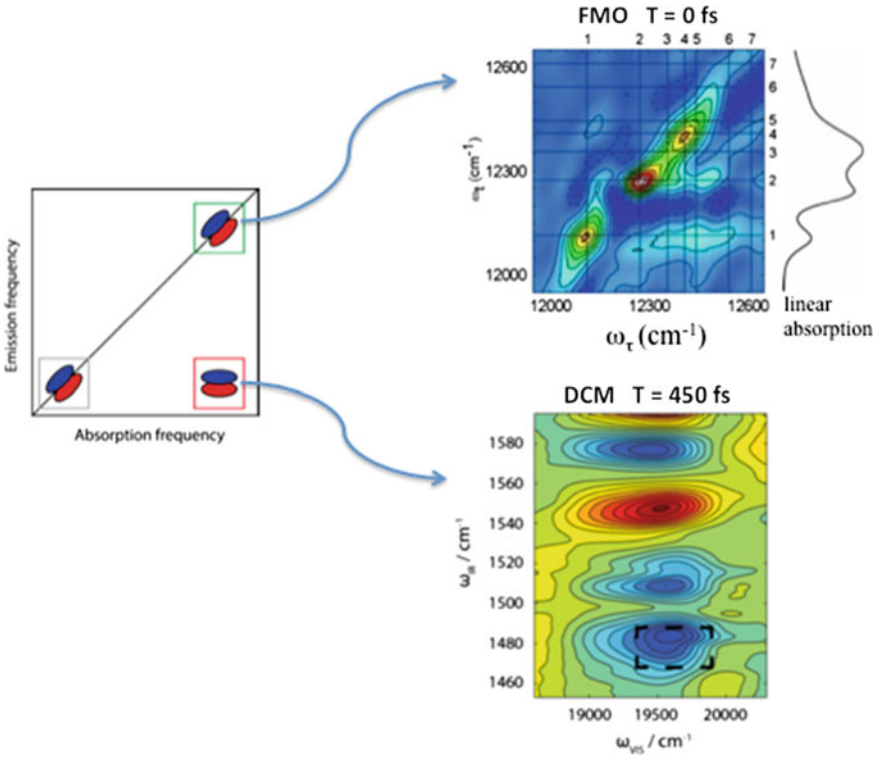

Fig. 2.1 Left: two-dimensional spectroscopies and their relative positions in frequency space. Both 2DIR and 2DES lie on the diagonal while 2DEV corresponds to an extreme cross peak. Right Upper: example experimental spectra for 2DES [1] with some of the typical information gained to the right. Right Lower: experimental 2DES spectrum for the dye DCM in methanol [2] along with typical information context

as a function of waiting time is that they correlate the electronic and nuclear dynamics so that, for example the degree of concertedness in a proton coupled electron transfer can be directly assessed from the changes and the spectral features along the two axes. The much higher spectral resolution of vibrational versus electronic spectra enable, for example, clear resolution of the 5- or 6-coordinate chlorophyll species in solution [3], or readily distinguishing chlorophyll b from chlorophyll a in the congested spectrum of a light harvesting complex containing both [4]. In both these cases the 2D electronic spectrum lacks the spectral resolution to distinguish these species. Perhaps nearly unique to chlorophyll bound in photosynthetic proteins, the fact that vibrational frequencies are little affected by whether the chlorophyll is electronically excited or not [5–7], but somewhat sensitive the specific binding site, enables a mapping of evolution in energy to evolution in space [4]. 2DEV spectroscopy in conjunction with high-level electronic structure calculation enables dynamics on complex potential energy services to be followed [8]. Here the vibrational intensity profiles as a function of waiting time as well as the 2DEV lineshapes provide impor-

tant new information [8]. The evolution of the 2DEV lineshape as characterized by the center line slope (CLS) appears to provide novel information [8–10]. The CLS decay provides vibrational dephasing rates and information on the relative strengths vibrational coupling to phonons in ground and excited electronic states. Because the CLS can be positive, negative, or zero depending on the sign of the correlation between the distribution of the electronic frequencies and that of the vibrational frequencies, it is sensitive to rapid changes in the electronic structure such as a reverse in direction of the molecular dipole moment above and just below a conical intersection.

Figure 2.2 shows a simple example of the center line slope and its decay in this case for a dye molecule (DDTCI in $CDCl_3$) undergoing solvation dynamics [9, 10]. In this case the CLS begins with a positive slope in both spectral dimensions which decays with the same 2 ps timescale to zero. In this case the CLS was determined by simply plotting the line of maximum points versus either frequency axis, though we have found that when the line is asymmetric the precision with which the CLS can be determined is higher when the slope is determined with respect to the visible axis because of the higher number of points in that dimension [8]. Although the CLS behavior shown in Fig. 2.2 is quite straightforward we have found much richer CLS behavior in 2DEV spectra taken for the major light-harvesting complex, LHCII [4, 11]. At first sight it might be expected that systems with ultrafast dynamics such as electronic energy transfer (EET), any correlation between vibrational and electronic frequencies would be very rapidly lost, this assumption is not correct for LHCII at

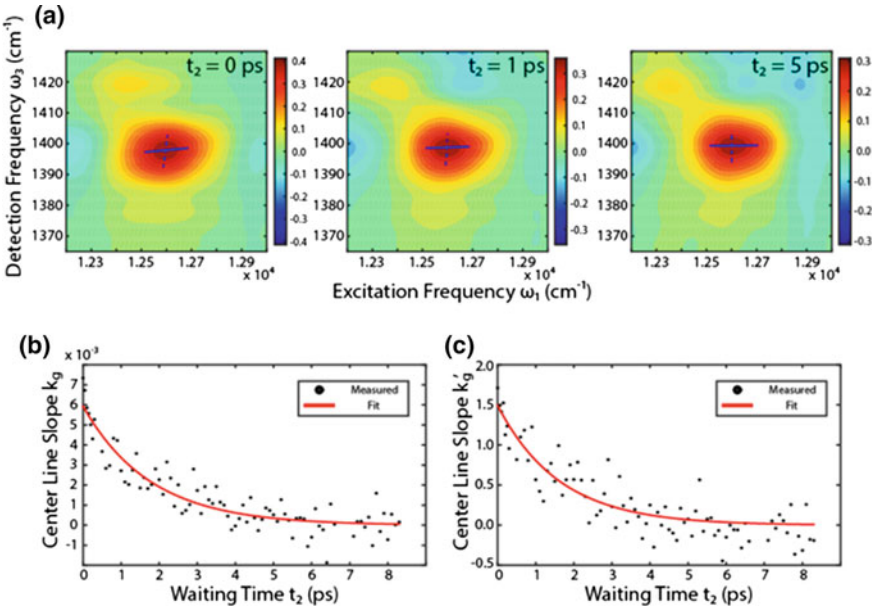

Fig. 2.2 Upper: Evolution of a single ground state bleach peak in the 2DEV spectrum of DTTCI in $CDCl_3$ [9]. The decay center line slope (CLS) of the peak obtained versus the electronic frequency axis **b** or the infrared frequency axis. **c** Both plots give the same decay time ~1.6 ps

77 K where a wide variety of rather complex CLS behavior is observed [11]. Part of the reason for this complex behavior likely arises from the bias in energy transfer rates to specific parts of the donor and acceptor inhomogeneous (on the EET timescale) distributions. We are in process of developing a full dynamic theory for the CLS in EET systems.

The comments above apply to individual molecules in an ensemble or to multi-component systems where the mixing (coupling) is relatively weak. In more strongly coupled systems the 2DEV spectrum becomes considerably more complex with multiple new pathways being opened up in vibronically mixed systems. In a strongly vibronic-coupled system, such as a molecular dimer with strong electronic coupling, there are a number of new factors that come into interpretation of a 2DEV spectrum. First, the initial populations of the various exciton levels, for example, the six excitons in a dimer with each monomer having a single vibration, will vary strongly with only the nearly pure electronic levels, and (near) resonant vibronic level(s) carrying significant oscillator strength. Second, for the third and fourth interactions the infrared transition moments must be considered. IR transitions that are mostly within one molecule will be significantly stronger than those involving "cross-molecule" excitation. Conversely, weak optical transitions that might not be discernable in the electronic spectrum or in a 2D electronic spectrum can become evident in a 2DEV spectrum through the IR transition moments. Additionally, relaxation pathways induced by vibronic coupling to the phonon bath must be considered. The combination of all these factors is required to analyze a strongly coupled vibronic system.

Two aspects of a moderately strongly coupled vibronic system that deserve comment are (1) peaks that involve coherences between vibronic states can be strong at short times. Such coherences decay on timescales of a few hundred (200–300) fs [12], rather slower than pure electronic coherences that might be observed in 2D electronic spectra. The amplitude of the vibronic coherences may also show weak oscillations [12]. (2) While in weakly coupled systems it is often possible to avoid vibrational excitation in the excited state by suitable selection of the visible pump bandwidth and center wavelength, this is likely to be more difficult in vibronic systems as a result of the level spacing and oscillator strengths. This means that simple discrimination of the ground and excited state features by the sign of the 2DEV peaks may no longer be possible as excited state stimulated IR emission becomes possible [12, 13].

To date 2DEV spectroscopy has been applied to the following systems: conical intersection dynamics [8, 14], proton-coupled electron transfer [15, 16], energy transfer dynamics [4, 11], solvation dynamics [2, 9, 17], vibration-phonon coupling [9, 10], vibronically mixed systems [12], and metal-to-ligand charge-transfer complexes [18]. Theoretical aspects have been explored in [9–13]. In the following after describing the experimental system we have constructed [2, 19] and signal extraction [19] we focus on an application to barrierless photochemical reactions.

2.3 Experimental Design

A schematic of the experimental setup, which is essentially a high time resolution transient IR absorption spectrometer with the addition of a pulse shaper into the visible pump beam, is shown in Fig. 2.3. The excitation laser is derived either directly from a Ti:Sapphire (Ti:Saph) regenerative amplifier (Coherent Legend Elite) seeded by a Ti:Saph oscillator (Coherent Micra), or from a home-build non-collinear optical parametric amplifier (NOPA). The IR probe pulse is derived from a home-built near-IR OPA equipped with difference frequency generation between the signal and idler to convert the laser to the mid-IR [20, 21].

After the pump beam passes through the prism compressor immediately following the NOPA, it is rotated by a half wave plate to the polarization required for the pulse shaper (Fastlite Dazzler). The pulse shaper is used to compress the pulse to nearly the Fourier transform limit, and to split the pulse into two identical pulse pairs with a controlled time delay t_1, as well as a controlled relative phase φ_{12}. The details of the phase cycling used to isolate the 2DEV signal are described below. The pump pulse pair is then reflected from a retroreflector mounted on a computer-controllable delay stage (Newport) which is used to control the relative delay between the visible pump pulse and the IR probe pulse t_2. The beam is then passed through another half wave plate mounted on a computer controllable rotation stage (Thorlabs) to control the relative polarization between the pump and probe beams, allowing for the measurement of the anisotropy response of the transient signal. The pump beam is then focused into the sample by a silver coated $f = 25$ cm 90° off-axis parabolic mirror (OAP) to a spot of ~250 μm, where it is spatially overlapped with the IR probe beam.

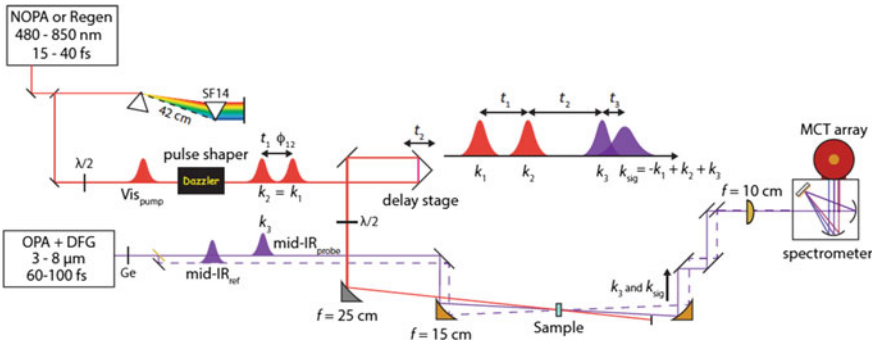

Fig. 2.3 Schematic of the 2DEV experimental setup. The visible pump beam is shown in red, and the IR probe beam is shown in purple. The t_1 time delay and ϕ_{12} relative phase difference between the pump pulse pair is generated and controlled by the pulse shaper (Dazzler), while the t_2 time delay between the pump and the probe is controlled with the delay stage. A reference beam (dashed purple line) follows next to the probe beam through the sample and is imaged onto a second array in the detector. The signal is self heterodyned by the collinear probe beam. The relative polarization between the pump and the probe is determined by the half wave plate in the pump beam before the focusing OAP

The IR beam, which, for alignment purposes, is combined with a mode-matched He–Ne on the mid-IR long-pass filter in the OPA, first passes through a series of Ge plates (removed during alignment with the He–Ne). These are used to compress the pulse by compensating for the other materials in the probe line, such as the ZnSe beam splitter, the CaF_2 sample windows and, if the experiment is performed at cryogenic temperatures, the ZnS and CaF_2 cryostat windows [22]. The reference beam is then split from the probe beam with a ZnSe beamsplitter (∼40% R). The probe and reference beams are focused through the sample by a $f = 15$ cm 90° gold coated OAP to a spot size of ∼160 μm, such that the focal spots of the probe and reference are displaced and only the probe is overlapped with the pump beam. The beams are then recollimated by a matched OAP, and focused onto the slit of a spectrometer (HORIBA TRIAX 190) with a $f = 10$ cm ZnSe lens, such that the probe and reference beams are imaged onto the two 64 element HgCdTe photodiode arrays of the detector (Infrared Associates). The signal is then passed through a 128-channel boxcar integrator (Infrared Systems Development) balanced to match the responses of the individual HgCdTe elements. The probe spectrum is then normalized by the reference spectrum on a pulse-to-pulse basis to mitigate the fluctuations in the IR laser power.

2.4 Signal Extraction

The 2DEV signal can be considered as arising from a time dependent third-order polarization, which can be calculated using standard perturbation theory approaches [23] as the triple convolution of the third-order response function $S^{(3)}(t_1, t_2, t_3)$ with the electric field of the laser pulses $E(t)$ given by

$$\begin{aligned} P^{(3)}(t) =& S^{(3)} \otimes E \otimes E \otimes E \\ =& \int_0^\infty \int_0^\infty \int_0^\infty S^{(3)}(\tau_1, \tau_2, \tau_3) E(t - \tau_1 - \tau_2 - \tau_3) \\ & E(t - \tau_2 - \tau_3) E(t - \tau_3) \mathrm{d}\tau_1 \mathrm{d}\tau_2 \mathrm{d}\tau_3 \end{aligned}$$

For a sequence of three short laser pulses, the electric field at the sample can be described as

$$E(t) = \sum_{i=1}^{3} A_i(t - t_1) \exp\left[-i\omega_i^0(t - t_i) - i\phi_i + i\mathbf{k}_i \cdot \mathbf{r}\right]$$

where A_i is the time dependent amplitude, ω_i^0 is the carrier frequency, ϕ_i is the carrier-envelope phase imparted by the pulseshaper and $\mathbf{k}_i$ is the wavevector.

Traditional degenerate or near-degenerate 2D spectroscopic techniques can take advantage of these phase matching conditions to generate the desired signal spatially separated from the other undesired signals by arranging the three beams in useful geometries, such as the square so-called boxcar geometry [24]. For highly non-degenerate experiments like 2DEV, however, the geometries necessary, while not impossible [25], become difficult and impractical. This is due to the nearly order of magnitude difference between the wavelengths of the visible pump pulses and the IR probe pulse, which affects the phase matching direction by the relation between the magnitude of the wavevector and the wavelength of the light $|\mathbf{k}| = 2\pi/\lambda$. Because of the practical difficulties of implementing the experimental geometries necessary for the background-free 2DEV signal, especially when accounting for the necessity of accurate and stable sub-wavelength delay control of the visible pulses for the interferometric measurement of the photon echo signal, it is highly advantageous to instead use the partially collinear pump-probe geometry $\mathbf{k}_1 = \mathbf{k}_2 \neq \mathbf{k}_3$ with phase cycling methods to isolate the desired signal from the background. In the pump-probe geometry, the signal that is detected will include the desired 2DEV signal together with the transient absorption arising from two interactions with either of the visible pump pulses and the static background of the probe beam. The total measured amplitude to third order is given by

$$\begin{aligned}\left|\tilde{S}_T^{(3)}(t_1,t_2,\omega_3;\Delta\phi_{12})\right|^2 &= \left|\left(\tilde{S}_{123}^{(3)}(t_1,t_2,\omega_3)+\tilde{S}_{113}^{(3)}(t_1,t_2,\omega_3)+\tilde{S}_{223}^{(3)}(t_1,t_2,\omega_3)+1\right)E_3(\omega_3)\right|^2 \\ &= \left|\tilde{S}_{123}^{(3)}(t_1,t_2,\omega_3)E_3(\omega_3)\right|^2+\left|\left(\tilde{S}_{113}^{(3)}(t_1,t_2,\omega_3)+\tilde{S}_{223}^{(3)}(t_1,t_2,\omega_3)+1\right)E_3(\omega_3)\right|^2 \\ &+ 2\mathrm{Re}\left[e^{i\Delta\phi_{12}}\tilde{S}_{123}^{(3)}(t_1,t_2,\omega_3)\left(\tilde{S}_{123}^{(3)}(t_1,t_2,\omega_3)+\tilde{S}_{223}^{(3)}(t_1,t_2,\omega_3)+1\right)^*\right]|E_k(t_3)|^2\end{aligned}$$

where

$$\tilde{S}_{ij3}^{(3)}(t_1,t_2,\omega_3)E_k(\omega_3) = \int e^{-i\omega_3 t_3}S^{(3)}(t_1,t_2,t_3)\otimes_{t_1}E_i^*(t_1)\otimes_{t_2}E_j(t_2)\otimes_{t_3}E_3(t_3)$$

is the convolution of the third-order response function with the electric fields of the laser pulses.

The cross-terms between the 2DEV signal and the transient absorptions terms cannot be completely removed, but because they scale as the square of a third-order field they will be negligible compared to the desired signal, which is linear in the third-order field. When the probe spectrum is removed in the division by the reference spectrum, we have then effectively isolated the desired 2DEV signal. To convert this to the purely absorptive 2DEV spectrum, this signal can be Fourier transformed about t_1, though it is typically beneficial to process the data further to improve the quality of the signal.

If it is desired to separate the rephasing pathways from the nonrephasing pathways, a time domain windowing method can be used. The separation will rely on the difference in the relative sign of the phase evolution for these pathways during t_1 and t_3, which means that they can only be separated if the number of relative phases used in the phase cycling $n \geq 3$, so that both the real and imaginary parts of the signal have

been obtained. Once the phase cycling has been applied, the signal must be Fourier transformed along ω_3 to the pure time domain response. Because only the positive values of t_1 have been measured, this places the rephasing signal in the quadrant with $t_3 \leq 0$, because of the opposite signs of the phase evolution during these time periods for these pathways, while the nonrephasing signal, which evolves with the same sign during these time periods, will be constrained to the $t_3 \geq 0$ quadrant. The separate rephasing and nonrephasing spectra can then be obtained by using an appropriate windowing function to select one or the other of these regions, then converting the signal back into the frequency domain using the Fourier transform about both t_1 and t_3. It is important to note that both rephasing and nonrephasing must contain $t_3 = 0$ when performing this apodization, otherwise the projection-slice theorem will cause a dramatic distortion of the spectrum. A demonstration of the phase control capabilities with the pulse shaper is shown in Fig. 2.4.

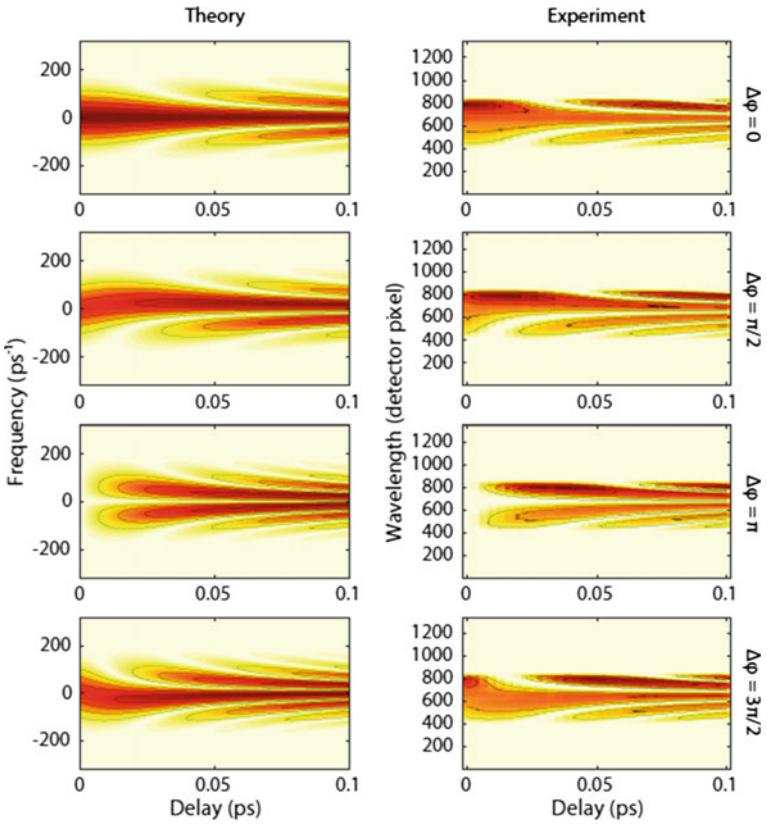

Fig. 2.4 Comparison between theoretical (left) and experimental (right) interference patterns between the pump pulse pair as a function of delay time for relative phases $\Delta\phi = 0, \pi/2, n,$ and $3\pi/2$

The interferogram generated by dispersing the pulse pair on a spectrometer is shown as a function of the delay between the pulses for a series of different relative phases between the pulses. The comparison between the measured interferograms and the interferograms calculated from a simple model shows strong agreement, which confirms that the pulse pair is being generated and controlled correctly.

2.5 Application to Barrierless Photochemical Reactions

A formalism to describe reactions that proceed without a barrier was given in 1983 by Bagchi et al. [26] Such reactions involve significant molecular rearrangement towards a region of the potential surface near to a conical intersection. Despite this early work, quantitative confrontation with real experimental systems was limited because of lack of tools to (a) calculate the electronic structure along the reaction path and (b) observe the system as it evolved on the initial and final potential surfaces. In the intervening 35 years electronic structure theory has advanced enormously and multidimensional spectroscopies have become key tools in unravelling the dynamics of complex systems. The 2DEV technique seems well-suited to address the conical intersection (CI)—related barrierless reactions because of its ability to correlate the evolution of the electronic and nuclear degrees of freedom. It thus seemed appropriate to revisit the photophysics of the triphenyl methane dyes that have served as exemplars of barrierless CI relaxation since at least the work of Forster and Hoffmann [27]. The structure of the two most common triphenyl methane dyes, crystal violet (CV) and malachite green (MG) are shown in Fig. 2.5 along with sketches of the potential surfaces as a function of the dihedral angle [8].

Figure 2.6a shows the 2D electronic spectrum for malachite green in methanol at three waiting times, recorded with 17 fs pulses. The spectra are fairly featureless but do show modulation with a frequency of 303 cm^{-1} corresponding to the in plane phenyl-C-phenyl motion observed in the Raman spectrum [28, 29]. Figure 2.6b shows the visible pump-IR probe spectrum of crystal violet. Three features are readily apparent—the ground state bleach (red contours), the rapid excited state decay (blue contours) and the delayed appearance of a new absorption band at ~1590 cm^{-1} which we assign to the twisted ground state formed after passage through the region of the CI (see below).

Figure 2.7a shows 2DEV spectra for CV in methanol where four distinct peaks are apparent and Fig. 2.7b gives 2DEV spectra for MG where in the latter five peaks are evident one with a delayed appearance.

The ability to resolve the dynamics in the 2DEV spectrum becomes more apparent when the time dependence of the amplitude of the peaks is plotted as in Fig. 2.8.

Taking the case of CV in methanol and propanol as an example, the fact that the 1513 cm^{-1} peak reaches the maximum promptly but the 1577 cm^{-1} peak has a slower and viscosity dependent rise suggests the two peaks arise from differing locations on the excited state potential surface sketched in Fig. 2.5. In combination with electronic structure and vibrational oscillator strength calculations we assign the 1513 cm^{-1}

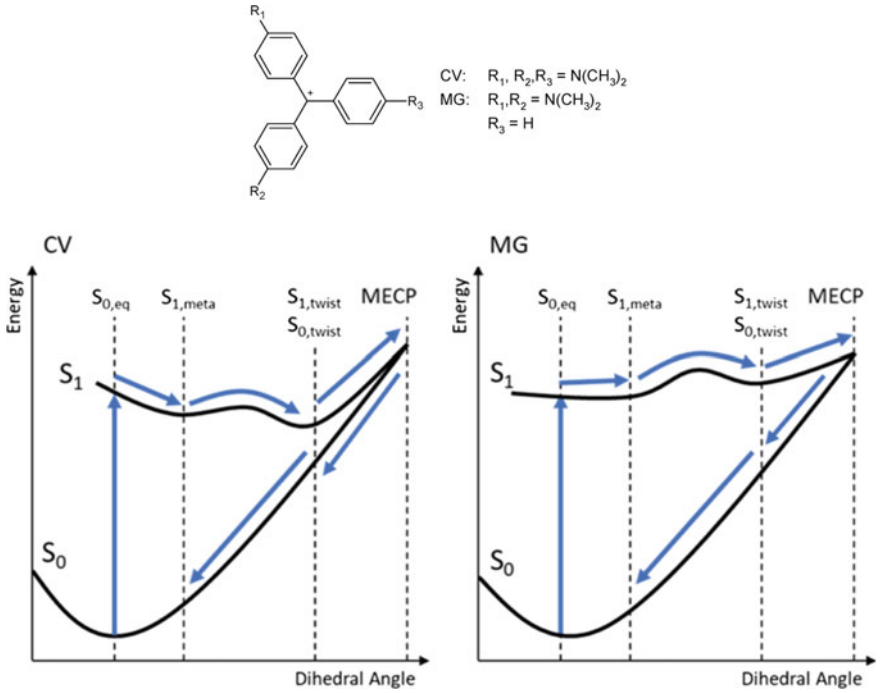

Fig. 2.5 (top) Structure of crystal violet and malachite green. (bottom) Schematic potential surfaces as a functions of dihedral angle for crystal violet (left) and malachite green (right) [8] MECP: Minimum energy crossing point

peak to the Franck Condon/$S_{1,\mathrm{meta}}$ region while the 1577 cm^{-1} peak is assigned to the S_1 minimum. Very apparent is the delayed and viscosity-dependent appearance of the 1589 cm^{-1} peak which we assign to the ground state immediately after passage through the CI (Note the different timescales on the plots for methanol and propanol). More evidence for this scenario comes from the center line slopes (CLS) for the two molecules shown in Fig. 2.9. Beginning with the crystal violet data we see that the CLS for the ground state bleach is positive, indicating positive correlation between the electronic and vibrational frequencies (the negative CLS after ~3 ps likely arises from overlap with the new twisted ground state band at 1589 cm^{-1}). In contrast the band assigned to $S_{1,\mathrm{min}}$ has a clear negative CLS initially while the twisted ground state band has a positive CLS immediately on appearance. This is not the case in malachite green where no sign change is evident in the three CLS plots in Fig. 2.9. These results are entirely consistent with the electronic structure calculations of Ge and Head-Gordon [8] who find that in CV the molecular dipole moment reverses direction between $S_{1,\mathrm{min}}$ and the twisted ground state (the equilibrium ground state in CV has no dipole moment). In contrast, for MG the direction of the molecular dipole moment remains the same above and below the CI. Thus, the CLS is a valuable

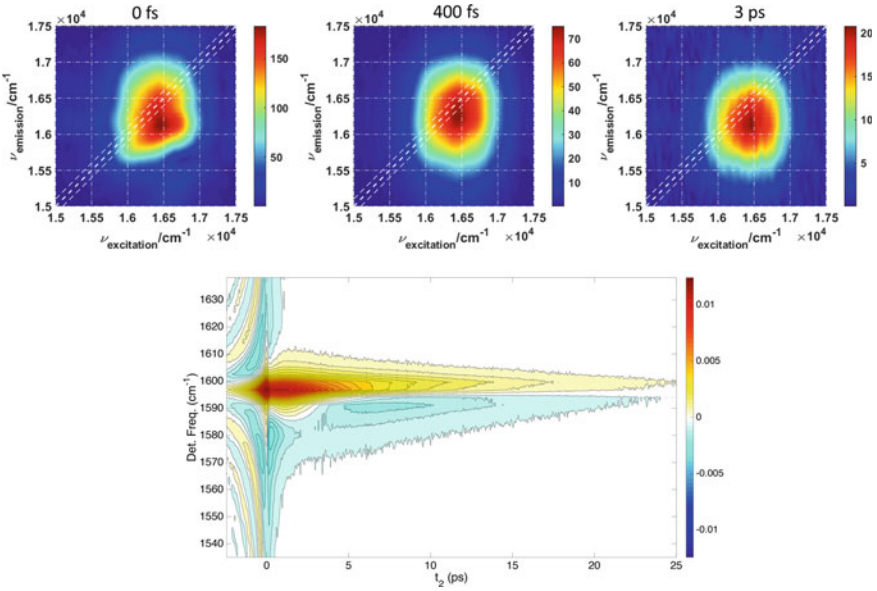

Fig. 2.6 Top: 2DES for malachite green in methanol at three waiting times. Bottom: Visible pump-IR probe data for crystal violet in MEOD

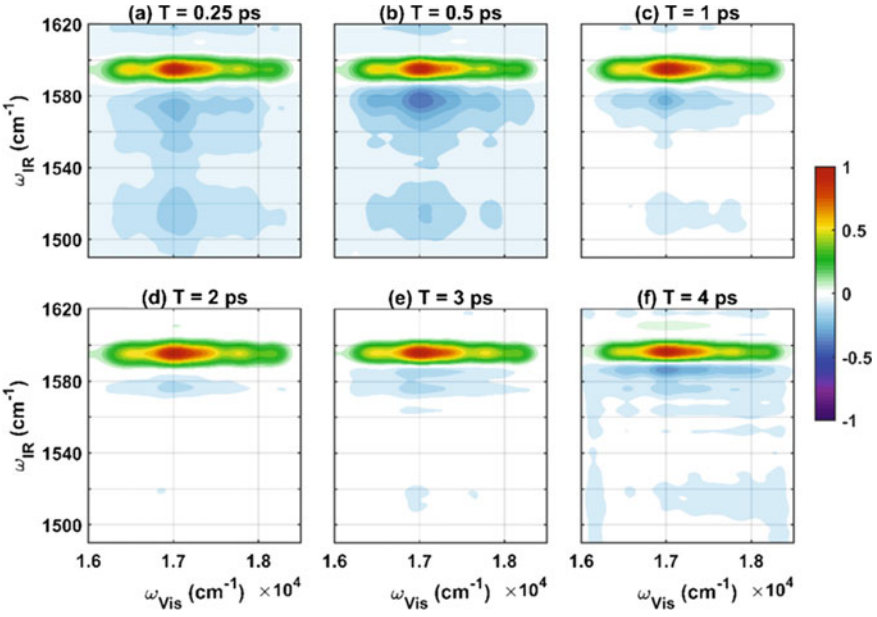

Fig. 2.7 2DEV spectra for crystal violet in MEOD at six waiting times [8]. The 2DEV spectra for malachite green in MEOD are similar to that for crystal violet

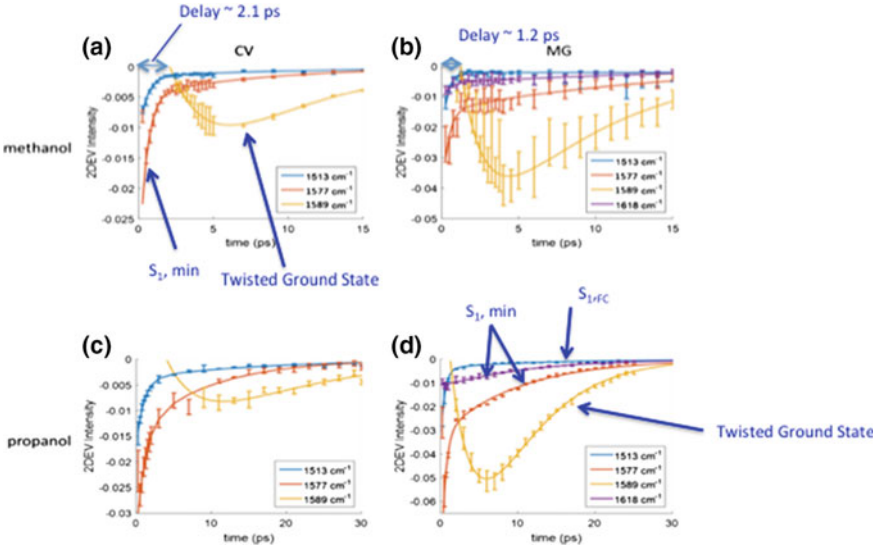

Fig. 2.8 Time dependence of the infrared peaks from the 2DEV spectra of crystal violet (left) and malachite green (right). Solvents methanol (**a**) and (**b**), propanol (**c**) and (**d**) The solid lines are bi-exponential fits to the data

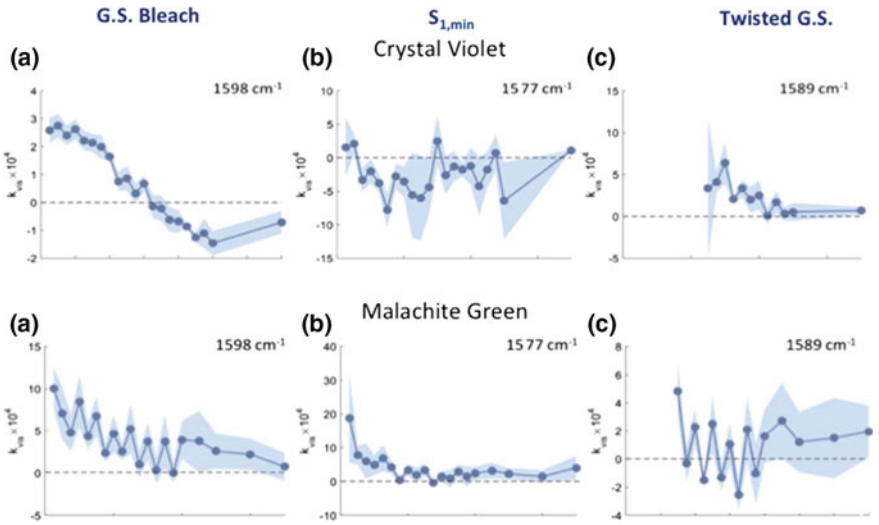

Fig. 2.9 Center line slopes for crystal violet (top row) and malachite green (bottom row) for the bands indicated on the figure. Solvent methanol

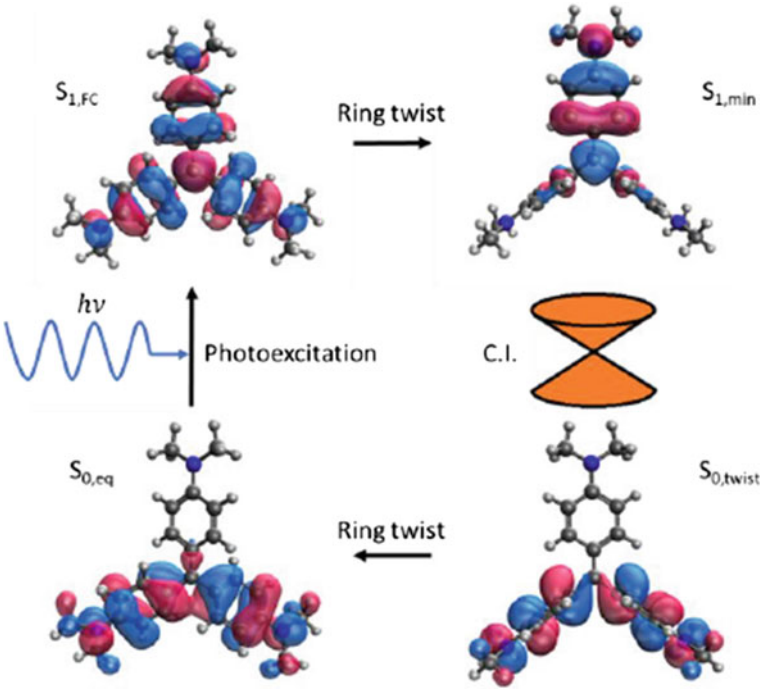

Fig. 2.10 A cartoon illustrating the photoinduced excitation, subsequent evolution and ultimate radiationless decay through conical intersection of CV. The orbitals pictured are the dominant virtual NTOs for $S_{1,FC}$ and $S_{1,min}$ and the dominant occupied NTOs for $S_{0,eq}$ and $S_{0,twist.}$ Reproduced with permission from [8]

tool for exploring the large changes in electronic structure accompanying conical intersection dynamics.

A summary of the sequence of events is given in Fig. 2.10 using the dominant natural transition orbitals (NTOs) [30] to illustrate the remarkable changes in electronic structure in the apparently simple system.

2.6 Concluding Comments

2DEV spectroscopy provides a significant addition to the tool box of coherent multidimensional spectroscopies. In addition to enhanced resolution of medium frequency vibrational features giving clear insight into reactions involving both nuclear and electronic rearrangements such as proton-coupled electron transfer, it provides novel information via the center line slope of the spectral features, and reveals vibronic coherences in strongly coupled systems. No doubt many other perspectives will

emerge from 2DEV spectroscopy of complex material and molecular systems as the theoretical underpinnings of the experiment continue to be developed.

Acknowledgements The development of 2DEV spectroscopy was supported by the US Department of Energy, Office of Science, Basic Energy Sciences, Chemical Sciences, Geosciences, and Biosciences Division under Field Work proposal 449A and by the National Science Foundation grant CHE-18000345. We are very grateful for the collaboration and expertise of Q. Ge and M. Head-Gordon on electronic structure calculations. S.O. was supported by a Fellowship from Deutsche Forschungsgemeinschaft (DFG), Forschungsstipendium, grant OL-555 1-1.

References

1. T. Brixner, J. Stenger, H.M. Vaswani et al., Two-dimensional spectroscopy of electronic couplings in photosynthesis. Nature **434**, 625–628 (2005). https://doi.org/10.1038/nature03429
2. T.A.A. Oliver, N.H.C. Lewis, G.R. Fleming, Correlating the motion of electrons and nuclei with two-dimensional electronic-vibrational spectroscopy. Proc. Natl. Acad. Sci. **111**, 10061–10066 (2014). https://doi.org/10.1073/pnas.1409207111
3. N.H.C. Lewis, G.R. Fleming, Two-dimensional electronic-vibrational spectroscopy of chlorophyll a and b. J. Phys. Chem. Lett. **7**, 831–837 (2016). https://doi.org/10.1021/acs.jpclett.6b00037
4. N.H.C. Lewis, N.L. Gruenke, T.A.A. Oliver et al., Observation of electronic excitation transfer through light harvesting complex ii using two-dimensional electronic-vibrational spectroscopy. J. Phys. Chem. Lett. **7**, 4197–4206 (2016). https://doi.org/10.1021/acs.jpclett.6b02280
5. Y. Jia, J.M. Jean, M.M. Werst et al., Simulations of the temperature dependence of energy transfer in the PSI Core Antenna. Biophys. J. **63**, 259–273 (1992). https://doi.org/10.1016/S0006-3495(92)81589-8
6. J.K. Gillie, G.J. Small, J.H. Golbeck, Nonphotochemical Hole Burning of the native Antenna complex of photosystem I (PSI-200). J. Phys. Chem. **93**, 1620–1627 (1989). https://doi.org/10.1021/j100341a085
7. K.K. Rebane, R.A. Avarmaa, Sharp line vibronic spectra of chlorophyll and its derivatives in solid solutions. Chem. Phys. **68**, 191–200 (1982). https://doi.org/10.1016/0301-0104(82)85094-5
8. E.C. Wu, Q. Ge, E.A. Arsenault et al., Two-dimensional electronic-vibrational spectroscopic study of conical intersection dynamics: an experimental and electronic structure study. Phys. Chem. Chem. Phys. **21**, 14153 (2019). https://doi.org/10.1039/C8CP05264F
9. N.H.C. Lewis, H. Dong, T.A.A. Oliver, G.R. Fleming, Measuring correlated electronic and vibrational spectral dynamics using line shapes in two-dimensional electronic-vibrational spectroscopy. J. Chem. Phys. **142**, 174202 (2015). https://doi.org/10.1063/1.4919686
10. H. Dong, N.H.C. Lewis, T.A.A. Oliver, G.R. Fleming, Determining the static electronic and vibrational energy correlations via two-dimensional electronic-vibrational spectroscopy. J. Chem. Phys. **142**, 174201 (2015). https://doi.org/10.1063/1.4919684
11. E.C. Wu, E.A. Arsenault, P. Bhattacharyya et al., Two-dimensional electronic spectroscopy and ultrafast excitonic and vibronic photosynthetic energy transfer. Faraday Discuss. **216**, 116–132 (2019). https://doi.org/10.1039/C8FD00190A
12. P. Bhattacharyya, G.R. Fleming, A near analytical approach to simulating 2DEV spectra in vibrationally assisted electronic energy transport (VAEET). J. Chem. Phys. Lett. (In Press)
13. J.D. Gaynor, M. Khalil, Signatures of vibronic coupling in two-dimensional electronic-vibrational and vibrational-electronic spectroscopies. J. Chem. Phys. **147**, 094202 (2017). https://doi.org/10.1063/1.4991745

14. T.A.A. Oliver, G.R. Fleming, Following coupled electronic-nuclear motion through conical intersections in the ultrafast relaxation of β-Apo-8′-carotenal. J. Phys. Chem. B **119**, 11428–11441 (2015). https://doi.org/10.1021/acs.jpcb.5b04893
15. E. Odella, S.J. Mora, B.L. Wadsworth et al., Controlling proton-coupled electron transfer in bioinspired artificial photosynthetic relays. J. Am. Chem. Soc. **140**, 15450–15460 (2018). https://doi.org/10.1021/jacs.8b09724
16. M.T. Huynh, S.J. Mora, M. Villalba et al., Concerted one-electron Two-proton transfer processes in models inspired by the Tyr-His couple of photosystem II. ACS Cent. Sci. **3**, 372–380 (2017). https://doi.org/10.1021/acscentsci.7b00125
17. F. Terenziani, A. Painelli, Two-dimensional electronic-vibrational spectra: modeling correlated electronic and nuclear motion. Phys. Chem. Chem. Phys. **17**, 13074–13081 (2015). https://doi.org/10.1039/C5CP01485A
18. J.D. Gaynor, A. Petrone, X. Li, M. Khalil, Mapping vibronic couplings in a solar cell dye with polarization-selective two-dimensional electronic-vibrational spectroscopy. J. Phys. Chem. Lett. **9**, 6289–6295 (2018). https://doi.org/10.1021/acs.jpclett.8b02752
19. N.H.C. Lewis, Two-dimensional electronic-vibrational spectroscopy. Ph.D. Thesis, (University of California, Berkeley, 2016)
20. P. Hamm, R.A. Kaindl, J. Stenger, Noise suppression in femtosecond mid-infrared light sources. Opt. Lett. **25**, 1798 (2000). https://doi.org/10.1364/OL.25.001798
21. A.J. Van Tassle Excited state structural dynamics of carotenoids and charge transfer system. Ph.D. Thesis, (University of California, Berkeley, 2006)
22. N. Demirdöven, M. Khalil, O. Golonzka, A. Tokmakoff, Dispersion compensation with optical materials for compression of intense Sub-100-fs Mid-Infrared Pulses. Opt. Lett. **27**, 433 (2002). https://doi.org/10.1364/OL.27.000433
23. S. Mukamel, *Principles of Nonlinear Optical Spectroscopy*. (Oxford University Press, 1995)
24. T. Brixner, T. Mančal, I.V. Stiopkin, G.R. Fleming, Phase-stabilized two-dimensional electronic spectroscopy. J. Chem. Phys. **121**, 4221–4236 (2004). https://doi.org/10.1063/1.1776112
25. P.M. Donaldson, H. Strzalka, P. Hamm, High sensitivity transient infrared spectroscopy: a UV/visible transient grating spectrometer with a heterodyne detected infrared probe. Opt. Express **20**, 12761 (2012). https://doi.org/10.1364/OE.20.012761
26. B. Bagchi, G.R. Fleming, D.W. Oxtoby, Theory of electronic relaxation in solution in the absence of an activation Barrier. J. Chem. Phys. **78**, 7375–7385 (1983). https://doi.org/10.1063/1.444729
27. T. Förster, G. Hoffmann, Die Viskositätsabhängigkeit der Fluoreszenzquantenausbeuten einiger Farbstoffsysteme. Zeitschrift für Phys Chemie **75**, 63–76 (1971). https://doi.org/10.1524/zpch.1971.75.1_2.063
28. L. He, N.-J. Kim, H. Li et al., Use of a fractal-like gold nanostructure in surface-enhanced Raman spectroscopy for detection of selected food contaminants. J. Agric. Food Chem. **56**, 9843–9847 (2008). https://doi.org/10.1021/jf801969v
29. E.J. Liang, X.L. Ye, W. Kiefer, Surface-enhanced Raman spectroscopy of crystal violet in the presence of halide and halate ions with near-infrared wavelength excitation. J. Phys. Chem. A **101**, 7330–7335 (1997). https://doi.org/10.1021/jp971960j
30. R.L. Martin, Natural transition orbitals. J. Chem. Phys. **118**, 4775–4777 (2003). https://doi.org/10.1063/1.1558471

Chapter 3
Nuclear Wave-Packet Dynamics in Two-Dimensional Interferograms of Excitation-Transfer Systems

Jeffrey A. Cina and Alexis J. Kiessling

Abstract We propose a general framework for calculating and interpreting multidimensional electronic spectroscopy signals in terms of the wave-packet-shaping, amplitude-transferring effects of femtosecond laser pulses on time-dependent molecular states. The chapter sets up basic expressions for two-dimensional wave-packet interferometry (WPI) experiments on an electronic energy-transfer (EET) system as a quantum yield-weighted sum of contributing overlaps between multi-pulse wave packets. Further, we identify the ranges of interpulse delay within which each overlap is not excluded by its order of pulse action from contributing to the WPI signal. Example calculations are carried out for the case of a spatially oriented, weakly-coupled EET dimer. Semiclassical analyses of the necessary conditions for phase-space coincidence between the bra and ket, the dynamical consequences of a site-energy difference between the two chromophores, and the sensitivity of contributions accessing or originating from doubly electronically excited states of the dimer to the possible presence of an exciton shift all provide physical interpretations of individual wave-packet overlaps.

3.1 Introduction

Optically phase-coherent two-dimensional electronic spectroscopy has proved itself in recent years as an effective technique for revealing unprecedentedly detailed information on electronic excitation transfer (EET) within chromophore arrays [1, 2]. Because the molecular systems under study often comprise several participating excitation sites and a large number of interacting vibrational modes, all present in

J. A. Cina (✉) · A. J. Kiessling
Department of Chemistry and Biochemistry and Oregon Center for Optical, Molecular and Quantum Science, University of Oregon, Eugene, OR 97403, USA
e-mail: cina@uoregon.edu

A. Kiessling
e-mail: kiesslingalexis@gmail.com

M. Cho (ed.), *Coherent Multidimensional Spectroscopy*,
Springer Series in Optical Sciences 226,
https://doi.org/10.1007/978-981-13-9753-0_3

a variety of overall orientations with respect to the polarization of the incident light pulses, their signals' simulation and interpretation can become rather involved [3–5].

Here, for the sake of sharpening our thinking about some basic aspects of the information content of multi-dimensional spectroscopy and its interpretation in terms of the underlying, entangled electronic and nuclear dynamics, we undertake an exercise of reframing the basic theory with an emphasis on the role of nonstationary nuclear wave functions under the influence of laser pulse- and energy transfer-driven transitions among relevant site, adiabatic, or spatially-extended exciton states. While our treatment conforms in its physical content with those based on nonlinear optical response functions, its set-up differs from conventional approaches in reversing the order of quantum-mechanical averaging and temporal integration over the external fields. It performs the latter operation *first*, with the interpretive and computational advantages that the analysis then turns on the dynamics of the nonstationary molecular states actually prepared and probed by phase-coherent, short-pulse optical spectroscopy.

This work expands on a previous study by Cina et al. [6], who investigated two-dimensional signals from model systems similar to that used for illustration here, but made some additional simplifying assumptions. The model used here consists of a dimer that interacts with four identically shaped laser pulses resonant with the bare electronic transition frequency of the constituent chromophores. The total time-dependent wave function is expressed as a sum of nuclear wave packets evolving in different electronic states that have various different interactions with the pulses. The quantum mechanical overlaps of these wave packets give rise to the 2D ES signal. The dynamics of an individual wave packet is determined by its episodes of motion under the relevant vibronic Hamiltonians describing both evolution on a particular electronic potential energy surface and energy-transfer and/or nonadiabatic transitions between surfaces, interspersed with pulse actions that shape it and also effect its inter-surface transfer. The resulting spectra, plotted with respect to combinations of pulse-to-pulse delay times, are interpreted in terms of these dynamics.

In addition to the prior analysis of Cina, Kilin, and Humble, other works somewhat similar in spirit include that carried out by Tiwari et al. [7] to explore the origin of oscillating peaks in 2D ES spectra and a theoretical study of the transfer and trapping of coherent vibrational motion in EET by Cina and Fleming [8]. The latter provided an explanation for the behavior of vibrational quantum beats observed in time-resolved polarized fluorescence up-conversion measurements of LH-1 by Bradforth et al. [9], and the analysis of Tiwari et al. endeavored to illuminate the roles of coherent electronic and vibrational dynamics in producing signal oscillations from EET systems. Both of those reports make use of models similar to the one studied here. Butkus et al. [10] explored similar questions, comparing calculated signals from a monomer model with only vibronic coupling and a dimer model with only electronic coupling. Biggs and Cina investigated the influence that preparing nonstationary states of nuclear motion can exert on EET after subsequent electronic excitation [11–13].

In a four-wave mixing (FWM) rendition of 2D ES, the experiments detect the interference between a laser pulse that serves as a local oscillator and a signal beam

emitted by the oscillating third-order dipole moments induced in the sample by the other three pulses [14]. While it is possible to describe this kind of signal using a wave-packet framework, we restrict ourselves for the present to wave-packet interferometry (WPI) by fluorescence detection. Two-dimensional fluorescence spectroscopy measurements employing optical phase modulation came into prominence with the works of Tekavec et al. [15] and Lott et al. [16]. With certain differences due to fluorescence-yield weighting of contributions from singly- versus doubly-excited electronic states, phase-modulated WPI signals effect an isolation of sum- and difference-phased overlap combinations that is similar to the separation in FWM approaches between different wave-vector-matched directions.

This chapter continues by describing an EET dimer model consisting of interacting chromophores whose states of electronic excitation are coupled to a collection of intra-complex or environmental vibrational degrees of freedom. Basic expressions are derived for the fluorescence-detected wave-packet interferometry signal resulting from the dimer's interaction with two optically phase-controlled ultrashort laser pulse-pairs. Contributions to the 2D WPI signal are calculated for the exemplary case of a spatially-oriented pair of weakly-coupled monomers with perpendicular electronic transition moments, each possessing a single Franck-Condon-active internal vibrational mode.

3.2 Energy-Transfer Dimer

We start by describing a molecular dimer model comprising four *site states*, $|\bar{g}g\rangle$, $|\bar{e}g\rangle$, $|\bar{g}e\rangle$, and $|\bar{e}e\rangle$, in which neither, one, or both of the monomers are electronically excited.[1] Such a complex can exhibit electronic energy (or excitation) transfer between the two singly excited states. The dimer Hamiltonian is $H = T + H_{el}(\hat{Q})$, where T is the nuclear kinetic energy. The electronic Hamiltonian in the site basis is

$$\begin{aligned} H_{el}(Q) = {} & |\bar{g}g\rangle V_{\bar{g}g}(Q)\langle\bar{g}g| + |\bar{e}g\rangle V_{\bar{e}g}(Q)\langle\bar{e}g| + |\bar{g}e\rangle V_{\bar{g}e}(Q)\langle\bar{g}e| \\ & + |\bar{e}e\rangle V_{\bar{e}e}(Q)\langle\bar{e}e| + J(Q)(|\bar{e}g\rangle\langle\bar{g}e| + |\bar{g}e\rangle\langle\bar{e}g|) \; . \end{aligned} \tag{3.1}$$

Q stands for the full collection of intramolecular and intermolecular nuclear coordinates, including those of any surrounding medium. Alternatively, the electronic Hamiltonian can be expressed in terms of the *adiabatic electronic states* as

$$\begin{aligned} H_{el}(Q) = {} & |0\rangle E_0(Q)\langle 0| + |\bar{1}(Q)\rangle E_{\bar{1}}(Q)\langle\bar{1}(Q)| \\ & + |1(Q)\rangle E_1(Q)\langle 1(Q)| + |2\rangle E_2(Q)\langle 2| \; . \end{aligned} \tag{3.2}$$

It is easy to specify the relationship between these two representations. Let

[1] The monomers may be the same or different. Our model neglects states such as $|\bar{e}'g\rangle$ or $|\bar{e}'e''\rangle$ in which one or both of the molecules occupy higher-lying electronic excited states.

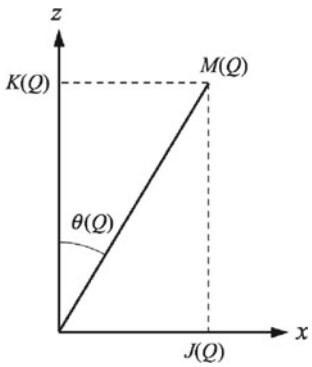

Fig. 3.1 Parameters of the electronic Hamiltonian. $J(Q)$ is the energy-transfer coupling at nuclear configuration Q. $K(Q)$ is half the local site-energy difference. $M(Q)$ is half the resultant energy difference between adiabatic singly-excited electronic states

$$\mathcal{P}_{\text{one}} = |\bar{e}g\rangle\langle\bar{e}g| + |\bar{g}e\rangle\langle\bar{g}e| \,, \tag{3.3}$$

$$\sigma_x = |\bar{e}g\rangle\langle\bar{g}e| + |\bar{g}e\rangle\langle\bar{e}g| \,, \tag{3.4}$$

$$\sigma_y = -i|\bar{e}g\rangle\langle\bar{g}e| + i|\bar{g}e\rangle\langle\bar{e}g| \,, \tag{3.5}$$

and

$$\sigma_z = |\bar{e}g\rangle\langle\bar{e}g| - |\bar{g}e\rangle\langle\bar{g}e| \,. \tag{3.6}$$

Introducing the following functions of nuclear coordinates,

$$K(Q) = \frac{1}{2}\big(V_{\bar{e}g}(Q) - V_{\bar{g}e}(Q)\big) \,, \tag{3.7}$$

$$L(Q) = \frac{1}{2}\big(V_{\bar{e}g}(Q) + V_{\bar{g}e}(Q)\big) \,, \tag{3.8}$$

$$M(Q) = \sqrt{J^2(Q) + K^2(Q)} \,, \tag{3.9}$$

and

$$\theta(Q) = \arctan\left(\frac{J(Q)}{K(Q)}\right) , \tag{3.10}$$

as illustrated in Fig. 3.1, allows us to rewrite (3.1) as

$$\begin{aligned} H_{el}(Q) &= |\bar{g}g\rangle\langle\bar{g}g|V_{\bar{g}g}(Q) + \sigma_x J(Q) + \sigma_z K(Q) + \mathcal{P}_{\text{one}} L(Q) + |\bar{e}e\rangle\langle\bar{e}e|V_{\bar{e}e}(Q) \\ &= |\bar{g}g\rangle\langle\bar{g}g|V_{\bar{g}g}(Q) + \mathcal{P}_{\text{one}} L(Q) \\ &\quad + e^{-i\sigma_y\theta(Q)/2}\sigma_z e^{i\sigma_y\theta(Q)/2} M(Q) + |\bar{e}e\rangle\langle\bar{e}e|V_{\bar{e}e}(Q) \,. \end{aligned} \tag{3.11}$$

The adiabatic eigenenergies appearing in (3.2) can be seen from (3.11) to be

$$E_0(Q) = V_{\bar{g}g}(Q) \,, \tag{3.12}$$

$$E_{\bar{1}}(Q) = L(Q) + M(Q) \,, \tag{3.13}$$

$$E_1(Q) = L(Q) - M(Q) \,, \tag{3.14}$$

and

$$E_2(Q) = V_{\bar{e}e}(Q) \,. \tag{3.15}$$

The ground and doubly-excited adiabatic eigenstates of the model dimer, $|0\rangle = |\bar{g}g\rangle$ and $|2\rangle = |\bar{e}e\rangle$, respectively, remain unchanged from the site basis. The singly-excited adiabatic states can be defined as

$$|\bar{1}(Q)\rangle = e^{-i\sigma_y\theta(Q)/2}|\bar{e}g\rangle \,, \tag{3.16}$$

and

$$|1(Q)\rangle = e^{-i\sigma_y\theta(Q)/2}|\bar{g}e\rangle \,. \tag{3.17}$$

The electronic Hamiltonian for this dimer has been diagonalized by a Q-dependent unitary transformation. But the remaining contribution to the full Hamiltonian, the nuclear kinetic-energy operator T, may couple the adiabatic electronic states of the single-excitation manifold in the presence of sufficiently rapid nuclear motion. We shall see shortly that the dipole moment operator connecting single-excitation states to the electronic ground state or to the doubly excited state become Q-dependent in the basis of adiabatic electronic states. This feature can complicate the description (using pulse propagators, as described below) of short-pulse-driven electronic transitions. Such complications do not arise in the site basis, with its nuclear coordinate-independent electronic states.

Another popular basis featuring Q-independent electronic states is the *exciton basis*. It consists of the four eigenstates of the electronic Hamiltonian evaluated at the equilibrium nuclear configuration of the electronic ground state $H_{el}(Q = 0)$: $|0\rangle$, $|1\rangle \equiv |1(0)\rangle$, $|\bar{1}\rangle \equiv |\bar{1}(0)\rangle$, and $|2\rangle$. The matrix elements of the electronic Hamiltonian in this basis are readily obtained. For example,

$$\begin{aligned}\langle\bar{1}|H_{el}(Q)|\bar{1}\rangle &= \langle\bar{1}|\bar{1}(Q)\rangle\langle\bar{1}(Q)|\bar{1}\rangle E_{\bar{1}}(Q) + \langle\bar{1}|1(Q)\rangle\langle 1(Q)|\bar{1}\rangle E_1(Q) \\ &= \langle\bar{e}g|e^{-i\frac{\delta\theta(Q)}{2}\sigma_y}|\bar{e}g\rangle\langle\bar{e}g|e^{i\frac{\delta\theta(Q)}{2}\sigma_y}|\bar{e}g\rangle E_{\bar{1}}(Q) \\ &\quad + \langle\bar{e}g|e^{-i\frac{\delta\theta(Q)}{2}\sigma_y}|\bar{g}e\rangle\langle\bar{g}e|e^{i\frac{\delta\theta(Q)}{2}\sigma_y}|\bar{e}g\rangle E_1(Q) \,,\end{aligned} \tag{3.18}$$

with $\delta\theta(Q) = \theta(Q) - \theta(0) \equiv \theta(Q) - \theta$. Simplification leads to

$$\langle\bar{1}|H_{el}(Q)|\bar{1}\rangle = L(Q) + M(Q)\cos\delta\theta(Q) \,. \tag{3.19}$$

By similar analyses,

$$\langle 1|H_{el}(Q)|1\rangle = L(Q) - M(Q)\cos\delta\theta(Q)\,, \tag{3.20}$$

and

$$\langle 1|H_{el}(Q)|\bar{1}\rangle = \langle \bar{1}|H_{el}(Q)|1\rangle = M(Q)\sin\delta\theta(Q)\,. \tag{3.21}$$

Using the definition of $\delta\theta(Q)$, we easily find

$$\cos\delta\theta(Q) = \frac{K(Q)K + J(Q)J}{M(Q)M}\,, \tag{3.22}$$

and

$$\sin\delta\theta(Q) = \frac{J(Q)K - K(Q)J}{M(Q)M}\,. \tag{3.23}$$

Combining these results and introducing the definitions $\delta J(Q) = J(Q) - J$ and $\delta K(Q) = K(Q) - K$, we arrive at the expression

$$\begin{aligned} H_{\rm el}(Q) = {} & |0\rangle\langle 0|E_0(Q) + |\bar{1}\rangle\langle\bar{1}|\Big\{L(Q) + M + \frac{K\delta K(Q) + J\delta J(Q)}{M}\Big\} \\ & + |1\rangle\langle 1|\Big\{L(Q) - M - \frac{K\delta K(Q) + J\delta J(Q)}{M}\Big\} \\ & + (|\bar{1}\rangle\langle 1| + |1\rangle\langle\bar{1}|)\Big\{\frac{K\delta J(Q) - J\delta K(Q)}{M}\Big\} + |2\rangle\langle 2|E_2(Q)\,, \end{aligned} \tag{3.24}$$

for the electronic Hamiltonian in the exciton basis.

In order to choose between the two nuclear coordinate-independent electronic bases in a given instance, we can compare the respective ratios of the off-diagonal matrix elements of their Hamiltonians to the difference between the two diagonal matrix elements within the singly-excited manifold. The site basis is seen to be favored by small values of the quantity

$$\Big|\frac{J(Q)}{V_{\bar{e}g}(Q) - V_{\bar{g}e}(Q)}\Big| = \frac{1}{2}\Big|\frac{J(Q)}{K(Q)}\Big|\,. \tag{3.25}$$

On the other hand, small values of

$$\left|\frac{K\delta J(Q) - J\delta K(Q)}{M}\,\frac{1}{2\big(M + \frac{K\delta K(Q) + J\delta J(Q)}{M}\big)}\right| = \frac{1}{2}\Big|\frac{K\delta J(Q) - J\delta K(Q)}{M^2 + K\delta K(Q) + J\delta J(Q)}\Big| \tag{3.26}$$

support a choice of the exciton basis. These criteria indicate that the site (exciton) basis is preferred under conditions of weak (strong) energy-transfer coupling.

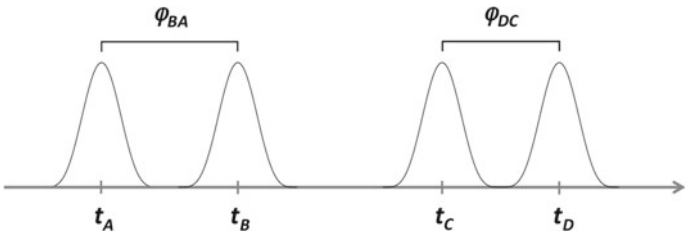

Fig. 3.2 Electric field envelopes in a 2D WPI experiment are shown schematically, along with their arrival times and controlled intrapulse-pair optical phase shifts

3.3 Whoopee Signal

3.3.1 Interaction Hamiltonian

Next, we develop basic formulas for the fluorescence-detected WPI signal from the dimer complex. In order to carry out this derivation, we add to the Hamiltonian a time-dependent perturbation accounting for the dimer's interaction with a sequence of four ultrashort laser pulses,

$$V(t) = \sum_{I=A,B,C,D} V_I(t)\,, \tag{3.27}$$

with

$$V_I(t) = -\hat{\mathbf{m}} \cdot \mathbf{E}_I(t)\,. \tag{3.28}$$

The electric fields are

$$\mathbf{E}_I(t) = \mathbf{e}_I E_I f_I\,(t - t_I(\mathbf{r}))\cos\left[\Omega\,(t - t_I\,(\mathbf{r})) + \varphi_I\right]\,, \tag{3.29}$$

in which $t_I(\mathbf{r}) = t_I + \mathbf{n}_I \cdot \mathbf{r}/c$. The quantity $\mathbf{e}_I$ in (3.29) is the polarization unit vector (assumed to be real) and $t_I(\mathbf{r})$ is the arrival time of the pulse at the molecular location ($\mathbf{r} = 0$), with t_I being the arrival time at some origin within the sample and $\mathbf{n}_I$ being a unit vector in the direction of the laser beam's spatial propagation. We are specializing to the common situation in which the optical phase *differences* $\varphi_{BA} \equiv \varphi_B - \varphi_A$ and $\varphi_{DC} \equiv \varphi_D - \varphi_C$ are under experimental control even though the individual φ_I may vary randomly on successive laser shots due to mechanical jitter in the optical setup. As illustrated in Fig. 3.2, the pulse sequence comprises two phase-controlled pulse-pairs. The variable intrapulse-pair delays $t_{BA} \equiv t_B - t_A$ and $t_{DC} \equiv t_D - t_C$, or their conjugate frequency variables, are the two "dimensions" of a 2D WPI experiment. The pulse arrivals at the sample origin obey $t_A \leq t_B$, $t_C \leq t_D$, and $t_A + t_B \leq t_C + t_D$ (as explained on p. 10).

The dipole operator is

$$\hat{\mathbf{m}} = \mathbf{m}_a \left(|\bar{e}g\rangle\langle\bar{g}g| + |\bar{e}e\rangle\langle\bar{g}e|\right) + \mathbf{m}_b \left(|\bar{g}e\rangle\langle\bar{g}g| + |\bar{e}e\rangle\langle\bar{e}g|\right) + \text{H.c.} \tag{3.30}$$

We can find this operator in the adiabatic electronic basis by calculating its matrix elements,

$$\begin{aligned}\langle\bar{1}(Q)|\hat{\mathbf{m}}|0\rangle &= \mathbf{m}_a\langle\bar{1}(Q)|\bar{e}g\rangle + \mathbf{m}_b\langle\bar{1}(Q)|\bar{g}e\rangle \\ &= \mathbf{m}_a \cos\frac{\theta(Q)}{2} + \mathbf{m}_b \sin\frac{\theta(Q)}{2}\,,\end{aligned} \tag{3.31}$$

$$\langle 1(Q)|\hat{\mathbf{m}}|0\rangle = -\mathbf{m}_a \sin\frac{\theta(Q)}{2} + \mathbf{m}_b \cos\frac{\theta(Q)}{2}\,, \tag{3.32}$$

$$\langle 2|\hat{\mathbf{m}}|\bar{1}(Q)\rangle = \mathbf{m}_a \sin\frac{\theta(Q)}{2} + \mathbf{m}_b \cos\frac{\theta(Q)}{2}\,, \tag{3.33}$$

and

$$\langle 2|\hat{\mathbf{m}}|1(Q)\rangle = \mathbf{m}_a \cos\frac{\theta(Q)}{2} - \mathbf{m}_b \sin\frac{\theta(Q)}{2}\,. \tag{3.34}$$

From these we obtain

$$\begin{aligned}\hat{\mathbf{m}} = {} & |\bar{1}(Q)\rangle\langle 0|\left\{\mathbf{m}_a \cos\frac{\theta(Q)}{2} + \mathbf{m}_b \sin\frac{\theta(Q)}{2}\right\} \\ & + |1(Q)\rangle\langle 0|\left\{-\mathbf{m}_a \sin\frac{\theta(Q)}{2} + \mathbf{m}_b \cos\frac{\theta(Q)}{2}\right\} \\ & + |2\rangle\langle\bar{1}(Q)|\left\{\mathbf{m}_a \sin\frac{\theta(Q)}{2} + \mathbf{m}_b \cos\frac{\theta(Q)}{2}\right\} \\ & + |2\rangle\langle 1(Q)|\left\{\mathbf{m}_a \cos\frac{\theta(Q)}{2} - \mathbf{m}_b \sin\frac{\theta(Q)}{2}\right\} + \text{H.c.}\end{aligned} \tag{3.35}$$

Setting $Q = 0$ in (3.35) yields the dipole operator in the exciton basis:

$$\begin{aligned}\hat{\mathbf{m}} = {} & |\bar{1}\rangle\langle 0|\left\{\mathbf{m}_a \cos\frac{\theta}{2} + \mathbf{m}_b \sin\frac{\theta}{2}\right\} + |1\rangle\langle 0|\left\{-\mathbf{m}_a \sin\frac{\theta}{2} + \mathbf{m}_b \cos\frac{\theta}{2}\right\} \\ & + |2\rangle\langle\bar{1}|\left\{\mathbf{m}_a \sin\frac{\theta}{2} + \mathbf{m}_b \cos\frac{\theta}{2}\right\} + |2\rangle\langle 1|\left\{\mathbf{m}_a \cos\frac{\theta}{2} - \mathbf{m}_b \sin\frac{\theta}{2}\right\} + \text{H.c.}\end{aligned} \tag{3.36}$$

3.3.2 2D Signal

The two-dimensional whoopee signal S depends on the quadrilinear contributions (proportional to $E_A E_B E_C E_D$) to the population of each of the several electronic excited states. For a sample having uniform dimer density ρ throughout an illuminated volume V, it can be written

$$S = \rho \int_V d^3r \left\{ Q_{\bar{e}e} P_{\bar{e}e}(\mathbf{r}) + Q_{\bar{e}g} P_{\bar{e}g}(\mathbf{r}) + Q_{\bar{g}e} P_{\bar{g}e}(\mathbf{r}) \right\}$$
$$= \rho \int_V d^3r \left\{ Q_2 P_2(\mathbf{r}) + Q_{\bar{1}} P_{\bar{1}}(\mathbf{r}) + Q_1 P_1(\mathbf{r}) \right\}, \tag{3.37}$$

where $P_\xi(\mathbf{r})$ is the quadrilinear portion of the ξ-state population of a dimer at position $\mathbf{r}$ and Q_ξ is the fluorescence quantum yield in that state.[2] The $\mathbf{r}$-dependence of the quadrilinear populations would become important if we wished to describe a set-up in which the four incident laser beams were noncollinear; in that case, wave-vector-matching conditions among the $\mathbf{n}_I$ would play a role analagous to or in concert with optical phase cycling in helping to isolate a particular quadrilinear contribution to the signal (i.e. one having a sum or difference optical phase combination, $\varphi_{DC} + \varphi_{BA}$ or $\varphi_{DC} - \varphi_{BA}$, respectively). In order to simplify subsequent formulas, we shall omit the $\mathbf{r}$-dependence from here on out, but it could easily be restored. The resulting formulas will apply as they are in the case of four collinear beams or in the in-principle-possible case of experiments on a single molecule, with the spatial integrals of (3.37) also being omitted in the latter instance.

3.3.2.1 Singly Excited-State Populations

We focus first on the contributions to (3.37) arising from the population of singly-excited electronic states. Among the 48 quadrilinear overlaps contributing (along with their complex conjugates) to the population of a given singly-excited state, we may omit the sixteen overlaps carrying an uncontrolled optical phase factor of the form $\exp\{\pm i(\varphi_A + \varphi_B) \pm i(\varphi_C + \varphi_D)\}$, as these average to negligibility over the many laser shots needed to accumulate a WPI signal. The remaining, phase-stable contributions to P_ξ can be broken into separately measurable sum- and difference-phased components (see Sect. 3.3.2.3). Thus $P_\xi = P_\xi^{(s)} + P_\xi^{(d)}$, where

$$\begin{aligned} P_\xi^{(s)} = 2\mathrm{Re}\big\{ &\langle \uparrow_A \downarrow_B \uparrow_C |\xi\rangle\langle\xi| \uparrow_D\rangle + \langle \uparrow_A \downarrow_D \uparrow_C |\xi\rangle\langle\xi| \uparrow_B\rangle + \langle \uparrow_C |\xi\rangle\langle\xi| \uparrow_B \downarrow_A \uparrow_D\rangle \\ &+ \langle \uparrow_A |\xi\rangle\langle\xi| \uparrow_B \downarrow_C \uparrow_D\rangle + \langle \uparrow_C \downarrow_B \uparrow_A |\xi\rangle\langle\xi| \uparrow_D\rangle + \langle \uparrow_C \downarrow_D \uparrow_A |\xi\rangle\langle\xi| \uparrow_B\rangle \\ &+ \langle \uparrow_C |\xi\rangle\langle\xi| \uparrow_D \downarrow_A \uparrow_B\rangle + \langle \uparrow_A |\xi\rangle\langle\xi| \uparrow_D \downarrow_C \uparrow_B\rangle \\ &+ \langle \uparrow_A \uparrow_C \downarrow_B |\xi\rangle\langle\xi| \uparrow_D\rangle + \langle \uparrow_A \uparrow_C \downarrow_D |\xi\rangle\langle\xi| \uparrow_B\rangle + \langle \uparrow_C |\xi\rangle\langle\xi| \uparrow_B \uparrow_D \downarrow_A\rangle \\ &+ \langle \uparrow_A |\xi\rangle\langle\xi| \uparrow_B \uparrow_D \downarrow_C\rangle + \langle \uparrow_C \uparrow_A \downarrow_B |\xi\rangle\langle\xi| \uparrow_D\rangle + \langle \uparrow_C \uparrow_A \downarrow_D |\xi\rangle\langle\xi| \uparrow_B\rangle \\ &+ \langle \uparrow_C |\xi\rangle\langle\xi| \uparrow_D \uparrow_B \downarrow_A\rangle + \langle \uparrow_A |\xi\rangle\langle\xi| \uparrow_D \uparrow_B \downarrow_C\rangle \big\}, \end{aligned} \tag{3.38}$$

and (by swapping Cs and Ds throughout)

[2] We do not include an average over any possible orientational distribution of the dimer at a given location, regarding this as being implicitly included in the spatial distribution of population.

$$
\begin{aligned}
P_{\xi}^{(d)} = 2\mathrm{Re}\big\{&\langle\uparrow_A\downarrow_B\uparrow_D\,|\xi\rangle\langle\xi|\,\uparrow_C\rangle + \langle\uparrow_A\downarrow_C\uparrow_D\,|\xi\rangle\langle\xi|\,\uparrow_B\rangle + \langle\uparrow_D\,|\xi\rangle\langle\xi|\,\uparrow_B\downarrow_A\uparrow_C\rangle \\
&+ \langle\uparrow_A\,|\xi\rangle\langle\xi|\,\uparrow_B\downarrow_D\uparrow_C\rangle + \langle\uparrow_D\downarrow_B\uparrow_A\,|\xi\rangle\langle\xi|\,\uparrow_C\rangle + \langle\uparrow_C\downarrow_D\uparrow_A\,|\xi\rangle\langle\xi|\,\uparrow_B\rangle \\
&+ \langle\uparrow_D\,|\xi\rangle\langle\xi|\,\uparrow_C\downarrow_A\uparrow_B\rangle + \langle\uparrow_A\,|\xi\rangle\langle\xi|\,\uparrow_C\downarrow_D\uparrow_B\rangle \\
&+ \langle\uparrow_A\uparrow_D\downarrow_B\,|\xi\rangle\langle\xi|\,\uparrow_C\rangle + \langle\uparrow_A\uparrow_D\downarrow_C\,|\xi\rangle\langle\xi|\,\uparrow_B\rangle + \langle\uparrow_D\,|\xi\rangle\langle\xi|\,\uparrow_B\uparrow_C\downarrow_A\rangle \\
&+ \langle\uparrow_A\,|\xi\rangle\langle\xi|\,\uparrow_B\uparrow_C\downarrow_D\rangle + \langle\uparrow_D\uparrow_A\downarrow_B\,|\xi\rangle\langle\xi|\,\uparrow_C\rangle + \langle\uparrow_D\uparrow_A\downarrow_C\,|\xi\rangle\langle\xi|\,\uparrow_B\rangle \\
&+ \langle\uparrow_D\,|\xi\rangle\langle\xi|\,\uparrow_C\uparrow_B\downarrow_A\rangle + \langle\uparrow_A\,|\xi\rangle\langle\xi|\,\uparrow_C\uparrow_B\downarrow_D\rangle\big\}\,. \qquad (3.39)
\end{aligned}
$$

Reading from left to right within any bra or ket, the pulses must act on the dimer in the order listed, irrespective of their order of temporal arrival, driving upward (absorptive) or downward (emissive) electronic transitions. Explicit expressions for the contributing multi-pulse amplitudes are developed subsequently. We have written the various quadrilinear populations so the displayed overlaps have phase signature $e^{-i\varphi_{BA}-i\varphi_{DC}}$ and $e^{-i\varphi_{BA}+i\varphi_{DC}}$ in $P_{\xi}^{(s)}$ and $P_{\xi}^{(d)}$, respectively. The first eight overlaps in each of the quadrilinear ξ-state populations do not access the doubly excited electronic state at any stage in the amplitude-transfer process described by the three-pulse bra or ket. In the last eight overlaps of $P_{\xi}^{(s)}$ and $P_{\xi}^{(d)}$, amplitude is generated in the doubly excited state by the action of the second pulse of the three-pulse bra or ket.

If we make the reasonable assumption that the quantum yields for fluorescence (or other action-spectroscopy signal) following excitation of the $\bar{e}g$- and $\bar{g}e$-states are equal, $Q_{\bar{e}g} = Q_{\bar{g}e} = Q_{\mathrm{one}}$, then the total quadrilinear population of both singly-excited site states $P_{\mathrm{one}}^{(s/d)} = P_{\bar{e}g}^{(s/d)} + P_{\bar{g}e}^{(s/d)}$ is all that matters. Expressions for $P_{\mathrm{one}}^{(s)}$ and $P_{\mathrm{one}}^{(d)}$ could be obtained from (3.38) and (3.39), respectively by replacing $|\xi\rangle\langle\xi|$ with $\mathcal{P}_{\mathrm{one}} = |\bar{e}g\rangle\langle\bar{e}g| + |\bar{g}e\rangle\langle\bar{g}e|$. But all the one- and three-pulse bras and kets appearing there generate amplitude only in the singly electronically-excited manifold. So the operator $|\xi\rangle\langle\xi|$ can simply be removed to give $P_{\mathrm{one}}^{(s/d)}$. The same sort of argument of course applies in the exciton basis.

The various quadrilinear overlaps differ in their dependence on the interpulse delays, and it is through this delay dependence that WPI data provide information on the dynamics of the energy-transfer system. For bookkeeping purposes—and without any sacrifice of experimental data—we require that $t_A \le t_B$, $t_C \le t_D$, and $(t_A + t_B)/2 \le (t_C + t_D)/2$. Assuming that all four pulses have identical envelopes, any data obtained with t_B less than t_A would coincide with those within the prescribed range having t_A and t_B interchanged and φ_{BA} changed in sign; a similar statement holds for data with t_D less than t_C. Data with the midpoint of t_C and t_D less than that of t_A and t_B exist in the prescribed range with t_A interchanged with t_C, t_B interchanged with t_D, and φ_{BA} swapped with φ_{DC}. An exhaustive range of interpulse delays thus spans a three-dimensional space $\{t_{BA}, t_{DC}, t_{CB}\}$ with t_{BA} and t_{DC} greater than or equal to zero and t_{CB} greater than or equal to $-(t_{DC} + t_{BA})/2$. Notice that under these restrictions, t_B can be before, between, or after t_C and t_D, and t_A can come before or after t_C, provided $t_{DC} + 2t_{CB} + t_{BA}$ remains nonnegative.

Because the pulses have short durations that sometimes preclude their acting in the required order, each of the wave-packet overlaps in (3.38) and (3.39) is restricted

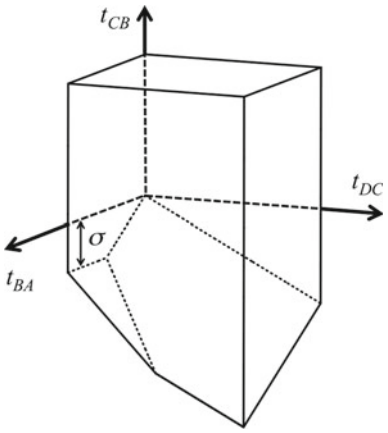

Fig. 3.3 Three-dimensional region of time-delay parameter space in which the ground-state-bleach contribution to the difference-phased 2D-WPI signal may be nonvanishing. The region shown is to be extended to arbitrarily large, positive values of t_{BA} and t_{DC}, and to arbitrarily large positive and negative values of t_{CB} (while maintaining t_{CB} greater than both $-(t_{DC} + t_{BA})/2$ and $-\sigma - t_{DC}$). The stimulated-emission overlap may be nonzero in the temporal region generated from that depicted here by reflection through the $t_{DC} = t_{BA}$ plane

in the range of interpulse delays for which it can make a contribution to the WPI signal. Let's identify the three-dimensional regions of the "delay space" within which each of the overlaps participating in $P_{\text{one}}^{(d)}$ may be active.

First we consider $\langle \uparrow_A \downarrow_B \uparrow_D \mid \uparrow_C \rangle$, which is responsible for bleaching the electronic ground state. Since the D pulse acts after the B pulse in this term, the overlap vanishes if t_D precedes t_B by more than approximately the pulse duration, whence $t_D - t_B > -\sigma$, or $t_{DC} + t_{CB} + \sigma > 0$. Together with the general restriction that $t_{DC} + 2t_{CB} + t_{BA}$ be nonnegative, this condition confines the overlap to the 3D temporal region plotted in Fig. 3.3. A similar argument for the stimulated-emission overlap, $\langle \uparrow_A \downarrow_C \uparrow_D \mid \uparrow_B \rangle$, shows that it can only exist within the 3D region where $t_{CB} + t_{BA} + \sigma > 0$ and $t_{DC} + 2t_{CB} + t_{BA} > 0$, which corresponds to the mirror image of the volume shown in Fig. 3.3 through the vertical plane $t_{DC} = t_{BA}$, containing the t_{CB} axis.

There are also fully three-dimensional regions of interpulse delays where the overlaps $\langle \uparrow_A \mid \uparrow_C \downarrow_D \uparrow_B \rangle$ and $\langle \uparrow_D \mid \uparrow_C \downarrow_A \uparrow_B \rangle$ may be nonnegligible. Since pulse D acts before pulse B in the first of these, its arrival times must obey $t_D - t_B < \sigma$, and $\langle \uparrow_A \mid \uparrow_C \downarrow_D \uparrow_B \rangle$ is therefore confined to the shared range of $t_{DC} + t_{CB} < \sigma$ and $t_{DC} + 2t_{CB} + t_{BA} > 0$ plotted in Fig. 3.4. For $\langle \uparrow_D \mid \uparrow_C \downarrow_A \uparrow_B \rangle$ on the other hand, pulse C must act before pulse A, whence $t_C - t_A < \sigma$. This overlap can make a nonvanishing contribution to $P_{\text{one}}^{(d)}$ when $t_{CB} + t_{BA} < \sigma$ and $t_{DC} + 2t_{CB} + t_{BA} > 0$. This region mirrors the volume shown in Fig. 3.4 through the $t_{DC} = t_{BA}$ plane. Note that the delay-range regions where both of these overlaps may contribute are largely limited to negative t_{CB}.

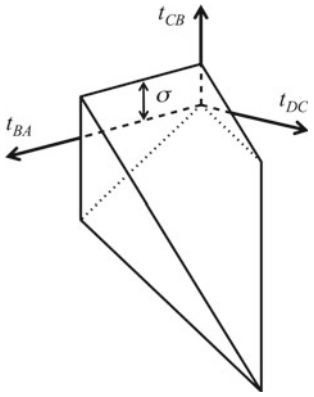

Fig. 3.4 Delay region in which the contribution of $\langle\uparrow_A \mid \uparrow_C\downarrow_D\uparrow_B\rangle$ to the difference-phased 2D-WPI signal may not vanish. The pictured volume is to be extended to arbitrarily large, positive values of t_{BA} and t_{DC}, while maintaining t_{CB} greater than $-(t_{DC}+t_{BA})/2$ and less than $\sigma - t_{DC}$. The region of possibly nonvanishing $\langle\uparrow_D \mid \uparrow_C\downarrow_A\uparrow_B\rangle$ is the mirror image of this one through the vertical $t_{DC} = t_{BA}$ plane

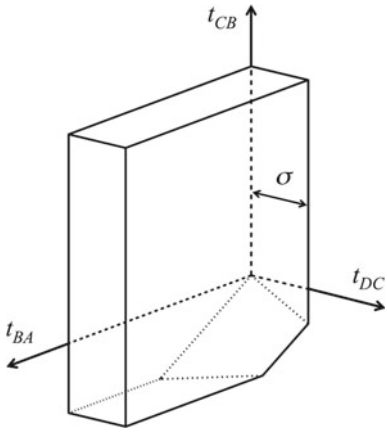

Fig. 3.5 Quasi-2D time-delay region in which the overlap $\langle\uparrow_A \mid \uparrow_B\downarrow_D\uparrow_C\rangle$ may contribute to the 2D-WPI signal; it is to be extended to arbitrarily large, positive values of t_{BA} and t_{CB}. Reflection in the plane $t_{DC} = t_{BA}$ yields the slab within which $\langle\uparrow_D \mid \uparrow_B\downarrow_A\uparrow_C\rangle$ may take nonzero values

In $\langle\uparrow_A \mid \uparrow_B\downarrow_D\uparrow_C\rangle$, the D pulse acts before the C pulse, despite the fact that by definition the arrival time t_D follows t_C; $t_{DC} < \sigma$. Since the B pulse also acts before the C pulse in this overlap, but t_C can precede t_B in the specified range of unique interpulse delays, $t_B - t_C$ has to be less than the pulse length, so $t_{CB} > -\sigma$ is required as well. Together with $t_{DC} + 2t_{CB} + t_{BA} > 0$, these conditions restrict $\langle\uparrow_A \mid \uparrow_B\downarrow_D\uparrow_C\rangle$ to the quasi-2D time-delay region illustrated in Fig. 3.5. The delay region for $\langle\uparrow_D \mid \uparrow_B\downarrow_A\uparrow_C\rangle$ is obtained by reflecting this slab in the $t_{DC} = t_{BA}$ plane.

The two remaining overlaps in $P^{(d)}_{\text{one}}$ which do not access the doubly-excited state are limited to quasi zero-dimensional delay regions. Since pulse B and D both act before pulse A in $\langle\uparrow_D\downarrow_B\uparrow_A \mid \uparrow_C\rangle$, this overlap cannot contribute unless t_{BA} and

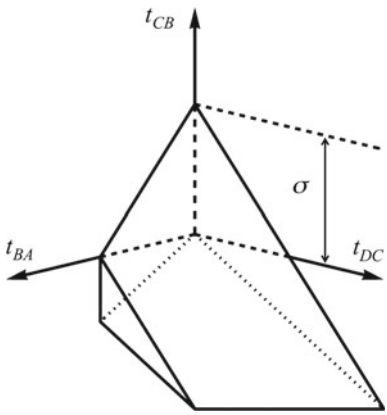

Fig. 3.6 Delay region where $\langle \uparrow_D \downarrow_B \uparrow_A | \uparrow_C \rangle$ may take nonnegligible values. This region is quasi zero-dimensional because it shrinks towards nonexistence in all three directions as the pulses become shorter. The overlap $\langle \uparrow_D \downarrow_C \uparrow_A | \uparrow_B \rangle$ may exist only inside a region mirroring this one through the $t_{DC} = t_{BA}$ plane

$t_D - t_A = t_{DC} + t_{CB} + t_{BA}$ are less than about σ. These conditions, together with the restriction to nonnegative $t_{DC} + 2t_{CB} + t_{BA}$, limit this overlap to the region shown in Fig. 3.6. The mirror image of this region through $t_{DC} = t_{BA}$ similarly confines $\langle \uparrow_D \downarrow_C \uparrow_A | \uparrow_B \rangle$.

It is apposite to recall that—despite their differing phase signatures, pulse orderings, and confining regions of time-delay space—the first eight overlaps appearing in each of (3.38) and (3.39) are essentially the same from the dimer's point of view; each term records a contribution to the population of the one-exciton manifold resulting from the interference between an amplitude generated by the action of a single resonant electric-field interaction and another generated by an excitation-deexcitation-reexcitation process driven by three sequential interactions with resonant fields. The pulse labels attached to the participating fields don't evince themselves in a single population-generation process, but only in the way the measured quadrilinear contribution to the singly-excited population varies with the experimentally specified pulse polarizations, intrapulse-pair phase shifts, and interpulse delays. The same is true among the second set of eight overlaps in (3.38) and (3.39); each of these represents the interference population between a singly-excited wave packet generated by the action of one pulse and another driven by a three-pulse process of excitation-excitation-deexcitation.

Each of the last eight overlaps in (3.38) and (3.39), those involving a three-pulse bra or ket whose amplitude visits the doubly-excited electronic state between the second- and third-acting pulse, can also be confined to a specified region of $\{t_{BA}, t_{DC}, t_{CB}\}$. Here we identify the delay-space volumes for the last eight quadrilinear overlaps contributing to $P^{(d)}_{\text{one}}$.

The overlap $\langle \uparrow_A \uparrow_D \downarrow_B | \uparrow_C \rangle$ is confined to negative or very short positive t_{CB}. Because it depends on pulse D acting before B, $t_{DC} + t_{CB}$ can be no larger than the pulse duration σ. The data-organizational requirement that the temporal midpoint of C and D follow that of A and B is the only other restriction, so this overlap's admissible delay range is the quasi-3D region displayed in Fig. 3.7.

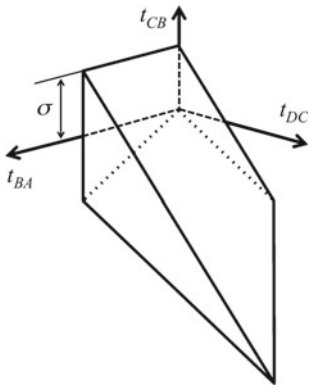

Fig. 3.7 Region of interpulse delays where the effects of the order of pulse action alone do not prevent $\langle\uparrow_A\uparrow_D\downarrow_B|\uparrow_C\rangle$ from taking significant values. This delay volume extends to arbitrarily large positive t_{BA} and t_{DC}, and arbitrarily large negative t_{CB}

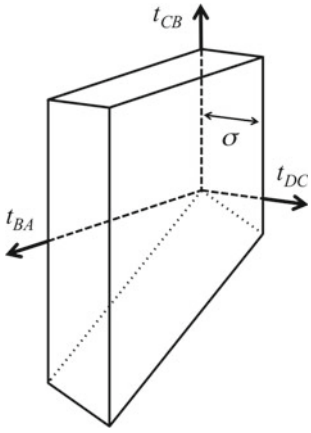

Fig. 3.8 Delay region where $\langle\uparrow_A\uparrow_D\downarrow_C|\uparrow_B\rangle$ may be nonzero. This pulse-duration-thick slab extends to arbitrarily large positive t_{BA} and t_{CB}, and to $t_{CB} \approx -t_{BA}/2$

The signal contribution from $\langle\uparrow_A\uparrow_D\downarrow_C|\uparrow_B\rangle$ can only be sizable in the quasi-2D delay region shown in Fig. 3.8. For t_{DC} must be less than σ and, as usual, $2t_{CB} + t_{BA} + t_{DC} > 0$. The condition $t_C - t_A = t_{CB} + t_{BA} > -\sigma$ imposes no additional restriction.

The three-pulse wave packet participating in $\langle\uparrow_D|\uparrow_B\uparrow_C\downarrow_A\rangle$ can only be formed under the stringent conditions $t_{BA} < \sigma$, $t_{CB} > -\sigma$, and $t_{CB} + t_{BA} < \sigma$, along with $2t_{CB} + t_{BA} + t_{DC} > 0$. These requirements restrict its nonnegligible contributions to the quasi one-dimensional t_{DC} range plotted in Fig. 3.9.

Contributions to the $P^{(d)}_{\text{one}}$ WPI signal from $\langle\uparrow_A|\uparrow_B\uparrow_C\downarrow_D\rangle$ can arise whenever $t_{CB} > -\sigma$. The condition $2t_{CB} + t_{BA} + t_{DC} > 0$ has an impact only at very small intrapulse-pair delays. This important overlap may therefore exist anywhere within the 3D delay volume portrayed in Fig. 3.10.

Because pulse D acts before A in its bra, $\langle\uparrow_D\uparrow_A\downarrow_B|\uparrow_C\rangle$ can only exist for very small values of all three interpulse delays. Thus $t_D - t_A = t_{DC} + t_{CB} + t_{BA} < \sigma$ combined with $2t_{CB} + t_{BA} + t_{DC} > 0$ confines nonnegligible values of this overlap to the quasi-1D region illustrated in Fig. 3.11. The overlap $\langle\uparrow_D\uparrow_A\downarrow_C|\uparrow_B\rangle$ is restricted

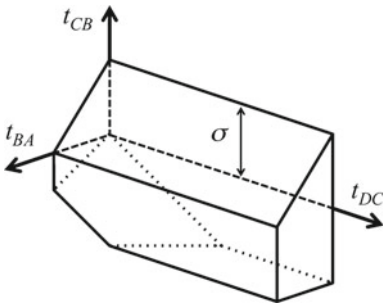

Fig. 3.9 Narrow region of delay-space to which nonnegligible contributions from $\langle \uparrow_D | \uparrow_B \uparrow_C \downarrow_A \rangle$ are confined

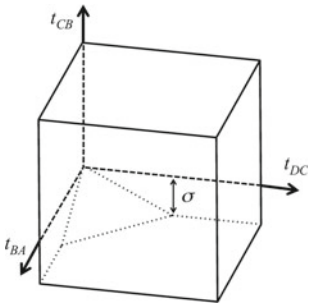

Fig. 3.10 Volume in $\{t_{BA}, t_{DC}, t_{CB}\}$, extending to indefinitely large values of all three delays, where $\langle \uparrow_A | \uparrow_B \uparrow_C \downarrow_D \rangle$ can in principle make a signal contribution

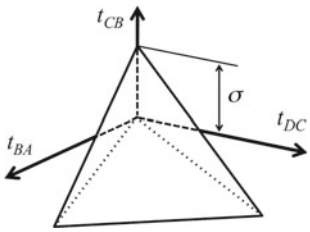

Fig. 3.11 The small delay-range region within which the overlaps $\langle \uparrow_D \uparrow_A \downarrow_B | \uparrow_C \rangle$ and $\langle \uparrow_D \uparrow_A \downarrow_C | \uparrow_B \rangle$ are expected to contribute to $P^{(d)}_{\text{one}}$

to the same region: $t_D - t_A$ must again be less than the pulse duration, and the condition $t_C - t_A = t_{CB} + t_{BA} < \sigma$ proves to be redundant.

The ket in $\langle \uparrow_D | \uparrow_C \uparrow_B \downarrow_A \rangle$ vanishes unless both $t_C - t_A = t_{CB} + t_{BA}$ and t_{BA} alone are less than the pulse duration. Along with $2t_{CB} + t_{BA} + t_{DC} > 0$, these lead to the delay region of significance sketched in Fig. 3.12.

It is worth recalling that outside its prescribed interpulse-delay region, a particular overlap vanishes simply because the delay combinations are inconsistent with the required order of pulse action in the participating three-pulse bra or ket. But criteria specific to the dimer's Hamiltonian, including internal molecular and host-medium nuclear degrees of freedom, will sometimes diminish the overlaps for certain delay combinations inside these regions. In multimode systems for instance, electronic dephasing driven by electronic-nuclear coupling will often severely limit the maximal intrapulse-pair delays t_{BA} and t_{DC} over which the electronic coherence on which a nonvanishing 2D-WPI signal depends can be effectively maintained. Because the *B*-

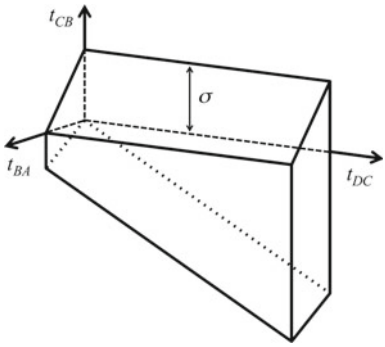

Fig. 3.12 Interpulse-delay region, extending to arbitrarily large positive t_{DC} and negative t_{CB}, where $\langle \uparrow_D | \uparrow_C \uparrow_B \downarrow_A \rangle$ may give rise to significant signal

and C-pulses are not phase-locked, signal contributions tend to be less susceptible to dynamical truncation along t_{CB}.

3.3.2.2 Doubly Excited-State Population

As indicated in (3.37), the quadrilinear portion of the population of the doubly-excited electronic state contributes to the 2D-WPI signal with a certain quantum yield $Q_{\bar{e}e} = Q_2 \equiv Q_{\text{two}}$. Eliminating as unmeasured the four overlaps appearing in the doubly-excited population whose optical phases are uncontrolled allows us to write P_{two} as a sum of two experimentally isolable portions,

$$P_{\text{two}}^{(s)} = 2\text{Re}\left\{\langle \uparrow_A \uparrow_C | \uparrow_B \uparrow_D \rangle + \langle \uparrow_A \uparrow_C | \uparrow_D \uparrow_B \rangle + \langle \uparrow_C \uparrow_A | \uparrow_B \uparrow_D \rangle + \langle \uparrow_C \uparrow_A | \uparrow_D \uparrow_B \rangle \right\}, \tag{3.40}$$

and (by interchanging Cs and Ds)

$$P_{\text{two}}^{(d)} = 2\text{Re}\left\{\langle \uparrow_A \uparrow_D | \uparrow_B \uparrow_C \rangle + \langle \uparrow_A \uparrow_D | \uparrow_C \uparrow_B \rangle + \langle \uparrow_D \uparrow_A | \uparrow_B \uparrow_C \rangle + \langle \uparrow_D \uparrow_A | \uparrow_C \uparrow_B \rangle \right\}. \tag{3.41}$$

Let's work out the region of $\{t_{BA}, t_{DC}, t_{CB}\}$ to which each of the difference-phased quadrilinear contributions to the population of the doubly-excited state, seen in (3.41), is exclusively confined. In $\langle \uparrow_A \uparrow_D | \uparrow_B \uparrow_C \rangle$, the pulses act in their nominal order (A before D and B before C), so the overlap can be nonnegligible in a three-dimensional region of delay-space. More specifically, t_C must exceed $t_B - \sigma$, or the B-pulse could not act before C; hence $t_{CB} > -\sigma$. But the bookkeeping restriction $t_D + t_C > t_B + t_A$ also requires $t_{CB} > -\frac{1}{2}(t_{DC} + t_{BA})$, which is slightly more restrictive for tiny intrapulse-pair delays. All three interpulses delays can take arbitrarily large positive values. These are the same restrictions as apply to $\langle \uparrow_A | \uparrow_B \uparrow_C \downarrow_D \rangle$, so the relevant delay volume is identical to Fig. 3.10.

In the ket of $\langle \uparrow_A \uparrow_D | \uparrow_C \uparrow_B \rangle$, C-pulse action precedes B-pulse action. In order that this overlap not vanish, t_{CB} must therefore be shorter than σ. As the general condition $t_{CB} > -\frac{1}{2}(t_{DC} + t_{BA})$ also applies, nonvanishing values can only reside in the delay region plotted in Fig. 3.13.

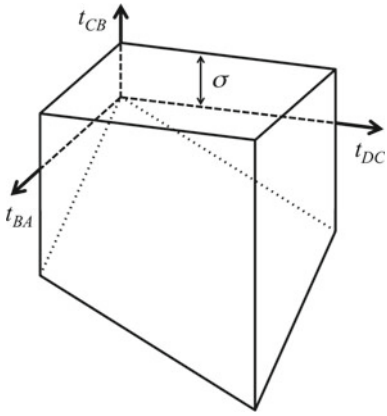

Fig. 3.13 Region of interpulse delays where $\langle \uparrow_A \uparrow_D | \uparrow_C \uparrow_B \rangle$ can be nonzero

The overlap $\langle \uparrow_D \uparrow_A | \uparrow_B \uparrow_C \rangle$ can only be nonnegligible when $t_D - t_A = t_{DC} + t_{CB} + t_{BA}$ is less than the pulse duration. But t_{CB} must exceed $-\frac{1}{2}(t_{BA} + t_{DC})$, so this contribution to $P^{(d)}_{\text{two}}$ can exist only in a quasi zero-dimensional region of very short interpulse delays. The same restrictions apply to $\langle \uparrow_D \uparrow_A | \uparrow_C \uparrow_B \rangle$, for nonnegligibility of this overlap again requires $t_{DC} + t_{CB} + t_{BA} < \sigma$. The weaker condition $t_{CB} < \sigma$ adds no additional constraint. The resulting common delay region coincides with that illustrated in Fig. 3.11 for $\langle \uparrow_D \uparrow_A \downarrow_B | \uparrow_C \rangle$ and $\langle \uparrow_D \uparrow_A \downarrow_C | \uparrow_B \rangle$.

3.3.2.3 Signal Isolation

As we have mentioned, it is possible to separate experimentally the sum-phased signal arising from (3.38) and (3.40), on one hand, and the difference-phased signal from (3.39) and (3.41), on the other. This is accomplished by combining WPI measurements $S(\varphi_{BA}, \varphi_{DC})$ having different combinations of the optical phase shifts φ_{BA} and φ_{DC}. In fact, the same "phase-cycling" methods enable the isolation of the quantum yield-weighted sum of the complex-valued quantities inside the braces of the first two or the second two of those expressions. We can illustrate the basic strategy with a simple example; more complicated schemes may have advantages in practice.

Writing the signal with particular phase shifts as

$$S(\varphi_{BA}, \varphi_{DC}) = 2\text{Re}\{e^{-i\varphi_{BA} - i\varphi_{DC}} \xi_s + e^{-i\varphi_{BA} + i\varphi_{DC}} \xi_d\}\,, \tag{3.42}$$

and denoting $\xi_{s/d} = \xi'_{s/d} + i\xi''_{s/d}$, leads to distinct combinations such as

$$S(0, 0) = 2(\xi'_s + \xi'_d)\,, \tag{3.43}$$

$$S(\tfrac{\pi}{2}, 0) = 2(\xi''_s + \xi''_d)\,, \tag{3.44}$$

$$S(0, \tfrac{\pi}{2}) = 2(\xi_s'' - \xi_d'')\,, \tag{3.45}$$

and

$$S(\tfrac{\pi}{2}, \tfrac{\pi}{2}) = 2(-\xi_s' + \xi_d')\,. \tag{3.46}$$

From these we can reconstruct the sought-after quantities

$$\xi_s = \tfrac{1}{4}\{S(0,0) - S(\tfrac{\pi}{2}, \tfrac{\pi}{2}) + iS(\tfrac{\pi}{2}, 0) + iS(0, \tfrac{\pi}{2})\}\,, \tag{3.47}$$

and

$$\xi_d = \tfrac{1}{4}\{S(0,0) + S(\tfrac{\pi}{2}, \tfrac{\pi}{2}) + iS(\tfrac{\pi}{2}, 0) - iS(0, \tfrac{\pi}{2})\}\,. \tag{3.48}$$

3.3.3 *One-, Two-, and Three-Pulse Kets*

Using time-dependent perturbation theory, we now seek explicit expressions for the various multi-pulse bras and kets whose overlaps determine the 2D-WPI signal from an EET complex. Under the dimer Hamiltonian $H = T + H_{\rm el}(\hat{Q})$ (see (3.1)) and the interaction potential $V(t)$, given in (3.27) with the pulse arrival times reckoned at $\mathbf{r} = 0$, the quantum mechanical state obeys

$$i\hbar\frac{\partial}{\partial t}|\Psi(t)\rangle = \big(H + V(t)\big)|\Psi(t)\rangle\,. \tag{3.49}$$

The initial condition is taken to be $|\Psi(t \ll t_A)\rangle = [t - t_A]|\bar{g}g\rangle|\psi_0\rangle$ (using the notation $[t] \equiv \exp\{-iHt/\hbar\}$), where $|\psi_0\rangle$ is some eigenket of the ground-state nuclear Hamiltonian, $T + \langle\bar{g}g|H_{\rm el}(Q)|\bar{g}g\rangle$. In the interaction picture, (3.49) becomes

$$i\hbar\frac{\partial}{\partial t}|\tilde{\Psi}(t)\rangle = \tilde{V}(t)|\tilde{\Psi}(t)\rangle\,, \tag{3.50}$$

with $\tilde{V}(t) = [-t + t_A]V(t)[t - t_A]$ and $|\tilde{\Psi}(t \ll t_A)\rangle = |\bar{g}g\rangle|\psi_0\rangle$.

Since the quadrilinear signal contributions all take the form of an overlap between a two-pulse bra and a two-pulse ket, or between a one-pulse bra and a three-pulse ket, it is enough to solve (3.50) through third order in the external fields:

$$|\tilde{\Psi}(t)\rangle \cong \left\{1 + \frac{1}{i\hbar}\int_{-\infty}^{t} d\tau\,\tilde{V}(\tau) + \left(\frac{1}{i\hbar}\right)^2\int_{-\infty}^{t} d\tau\int_{-\infty}^{\tau} d\bar{\tau}\,\tilde{V}(\tau)\tilde{V}(\bar{\tau}) + \left(\frac{1}{i\hbar}\right)^3\int_{-\infty}^{t} d\tau\int_{-\infty}^{\tau} d\bar{\tau}\int_{-\infty}^{\bar{\tau}} d\bar{\bar{\tau}}\,\tilde{V}(\tau)\tilde{V}(\bar{\tau})\tilde{V}(\bar{\bar{\tau}})\right\}|\bar{g}g\rangle|\psi_0\rangle\,. \tag{3.51}$$

This perturbative solution can be rewritten in terms of *pulse propagators* which encapsulate the effect of each finite-duration laser pulse in the instantaneous action

of a single quantum mechanical operator. Upon reversion to the Schrödinger picture, this reframing results in an equivalent solution,

$$
\begin{aligned}
|\Psi(t)\rangle = \Big\{ & [t - t_A] + i \sum_{I=A,B,C,D} [t - t_I] P_I(t - t_I; \tau) [t_{IA}] \\
& + i^2 \sum_{IJ} [t - t_J] P_J(t - t_J; \tau) [t_{JI}] P_I(\tau + t_{JI}; \bar{\tau}) [t_{IA}] \\
& + i^3 \sum_{IJK} [t - t_K] P_K(t - t_K; \tau) [t_{KJ}] P_J(\tau + t_{KJ}; \bar{\tau}) [t_{JI}] \\
& \times P_I(\bar{\tau} + t_{JI}; \bar{\bar{\tau}}) [t_{IA}] \Big\} |\bar{g} g\rangle |\psi_0\rangle \,,
\end{aligned}
\tag{3.52}
$$

in which the Ith pulse propagator is

$$
P_I(t; \tau) = \frac{E_I}{\hbar} \int_{-\infty}^{t} d\tau \, f_I(\tau) \cos(\Omega\tau + \varphi_I) \, [-\tau] \, \mathbf{e}_I \cdot \hat{\mathbf{m}} \, [\tau] \,. \tag{3.53}
$$

The first argument of a pulse propagator is the upper integration limit and the second designates the variable of integration.

By extracting terms from (3.52) we can develop formulas for the wave-packet overlaps contributing to the 2D-WPI signal using any electronic basis. Portions of the two- and three-pulse sums in this expression of quadratic or cubic order in the field-strength of an individual pulse are of course irrelevant. We bypass the adiabatic electronic basis in favor of the two fixed bases, letting $|\xi\rangle$ denote either a site or an exciton state. Electronic matrix elements of the pulse propagator (3.53) can be conveniently expressed in terms of reduced pulse propagators,

$$
p_I^{(\xi\bar{\xi})}(t; \tau) = \int_{-\infty}^{t} \frac{d\tau}{\sigma} \, f_I(\tau) e^{\mp i \Omega \tau} [-\tau]_{\xi\xi} [\tau]_{\bar{\xi}\bar{\xi}} \,, \tag{3.54}
$$

by making a rotating-wave approximation and invoking one of the forms (3.30) or (3.36) for the dipole operator. We have written $\langle \xi | [\tau] | \bar{\xi} \rangle = [\tau]_{\xi\bar{\xi}}$ and made a significant simplification by assuming that electronic transitions between different singly excited states *in the appropriate basis* can be neglected on the timescale of the pulse duration. The upper (lower) sign in (3.54) applies in the case of an absorptive (emissive) transition $\xi \leftarrow \bar{\xi}$ ($\bar{\xi} \rightarrow \xi$). With the same approximations and conventions, the nonvanishing elements of the overall pulse propagator (3.53) can be written as

$$
\langle \xi | P_I(t; \tau) | \bar{\xi} \rangle = F_I^{(\xi\bar{\xi})} e^{\mp i \varphi_I} \, p_I^{(\xi\bar{\xi})}(t; \tau) \,, \tag{3.55}
$$

where $F_I^{(\xi\bar{\xi})} \equiv F_I \langle \xi | \hat{\mathbf{m}} \cdot \mathbf{e}_I | \bar{\xi} \rangle$ with $F_I = E_I \sigma / 2\hbar$.[3]

[3]Note that any polarization dependence of a 2D-WPI signal enters through the $F_I^{(\xi\bar{\xi})}$.

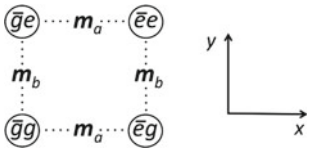

Fig. 3.14 Site-state labels arranged so that each pair is separated in the direction of the monomer transition moment that connects them

3.4 Illustrative Calculations

3.4.1 Overlaps

The stage is set for a variety of calculations of WPI signals from EET dimers and their interpretation in terms of the underlying nuclear wave-packet and energy-transfer dynamics. For illustration, we drastically pare the vast range of possible molecular parameters expressible in terms of the electronic Hamiltonian (3.1) and experimental choices by investigating the difference-phased fluorescence-detected signal from a space-fixed dimer with perpendicularly oriented monomer transition dipoles, $\mathbf{m}_a = m_a\hat{\mathbf{x}}$ and $\mathbf{m}_b = m_b\hat{\mathbf{y}}$.[4] We restrict attention to the situation in which the A, B, C, and D pulses arrive in their nominal order and are short enough that temporal pulse overlap can be neglected.[5] Consulting the relevant delay regions shown in Sects. 3.3.2.1 and 3.3.2.2 confirms inspection of (3.39) and (3.41) in showing that, under these circumstances, the quadrilinear singly- and doubly-excited populations simplify to

$$P^{(d)}_{\text{one}} = 2\text{Re}\big\{\langle\uparrow_A\downarrow_B\uparrow_D \mid \uparrow_C\rangle + \langle\uparrow_A\downarrow_C\uparrow_D \mid \uparrow_B\rangle + \langle\uparrow_A \mid \uparrow_B\uparrow_C\downarrow_D\rangle\big\}\,, \tag{3.56}$$

and

$$P^{(d)}_{\text{two}} = 2\text{Re}\big\{\langle\uparrow_A\uparrow_D \mid \uparrow_B\uparrow_C\rangle\big\}\,. \tag{3.57}$$

We assume that the electronic excitation-transfer coupling is sufficiently weak that the site states are an appropriate electronic basis. Provided the interpulse delays are not too long, the condition $|Jt_{IK}|/\hbar \ll 1$ then ensures that the WPI signal will be at most of first order in J. It is easy to show that if all four laser pulses have the same (x or y) polarization, then first-order EET cannot contribute to the signal. To see this, we can arrange the site-state labels as in Fig. 3.14, so the directions between them are those of the connecting transition moments. Four x-polarized pulses combined with a single EET-driven amplitude transfer can then be seen to generate one- and three-pulse wave packets in *different* electronic states, as illustrated in Fig. 3.15; their

[4] The net signal from an isotropic sample of dimers with a certain internal geometry would be a weighted sum of signals from a handful of representative space-fixed orientations.

[5] Specifically, these assumptions mean that t_{CB} is positive and greater than the pulse duration. In addition, since t_{BA} and t_{DC} are defined to be positive, they also mean that pulse-overlap effects will be ignored when either is very short.

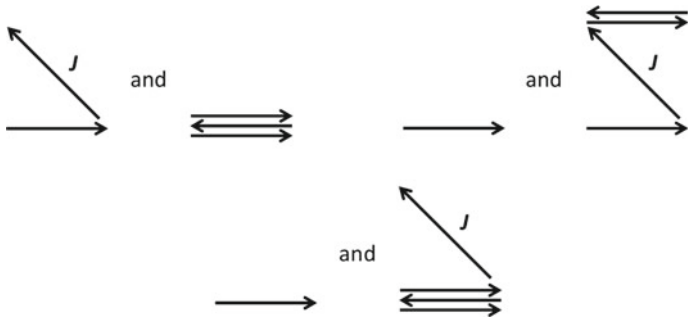

Fig. 3.15 Three combinations of one- and three-pulse states formed by all x-polarized pulses, with one state or the other being linear in J. Each of the three pairs forms a vanishing wave-packet overlap

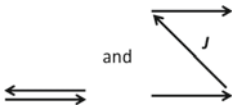

Fig. 3.16 Illustration that a pair of two-pulse wave packets, one of them linear in J, formed by four x-polarized pulses produce a vanishing overlap

overlaps vanish and hence make no contribution to P_{one}. Four x-pulses are similarly unable to contribute to P_{two} linearly in J, as Fig. 3.16 reveals.

As an example of a polarization combination that produces a nonzero difference-phased interference signal of first order in J from our oriented model dimer (and no signal in the absence of energy transfer), we consider the case $\mathbf{e}_A = \hat{\mathbf{y}}$, $\mathbf{e}_B = \mathbf{e}_C = \mathbf{e}_D = \hat{\mathbf{x}}$. The sequences of pulse- and EET-driven electronic transitions making up the quadrilinear overlaps of $P_{\text{one}}^{(d)}$ are sketched in Fig. 3.17, while those responsible for $P_{\text{two}}^{(d)}$ are illustrated in Fig. 3.18.[6]

In the simple version of the dimer Hamiltonian (3.1) used here, each monomer will be assigned a single internal vibrational mode, so the kinetic energy is

$$T = \frac{p_a^2}{2m} + \frac{p_b^2}{2m}\,, \tag{3.58}$$

and the site-state potential functions are

$$V_{\bar{g}g}(q_a, q_b) = \frac{m\omega^2}{2}(q_a^2 + q_b^2)\,, \tag{3.59}$$

$$V_{\bar{e}g}(q_a, q_b) = \epsilon_{\bar{e}g} + \frac{m\omega^2}{2}\big((q_a - d)^2 + q_b^2\big)\,, \tag{3.60}$$

[6] 2D interferograms from $\langle \uparrow_A | \uparrow_B \uparrow_C \downarrow_D \rangle$ alone in model dimers akin to that considered here, under the same polarization conditions—but with arbitrarily abrupt laser pulses—were the subject of earlier work by Cina et al. [6].

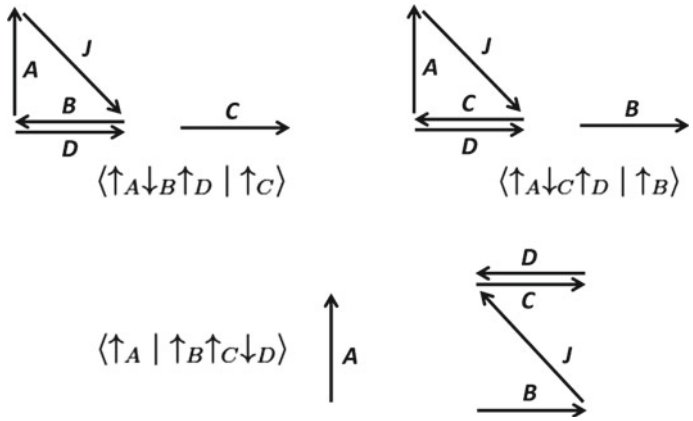

Fig. 3.17 Sequence of electronic transitions under $A_y B_x C_x D_x$ polarization in each pair of states whose overlap contributes to $P^{(d)}_{\text{one}}$ at first order in J

Fig. 3.18 Electronic transitions under $A_y B_x C_x D_x$ polarization in the two states whose overlap determines $P^{(d)}_{\text{two}}$ at first order in J

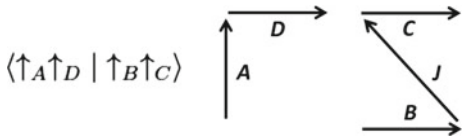

$$V_{\bar{g}e}(q_a, q_b) = \epsilon_{\bar{g}e} + \frac{m\omega^2}{2}\left(q_a^2 + (q_b - d)^2\right), \tag{3.61}$$

and

$$V_{\bar{e}e}(q_a, q_b) = \epsilon_{\bar{e}e} + \frac{m\omega^2}{2}\left((q_a - d)^2 + (q_b - d)^2\right). \tag{3.62}$$

We focus on a case of "downhill" energy transfer with $\epsilon_{\bar{e}g} - \epsilon_{\bar{g}e} = m\omega^2 d^2$, so the intersection line between the singly-excited site-state potentials passes through the minimum point $(q_a, q_b) = (d, 0)$ of the higher-energy, "donor-state" potential, as shown in Fig. 3.19. We pick a moderate Franck-Condon displacement $d = q_{\text{rms}}$, where $q_{\text{rms}} = \sqrt{\hbar/2m\omega}$. The condition (3.25) for weak energy-transfer coupling underlying our choice of the site basis here implies $|J| \ll m\omega^2 d^2 = \hbar\omega/2$. We treat J as a constant, dismissing any nuclear-coordinate dependence.

The weak-coupling condition just invoked ensures $|Jt_{IK}/\hbar| \ll \omega t_{IK}/2$ in the present instance. So the effect of energy transfer is small and can be treated perturbatively through first order in J, as we wish to do, over interpulse delays up to several vibrational periods in length. Other than assuming that weak coupling is operative and stating the sign of J, we need not specify it any more precisely. In the WPI signal calculations presented below the sign of J is taken positive; all the interferograms would change sign if it were instead made negative.

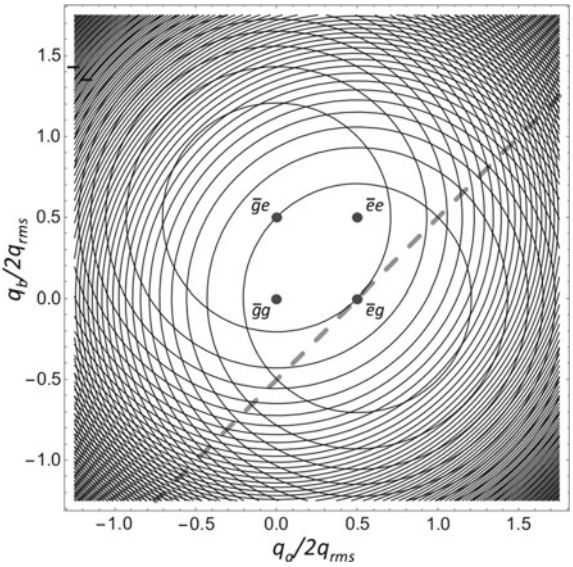

Fig. 3.19 Plot of $V_{\bar{e}g}$ and $V_{\bar{g}e}$ with their minima labeled. Dashed diagonal is the line of intersection between $V_{\bar{e}g}$ and $V_{\bar{g}e}$ for the chosen bare site-energy difference. Minimum points of $V_{\bar{g}g}$ and $V_{\bar{e}e}$ are also shown

From (3.52) we extract formulas for each of the wave packets appearing in (3.56) and (3.57). We find, for instance,

$$|\uparrow_C\rangle = ie^{-i\varphi_C} \sum_{\xi,\xi_1=\bar{e}g,\bar{g}e} |\xi\rangle F_C^{(\xi_1\,\bar{g}g)}[t-t_C]_{\xi\,\xi_1}\, p_C^{(\xi_1\,\bar{g}g)}[t_{CA}]_{\bar{g}g\,\bar{g}g}|\psi_0\rangle\,, \tag{3.63}$$

and

$$\begin{aligned}|\uparrow_A\downarrow_B\uparrow_D\rangle = -ie^{i\varphi_{BA}-i\varphi_D} \sum_{\xi,\xi_2,\xi_3,\xi_4=\bar{e}g,\bar{g}e} |\xi\rangle F_D^{(\xi_2\,\bar{g}g)} F_B^{(\bar{g}g\,\xi_3)} F_A^{(\xi_4\,\bar{g}g)} \\ \times [t-t_D]_{\xi\,\xi_2}\, p_D^{(\xi_2\,\bar{g}g)}[t_{DB}]_{\bar{g}g\,\bar{g}g}\, p_B^{(\bar{g}g\,\xi_3)}[t_{BA}]_{\xi_3\,\xi_4}\, p_A^{(\xi_4\,\bar{g}g)}|\psi_0\rangle\,. \end{aligned} \tag{3.64}$$

Because temporal pulse overlap is being neglected, we have replaced the first argument of each reduced pulse propagator by infinity and written $p_I^{(\xi\bar{\xi})}(\infty;\tau) = p_I^{(\xi\bar{\xi})}$.

The "observation time" t disappears when we take the inner product between the wave packets (3.63) and (3.64) and sum over the state index ξ. Since unitary evolution of both wave packets, including subsequent energy transfer, does not affect their contribution to the singly-excited population, the resulting overlap can be formally evalutated at $t = t_D$:

$$\begin{aligned}\langle\uparrow_A\downarrow_B\uparrow_D|\uparrow_C\rangle = -e^{-i\varphi_{BA}+i\varphi_{DC}} \sum_{\xi_1\,\xi_2\,\xi_3\,\xi_4} F_A^{(\bar{g}g\,\xi_4)} F_B^{(\xi_3\,\bar{g}g)} F_D^{(\bar{g}g\,\xi_2)} F_C^{(\xi_1\,\bar{g}g)}\langle\psi_0| \\ \times\, p_A^{(\bar{g}g\xi_4)}[-t_{BA}]_{\xi_4\xi_3} p_B^{(\xi_3\bar{g}g)}[-t_{DB}]_{\bar{g}g\,\bar{g}g} p_D^{(\bar{g}g\xi_2)}[t_{DC}]_{\xi_2\xi_1} p_C^{(\xi_1\bar{g}g)}[t_{CA}]_{\bar{g}g\,\bar{g}g}|\psi_0\rangle. \end{aligned} \tag{3.65}$$

The overlap (3.65) serves as a template for the others appearing in (3.56) and (3.57), which can be written out directly:

$$\langle\uparrow_A\downarrow_C\uparrow_D \mid \uparrow_B\rangle = -e^{-i\varphi_{BA}+i\varphi_{DC}} \sum_{\xi_1\,\xi_2\,\xi_3\,\xi_4} F_A^{(\bar{g}g\,\xi_4)} F_C^{(\xi_3\,\bar{g}g)} F_D^{(\bar{g}g\,\xi_2)} F_B^{(\xi_1\,\bar{g}g)} \langle\psi_0| \tag{3.66}$$
$$\times\, p_A^{(\bar{g}g\xi_4)}[-t_{CA}]_{\xi_4\xi_3} p_C^{(\xi_3\bar{g}g)}[-t_{DC}]_{\bar{g}g\,\bar{g}g} p_D^{(\bar{g}g\xi_2)}[t_{DB}]_{\xi_2\xi_1} p_B^{(\xi_1\bar{g}g)}[t_{BA}]_{\bar{g}g\,\bar{g}g}|\psi_0\rangle\,,$$

$$\langle\uparrow_A \mid \uparrow_B\uparrow_C\downarrow_D\rangle = -e^{-i\varphi_{BA}+i\varphi_{DC}} \sum_{\xi_1\,\xi_2\,\xi_3\,\xi_4} F_A^{(\bar{g}g\,\xi_1)} F_D^{(\xi_2\,\bar{e}e)} F_C^{(\bar{e}e\,\xi_3)} F_B^{(\xi_4\,\bar{g}g)} \langle\psi_0| \tag{3.67}$$
$$\times\, p_A^{(\bar{g}g\,\xi_1)}[-t_{DA}]_{\xi_1\xi_2}\, p_D^{(\xi_2\,\bar{e}e)}[t_{DC}]_{\bar{e}e\,\bar{e}e}\, p_C^{(\bar{e}e\,\xi_3)}[t_{CB}]_{\xi_3\xi_4}\, p_B^{(\xi_4\,\bar{g}g)}[t_{BA}]_{\bar{g}g\,\bar{g}g}|\psi_0\rangle\,,$$

and

$$\langle\uparrow_A\uparrow_D \mid \uparrow_B\uparrow_C\rangle = e^{-i\varphi_{BA}+i\varphi_{DC}} \sum_{\xi_1\,\xi_2\,\xi_3\,\xi_4} F_A^{(\bar{g}g\,\xi_1)} F_D^{(\xi_2\,\bar{e}e)} F_C^{(\bar{e}e\,\xi_3)} F_B^{(\xi_4\,\bar{g}g)} \langle\psi_0| \tag{3.68}$$
$$\times\, p_A^{(\bar{g}g\,\xi_1)}[-t_{DA}]_{\xi_1\xi_2}\, p_D^{(\xi_2\,\bar{e}e)}[t_{DC}]_{\bar{e}e\,\bar{e}e}\, p_C^{(\bar{e}e\,\xi_3)}[t_{CB}]_{\xi_3\xi_4}\, p_B^{(\xi_4\,\bar{g}g)}[t_{BA}]_{\bar{g}g\,\bar{g}g}|\psi_0\rangle\,.$$

It is to be noted that $\langle\uparrow_A\uparrow_D \mid \uparrow_B\uparrow_C\rangle$, which describes excited-state absorption from the singly- to the doubly-excited electronic manifold, equals minus $\langle\uparrow_A \mid \uparrow_B\uparrow_C\downarrow_D\rangle$, which accounts for "bleaching" of the singly-excited states in the same process. The degree to which the contributions of these overlaps cancel in the WPI signal depends on the relative fluorescence quantum yield following double and single excitation.

Each of the overlaps (3.65)–(3.68) contains two periods of free molecular evolution in the singly-excited manifold of the form $[t_{KL}]_{\xi\,\bar{\xi}}$ during which site-to-site electronic excitation transfer may not or must occur, according to whether ξ is or isn't equal to $\bar{\xi}$; these free molecular-evolution operators consist exclusively of terms of even or odd powers of J, respectively. Thus, an expansion of the signal through first order in J could be found by collecting terms of zeroth and first order in (3.65)–(3.68). But the task is simplified when we consider the chosen dimer orientation and the polarization directions. For the y-polarized A-pulse we have

$$\begin{aligned} F_A^{(\bar{g}g\,\bar{e}g)} &= 0\,; \\ F_A^{(\bar{g}g\,\bar{g}e)} &= m_b F_A \end{aligned} \tag{3.69}$$

(see below (3.55)). For $I = B, C,$ and D, which are x-polarized,

$$\begin{aligned} F_I^{(\bar{g}g\,\xi)} &= \delta_{\xi\,\bar{e}g} m_a F_I\,, \\ F_I^{(\bar{e}g\,\xi)} &= \delta_{\xi\,\bar{g}g} m_a F_I\,, \\ F_I^{(\bar{g}e\,\xi)} &= \delta_{\xi\,\bar{e}e} m_a F_I\,, \\ F_I^{(\bar{e}e\,\xi)} &= \delta_{\xi\,\bar{g}e} m_a F_I\,. \end{aligned} \tag{3.70}$$

Under these circumstances, net transfer occurs during one particular evolution interval in each of the contributing overlaps. All of them vanish at zeroth order in J, and the sought-after first-order overlaps reduce to

$$\langle\uparrow_A\downarrow_B\uparrow_D \mid \uparrow_C\rangle = -e^{-i\varphi_{BA}+i\varphi_{DC}}\mathcal{F}\langle\psi_0|p_A^{(\bar{g}g\,\bar{g}e)}[-t_{BA}]^{(1)}_{\bar{g}e\,\bar{e}g}\,p_B^{(\bar{e}g\,\bar{g}g)} \times [-t_{DB}]_{\bar{g}g\,\bar{g}g}\,p_D^{(\bar{g}g\,\bar{e}g)}[t_{DC}]^{(0)}_{\bar{e}g\,\bar{e}g}\,p_C^{(\bar{e}g\,\bar{g}g)}[t_{CA}]_{\bar{g}g\,\bar{g}g}|\psi_0\rangle\,, \tag{3.71}$$

$$\langle\uparrow_A\downarrow_C\uparrow_D \mid \uparrow_B\rangle = -e^{-i\varphi_{BA}+i\varphi_{DC}}\mathcal{F}\langle\psi_0|p_A^{(\bar{g}g\,\bar{g}e)}[-t_{CA}]^{(1)}_{\bar{g}e\,\bar{e}g}\,p_C^{(\bar{e}g\,\bar{g}g)} \times [-t_{DC}]_{\bar{g}g\,\bar{g}g}\,p_D^{(\bar{g}g\,\bar{e}g)}[t_{DB}]^{(0)}_{\bar{e}g\,\bar{e}g}\,p_B^{(\bar{e}g\,\bar{g}g)}[t_{BA}]_{\bar{g}g\,\bar{g}g}|\psi_0\rangle\,, \tag{3.72}$$

$$\langle\uparrow_A \mid \uparrow_B\uparrow_C\downarrow_D\rangle = -e^{-i\varphi_{BA}+i\varphi_{DC}}\mathcal{F}\langle\psi_0|p_A^{(\bar{g}g\,\bar{g}e)}[-t_{DA}]^{(0)}_{\bar{g}e\,\bar{g}e}\,p_D^{(\bar{g}e\,\bar{e}e)} \times [t_{DC}]_{\bar{e}e\,\bar{e}e}\,p_C^{(\bar{e}e\,\bar{g}e)}[t_{CB}]^{(1)}_{\bar{g}e\,\bar{e}g}\,p_B^{(\bar{e}g\,\bar{g}g)}[t_{BA}]_{\bar{g}g\,\bar{g}g}|\psi_0\rangle\,, \tag{3.73}$$

and

$$\langle\uparrow_A\uparrow_D \mid \uparrow_B\uparrow_C\rangle = e^{-i\varphi_{BA}+i\varphi_{DC}}\mathcal{F}\langle\psi_0|p_A^{(\bar{g}g\,\bar{g}e)}[-t_{DA}]^{(0)}_{\bar{g}e\,\bar{g}e}\,p_D^{(\bar{g}e\,\bar{e}e)} \times [t_{DC}]_{\bar{e}e\,\bar{e}e}\,p_C^{(\bar{e}e\,\bar{g}e)}[t_{CB}]^{(1)}_{\bar{g}e\,\bar{e}g}\,p_B^{(\bar{e}g\,\bar{g}g)}[t_{BA}]_{\bar{g}g\,\bar{g}g}|\psi_0\rangle\,, \tag{3.74}$$

where $\mathcal{F} = m_a^3 m_b F_A F_B F_C F_D$. Free-evolution operators of zeroth and first order in J within the singly excited manifold are marked with superscripts. More explicitly, $[t] \cong [t]^{(0)} + [t]^{(1)}$, where $[t]^{(0)} = \exp\{-iH^{(0)}t/\hbar\}$ (with $H^{(0)}$ being $T + H_{\rm el}(Q)$ in which J is set to zero) and, by first-order time-dependent perturbation theory,

$$[t]^{(1)} = -\frac{iJ}{\hbar}\int_0^t d\tau\,[t-\tau]^{(0)}\big(|\bar{e}g\rangle\langle\bar{g}e| + |\bar{g}e\rangle\langle\bar{e}g|\big)[\tau]^{(0)}\,. \tag{3.75}$$

In the calculated interferograms shown here, the common envelope function for all four pulses is taken to be $f(t) = \exp\{-t^2/2\sigma^2\}$ with $\sigma = 0.09(2\pi/\omega) \equiv 0.09\tau_v$. From (3.54), the reduced pulse propagators,

$$p^{(\xi\bar{\xi})} = \int_{-\infty}^{\infty}\frac{d\tau}{\sigma}\,e^{-\tau^2/2\sigma^2}e^{\mp i\Omega\tau}[-\tau]^{(0)}_{\xi\xi}[\tau]^{(0)}_{\bar{\xi}\bar{\xi}}\,, \tag{3.76}$$

are seen to become proportional to Fourier components of the envelope evaluated at the offset between Ω and the $\bar{\xi}$-to-ξ vibronic transition frequency.

In order to calculate the WPI signal from the excited-state populations, we have to specify the relative fluorescence quantum yield from the singly- and doubly-excited manifolds. We set $Q_{\rm one} = 1$ and illustrate several possibilities by taking $Q_{\rm two} = 0$, 1, or 2. The first choice would be appropriate if some rapid, nonradiative process were to shut off fluorescence from doubly-excited dimers; the second applies if the dimer

undergoes quick internal conversion to the singly-excited manifold prior to radiative decay; and the last value would be applicable if simultaneously excited monomers within a dimer decay by emitting one photon each.

We have not yet stated a value for the bare electronic energy $\epsilon_{\bar{e}e}$ seen in (3.62). One could imagine that it is simply the sum of the individual excitation energies, $\epsilon_{\bar{e}g}$ and $\epsilon_{\bar{g}e}$, and some of our calculations will make this assumption. It's also possible, however, that an "exciton shift" alters the excitation energy for one monomer when the other is already excited, perhaps lowering it due to stronger dispersion interactions between two excited monomers than between one excited and another unexcited species. We'll entertain the possible effect of a nonvanishing exciton shift by considering a particular choice, $\epsilon_{\bar{e}e} = \epsilon_{\bar{e}g} + \epsilon_{\bar{g}e} - \hbar\omega/2$. Due to the phase-sensitive nature of 2D WPI, even this small shift will be seen to influence nonnegligibly the form of the calculated interferograms. A significantly stronger exciton shift might even move singly-to-doubly-excited transitions outside the power spectrum of the laser pulses, driving the relevant matrix elements of $p_C^{(\bar{e}e\,\bar{g}e)}$ and $p_D^{(\bar{g}e\,\bar{e}e)}$ effectively to zero in (3.73) and (3.74) and eliminating contributions from those overlaps. This consequence of a strong exciton shift could be similar to that of a $Q_{\text{two}} = Q_{\text{one}}$ cancelation between the same two overlaps.

Shown below are the real part and the absolute value of each of the contributing overlaps as well as those of the quantum yield-weighted sum of overlaps ξ_d determining the measured 2D signal (see Sect. 3.3.2.3), calculated under the conditions just described. All the time-evolution operators and pulse propagators are represented as matrices in a two-dimensional harmonic oscillator basis. The waiting time is set to half a vibrational period ($t_{CB} = \tau_v/2$) to allow optically generated excited-state wave packets at most one pass through the $V_{\bar{e}g} = V_{\bar{g}e}$ intersection during this interval. The overlaps are multiplied by $\exp\{i\Omega(t_{DC} - t_{BA})\}$ to eliminate optical-frequency oscillations and by $\exp\{i\varphi_{BA} - i\varphi_{DC}\}$ to specify the $\varphi_{BA} = \varphi_{DC} = 0$ case. All overlaps and signals are plotted in units of $|J|/\hbar\omega$ times $m_a^3 m_b F_A F_B F_C F_D$.

Figure 3.20 plots $\langle\uparrow_A\downarrow_B\uparrow_D|\uparrow_C\rangle$ and $\langle\uparrow_A\downarrow_C\uparrow_D|\uparrow_B\rangle$, which appear in $P_{\text{one}}^{(d)}$. Since the three-pulse bra in each of these overlaps does not access the doubly excited state, they would be impervious to the presence of an exciton shift. In Fig. 3.21 is seen the overlap $\langle\uparrow_A|\uparrow_B\uparrow_C\downarrow_D\rangle$, also appearing in $P_{\text{one}}^{(d)}$, whose three-pulse ket involves $\bar{e}e$-state wave-packet dynamics between t_C and t_D. This overlap will be recalculated below with an exciton shift included. It is not necessary to make a separate plot for the overlap $\langle\uparrow_A\uparrow_D|\uparrow_B\uparrow_C\rangle$ determining $P_{\text{two}}^{(d)}$, as it equals minus $\langle\uparrow_A|\uparrow_B\uparrow_C\downarrow_D\rangle$ without or with an exciton shift.

For the model dimer under study, it is possible to understand many key features of the delay dependence of the overlaps shown in Figs. 3.20 and 3.21 in terms of the underlying energy-transfer and nuclear wave-packet dynamics. The vanishing of $\langle\uparrow_A\downarrow_B\uparrow_D|\uparrow_C\rangle$ for $t_{BA} = 2n\tau_v$ is a striking consequence of the half-quantum offset between $\epsilon_{\bar{e}g}$ and $\epsilon_{\bar{g}e}$. We see from (3.71) that first-order energy transfer must occur during t_{BA} for this overlap to be nonzero. When $t_{BA} = 2n\tau_v$, this EET event could take place during any $2\tau_v$-long interval, so we can write

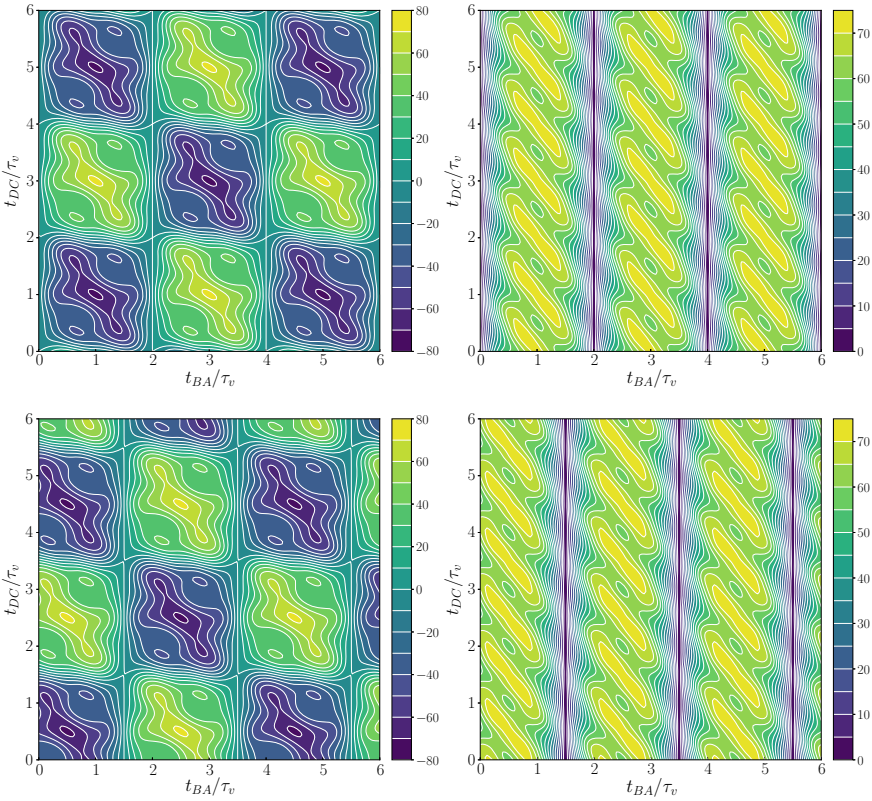

Fig. 3.20 The two upper panels are the real part (left) and absolute value (right) of $\langle \uparrow_A \downarrow_B \uparrow_D | \uparrow_C \rangle$. Intrapulse-pair delays are in vibrational periods $\tau_v = 2\pi/\omega$, and the waiting time is fixed at $t_{CB} = \tau_v/2$. Lower panels are for $\langle \uparrow_A \downarrow_C \uparrow_D | \uparrow_B \rangle$. Neither of these overlaps would be affected by an "exciton shift" in the singly-to-doubly-excited transition energy

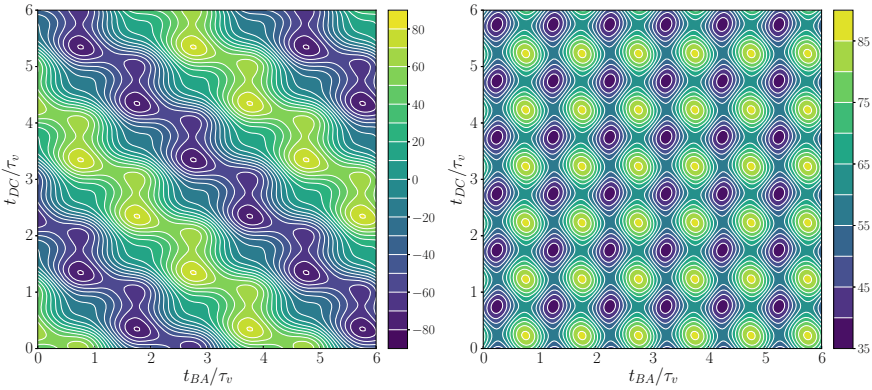

Fig. 3.21 The left panel gives $\mathrm{Re}\{\langle \uparrow_A | \uparrow_B \uparrow_C \downarrow_D \rangle\}$ (or $-\mathrm{Re}\{\langle \uparrow_A \uparrow_D | \uparrow_B \uparrow_C \rangle\}$) for the model dimer without an exciton shift, and the right panel shows its absolute value

$$
\begin{aligned}
[-2n\tau_v]^{(1)}_{\bar{g}e\,\bar{e}g} &= [-2\tau_v]^{(1)}_{\bar{g}e\,\bar{e}g}\,[-2(n-1)\tau_v]^{(0)}_{\bar{e}g\,\bar{e}g} \\
&\quad + [-2\tau_v]^{(0)}_{\bar{g}e\,\bar{g}e}\,[-2\tau_v]^{(1)}_{\bar{g}e\,\bar{e}g}\,[-2(n-2)\tau_v]^{(0)}_{\bar{e}g\,\bar{e}g} \\
&\quad + \cdots + [-2(n-1)\tau_v]^{(0)}_{\bar{g}e\,\bar{g}e}\,[-2\tau_v]^{(1)}_{\bar{g}e\,\bar{e}g}\ . \qquad (3.77)
\end{aligned}
$$

We can break up the first-order factors as

$$
\begin{aligned}
[-2\tau_v]^{(1)}_{\bar{g}e\,\bar{e}g} &= -\frac{iJ}{\hbar}\int_0^{-2\tau_v} d\tau\,[-2\tau_v-\tau]^{(0)}_{\bar{g}e\,\bar{g}e}\,[\tau]^{(0)}_{\bar{e}g\,\bar{e}g} \\
&= -\frac{iJ}{\hbar}\int_0^{-\tau_v} d\tau\,[-2\tau_v-\tau]^{(0)}_{\bar{g}e\,\bar{g}e}\,[\tau]^{(0)}_{\bar{e}g\,\bar{e}g} \\
&\quad -\frac{iJ}{\hbar}\int_{-\tau_v}^{-2\tau_v} d\tau\,[-2\tau_v-\tau]^{(0)}_{\bar{g}e\,\bar{g}e}\,[\tau]^{(0)}_{\bar{e}g\,\bar{e}g} \\
&= -\frac{iJ}{\hbar}\int_0^{-\tau_v} d\tau\,[-2\tau_v-\tau]^{(0)}_{\bar{g}e\,\bar{g}e}\,[\tau]^{(0)}_{\bar{e}g\,\bar{e}g} \\
&\quad -\frac{iJ}{\hbar}e^{i\frac{\tau_v}{\hbar}(\epsilon_{\bar{e}g}-\epsilon_{\bar{g}e})}\int_0^{-\tau_v} d\bar{\tau}\,[-2\tau_v-\bar{\tau}]^{(0)}_{\bar{g}e\,\bar{g}e}\,[\bar{\tau}]^{(0)}_{\bar{e}g\,\bar{e}g} = 0\,; \qquad (3.78)
\end{aligned}
$$

the nuclear wave packet generated in the $\bar{e}g$-state by EET during the second half of each $2\tau_v$-interval is opposite in sign from that formed during the first half, giving rise to complete destructive interference and no net amplitude transfer. The first-order evolution operator in (3.77) therefore vanishes entirely.

A necessary condition for $\langle\uparrow_A\downarrow_B\uparrow_D|\uparrow_C\rangle$ to have a sizable value is that the overlapped one- and three-pulse wave packets reside in similar regions of phase space. That is to say, the expectation values of their coordinate and momentum must nearly coincide, for both a and b modes. Schematic diagrams for both modes of both wave packets are sketched in Fig. 3.22. The A pulse excites the dimer to the $\bar{g}e$ state, where b-mode motion ensues. The local splitting between the two site-states becomes larger than its Franck-Condon value of $\hbar\omega/2$ at positive q_b, so the most likely elapsed times before an energy-transfer transition to $\bar{e}g$, denoted by t_{JA}, will be integer multiples of τ_v. The condition for a-mode coincidence can then be written

$$
\begin{aligned}
\omega d\big(1-e^{-i\omega t_{DC}}\big) &= \omega d\big(1-e^{-i\omega t_{BJ}}\big)e^{-i\omega t_{DB}} \\
&\approx \omega d\big(1-e^{-i\omega t_{BA}}\big)e^{-i\omega t_{DC}-i\omega\frac{\tau_v}{2}}\ , \qquad (3.79)
\end{aligned}
$$

which reduces to $t_{DC}+t_{BA}=m\tau_v$ and rationalizes the slanted form of the peaks in the upper right panel of Fig. 3.20. The b-mode coincidence requirement $0=\omega d(1-\exp\{-i\omega t_{JA}\})$ simply reinforces the condition $t_{JA}\approx n\tau_v$.

The exciton shift affects the two contributing overlaps which involve wave-packet motion in the doubly excited electronic state. $\langle\uparrow_A\,|\,\uparrow_B\uparrow_C\downarrow_D\rangle$ with the chosen exciton shift (see p. 27) is illustrated in Fig. 3.23. $\langle\uparrow_A\uparrow_D\,|\,\uparrow_B\uparrow_C\rangle$ has the opposite sign. The complex-valued overlap itself changes drastically between Figs. 3.21 and 3.23, illustrating the sensitivity of the overlaps determining the 2D-WPI signal to small

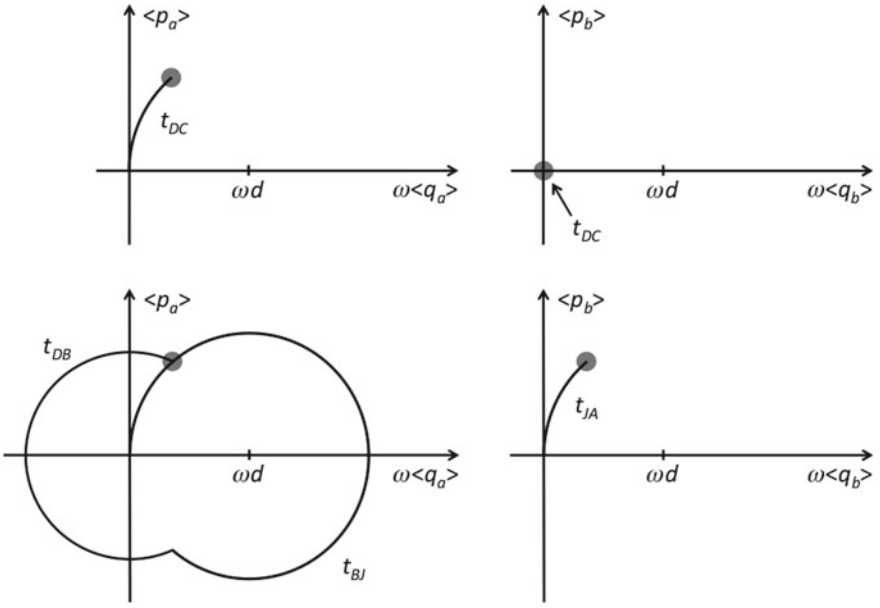

Fig. 3.22 The upper two panels show approximate phase-space paths for $|\uparrow_C\rangle$ while the lower two show those for $|\uparrow_A\downarrow_B\uparrow_D\rangle$, in the case $t_{CB} = \tau_v/2$

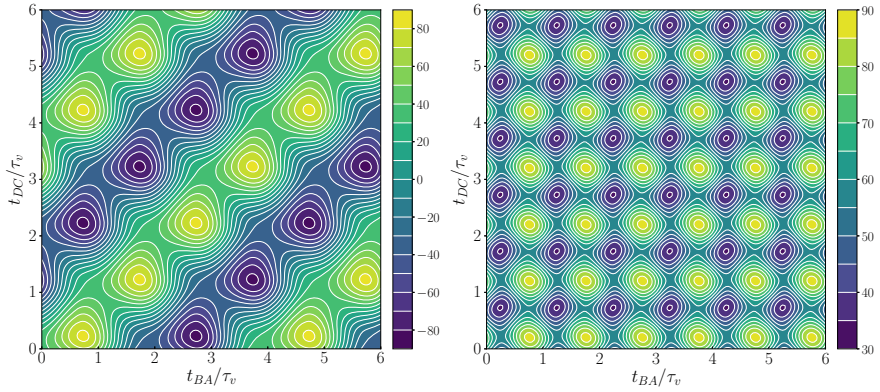

Fig. 3.23 The left panel shows $\mathrm{Re}\{\langle\uparrow_A \mid \uparrow_B\uparrow_C\downarrow_D\rangle\}$ (or $-\mathrm{Re}\{\langle\uparrow_A\uparrow_D \mid \uparrow_B\uparrow_C\rangle\}$) for the model dimer *with* an exciton shift, and the right panel plots its absolute value

changes in the relative phase of the interfering wave packets. The absolute value of the overlap changes only slightly as a result of this small shift, reflecting minute changes in the location of the dimer's singly-to-doubly-excited vibronic transition energies within the power spectrum of the pulses.

The bra and ket trajectories whose final-point coincidence determines the delay combinations of maximal overlap visible in the right panels of Figs. 3.21 and 3.23

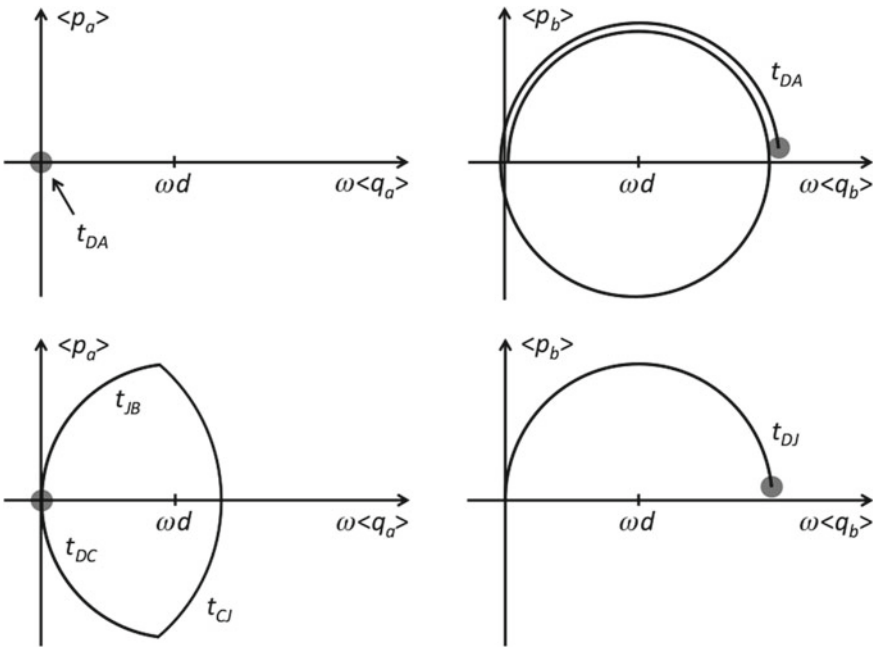

Fig. 3.24 The top (bottom) panels show momentum-versus-position expectation-value trajectories for the bra (ket) of $\langle \uparrow_A \mid \uparrow_B \uparrow_C \downarrow_D \rangle$. Coincidence between the endpoints of these phase-space paths is a prerequisite for this overlap to be large

are drawn schematically in Fig. 3.24. The requirement for agreement between the two a-mode ending points can be written

$$0 = \omega d\big[\big(1 - e^{-i\omega t_{JB}}\big)e^{-i\omega(t_{CB}-t_{JB})} - 1\big]e^{-i\omega t_{DC}} + \omega d\,, \tag{3.80}$$

where $t_{CB} = \tau_v/2$ and t_{JB} estimates the delay between B-pulse arrival and amplitude transfer by EET from $\bar{e}g$ to $\bar{g}e$. This requirement reduces to $t_{DC} = k\tau_v + t_{JB}$. The corresponding condition for the b-mode is

$$\omega d\big(1 - e^{-i\omega t_{DA}}\big) = \omega d\big(1 - e^{-i\omega t_{DJ}}\big)\,, \tag{3.81}$$

or $t_{BA} = l\tau_v - t_{JB}$. Since $t_{JB} \approx \tau_v/4$ in the present situation, the coincidence requirements predict peaks at $(t_{BA}, t_{DC}) \approx (l - \frac{1}{4}, k + \frac{1}{4})\tau_v$, just as seen in the absolute-value plots.

It is interesting that, in the weak EET-coupling situation illustrated here, purely classical descriptions of intramolecular nuclear motion provide reliable explanations for the delay-dependence of 2D WPI signal intensity despite the fact that the spatial range of motion is similar to the width of the nuclear wave packets.

Despite the close similarity between the right-hand panels of Figs. 3.21 and 3.23, the phase dependence exhibited on the left is quite different. The residual electronic phase factor of the aliased overlap is

$$\begin{aligned} e^{i\Omega(t_{DC}-t_{BA})}\langle\uparrow_A \mid \uparrow_B\uparrow_C\downarrow_D\rangle \sim \exp\Bigg\{ & \frac{i}{\hbar}\left(\epsilon_{\bar{g}e}+\frac{\Delta\epsilon}{2}\right)\left(t_{DC}-t_{BA}\right) \\ & + \frac{i}{\hbar}\epsilon_{\bar{g}e}\left(t_{DC}+\frac{\tau_v}{2}+t_{BA}\right) - \frac{i}{\hbar}\left(2\epsilon_{eg}+\Delta\epsilon+\delta\epsilon\right)t_{DC} \\ & + \frac{i}{\hbar}\epsilon_{\bar{g}e}\left(t_{JB}-\frac{\tau_v}{2}\right) - \frac{i}{\hbar}\left(\epsilon_{\bar{e}g}+\Delta\epsilon\right)t_{JB}\Bigg\} \\ = \exp\Bigg\{ & -\frac{i}{\hbar}\Delta\epsilon\left(\frac{t_{DC}+t_{BA}}{2}+t_{JB}\right) - \frac{i}{\hbar}\delta\epsilon\, t_{DC}\Bigg\} \end{aligned} \tag{3.82}$$

(see p. 26), where $\Delta\epsilon = \epsilon_{\bar{e}g} - \epsilon_{\bar{g}e} = \hbar\omega/2$ is the site-energy offset and $\delta\epsilon = 0, -\hbar\omega/2$ is the exciton shift. In the absence of the latter,

$$e^{i\Omega(t_{DC}-t_{BA})}\langle\uparrow_A \mid \uparrow_B\uparrow_C\downarrow_D\rangle \sim \exp\left\{-i\omega\left(\frac{t_{DC}+t_{BA}}{4}+\frac{t_{JB}}{2}\right)\right\}, \tag{3.83}$$

while in its presence,

$$e^{i\Omega(t_{DC}-t_{BA})}\langle\uparrow_A \mid \uparrow_B\uparrow_C\downarrow_D\rangle \sim \exp\left\{i\omega\left(\frac{t_{DC}-t_{BA}}{4}-\frac{t_{JB}}{2}\right)\right\}. \tag{3.84}$$

Equations (3.83) and (3.84) account for the constant phase of the overlap along lines of constant $t_{DC}+t_{BA}$ and $t_{DC}-t_{BA}$ seen in Figs. 3.21 and 3.23, respectively.

3.4.2 Signals

While the delay dependence of the individual overlaps is relatively easy to analyze in terms of wave-packet dynamics, the 2D-WPI signal (3.37) comprises a quantum-yield-weighted sum of the several contributing overlaps. Under the assumptions described on p. 10, the difference-phased whoopee signal from our model dimer becomes

$$S^{(d)} \propto Q_{\text{one}}P^{(d)}_{\text{one}} + Q_{\text{two}}P^{(d)}_{\text{two}} = 2\text{Re}\{e^{-i\varphi_{BA}+i\varphi_{DC}}\xi_d\}, \tag{3.85}$$

where the relevant quadrilinear populations are given by (3.56) and (3.57). Since one of the equal-and-opposite overlaps involving access to the doubly excited state contributes to $P^{(d)}_{\text{one}}$ and the other determines $P^{(d)}_{\text{two}}$, their degree of cancellation will depend on the relative quantum yield from populations in the singly- and doubly-

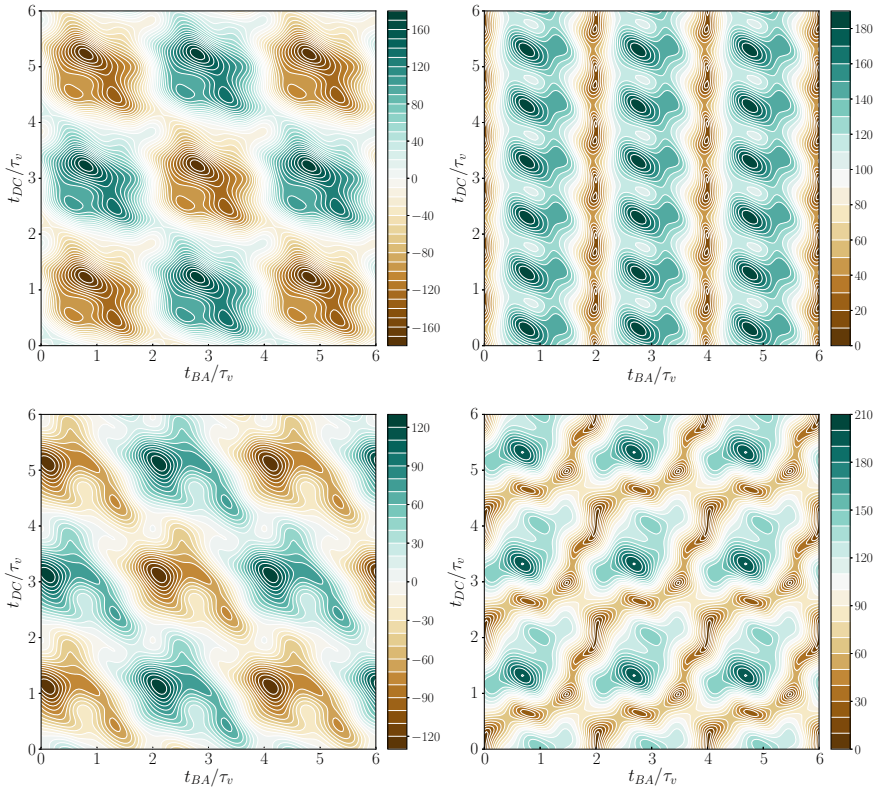

Fig. 3.25 The top two panels exhibit $\mathrm{Re}\{\xi_d\} = \xi_d'$ and $|\xi_d|$ for the EET dimer with $Q_{\mathrm{two}}/Q_{\mathrm{one}} = 0$ in the absence of an exciton shift. Their forms in the presence of a small, negative shift are shown in the bottom row

excited manifolds. As described on p. 27, we shall examine calculated signals for $Q_{\mathrm{two}}/Q_{\mathrm{one}} = 0$, 1, and 2.

Figure 3.25 presents the 2D interferogram determined by the calculated overlaps in the case $Q_{\mathrm{two}}/Q_{\mathrm{one}} = 0$. In the top (bottom) row are the real part and absolute value of ξ_d without (with) an exciton shift. Although $\langle \uparrow_A \uparrow_D \mid \uparrow_B \uparrow_C \rangle$ fails to contribute in this case, the interferogram remains sensitive to the exciton shift through $\langle \uparrow_A \mid \uparrow_B \uparrow_C \downarrow_D \rangle$; both complex-valued and absolute interferograms differ markedly in the two cases.

If $Q_{\mathrm{two}}/Q_{\mathrm{one}} = 1$, the case of equal fluorescence yields from the singly- and doubly-excited manifolds, then $\langle \uparrow_A \mid \uparrow_B \uparrow_C \downarrow_D \rangle$ and $\langle \uparrow_A \uparrow_D \mid \uparrow_B \uparrow_C \rangle$ cancel each other exactly; the interference signal becomes independent of any exciton shift. The 2D WPI signal, illustrated in Fig. 3.26, is now determined by the two remaining overlaps contributing to $P_{one}^{(d)}$.

Sensitivity to the exciton shift returns when $Q_{\mathrm{two}}/Q_{\mathrm{one}} = 2$, meaning that the doubly-excited state is twice as productive of fluorescent photons as a singly-excited state. Here, the contribution from $\langle \uparrow_A \uparrow_D \mid \uparrow_B \uparrow_C \rangle$ outweighs that from $\langle \uparrow_A \mid \uparrow_B \uparrow_C \downarrow_D . \rangle \xi_d$ for the EET dimer for this yield ratio is shown in Fig. 3.27.

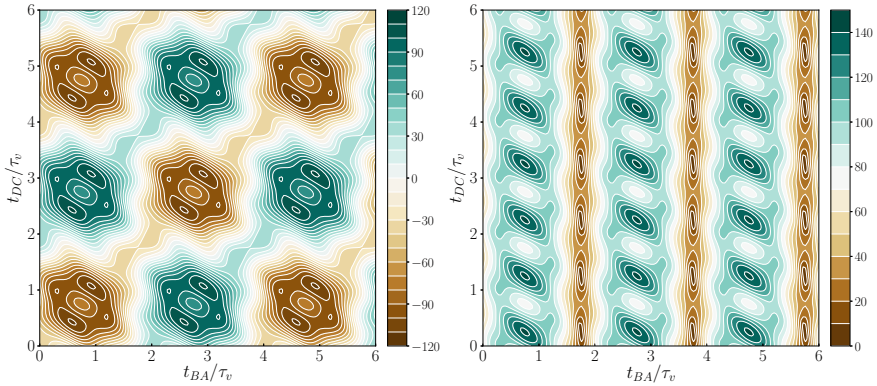

Fig. 3.26 The real part and absolute value of the WPI signal for $Q_{\text{two}}/Q_{\text{one}} = 1$, which is not affected by an exciton shift

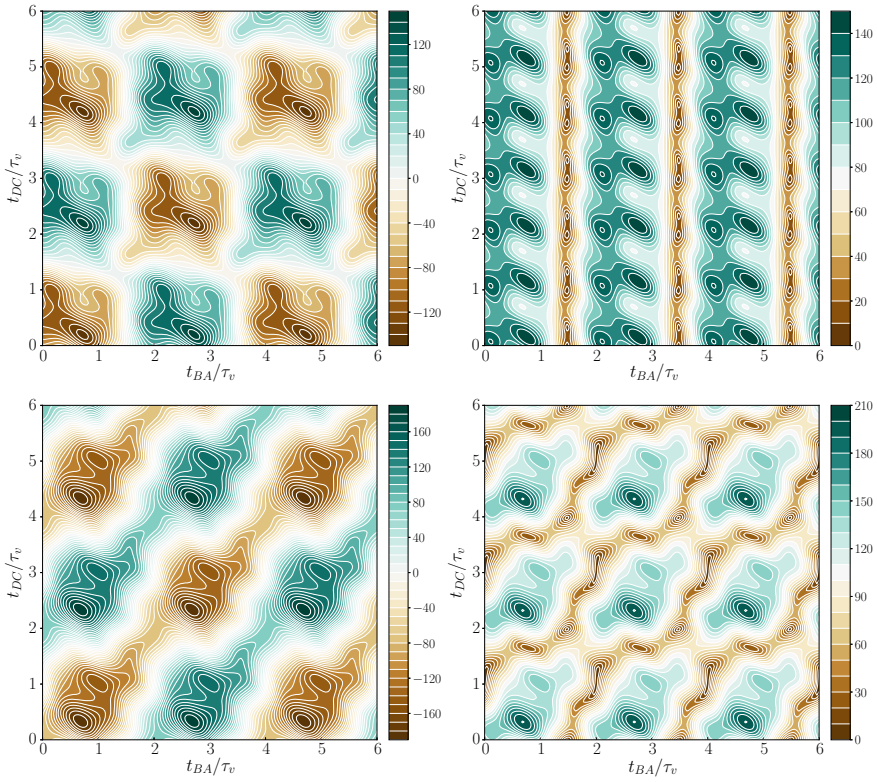

Fig. 3.27 The top panels show ξ_d with $Q_{\text{two}}/Q_{\text{one}} = 2$ and no exciton shift. The bottom two include a small down-shift for singly-to-doubly excited transitions

The calculations presented in this section illustrate the physical information content and dynamical interpretation of two-dimensional wave-packet interferometry signals from an energy-transfer dimer for a specific set of molecular features and experimental parameters. Many elaborations and generalizations remain to be investigated. While the present illustrative calculations yield interferograms of undiminished signal intensity with increasing t_{BA} and t_{DC}, more realistic simulations including (perhaps weak) electronic-nuclear coupling for a large number of intra- and intermolecular modes would of course exhibit "optical dephasing." As a result, increasing intrapulse-pair delays would be accompanied by decreasing signal size [3].

3.5 Conclusion

This chapter spells out a straightforward, general framework for calculating and interpreting multidimensional electronic spectroscopy signals in terms of the wave-packet-shaping, amplitude-transferring effects of femtosecond laser pulses on time-dependent molecular states. It sets up the basic expressions for two-dimensional wave-packet interferometry experiments on an energy-transfer system as a quantum yield-weighted sum of contributing overlaps between multi-pulse wave packets, and identifies the ranges of interpulse delay within which each overlap is not excluded by its order of pulse action from contributing to the WPI signal.

Example calculations are presented for a spatially oriented, weakly coupled EET dimer for whose individual overlaps physical interpretations are readily found using semiclassical analyses of the necessary conditions for phase-space coincidence between the bra and ket, the dynamical consequences of a site-energy difference between to two chromophores, and the sensitivity of contributions accessing or originating from doubly electronically excited states of the dimer to the possible presence of an exciton shift.

The version of the model used for illustration is among the simplest conceivable for basic examination of the information content of 2D ES in the context of electronic excitation transfer, and many possibilities exist for increasing its complexity. One possible change would be to incorporate electronic decoherence by adding site-state-dependent electronic-nuclear coupling to a multiplicity of intra- and intermolecular modes of various frequencies [3]. Another natural step is to increase the number of participating monomers. For example, a tetramer of chromophores arranged in a square geometry could give rise to a conical intersection between single-exciton states, which would in principle generate geometric-phase effects in the EET dynamics. In addition, the occurrence of excitation transfer to more than one neighboring chromophore could result in spatial interference akin to that seen in double-slit experiments. For instance, excitation could transfer from an individual chromophore to the non-adjacent one by taking more than one pathway. Of interest would be the extent to which electronic-nuclear coupling suppresses the resulting interference in excitation transfer by "observing" through which of the neighboring chromophores the excitation was passed. Possibilities may also exist for altering the interference by prior preparation of nuclear motion in the electronic ground state via impulsive stimulated Raman excitation.

Acknowledgements This work was supported by a grant from the US National Science Foundation. JAC thanks Professor Cathy Wong, University of Oregon, for helpful conversations.

References

1. Y. Lee, M. Gorka, J.H. Golbeck, J.M. Anna, Ultrafast energy transfer involving the red chlorophylls of cyanobacterial photosystem I probed through two-dimensional electronic spectroscopy. J. Am. Chem. Soc. **140**, 11631–11638 (2018). https://doi.org/10.1021/jacs.8b04593
2. V. Tiwari, Y.A. Matutes, A. Konar, Z. Yu, M. Ptaszek, D.F. Bocian, D. Holten, C. Kirmaier, J.P. Ogilvie, Strongly coupled bacteriochlorin dyad studied using phase-modulated fluorescence-detected two-dimensional electronic spectroscopy. Opt. Express **26**, 22327–22341 (2018). https://doi.org/10.1364/OE.26.022327
3. M. Cho, H.M. Vaswani, T. Brixner, J. Stenger, G.R. Fleming, Exciton analysis in 2D electronic spectroscopy. J. Phys. Chem. B. **109**, 10542–10556 (2005). https://doi.org/10.1021/jp050788d
4. S.J. Jang, B. Mennucci, Delocalized excitons in natural light-harvesting complexes. Rev. Mod. Phys. **90**, 035003 (2018). https://doi.org/10.1103/RevModPhys.90.035003
5. M.K. Lee, K.B. Bravaya, D.F. Coker, First-principles models for biological light-harvesting: phycobiliprotein complexes from cryptophyte algae. J. Am. Chem. Soc. **139**, 7803–7814 (2017). https://doi.org/10.1021/jacs.7b01780
6. J.A. Cina, D.S. Kilin, T.A. Humble, Wave packet interferometry for short-time electronic energy transfer: multidimensional optical spectroscopy in the time domain. J. Chem. Phys. **118**, 46–61 (2003). https://doi.org/10.1063/1.1519259
7. V. Tiwari, W.K. Peters, D.M. Jonas, Electronic resonance with anticorrelated pigment vibrations drives photosynthetic energy transfer outside the adiabatic framework. P. Natl. Acad. Sci. USA **110**, 1203–1208 (2013). https://doi.org/10.1073/pnas.1211157110
8. J.A. Cina, G.R. Fleming, Vibrational coherence transfer and trapping as sources for long-lived quantum beats in polarized emission from energy transfer complexes. J. Phys. Chem. A. **108**, 11196–11208 (2004). https://doi.org/10.1021/jp047015u
9. S.E. Bradforth, R. Jimenez, F. van Mourik, R. van Grondelle, G.R. Fleming, Excitation transfer in the core light-harvesting complex (LH-1) of Rhodobacter sphaeroides: an ultrafast fluorescence depolarization and annihilation study. J. Phys. Chem. **99**, 16179–16191 (1995). https://doi.org/10.1021/j100043a071
10. V. Butkus, D. Zigmantas, L. Valkunas, D. Abramavicius, Vibrational versus electronic coherences in 2D spectrum of molecular systems. Chem. Phys. Lett. **545**, 40–43 (2012). https://doi.org/10.1016/j.cplett.2012.07.014
11. J.D. Biggs, J.A. Cina, Using wave-packet interferometry to monitor the external vibrational control of electronic excitation transfer. J. Chem. Phys. **131**, 224101 (2009). https://doi.org/10.1063/1.3257596
12. J.D. Biggs, J.A. Cina, Calculations of nonlinear wave-packet interferometry signals in the pump-probe limit as tests for vibrational control over electronic excitation transfer. J. Chem. Phys. **131**, 224302 (2009). https://doi.org/10.1063/1.3257597
13. See also: S. Tomasi, S. Baghbanzadeh, S. Rahimi-Keshari, I. Kassal, Coherent and controllable enhancement of light-harvesting efficiency (2018). arXiv:1810.03251v1 [physics.chem-ph]
14. D.M. Jonas, Two-dimensional femtosecond spectroscopy. Annu. Rev. Phys. Chem. **54**, 425–463 (2003). https://doi.org/10.1146/annurev.physchem.54.011002.103907
15. P.F. Tekavec, G.A. Lott, A.H. Marcus, Fluorescence-detected two-dimensional electronic coherence spectroscopy by acousto-optic phase modulation. J. Chem. Phys. **127**, 214307 (2007). https://doi.org/10.1063/1.2800560
16. G.A. Lott, A. Perdomo-Oritz, J.K. Utterback, J.R. Widom, A. Aspuru-Guzik, A.H. Marcus, Conformation of self-assembled porphyrin dimers in liposome vesicles by phase-modulation 2D fluorescence spectroscopy. P. Natl. Acad. Sci. USA **108**, 16521–16526 (2011). https://doi.org/10.1073/pnas.1017308108

Chapter 4
The Development and Applications of Phase Cycling in Multidimensional Optical Spectroscopy

Howe-Siang Tan

Abstract Although most experiments are performed using a non-collinear beam geometry, multidimensional optical spectroscopy experiments can also be performed using collinear and partially collinear beam geometries. Phase cycling is an important procedure to enable multidimensional optical spectroscopy experiments to be performed in collinear and partially collinear beam geometries. In this chapter, we present the general theory of phase cycling and summarizes the development and applications of the phase cycling procedures in various multidimensional optical spectroscopies. These applications include fully collinear two dimensional optical spectroscopy, pump-probe geometry third order and fifth order two dimensional optical spectroscopies, and fifth order three dimensional optical spectroscopy.

4.1 Introduction

Coherent Multidimensional Optical Spectroscopy (CMDOS) is an important and essential tool in the study of various physical, chemical, and biological systems [1–3]. In CMDOS, nonlinear optical signals representative of the samples' response functions are obtained as a function of the inputs of multiple pulses. The most typical of CMDOS is the third order two-dimensional optical spectroscopy (2DOS). 2DOS can be viewed as the two dimensional Fourier transform of a three-pulse photon echo signal $s(t; \tau, T)$. Here, τ is the delay between the first and second pulses and is typically termed the first coherence time. T is the delay between the second and third pulses and is termed the population (or waiting) time. T is analogous to the pump probe delay in a transient absorption experiment. Further developments has led to optical spectroscopies of higher order and higher dimensions.

As there exists in general, huge number of possible nonlinear optical signals apart from the desired photon echo signal, a sound experimental design is needed to

H.-S. Tan (✉)
Division of Chemistry and Biological Chemistry, School of Physical and Mathematical Sciences, Nanyang Technological University, 21 Nanyang Link, Singapore 637371, Singapore
e-mail: howesiang@ntu.edu.sg

M. Cho (ed.), *Coherent Multidimensional Spectroscopy*,
Springer Series in Optical Sciences 226,
https://doi.org/10.1007/978-981-13-9753-0_4

isolate and acquire the desired signal. There are several techniques in the experimental implementation of CMDOS. The most common approach is to use directional phase matching. In phase matching, pulses incident at different directions result in the different nonlinear signals exiting the sample at different distinct directions. The desired nonlinear signal can then be selectively measured in a distinctive direction. The other approach is to perform CMDOS using all interacting pulses in a collinear beam geometry. In this approach, as all signals are emitted in the same collinear direction, the interpulse phases are managed in order to extract the signal of the desired process. This is the basis of the phase cycling procedure. In phase cycling, we repeat an experiment with a series of different pulse phases. Judicious linear combination of these phase dependent data will then yield the spectrum of the desired nonlinear optical process.

The first discussion and theoretical study of using phase cycling in CMDOS was found in an article by Keusters et al. [4]. It showed that directional selective phase matching and phase selective phase cycling are theoretically equivalent and propose that a $1 \times 4 \times 4 = 16$-step phase cycling scheme can be performed using three collinear phase coherent pulses to measure a two-pulse photon echo two-dimensional optical spectrum. The phase cycling scheme comprises of repetitions of the experiment with the cycling of the phase of the second and third pulses through 0°, 90°, 180°, and 270° relative to the phase of the first pulse. The summation of the 16 sets of data with specific weights will then yield the desired photon echo 2DOS spectrum. This was experimentally demonstrated by acquiring the electronic 2DOS spectrum of rubidium atoms [5]. However, at that time, no procedure was available to determine what other phase cycling schemes can perform the same task. A general theory of phase cycling and phase cycling scheme selection procedure was later presented [6]. This study also included additional CMDOS experiments that can be performed using phase cycling. These include obtaining the 2DOS spectrum of purely absorptive three-pulse echo experiments and 2DOS that correlates two-quanta transitions to one-quantum transitions. It was recognized that there will be experiments that will make use of both directional phase matching and phase cycling [4]. This was made possible with the advent of 2DOS performed in a 'pump-probe' beam geometry [7]. Phase cycling was first used in pump-probe 2DOS in the mid infrared (MIR) [8] and soon applied to visible electronic 2DOS [9]. Phase cycling was also extended to enable fifth order three dimensional optical spectroscopy (5O3DOS) to be performed in a pump-probe geometry [10].

In Sect. 4.2, we present the general theory of phase cycling and the procedure on how a phase cycling scheme can be selected given a particular experimental configuration. In Sect. 4.3, we will present in more details, the CMDOS signals obtainable from different possible experimental configurations, and the appropriate phase cycling scheme and data management needed to acquire the CMDOS spectra of interest.

4.2 Theory of Phase Cycling

In a non-linear optical spectroscopic experiment, a sample interacts with an electric field $E(t)$ consisting a series of optical pulses

$$E(t) = \sum_i A_i(t + \tau_i) \exp(-i[\omega_i t + \boldsymbol{k}_i \cdot \boldsymbol{r} + \phi_i]) \tag{4.1}$$

where A_i are the envelope functions of the interacting pulses with delays τ_i. Under the framework of the time dependent diagrammatic perturbation theory [3, 11], the nonlinear optical signals resulting from different processes acquire the phase terms $\exp(\pm i \boldsymbol{k}_i \cdot \boldsymbol{r})$ and $\exp(\pm i \phi_i)$ with each successive interactions [4]. If the interacting pulses are all non-collinear, the signal pulses will acquire a net direction $\boldsymbol{k}_{\text{sig}}$, while the phase terms ϕ_i will in general cancel out spatially. On the other hand, if the interacting pulses are collinear, the final directional $\boldsymbol{k}$ will be in the same direction as the collinear pulses, and hence will have no directional discriminating effect as in the phase matching case. However, in the collinear geometry, the pulse phases ϕ_i may interfere constructively or destructively, thus enabling us to perform phase cycling. For nonlinear experiments that have a combination of collinear and noncollinear beam geometry, phase cycling can be applied to portions of experiments that are collinear.

We shall discuss a most common example as a conceptual illustration, before laying out the general equations for phase cycling. Figure 4.1a depicts the coherence transfer pathways or double sided Feynman diagrams (DSFD) [3, 11] for a three pulse photon echo (rephasing) process performed using a phase matching approach detected in the $\boldsymbol{k}_{\text{sig}} = -\boldsymbol{k}_1 + \boldsymbol{k}_2 + \boldsymbol{k}_3$ direction.

Likewise for an experiment with three collinear pulses, the signal will acquire a phase of $\phi_{\text{sig}} = -\phi_1 + \phi_2 + \phi_3$. Typically the photon echo signal is not detected collinearly as it is weak, so it is converted into population and detected as a population based action spectrum such as fluorescence and photoconductivity [12, 13]. This necessitates an extra pulse to convert the polarization to population. This is illustrated in Fig. 4.1b where the final population acquires a phase term of $\phi_{\text{sig}} = -\phi_1 + \phi_2 + \phi_3 - \phi_4$. The area shaded in grey denotes where phase cycling is applied over. The phase term ϕ_{sig} 'tags' different processes, much like how $\boldsymbol{k}_{\text{sig}}$ serves to discriminate between different processes, and forms the basis of phase cycling. This desired signal will

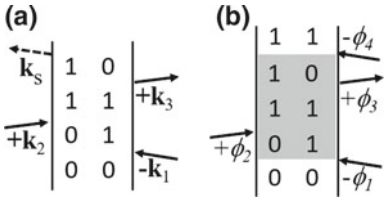

Fig. 4.1 Double sided Feynman Diagram (DSFD) a three pulse photon echo (rephasing) process for **a** phase matching noncollinear beam geometry, **b** phase cycling collinear beam geometry

have the population signal $\tilde{p}_{\text{echo}} \exp[i(-\phi_1 + \phi_2 + \phi_3 - \phi_4)]$. This signal however, is just one of the many component signals of the total pulse phase dependent signal $P(\phi_1, \phi_2, \phi_3, \phi_4)$ that one measures

$$P(\phi_1, \phi_2, \phi_3, \phi_4) = \sum_{\{\alpha_j\}} \tilde{p}(\alpha_1, \alpha_2, \alpha_3, \alpha_4) \exp[i(\alpha_1\phi_1 + \alpha_2\phi_2 + \alpha_3\phi_3 + \alpha_4\phi_4)] \tag{4.2}$$

where $\{\alpha_j\}$ denotes all possible kinds of processes arising from all possible combinations of interactions. The aim of a phase cycling scheme is to perform experiments to obtain selectively only the $\tilde{p}_{\text{echo}}$ signal.

We now consider some conditions placed on the $\{\alpha_j\}$ values.

$$\alpha_1 + \alpha_2 + \alpha_3 + \alpha_4 = 0 \tag{4.3}$$

This condition arises from the fact that the measurable signal comes from the diagonal or population elements of the density matrix. This can be understood by inspecting a DSFD that traces the evolution of the density matrix of a system interacting with the light fields. To start from an initial diagonal element of a density matrix and finally ending in another diagonal element requires that the total number of arrows pointing to the right equates the number of arrows pointing to the left (Fig. 4.1b is an example). As we typically do not control the absolute pulse phases and can only maintain interpulse phase relations, (4.2) [upon substituting (4.3)] gives

$$P(\phi_{21}, \phi_{31}, \phi_{41}) = \sum_{\{\alpha_j\}} \tilde{p}(\alpha_2, \alpha_3, \alpha_4) \exp[i(\alpha_2\phi_{21} + \alpha_3\phi_{31} + \alpha_4\phi_{41})] \tag{4.4}$$

Without a lack of generality, we have referenced the interpulse phase relation to the first pulse, $\phi_{j1} = \phi_j - \phi_1$. The measured signal $P(\phi_{21}, \phi_{31}, \phi_{41})$ contains all the terms with an even number of interactions with the four interacting light fields. Mathematically, to extract any signal $\tilde{p}(\alpha_2, \alpha_3, \alpha_4)$ such as the desired echo signal $\tilde{p}(+1, +1, -1)$ from $P(\phi_{21}, \phi_{31}, \phi_{41})$, we need to take the three dimensional Fourier transform of $P(\phi_{21}, \phi_{31}, \phi_{41})$

$$\begin{aligned}\tilde{p}(\alpha_2, \alpha_3, \alpha_4) \sim \iiint_0^{2\pi} \mathrm{d}\phi_{41}\mathrm{d}\phi_{31}\mathrm{d}\phi_{21} P(\phi_{21}, \phi_{31}, \phi_{41}) \\ \times \exp(-i\alpha_2\phi_{21}) \exp(-i\alpha_3\phi_{31}) \exp(-i\alpha_4\phi_{41})\end{aligned} \tag{4.5}$$

Experimentally, we can only sample the ϕ_{21}-space, ϕ_{31}-space and ϕ_{41}-space finite many times by performing the multipulse experiments with different interpulse phases. This necessitates a discrete Fourier transform evaluation of the Fourier series coefficient

$$\tilde{p}(\alpha_2, \alpha_3, \alpha_4) = \frac{1}{K_2 K_3 K_4} \sum_{k_2=0}^{K_2-1} \sum_{k_3=0}^{K_3-1} \sum_{k_4=0}^{K_4-1} P(k_2 \Delta\phi_{21}, k_3 \Delta\phi_{31}, k_4 \Delta\phi_{41}) \times \exp(-i\alpha_2 \cdot k_2 \Delta\phi_{21}) \exp(-i\alpha_3 \cdot k_3 \Delta\phi_{31}) \exp(-i\alpha_4 \cdot k_4 \Delta\phi_{41}) \tag{4.6}$$

with K_2, K_3 and K_4 being the number of sample points in the ϕ_{21}-space, ϕ_{31}-space and ϕ_{41}-space, respectively. The relationships between the continuous and discrete variables are

$$\begin{aligned} \mathrm{d}\phi_{21} \rightarrow \Delta\phi_{21} \equiv \tfrac{2\pi}{K_2}, \quad \phi_{21} \rightarrow k_2 \Delta\phi_{21} \\ \mathrm{d}\phi_{31} \rightarrow \Delta\phi_{31} \equiv \tfrac{2\pi}{K_3}, \quad \phi_{31} \rightarrow k_3 \Delta\phi_{21} \\ \mathrm{d}\phi_{41} \rightarrow \Delta\phi_{41} \equiv \tfrac{2\pi}{K_4}, \quad \phi_{41} \rightarrow k_4 \Delta\phi_{21} \end{aligned} \tag{4.7}$$

Experimentally, this means a series of $1 \times K_2 \times K_3 \times K_4$ experiments need to be repeated at the different interpulse phases ϕ_{21}, ϕ_{31} and ϕ_{41}. The desired Fourier coefficient $\tilde{p}(\alpha_2, \alpha_3, \alpha_4)$ can then be extracted by the summation of these experiments with the appropriate weights as defined in (4.6).

The periodic property of discrete Fourier transform introduces aliased signals. In a $1 \times K_2 \times K_3 \times K_4$ phase-cycling experiment, the weighted sum of the phase dependent population cannot distinguish between the signals

$$\tilde{p}(\alpha_2, \alpha_3, \alpha_4) \quad \text{and} \quad \tilde{p}(\alpha_2 + pK_2, \alpha_3 + qK_3, \alpha_4 + rK_4) \tag{4.8}$$

where p, q and r are integers. The aliased signals can be suppressed by choosing the appropriate phase cycling scheme. We will outline here the procedure to select the appropriate phase-cycling scheme. Assuming that we can ignore sixth- and higher-order contributions, we will have an additional condition for the $\{\alpha_j\}$ values

$$|\alpha_1| + |\alpha_2| + |\alpha_3| + |\alpha_4| \leq 4 \tag{4.9}$$

The aim is in choosing an appropriate phase cycling scheme that will minimize the number of total phase cycling steps but still be able to uniquely obtain the desired signal free of aliasing. This can be done easily by enumerating all possible $\alpha_2, \alpha_3, \alpha_4$ values that satisfy (4.3) and (4.9). The phase cycling scheme selection criteria is in determining K_2, K_3 and K_4, such that the number of cycles $1 \times K_2 \times K_3 \times K_4$ are minimized but simultaneously avoiding the aliasing of (4.8).

For the case mentioned here, there is a total of 55 possible $\alpha_2, \alpha_3, \alpha_4$ values and to obtain exclusively the rephasing echo signal, $\tilde{p}(\alpha_2 = +1, \alpha_3 = +1, \alpha_4 = -1)$, a $1 \times 3 \times 3 \times 3 = 27$ phase cycling scheme is needed [6].

We now consider the general case for a n-pulse experiment, and set up the necessary phase cycling equations. These n-pulses can be the collinear part of a higher pulse number experiment, giving rise to a pulse phases dependent final measured signal $S(\phi_1, \phi_2, \ldots, \phi_n)$.

The total signal from the n-pulse experiment can be expressed as a summation over all possible set of $\{\alpha_j\}$ values which represents all the different nonlinear optical processes.

$$S(\phi_1, \phi_2, \ldots, \phi_n) = \sum_{\{\alpha_j\}} \tilde{s}(\alpha_1, \alpha_2, \ldots, \alpha_n) \exp[i(\alpha_1\phi_1 + \alpha_2\phi_2 + \cdots + \alpha_n\phi_n)] \tag{4.10}$$

We can lay down the general conditions of what these $\{\alpha_j\}$ values can be

$$\sum_j^n \alpha_j = 0 \tag{4.11}$$

where α_j denotes the interactions with the system by pulse j. The sum of these values leads to zero for a population state. In principle, it is possible to consider interactions leading up to polarization, in which case, the sum will then lead to 1. Another condition on the $\{\alpha_j\}$ values arises from the consideration of the order of nonlinearity M that we need to consider in an experiment.

$$\sum_j^n |\alpha_j| = M \tag{4.12}$$

Typically we cannot control the absolute phases and can only maintain interpulse phase relations. Without any lack of generality, we reference the interpulse phase to the first pulse and obtain from (4.10)

$$\begin{aligned} S(\phi_{21}, \ldots, \phi_{n1}) = \sum_{\{\alpha_j\}} & \tilde{s}(\alpha_1, \alpha_2, \ldots, \alpha_n) \\ & \exp\left[i\left(\left[\Sigma_j \alpha_j\right]\phi_1 + \alpha_2\phi_{21} + \cdots + \alpha_n\phi_{n1}\right)\right] \end{aligned} \tag{4.13}$$

For measurements from population density matrix elements, the first term of above equation reduces to zero according to (4.11). In order to extract a particular $\tilde{s}(\alpha_1, \alpha_2, \ldots, \alpha_n)$ term, we need to perform a $(n-1)$-Dimensional Fourier transform

$$\begin{aligned} \tilde{s}(\alpha_2, \ldots, \alpha_n) \sim \iint \cdots \int_0^{2\pi} & \mathrm{d}\phi_{n1} \ldots \mathrm{d}\phi_{21} S(\phi_{21}, \ldots, \phi_{n1}) \\ & \times \exp(-i\alpha_2\phi_{21}) \ldots \exp(-i\alpha_n\phi_{n1}) \end{aligned} \tag{4.14}$$

In the discrete Fourier transform form, we have the phase cycling equation

$$\tilde{s}(\alpha_2,\ldots,\alpha_n) = \frac{1}{K_2\ldots K_n}\sum_{k_2=0}^{K_2-1}\cdots\sum_{k_n=0}^{K_n-1} S(k_2\Delta\phi_{21},\ldots,k_n\Delta\phi_{n1}) \times \exp(-i\alpha_2\cdot k_2\Delta\phi_{21})\ldots\exp(-i\alpha_n\cdot k_n\Delta\phi_{n1}) \quad (4.15)$$

We shall now discuss the applications of these expressions, especially (4.11), (4.12) and (4.15) to various different types of CMDOS experiments performed in different configurations.

4.3 Applications to Specific Configurations

4.3.1 2DOS in a Collinear Beam Geometry

We have started our discussion in the previous section with the collinear four-pulse photon echo process. In general, there are two processes of interest, Fig. 4.2a, b depict the DSFDs for the non-rephasing (anti-echo) and rephasing (echo) processes respectively.

As mentioned in the earlier section, the conditions on $\{\alpha_j\}$ for such experiments are

$$\alpha_1+\alpha_2+\alpha_3+\alpha_4 = 0 \quad \text{and} \quad |\alpha_1|+|\alpha_2|+|\alpha_3|+|\alpha_4| \le 4 \quad (4.16)$$

The argument has already been made earlier that a $1 \times 3 \times 3 \times 3 = 27$ phase cycling scheme is needed to exclusively select the rephasing $\tilde{s}(\alpha_2,\alpha_3,\alpha_4 = +1,+1,-1)$ signal. The same data set can also be processed to acquire the nonrephasing signal $\tilde{s}(\alpha_2,\alpha_3,\alpha_4 = -1,+1,-1)$ by using different coefficients for the summation. Upon closer observation, there is a possibility of reducing the phase cycling steps further. From the DSFDs in Fig. 4.2, it can be seen that the rephasing process $\tilde{s}(\alpha_2,\alpha_3,\alpha_4 = +1,+1,-1)$ and nonrephasing signal $\tilde{s}(\alpha_2,\alpha_3,\alpha_4 = -1,+1,-1)$ has oscillatory terms $\exp(+i\omega_{10}\tau - i\omega_{10}t)$ and $\exp(-i\omega_{10}\tau - i\omega_{10}t)$ repectively. Upon 2D Fourier transform to yield the 2D spectra, the $\tilde{s}(\alpha_2,\alpha_3,\alpha_4 = +1,+1,-1)$ and $\tilde{s}(\alpha_2,\alpha_3,\alpha_4 = -1,+1,-1)$ signals will be located in the positions centered at $(\omega_\tau,\omega_t) = (-\omega_{10},\omega_{10})$ and $(\omega_\tau,\omega_t) = (\omega_{10},\omega_{10})$

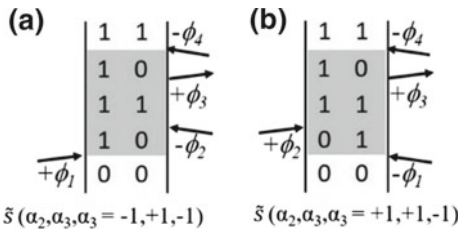

Fig. 4.2 DSFDs of **a** non-rephasing, and **b** rephasing processes from a four pulse collinear 2DOS experiment

respectively. The two signals are thus distinctly located on different quadrants of the 2D spectrum. Therefore with a $1 \times 2 \times 2 \times 2 = 8$ phase cycling scheme, which due to aliasing, will simultaneously acquire both signals on the same 2D spectrum, the two signals being on two different quadrants of the 2D spectrum, can be easily differentiated.

Phase cycling based 2DOS performed in a collinear configuration has the advantage that it can be applied to experimental situations where the sample volume is very small, or in a restricted geometry [4], in which case action spectroscopies that measures populations as fluorescence or photocurrent can be used [12, 13]. Applications of phase cycling enabled collinear 2DOS experiments, include measuring the 2D spectrum of a sample in a flow capillary [14]. Sub-micron spatial resolution at diffraction limit was also achieved with collinear 2DOS performed through a microscope objective lens [15]. By confocal imaging of the fluorescence signal followed by a spatial filter, it is also possible to utilize noncollinear beam geometry to perform what can be measured in a collinear beam geometry [16].

Collinear geometry 2DOS can also be carried out using a three pulse train, whereby the sample interacts twice with the second pulse and the third pulse converts the polarization to population. One can interpret this experiment as a subset of the four pulse collinear 2DOS experiment discussed above, with no delay between the second and third pulses resulting in zero population time, $T = 0$.

In this case, the conditions on the values of $\{\alpha_j\}$ becomes

$$\alpha_1 + \alpha_2 + \alpha_3 = 0 \quad \text{and} \quad |\alpha_1| + |\alpha_2| + |\alpha_3| \leq 4 \tag{4.17}$$

Historically, this was the first phase cycling problem that was first identified [4] and demonstrated experimentally [5]. It was first recognized that a $1 \times 4 \times 4 = 16$-step phase-cycling scheme can selectively measure the photon echo signal $\tilde{s}(\alpha_2, \alpha_3 = +2, -1)$. It was later determined theoretically that a $1 \times 5 \times 2 = 10$-step phase-cycling scheme is sufficient [6]. It should be pointed out that for a three pulse collinear 2DOS, the non-rephasing process $\tilde{s}(\alpha_2, \alpha_3 = 0, -1)$ is not easily measurable as it will be drowned out by a second order process signal which has an identical phase label, and cannot be separated by phase cycling.

Apart from the process depicted in Fig. 4.3a, at least two other processes can also

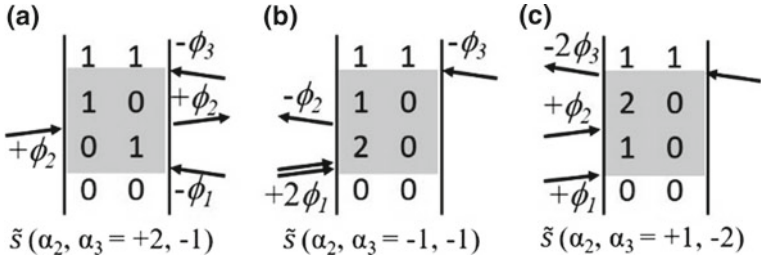

Fig. 4.3 DSFDs of processes measured using three pulse collinear beam geometry. **a** Photon echo (zero waiting time), **b** 2Q-2D, **c** 1Q-2Q correlation

be measured. Figure 4.3b depicts an experiment to measure third-order 2Q-2D spectrum $\tilde{s}(\alpha_2, \alpha_3 = -1, -1)$ where the first two interactions with the first pulse create a double quantum coherence in the system [17]. This is allowed to evolve over the first coherence time period until the second pulse sets it back to one-quantum coherence to evolve over the second coherence time. The interaction by a third pulse brings the process to the population state to be detected. Figure 4.3c depicts another process that is related to the third order 2Q-2D process. This process is termed the 1Q-2Q 2D correlation spectrum. This pathway can be represented by $\tilde{s}(\alpha_2, \alpha_3 = +1, -2)$. In this process, the interaction with the first pulse creates a one-quantum coherence, oscillating during the first coherence time period. One interaction with the second pulse transfers the one-quantum coherence to a double-quantum coherence that oscillates during the second coherence time period. With a $1 \times 4 \times 4 = 16$-step phase-cycling scheme, all three processes (Fig. 4.3a–c) can be obtained from same set of data [6]. This has been experimentally demonstrated by Brixner et al. in measuring the 2DOS, 2Q-2D and 1Q-2Q fluorescence spectra of cresyl violet [18].

4.3.2 2DOS in a Pump Probe Beam Geometry

2DES performed in a partially collinear or pump–probe beam geometry involves interactions with two collinear excitation pulses with precise control in the delay τ and interpulse phase ϕ_{21} which can be easily produced using an optical pulse shaper. In an analogy of 'pump-probe' spectroscopy one can view the first two collinear pulses as a two-pulse 'pump'. Considering the photon echo signals, two interactions from this first two pulses brings it to a population state. A third pulse that is noncollinear with the first two pulses with a delay of T after the first two pulses, provides the third interaction. This third pulse can thus be viewed as a 'probe' pulse. As the emitted signal is in the same direction as the third excitation pulse, the third pulse also acts as a local oscillator that heterodyne-detects the signal and frequency resolved after a spectrometer with a square-law detector to give a signal $S(\phi_{21}; \tau, \omega_t)$. This approach was first demonstrated in the MIR without the use of a pulse shaper by Tokmakoff et al. [7]. Subsequently, it was implemented in MIR [8], visible [9] and ultraviolet [19] wavelengths using a pulse shaper.

As the first two pulses and interactions are collinear leading to a population state, we can apply phase cycling procedure over these two pulses. Figure 4.4 depicts the possible DSFDs of third order nonlinear optical processes that arise from such geometry. They consist of the non-rephasing (Fig. 4.4a), rephasing (Fig. 4.4b) and conventional pump probe (Fig. 4.4c and d) processes. Usually, only the processes depicted in Fig. 4.4a, b are desired.

For brevity, assuming that the interaction pulses are delta functions in time, the measured signal $S(\phi_{21}; \tau, \omega_t)$ which contains the DSFDs depicted in Fig. 4.4, can be described as

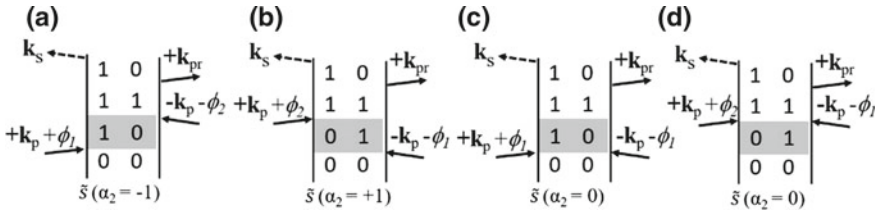

Fig. 4.4 DSFDs for third order signals from a pump-probe geometry 2DOS experiment. **a** Non-rephasing, **b** rephasing, **c** pump-probe from interactions only from first pulse, **d** pump-probe from interactions only from second pulse

$$\begin{aligned} S(\phi_{21};\tau,\omega_t) &= \Re e\big[F_R(\tau,\omega_t-\omega_{10})\exp(i\omega_{10}\tau)\exp(i\phi_{21}) \\ &\quad + F_{NR}(\tau,\omega_t-\omega_{10})\exp(-i\omega_{10}\tau)\exp(-i\phi_{21}) + PP\big] \\ &= \big\{F_R + F_{NR}^*\big\}(\tau,\omega_t-\omega_{10})\exp(i\omega_{10}\tau)\exp(i\phi_{21}) \\ &\quad + \big\{F_{NR} + F_R^*\big\}(\tau,\omega_t-\omega_{10})\exp(-i\omega_{10}\tau)\exp(-i\phi_{21}) + PP \end{aligned} \tag{4.18}$$

The real value arises from heterodyne detection [3]. The PP term contains all signals that are ϕ_{21}-independent and will also have no $\exp(i\omega_{10}\tau)$ or $\exp(-i\omega_{10}\tau)$ dependence. PP usually dominates any set of data taken as they include the pump–probe signals from individual pulses and linear absorption contributions. Upon Fourier transform about τ, of (4.18) to yield a 2D spectrum, we have

$$\begin{aligned} S(\phi_{21};\omega_\tau,\omega_t) &\equiv \sum_{\{\alpha_j\}} \tilde{s}(\alpha_2;\omega_\tau,\omega_t)\exp[i\alpha_2\phi_{21}] \\ &= F_R(\omega_\tau+\omega_{10},\omega_t-\omega_{10})\exp(i\phi_{21}) \\ &\quad + F_{NR}^*(\omega_\tau+\omega_{10},\omega_t-\omega_{10})\exp(i\phi_{21}) \\ &\quad + F_R^*(\omega_\tau-\omega_{10},\omega_t-\omega_{10})\exp(-i\phi_{21}) \\ &\quad + F_{NR}(\omega_\tau-\omega_{10},\omega_t-\omega_{10})\exp(-i\phi_{21}) + PP(\omega_\tau,\omega_t-\omega_{10}) \end{aligned} \tag{4.19}$$

As after two interaction, it is in the population state, the conditions of (4.11) and (4.12) becomes

$$\alpha_1 + \alpha_2 = 0 \quad \text{and} \quad |\alpha_1| + |\alpha_2| \le 2 \tag{4.20}$$

The second condition above arises if we restrict ourselves to processes of third and lower orders while ignoring higher order terms, we need consider only up to two interactions from the first two pulses.

The phase cycling equation for this case can then be expressed as

$$\tilde{s}(\alpha_2;\tau,\omega_t) = \frac{1}{K_2}\sum_{k_2=0}^{K_2-1} S(k_2\Delta\phi_{21};\tau,\omega_t) \times \exp(-i\alpha_2\cdot k_2\Delta\phi_{21}) \tag{4.21}$$

where a $1 \times K_2$ phase cycling is implemented over the second pulse. From (4.20), it can be seen that the possible values of α_2 are $-1 \leq \alpha_2 \leq +1$. To prevent aliasing, the smallest K_2 value is $K_2 = 3$ [20]. However, the rephasing and non-rephasing signals cannot naturally be separated. This can be seen when phasing cycling is used to select the $\tilde{s}(\alpha_2 = +1)$ terms, both the F_R and F_{NR}^* signal will be collected in the same position centred at $(\omega_\tau, \omega_t) = (-\omega_{10}, \omega_{10})$. Due to the measurement of only the real part of the combined rephasing and nonrephasing signals, only pure absorptive peakshapes are obtained. For many applications this is an asset, as it does away with the need of phasing to acquire an absorptive spectrum [2]. The 1×3 phase cycling has been experimentally demonstrated in the visible [21] and in the IR [22].

However, it turns out that for normal usage, a 1×2 phase cycling scheme suffices. A 1×2 phase cycling scheme suffices to separate away the $\tilde{s}(\alpha_2 = 0)$ *PP* terms. Although the same 1×2 phase cycling scheme will cause both $\tilde{s}(\alpha_2 = +1)$ and $\tilde{s}(\alpha_2 = -1)$ terms to be selected, they will appear on distinctly different regions of the 2D spectrum [20]. The $\tilde{s}(\alpha_2 = +1)$ signals will appear centred at $(\omega_\tau, \omega_t) = (-\omega_{10}, \omega_{10})$ and the $\tilde{s}(\alpha_2 = -1)$ signals will appear centred at $(\omega_\tau, \omega_t) = (\omega_{10}, \omega_{10})$. Both these signals are mirror images of each other. Typically, only the former signal at the $(\omega_\tau, \omega_t) = (+\text{ve}, +\text{ve})$ part of the spectrum is presented as the 2D spectra.

Phase cycling enabled pump probe 2DOS has been gradually adopted by increasing number of 2DOS practitioners. Examples of applications of this approach include the measurement of spectral diffusion dynamics of vibrational and electronic transitions [22, 23], elucidating excitation energy transfer pathways in photosynthetic light harvesting systems [24], exciton dynamics in colloidal CdSe quantum dots [25], and singlet fission dynamics [26].

We can expand the pump probe method to study processes of higher order. In fifth order two-quanta 2D spectroscopy (5O2Q2D) [27], (DSFD depicted in Fig. 4.5), the double quanta coherence over the first coherence period τ is created by two interactions with a first pulse, followed by two interactions with a second pulse. After a population time T, where the population of the two-quanta state relaxes to a one-quantum state, an interaction with the third pulse ('probe' pulse) brings it to a one-quantum coherence. 5O2Q2D allows the study of correlations between a two-quanta coherence a one-quantum coherence over a variable time delay of T. Furthermore, both 'non-rephasing' (Fig. 4.5a) and 'rephasing' (Fig. 4.5b) can be measured to acquire a purely absorptive spectrum.

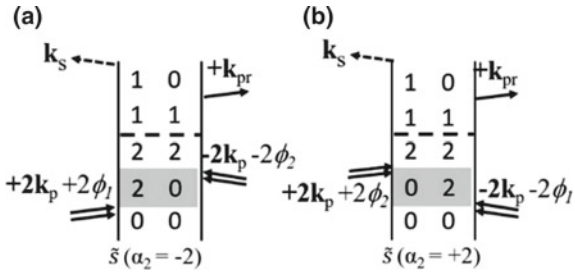

Fig. 4.5 DSFDs of **a** non-rephasing, **b** rephasing processes of fifth order two-quanta 2DOS with four puls collinear beam geometry

The measured signals in a pump probe 2D experiment will include the processes from DSFDs from Fig. 4.4 representing the one-quantum 2D signals and Fig. 4.5 representing the two-quanta 2D signals, and can be expressed as

$$\begin{aligned} S(\phi_{21};\tau,\omega_t) = \Re e\big[& F_{2QR}(\tau,\omega_t-\omega_{10})\exp(i\omega_{20}\tau)\exp(i2\phi_{21}) \\ & + F_{2QNR}(\tau,\omega_t-\omega_{10})\exp(-i\omega_{20}\tau)\exp(-i2\phi_{21}) \\ & + F_{1QR}(\tau,\omega_t-\omega_{10})\exp(i\omega_{10}\tau)\exp(i\phi_{21}) \\ & + F_{1QNR}(\tau,\omega_t-\omega_{10})\exp(-i\omega_{10}\tau)\exp(-i\phi_{21}) + PP\big] \end{aligned} \tag{4.22}$$

The aim of the phase cycling scheme is to be able to differentiate between the third order and fifth order signals. If we consider up to the fifth order signals, the conditions on α_1 and α_2 becomes

$$\alpha_1 + \alpha_2 = 0 \quad \text{and} \quad |\alpha_1| + |\alpha_2| \leq 4 \tag{4.23}$$

It can be seen that $-2 \leq \alpha_2 \leq +2$ and a 1×5 phase cycling scheme will be needed to fully discriminate all the terms with different α_2 values without any aliasing. However, a 1×4 phase cycling scheme should suffice for most cases. In a 1×4 phase cycling scheme, the $\alpha_2 = +2$ and $\alpha_2 = -2$ signals cannot be exclusively separated, However, upon Fourier transform about τ, the $\tilde{s}(\alpha_2 = +2)$ signals will appear centred at $(\omega_\tau, \omega_t) = (-\omega_{20}, \omega_{10})$ and the $\tilde{s}(\alpha_2 = -2)$ signals will appear centred at $(\omega_\tau, \omega_t) = (\omega_{20}, \omega_{10})$. Both these signals are purely absorptive and are mirror image of each other, on opposite sides of the ω_τ axis, thus allowing them to be presented separately. The pump probe geometry 2Q 2DOS with a 1×4 phase cycling scheme has been experimentally applied recently to measure the 2DOS of biexcitons in a J-aggregate. The T dependent annihilation dynamics can be used to measure the exciton diffusion constant [28].

4.3.3 Fifth Order 3DOS in a Pump Probe Beam Geometry

It is a natural progression in technique development to extend the well-established two-dimensional (2D) third-order optical spectroscopies to three-dimensional fifth-order optical spectroscopies [29] (5O3DOS). In a full version of 5O3DOS, the time t - dependent signal $s(t; \tau_1, T_1, \tau_2, T_2)$ resulting from five interactions with five pulses with delays τ_1, T_1, τ_2 and T_2 between first till fifth pulse is collected. The signal is Fourier transform over the three coherence time periods τ_1, τ_2 and t to give the three spectral axes with the two population or waiting times T_1 and T_2 as parameters. A limited form of 5O3DOS can be performed using four pulses (including the local oscillator), as is demonstrated in the MIR [30] and visible [31] wavelengths where multiple interactions are achieved by the second and third pulses, to measure the fifth-order signal. A full form of 5O3DOS with control over both the population times was performed in the MIR using a non-collinear phase-matching geometry with six pulses (including the local oscillator) independently controlled using computer-controlled mechanical translational stages [32]. A full form of 5O3DOS was demonstrated in the visible using a pump-probe geometry which is an adaptation of the technique used to perform pump probe 2DOS [10] presented in Sect. 4.3.2. In this approach, the first four "pump" pulses are provided collinearly by a pulse shaper, followed by subsequent interaction by a non-collinear probe pulse. Just like in the pump probe 2DOS case, where the phase cycling is performed over the two collinear pulse train, phase cycling can be performed over the four collinear pulses in the 5O3DOS (marked out in grey in Fig. 4.6).

The phase cycling over the four pump pulses leading to a population period in the second waiting time is reminiscent of the collinear 2DOS experiment where a four wave mixing process leads to a population state (Sect. 4.3.1). The conditions on the values of $\{\alpha_j\}$ becomes

$$\alpha_1 + \alpha_2 + \alpha_3 + \alpha_4 = 0 \quad and \quad |\alpha_1| + |\alpha_2| + |\alpha_3| + |\alpha_4| \leq 4 \tag{4.24}$$

The pump probe signal becomes

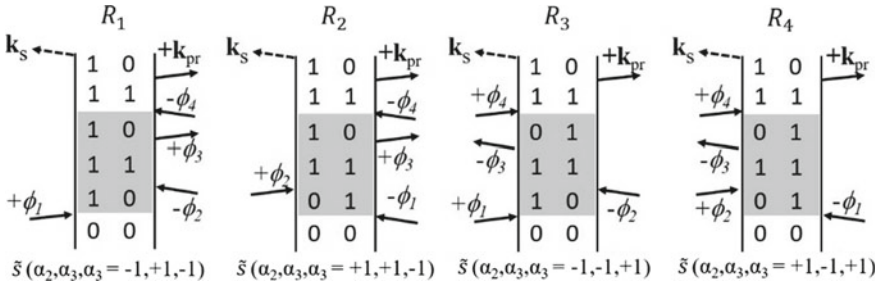

Fig. 4.6 DSFDs of the processes in a fifth order 3D optical spectroscopy measured with a pump-probe beam geometry

$$
\begin{aligned}
S(\phi_{21},\phi_{31},\phi_{41};\tau_1,\tau_2,\omega_t) = \Re e[&R_1(\tau_1,\tau_2,\omega_t-\omega_{10})\exp[-i(\omega_{10}\tau_1+\omega_{10}\tau_2)]\\
&\exp[i(-\phi_{21}+\phi_{31}-\phi_{41})]\\
&+R_2(\tau_1,\tau_2,\omega_t-\omega_{10})\exp[-i(-\omega_{10}\tau_1+\omega_{10}\tau_2)]\\
&\exp[i(\phi_{21}+\phi_{31}-\phi_{41})]\\
&+R_3(\tau_1,\tau_2,\omega_t-\omega_{10})\exp[i(-\omega_{10}\tau_1+\omega_{10}\tau_2)]\\
&\exp[i(-\phi_{21}-\phi_{31}+\phi_{41})]\\
&+R_4(\tau_1,\tau_2,\omega_t-\omega_{10})\exp[i(\omega_{10}\tau_1+\omega_{10}\tau_2)]\\
&\exp[i(\phi_{21}-\phi_{31}+\phi_{41})]+\ldots] \qquad (4.25)
\end{aligned}
$$

Upon Fourier transform about the τ_1 and τ_2 axes, we have

$$
\begin{aligned}
S\big(\phi_{21},\phi_{31},\phi_{41};\omega_{\tau_1},\omega_{\tau_2},\omega_t\big) &\equiv \sum_{\{\alpha_j\}}\tilde{s}\big(\alpha_2\ldots;\omega_{\tau_1},\omega_{\tau_2},\omega_t\big)\\
&\quad\exp[i(\alpha_2\phi_{21}+\alpha_2\phi_{21}+\alpha_2\phi_{21})]\\
&=\big\{R_1+R_4^*\big\}\big(\omega_{\tau_1}-\omega_{10},\omega_{\tau_2}-\omega_{10},\omega_t-\omega_{10}\big)\\
&\quad\exp[i(-\phi_{21}+\phi_{31}-\phi_{41})]\\
&\quad+\big\{R_2+R_3^*\big\}\big(\omega_{\tau_1}+\omega_{10},\omega_{\tau_2}-\omega_{10},\omega_t-\omega_{10}\big)\\
&\quad\exp[i(\phi_{21}+\phi_{31}-\phi_{41})]\\
&\quad+\big\{R_3+R_2^*\big\}\big(\omega_{\tau_1}-\omega_{10},\omega_{\tau_2}+\omega_{10},\omega_t-\omega_{10}\big)\\
&\quad\exp[i(-\phi_{21}-\phi_{31}+\phi_{41})]\\
&\quad+\big\{R_4+R_1^*\big\}\big(\omega_{\tau_1}+\omega_{10},\omega_{\tau_2}+\omega_{10},\omega_t-\omega_{10}\big)\\
&\quad\exp[i(\phi_{21}-\phi_{31}+\phi_{41})]+\ldots \qquad (4.26)
\end{aligned}
$$

It can be seen from (4.26) that it is not possible to obtain a signal representing only one particular process R_i, as all terms are a sum of two processes. However, this is not too much of an issue, as the applications so far have required the measurement of purely absorptive 5O3DOS spectrum, in which case all four of the processes in Fig. 4.6 will need to be measured and combined. As this case is similar to the four pulse collinear 2DOS, there is a total of 55 possible $\alpha_2,\alpha_3,\alpha_4$ values that satisfy the conditions in (4.24). To obtain any one of the term in (4.26) exclusively, a $1\times 3\times 3\times 3=27$ phase cycling scheme is needed. The acquired terms can then be manipulated according to the recipe outlined in [33] to obtain the purely absorptive 5O3DOS spectrum. This phase cycling enabled pump probe geometry 5O3DOS has been used to study the multi-step excitation energy transfer process in plant light harvesting complex LHCII [34].

In preceding discussions, the expressions are presented in the non-rotating frame. That is, the oscillation over the τ period will proceed at the transition frequencies. The discussions are all valid even in the partially rotating frame case, so long as the reference frame is chosen so that no signal overlaps with its mirror imaged aliased signals [21].

4.4 Summary

In this chapter, we have described the concept and the various applications of phase cycling in coherent multidimensional optical spectroscopy. It has found applications in CMDOS performed in a collinear beam geometry, especially useful for small sample volumes and for microscopic spatial resolution. It has also found applications in a series of 'pump-probe' beam geometry CMDOS, including third order and fifth order 2D and fifth order 3D optical spectroscopies. It should be noted that all these phase cycling enabled pump-probe CMDOS techniques can be performed using one setup with minimal opto-mechanical adjustments. This is done by inserting an optical pulse shaper in the 'pump' beam line in a conventional pump-probe transient absorption setup [9, 35]. Further development will no doubt add to the variety of these spectroscopic techniques. In thinking about future designs of CMDOS configurations, phase cycling schemes should be incorporated and used in conjunction with directional phase matching to increase the versatility and range of applications in CMDOS.

Acknowledgements This work is supported by grants from the Singapore Ministry of Education Academic Research Fund (Tier 2 MOE2015-T2-1-039 and Tier 1 RG16/15).

References

1. D.M. Jonas, Two-dimensional femtosecond spectroscopy. Annu. Rev. Phys. Chem. **54**, 425–463 (2003). https://doi.org/10.1146/annurev.physchem.54.011002.103907
2. F.D. Fuller, J.P. Oilivie, Experimental implementations of two-dimensional Fourier transform electronic spectroscopy, Annu. Rev. Phys. Chem. **66**, 667–90 (2015). https://doi.org/10.1146/annurev-physchem-040513-103623
3. P. Hamm, M.T. Zanni, *Concepts and Methods of 2D Infrared Spectroscopy* (Cambridge University Press, 2011)
4. D. Keusters, H.S. Tan, W.S. Warren, Role of pulse phase and direction in two-dimensional optical spectroscopy. J. Phys. Chem. A **103**, 10369–10380 (1999). https://doi.org/10.1021/jp992325b
5. P. Tian, D. Keusters, Y. Suzaki, W.S. Warren, Femtosecond phase-coherent two-dimensional spectroscopy. Science **300**, 1553–1555 (2003). https://doi.org/10.1126/science.1083433
6. H.-S. Tan, Theory and phase-cycling scheme selection principles of collinear phase coherent multi-dimensional optical spectroscopy. J. Chem. Phys. **129**, 124501 (2008). https://doi.org/10.1063/1.2978381
7. L.P. DeFlores, R.A. Nicodemus, A. Tokmakoff, Two-dimensional Fourier transform spectroscopy in the pump-probe geometry. Opt. Lett. **32**, 2966–2968 (2007). https://doi.org/10.1364/OL.32.002966
8. S.H. Shim, D.B. Strasfeld, Y.L. Ling, M.T. Zanni, Automated 2D IR spectroscopy using a mid-IR pulse shaper and application of this technology to the human islet amyloid polypeptide. Proc. Natl. Acad. Sci. U.S.A. **104**, 14197–14202 (2007). https://doi.org/10.1073/pnas.0700804104
9. J.A. Myers, K.L.M. Lewis, P.F. Tekavec, J.P. Ogilvie, Two-color two-dimensional Fourier transform electronic spectroscopy with a pulse-shaper. Opt. Express **16**, 17420–17428 (2008). https://doi.org/10.1364/OE.16.017420

10. Z. Zhang, K.L. Wells, H.S. Tan, Purely absorptive fifth-order three-dimensional electronic spectroscopy. Opt. Lett. **37**, 5058–5060 (2012). https://doi.org/10.1364/OL.37.005058
11. S. Mukamel, in *Principles of Nonlinear Optical Spectroscopy* (Oxford University Press, 1995)
12. G. Nardin, T.M. Autry, K.L. Silverman, S.T. Cundiff, Multidimensional coherent photocurrent spectroscopy of a semiconductor nanostructure. Opt. Express **21**, 28617–28627 (2013). https://doi.org/10.1364/oe.21.028617
13. F.A. Damtie, A. Wacker, T. Pullerits, K.J. Karki, Two-dimensional action spectroscopy of excitonic systems: explicit simulation using a phase-modulation technique. Phys. Rev. A **96**, 053830 (2017). https://doi.org/10.1103/physreva.96.053830
14. S. Draeger, S. Roeding, T. Brixner, Rapid-scan coherent 2D fluorescence spectroscopy. Opt. Express **25**, 3259–3267 (2017). https://doi.org/10.1364/oe.25.003259
15. S. Goetz, D.H. Li, V. Kolb, J. Pflaum, T. Brixner, Coherent two-dimensional fluorescence microspectroscopy. Opt. Express **26**, 3915–3925 (2018). https://doi.org/10.1364/oe.26.003915
16. A.K. De, D. Monahan, J.M. Dawlaty, G.R. Fleming, Two-dimensional fluorescence-detected coherent spectroscopy with absolute phasing by confocal imaging of a dynamic grating and 27-step phase-cycling. J. Chem. Phys. **140**, 194201 (2014). https://doi.org/10.1063/1.4874697
17. E.C. Fulmer, P. Mukherjee, A.T. Krummel, M.T. Zanni, A pulse sequence for directly measuring the anharmonicities of coupled vibrations: two-quantum two-dimensional infrared spectroscopy. J. Chem. Phys. **120**, 8067–8078 (2004). https://doi.org/10.1063/1.1649725
18. S. Mueller et al., Fluorescence-detected two-quantum and one-quantum-two-quantum 2D electronic spectroscopy. J. Phys. Chem. Lett. **9**, 1964–1969 (2018). https://doi.org/10.1021/acs.jpclett.8b00541
19. N. Krebs, I. Pugliesi, J. Hauer, E. Riedle, Two-dimensional Fourier transform spectroscopy in the ultraviolet with sub-20 fs pump pulses and 250–720 nm supercontinuum probe. New. J. Phys. **15**, 085061 (2013). https://doi.org/10.1088/1367-2630/15/8/085016
20. S. Yan, H.S. Tan, Phase cycling schemes for two-dimensional optical spectroscopy with a pump-probe beam geometry. Chem. Phys. **360**, 110–115 (2009). https://doi.org/10.1016/j.chemphys.2009.04.019
21. Z. Zhang, K.L. Wells, E.W.J. Hyland, H.-S. Tan, Phase-cycling schemes for pump–probe beam geometry two-dimensional electronic spectroscopy. Chem. Phys. Lett. **550**, 156–161 (2012). https://doi.org/10.1016/j.cplett.2012.08.037
22. S.K.K. Kumar, A. Tamimi, M.D. Fayer, Comparisons of 2D IR measured spectral diffusion in rotating frames using pulse shaping and in the stationary frame using the standard method. J. Chem. Phys. **137**, 184201 (2012). https://doi.org/10.1063/1.4764470
23. K.L. Wells, Z.Y. Zhang, J.R. Rouxel, H.S. Tan, Measuring the spectral diffusion of chlorophyll a using two-dimensional electronic spectroscopy. J. Phys. Chem. B. **117**, 2294–2299 (2013). https://doi.org/10.1021/jp310154y
24. K.L. Wells, P.H. Lambrev, Z.Y. Zhang, G. Garab, H.S. Tan, Pathways of energy transfer in LHCII revealed by room-temperature 2D electronic spectroscopy. Phys. Chem. Chem. Phys. **16**, 11640–11646 (2014). https://doi.org/10.1039/c4cp00876f
25. H. Seiler, S. Palato, P. Kambhampati, Investigating exciton structure and dynamics in colloidal CdSe quantum dots with two-dimensional electronic spectroscopy. J. Chem. Phys. **149**, 074702 (2018). https://doi.org/10.1063/1.5037223
26. A. Mandal et al., Two-dimensional electronic spectroscopy reveals excitation energy-dependent state mixing during singlet fission in a terrylenediimide dimer. J. Am. Chem. Soc. **140**, 17907–17914 (2018). https://doi.org/10.1021/jacs.8b08627
27. B. Bruggemann, T. Pullerits, Nonperturbative modeling of fifth-order coherent multidimensional spectroscopy in light harvesting antennas. New. J. Phys. **13**, 025024 (2011). https://doi.org/10.1088/1367-2630/13/2/025024
28. J. Dostal, et al., Direct observation of exciton-exciton interactions. Nat. Commun. **9**, 2466 (2018). https://doi.org/10.1038/s41467-018-04884-4
29. P. Hamm, Three-dimensional-IR spectroscopy: Beyond the two-point frequency fluctuation correlation function. J. Chem. Phys. **124**, 124506 (2006). https://doi.org/10.1063/1.2178811

30. F. Ding, M.T. Zanni, Heterodyned 3D IR spectroscopy. Chem. Phys. **341**, 95–105 (2007). https://doi.org/10.1016/j.chemphys.2007.06.010
31. A.F. Fidler, E. Harel, G.S. Engel, Dissecting hidden couplings using fifth-order three-dimensional electronic spectroscopy. J. Phys. Chem. Lett. **1**, 2876–2880 (2010). https://doi.org/10.1021/jz101064j
32. S. Garrett-Roe, P. Hamm, Purely absorptive three-dimensional infrared spectroscopy. J. Chem. Phys. **130**, 164510 (2009). https://doi.org/10.1063/1.3122982
33. Z.Y. Zhang, K.L. Wells, M.T. Seidel, H.S. Tan, Fifth-order three-dimensional electronic spectroscopy using a pump-probe configuration. J. Phys. Chem. B. **117**, 15369–15385 (2013). https://doi.org/10.1021/jp4046403
34. Z.Y. Zhang, P.H. Lambrev, K.L. Wells, G.Z. Garab, H.S. Tan, Direct observation of multistep energy transfer in LHCII with fifth-order 3D electronic spectroscopy. Nat. Commun. **6**, 2914 (2015). https://doi.org/10.1038/ncomms8914
35. S.H. Shim, M.T. Zanni, How to turn your pump-probe instrument into a multidimensional spectrometer: 2D IR and Vis spectroscopies via pulse shaping. Phys. Chem. Chem. Phys. **11**, 748–761 (2009). https://doi.org/10.1039/B813817F

Chapter 5
Four-Dimensional Coherent Spectroscopy

Elad Harel

Abstract The ground- and excited-state electronic and vibrational structure of condensed-phase systems dictates many of their functions. This structure, however, is oftentimes difficult to observe experimentally as the system increases in size and complexity due to short lifetimes and rapid decoherence. One powerful, and, general, approach to elucidating these interactions is to perform increasingly higher-order and higher-dimensionality optical spectroscopies, which have found success in a wide variety of chemical and biological systems and materials. While this approach indeed leads to increased spectral resolution by spreading the spectral information across multiple, coherently coupled dimensions, it also increases the number of signal pathways, and the signal strength falls exponentially. Experiment complexity, long acquisition times, and challenging spectroscopic interpretation has, thus far, made this approach impractical beyond three dimensions. Here, we discuss advances in four-dimensional spectroscopy that addresses, and overcomes, these challenges. We demonstrate that resonance may be used to control which pathways contribute to the signal, thereby greatly simplifying the physical interpretation in comparison to lower-order and fully-resonant experiments. Further, we show that contrary to expectation, and given the dramatically lower signal strength, orders-of-magnitude higher dynamic range is achievable than with lower-order measurements. The analogy of ideas presented here for sampling and reconstruction to existing approaches in NMR are discussed. Finally, we outline a strategy to utilize these methods to interrogate complex molecular systems in solution, show experimental results on organic molecules, and discuss prospects for studying more complex systems such as semiconductor nanocrystals and photosynthetic proteins.

E. Harel (✉)
Department of Chemistry, Northwestern University, Illinois, USA
e-mail: elharel@northwestern.edu

M. Cho (ed.), *Coherent Multidimensional Spectroscopy*,
Springer Series in Optical Sciences 226,
https://doi.org/10.1007/978-981-13-9753-0_5

5.1 Introduction

The influence of electronic-vibrational coupling on excited-state dynamics is well understood in simple, gas-phase molecules, but in more complex systems in solution the large number of quantum-mechanical degrees-of-freedom, especially when considering the influence of the environment, has proven a major challenge for the proper interpretation of spectroscopic experiments. One difficulty is the disparate time and energy scales of the inter- and intra-molecular interactions involved, which can differ by many orders of magnitude. Yet, these interactions are critical in understanding transport of electrons, holes, and excitons in single molecules, molecular aggregates, and solids in the process of a chemical reaction or while moving charge or energy. Recent experimental and theoretical works has demonstrated that exciton-vibrational coupling creates vibronic states whose interactions may dictate the rate of energy transfer in photosynthetic pigment-protein interactions [1], the efficiency and rates of singlet-fission [2], and the rates of carrier relaxation in quantum dots [3]. Coupling of carriers to phonons has a major influence on the properties of semiconductors and their use in a wide variety of applications from lasing, photovoltaics, wave guiding, and lighting. These phonons, which may be acoustic or optical span a wide range of energies across the THz spectral region. Excitons, typically, have absorption bands across a much higher energy range, from the near-infrared to the ultraviolet. The broad range of energies, time, and length scales makes a holistic view of charge and energy transport challenging from both an experimental and theoretical perspective (Fig. 5.1).

As early as the 1970s, Ernst suggested that, as with 2D NMR, 2D infrared spectroscopy could be used to understand the coupling between vibrational modes, thereby tracking structural changes on an ultrafast time scale. More generally, two-dimensional spectroscopy, including 2D electronic spectroscopy, first demonstrated by Jonas and co-workers [4], promised to provide new insights on both the structure and dynamics of complex, condensed-phase systems. As light sources increased in bandwidth and time resolution, larger windows of energy and time space could be accessed, but the effects of broad lines and hard-to-interpret signals still limited their application to relatively small systems (or systems with a small number of well-resolved states). As with NMR, where higher dimensionality experiments proved critical for solving the structure of large proteins and other challenging targets [5], there have been a concerted effort to do the same in the optical domain.

There have been many notable successes in extending multi-dimensional spectroscopy to higher order and higher dimensions, although a comprehensive review is well beyond the scope of this chapter (see review by Cundiff [6]). As early as 2000, Park and Cho showed theoretically that 3D vibrational spectroscopy could reveal three-mode coupling constants in molecules [7], while the work of Hamm and coworkers further considered the effect of non-Gaussian solvation effects on the nonlinear response [8]. Experimentally, Ding and Zanni were among the first to report 3D IR spectra on the molecule $W(CO)_6$ in solution [9]. Other 3D IR experiments were carried out on a diverse range of systems, including the OH stretch of liquid

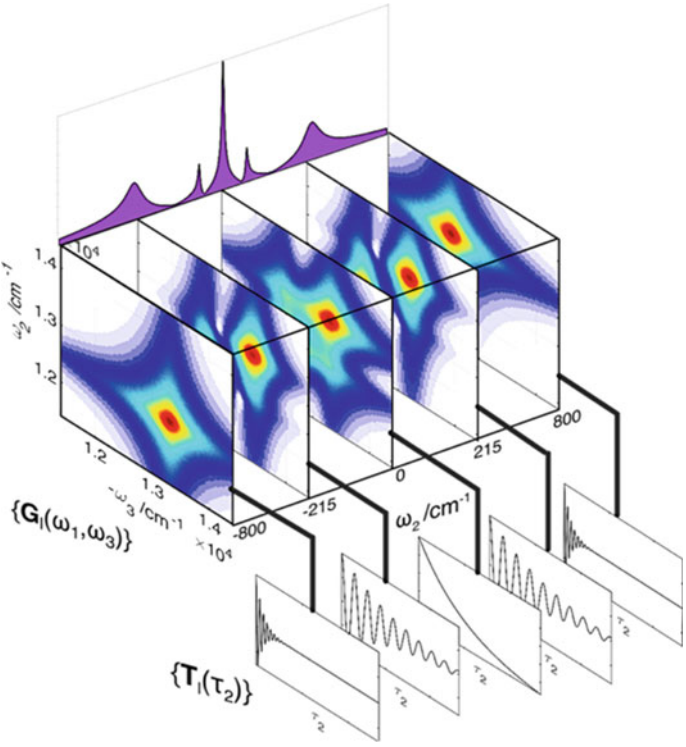

Fig. 5.1 Illustration of a 3D electronic spectrum, where cuts through the low-frequency dimension show a 2D electronic 'beating spectrum'

water and ice [10]. Fifth-order 3D electronic spectroscopy was demonstrated by this author and the Engel group on the cyanine dye, IR-144, which has a long history in the development of 2D ES, as well as some of the initial experiments on 4D coherent spectroscopy discussed here [11]. By spreading the response across three dimensions, a vibronic cross peak that was hidden in lower-order projections was easily resolved. Another important application of 3D ES was in third-order experiments, where the waiting time dimension is Fourier transformed. Many different systems have been studied using this approach including semiconductors, atomic vapors, and photosynthetic pigments and complexes.

With the success of third-order 2D IR, considerable effort was put forth in order to execute fifth-order 2D Raman spectroscopy. First proposed by Tanimura and Mukamel [12], 2D Raman is complimentary to 2D IR (without population dynamics, whose inclusion which would require a seventh-order process) but offers the advantage of far greater spectral bandwidth and access to Raman active modes. A great advantage of using a time-domain approach is the ability to observe transitions in the low-frequency range (0–200 cm^{-1}) that encode, for instance, intermolecular solvent interactions. This spectral range is difficult to access using frequency-domain Raman

spectroscopy, especially in systems that exhibit broadband fluorescence. Unfortunately, it turns out that lower-order cascades co-propagate with the desired fifth-order emitted field. Despite significant effort, separating the much weaker fifth-order signal from the third-order cascade proved extremely challenging [13, 14]. Moreover, even if the signals could be isolated from one another, the method was only applicable to pure solvents using very intense laser pulses because of the non-resonance nature of the interaction. Recently, an effort lead by the Moran group, used resonant excitation to measure true, fifth-order 2D Raman spectra of molecules in dilute solution [15–17]. The method was implemented using both a broadband, time-domain approach and with mixed, time-frequency femtosecond-stimulated Raman. However, since only two temporal dimensions are scanned, there is no direct information on the electronic states or electronic-vibrational coupling, and the large number of signal pathways makes interpretation of the signals more challenging. As will be discussed later, using purely resonant excitation greatly amplifies the signal, but anharmonic coupling information is generally not recoverable because the signal manifests only as subtle changes in the relative peak intensities in the 2D Raman spectrum.

Here, we discuss a novel method to acquire four-dimensional coherent spectra using a method we call Gradient-Assisted Multidimensional Electronic Raman Spectroscopy or GAMERS. We show that GAMERS offers dramatically higher spectral resolution for condensed-phase system than any other optical spectroscopy in the spectral range from THz to the visible. Despite being weak, the unique properties of the signal make it easier to separate from noise, resulting in significantly higher dynamic range compared to lower-order methods. We briefly summarize the theory behind GAMERS and discuss the new physical information it provides, including unique spectral signatures of anharmonicity, electronic coherence, and other non-trivial effects. We end with some applications of the method to conjugated dyes and colloidal quantum dots.

5.2 Gradient Assistant Multidimensional Electronic Raman Spectroscopy—GAMERS

The GAMERS method builds on a single-shot version of 2D electronic spectroscopy (2D ES) called GRadient-Assisted Photon Echo Spectroscopy or GRAPES [18–20]. In traditional 2D ES, three resonant pulses are used to correlate the excitation and emission or excited-state absorption of a system in time. The first pulse creates a single-quantum coherence (SQC) between the ground and excited states, which evolves for some time, τ. Fourier transformation of the time dimension reproduces the ground-state absorption spectrum. The next pulse transforms the SQC to a zero-quantum coherence (ZQC), which may either be a population or a coherence between multiple excited states. Formally, populations are diagonal elements of the density matrix of the form $|a\rangle\langle a|$, while coherences are given by the off-diagonal elements $|a\rangle\langle b|$ where $a \neq b$. The system remains in the ZQC for a period of time, T, before

the next pulse arrives and generates another ZQC. In the particular phase-matched direction known as a photon echo, the first SQC has opposite phase to the last SQC (e.g. a $|a\rangle\langle b|$ coherence is generated during τ, while a $|b\rangle\langle a|$ coherence is generated during the final period, t, prior to signal emission). Other phase-matched 2D or 3D experiments are possible in which higher quanta coherences are generated, but they will not be discussed here. In GRAPES, the exact same information is acquired as in the third-order photon echo experiment, except the τ dimension is not scanned in a point-by-point fashion. Rather, the phase fronts of the pulses are tilted in such a way that there is a one-to-one mapping of the τ delay to a spatial location along one axis of the sample. This arrangement effectively multiplexes the acquisition so that all the τ points are collected at once. More details on the implementation of this geometry will be discussed a bit later.

In GAMERS [21], an additional pulse is added prior to the third-order photon echo sequence. This 'pre-pulse' is non-resonant with the $S_0 \rightarrow S_1$ transition of the molecule, so that, by means of impulsive Raman scattering, a ground-state coherence is generated. This ZQC is allowed to evolve for a time T_0, which, after Fourier transformation, encodes information on the Raman-allowed vibrational frequencies on the ground electronic state. In all, the 4D GAMER spectrum maps electronic—electronic (2D SQC), vibrational–vibrational (2D ZQC), and electronic–vibrational (2D SQC-ZQC) interactions. The 4D spectrum $\hat{S}\left(\omega_{T_0}, \omega_\tau, \omega_T, \omega_t\right)$ is composed of two "Raman-like" ZQC dimensions (ω_{T_0} and ω_T) that resolve vibrational and low-frequency electronic coherences and two "optical" SQC dimensions (ω_τ and ω_t, known as the excitation and detection dimensions, respectively) that resolve high-frequency electronic coherences. The second ZQC dimensions is "Raman-like" is because, due to resonance, there are two possible coherences generated, one on the ground-state and another on the excited state (via a ground-state bleach or excited-state emission pathways). In fact, this ambiguity has led to much debate in the field on the origin of certain 'beating signals' that were observed in 2D ES experiments on photosynthetic pigment-protein complexes [22, 23].

In order to better visualize the 4D spectrum, 2D slices and projections are often helpful in isolating and assigning features [21]. For example, at each point in the (ω_τ, ω_t) plane, one can extract a 2D spectrum containing the vibrational modes that couple to the electronic transition at the chosen point[21212121]. Similarly, at each point in the $\left(\omega_{T_0}, \omega_T\right)$ plane, one can extract a 2D 'beating' spectrum that reveals which electronic transitions couple to the vibrational mode at the chosen $\left(\omega_{T_0}, \omega_T\right)$ point. Importantly, there are also mixed electronic–vibrational slices in which the signal is displayed as a function of one electronic dimension (ω_τ or ω_t) and one vibrational dimension (ω_{T_0} or ω_T). These slices are particularly useful for highlighting differences in vibrational frequencies between different electronic states or for revealing relative electronic–vibrational (e.g., exciton–phonon) couplings. In all, there are six different 2D projections of the 4D data cube, and many thousands of different 2D slices that can be chosen to highlight specific pathways and features. The total number of data points in each hypercube is at least 10^8, and in some case much more depending on the resolution and bandwidth of the experiment. Dealing with such large data presents its own challenges associated with data handling and processing.

Therefore, it is very useful to understand the signal pathways that contribute to the GAMER spectrum, which then informs precisely which locations to examine in the sparse spectral space.

To track the different signal contributions, it is useful to think of GAMERS as a third-order, rather than fifth-order, process that starts from an initial, ground-state coherence [24]. Since the interactions of the resonant and non-resonant pulses are physically distinct, with the former operating according to the dipole-moment operator, while the latter is through the electronic polarizability, this separation of a fifth-order process to a second- plus third-order process is justified. To first-order in perturbation theory, the density matrix in the interaction representation after interaction with the non-resonant pre-pulses is given by

$$\tilde{\rho}_{\mu,\mu'}(t) = \rho^{(\mathrm{eq})}_{\mu,\mu'} - \frac{i}{\hbar}\Delta\rho^{(\mathrm{eq})}_{\mu,\mu'}\int_0^t \mathrm{d}t'\, H'_{\mu,\mu'}\left(t'\right)\exp\left(i\omega_{\mu,\mu'}t'\right)$$

Therefore, the initial coherence depends on the intensity envelope, $H'(t)$, of the non-resonant pulse and requires that the pulse duration be shorter than the vibrational period, $\left(\omega_{\mu,\mu'}\right)^{-1}$. In practice, the non-resonant pulse is actually near-resonant (usually red-shifted of the absorption band) and temporally short to excite as large of a bandwidth as the pulse spectrum supports. The expression above for the density operator may then be thought of as the initial state in a third-order photon echo spectroscopy [25]. The same third-order pathways may be drawn using a diagrammatic representation of the density matrix after each field-matter interaction.

One important feature of GAMERS is that it makes assigning signals to specific coherence pathways more straightforward than lower-order methods. For instance, the ambiguity of many early 2D ES experiments that report on beating signals during the time period T is a result of the difficulty in distinguishing between the R_3 (R_3*) and R_4 (R_4*) pathways; the former consists of electronically excited states, while the latter is confined to the ground state. The '*' indicates negative frequencies during T_0, which occur because there the interaction with the two Raman pre-pulses can occur on either side of the density matrix (note, there is no specific time-ordering enforced between the interactions with pulse 0 and 0'). Fortunately, the signals naturally separate into different quadrants of the 4D spectrum. As it relates to energy transfer this distinction is critical, as the latter pathway is not at all related to excited-state dynamics and, therefore, cannot play any role in transport [26]. A key advantage of GAMERS is that the SQC generated during T_0 must be on the ground state, while during the period T coherences may be on either electronic surface. Therefore, after taking careful account of differences caused by selection rules, examination of correlations between the two SQCs allows for the determination of the origin of coherence signals assuming that there are resolvable shifts in energy (or lifetimes) caused by differences in the ground and excited-state potential surfaces (see Fig. 5.3). This is not the case for lower-order methods, where no such ground-state reference exists. It is important to realize, however, that if the ground and excited-state frequencies are identical, then there is no spectroscopic means of distinguishing them without

resorting to some alternate detection method such as fluorescence, which can only come from an excited state pathway.

As eluded to earlier, the resonance condition is critical for predicting which type of physical effects will be detected by any particular multi-dimensional spectroscopy. In a non-resonant experiment, such as fifth-order 2D Raman, the signal can only arise when there is anharmonic coupling between vibrational modes. This makes the method sensitive to non-trivial effects such as intermolecular coupling in liquids, but it comes at the cost of very low signal (hence, the need to perform the experiment in a pure solvent). When there is a competing process such as cascades, a problem exacerbated at high concentrations, the signal of interest can be hard or impossible to isolate. On the flip side, a fully resonant 6WM experiment completely overcomes the cascade problem, but now the signal is only sensitive to the Franck–Condon overlap between the ground and excited states. While anharmonicity effects the transition moments, and, hence, the intensity of peaks in the spectrum, it is extremely difficult to quantify the coupling based on relative amplitudes. GAMERS, on the other hand, combines resonant and non-resonant excitation, thereby making it sensitive to non-trivial effects such as anharmonic coupling and electron-vibrational coupling, while also avoiding the cascade problem. The signal strength is intermediate between the two extremes, but with advances in signal detection and analysis, the experiment can be done at the same concentrations used in the corresponding third-order resonant spectroscopy.

5.3 Practical Implementation of 4D Spectroscopy

As discussed above, GAMERS is a fifth-order nonlinear spectroscopy in which five excitation pulses stimulate an emitted six-wave mixing (6WM) signal field that varies as a function of the relative delays between pulses. As shown in Fig. 5.2b, the photon-echo signal of GAMERS is measured in the phase-matched direction, $\hat{k}_{6\mathrm{WM}} = -\hat{k}_0 + \hat{k}_{0'} - \hat{k}_1 + \hat{k}_2 + \hat{k}_3$. An immediate problem that arises when trying to execute a four-dimensional experiment is the large number of data points resulting from each time dimension, combined with the low signal-to-noise that necessitates long signal averaging. For instance, if each spectral dimension contains 256 points, then over four billion data points, typically at 16-bit resolution, are required to capture the 4D spectrum. Since the signal is very weak—about 10^{-4} of the strength of a typical 4WM experiment—a brute force measurement, sampling all four temporal dimensions at these rates and signal averaging would require hundreds of years. Even when multiplexing by using a spectrometer to resolve the probe frequencies (if sufficient signal exists), sampling could take many months. Exposure to many laser pulses (>200,000 per second), even at very low pulse intensities, usually degrades the sample in a matter of hours.

One important means by which to reduce the acquisition time is to employ the GRAPES geometry using a cylindrical optic in which light is focused along only direction. In the unfocused direction, the wavefront of beam 2 is oriented parallel to

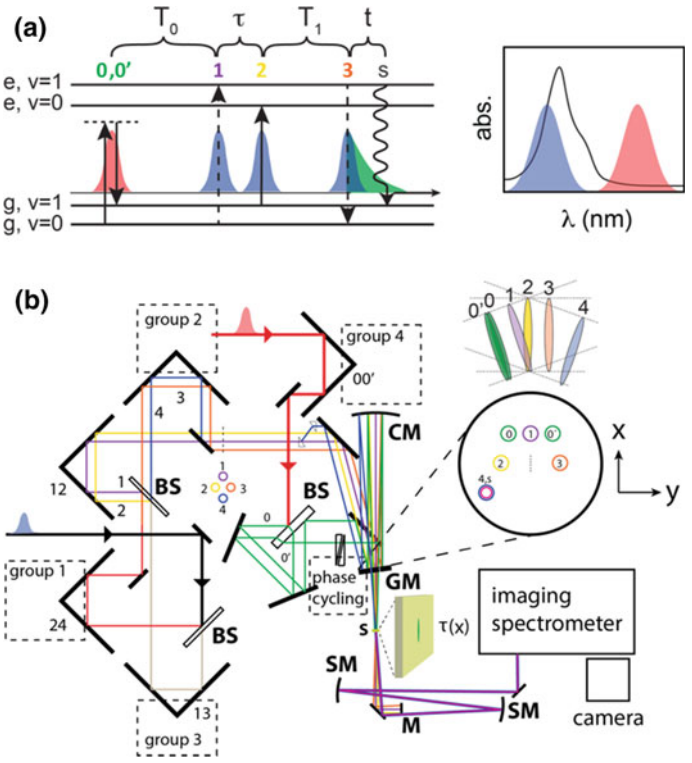

Fig. 5.2 Overview of GAMERS. **a** Pulse sequence involving five field-matter interactions. The first two pulses, 0 and 0', create a ground-state coherence which evolves for a time T_0. These pulses are off-resonance with the absorption of the molecule. The next three pulses are resonant and create single- and zero-quantum coherences during the delays τ, T_1, and t. **b**. Experimental setup showing the generation of six pulses (0, 0', 1, 2, 3, and 4 = local oscillator). A Sagnac interferometer is used to passively phase stabilize the non-resonant pulses, which are coincident in time but excite from different directions. The inset shows the beam geometry and the pulse-front tilt of each pulse relative to the sample position (along *x*). The signal comes out in a unique, phase-matched direction and overlaps with the local oscillator on a camera after passing through an imaging spectrometer. Due to spatial-temporal multiplexing (GRAPES), only T_0 and T_1 need to be scanned. **BS** = beam splitter, **CM** = cylinder mirror, **GM** = GRAPES mirror assembly, **SM** = spherical mirror, **M** = mask

the sample, while beam 1 is tilted by a few degrees using a mirror. This arrangement creates a delay of about 100–200 fs per millimeter depending on the exact geometry used. Since SQC times of molecules in solution are typically short, this is sufficient to encode the full range of τ delays, with only a small apodization caused by the, possibly, non-uniform spatial intensity of the pulses (which can be corrected to a large degree during processing). The GRAPES geometry, however, requires careful geometric considerations in order to not inadvertently introduce other spatially dependent time delays in the pulse sequence. As shown in Fig. 5.2b, the beam geometry is such that the pre-pulses are arranged along the same horizontal axis as the first

resonant excitation beam (labelled as '1'). This ensures that the pulse front of beams 0, 0', and 1 are all parallel at the sample so that no spatiotemporal gradient exists among them. These pulses are tilted relative to pulse 2 in the GRAPES geometry, while pulse 3 is parallel to pulse 2 and to the line of focus at the sample. The local oscillator, pulse 4, which is needed to resolve the signal phase, is positioned in a plane below the sample and, therefore, tilted relative to all the other pulses and to the emitted signal. The effects of this tilt must be carefully considered when processing the data to ensure the signal is not rotated in phase along the spatiotemporal axis. Calibration of all the pulses, their tilts and phase, therefore, is an important aspect of retrieving accurate spectra. As with GRAPES, the signal and local oscillator are reimaged onto the slit of an imaging spectrometer after passing through a mask that blocks all the excitation light. Further schemes such as phase cycling are used to eliminate scattering contributions to the signal. Note, acquiring the absolute phase, so-called 'phasing', is more difficult in GAMERS because the projection-slice theorem would require pumping with the non-resonant pulses and probing with a resonant pulse. While theoretically possible to measure, the 5th-order signal would then be buried in a background 7–8 orders of magnitude larger, making signal extraction nearly impossible (Fig. 5.3).

In the original implementation (unpublished) of GAMERS, the output of a high-repetition rate (200 kHz) Yb amplifier was used as the pre-pulse ($\hat{k}_0$ and $\hat{k}_{0'}$), but because the bandwidth was limited (<10 nm), the spectra were highly distorted and showed few high-resolution vibrational modes along ω_{T_0}. The amplifier was replaced with an ultra-short non-collinear optical parametric amplifier (NOPA) with considerably more bandwidth (up to 1500 cm^{-1}), but considerably lower power. Still, by placing the center frequency closer to resonance, considerably more signal was generated and a larger number of vibrational modes could be observed along ω_{T_0}. To test whether the signal generated was truly fifth-order and not a lower-order cascade, the pre-pulses were directed to be colinear so that both the four-wave mixing (4WM) and 6WM signals could co-propagate. In this arrangement, one could directly compare the phase of the signals, which were predicted to be exactly 180° out of phase owing to the two additional interactions in the 6WM experiment. In addition, we carried out concentration dependent studies that showed that the signal scaled linearly with the concentration of the analyte after carefully considering reabsorption effects that occur at high optical densities. Even without these validation experiments, it is easy to understand why cascaded signals to not dominate the GAMERS signal. Since three of the pulses are resonant with the low concentration analyte, the non-resonant signal is strongly suppressed. In fact, one advantage of GAMERS over 4WM) experiments such as 2D ES is that there is no measurable signal from the solvent, which greatly simplifies interpretation of the spectra, especially when assigning the vibrational modes.

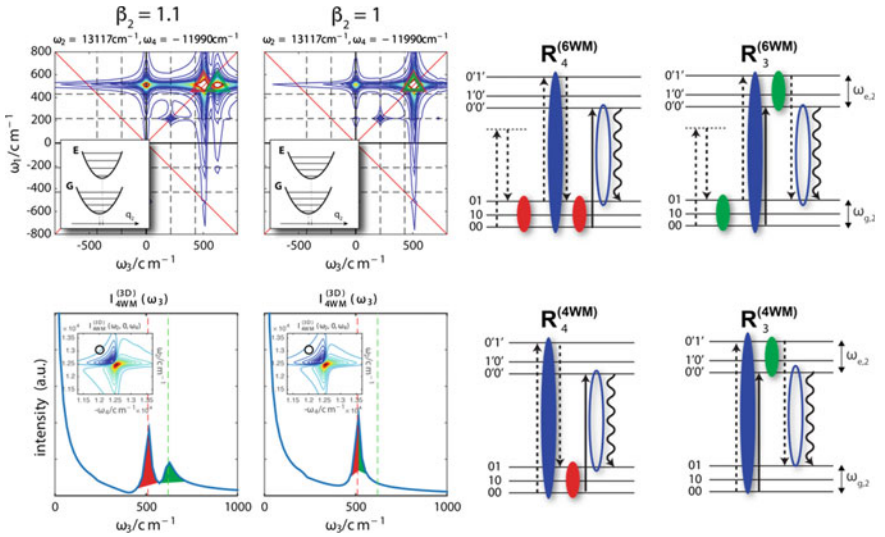

Fig. 5.3 Distinguishing ground from excited-state coherences. **Top Left**: 2D ZQC-ZQC cut through a simulated 4D GAMER spectrum of a displaced harmonic oscillator system with different curvatures of the excited state (beta = 1 and 1.1). Two vibrational modes are included in the model. Note new peak appears in beta = 1.1 model along only one axis because the first ZQC coherence acts as a reference. **Top Right**: Feynman pathways for 6WM, in which the second ZQC is either on the ground (R_4) or exited (R_3) manifolds. Dark ovals indicate a positive coherence, while open ovals indicate a negative coherence frequency. **Bottom Left**: Simulated 2D electronic spectra and ZQC spectrum for the corresponding models in top left. If the excited-state frequencies differ from those in the ground-state, multiple peaks appear, but there is no way to assign them to their respective potential surfaces. **Bottom Right**: Corresponding Feynman pathways for 4WM process

A major disadvantage, however, of the collinear geometry in which $\hat{k}_0 \approx \hat{k}_{0'}$, is that the 6WM signal is buried in the ~1000x or more 4WM signal, greatly limiting dynamic range. This can be seen in the 2D ZQC spectra from IR144 in Fig. 5.4, where the peaks are not much stronger than the noise. It is important to note that most of the noise accumulates along $\omega_T = 0$ and $\omega_{T_0} = 0$ because the corresponding time delays are sampled slowly (so-called indirect noise). In the Fourier domain, such indirect sampling causes large amplitude noise in the spectra. As theory predicts, most of the signal is accumulated in the all positive and all negative quadrants in the (ω_T, ω_{T_0}) plane, while there is some noticeable peaks in the lower right quadrant. Examining the corresponding 2D ZQC 'beat maps' reveals the Feynman pathways associated with each of these vibrational peaks. While most of the signal intensity is on the diagonal, indicating modes that are activated both by the polarizability and Franck–Condon overlap, there is noticeable signal intensity off the diagonal indicating some degree of mode coupling, especially between low-frequency modes. A salient feature of the beating maps is that they are considerably narrower than the overall third-order 2D electronic spectra because they only involve pathways that pass through specific vibrational states, either on the ground or excited states or both. Yet, the SNR in

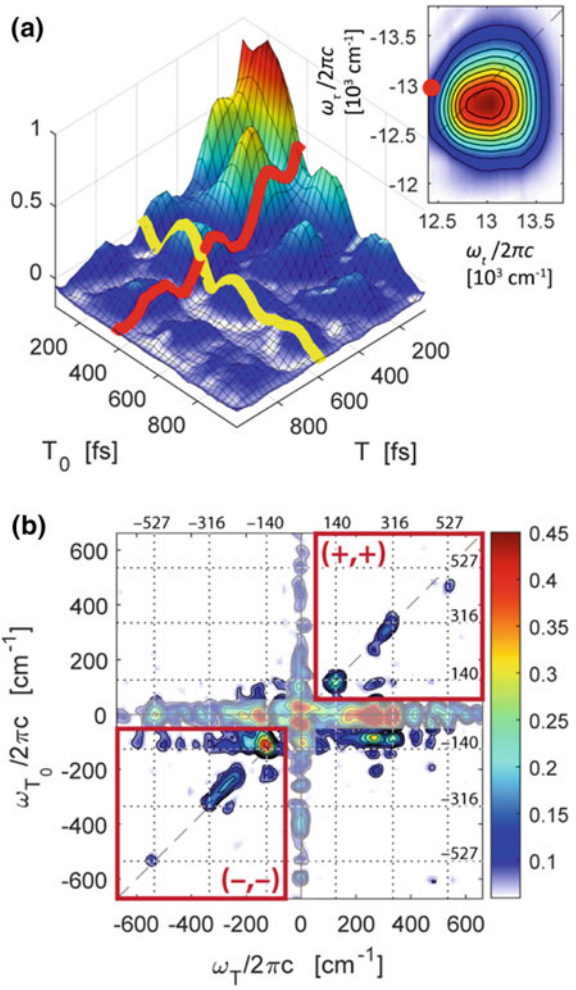

Fig. 5.4 **a** Two-dimensional interferogram showing 'beating' signal at one point in the (ω_τ, ω_t) plane. **b** 2D Raman-like spectrum at one point in the (ω_{T_0}, ω_T) plane (red circle in figure a)

this experiment is not sufficient to obtain any real quantitative information about this system, and the prospect for looking at more complex systems at higher resolution is bleak using the above-mentioned approaches. The need to improve the sensitivity motivates the exploration of novel experimental approaches that could dramatically decrease the acquisition time, and hence the indirect noise, as well as data processing methods that could isolate small features. The latter problem of dynamic range is particularly acute in 6WM experiments because the large number of field-matter interactions dramatically scales the signals in a nonlinear way. This is likely the reason why vibrational modes observed in Raman experiments were oftentimes not seen in 2D ES experiments that should have theoretically observed them. In GAMERS, the number of observed modes appears to decrease, but this is simply a result of the limited dynamic range associated with the low signal-to-noise.

In order to isolate the coherences in GAMERS, it is necessary to remove the non-oscillatory background, which results from excited-state contributions to the signal. While the population dynamics are interesting to explore as they allow access to regions of the excited-state potential may not be excited from a thermalized ground state population, we discard them here. To obtain a coherence-only 4D spectrum, the signal is fit to a sum of exponential decays, or alternatively a global fitting algorithm is used to simultaneously fit the entire background signal. After background subtraction, only the oscillatory parts of the signal remain, which, after Fourier transformation yield the final 4D coherence-only spectra. We should mention that it is also possible to use global analysis to yield "oscillation maps" if the imaginary parts of the exponential are included in the fit. In many cases, this yields better results than using the Fourier transform and also allows one to easily eliminate noise contributions from known sources (e.g. periodic laser intensity fluctuations), and even solvent (although not an issue in GAMERS).

While technically possible in limited situations, measuring the 4D GAMER spectra by sampling T_0 and T systematically on a rectalinear grid according to the Nyquist criteria, this uniform sampling schedule is extremely time consuming even with the speedup afforded by spatial multiplexing. As mentioned above, it leads to significant noise around the low-frequency regions where there is potentially important molecular information about vibrational coupling. A major improvement to the sensitivity and data acquisition speed of GAMERS was realized through the development of novel schemes for sampling the T_0 and T dimensions more efficiently [27]. Instead of uniform sampling, one can utilize a non-uniform schedule that takes advantage of the sparsity of the signal by acquiring along radial lines at a range of angles through the origin of the (T_0, T) plane as shown in Fig. 5.5 [28]. Critically, this

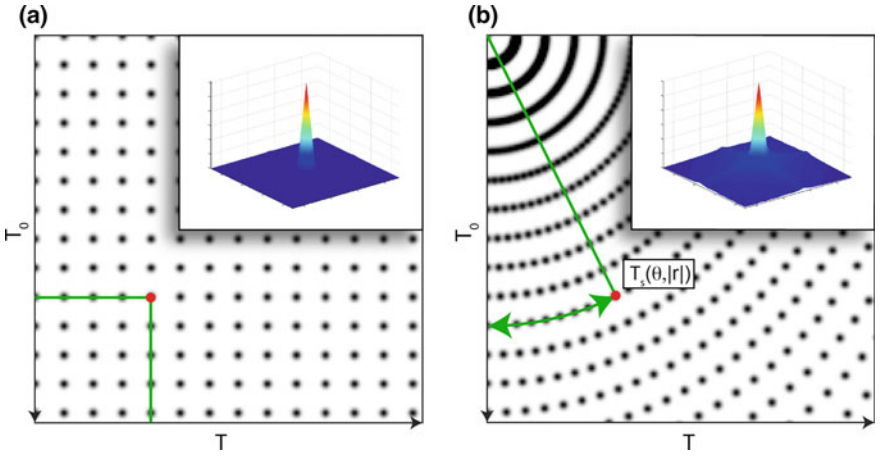

Fig. 5.5 **a** Uniform sampling in T/T_0 plane. Inset shows point-spread function. **b** Non-uniform sampling along radial lines defined by an angle and distance from the origin. Inset shows point-spread function with more pronounced tails than in the uniform sampling case

schedule includes more points near $T = T_0 = 0$ where the signal is strongest prior to dephasing. Instead of an n^2 scaling, the (ω_{T_0}, ω_T)-dependence of the 6WM signal can be characterized with only n-scaling in sample points multiplied by the number of radial slices, which may by much smaller than n. Radial scanning was first introduced in X-ray tomography using the Radon transform which reconstructs 2D tomograms from 1D projections. While the most straightforward application of the Radon transform is for imaging applications, it may also be utilized for spectroscopy after applying the projection–slice theorem, which states that the Fourier transform of a slice through the (T_0, T) plane contains the projection of the signal onto the same line in the (ω_{T_0}, ω_T) plane [29]. Recording projections of the signal from a sufficient number of slice angles results in recovery of the full 2D spectrum (see Fig. 5.6). In practice, we find that for GAMERS only about 8 or 16 slices are necessary to faithfully reconstruct the 2D ZQC spectra, which corresponds to as little as a 3% sampling rate (i.e. the ratio of sampling compared to Nyquist). Previously we have explored other sub-sampling schemes such as compressive sensing (CS) [30, 31], but the advantage here is the recovery of the spectrum is mathematically unique and does not require solving an underdetermined set of linear equations. Importantly, it is significantly more robust to noise, while achieving much lower sampling rates.

As in the uniform sampling case, the first step to recover the 4D GAMER spectrum is to remove the population dynamics using a multi-exponential model (i.e. global analysis). For each slice, the oscillatory components are Fourier transformed to produce a frequency-domain projection in the (ω_{T_0}, ω_T) plane, which may then be used to reconstruct the 2D spectrum using a filtered-back-projection (FBP) method [32]. In FBP, each projection back propagates through the entire 2D plane, and the results are summed over all the different projection angles. Since real signals appear in each

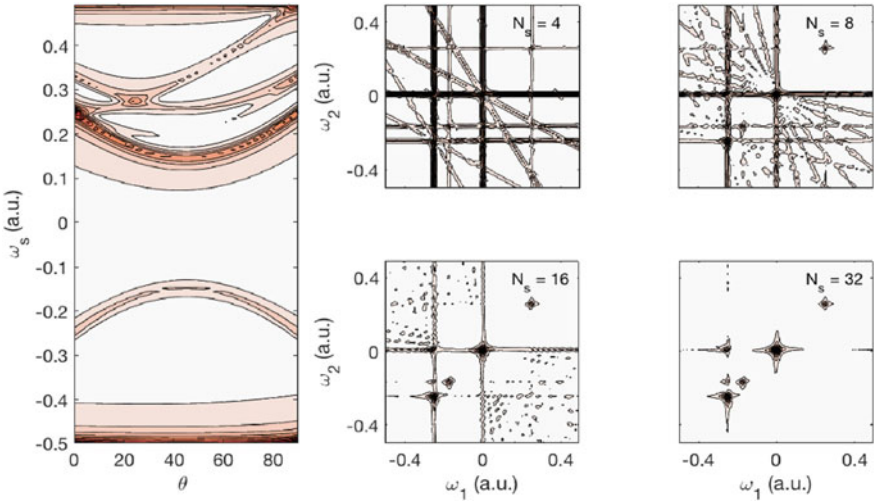

Fig. 5.6 Left: Sinogram showing projections as a function of slice angle ($N_s = 32$). Right: Results of inverse Radon transform on simulated data with $N_s = 4, 8, 16$, and 32 slices equally spaced between 0° and 90°

projection, the FBP) procedure builds amplitude where the back projections overlap. With enough slices, the true signal locations are revealed. Note, this procedure is repeated for each point along ω_τ and ω_t, which can require considerable computational resources. It is important to mention that due to causality, only the positive time quadrant is sampled so that, unlike conventional tomography (e.g. computed tomographic imaging), there is no direct access to angles beyond 90°. In NMR, this issue has been addressed [33] by combining the results of different experiments with control over the phase of the pulses to extend the range to the full 180°. Application of this approach to GAMERS will be the subject of future work.

While FBP is stable and computationally efficient, it introduces undesirable artifacts at low slice numbers such as streaks and ridges across the spectrum from the back-projection procedure (see Fig. 5.6). As the number of slices grows, the spectrum converges exactly to the 2D Fourier transform result since this just amounts to simply changing between rectangular and polar coordinates. Unfortunately, the effect of the ridges is to severely limit the dynamic range of the experiment since weak 'real' signals (i.e. those that appear in all slices and, ideally, have a molecular origin) have to compete with ridges that may have resulted from noise in only a single slice. These effects are easily seen in the simulations in Fig. 5.6 for a small number of slices. While FBP is a dramatic improvement over Fourier sampling, offering at least an order of magnitude improvement in SNR with less than 16% of the acquisition time, it still remains problematic for spectroscopic applications where artifacts may be misinterpreted as real signals. Fortunately, there is a way to eliminate the ridge structure completely using a method called lowest-value (LV) reconstruction[34], which exploits the fact that true spectral features must appear in each projection (even if at some angles, peaks obscure one another). Signals that are not real are likely to only appear in a small number of projections, but statistically unlikely to appear in all of them. LV compares the signals from each back-projection and simply takes the smallest value among all of them. Ridge features arising from non-real signals are replaced by noise, while real signals are replaced by their smallest value, which are equivalent within the noise level. LV improves with more projections since the likelihood of noise appear in all back-projections rapidly diminishes. In GAMERS, we have found that a major source of noise is from periodic laser amplitude fluctuations. Typically, these are not of great concern when the integration time is long (>1 s), but during rapid scanning of the stage positions, these fluctuations are on the same order in strength as the molecular signals. LV can be exploited to eliminate these noise sources because each slice direction amounts to different step sizes along T and T_0. In lab time, this means that the laser amplitude noise is sampled at different rates during each slice, and, therefore, the peaks in the noise spectrum move around (depending on the noise frequency and aliasing effects). However, the real signals from the molecular vibrations do not move (as long as the sampling fulfills the Nyquist criteria). Therefore, LV dramatically reduces laser noise as well as most other noise source that results from laboratory-based fluctuations. This can be clearly seen in the experimental results from Fig. 5.7.

While LV eliminates a large portion of the noise, it also inadvertently eliminates real signal peaks as well. The reason is that LV is not additive like FBP or FT, so that

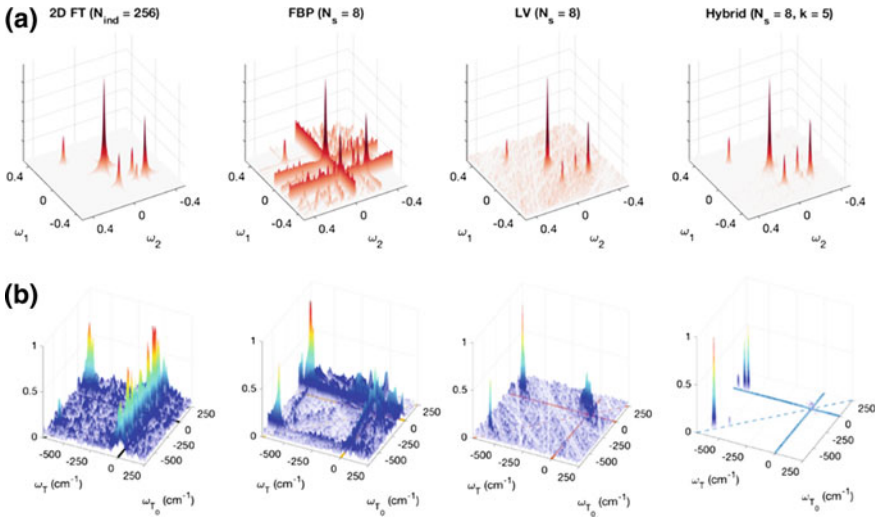

Fig. 5.7 **a** Comparison of simulated 2D Raman-like spectra (i.e., 2DBS spectra). From left to right: 2D FT; FBP with $N_s = 8$ slices showing strong ridge patterns; LV reconstruction eliminates most of the ridge structure; hybrid-LV with $k = 5$ bins completely eliminates ridges and recovers most of the spectral features including relative peak heights and peak positions. **b** Comparison of experimental 2D Raman-like spectra (i.e., 2DBS spectra) at one point in the 2D SQC spectrum of Nile Blue reconstructed using various methods. From left to right: 2D FT; FBP with $N_s = 32$ slices; LV reconstruction; and hybrid-LV with $k = 5$ bins

there is no building of signal amplitude. If one peak is smaller than the largest noise component along any slice in its direction, it will be eliminated. Fortunately, there is means by which to get the additive advantage of FBP and the artifact elimination advantage of LV using a hybrid approach (HBLV). The idea is to group the projections into k bins, so that among n projections, there are $\binom{n}{k}$ different bin sets. For each set, a 2D FBP spectra is generated, so that the k back-projections are effectively summed (after applying a suitable filter). These spectra are then compared to one another and the lowest value is selected among them. For instance, if 16 projections are taken and $k = 8$, then there would be 12,870 different 2D FBP spectra. LV would then choose the lowest value at each point in the 2D spectra. By adjusting the value of k, one goes from full FBP ($k = n$) to LV ($k = 1$). A larger bin size causes more signal buildup, but at the cost of introducing ridge artifacts. The major advantage of HBLV is the statistical nature of the reconstruction. In the example above, a single (lowest) value is selected among 12,870 different spectra. This results in a nearly complete suppression of noise, which is generally uncorrelated across all the different projections. In the simulation, HBLV recovers the ideal FT, both in terms of peak location and relative amplitudes, even with only 3% of the Nyquist sampling rate. Surprisingly, the improvement in the experiment is far more dramatic because of noise suppression, which works in a nonlinear fashion. With a greatly reduced

acquisition time, indirect noise is strongly suppressed, and the statistical nature of HBLV further reduces systematic noise.

5.4 HBLV-Reconstructed GAMERS Spectra of Nile Blue

HBLV GAMERS was applied to the study of the fluorescent dye molecule, Nile blue (NB), whose molecular formula is $C_{20}H_{20}N_3O^+$. NB has been studied by many methods including resonance Raman spectroscopy (RRS), transient-grating, and 2D electronic spectroscopy. RRS studies have identified dozens of vibronic modes [35], but as with many other fluorescent systems, it is challenging to observe low-frequency modes below about 200 cm^{-1}. Additionally, the RR spectrum of NB suffers from spectral congestion, and is sensitive to the excitation frequency. When modes overlap, quantifying the degree of vibronic coupling is very difficult, and requires fitting procedures which are prone to finding local, rather than global minima. The RR spectra may be used to model the absorption and emission spectra which can be broad and featureless at room temperature and in solution, but without accurate estimations of the HR factors, this may be difficult. Here, we demonstrate the GAMERS can easily resolve the vibronic structure and see features completely obscured by homogeneous and inhomogeneous broadening. More fundamentally, GAMERS observe coupling between vibrational modes that cannot be accessed using any other method.

The HBLV method was applied to NB as described above using the exact same data set as for FBP (n = 32 slices). Since the number of LV sets rises exponentially with the bin number, k, it becomes computationally prohibitive to use $k > 5$ for this large slice number. A smaller slice number was also used (n = 16) with comparable results, but employing a larger k. For k = 5 and n = 32, the number of 2D FBP spectra is 201,376 for each point in the 2D electronic spectrum. In order to reduce the computational load, back-projections were pre-calculated for each projection and then summer in different combinatorial ways prior to use of the LV method. Only a few seconds was needed to calculate the HBLV spectrum per point in the 2D electronic spectrum. It is important to note that this procedure does not alter the line shape of the electronic spectral features, but it may artificially narrow the vibrational spectral lines. This arises from the choice of filter in the FBP algorithm, and also the cumulative effects of taking the lowest value around the baseline of each peak. Because of the potentially detrimental effects of improper interpolation on LV, a special procedure was devised in order to avoid interpolation altogether using a complex Fourier transform algorithm.

In all, there are six 2D projections of the full 4D coherence-only spectrum along the remaining two dimensions. The first projection shown in the 2D ZQC spectrum, averaged along the remaining SQC dimensions (Fig. 5.7b). It shows a series of diagonal and off-diagonal vibrational peaks at ($\pm$ 590 cm^{-1}, $\pm$ 590 cm^{-1}) and the corresponding off-diagonal positions at ($\pm$ 590 cm^{-1}, 0 cm^{-1}). The signal is primarily in the (+/+) and (−/−) quadrants, which arises because the signal is casual so that only positive times are sampled. However, theory also predicts that the signal

in the other two opposing quadrants should be small due to a lack of significant anharmonicity. Note, that the FT results do indeed match this prediction although some non-negligible signal is seen in the lower-right quadrant. As was mentioned before, there are ways to manipulate the phase of the signal to acquire the opposing quadrants, but this was not done here. It may appear surprising that such a small number of peaks appear given that more than 40 peaks are observed in Raman spectroscopy. This is due to the large difference in dynamic range between traditional Raman and GAMERS owing to the six field-matter interactions in the latter process which causes a nonlinear scaling in the relative peak strength. Strong transitions are amplified compared to weak transitions, which explains why the strong 590 cm^{-1} mode dominates all other signals. The linear scaling of the 2D spectrum, however, masks the enormous dynamic range offered by HBLV, which can reach 10,000:1. As shown in Fig. 5.8, many dozen of peaks are observed when plotting on a nonlinear scaling. Unlike FT or FBP, where the dynamic range is no better than 10:1, HBLV completely suppresses noise, which is not possible by traditional methods. It is interesting to observe that indeed cross peaks are present, especially between highly delocalized low-frequency modes and higher frequency vibrations, although direct coupling between high-frequency modes is not seen in NB, while it is observed for the cyanine dye, IR 144 (not shown). Other 2D projections show, most notably the four

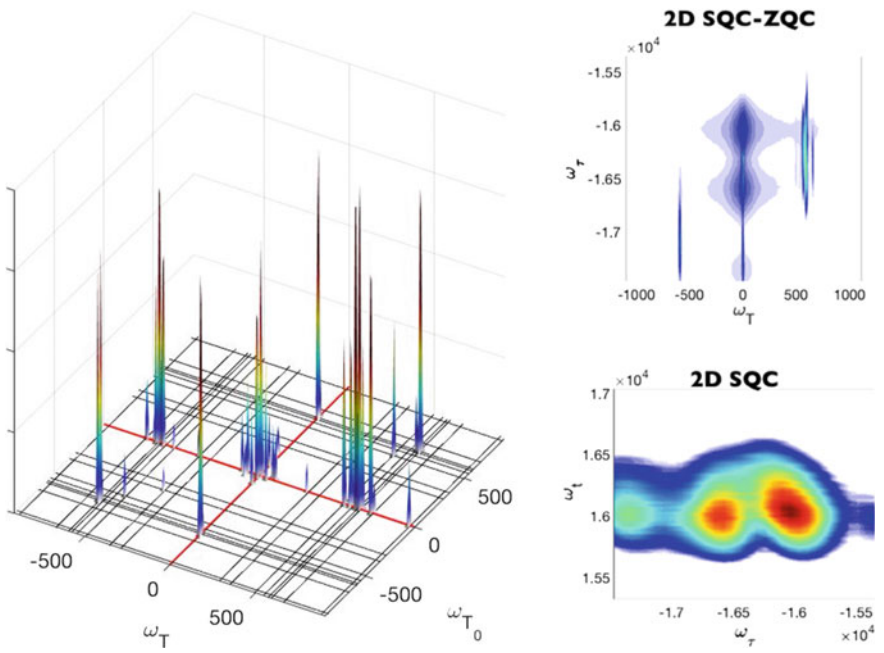

Fig. 5.8 Left: Experimental HBLV-reconstructed 2D ZQC (2D Raman-like) spectrum of NB and zoomed-in regions showing cross peak features. Black lines indicate modes identified by resonance Raman spectroscopy. Spectrum is displayed on a log scale. **Top Right**: SQC-ZQC projection spectrum (one of four). **Bottom Right**: SQC-SCQ projection spectrum. Units are cm^{-1}

2D ZQC-SQC maps, the effects of vibronic coupling between various modes, most prominently at 590 cm^{-1}, and the first electronic transition. In the 2D SQC spectrum, we clearly observe a vibronic progression (blue-shifted from main $S_0 \rightarrow S_1$ transition at ~16,500 cm^{-1}), which appeared as only a weak shoulder in the absorption spectrum.

5.5 Conclusions

We have demonstrated a novel 4D spectroscopy which we call GAMERS that combines resonant and non-resonant excitation. GAMERS is highly sensitive to non-trivial effects such as vibronic coupling, anharmonicity, electronic coherence, and mode coupling. A brief theoretical description of the optical response was given, highlighting the ability to access new physical information not available from purely resonant or non-resonant fifth-order electronic spectroscopies. Further, we discussed details of the experimental setup and analysis which allows for practical implementation of the technique in a reasonable amount of time, even when the signal strength is very low. Novel reconstruction strategies were discussed, showcasing the unique ability of GAMERS to achieve extremely high dynamic range, well beyond lower-order methods such as third-order 2D or 3D ES. While the focus here was on fifth-order 4D spectroscopy, we have also performed fifth-order 3D spectroscopy where one of the time delays (either T or T_0) was held fixed. This manifestation of GAMERS was applied to colloidal CdSe quantum dots [3], and proved instrumental in uncovering excitonic coupling to acoustic and optical phonon modes. Full 4D spectroscopy on these systems is now under way, in which excitonically selective 2D THz Raman spectra may be recorded to understand phonon-phonon coupling in these systems. Future technical and theoretical advancements will position GAMERS to uncover new chemical physics in increasingly complex molecular systems where lower-order methods are highly averaged and conceal critical spectral and dynamical features.

References

1. D.M. Jonas, Vibrational and nonadiabatic coherence in 2D electronic spectroscopy, the Jahn-Teller effect, and energy transfer. Annu. Rev. Phys. Chem. **69**(69), 327–352 (2018)
2. R. Tempelaar, D.R. Reichman, Vibronic exciton theory of singlet fission. III. How vibronic coupling and thermodynamics promote rapid triplet generation in pentacene crystals. J. Chem. Phys. **148**(24), 244701 (2018)
3. A.P. Spencer, W.O. Hutson, S. Irgen-Gioro, E. Harel, Exciton-phonon spectroscopy of quantum dots below the single-particle homogeneous line width. J. Phys. Chem. Lett. **9**(7), 1503–1508 (2018)
4. J.D. Hybl, A.A. Ferro, D.M. Jonas, Two-dimensional Fourier transform electronic spectroscopy. J. Chem. Phys. **115**(14), 6606–6622 (2001)

5. R.R. Ernst, G. Bodenhausen, A. Wokaun, *Principles of Nuclear Magnetic Resonance in One and Two Dimensions*. (Clarendon Press, Oxford University Press, Oxford England, New York, 1988), p xxiv, 610p. Reprinted 1988 (with corrections)
6. S.T. Cundiff, Optical three dimensional coherent spectroscopy. Phys. Chem. Chem. Phys. **16**(18), 8193–8200 (2014)
7. K. Park, M.H. Cho, Theoretical description of the nonlinear response functions associated with eight distinctive three-dimensional vibrational spectroscopies. J. Chem. Phys. **112**(11), 5021–5036 (2000)
8. P. Hamm, Three-dimensional-IR spectroscopy: beyond the two-point frequency fluctuation correlation function. J. Chem. Phys. **124**, 124506 (2016)
9. F. Ding, M.T. Zanni, Heterodyned 3D IR spectroscopy. Chem. Phys. **341**(1–3), 95–105 (2007)
10. S. Garrett-Roe, F. Perakis, F. Rao, P. Hamm, Three-dimensional infrared spectroscopy of isotope-substituted liquid water reveals heterogeneous dynamics. J. Phys. Chem. B **115**(21), 6976–6984 (2011)
11. A. Fidler, E. Harel, G. Engel, Dissecting hidden couplings using fifth-order three-dimensional electronic spectroscopy. J. Phys. Chem. Lett. **1**(19), 2876–2880 (2010)
12. Y. Tanimura, S. Mukamel, 2-dimensional femtosecond vibrational spectroscopy of liquids. J. Chem. Phys. **99**(12), 9496–9511 (1993)
13. K.C. Wilson, B. Lyons, R. Mehlenbacher, R. Sabatini, D.W. McCamant, Two-dimensional femtosecond stimulated Raman spectroscopy: observation of cascading Raman signals in acetonitrile. J. Chem. Phys. **131**(21), 214501 (2009)
14. D.A. Blank, L.J. Kaufman, G.R. Fleming, Fifth-order two-dimensional Raman spectra of CS2 are dominated by third-order cascades. J. Chem. Phys. **111**(7), 3105–3114 (1999)
15. B.P. Molesky, Z.K. Guo, T.P. Cheshire, A.M. Moran, Perspective: two-dimensional resonance Raman spectroscopy. J. Chem. Phys. **145**(18), 180901 (2016)
16. B.P. Molesky, Z.K. Guo, T.P. Cheshire, A.M. Moran, Two-dimensional resonance Raman spectroscopy of oxygen- and water-ligated myoglobins. J. Chem. Phys. **145**(3), 034203 (2016)
17. B.P. Molesky, Z.K. Guo, T.P. Cheshire, A.M. Moran, Multidimensional resonance raman spectroscopy by six-wave mixing in the deep UV. J. Chem. Phys. **141**(11), 114202 (2014)
18. E. Harel, A. Fidler, G. Engel, Single-shot gradient-assisted photon echo electronic spectroscopy. J. Phys. Chem. A **115**(16), 3787–3796 (2011)
19. E. Harel, P.D. Long, G.S. Engel, Single-shot ultrabroadband two-dimensional electronic spectroscopy of the light-harvesting complex LH2. Opt. Lett. **36**(9), 1665–1667 (2011)
20. E. Harel, A. Fidler, G. Engel, Real-time mapping of electronic structure with single-shot two-dimensional electronic spectroscopy. Proc. Natl. Acad. Sci. USA **107**(38), 16444–16447 (2010)
21. A.P. Spencer, W.O. Hutson, E. Harel, Quantum coherence selective 2D Raman–2D electronic spectroscopy. Nat. Commun. **8**, 14732 (2017)
22. G.S. Engel, T.R. Calhoun, E.L. Read, T.-K. Ahn, T. Mancal, Y.-C. Cheng, R.E. Blankenship, G.R. Fleming, Evidence for wavelike energy transfer through quantum coherence in photosynthetic systems. Nature **446**(7137), 782–786 (2007)
23. H.G. Duan, V.I. Prokhorenko, R.J. Cogdell, K. Ashraf, A.L. Stevens, M. Thorwart, R.J.D. Miller, Nature does not rely on long-lived electronic quantum coherence for photosynthetic energy transfer. Proc. Natl. Acad. Sci. USA **114**(32), 8493–8498 (2017)
24. E. Harel, Four-dimensional coherent electronic Raman spectroscopy. J. Chem. Phys. **146**(15), 154201 (2017)
25. S. Mukamel *Principles of Nonlinear Optical Spectroscopy*. (Oxford University Press, New York, 1995), p. xviii, 543p.
26. R. Tempelaar, T.L.C. Jansen, J. Knoester, Vibrational beatings conceal evidence of electronic coherence in the FMO light-harvesting complex. J. Phys. Chem. B **118**(45), 12865–12872 (2014)
27. W.O.S.A.P. Hutson, E. Harel, Ultrafast four-dimensional coherent spectroscopy by projection reconstruction. J. Phys. Chem. Lett. **9**, 1034–1040 (2018)
28. W.O. Hutson, A.P. Spencer, E. Harel, Ultrafast four-dimensional coherent spectroscopy by projection reconstruction. J. Phys. Chem. Lett. **9**, 1034–1040 (2018)

29. R.N. Bracewell, *The Fourier Transform and Its Applications*, 3rd edn. (McGraw Hill, Boston, 2000), p. 616
30. A.P. Spencer, B. Spokoyny, S. Ray, F. Sarvari, E. Harel, Mapping multidimensional electronic structure and ultrafast dynamics with single-element detection and compressive sensing. Nat. Commun. **7**, 10434 (2016)
31. J.A. Dunbar, D.G. Osborne, J.M. Anna, K.J. Kubarych, Accelerated 2D-IR using compressed sensing. J. Phys. Chem. Lett. **4**(15), 2489–2492 (2013)
32. R.M. Merserea, A.V. Oppenhei, Digital reconstruction of multidimensional signals from their projections. Proc. IEEE **62**(10), 1319–1338 (1974)
33. E. Kupce, R. Freeman, Reconstruction of the three-dimensional NMR spectrum of a protein from a set of plane projections. J. Biomol. NMR **27**(4), 383–387 (2003)
34. C.D. Ridge, V.A. Mandelshtam, On projection-reconstruction NMR. J. Biomol. NMR **43**(3), 151–159 (2009)
35. M.K. Lawless, R.A. Mathies, Excited-state structure and electronic dephasing time of nile blue from absolute resonance raman intensities. J. Chem. Phys. **96**(11), 8037–8045 (1992)

Chapter 6
Two-Dimensional Electronic Spectroscopy of Gold Nanorods: Nodal Line Slope Analysis and Spectral Interference

Hanju Rhee and Minhaeng Cho

Abstract Two-dimensional (2D) electronic spectroscopy (ES) has been used to investigate the electronic coupling and dynamics of coupled multi-chromophore systems. In particular, off-diagonal features on 2D ES spectra provide critical information, such as on the electronic couplings, excitation transfer rates and molecular conformational changes between the involved electronic states. Recently, a 2D ES study has been performed on plasmonic gold nanorods with the surface plasmonic resonance excitation of free electrons. To gain quantitative information on the degree of dynamical inhomogeneity of polydisperse gold nanorods, nodal line slope analyses of the time-resolved 2D ES spectra with varying center wavelengths of pump and probe pulses have been carried out and shown to be of use for investigating broad distributions of dimensionally heterogeneous gold nanorods. In addition, due to the strong nonlinear surface plasmonic resonance response of gold nanorods, we observed unusual spectral fringe patterns in their 2D ES spectra, which were not observed in organic chromophores, in a reverse time-ordered pulse sequence. This was shown to be further critical evidence of the inhomogeneously broadened longitudinal surface plasmonic resonance band of gold nanorods. In this chapter, we present a detailed description of the 2D ES responses of gold nanorods that are associated with ultrafast electron heating, coherent electron dynamics, and the subsequent relaxation processes.

H. Rhee
Korea Basic Science Institute, Seoul 02841, Republic of Korea

M. Cho (✉)
Center for Molecular Spectroscopy and Dynamics, Institute for Basic Science (IBS), Seoul 02841, Republic of Korea
e-mail: mcho@korea.ac.kr

Department of Chemistry, Korea University, Seoul 02841, Republic of Korea

M. Cho (ed.), *Coherent Multidimensional Spectroscopy*,
Springer Series in Optical Sciences 226,
https://doi.org/10.1007/978-981-13-9753-0_6

6.1 Introduction

Gold nanoparticles of various sizes and shapes show intriguing optical properties and have thus been widely used in a variety of applications to molecular imaging, drug delivery, photothermal therapy and optoelectronic devices [1–4]. Elucidating the general interplay between the size and shape of nanoparticles and their electronic, photothermal, and optical properties is critical not only for further understanding of the underlying physics behind nanophotonics but also for providing guidelines for the future design of nanoparticles in practical applications [1, 4, 5].

Gold nanorods (AuNRs), which are elongated nanoparticles with a short and a long axis, have attracted a great deal of attention due to the optical tunability of their surface plasmon resonance bands via changing their aspect (length-to-width) ratio (R). Here, surface plasmon resonance (SPR) is a collective oscillation of conduction band electrons coupled to incident electromagnetic fields [1–4]. Unlike molecular excitation involving a superposition of two or multiple eigenstates, SPR leads to coherent linear oscillations (superposition of linear translation modes) of quasi-free electrons in the presence of an electric field (Fig. 6.1). Due to its elongated structure, the AuNR has two different SPR modes: transverse and longitudinal SPR (TrSPR and LgSPR) modes oscillating along its short and long axes, respectively. In particular, the LgSPR band, which appears in the longer wavelength region, strongly depends on the size and shape of the nanorod, showing a characteristic red-shift of the maximum absorption frequency with increasing aspect ratio (R) [1–4]. Their aspect ratio-dependent spectroscopic nature as well as exceptionally strong SPR responses make AuNRs promising for a variety of optical sensor applications [1, 5].

Synthesized AuNRs usually have a broad size distribution (polydisperse). The polydispersity of the aspect ratio of AuNRs gives rise to a significant inhomogeneous broadening of the LgSPR band, potentially making the optical sensing of local environments with AuNRs less effective because AuNRs with different aspect ratios

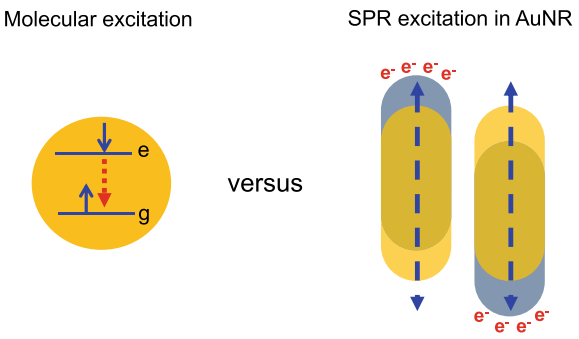

Fig. 6.1 Molecular excitation versus SPR excitation in AuNR. For a molecule, a superposition of two (or multiple) eigenstates (wavefunctions) are created by a single electron excitation. For an AuNR, however, a superposition of linear translation modes (collective and coherent linear oscillations) of many quasi-free electrons in the presence of electric field is produced by SPR excitation

cause spectral congestion of overlapping SPR bands. Therefore, the monodispersity of AuNRs and their resulting narrow SPR bandwidth are important for improved optical sensitivity. Transmission electron microscopy (TEM) images are often used to examine the dimensional heterogeneity of synthesized nanorods. TEM, however, has difficulties related to not only sample preparation but also obtaining reproducible results from the limited number of images usually available for statistical analysis. As a simpler optical spectroscopic method, one can extract information on the aspect ratio distribution by fitting an experimentally measured LgSPR band to a set of calculated homogeneously broadened spectra for AuNRs with different aspect ratios [6]. However, it remains challenging or even impossible to clearly differentiate homogeneous and inhomogeneous line broadenings for an ensemble of AuNRs in steady-state or pump-probe transient absorption (TA) spectroscopy [2, 3, 7–17].

Two-dimensional (2D) electronic spectroscopy (ES) [18–27] has often been used to investigate the electronic coupling and dynamics of coupled multi-chromophore systems such as photosynthetic light-harvesting complexes [19, 20]. By analyzing the off-diagonal signals on 2D ES spectra, one can obtain information, such as on the electronic couplings, excitation transfer rates and molecular conformational changes between the involved electronic states of the molecule or molecular complexes of interest [20, 21]. So far, 2D ES studies have mainly focused on molecular systems involving transitions between the discrete quantum states of electrons bound to nuclei. In contrast, 2D ES studies on plasmonic metal nanoparticle systems involving SPR excitation of free electrons have been hardly performed. This is probably because 2D ES of plasmonic AuNR systems does not show any distinct features, such as off-diagonal peaks, that can provide useful information on the structure or electronic couplings of molecular systems. Other than off-diagonal signals, however, there remain useful observables extractable from 2D ES spectra. One of them is the nodal line slope (NLS) [21, 22], which has proven to be of critical use for gaining information on the degree of dynamic inhomogeneity of solvated molecular systems in condensed phases. This NLS analysis can additionally be used to examine the aspect ratio inhomogeneity of AuNRs in a broad distribution because nodal lines, created by rapid electron heating after SPR excitation of AuNRs, are easily observed on AuNR 2D ES spectra. Furthermore, due to the strong nonlinear SPR response of AuNR [7, 8], unusual spectral fringe patterns that are not often observed in organic chromophores are observed in the 2D ES spectra of AuNRs in a reverse time-ordered pulse sequence, which can be further critical evidence of the inhomogeneously broadened LgSPR band of AuNRs [28].

6.2 Photo-Induced Electron Dynamics

The electron dynamics of AuNRs excited by ultrashort pulses have been extensively studied and well characterized [7–17]. The involved relaxation processes show somewhat different aspects from those of excited molecules. In molecular excitation, a single electron is usually excited in such a way that no electron-electron collisions

occur within each molecule. However, the electronic oscillations of multiple two-level systems (chromophores) in condensed phases start to decohere due to electron-bath interactions, followed by electronic population relaxation to the bath degree of freedom [21]. In the LgSPR excitation of AuNRs, however, electron-electron (e-e) collisions (or scatterings) dominantly occur within each AuNR, and lead to electron heating (0.1–1 ps) as well as decoherence (5–20 fs) in the LgSPR mode. The hot electrons are then thermally equilibrated with lattice phonons via electron-phonon (e-ph) scatterings (2–5 ps), and then the dissipation of the excited lattice phonon modes to the surrounding bath degree of freedom via phonon-phonon (ph-ph) scatterings (~100 ps) [9–17]. Figure 6.2 displays a typical TA time trace showing the relaxation processes of photo-excited AuNR. In addition to the stepwise TA signal decay behavior, a slowly oscillating component is often observed during the phonon-phonon relaxation process, which can be attributed to the coherent excitation of extensional vibrational modes along the longitudinal axis of AuNR [2, 16].

Pump-probe TA spectroscopy of molecules involves transitions between discrete eigenstates (Fig. 6.3a). Pump photons initially excite molecules from the ground state (g) to an excited state (e). Then, the probe photons interact with the excited molecules causing further absorption (TA > 0) to higher excited states (f) and stimulated emission (TA < 0) back to the ground state (g). In this case, the TA signal may show various spectral features depending on the electronic structure of the molecule under investigation. However, the TA signal of AuNR upon LgSPR excitation can simply be explained by the change in dielectric constant (i.e., changes in both absorption and refractive index) from a rapid increase of electronic temperature by electron heating (Fig. 6.3b), which leads to spectral red-shift and line broadening of the LgSPR band (Fig. 6.3c). As a result, a negative TA signal ($\Delta A < 0$) appears in the higher frequency

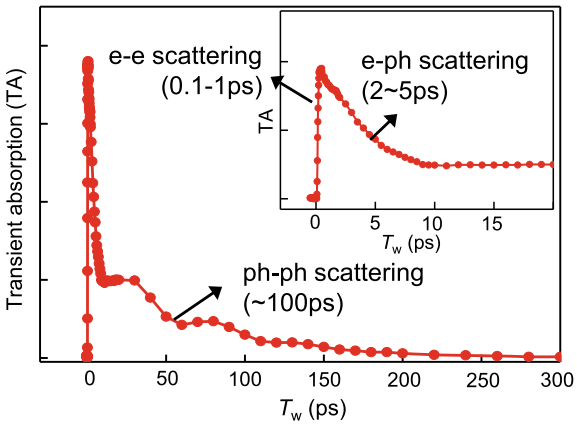

Fig. 6.2 TA time profile showing typical photo-induced relaxation processes of AuNRs. The TA trace was obtained at the probe wavelength of 850 nm after excitation at the pump center wavelength of $\lambda_{pump\_c} = 800$ nm for silica-coated AuNRs with the average $R = 3.84$ (see Fig. 6.4). Note that a slowly oscillating component observed together during the phonon-phonon relaxation process is due to a coherent excitation of extensional vibrational modes along the long axis of AuNR

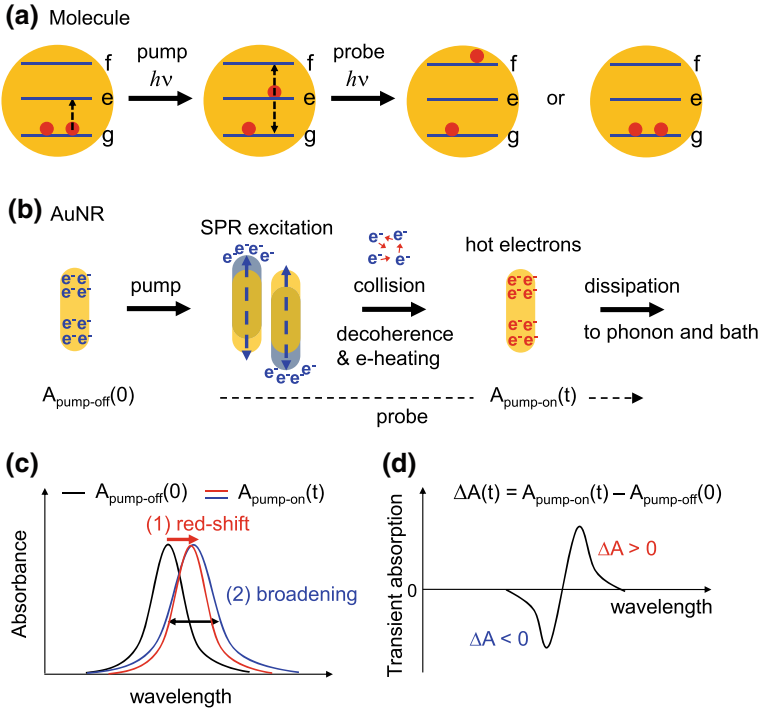

Fig. 6.3 Photo-induced processes of **a** molecule and **b** AuNR in pump-probe experiment. In a molecule, a single electron excited from the ground (g) to first excited (e) states by the pump can undergo either a further excitation to the higher excited state (**f**) (excited state absorption, ESA) or a de-excitation to the ground state (stimulated emission, SE). Usually, complicated TA spectra by overlapping ESA and SE signals are observed depending on the electronic structure of the involved excited states. In an AuNR, a SPR excitation by the pump induces a coherent and collective oscillation of conduction electrons. Then, electron dephasing and heating occur by electron-electron collisions. Hot electrons generated by the electron heating (e-heating) further undergo a heat dissipation to the phonon and bath modes. **c** Spectral red-shift and line broadening of the LgSPR band of AuNRs by electron heating. **d** TA spectrum ($\Delta A(t)$) obtained at a pump-probe delay time t after the electron heating is done. Due to the spectral red-shift and broadening, ΔA has positive and negative values at the longer and shorter wavelengths, respectively, which is the characteristic TA spectral feature for the LgSPR band of AuNRs

(shorter wavelength) region while a positive TA signal ($\Delta A > 0$) appears in the lower frequency (longer wavelength) region (Fig. 6.3d), which is the characteristic spectral signature of the TA signal observed in the LgSPR band of AuNR.

6.3 Transient Absorption

For ideally monodisperse AuNRs, the LgSPR bandwidth is dominated by homogeneous line broadening. All the nanorods therefore undergo the same SPR excitation-and-subsequent relaxation processes, giving rise to the same TA spectral change regardless of pump (excitation) frequency. However, for an ensemble of highly polydisperse AuNRs with different aspect ratios, the LgSPR band is inhomogeneously broadened so that the AuNRs with smaller R are dominantly excited by higher frequency excitation fields while those with larger R are excited by lower frequency fields (Fig. 6.4a). In this case of an inhomogeneous line broadening limit, the entire LgSPR band can be represented by a collection of homogeneously broadened LgSPR bands with different center frequencies. If a pump (excitation) beam with a bandwidth narrower than that of the LgSPR band is used in a pump-probe TA experiment, as shown in Fig. 6.4a, selective excitations of just subensembles of the AuNRs are achieved [28].

Figure 6.4b shows the TA spectra of AuNRs excited with different pump center wavelengths ($\lambda_{pump} = 720, 760, 800$ nm in Fig. 6.4a) at $T_w = 1$ ps of pump-probe delay (waiting) time. Note that the pump spectral bandwidth is narrower than the LgSPR bandwidth of the silica-coated AuNRs (length: 35–41 nm, width: 9–11 nm, average aspect ratio: 3.84) used in the TA measurement [28]. All the individual TA spectra exhibit negative and positive TA signals at the higher and lower frequency regions, respectively, with the nodal point red-shifted from the excitation wavelength, which is the characteristic pump-probe TA spectral signature created by electron heating after a femtosecond excitation of LgSPR modes as shown in Fig. 6.3. It is noteworthy that the nodal point of the TA spectrum red-shifts as the excitation wavelength increases. This indicates that the LgSPR band is significantly inhomogeneously broadened so that the subensembles of AuNRs with different aspect ratios, which are selectively excited with varying pump wavelength, produce their own TA spectra with different

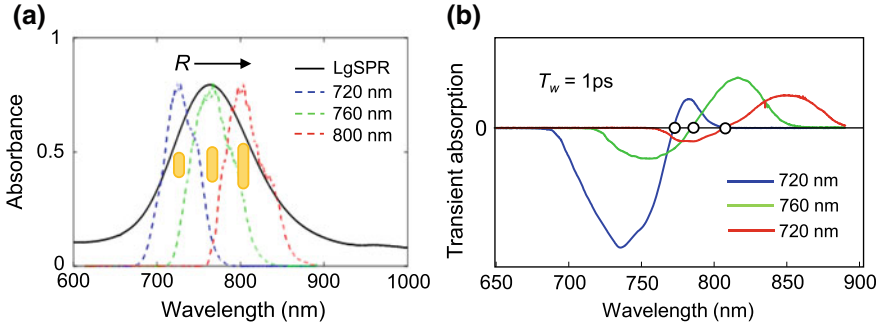

Fig. 6.4 **a** LgSPR absorption band (black solid line) of silica-coated AuNRs with the average R = 3.84 and the pump laser spectra (dashed line) of different center wavelengths (blue: 720 nm, green: 760 nm, red: 800 nm) used for TA measurement. **b** TA spectra measured at 1 ps of pump-probe delay time (T_w) with different pump center wavelengths in (**a**). This figure is adapted from Fig. 6.1 in [28]

nodal points. Another notable feature of Fig. 6.4b is that the positive TA signal is much smaller than the negative one when the sample is excited at the blue edge ($\lambda_{pump} = 720$ nm) of the LgSPR band. This implies that inhomogeneous broadening is still dominant even within a pump bandwidth narrower than the entire LgSPR band. That is to say, the positive TA signal from a subensemble of AuNRs excited at the blue edge of the pump spectrum interferes with the negative TA signal from another subensemble of AuNRs excited at the red edge, leading to a significant cancellation of the TA signal [28]. It should be noted that one-dimensional (1D) pump-probe TA spectroscopy, however, does not provide detailed information on how significantly the LgSPR band is inhomogeneously broadened within the pump bandwidth. The next section will show how the degree of aspect ratio inhomogeneity of AuNRs can be investigated by analyzing the slope of the nodal line on each 2D ES spectrum.

6.4 Two-Dimensional Electronic Spectroscopy

6.4.1 Nodal Line Slope Analysis: Basic Concept

In principle, a 2D ES spectrum can be represented by a collection of TA spectra (y-axis) of the probe beam as the excitation wavelength or frequency (x-axis) is varied. Due to electron heating after LgSPR excitation by the pump beam (Fig. 6.3b), the band undergoes both the spectral red-shift and line broadening, producing positive and negative TA signals at lower and higher probe frequency regions, respectively, as shown in Fig. 6.3c, d. For a homogeneous system with AuNRs of uniform aspect ratio, the TA spectra (y-axis) created by varying the pump wavelength (x-axis) would, regardless of pump wavelength, all show the same spectral shape and nodal point wavelength (NPW), which is the probe wavelength at which the nodal line crosses the vertical line at the pump center wavelength [28]. As a result, the nodal line connecting all the nodal points of the TA spectra would be parallel to the pump wavelength axis (x-axis), giving NLS = 0. However, as inhomogeneous broadening becomes significant, the nodal line slope (NLS) increases depending on the aspect ratio inhomogeneity of AuNRs and should have finite values larger than zero.

The simulation results in Fig. 6.5 show that 2D ES is capable of distinguishing between ensembles of AuNRs with different aspect ratio distributions (ΔR: standard deviation of R) and how the NLS on the 2D ES spectra varies with the degree of aspect ratio inhomogeneity (β). For simplicity, we assume that the absorption spectra (Figs. 6.5a–c) can be given by a Voigt function, which is the convolution of homogeneously (Lorentzian) and inhomogeneously (Gaussian) broadened line shape functions. It should be noted that β is defined as the ratio of the inhomogeneous ($\Delta\omega_{in}$) to homogeneous ($\Delta\omega_h$) line broadenings, i.e., $\beta = \Delta\omega_{in}/\Delta\omega_h$, where $\Delta\omega_h$ and $\Delta\omega_{in}$ are the full widths at half maximum (FWHM) of the corresponding Lorentzian and Gaussian functions, respectively. Three cases of AuNR systems with large ($\beta = 3$), intermediate ($\beta = 1$) and small ($\beta = 0.33$) ΔR are compared in Fig. 6.5. For $\beta = 0.33$,

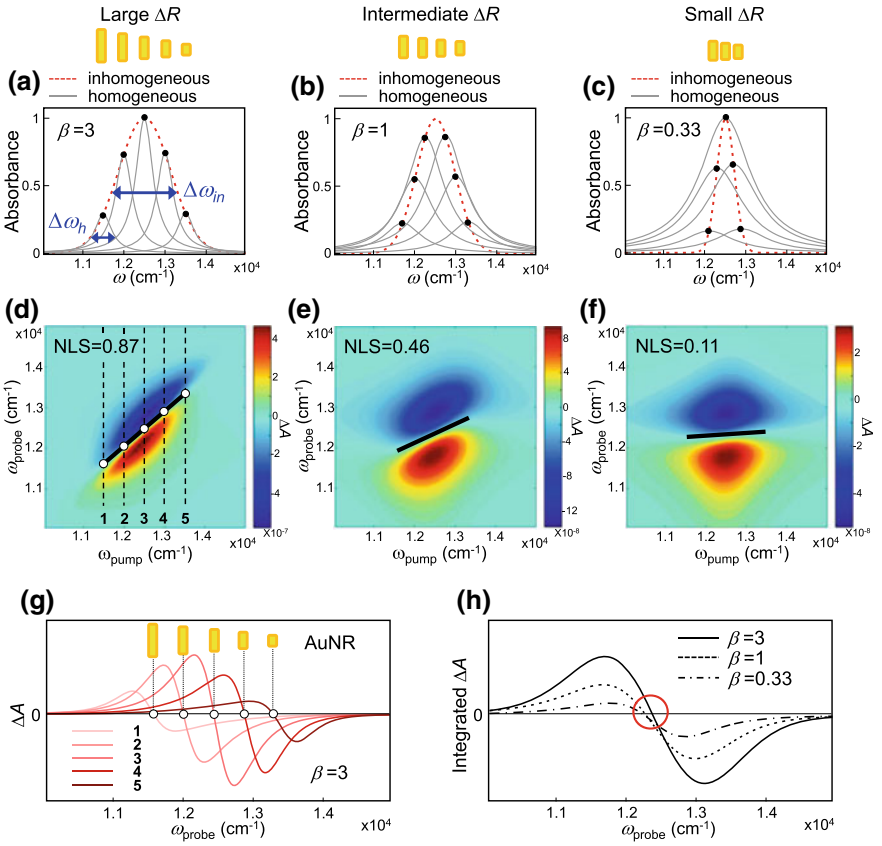

Fig. 6.5 Simulation on **a**–**c** LgSPR bands, **d**–**f** 2D ES spectra and nodal line slopes of AuNRs with different aspect ratio inhomogeneity: Large ($\beta = 3$), intermediate ($\beta = 1$) and small ($\beta = 0.33$) ΔR. The homogeneous (blue solid) and inhomogeneous (red dashed) line broadenings contributing to the LgSPR band are assumed to be Lorentzian ($\Delta\omega_h$: FWHM) and Gaussian ($\Delta\omega_{\text{in}}$: FWHM) functions, respectively. The degree of inhomogeneity is defined as the ratio of $\Delta\omega_{\text{in}}$ to $\Delta\omega_h$, i.e., $\beta = \Delta\omega_{\text{in}}/\Delta\omega_h$. Calculating 2D ES spectra, it is assumed that each homogeneous band undergoes a red-shift of the peak by 30 cm^{-1} and a spectral broadening by 2% of the original bandwidth by the electron heating of AuNRs. **g** Slice spectra (black dashed lines: **1–5** in (**d**)) taken at different pump frequencies of the 2D ES spectrum for $\beta = 3$. **h** Projected (integrated) spectra of the 2D ES in **d**–**f** onto the probe frequency axis (y-axis), which are essentially equivalent to the pump-probe TA spectra, for $\beta = 3$ (solid), 1 (dashed), 0.33 (dash-dotted). This figure is from Fig. 6.3 in [28], which was published under a Creative Commons license

where homogeneous broadening dominates inhomogeneous broadening, the nodal line is almost parallel to the pump frequency axis (x-axis) so that the NLS value is close to zero (NLS = 0.11). However, the NLS sensitively varies with increasing β and approaches unity as $\Delta\omega_{\text{in}}$ becomes much larger than $\Delta\omega_h$ (NLS = 0.87 for β = 3). This indicates that the NLS of 2D ES can be a decisive measure of the aspect ratio inhomogeneity of AuNRs [28].

One of the advantages of 2D ES over 1D pump-probe TA spectroscopy is its capability of resolving each individual spectral signature and electron dynamics of a given homogeneous subensemble in a heterogeneous system. In 2D ES, AuNRs with different aspect ratios are selectively photo-excited by varying pump frequency, so their pump-induced TA spectra (y-axis) can spread out along the pump frequency axis (x-axis). The slice probe spectra of AuNR under β = 3 (a highly inhomogeneous case) taken at different pump frequencies (**1–5** in Fig. 6.5d) of the 2D ES spectrum represent the individual TA spectra of AuNR subensembles and are plotted together in Fig. 6.5g. The nodal points extracted from the individual TA spectra of AuNRs with different aspect ratios are clearly separated and red-shift with pump frequency. However, such spectral features disappear in 1D pump-probe TA spectra because the contributions from different-sized AuNRs are averaged out. Indeed, in the spectra projected onto the probe frequency axis, which are equivalent to the pump-probe TA spectra, the nodal point frequencies hardly depend on the degree of aspect ratio inhomogeneity at all and are almost insensitive to β (Fig. 6.5h). This indicates that using pump-probe spectroscopy it is difficult to separately obtain the spectral signatures of different-sized AuNRs or investigate their relaxation dynamics simultaneously. In Sect. 6.4.3 we will show that the time evolutions of the NLS and nodal point wavelength (NPW) extracted from the 2D ES spectra enable us to investigate the homogeneous (heterogeneity-free) dephasing or relaxation of photo-excited AuNRs.

6.4.2 *Pulse Shaper-Based 2D ES Setup (Pump-Probe Geometry)*

By varying waiting times (T_w), two-dimensional electronic spectra are plotted with respect to two (independently controllable) frequencies that correspond to the excitation (ω_{pu}) and emission (ω_{pr}) axes. In general, there are two ways to plot a 2D spectrum in the frequency and time domains: one (frequency domain) is to measure broadband probe (emission) spectra while varying the frequency (ω_{pu}) of the narrowband pump (excitation) beams, and the other (time domain) is to measure broadband probe spectra while scanning the time delay (τ) between two broadband excitation pulses (twin pulses generated by a pulse shaper in our case). Current 2D spectroscopy experiments usually employ the two-dimensional Fourier transform (FT) method because the frequency domain method, which utilizes temporally broad pump pulses, inevitably loses the time resolution with respect to T_w.

Our pulse shaper-based FT 2D ES setup in a two-beam pump-probe geometry is depicted in Fig. 6.6a, where a pair of co-propagating replica pulses (E_{pu1} and E_{pu2}) from the pulse shaper is used as two pump pulses and another time-delayed (non-collinearly propagating with the pump pulses) pulse (E_{pr}) from E_{pu2} by T_w (waiting time) is used as a probe pulse [26–28]. The role of scanning τ, controlled by the pulse shaper, is essentially to give the same effect as varying the excitation frequency (ω_{pu}) as follows. Each broadband excitation pulse, $E_{pu1}(\omega_{pu})$ and $E_{pu2}(\omega_{pu})$, can be decomposed into constituting electric field components with different optical frequencies (ω_n). As τ is scanned, τ-varying interference between these electric field waves from the two excitation pulses results in intensity modulations $I(\omega_n,\tau)$ with the corresponding frequencies. Consequently, the individual AuNRs with different

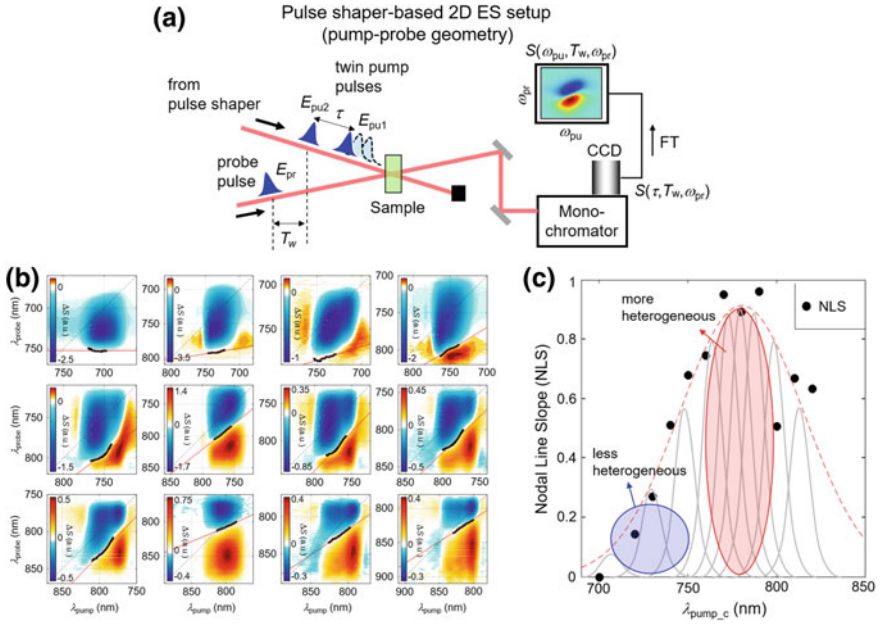

Fig. 6.6 **a** Pulse shaper-based 2D ES setup in pump-probe two-beam geometry. $E_{pu1,2}$: twin pump pulses generated from the pulse shaper, E_{pr}: probe pulse, CCD: charge-coupled device detector. **b** 2D ES spectra of the AuNRs measured at $T_w = 1$ ps varying the center wavelengths of both the pump and probe pulses from 700 nm to 820 nm. The thick black line in each panel represents a collection of nodal points at which the 2D signal is zero and the red line is the linear fit to the nodal points. **c** Wavelength dependence of the NLS (black circles) of the 2DES spectra of the AuNRs, which well fits to a Gaussian line shape with an FWHM of 1320 cm^{-1} approximately matching the LgSPR band shown in Fig. 6.4a. The individual homogeneous LgSPR peaks (gray lines) for AuNRs with different aspect ratios are drawn together to show an unequal distribution of aspect ratio inhomogeneity across the LgSPR band. A more diverse and denser distribution of AuNRs with different aspect ratios around the center of the LgSPR band (red shaded area) leads to a more heterogeneous excitation of AuNRs by the relatively narrowband pump than at the band edges (blue shaded area), producing a higher NLS (NLS ~1 at 780 nm, NLS ~0 at 700 nm). This figure is adapted from Fig. 6.4 in [28]

aspect ratios (R_n) are selectively excited with each $I(\omega_n,\tau)$. That is to say, they are individually tagged with the intensity modulations at different temporal periods with respect to τ. After waiting time T_w, the excited hot electrons of the AuNRs are probed by the time-delayed $E_{pr}(\omega_{pr})$, which is spectrally dispersed by a monochromator and then detected with a CCD (charge-coupled device) detector. Finally, the FT of the τ-dependent interferogram $S(\tau,T_w,\omega_{pr})$ with respect to τ provides the 2D correlation spectrum, $S(\omega_{pu},T_w,\omega_{pr})$, between ω_{pu} (excitation or pump) and ω_{pr} (emission or probe) frequencies [21]. In summary, the role of the τ-scan-and-FT of the signal in our method is to provide a way (1) to spectrally resolve broadband pump beams, then (2) to individually excite the AuNRs with different aspect ratios, and finally (3) to spread the correlated emission spectra (ω_{pr}) with each excitation frequency (ω_{pu}) on the 2D frequency axes [28].

6.4.3 2D ES Spectra and Nodal Line Slope Analysis: Experiment

In general, it is difficult to obtain detailed information on the dimensional distribution of the AuNR system only from the 1D absorption or TA spectra. As shown in the simulations (Fig. 6.5), however, the 2D ES provides a way to judge the degree of aspect ratio inhomogeneity of AuNRs using the nodal line slope (NLS) of the 2D ES spectrum measured at a particular waiting time. Figure 6.6b displays the 2D ES spectra and the NLS of the silica-coated AuNRs measured at various pump center wavelengths ($\lambda_{pump\_c} = 700 \sim 820$ nm) at $T_w = 1$ ps, which corresponds to the waiting time after the completion of electron heating. Note that the bandwidth of the pump beam used is narrower than the LgSPR band under investigation, allowing a selective examination of the aspect ratio inhomogeneity of the subsets of the AuNRs (parts of the LgSPR band) excited by the pump. The NLS values (black circles) in Fig. 6.6c, which are obtained from a linear fit (red line) to a number of nodal points (black points) around λ_{pump_c} in Fig. 6.6b, vary with the pump center wavelength according to a Gaussian-shaped dependence, which approximately follows the absorption line shape of the LgSPR band. The NLS value has a maximum (close to unity) around 780 nm, which indeed corresponds to the center wavelength of the LgSPR band while it decreases as λ_{pump_c} approaches the red or blue edge of the LgSPR band. These unequal NLS values across the LgSPR band indicate that the degree and nature of the aspect ratio distributions of the individual AuNR subensembles are different significantly at both the center and the two edges of the LgSPR band. The NLS value being close to unity at the LgSPR band maximum means that the inhomogeneous broadening of the AuNR system investigated is much larger than the homogeneous one. That is to say, a subset of the AuNRs around the LgSPR band maximum (red shaded area in Fig. 6.6c), which is selectively excited by the relatively narrowband pump, has a diverse and dense distribution of homogeneous subensembles of AuNRs (gray lines in Fig. 6.6c), so that the pump causes a considerably heterogeneous

excitation of the AuNRs. On the other hand, a less heterogeneous excitation of the AuNRs is induced by the pump tuned to the band edge (blue shaded area in Fig. 6.6c) because the aspect ratio distribution of the AuNRs is more discrete and less dense at either edge of the LgSPR band.

In addition to the spectral dependence of NLS due to an unequal aspect ratio distribution across the LgSPR band, it is noteworthy that the NLS and NPW are waiting time-dependent, as is apparent in Fig. 6.7. Since the NLS and NPW are free from inhomogeneous line broadening contributions, their time-dependent changes are direct signatures of homogeneous relaxation dynamics after photo-excitation of the LgSPR modes of AuNRs. The transient behaviors of the NLS and NPW at T_w < 300 fs can be attributed to ultrafast electron dynamics, such as the dephasing of the coherent oscillations of plasmonic electrons and rapid electron heating in each AuNR, which are induced by the e-e scattering (collision) process [17, 28]. On the other hand, the subsequent monotonic decay of the NLS and the slow blue-shift of the NPW over similar time scales (a few ps) result from homogeneous dephasing due to e-ph couplings. These heterogeneity-free electron-electron (e-e) or electron-phonon (e-ph) relaxation dynamics of AuNRs cannot be observed in conventional pump-probe spectroscopy because the corresponding pump-probe signals result from

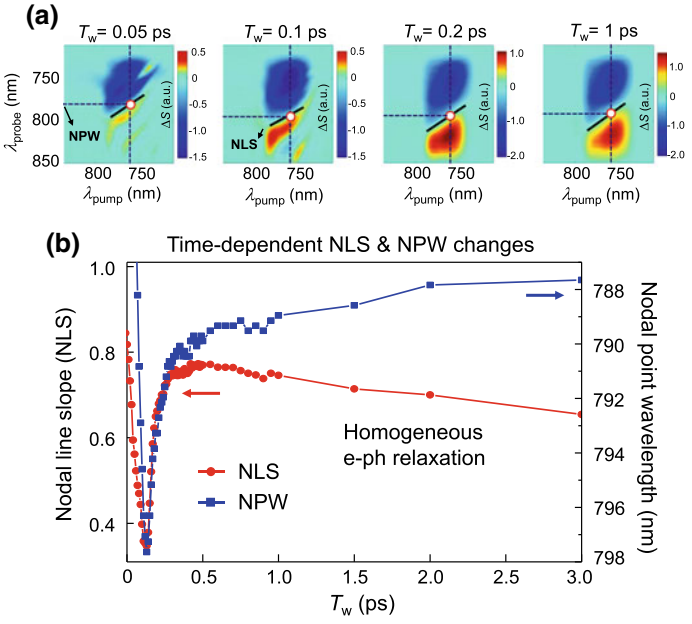

Fig. 6.7 **a** Time evolution of 2D ES spectra measured with the pump center wavelength of λ_{pump_c} = 760 nm at different waiting times (T_w = 0.05 ps, 0.1 ps, 0.2 ps and 1 ps). **b** Time-dependent nodal line slope (NLS, red circle) and nodal point wavelength (NPW, blue square) changes of the 2D ES spectra in (**a**) as a function of waiting time (T_w). Here, the NPW is the probe wavelength at which the nodal line and vertical dashed line corresponding to λ_{pump_c} = 760 nm in (**a**) are crossing with each other. This figure is adapted from Fig. 6.5 in [28]

averaging all the transient dynamics and relaxations of the entire heterogeneous AuNRs.

6.4.4 Comparison Between Nonlinear Signals in Positive and Negative Waiting Times

2D ES is a four-wave-mixing (4WM) process involving three field-matter interactions with incident pulses and one field-matter interaction with the signal field. In the photon echo geometry often used in 2D ES experiments, where three laser beams are noncollinearly incident to the sample, a third-order signal field is generated in a specific direction different from those of the incident beams due to the corresponding phase-matching condition. Then, the thus generated 2D ES signal field is heterodyne-detected by allowing it to interfere with another laser field called a local oscillator (LO) [19–21]. The amplitude and phase of the 2D ES signal electric field can be measured with respect to the delay times between the involved laser pulses. In pump-probe-type 2D ES, on the other hand, the generated signal field interferes with the collinearly propagating incident laser field (probe) after the sample and, consequently, only the absorptive part of the interference term is detected. This technique is often called self-heterodyne-detection [26–29]. Below we compare the observables in normal (positive waiting time, $T_w > 0$) and reverse (negative waiting time, $T_w < 0$) time-orderings of the twin pump pulses and one probe pulse, and explain why spectral fringe patterns are observed only in the negative waiting time domain.

Normal 2D ES measurement ($T_w > 0$). In the pump-probe-type 2D ES experimental setup shown in Fig. 6.8a, collinearly propagating twin pump pulses (pu1 and pu2) originate from the pulse shaper, which controls the time delay (τ) between them, and are injected into the sample. For a normal time-ordered pulse sequence, the probe pulse (pr) is delayed from pu2 by the waiting time T_w, i.e., $T_w > 0$. After three field-matter interactions with the sample in the order of pu1→pu2→pr with wavevectors of $\mathbf{k}_{\mathrm{pu1}}$, $\mathbf{k}_{\mathrm{pu2}}$ and $\mathbf{k}_{\mathrm{pr}}$, respectively, the 2D ES signal field ($\mathbf{k}_{\mathrm{s}}$) is generated in the same direction as the probe wavevector ($\mathbf{k}_{\mathrm{s}} = -\mathbf{k}_{\mathrm{pu1}} + \mathbf{k}_{\mathrm{pu2}} + \mathbf{k}_{\mathrm{pr}} = \mathbf{k}_{\mathrm{pr}}$) and interferes with the probe beam itself (Fig. 6.8b). The interference term between the 2D ES signal field and the probe beam is then detected by a spectrometer. The 2D ES spectra measured at positive waiting times ($T_w > 0$) exhibit both positive and negative peaks with a nodal line separating the two, as shown in Fig. 6.6b.

Transient grating at negative waiting times ($T_w < 0$). Now, let us consider another pulse sequence and 4WM field-matter interactions at negative waiting times ($T_w < 0$), as schematically shown in Figs. 6.8c–d. From the definition of the waiting time, which is the delay time of the probe pulse (pr) from the second pump pulse (pu2), the probe pulse (pr) precedes the second pump pulse (pu2) by $|T_w|$ at negative waiting times. When the delay time τ is scanned from 0 to a finite time for the 2D ES measurement, the pump 1 (pu1) and probe (pr), which propagate differently in space, can overlap in time and thus interact with the AuNRs to generate a transient

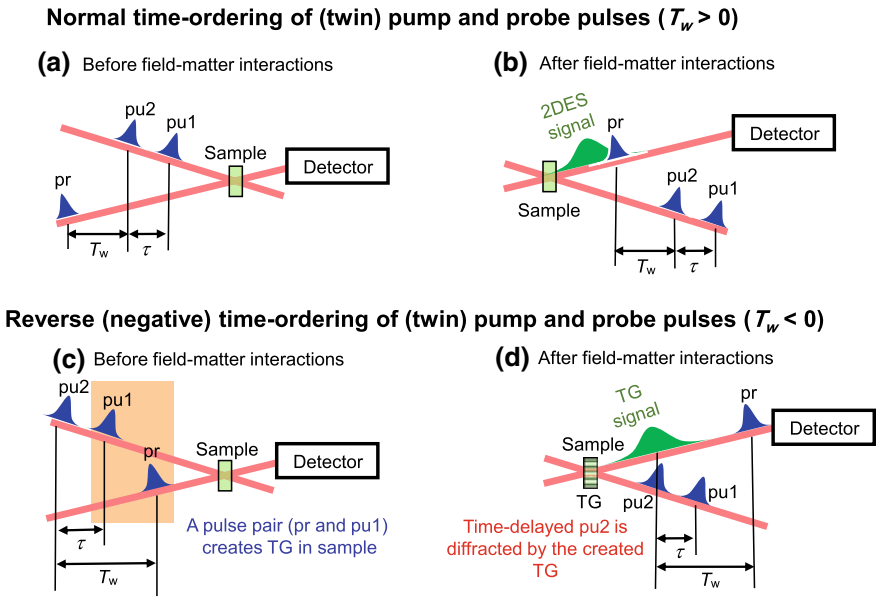

Fig. 6.8 Comparison between pulse sequences and generated third-order signals (2D ES and TG signals) before and after field-matter interaction in **a**–**b** normal ($T_w > 0$) and **c**–**d** reverse ($T_w < 0$) time orderings of twin pump and probe pulses. At positive waiting times ($T_w > 0$), the 2D ES signal interfering with the probe pulse is normally detected. In contrast, another third-order signal called transient grating (TG), which results from a diffraction of the time-delayed second pump pulse (pu2) due to a TG in the sample created by the first pump (pu1) and probe (pr) pulses, is heterodyned detected with the preceding probe pulse at negative waiting times ($T_w < 0$)

spatial grating (TG) inside the sample due to a non-parallel overlap of the wave fronts of the pu1 and pr fields [30]. The following second pump pulse (pu2) is then diffracted by the created TG ($\mathbf{k}_{TG}$) in the same direction as the probe wavevector ($\mathbf{k}_{TG} = \mathbf{k}_{pr}$), and consequently the TG signal field can interfere with the preceding probe field by $|T_w|$. The time delay between the probe pulse and the generated TG signal field is fixed at $|T_w|$ regardless of the scanning delay time τ. Therefore, one can measure the spectral interference between those time-separated fields (TG signal and probe), which produce a spectral fringe pattern with a fringe spacing of $1/|T_w|$ along the probe frequency axis (y-axis) in a given 2D ES spectrum. The following section gives further detailed descriptions of how the TG can create a spectral fringe pattern on the 2D ES spectrum and explain how the spectral interference is related to the aspect ratio inhomogeneity of AuNRs.

6.4.5 Spectral Interference by Transient Grating (TG) in 2D ES

The TG is a temporal and spatial grating created by spatially regular and interferometric SPR excitation across the sample, which is induced by noncollinear mixing of the pu1 and pr fields into the sample at $T_w < 0$, as shown in Figs. 6.8c–d. During scanning the delay time (τ) between the pu1 and pu2, two pulse sequences, pr $\rightarrow$ pu1 $\rightarrow$ pu2 ($\mathbf{k}_{\mathrm{TG}} = \mathbf{k}_{\mathrm{pr}} - \mathbf{k}_{\mathrm{pu1}} + \mathbf{k}_{\mathrm{pu2}}$) and pu1 $\rightarrow$ pr $\rightarrow$ pu2 ($\mathbf{k}_{\mathrm{TG}} = -\mathbf{k}_{\mathrm{pu1}} + \mathbf{k}_{\mathrm{pr}} + \mathbf{k}_{\mathrm{pu2}}$), are involved, which have the same phase-matching condition for the TG, i.e., $\mathbf{k}_{\mathrm{TG}} = \mathbf{k}_{\mathrm{pr}}$ at a fixed negative waiting time, T_w. Consequently, the TG signal field spectrally interferes with the preceding probe pulse by $|T_w|$ in the probe frequency domain (ω_{pr}). Since the spatial phase of the TG across the sample sensitively varies with the time delay ($\tau' = |T_w| - |\tau|$) between pu1 and pr and oscillates at optical frequencies ($\omega_{\tau'}$) of the incident electric fields (pu1 and pr) with respect to τ', scanning τ' results in the temporal modulation of the spectral interference signal between the pu1 and pr fields. Fourier transformation of this modulated spectral interferogram, $S(\tau', T_w, \omega_{\mathrm{pr}})$, with respect to τ' yields the spectral interferometric 2D ES spectra, $S(\omega_{\tau'}, T_w, \omega_{\mathrm{pr}})$.

Figure 6.9a shows the spectral fringe patterns on the experimentally measured 2D ES spectra of the silica-coated AuNRs with an inhomogeneous aspect ratio distribution (length: 35–41 nm, width: 9–11 nm, average aspect ratio: 3.84) at $T_w = -150$ fs, -50 and 0 fs. One of the characteristic features of those interference patterns is the fringe spacing increasing according to $1/|T_w|$ as $|T_w|$ goes to zero, which is also clearly shown in the slice spectra (Fig. 6.9b) taken at the center frequencies (vertical solid lines) of the 2D ES spectra in Fig. 6.9a. To further investigate the $|T_w|$-dependence of the spectral interference, one can perform a Fourier transformation of the spectral fringe patterns in Fig. 6.9b to analyze the resulting time domain signals with respect to the waiting time (Fig. 6.9d). Note that when two pulses are separated in time by t_{d}, the Fourier transformed time domain signal from the spectral fringe created by the two signal pulses peaks at $t = t_{\mathrm{d}}$ [31]. Although the Fourier transformed signals are relatively broad and do not show ideally sharp peaks in time due to the finite chirp of the laser pulses used in experiment, the first moment of the Fourier transformed time domain signal can give meaningful information on the average delay time between the signals involved in spectral interference. As expected, the t_{d}-versus-T_w plot in the inset of Fig. 6.9d shows that the average delay time (t_{d}) decreases in linear proportion to $|T_w|$ at negative waiting times. This experimental observation is in good agreement with the explanation about the origin of spectral interference above, which is based on the TG-induced diffraction of the second pump pulse (pu2) that is time-delayed from the probe (pr) by $|T_w|$.

Another notable feature of the spectral interference on the 2D ES spectra of the AuNR is the diagonal elongation of the fringe pattern (Figs. 6.9a and 6.10a), which is in close connection to the aspect ratio inhomogeneity of the AuNRs. The strong SPR effect of the AuNRs, created by the interfering pu1 and pr fields, significantly modulates the refractive index in a regular spacing across the sample.

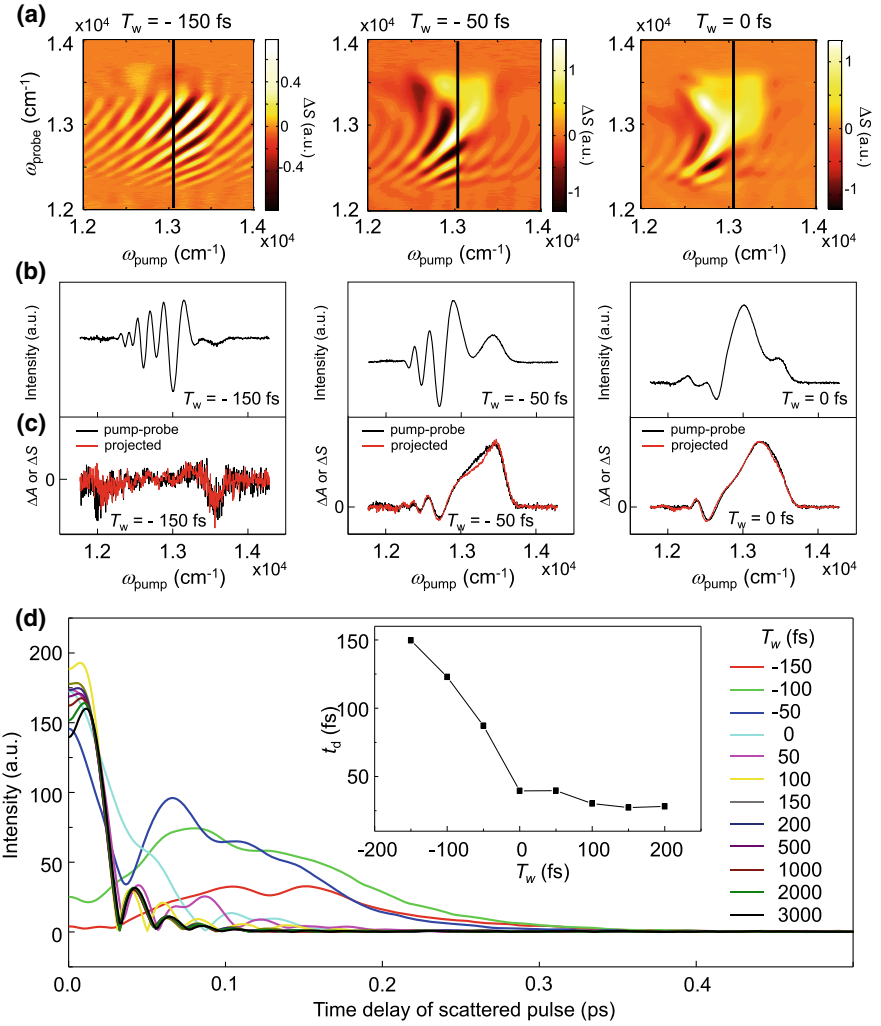

Fig. 6.9 **a** Spectral interference patterns in the 2D ES spectra of AuNRs measured at waiting times of $T_w = -150$, -50, and 0 fs. The center wavelengths of both the pump and probe pulses are 770 nm. **b** Slice spectra (vertical lines) taken at $\omega_{pump} = 13{,}000\ cm^{-1}$ ($\lambda_{pump} = 770$ nm) in the 2D ES spectra of (**a**). **c** Comparison between the pump-probe TA (black lines) and projected (red lines) spectra onto the probe frequency axis (y-axis) in the 2D ES spectra measured at the corresponding waiting times (T_w). **d** Fourier transformed signals of the slice spectra in (**b**) at $\omega_{pump} = 13{,}000\ cm^{-1}$ ($\lambda_{pump} = 770$ nm). Inset: First moment (t_d) of the time-domain signal in (**d**) as a function of waiting time (T_w)

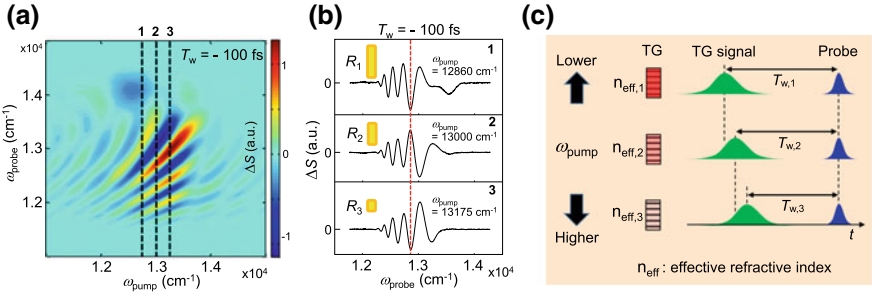

Fig. 6.10 **a** 2D ES spectrum of the AuNRs measured at $T_w = -100$ fs. **b** Slice spectra taken at different pump frequencies, $\omega_{\text{pump}} = 12{,}860$, 13,000 and 13,175 cm^{-1} (vertical dashed lines in (**a**)), which excite different-sized AuNRs with R_j, in the 2D ES spectrum at $T_w = -100$ fs. **c** Pump frequency dependence of time delay between the TG signal and probe pulse at negative (reverse time ordering in Fig. 6.8c–d) waiting times ($T_w < 0$). The spatially modulated refractive index by the strong SPR effect of AuNRs creates a TG in the sample, which can lead to a further time delay ($T_{w,j}$) of the TG signal from the preceding probe pulse by modulating the velocity of the TG signal field. This time delay ($T_{w,j}$) is pump frequency dependent because the effective refractive indices ($n_{\text{eff},j}$) induced by the TG change with the size of the AuNRs with different aspect ratios (R_j), which are individually excited by different pump frequencies. This figure is adapted from Fig. 6.6 in [28]

This spatially modulated refractive index not only gives rise to the diffraction of the pu2 beam in space, but can also further time-delay the TG signal field from the probe pulse by modulating its velocity at the sample. Furthermore, since with varied pump frequencies (ω_{pump}) the TG-inducing beams (pu1 and pr) can individually excite AuNR subensembles with different aspect ratios (R_i) and therefore different effective refractive indices ($n_{\text{eff},i}$), the delay time ($T_{w,i}$) between the TG and probe pulse is dependent on pump frequency (ω_{pump}). Thus, $T_{w,i}$ is larger at lower ω_{pump} (Fig. 6.10c). As a consequence, as shown in Fig. 6.10b, the spectral interferogram along the probe frequency axis is phase-shifted depending on ω_{pump}, i.e., the aspect ratio (R_i) of the AuNRs, producing the diagonally elongated fringe pattern on the 2D ES spectrum [28]. However, this spectral fringe, which contains information on the inhomogeneous dimensional distribution of the AuNRs investigated, disappears in the pump-probe spectra (black lines in Fig. 6.9c), which is equivalent to the average spectra (red lines in Fig. 6.9c) projected onto the probe axis, because the oscillating positive and negative signals on the 2D spectrum along the pump frequency axis are averaged out.

6.5 A Few Concluding Remarks

In the present chapter, we presented our recent 2D ES results for AuNRs featuring a broad dimensional distribution. Although a vast quantity of literature has been published reporting the optical properties of AuNR with respect to size, aspect ratio, surface ligand, shape, and so on, measured using linear absorption spectroscopy and

the time-resolved pump-probe (or transient absorption) measurement method, these spectroscopic techniques cannot provide incisive information about homogeneous dephasing processes involving e-e, e-ph, and ph-ph scatterings. This is because those spectroscopic observables are intrinsically not free from the dimensional heterogeneity of AuNRs in condensed phases. Our 2D ES studies of AuNRs with selective excitations of LgSPR modes provide quantitative information about the homogeneous relaxation dynamics of gold nanorods excited by femtosecond laser pulses. Despite the success of 2D ES application to the study of heterogeneous AuNR samples, due to the pump pulse bandwidth being narrower than the entire LgSPR bandwidth, we could not obtain the entire 2D electronic spectra of the AuNRs used. It will be of great interest to carry out a 2D ES study of the same sample with continuum pump and probe pulses so that the entire ensembles of the AuNRs are excited simultaneously and their ultrafast electron dynamics can be probed with sub-10 fs pulses in real time. In the future, a two-quantum 2D ES technique that utilizes a slightly different phase-matching condition would be useful for studying the large-amplitude longitudinal electronic oscillations of quasi-free electrons in AuNRs and other metallic nanoparticles, and could reveal unexpected electron correlations in such multi-electronic excitation systems.

Acknowledgements This work was supported by IBS-R023-D1 for MC and C39212 (KBSI grant) for HR.

References

1. X. Huang, S. Neretina, M.A. El-Sayed, Gold nanorods: from synthesis and properties to biological and biomedical applications. Adv. Mater. **21**, 4880–4910 (2009)
2. G.V. Hartland, Coherent excitation of vibrational modes in metallic nanoparticles. Annu. Rev. Phys. Chem. **57**, 403–430 (2006)
3. S. Link, M.A. El-Sayed, Shape and size dependence of radiative, non-radiative and photothermal properties of gold nanocrystals. Int. Rev. Phys. Chem. **19**, 409–453 (2000)
4. J. Pérez-Juste, I. Pastoriza-Santos, L.M. Liz-Marzán, P. Mulvaney, Gold nanorods: synthesis, characterization and applications. Coord. Chem. Rev. **249**, 1870–1901 (2005)
5. G. Raschke et al., Biomolecular recognition based on single gold nanoparticle light scattering. Nano Lett. **3**, 935–938 (2003)
6. S. Eustis, M.A. El-Sayed, Determination of the aspect ratio statistical distribution of gold nanorods in solution from a theoretical fit of the observed inhomogeneously broadened longitudinal plasmon resonance absorption spectrum. J. Appl. Phys. **100**, 044324 (2006)
7. H. Baida et al., Ultrafast nonlinear optical response of a single gold nanorod near its surface plasmon resonance. Phys. Rev. Lett. **107**, 057402 (2011)
8. M. Zavelani-Rossi et al., Transient optical response of a single gold nanoantenna: the role of plasmon detuning. ACS Photonics **2**, 521–529 (2015)
9. T.S. Ahmadi, S.L. Logunov, M.A. El-Sayed, Picosecond dynamics of colloidal gold nanoparticles. J. Phys. Chem. **100**, 8053–8056 (1996)
10. C. Voisin, N.D. Fatti, D. Christofilos, F. Vallée, Ultrafast electron dynamics and optical nonlinearities in metal nanoparticles. J. Phys. Chem. B **105**, 2264–2280 (2001)
11. M. Hu, G.V. Hartland, Heat dissipation for Au particles in aqueous solution: relaxation time versus size. J. Phys. Chem. B **106**, 7029–7033 (2002)

12. K. Yu, L. Polavarapu, Q.-H. Xu, Excitation wavelength and fluence dependent femtosecond transient absorption studies on electron dynamics of gold nanorods. J. Phys. Chem. A **115**, 3820–3826 (2011)
13. S. Link, C. Burda, M.B. Mohamed, B. Nikoobakht, M.A. El-Sayed, Femtosecond transient-absorption dynamics of colloidal gold nanorods: Shape independence of the electron-phonon relaxation time. Phys. Rev B **61**, 6086–6090 (2000)
14. C. Voisin et al., Ultrafast electron-electron scattering and energy exchanges in noble-metal nanoparticles. Phys. Rev B **69**, 195416 (2004)
15. O.P. Varnavski, T. Goodson III, M.B. Mohamed, M.A. El-Sayed, Femtosecond excitation dynamics in gold nanospheres and nanorods. Phys. Rev B **72**, 235405 (2005)
16. M. Hu et al., Vibrational response of nanorods to ultrafast laser induced heating: theoretical and experimental analysis. J. Am. Chem. Soc. **125**, 14925–14933 (2003)
17. H. Harutyunyan et al., Anomalous ultrafast dynamics of hot plasmonic electrons in nanostructures with hot spots. Nat. Nanotech. **10**, 770–774 (2015)
18. D. Jonas, Two-dimensional femtosecond spectroscopy. Ann. Rev. Phys. Chem. **54**, 425–463 (2003)
19. T. Brixner et al., Two-dimensional spectroscopy of electronic couplings in photosynthesis. Nature **434**, 625–628 (2005)
20. M. Cho, Coherent two-dimensional optical spectroscopy. Chem. Rev. **108**, 1331–1418 (2008)
21. M. Cho, *Two-dimensional Optical Spectroscopy* (CRS Press, 2009)
22. K. Kwac, M. Cho, Two-color pump-probe spectroscopies of two- and three-level systems: 2-dimensional line shapes and solvation dynamics. J. Phys. Chem. A **107**, 5903–5912 (2003)
23. J. Kim, S. Mukamel, G.D. Scholes, Two-dimensional electronic double-quantum coherence spectroscopy. Acc. Chem. Res. **42**, 1375–1384 (2009)
24. E. Harel, G.S. Fidler, G.S. Engel, Real-time mapping of electronic structure with single-shot two-dimensional electronic spectroscopy. Proc. Natl. Acad. Sci. **107**, 16444–16447 (2010)
25. S.M. Gallagher Faeder, D.M. Jonas, Two-dimensional electronic correlation and relaxation spectra: theory and model calculations. J. Phys. Chem. A **103**(49), 10489–10505 (1999).
26. J.A. Myers, K.L.M. Lewis, P.F. Tekavec, J.P. Ogilvie, Two-color two-dimensional Fourier transform electronic spectroscopy with a pulse-shaper. Opt. Express **16**, 17420–17428 (2008)
27. K.-H. Song et al., Quantum beats and phase shifts in two-dimensional electronic spectra of zinc naphthalocyanine monomer and aggregate. J. Phys. Chem. Lett. **6**, 4314–4318 (2015)
28. A. Lietard, C.-S. Hsien, H. Rhee, M. Cho, Electron heating and thermal relaxation of gold nanorods revealed by two-dimensional electron spectroscopy. Nat. Commun. **9**, 891 (2018)
29. L.P. DeFlores, R.A. Nicodemus, A. Tokmakoff, Two-dimensional Fourier transform spectroscopy in the pump-probe geometry. Opt. Lett. **32**, 2966–2968 (2007)
30. S. Mukamel, *Principles of Nonlinear Optical Spectroscopy*. (Oxford University Press, 1995)
31. L. Lepetit, G. Cheriaux, M. Joffre, Linear techniques of phase measurement by femtosecond spectral interferometry for applications in spectroscopy. J. Opt. Soc. Am. B **12**, 2467–2474 (1995)

Chapter 7
Fully Coherent Schrodinger Cat State Spectroscopy and the Future of CMDS

John C. Wright

Abstract Spectroscopy is one of the most powerful techniques in all of science and technology because of its ability to directly access the individual quantum states of matter and measure their dynamics. Frequency domain methodologies are used extensively to acquire spectra over wide ranges of wavelengths for identifying a system's quantum states. Often, the spectra become spectroscopic fingerprints of individual molecular species. Time domain methodologies have long been used to measure quantum state dynamics on time scales ranging from many seconds to attoseconds. These ultrafast methods typically create one dimensional (1D) spectra and become compromised in studying complex samples where the presence of multiple species creates spectral congestion. This chapter explores the tradeoffs between time and frequency domain methods, pulse width and sensitivity, and the ability to create multidimensional spectral fingerprints that are essential for studying complex materials.

7.1 Introduction

Spectroscopy is one of the most powerful techniques in all of science and technology because of its ability to directly access the individual quantum states of matter and measure their dynamics. Frequency domain methodologies are used extensively to acquire spectra over wide ranges of wavelengths for identifying a system's quantum states. Often, the spectra become spectroscopic fingerprints of individual molecular species. Time domain methodologies have long been used to measure quantum state dynamics on time scales ranging from many seconds to attoseconds. These ultrafast methods typically create one dimensional (1D) spectra and become compromised in studying complex samples where the presence of multiple species creates spectral congestion. This chapter explores the tradeoffs between time and frequency domain

J. C. Wright (✉)
Department of Chemistry, University of Wisconsin, Madison, WI 53706, USA
e-mail: wright@chem.wisc.edu

M. Cho (ed.), *Coherent Multidimensional Spectroscopy*,
Springer Series in Optical Sciences 226,
https://doi.org/10.1007/978-981-13-9753-0_7

methods, pulse width and sensitivity, and the ability to create multidimensional spectral fingerprints that are essential for studying complex materials.

Fully coherent CMDS methods have great promise for creating multidimensional fingerprints [1]. They are based on exciting multiple vibrational and electronic states to create a nonlinear polarization that re-emits an output beam [2–11]. Figure 7.1 shows two examples of three excitation pulses exciting resonances with different quantum states. The interactions with the pulses are time ordered from left to right. Each interaction creates a quantum mechanical superposition state consisting of the original and final states of the transition. The superposition state is called a coherence. After the third pulse, the excitations have created a coherence between states *c* and *b* that oscillates in time. The coherence associated with each molecule in the entire ensemble of molecules within the excitation volume corresponds to an oscillating nonlinear polarization that creates the output beam given by the last arrow. It is that output beam which is measured. Establishing resonance with a specific quantum state on a specific molecule or material component can enhance all of the other resonances that are coupled to it. The multiple resonances create multidimensional spectra that isolate the coupled states for a specific molecule or component. Establishing resonance with a different quantum state then isolates other coupled states on other molecules or components. Thus, CMDS methods can dissect spectra into those states that are coupled and belong to the same molecule or component [12–15].

CMDS methods are usually classified into frequency and time domain methods [3, 4, 16]. Time domain methods have been very successful in resolving dynamics for a wide variety of molecular and materials systems [17, 18]. They are based on a partially coherent pathway like that shown in Fig. 7.1a [6, 8–10]. Here, the first two pulses populate state *b*. The diagram shows population relaxation that transfers the

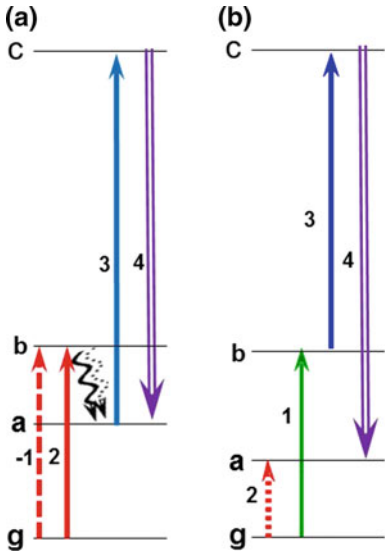

Fig. 7.1 WMEL diagrams showing the sequence of 3 excitations (left to right) for a partially coherent pathway (**a**) and a fully coherent pathway (**b**). Interaction 4 creates the output. Solid and dotted arrows identify transitions defining the two states involved in the output emission

population to state *a*. The third pulse excites state *c* that together with state *a* creates the output pulse. There are two coherences in this diagram. The first is between states *b* and *g* and the second is between states *a* and *c* and they oscillate at the frequency differences, ω_{bg} and ω_{ca}. Two dimensional spectra are acquired by overlapping the output beam created by the *ca* coherence with a fourth beam called a local oscillator and measuring the beating between the electric fields of the output pulse and the local oscillator. This heterodyne detection resolves the phase oscillations of individual coherences. Fourier transforming the data then creates multidimensional spectra. Long term pulse phase stability of ~λ/50 is needed over the measurement time to avoid artifacts [6]. Typically, the central excitation frequencies are fixed so the range of states that are excited is constrained by the pulse bandwidth. For example, 35 fs pulses can excite states over a ~420 cm^{-1} range. It is also possible to use a different excitation frequency for pulse 3 (see Fig. 7.1a) if the first two excitation fields create a static population. The static population isolates the phase oscillations of the first and last coherences [19–21]. This strategy makes it possible to perform vibrational-electronic spectroscopy (2DEV) where a vibrational population is first excited with a pump and the electronic output coherence is excited by the probe pulse [22]. The time domain methods have the multiplex advantage where each set of pulses creates data covering the entire frequency range. Multidimensional spectra can even be collected on a single shot of pulses [23].

Fully coherent multidimensional spectroscopy methods based on frequency domain methods have been very successful in acquiring multidimensional spectra of electronic and vibrational states for a wide variety of molecular and materials systems [5, 12–14, 16, 24–32]. Rather than resolving the phase oscillations of the individual coherences, they measure the resonance enhancement of the output intensity while scanning the excitation pulse frequencies. These methods require phase stability only during the excitation pulse interactions [1]. They don't require the long term phase stability of time domain methods where the phase oscillations are resolved by changing the pulse time delays. Instead, the phase stability requirement is enforced by the spatial and temporal modulations of the output nonlinear polarization. The freedom from long term phase stability between excitation pulses has a number of important consequences:

1. It becomes possible to use three independently tunable excitation beams so any combination of vibrational and electronic states can be excited.
2. The range of accessible frequencies is not constrained by the bandwidth of the excitation pulses.
3. There is a wide range of fully coherent pathways that provide complementary capabilities for probing different aspects of the sample.
4. Fully coherent spectroscopies directly probe couplings between quantum states and avoid relaxation effects that cause time dependent spectral changes. They create multidimensional spectral fingerprints that become a powerful probe of complex materials.
5. Many fully coherent spectroscopies have output transitions in the visible or ultraviolet that are easily detected by photomultipliers and other single photon detec-

tors while still acquiring vibrational spectra in the infrared. The output beams can also occur at different frequencies from the excitation pulses so they can be spectrally resolved and avoid interference from scattered light.

6. When CMDS methodologies are used for creating spectral contrast in microscopic imaging applications, the spatial resolution will be defined by the shortest excitation wavelength since the shortest wavelength has the shortest diffraction limit.

This chapter focuses on frequency domain CMDS and its relationship to time domain CMDS methods. Although time domain methods dominate the field of CMDS, frequency domain CMDS is well-suited for the most common use of spectroscopy that involve acquisition of spectra over very wide ranges of frequencies [16]. In particular, the fully coherent CMDS pathways are particularly important for wide-spread applications because of the selectivity acquired from 3D spectral fingerprints. The 3D fingerprints are immune to changes caused by relaxation because fully coherent pathways create quantum mechanical Schrodinger cat states that collapse if relaxation occurs. Frequency domain methods also provide the lowest detection limits because the excitation pulse width is comparable or longer than the dephasing times so the coherence amplitudes can approach the steady state values.

7.2 Schrodinger Cat States and Coherent Multidimensional Spectroscopy

Schrodinger cat states are quantum mechanical superposition states where a system exists simultaneously in multiple, entangled quantum states [33]. Entangled quantum states are one of the most surprising consequences of quantum mechanics because measurement of a quantum state collapses the cat state and provides an instantaneous snapshot of the quantum states [34]. The classic example is parametric down-conversion where interactions in a nonlinear crystal creates a cat state where the original pump photon and signal and idler photons are simultaneously present [35]. The photons are entangled in frequency and direction by energy and momentum conservation so $\omega_{\text{pump}} = \omega_{\text{signal}} + \omega_{\text{idler}}$ and $\vec{k}_{\text{pump}} = \vec{k}_{\text{signal}} + \vec{k}_{\text{idler}}$. They are also entangled in polarization by type I or type II phase matching. If an observation occurs that identifies the frequency, direction, or polarization, the observation collapses the cat state to a pump, signal, or idler photon [35]. Observation of a particular photon depends on its probability but subsequent observations of the other photons is then determined.

Coherent multidimensional spectroscopy (CMDS) is based on using multiple coherent excitation pulses to entangle the photon fields and the vibrational and/or electronic quantum states of a sample [1, 3, 36]. The most important capability of CMDS is its ability to isolate only those quantum states that are coupled so excitation of one affects the others. The sample's coupled quantum states form a superposition state called a multiple quantum coherence. It is time dependent and oscillates

at all frequency combinations of its states. The entanglement is lost when interactions collapse the cat state. The cat state collapses when its quantum mechanical phase relationships become randomized, either by measurement or interaction with the environment or vacuum photons. Upon collapse, the multiplicity of the cat state is lost and specific states of the sample and photon fields are populated with probabilities proportional to the square of their cat state amplitudes. The measurement is impervious to population relaxation effects that change the nature of the states because the relaxation effects would destroy the cat state.[1] The measurement can be the intensity of the new photon fields created by the coherence or the intensity change in the excitation fields. The act of measuring one defines any subsequent measurement of the others.

We first describe a fully coherent CMDS pathway that illustrates the creation of a four quantum Schrodinger cat state [11]. Tunable coherent pulses with frequencies ω_1, ω_2, and ω_3 are tuned to resonances with a molecule and excite three different quantum states that form a quantum mechanical coherence involving the ground state and three excited states. The wave function is time dependent with spatial and temporal properties given by $\Psi(x,t) = \sum_{\substack{n=\text{all quantum}\\ \text{states}}} c_n(t)\psi_n(x)\left[e^{i\omega_n t} + e^{-i\omega_n t}\right]$ where c_n is the amplitude for state n in the superposition state. This superposition state is entangled with the photon quantum states and together form the Schrodinger cat state. Observables depend on the product of an amplitude and its complex conjugate. For example, the diagonal $\rho_{nn} \equiv c_n c_n^*$ density matrix elements define the probability of population in state n while the off-diagonal $\rho_{nm} \equiv c_n c_m^*$ define the probability of a $\omega_{mn} \equiv \omega_m - \omega_n$ transition involving states m and n. In Dirac's bracket notation, $\langle m|\, n\rangle$, the m and n designate the bra and ket states, respectively, and differ in phase by π. When a transition occurs at ω_{nm}, the cat state collapses into a specific molecular state and specific photon states. Figure 7.1b shows a wave mixing energy level diagram (WMEL) [37] where three photons sequentially and impulsively excite states a, b, and c to form a cat state consisting of g, a, b, and c. Here, the time ordering of the transitions proceeds from left to right. The numbers denote the different frequencies of the excitation pulses, not the time ordering of the interactions. The last arrow is the output transition created by the free induction decay of the ρ_{ca} coherence. The solid arrows diagram the path for reaching state c and the dotted arrows diagram the path for reaching state a. The entire coherent pathway can be summarized by the notation $gg \overset{-2}{\rightarrow} ga \overset{1}{\rightarrow} ba \overset{3}{\rightarrow} ca$ where the numbers designate the frequencies and the signs depend on the phase matching. The output photon frequency is ω_{ca}. Energy conservation requires $\omega_1 - \omega_2 + \omega_3 = \omega_4 = \omega_{ca}$. The ω_1 and ω_3 excitation fields have all lost a photon, the ω_2 and ω_4 fields have gained a photon, and the molecule is left in state a. Momentum conservation requires $\vec{k}_4 = \vec{k}_1 - \vec{k}_2 + \vec{k}_3$. Of course, output beams would also occur at all $\omega_4 = \pm n_1\omega_1 \pm n_2\omega_2 \pm n_3\omega_3$ frequency combinations and all directions $n_1\vec{k}_4 = \pm n_1\vec{k}_1 \pm n_2\vec{k}_2 \pm n_3\vec{k}_3$ where $n = 0, 1, \ldots$ Each would correspond to a different process with different characteristics and WMEL diagrams. This same picture applies to partially coherent CMDS pathways that are used when relaxation

[1] The exception is coherent transfer where the environment causes a coherent evolution of a state without randomization of the quantum mechanical phase.

dynamics are studied [3]. Figure 7.1a is an example of a partially coherent CMDS pathway where there is an intermediate population that can undergo relaxation. The numbered arrows now label the excitation pulse time ordering. The first interaction forms a cat state involving states g and b. The second interaction creates a population in state b, that relaxes to state a and collapses the first cat state. The third interaction excites the aa state population to form a cat state involving states a and c. The output photon free emission decay results from collapse of the last cat state. The pathway summary is $gg \overset{-1}{\rightarrow} gb \overset{2}{\rightarrow} bb \overset{\text{NR}}{\Rightarrow} aa \overset{3}{\rightarrow} ca$ where the double arrow represents non-radiative (NR) population decay.

This pathway directly measures population dynamics where the excited molecular state relaxes to a different state and spectral diffusion where environmental changes change the state frequencies [38]. It is also important for relaxation assisted enhancement of weak transitions if state b absorbs strongly and transfers population to state a that is weakly absorbing [19, 39, 40]. If pulse 3 appears before relaxation occurs, the corresponding pathway becomes $gg \overset{-1}{\rightarrow} gb \overset{2}{\rightarrow} bb \overset{3}{\rightarrow} cb$. This pathway describes excited state absorption (ESA). Together with the $gg \overset{-1}{\rightarrow} gb \overset{2}{\rightarrow} bb \overset{3}{\rightarrow} bg$ photo-bleaching pathway (PB) and $gg \overset{-1}{\rightarrow} gb \overset{2}{\rightarrow} gg \overset{3}{\rightarrow} bg$ stimulated emission pathway (SE), they describe the pump-probe, transient grating, transient absorption, and photon echo methods that are used extensively for measuring quantum state dynamics [10]. The last pulse in the partially coherent pathway of Fig. 7.1a acts as a 1D probe of the dynamics.

It is also possible to replace the last pulse with three pulses that correspond to a fully coherent CMDS pathway such as that in Fig. 7.1b [1]. This pump-fully coherent CMDS probe provides much greater selectivity. The cat state nature of fully coherent CMDS has the important constraint that any relaxation process destroys the state so fully coherent CMDS methods are a direct probe of the coupling between states and are immune to the changes in these states as a result of relaxation. The multiple states within the cat state are a multidimensional spectral fingerprint that provides high selectivity for the specific species in a complex sample [36]. The cat state nature of the probe insures that relaxation dynamics only occurs during the time between the pump and CMDS probe pulses. Figure 7.2 shows examples of such methods. They include methods where the pump involves one and two photon absorption. Two photon pump methods have the advantage that they can probe the same state that is pumped without interference from pump pulse light scattering.

Although population relaxation destroys a cat state, coherence transfer does not. Coherence transfer occurs when a state within the cat state evolves to a different state because of a coherent interaction with the thermal bath. The key idea is coherence transfer maintains the overall quantum mechanical phase without collapsing the cat state. Coherence transfer has clearly been observed in vibrational spectra [41–43] and it may also be important in photosynthetic systems [17, 44, 45]. Its role in photosynthetic systems is obscured by the presence of vibronic effects [46, 47].

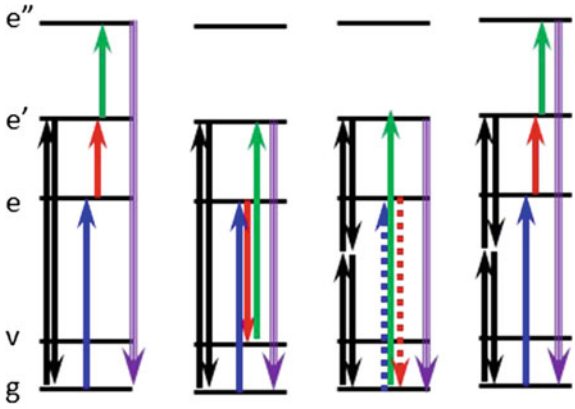

Fig. 7.2 Example pathways for pump (black arrows)-fully coherent probe (colored arrows)

7.3 Comparisons Between Time and Frequency Domain Methods

The field of CMDS is evolving rapidly and there have been many different experimental implementations. In order to compare the different approaches, we will focus on determining the ρ_{nm} coherence formed from a previous coherence in order to highlight the effects of pulse width. Each CMDS method is based on exciting a series of transitions that result in the final output coherence. The amplitude of each transition depends on the ratio of the Rabi frequency to the dephasing rate and the ratio of the excitation pulse temporal width to the dephasing time [5]. The buildup and decay of a coherence can be described in a closed form equation if the excitation pulse is a rectangular excitation pulse that is resonant and lasts for Δt seconds. The temporal dependence is given by $\frac{\Omega}{2\Gamma_{nm}}\left(1-e^{-\Gamma_{nm}\Delta t}\right)$ where Ω is the Rabi frequency, $\Omega \equiv \frac{\vec{\mu}\cdot\vec{E}}{\hbar}$, and Γ_{nm} is the dephasing rate of the transition between states m and n. Figure 7.3 shows an example of the transient for the coherence ρ_{ag} that is formed from a ground state population. The coherence builds towards a steady state over a time that depends on the dephasing rate but then undergoes free induction decay when the pulse (blue trace) turns off. For a four-wave mixing experiment in a two-level system, the amplitude of the output coherence after three interactions will be $\left[\frac{\Omega}{2\Gamma_{nm}}\left(1-e^{-\Gamma_{nm}\Delta t}\right)\right]^3\rho_{gg}$ where ρ_{gg} is typically 1. For the more general case, the transition moment and dephasing rate will be different for each transition. Table 7.1 illustrates the dependence on each variable. The table assumes a typical excitation intensity of 10^{10} watts/cm^2 regardless of Δt. This assumption is justified because higher instantaneous intensities can cause sample damage.

The table compares examples of the dephasing rate and transition moment for weak vibrational modes (typically $\mu \approx 0.01\,D$ and $\Gamma \approx 10^{12}\,s^{-1}$), the strongest vibrational modes (for carbonyl modes, $\mu \approx 0.3\,D$ and $\Gamma \approx 4\times10^{13}\,s^{-1}$), and typical electronic states (typically $\mu \approx 1\,D$ and $\Gamma \approx 5\times10^{15}\,s^{-1}$) with typical excitation pulse widths for picosecond (1 ps) and femtosecond (35 fs) CMDS [48,

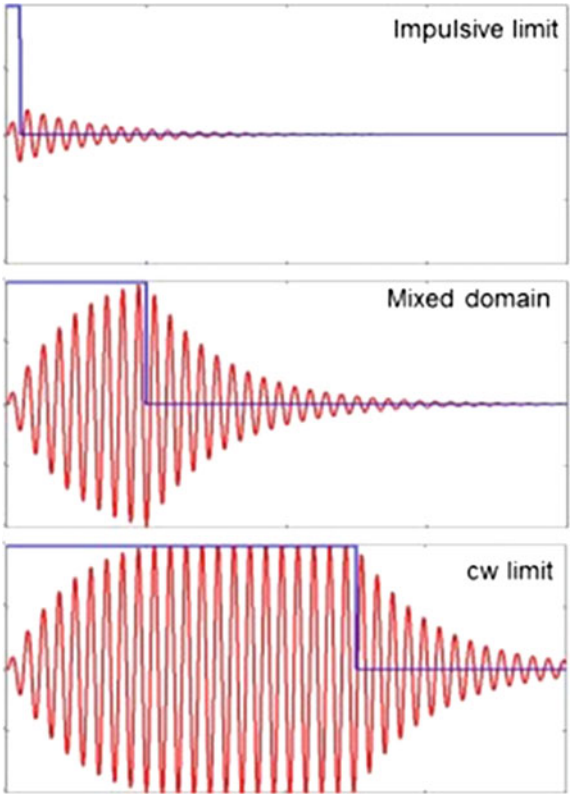

Fig. 7.3 Transients for exciting a coherence with different rectangular pulse widths (blue). Adapted from [76]. Copyright 2019 American Chemical Society

Table 7.1 Effect of pulse width on representative weak and strong vibrational transitions and electronic transitions

I_{excit} (watts/cm^2)	10^{10}					
Δt (ps)	1			0.035		
Γ (sec^{-1})	10^{12}	4.7×10^{12}	5×10^{13}	10^{12}	4.7×10^{12}	5×10^{13}
μ (Debye)	0.01 D	0.3 D	1D	0.01 D	0.3 D	1D
Ω (s^{-1})	4×10^{10}	10^{12}	10^{12}	4×10^{10}	10^{12}	4×10^{12}
$1 - e^{-\Gamma \Delta t}$	0.6	1.0	1.0	0.03	0.15	0.8
ρ_{final}/ρ_{init}	0.01	0.12	0.04	6×10^{-4}	0.018	0.03
ρ_{out}	1×10^{-6}	0.002	5×10^{-5}	3×10^{-10}	6×10^{-6}	3×10^{-5}

49]. The Rabi frequency in the table depends on the transition moment and the amplitude of the coherence depends on the dephasing rate and pulse width. For a picosecond pulse, a weak vibrational mode reaches 60% of the steady state value during Δt but the femtosecond pulse reaches only 3% of the steady state value. That difference results in an output coherence that is 4 orders of magnitude weaker for the femtosecond pulse. The differences are similar for the strong vibrational mode. Note, however, that the femtosecond output coherence for the strong vibrational transition is 6x larger than the picosecond output coherence for the weak vibrational mode. This difference is at the heart of why picosecond infrared CMDS can access the weak vibrational states [29, 48, 50] while femtosecond 2DIR CMDS accesses only the strongest vibrational modes [19, 39, 40]. These differences disappear for electronic CMDS like 2D-ES because the fast dephasing rates of electronic states allow both approaches to reach the steady state values.

The output coherence creates a macroscopic output polarization given by $P_{\text{out}} = NF\mu_{\text{out}}\rho_{\text{out}}$ where F is the field enhancement factor for the three excitation fields [5]. The electric field amplitude that is launched by the nonlinear polarization is defined by $\frac{\mathrm{d}E^{o}_{\text{out}}}{\mathrm{d}z} = \frac{2\pi i F\omega P^{o}_{NL}}{nc} e^{i\Delta\vec{k}z}$ where F is the field enhancement factor for the output field and Δk is the phase mismatch factor between the nonlinear polarization and the output field it creates. This output field can be very strong because unlike incoherent processes such as fluorescence, there is a phase relationship between all of the molecules in the excitation volume. The emission from all the molecules can be constructive and therefore cooperative. It creates a beam with a direction defined by constructive interference between the emission of the individual molecules in the excited ensemble. The intensity that is actually measured depends on the particular methodology that is employed. The intensity can be measured directly by homodyne detection in which case the intensity is $I = \frac{2\pi}{cn}\left|E_{\text{out}}\right|^2$. Fully coherent pathways that result in spectrally resolved output beams can have detection limits defined by the ability to measure individual photons.

The beam can also be heterodyned by overlapping the output field with either one of the excitation beams or an additional beam that acts as a local oscillator. The frequencies in the overlapped beams will beat at frequencies that depend on the differences between the beams. Heterodyne detection requires the frequencies present in the heterodyned beams to be similar so a detectable beat frequency can occur. This approach allows heterodyne detection to resolve the phase oscillations in the output field and define its frequencies. The intensity is given by $I = \frac{2\pi}{cn}\left|E_{\text{out}} + E_{\text{heterodyne}}\right|^2$. Heterodyne detection can create large signal levels if $E_{heterodyne}$ is larger than E_{out} so $\left|E_{\text{heterodyne}}E_{\text{out}}\right| > |E_{\text{out}}|^2$. The minimum detection limit depends on discriminating between the signal, $\left|E_{\text{heterodyne}}E_{\text{out}}\right|$, and uncorrected fluctuations in the local oscillator intensity, $|\Delta E_{\text{LO}}|^2$. Typically, $\left|\frac{\Delta E_{\text{LO}}}{E_{\text{LO}}}\right|^2 \approx 0.02$.

Our work has shown that the detection limits are similar for each approach and that homodyne detection presents the fewest problems with maintaining adequate phase stability. The only challenge is the quadratic dependence on the excitation intensity. The higher order dependence requires a detection strategy with a wide dynamic range

since signals range from large numbers of photons/pulse to fewer than one/excitation pulse. The work presented here uses homodyne detection exclusively.

Table 7.1 also shows that the $\rho_{\text{final}}/\rho_{\text{init}}$ values for picosecond vibrational CMDS are large enough that higher order processes become possible. Higher order process allow additional excitation beams to create additional transitions or multiple interactions with individual beams that excite higher overtone and combination band states on a vibrational ladder [41–43, 51–53]. Resolving the higher order vibrational state overtones and combination bands then makes it possible to probe the multidimensional potential energy surface of a molecule.

7.4 Experimental Implementations of Coherent Multidimensional Spectroscopy

Figure 7.4 diagrams a typical frequency domain CMDS experiment. Three tunable excitation pulses are focused into the sample where they create coherences throughout the excitation volume. Their emission can be cooperative and bright in specific directions where the fields emitted from individual molecules constructively interfere. These directions are defined by the output frequency and phase matching conditions, $\omega_{out} = \pm\omega_1 \pm \omega_2 \pm \omega_3 \pm \ldots$ and $\vec{k}_4 = \pm\vec{k}_1 \pm \vec{k}_2 \pm \vec{k}_3 \pm \ldots$, respectively, for third and higher order processes. Here, $|k| \equiv \frac{n\omega}{c}$ and n is the refractive index. These beams are emitted simultaneously. One beam is chosen for measurement and the others are blocked. The presence of an output beam that is different from the excitation beams in direction, frequency, and/or polarization makes it easier to isolate the output beam. In this example, a monochromator isolates the frequency of the output pulse and the beam intensity is measured directly (homodyne detection). The cooperative nature of the emission results in a quadratic dependence on molecular concentration instead of the linear dependence that results if the emission is incoherent.

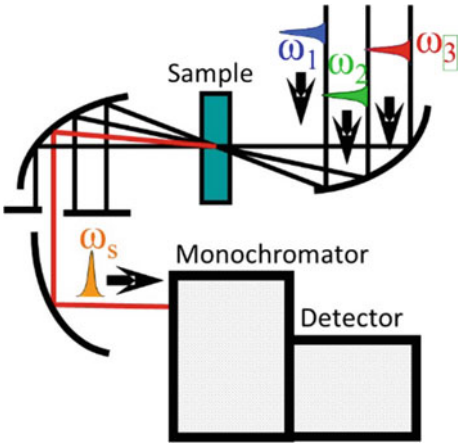

Fig. 7.4 Diagram of components in a frequency domain CMDS experiment

The most challenging problem for implementing frequency domain CMDS is scanning the excitation frequencies [54]. The frequencies of the excitation pulses with nanosecond excitation pulses can be easily scanned with optical parametric oscillators (OPOs). Nanosecond CMDS has resulted in 3D CMDS experiments that can resolve more than a million rotational peaks from gas phase molecules as complex as NO_2 where the state density is so high that 1D spectra are nearly featureless [55–57]. Continuous scanning is much more difficult with commercial picosecond and femtosecond laser systems. Commercial ultrafast systems are designed to set the output frequency to a specific value and acquire transients at that frequency. They are not designed to scan continuously across wide frequency ranges. Changing the frequency changes temporal, spatial, and line shapes of the excitation pulses and all of these changes must be corrected in order to accomplish spectral scanning.

Typically, a commercial OPA is pumped by a picosecond or femtosecond pulse from a Ti: sapphire oscillator which was amplified by a regenerative amplifier [58]. The conversion of the pump beam is based on parametric difference frequency generation that creates a signal and idler beam such that $\omega_{\text{pump}} = \omega_{\text{signal}} + \omega_{\text{idler}}$. There are different strategies for implementing spectral scanning but they all require changing the angles of nonlinear crystals and the time delays between pulses. We will use the femtosecond Light Conversion TOPAS optical parametric amplifier (OPA) as a specific example of the challenges in continuous scanning [54]. A beam splitter divides a pump beam into 97% and 3% components— the former passing into a power amplifier and the latter passing into an OPA. The 3% component is further divided in a 1:4 ratio. The smaller portion is focused into a ~3 mm thick sapphire crystal to generate white light which is subsequently chirped in a ~1 cm thick ZnSe crystal. The larger portion (now called the pump) is spatially overlapped with the white light beam. The time delay of the pump is adjusted to temporally overlap the part of the white light pulse with the desired frequency to be amplified. The pump and white light pass into a 1 mm thick BBO crystal where the BBO crystal angle is adjusted to phase match the production of the difference frequency (called the idler) between the pump and signal.

Figure 7.5 shows the dependence of the signal frequency and intensity on the positions of the crystal angle and pump delay time [54]. A spectrum is taken at each pixel defined by the angle and delay settings and the spectrum is fit to a Gaussian in order to define the intensity and central frequency for that pixel. The goodness of fit is also measured for each pixel and if the fit is poor at some positions, the OPA or regenerative amplifier alignment must be adjusted. The color bar in Fig. 7.5a shows how the intensity of the signal changes as a function of the crystal angle and pump delay. The labeled lines identify the contour of constant frequency (cm^{-1}) for the signal. The color bar in Fig. 7.5b shows how the center frequency of the signal changes as a function of the crystal angle and pump delay. The lines identify the contour of constant intensity. Note that changing the frequency requires a positively correlated movement of angle and delay but optimizing the intensity requires a negatively correlated movement. The correlation between the motors depends on the competition between the large gain bandwidth of BBO in the near-IR and the temporal dispersion profile of the ZnSe crystal. As a result, there is neither a single

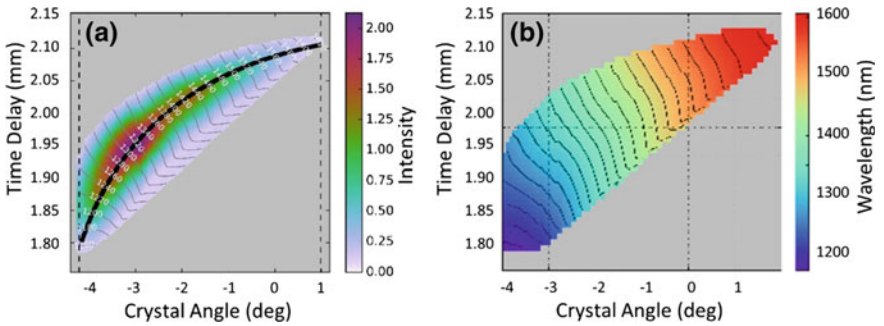

Fig. 7.5 **a** Shows the dependence of the signal output intensity on the crystal angle and the position of the time delay of the OPA. **b** Shows dependence of the signal output wavelength on the same two parameters

crystal angle nor a single delay that uniquely defines the output color. A strategy that optimizes the intensity at a series of different frequencies does a poor job of creating a calibration curve for scanning frequencies because the ratio of delay/angle for maximum intensity does not in general have a smooth dependence on the frequency. As a result, the correlation between nearby frequencies suffers. Although this behavior does not affect measuring transients at specific frequencies, the loss in correlation between angle and delay settings creates artifacts and noise in frequency scans. The quality of frequency scans requires a tuning curve that optimizes correlation between the angle and delay changes even though the intensity at any particular frequency could be improved by slight changes in the angle and delay. The tuning curve is calibrated by performing a polynomial fit to the maximum intensity dependence on peak frequency as a function of the angle and delay settings. The solid black line in Fig. 7.5a is an example of such a calibration curve. The calibration curve is stable over many days but there are environmental changes in temperature and humidity that affect the system, particularly the factors that control the white light generation. For that reason, the system is automated, so the calibration strategy defined above can be performed quickly and accurately.

The OPA idler output typically creates ~0.5–3 μJ pulses that serve as the input seed for amplification by a power amplifier that is pumped by the 97% portion from the original beam splitter. The power amplifier is a ~1 mm thick BBO crystal that amplifies the input seed beam from the OPA output by a factor of 200–300 to create intense signal and idler beams. When the OPA scans the seed frequency, the BBO angle and the delay between the seed and intense pump beams must be changed to preserve phase matching and temporal overlap. These changes must also be included in the calibration procedures required for spectral scans. Figure 7.6 shows the dependence of the intensity and frequency on the BBO crystal angle (x-axis) and delay time between the pump and seed beams (y-axis) [54]. It is clear that the maximum intensity for any specific seed frequency can occur at angle and delay settings where the central frequency is different from the seed frequency.

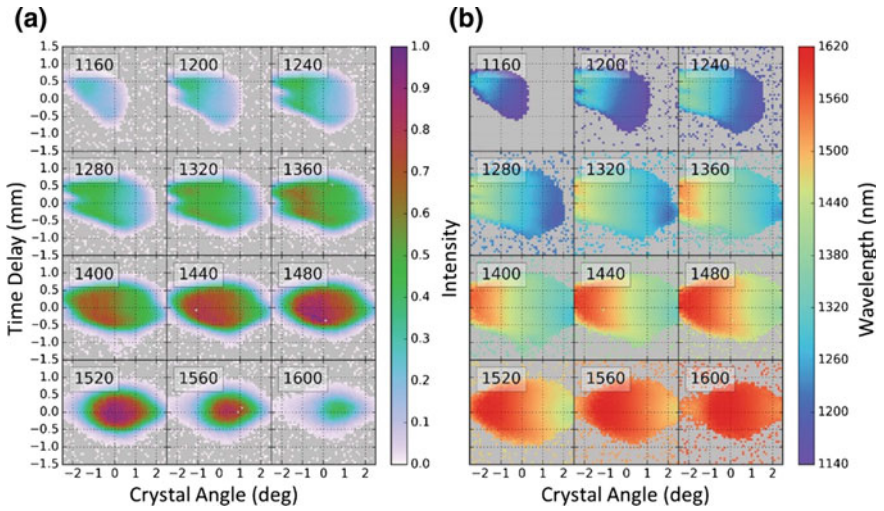

Fig. 7.6 **a** Shows the dependence of the signal output intensity on the crystal angle and the position of the time delay of the power amplifier. **b** Shows dependence of the signal output wavelength on the same two parameters

For example, the maximum intensity at $\omega_{\text{signal}} = 1360\ \text{cm}^{-1}$ in Fig. 7.6a occurs at (–1.8, 0.4) while the central frequency in Fig. 7.6b occurs at ~1480 nm for that position. This shift results because the power amplifier gain profile can cause the central frequency in the input seed pulse to be amplified asymmetrically across its bandwidth, particularly if the seed frequency is near the edge of the tuning range. The asymmetrical amplification can result in distortions of the ideal Gaussian distribution including the development of shoulders or splitting that depend on the phase-matching function during its amplification.

In order to tune the excitation frequencies across the infrared, visible, and ultraviolet, the signal, idler, and Ti:sapphire pump beams are focused into nonlinear mixing crystals where phase matching can create new frequencies at double or quadrupole the signal or idler frequencies, the sum of the pump and signal or idler frequencies, or the difference frequency between the signal and idler frequencies. As the signal and idler frequencies change, the angle of the nonlinear crystal responsible for these nonlinear processes must also change in order to preserve phase matching. Since the efficiency of the nonlinear mixing crystals depend only on the phase matching, the optimization required during frequency scans only requires one additional crystal angle to be tuned.

The changes in the crystal angles and delay times that occur upon scanning the excitation frequencies also leads to changes in the excitation beam directionality and temporal position. If the excitation beams are spatially and temporally overlapped at one set of frequencies, the directional and temporal changes will destroy the overlap if the frequencies are changed. For that reason, it is also necessary to correct the directionality and temporal changes during spectral scans. The directionality

changes can be controlled by a pair of mirrors that adjust beam position and angle and the temporal changes can be controlled by time delay optics. These corrections are required for each excitation beam. Computer control and software must simultaneously correct the angles and delays in the OPAs and in the beam directionality and temporal positions during any spectral scan. The calibration for these corrections occurs during the calibration for the OPAs frequency scans. The changes in directionality are monitored by the displacement of the focal spot through a pinhole and the changes in temporal position are monitored by overlapping the beams in a nonlinear, non-resonant material such as a semiconductor, transparent window, or solvent.

7.5 Mixed Frequency/Time Domain Experiments-When the Pulse Width Rivals the Dephasing Time

There are substantial advantages for experiments in a mixed frequency/time domain where the pulse widths are long enough to excite specific quantum states but short enough to measure their coherent and incoherent dynamics [59]. In this regime, the spectral line shapes fall between the steady state and impulsive limits. The mixed domain optimizes the output signal since the pulse lengths are long enough to approach the steady state limit. It also optimizes the spectral range by allowing tunable excitation frequencies since phase relationships are only needed during the creation of the cat state. However, operating in the mixed frequency/time domain also complicates the spectral interpretation since the spectra now have driven components that depend on the excitation frequencies and free induction decay components that depend upon the coherent state frequencies and the detuning from resonance. The interpretation of spectral line shapes must then distinguish between whether the spectra reflect the properties of the sample or the properties of the methodology. In many cases, it becomes important to numerically integrate the Liouville equation using the actual temporal envelope of the excitation field, $E^o(t)$.

Figure 7.7 shows the temporal dependence of a ρ_{ij} coherence (colored transients) by a Gaussian excitation pulse (gray) for three different dephasing rates, Γ_{ij}, that are normalized to the excitation pulse width (σ_t). Figure 7.8 shows the temporal evolution of the coherence's instantaneous frequencies for five values of $\Gamma_{ij}\sigma_t$ ranging from no dephasing to infinitely fast dephasing while the excitation frequency is slightly detuned from the coherence frequency, $\left(\omega - \omega_{ij}\right)/\sigma_\omega = 0.1$. The color bar depicts the instantaneous frequency difference from the free induction decay frequency. If there is no dephasing, the frequency at the earliest stage is that of the excitation source but the frequency changes to the free induction decay frequency after the pulse is over. If the dephasing is infinitely fast, the coherence remains at the excitation frequency and vanishes after the pulse. Figure 7.9 shows the dependence of the coherence frequency evolution on the detuning of the excitation frequency relative to the excitation pulse spectral width, $\left(\omega - \omega_{ij}\right)/\sigma_\omega$, with $\Gamma_{ij}\sigma_t = 1$. When the excitation frequency is

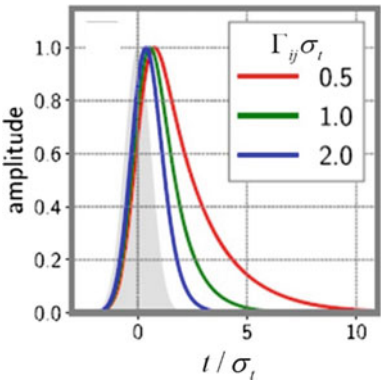

Fig. 7.7 Output pulse shape dependence on the relative temporal width of a Gaussian excitation pulse and the sample dephasing rate. Reprinted from [59], with the permission of AIP Publishing

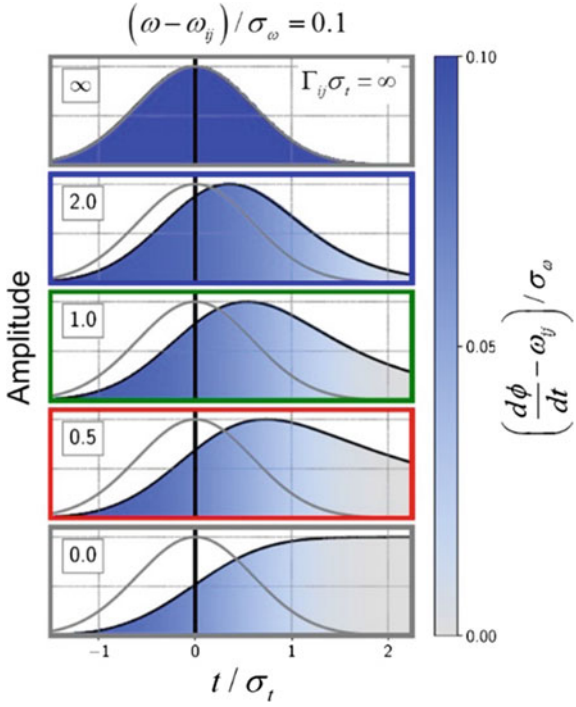

Fig. 7.8 Dependence of the instantaneous frequency of a coherence on the relative pulse width and dephasing rate for a small detuning from resonance. The gray Gaussian defines the excitation pulse. Reprinted from [59] with permission of AIP Publishing

resonant with ω_{ij}, the instantaneous frequency is unchanged throughout the evolution of the coherence but when it is detuned, the frequency changes from driven at early times to free induction decay at later times. These changes have effects on the line shapes of spectral features that depend on the relative time ordering of the excitation pulses.

Figure 7.10 shows the effects of the relative detuning on the line shapes and instantaneous frequencies for the $\rho_{gg} \overset{1}{\rightarrow} \rho_{ig} \overset{-2,2'}{\rightarrow} \rho_{ig}'$ pathway and $\vec{k}_4 = \vec{k}_1 - \vec{k}_2 + \vec{k}_{2'}$

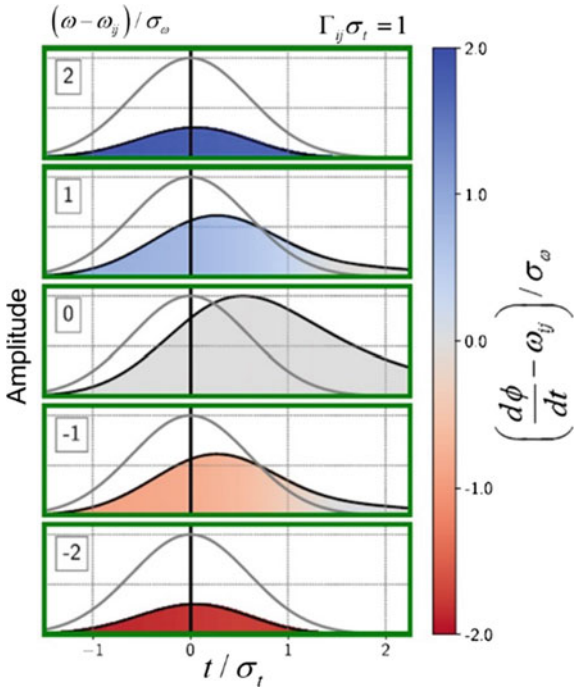

Fig. 7.9 Dependence of the instantaneous frequency on the detuning/pulse width ratio for $\Gamma_{ij}\sigma_t = 1$. Reprinted from [59] with permission of AIP Publishing

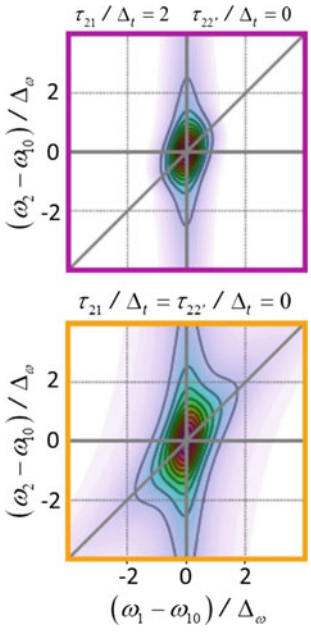

Fig. 7.10 Line shape changes when pulses 2 and 2' arrive after 1 versus when they are all temporally overlapped. Reprinted from [59] with permission of AIP Publishing

phase matching. If the-2 and 2' pulses arrive much after pulse 1, the 2D spectral shape depends independently on ω_1 and ω_2 because free induction decay determines the frequency of the first coherence, ρ_{ig}. However, if the pulses are temporally overlapped, the 2D spectral shape depends on $\omega_1 - \omega_2$ because the frequency of the ρ'_{ig} coherence is driven by both frequencies. Even though these spectra are measuring the properties of the same transition, the line-shapes are very different and could be misinterpreted. For example, the diagonal character of the lower spectrum could be attributed to the narrowing of inhomogeneous broadening which also appears as a diagonal feature. A more thorough discussion of these effects appears in Kohler et al [59]. The important message is realizing that when the temporal pulse width and dephasing time are comparable, the spectra should be simulated by including the effects of a finite pulse to avoid misinterpretations.

7.6 The Multiplicity of CMDS Coherence Pathways

Just as NMR consists of a family of different methods, CMDS also has a family. The family of CMDS methods is defined by the time ordering, phase matching, number of excitation pulses, and the nature of the excited quantum states. Each has special characteristics and capabilities. Figure 7.11 shows examples of pathways involving different combinations of vibrational and electronic states. We point out three important factors that distinguish particular pathways.

1. The involvement of an electronic state resonantly enhances the output signal, but it also translates the measurement into the visible or ultraviolet region where there are excellent detectors. The electronic state can also be non-resonant or

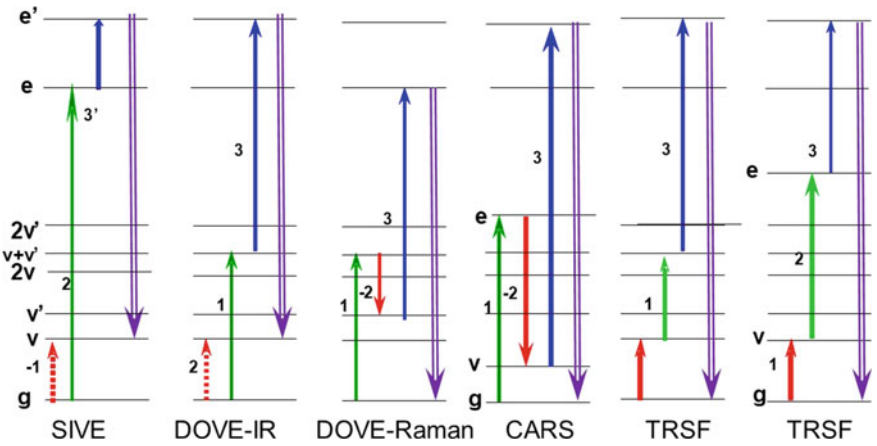

Fig. 7.11 Different examples of fully coherent CMDS pathway

virtual where many electronic states contribute enhancement rather than just the state closest to resonance.

2. The pathways where the final transition returns the system to its initial state are parametric pathways and do not impart energy to the sample. The pathways that terminate at a different state are non-parametric and do impart energy to the sample. The sample finishes in an excited state. For example, the DOVE-IR pathway in Fig. 7.11 is nonparametric while the CARS pathway is parametric.
3. The relative phases of the coherences in a pathway are also very important, especially how well the pathways can resolve inhomogeneous broadening. Each coherence has a phase factor that controls the response to inhomogeneous broadening. For example, the gv and $v'g$ coherences in the pathway $gg \rightarrow gv \rightarrow v + v'$, $g \rightarrow v'g$ evolve as $e^{-i\omega_{vg}t}$ and $e^{i\omega_{v'g}t}$, respectively. Inhomogeneous broadening creates a distribution of ω_{vg} and $\omega_{v'g}$ values so the coherence phase angles diverse in time and the signal disappears. However, if the inhomogeneous broadening results in correlated changes in ω_{vg} and $\omega_{v'g}$, the phase evolution during the gv coherence time evolution can be reversed by the phase evolution of the gv' coherence since the phase of the final coherence depends on $e^{-i\omega_{vg}t_1}\ e^{i\omega_{v'g}t_3}$. The rephasing results in a second enhancement called an echo [60–62].

7.7 CMDS Spectroscopy of Complex Systems

The greatest promise for wide-spread CMDS applications is probing complex systems where there are many components, each with their own quantum states. Spectral congestion dominates in these systems and the ability to resolve individual components is compromised [12]. There are a number of characteristics of Schrodinger cat states that make them ideal for studying complex materials. When they collapse and emit a photon, the initial and final states of the transition must be coupled. When the collapse occurs, all of the information about the resonances that formed those states is encoded in the output. The collapse also insures that the information is not perturbed by relaxation processes because any relaxation collapses the cat state before emission occurs. The output is therefore an instantaneous probe of the quantum states. Coherent transfer is the one exception [41–43, 63]. Coherent transfer occurs when fluctuations of the environment cause a transition between states without perturbing the phase of the cat state. Coherent transfer is normally ignored in the secular approximation where a Markovian thermal bath is assumed to have no memory of its earlier frequency fluctuation [64–66]. Coherent transfer is therefore a direct probe of the nature of the thermal bath.

Cobalamin is a model system for demonstrating the capabilities of Schrodinger cat state spectroscopies in complex materials. Cobalamin is a cofactor for many enzymatic reactions [67–69]. The vitamin B_{12} structure is shown in Fig. 7.12. The cobalt ion is ligated by a corrin ring with a CN upper axial ligand. In the active

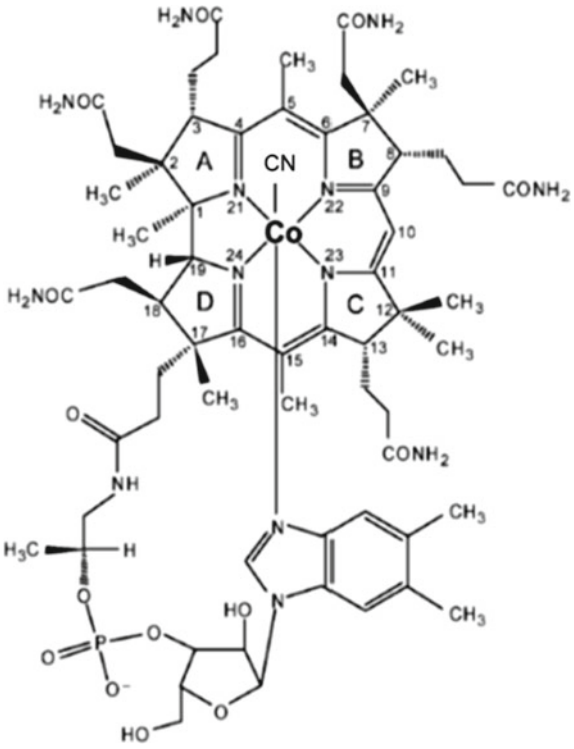

Fig. 7.12 Molecular structure of cyano-cobalamin (vitamin B12)

form, the CN upper axial ligand is replaced by a methyl or adenosine (Ado). The lower axial ligand is dimethylbenzimidazole (DMB). The active form inserts inside the barrel structure of an enzyme with the upper ligand facing outwards. When a substrate such as ethanol amine enters the barrel, the rate constant for Co-C bond scission increases by 12 orders of magnitude [67, 70–74]. The CN radical leaves and reacts with the substrate and then returns. There is great interest in understanding the mechanism by which the substrate causes such an enhancement in the rate of bond scission. The reaction coordinates for this mechanism must involve physical changes in the cobalamin structure which in turn cause changes in the electronic states controlling bond strength [75]. Since physical changes in structure involve vibrational coordinates, the reaction coordinates can be identified by mapping the vibrational and electronic states that are coupled. The formation of Schrodinger cat states therefore provides a strategy for identifying the reaction coordinates.

Figure 7.13 summarizes the first multidimensional spectroscopy of cobalamin [36]. The TRSF pathway used to obtain this spectrum appears on the right. The Schrodinger cat state is formed by three successive excitations to a fundamental vibrational mode ($g \xrightarrow{1} v$), an overtone or combination state ($v \xrightarrow{2} v + v'$), and an electronic or vibronic state ($v + v' \xrightarrow{3} e$). The e and g states are in a coherent superpo-

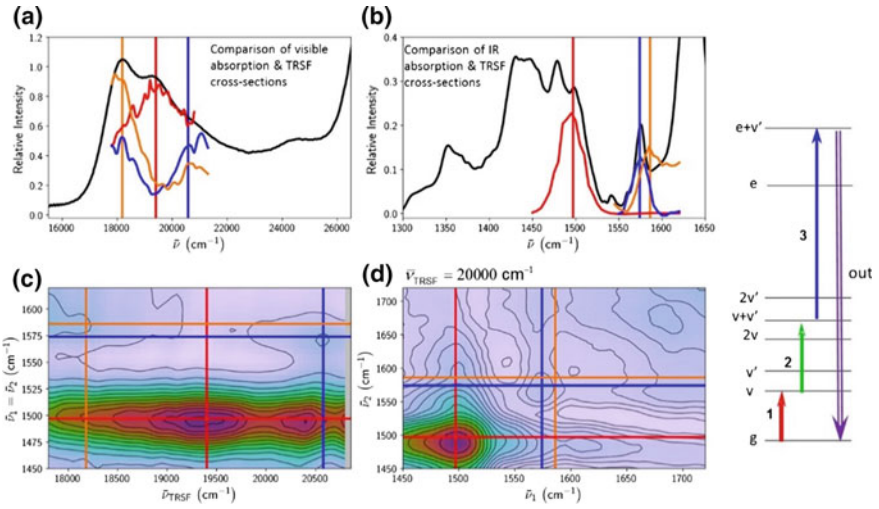

Fig. 7.13 The visible and IR absorption spectra appear in **a** and **b**, respectively (balck traces). **c** shows the CMDS spectrum where x is the electronic frequency and y is the IR frequencies. **b** shows the 2D IR spectrum when the electronic excitation is 30,000 cm^{-1}. The colored lines correlate with those in **a** and **b** to show the corresponding frequencies. The WMEL diagram defines the nature of the transitions involved in the spectra. Adapted from [36]. Copyright 2018 American Chemical Society

sition and oscillate at their difference frequency, ω_{eg}, if the driving fields are absent (i.e. free induction decay). If the fields are driving the coherences, the output occurs at $\omega_1 + \omega_2 + \omega_3$. The coherence launches the directional output beam that is measured. The experimental variables are the frequencies of the three excitation pulses, their relative time delay, and the frequency of the output. The data set results from a series of spectral scans where some frequencies are fixed while the others were scanned. By systematically repeating these spectral scans at different fixed frequencies, an entire data set can be acquired with all the excitation frequencies and the corresponding output intensities.

The spectra in the figure are cross-sections through this data set with the colors defining the amplitude (i.e. square root of the intensity) of the output beam. In Fig. 7.13c, the ω_1 and ω_2 frequencies were both scanned together so $\omega_1 = \omega_2$ while the ω_3 frequency was scanned so the output always remained at $\omega_{\text{TRSF}} = \omega_1 + \omega_2 + \omega_3$, the frequency of the electronic states. Thus, the x-axis shows the electronic frequencies and the y-axis shows the vibrational frequencies. In this case, the second interaction creates an overtone state. Any anharmonicity is obscured with this scanning strategy because of the frequency differences.

Figure 7.13d scans the ω_1 (x-axis) and ω_2 (y-axis) infrared frequencies but it also scans ω_3 such that $\omega_{\text{TRSF}} = \omega_1 + \omega_2 + \omega_3 = 20{,}000\ \text{cm}^{-1}$. This strategy identifies the vibrational states that are coupled to electronic states at 20,000 cm^{-1}. Diagonal peaks correspond to overtones formed after the second interaction and the departures from the diagonal define the anharmonicity. Cross peaks correspond to combination bands

where different modes are coupled by anharmonicity. The vertical and diagonal lines denote three different vibrational frequencies at 1497, 1572, and 1585 cm^{-1}. Note that the spectrum does not contain a feature at 1585 cm^{-1}. The Fig. 7.13c spectrum shows that 20,000 cm^{-1} is a frequency that is not resonant with any vibrational mode. There is enough resonance enhancement to reveal the 1497 and 1572 cm^{-1} features in Fig. 7.13d but not enough to see the 1585 cm^{-1} feature. The Fig. 7.13c spectrum also shows that the 1497 cm^{-1} mode is resonantly enhanced at 19,400 cm^{-1}, the 1572 cm^{-1} modes is resonantly enhanced at 20,520 cm^{-1}, and the 1585 cm^{-1} mode is resonantly enhanced at 18170 cm^{-1}.

The top set of spectra compare the 2D spectra in Fig. 7.13c, d with the visible and infrared absorption spectra shown in black in Fig. 7.13a, b. The vertical lines in Fig. 7.13a correspond to the same vertical lines in Fig. 7.13c. The curves with the same color in Fig. 7.13a are cross-sections of Fig. 7.13c along the horizontal lines of the same color. They show that each of the vibrational modes are resonantly enhanced at different parts of the absorption because they are coupled to specific states within the absorption spectrum. The same ideas apply in comparing the infrared absorption spectrum with slices in the 2D TRSF spectra. The vertical lines in Fig. 7.13b correspond to the same vertical lines in Fig. 7.13c, d. The colored curves in Fig. 7.13b correspond with vertical cross-sections along the same colored lines in Fig. 7.13c. In each case, the cross-sections in the multidimensional TRSF spectra dissect the electronic and vibrational states lying within the broad spectra. The dissection is based upon the fundamental nature of the Schrodinger cat state requiring coupled states.

7.8 The Future of CMDS Schrodinger Cat State Spectroscopy

The work described above is very much in its infancy. The reaction coordinates for cobalamin bond scission are undoubtedly complicated and revealing them requires a more extensive exploration of the vibrational and electronic state coupling. Low frequency Co-C stretch and other wagging and torsional modes are likely to be part of the reaction surface. The TRSF pathway described above is a powerful way to excite the higher frequency modes but application to lower frequency modes is more challenging. The DOVE and CARS pathways provide alternatives to excitation of low frequency modes because they form the combination bands used in DOVE pathways and they can be accessed by the Raman transitions accessed in CARS. Both DOVE and CARS access the electronic states. The reaction coordinates must involve potential energy surfaces that have strong anharmonicities because they result in bond scission. As a result, the coupling between the states must also be strong. These ideas motivate a comprehensive exploration of the coupling between states throughout the infrared, visible, and ultraviolet regions.

In addition to defining the reaction coordinates, it may also be possible to determine the potential energy surface for the reaction coordinates. We have shown that an increased fluence raises the Rabi frequency sufficiently that multiple interactions can occur during a single excitation pulse [52]. It is then feasible to climb vibrational ladders to much higher v quantum numbers where anharmonicities become important. Since multidimensional spectroscopy excites coupled vibrational modes, these ladders can include not only overtones but also the combination bands that make it possible to measure the multidimensional reaction coordinates potential energy surface. Figure 7.14 shows an example of this strategy for a simple rhodium dicarbonyl chelate. The WMEL diagram shows a series of interactions with the asymmetric and symmetric C = O stretch modes energy levels, labeled by a and b, respectively. The first laser at ω_1 is fixed for resonance with the higher energy symmetric mode at 2078 cm^{-1}, ω_2 is scanned across both modes, and the monochromator is scanned across symmetric stretch mode. At low intensities, the spectrum has two peaks, a diagonal peak when both lasers are exciting the same symmetric mode and a cross-peak when they are exciting different modes. At high intensities, 18 additional features

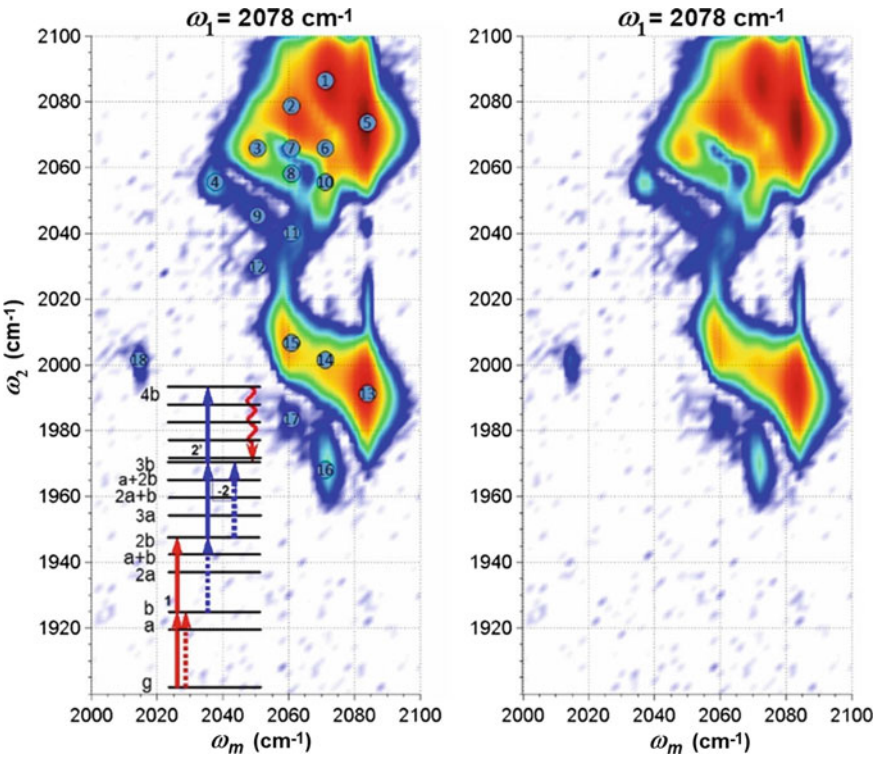

Fig. 7.14 Two dimensional spectrum of a rhodium dicarbonyl chelate at high excitation intensities. The numbered positions correspond to particular higher order pathways. The one sketched corresponds to feature 3

emerge. Each corresponds to a number of different interactions with the excitation fields. For example, the peak labeled 3 is created by the 4b, 3b overtone coherence using the pathway shown in the left corner. The other peaks correspond to other coherences involving different combinations of the a and b modes. The figure provides the anharmonicities for the overtones and combination bands up to $v = 6$. Fitting of the anharmonicity values using a Morse potential then provides an accurate model of the potential energy surface [53]. Widespread implementation of this strategy would provide the most fundamental information about reaction mechanisms.

There is great potential for applications of these fully coherent CMDS methods throughout the fields of chemistry and biochemistry. Since spectroscopy is used extensively throughout all fields of science and technology, CMDS methods are likely to become a dominant tool for spectroscopy of the complex materials that will be important in our global future. There are certain barriers currently preventing its widespread applications [1, 2, 76]. First, the field of CMDS needs to expand the range of the problems that it tackles, especially in areas beyond physical chemistry. Currently, the field focuses on dynamics, which are certainly important, but most spectroscopy in science and technology involves wide spectral ranges far beyond those common in the field today. Second, the field needs industrial partners to simplify the technology and reduce costs. These are challenges that can be solved but it requires a vision and commitment from scientists and society.

Acknowledgements This work was supported by the Division of Chemistry at the National Science Foundation under grant CHE-1709060. The author acknowledges with great appreciation the contributions and insights from his many graduate and postgraduate students who have worked on different aspects of this project over the last 40 years. Without them, this project would have collapsed long ago.

References

1. J.C. Wright, Analytical chemistry, multidimensional spectral signatures, and the future of coherent multidimensional spectroscopy. Chem. Phys. Lett. **662**, 1–13 (2016)
2. J.C. Wright, Applications of the new family of coherent multidimensional spectroscopies for analytical chemistry. Annu. Rev. Anal. Chem. **10**, 45–70 (2017)
3. J.C. Wright, Multiresonant coherent multidimensional spectroscopy (ed. by S.R. Leone, P.S. Cremer, J.T. Groves, M.A. Johnson) Ann. Rev. Phys. Chem. **62**, 209–230 (2011)
4. J.C. Wright, Coherent multidimensional vibrational spectroscopy. Int. Rev. Phys. Chem. **21**, 185–255 (2002)
5. J.C. Wright, R.J. Carlson, G.B. Hurst, J.K. Steehler, M.T. Riebe, B.B. Price, D.C. Nguyen, S.H. Lee, Molecular, multiresonant coherent four wave mixing spectroscopy. Int. Rev. Phys. Chem. **10**, 349–390 (1991)
6. D.M. Jonas, Two-dimensional femtosecond spectroscopy. Annu. Rev. Phys. Chem. **54**, 425–463 (2003)
7. M. Cho, *Two Dimensional Optical Spectroscopy*, 1st edn. (CRC Press, Boca Raton, 2009)
8. M. Cho, Coherent two-dimensional optical spectroscopy. Chem. Rev. **108**, 1331–1418 (2008)
9. M. Cho, Two dimensional vibrational spectroscopy, in *Advances in Multi-Photon Processes and Spectroscopy*, S.H. Lin, A.A. Villaeys, Y. Fujimura, vol. 12, 1st edn. (World Scientific, Singapore, 1999), pp 1–72

10. S. Mukamel, Multidimensional femtosecond correlation spectroscopies of electronic and vibrational excitations. Annu. Rev. Phys. Chem. **51**, 691–729 (2000)
11. S. Mukamel, *Principles of Nonlinear Optical Spectroscopy*, 1st edn. (Oxford University Press, New York, 1995)
12. W. Zhao, J.C. Wright, Spectral simplification in vibrational spectroscopy using doubly resonant infrared four wave mixing. J. Am. Chem. Soc. **121**, 10994–10998 (1999)
13. W. Zhao, J.C. Wright, Measurement of chi(3) for doubly vibrationally enhanced four wave mixing spectroscopy. Phys. Rev. Lett. **83**, 1950–1953 (1999)
14. R.J. Carlson, J.C. Wright, Enhanced selectivity by mode selection with four wave mixing. Anal. Chem. **63**, 1449–1451 (1991)
15. R.J. Carlson, J.C. Wright, Analysis of vibrational correlations and couplings in the lowest two singlet states of pentacene by fully resonant four wave mixing. J. Chem. Phys. **92**, 5186–5195 (1990)
16. A.V. Pakoulev, M.A. Rickard, K.A. Meyers, K. Kornau, N.A. Mathew, D.C. Thompson, J.C. Wright, Mixed frequency/time domain optical analogues of heteronuclear multidimensional NMR. J. Phys. Chem. A **110**, 3352–3355 (2006)
17. T. Brixner, J. Stenger, H.M. Vaswani, M. Cho, R.E. Blankenship, G.R. Fleming, Two-dimensional spectroscopy of electronic couplings in photosynthesis. Nature **434**, 625–628 (2005)
18. M.H. Cho, T. Brixner, I. Stiopkin, H. Vaswani, G.R. Fleming, Two dimensional electronic spectroscopy of molecular complexes. J. Chin. Chem. Soc. **53**, 15–24 (2006)
19. D.V. Kurochkin, S.R.G. Naraharisetty, I.V. Rubtsov, Dual-frequency 2D IR on interaction of weak and strong IR modes. J. Phys. Chem. A **109**, 10799–10802 (2005)
20. I.V. Rubtsov, J.P. Wang, R.M. Hochstrasser, Dual-frequency 2D-IR spectroscopy heterodyned photon echo of the peptide bond. Proc. Natl. Acad. Sci. USA **100**, 5601–5606 (2003)
21. I.V. Rubtsov, J. Wang, R.M. Hochstrasser, Dual frequency 2D-IR of peptide amide-A and amide-I modes. J. Chem. Phys. **118**, 7733–7736 (2003)
22. N.H.C. Lewis, G.R. Fleming, Two-dimensional electronic-vibrational spectroscopy of chlorophyll a and b. J. Phys. Chem. Lett. **7**, 831–837 (2016)
23. E. Harel, A.F. Fidler, G.S. Engel, Real-time mapping of electronic structure with single-shot two-dimensional electronic spectroscopy. Proc. Natl. Acad. Sci. USA **107**, 16444–16447 (2010)
24. S.H. Lee, J.K. Steehler, D.C. Nguyen, J.C. Wright, Site selective nonlinear four wave mixing by MENS and MEPS. Appl. Spectrosc. **39**, 243–253 (1985)
25. J.K. Steehler, J.C. Wright, Parametric and non-parametric four wave mixing in pentacene:p-terphenyl. J. Chem. Phys. **83**, 3200–3208 (1985)
26. M.T. Riebe, J.C. Wright, Nonlinear line narrowing spectroscopy in mixed organic crystals. Chem. Phys. Lett. **138**, 565–570 (1987)
27. M.T. Riebe, J.C. Wright, Spectral line narrowing and saturation effects in fully resonant non-degenerate four wave mixing. J. Chem. Phys. **88**, 2981–2994 (1988)
28. R.J. Carlson, D.C. Nguyen, J.C. Wright, Analysis of vibronic mode coupling in pentacene by fully resonant four wave mixing. J. Chem. Phys. **92**, 1538–1546 (1990)
29. W. Zhao, J.C. Wright, Doubly vibrationally enhanced four wave mixing spectroscopy- the optical analogue to 2D NMR. Phys. Rev. Lett. **84**, 1411–1414 (2000)
30. A.V. Pakoulev, M.A. Rickard, K.M. Kornau, N.A. Mathew, L.A. Yurs, S.B. Block, J.C. Wright, Mixed Frequency-/time-domain coherent multidimensional spectroscopy: research tool or potential analytical method? Acc. Chem. Res. **42**, 1310–1321 (2009)
31. L.A. Yurs, S.B. Block, A.V. Pakoulev, R.S. Selinsky, S. Jin, J.C. Wright, Multiresonant coherent multidimensional electronic spectroscopy of colloidal PbSe quantum dots. J. Phys. Chem. C **115**, 22833–22844 (2011)
32. K.J. Czech, B.J. Thompson, S. Kain, Q. Ding, M.J. Shearer, R.J. Hamers, S. Jin, J.C. Wright, Measurement of ultrafast excitonic dynamics of few-layer MoS2 using state-selective coherent multidimensional spectroscopy. ACS Nano **9**, 12146–12157 (2015)
33. E. Schrodinger, The current situation in quantum mechanics. Naturwissenschaften **23**, 807–812 (1935)

34. R. Horodecki, P. Horodecki, M. Horodecki, K. Horodecki, Quantum entanglement. Rev. Mod. Phys. **81**, 865–942 (2009)
35. Y. Shih, Entangled biphoton source-property and preparation. Rep. Prog. Phys. **66**, 1009–1044 (2003)
36. J.D. Handali, K.F. Sunden, B.J. Thompson, N.A. Neff-Mallon, E.M. Kaufman, T.C. Brunold, J.C. Wright, Three dimensional triply resonant sum frequency spectroscopy revealing vibronic coupling in cobalamins: toward a probe of reaction coordinates. J. Phys. Chem. A **122**, 9031–9042 (2018)
37. D. Lee, A.C. Albrecht, *Advances in Infrared and Raman Spectroscopy*, vol. 12, 1st edn. (Wiley-Heyden, Chichester, 1985)
38. S.T. Roberts, J.J. Loparo, A. Tokmakoff, Characterization of spectral diffusion from two-dimensional line shapes. J. Chem. Phys. **125**, 8 (2006)
39. N.I. Rubtsova, I.V. Rubtsov, Vibrational energy transport in molecules studied by relaxation-assisted two-dimensional infrared spectroscopy. Annu. Rev. Phys. Chem. **66**, 717–738 (2015)
40. D.V. Kurochkin, S.R.G. Naraharisetty, I.V. Rubtsov, A relaxation-assisted 2D IR spectroscopy method. Proc. Natl. Acad. Sci. USA **104**, 14209–14214 (2007)
41. A.V. Pakoulev, M.A. Rickard, N.A. Mathew, K.M. Kornau, J.C. Wright, Frequency-domain time-resolved four wave mixing spectroscopy of vibrational coherence transfer with single-color excitation. J. Phys. Chem. A **112**, 6320–6329 (2008)
42. M.A. Rickard, A.V. Pakoulev, N.A. Mathew, K.M. Kornau, J.C. Wright, Frequency- and time-resolved coherence transfer spectroscopy. J. Phys. Chem. A **111**, 1163–1166 (2007)
43. M.A. Rickard, A.V. Pakoulev, K. Kornau, N.A. Mathew, J.C. Wright, Interferometric coherence transfer modulations in triply vibrationally enhanced four-wave mixing. J. Phys. Chem. A **110**, 11384–11387 (2006)
44. G.S. Engel, T.R. Calhoun, E.L. Read, T.K. Ahn, T. Mancal, Y.C. Cheng, R.E. Blankenship, G.R. Fleming, Evidence for wavelike energy transfer through quantum coherence in photosynthetic systems. Nature **446**, 782–786 (2007)
45. E. Harel, G.S. Engel, Quantum coherence spectroscopy reveals complex dynamics in bacterial light-harvesting complex 2 (LH2). Proc. Natl. Acad. Sci. USA **109**, 706–711 (2012)
46. A.W. Chin, J. Prior, R. Rosenbach, F. Caycedo-Soler, S.F. Huelga, M.B. Plenio, The role of non-equilibrium vibrational structures in electronic coherence and recoherence in pigment–protein complexes. Nat. Phys. **9**, 113–118 (2013)
47. N. Christensson, H.F. Kauffmann, T. Pullerits, T. Mancal, Origin of long-lived coherences in light-harvesting complexes. J. Phys. Chem. B **116**, 7449–7454 (2012)
48. K. Kwak, S. Cha, M.H. Cho, J.C. Wright, Vibrational interactions of acetonitrile: Doubly vibrationally resonant IR-IR-visible four-wave-mixing spectroscopy. J. Chem. Phys. **117**, 5675–5687 (2002)
49. M. Spexard, D. Immeln, C. Thöing, T. Kottke, Infrared spectrum and absorption coefficient of the cofactor flavin in water. Vib. Spectrosc. **57**, 282–287 (2011)
50. K.M. Murdoch, N.J. Condon, W. Zhao, D.M. Besemann, K.A. Meyer, J.C. Wright, Isotope and mode selectivity in two dimensional vibrational four wave mixing spectroscopy. Chem. Phys. Lett. **335**, 349 (2001)
51. N.A. Mathew, S.B. Block, L.A. Yurs, K.M. Kornau, A.V. Pakoulev, J.C. Wright, Multiply enhanced odd-order wave mixing spectroscopy. J. Phys. Chem. A **113**, 13562–13569 (2009)
52. N.A. Mathew, L.A. Yurs, S.B. Block, A.V. Pakoulev, K.M. Kornau, J.C. Wright, Multiple quantum coherence spectroscopy. J. Phys. Chem. A **113**, 9261–9265 (2009)
53. N.A. Mathew, L.A. Yurs, S.B. Block, A.V. Pakoulev, K.M. Kornau, E.L. Sibert, J.C. Wright, Fully and partially coherent pathways in multiply enhanced odd-order wave-mixing spectroscopy. J. Phys. Chem. A **114**, 817–832 (2010)
54. S. Kain, Transition of frequency domain coherent multidimensional spectroscopy to the femtosecond time regime with application to nanoscale semiconductors. University of Wisconsin-Madison (2018)
55. P.C. Chen, High resolution coherent 2D spectroscopy. J. Phys. Chem. A **114**, 11365–11375 (2010)

56. B.R. Strangfeld, T.A. Wells, P.C. Chen, Rotational and vibrational pattern interpretation for high-resolution coherent 3D spectroscopy. J. Phys. Chem. A **118**, 6846–6857 (2014)
57. T.A. Wells, A.K. Muthike, J.E. Robinson, P.C. Chen, High resolution coherent three dimensional spectroscopy of NO2. J. Chem. Phys. **142**, 11 (2015)
58. S. Backus, C.G. Durfee, M.M. Murnane, H.C. Kapteyn, High power ultrafast lasers. Rev. Sci. Instrum. **69**, 1207–1223 (1998)
59. D.D. Kohler, B.J. Thompson, J.C. Wright, Frequency-domain coherent multidimensional spectroscopy when dephasing rivals pulsewidth: disentangling material and instrument response. J. Chem. Phys. **147**, 17 (2017)
60. C.A. Walsh, M. Berg, L.R. Narasimhan, M.D. Fayer, Optical dephasing of chromophores in an organic glass - picosecond photon-echo and hole burning experiments. Chem. Phys. Lett. **130**, 6–11 (1986)
61. T.J. Aartsma, D.A. Wiersma, Photon-echo spectroscopy of organic mixed crystals. Phys. Rev. Lett. **36**, 1360–1362 (1976)
62. R.G. Brewer, R.L. Shoemaker, Photon echo and optical nutation in molecules. Phys. Rev. Lett. **27**, 631–634 (1971)
63. M. Khalil, N. Demirdoven, A. Tokmakoff, Vibrational coherence transfer characterized with Fourier-transform 2D IR spectroscopy. J. Chem. Phys. **121**, 362–373 (2004)
64. Dijkstra, A. G.; Tanimura, Y. Non-Markovian Entanglement Dynamics in the Presence of System-Bath Coherence. *Phys Rev Lett* **2010**, *104*
65. P. Rebentrost, R. Chakraborty, A. Aspuru-Guzik, Non-Markovian quantum jumps in excitonic energy transfer. J. Chem. Phys. **131**, 184102 (2009)
66. A. Ishizaki, Y. Tanimura, Nonperturbative non-Markovian quantum master equation: validity and limitation to calculate nonlinear response functions. Chem. Phys. **347**, 185–193 (2008)
67. N. Shibata, H. Tamagaki, N. Hieda, K. Akita, H. Komori, Y. Shomura, S. Terawaki, K. Mori, N. Yasuoka, Y. Higuchi, T. Toraya, Crystal structures of ethanolamine ammonia-lyase complexed with coenzyme B-12 analogs and substrates. J. Biol. Chem. **285**, 26484–26493 (2010)
68. M. Fukuoka, Y. Nakanishi, R.B. Hannak, B. Krautler, T. Toraya, Homoadenosylcobalamins as probes for exploring the active sites of coenzyme B12-dependent diol dehydratase and ethanolamine ammonia-lyase. FEBS J. **272**, 4787–4796 (2005)
69. P.M. Kozlowski, T. Kamachi, M. Kumar, T. Nakayama, K. Yoshizawa, Theoretical analysis of the diradical nature of adenosylcobalamin cofactor-tyrosine complex in B-12-dependent mutases: inspiring PCET-driven enzymatic catalysis. J. Phys. Chem. B **114**, 5928–5939 (2010)
70. E.N.G. Marsh, G.D.R. Meléndez, Adenosylcobalamin enzymes: theory and experiment begin to converge. Biochim. Biophys. Acta **1824**, 1154–1164 (2012)
71. E.N.G. Marsh, D.P. Patterson, L. Li, Adenosyl radical: reagent and catalyst in enzyme reactions. ChemBioChem **11**, 604–621 (2010)
72. R.J. Sension, D.A. Harris, A. Stickrath, A.G. Cole, C.C. Fox, E.N.G. March, Time-resolved measurements of the photolysis and recombination of adenosylcobalamin bound to glutamate mutase. J. Phys. Chem. B **109**, 18146–18152 (2005)
73. N. Shibata, J. Masuda, Y. Morimoto, N. Yasuoka, T. Toraya, Substrate-induced conformational change of a coenzyme B12-dependent enzyme-crystal structure of the substrate-free form of diol dehydratase. Biochem.-Us **41**, 12607–12617 (2001)
74. T.A. Stich, A.J. Brooks, N.R. Buan, T.C. Brunold, Spectroscopic and computational studies of Co3 + -corrinoids: spectral and electronic properties of the B-12 cofactors and biologically relevant precursors. J. Am. Chem. Soc. **125**, 5897–5914 (2003)
75. B.D. Garabato, P. Lodowski, M. Jaworska, P.M. Kozlowski, Mechanism of Co-C photodissociation in adenosylcobalamin. Phys. Chem. Chem. Phys. **18**, 19070–19082 (2016)
76. J. C. Wright, Fundamental studies of relationships between experimental nonlinear coherent vibrational spectroscopies. J. Phys. Chem. Lett. **10**, 2767–2774 (2019)

Chapter 8
Noncovalent Interactions of Hydrated DNA and RNA Mapped by 2D-IR Spectroscopy

Benjamin P. Fingerhut and Thomas Elsaesser

Abstract Biomolecules couple to their aqueous environment through a variety of noncovalent interactions. Local structures at the surface of DNA and RNA are frequently determined by hydrogen bonds with water molecules, complemented by non-specific electrostatic and many-body interactions. Structural fluctuations of the water shell result in fluctuating Coulomb forces on polar and/or ionic groups of the biomolecular structure and in a breaking and reformation of hydrogen bonds. Two-dimensional infrared (2D-IR) spectroscopy of vibrational modes of DNA and RNA gives insight into local hydration geometries, elementary molecular dynamics, and the mechanisms behind them. In this chapter, recent results from 2D-IR spectroscopy of native and artificial DNA and RNA are presented, together with theoretical calculations of molecular couplings and molecular dynamics simulations. Backbone vibrations of DNA and RNA are established as sensitive noninvasive probes of the complex behavior of hydrated helices. The results reveal the femtosecond fluctuation dynamics of the water shell, the short-range character of Coulomb interactions, and the strength and fluctuation amplitudes of interfacial electric fields.

8.1 Vibrational Probes of Interactions and Dynamics in Aqueous Systems

Liquid water represents the medium in which most biological processes occur. The structure of bulk water at ambient temperature, its structural fluctuations, and their impact on chemical and biological processes have been the subject of extensive experimental and theoretical research over the last decades. On the experimental side, vibrational spectroscopy with a femtosecond time resolution has played a key role in identifying and separating the different contributions to water dynamics in

B. P. Fingerhut · T. Elsaesser (✉)
Max-Born-Institute, 2a Max-Born-St., 12489 Berlin, Germany
e-mail: elsasser@mbi-berlin.de

B. P. Fingerhut
e-mail: fingerhut@mbi-berlin.de

M. Cho (ed.), *Coherent Multidimensional Spectroscopy*,
Springer Series in Optical Sciences 226,
https://doi.org/10.1007/978-981-13-9753-0_8

the electronic ground state of the bulk liquid. In most experiments, excitations of the OH stretching and, to lesser extent, OH bending vibration of the water molecule have served for probing structure fluctuations, intermolecular energy exchange, as well as hydrogen bond breaking and reformation. Two-dimensional infrared (2D-IR) spectroscopy has allowed for extracting frequency fluctuation correlation functions (FFCFs) of the liquid, in which the different types of molecular dynamics give rise to different decay components. Moreover, vibrational relaxation processes and energy dissipation in the liquid have been studied both for intra- and intermolecular water modes, including the transient librational response. Theoretical calculations and molecular dynamics simulations have addressed the relevant molecular interactions and driving forces behind the different processes. In the present context, we briefly summarize a few key aspects of the dynamics of bulk H_2O, more detailed information can be found in recent review articles [1–3].

Water molecules in bulk H_2O form, on the average, four hydrogen bonds (H bonds), two in which the OH groups act as hydrogen donors, and two in which the oxygen atom serves as hydrogen acceptor. At ambient temperature, molecular degrees of freedom in a wide frequency range below the intramolecular OH bending and stretching modes are thermally excited, leading to stochastic motions of water molecules on a multitude of time scales. Such structural fluctuations give rise to fluctuating electric fields which originate from the dipolar character of the water molecule with a liquid-phase electric dipole moment of approximately 2.9 Debye [4]. The fastest fluctuations occur in the sub-100 fs time domain and are connected with librational motions essentially localized on individual water molecules. Slower sub-picosecond structure changes are due to delocalized librational degrees of freedom as well as hydrogen bond stretching and bending motions. The lifetime of hydrogen bonds is on the order of 1 ps, resulting in a rapid change of the extended hydrogen bond network in the liquid. According to the so-called jump model, the breaking and reformation of H bonds is connected with a jump-like angular reorientation of water molecules induced by fluctuations in the fourfold coordination of water molecules [5]. The rotational reorientation time of water molecules has a value of approximately 2.5 ps. All such processes result in a decay of structural correlations between water molecules.

The intramolecular OH stretching and bending modes of H_2O display lifetimes of some 200 fs. For OH stretching excitations, intermolecular excitation transfer between neighboring water molecules has been observed on a time scale of 100 fs. The dissipation of vibrational excess energy involves a transfer from the intramolecular vibrations to librations of a sub-100 fs lifetime and a subsequent redistribution among low-frequency degrees of freedom. As a result, a quasi-thermal ground state characterized by a vibrational excess temperature is formed within 1–2 ps [6].

A biomolecule embedded in water introduces both steric boundary conditions and specific interaction sites for water molecules in the first and second layer of the hydration shell. Vice versa, the degree of hydration has a marked impact on the structure of biomolecules, e.g., on the particular double-helical form of DNA [7]. Recent years have witnessed a change in perception of these first few water layers, from a passive bystander to an active player in determining structural stability and

dynamics of biological entities. Equilibrium geometries of DNA and RNA have extensively been studied by x-ray diffraction and positions of water oxygens and counterions, typically for crystallized samples at a limited hydration level, have been identified [8–11]. In DNA and RNA structures, the ionic phosphate groups of the sugar-phosphate backbone represent primary hydration sites at which each of the two free oxygen atoms accepts up to three hydrogen bonds with first-layer water molecules. The sugar OH groups and NH and carbonyl groups of nucleic bases can form hydrogen bonds to water as well. While the first water layer displays a substantial structural heterogeneity, the impact of the biomolecule on the hydration shell structure is limited to a few, typically less than 5 water layers [3]. It should be noted that x-ray diffraction preferentially maps immobilized water molecules at particular interaction sites while mobile waters have remained elusive.

Noncovalent interactions and water dynamics in hydration shells are currently understood only in part. In particular, the dynamics of hydrating water have remained controversial. A dramatic slowing down of structural fluctuations and rotational motions due to a more rigid water structure has been claimed on the basis of solvation studies in which electronic chromophores were attached to or incorporated in biomolecular structures [12–14]. After electronic excitation by an ultrashort optical pulse, the transient red-shift of emission has been followed to derive the FFCF of the aqueous environment. Such FFCFs display kinetic components extending into the nanosecond range and beyond which have been assigned to water dynamics. In contrast, nuclear magnetic resonance, ultrafast infrared studies, and molecular dynamics simulations point to a moderate slowing down of water dynamics in hydration shells by a factor of 3–5 only, with the fastest components well in the femtosecond time domain [15–17]. Obviously, the different experimental methods monitor different aspects of the highly complex dynamic scenario. Moreover, some of the probes are invasive, i.e., they impact solvation geometries and molecular arrangements substantially.

Insight into the spatial extent, dynamic nature and microscopic origins of the coupling of water with the biomolecule provides a basis for a deeper understanding of biomolecular interactions which are governed by the hydration/de-hydration forces at the interface. Functional groups of biomolecules which are located at the interface to the water shell hold particular potential for probing interactions, in particular hydrogen bonding and electrostatic couplings, as well as hydration dynamics. In DNA and RNA, vibrations of the helix backbone represent noninvasive probes which interact with the water shell and embedded counterions [18]. Two-dimensional infrared (2D-IR) spectroscopy [19, 20] with a femtosecond time resolution gives insight into the coupled dynamics of biomolecules and their water shells, into anharmonic couplings and excitation transfer between backbone vibrations, and into energy exchange between the two subsystems [18, 21–23]. This method together with in-depth theory and simulation has successfully been applied to native and artificial DNA and RNA structures and to model systems providing specific information on particular types of interactions [24–26]. In this chapter, we discuss recent results from such research. After a brief introduction in the methods (Sect. 8.2), 2D-IR spectra of artificial DNA and RNA oligomers at different levels of hydration are presented in Sect. 8.3, includ-

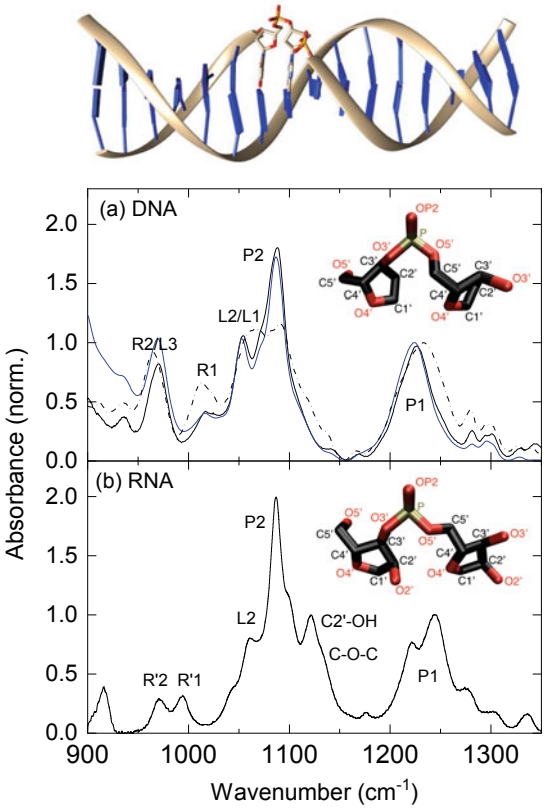

Fig. 8.1 Top panel: Schematic of a B-DNA double helix with two backbone strands (grey) and base pairs (blue). **a** Infrared absorption bands of DNA backbone modes. The absorbance $A = -\log(\mathrm{T})$ (T: sample transmission) is plotted as a function of wavenumber for double-stranded oligomers containing 23 alternating adenine-thymine pairs at a hydration level of 92% relative humidity (r.h., black dash-dotted line) and for full hydration (black solid line). Blue line: absorption spectrum of fully hydrated salmon testes DNA with some 2000 base pairs. The absorbance is normalized to the peak of the asymmetric PO_2^- stretching band P1. The other bands are due to the symmetric PO_2^- vibration P2, the ribose vibrations $R_{1,2}$ and the linker modes $L_{1,2,3}$. Inset: backbone segment of B-DNA. **b** Backbone absorption spectrum of a fully hydrated RNA double stranded helix containing 23 adenine-uracil base pairs. Inset: backbone segment of an A-RNA helix

ing an analysis of 2D lineshapes and the highly complex intermode coupling patterns. Section 8.4 discusses electric fields at the DNA surface, their fluctuations and their spatial range. Conclusions are given in Sect. 8.5, together with an outlook on how to map interactions of DNA and RNA with ions in their environment.

8.2 Experimental and Theoretical Methods

This section gives a short description of sample preparation (Sect. 8.2.1) and the methods of nonlinear vibrational spectroscopy applied in the present study (Sect. 8.2.2). We then describe a hierarchy of theoretical methods that provide an understanding of the noncovalent interactions of biomolecules with their surrounding (Sect. 8.2.3). A summary on the applicability for various system sizes and time scales is given.

8.2.1 Preparation and Linear Infrared Spectra of Hydrated DNA and RNA Samples

Different DNA and RNA structures with different counterions were studied at hydration levels from 0% relative humidity (r.h.) corresponding to two water molecules per base pair up to full hydration with more than 150 water molecules per base pair. Here, we focus on results for double stranded DNA oligomers containing 23 alternating adenine-thymine (A-T) base pairs and native salmon testes DNA which contains approximately 2000 base pairs, among them 41% guanine-cytosine (G-C) and 59% A-T pairs. As a prototypical RNA structure, we use double-stranded oligomers with 23 alternating adenine-uracil (A-U) base pairs in Watson-Crick geometry. Fully hydrated samples were prepared by dissolving the DNA and RNA helices and their Na^+ counterions in water or an 0.1 M aqueous NaCl solution. The concentration of salmon testes DNA was on the order of 10^{-4} M while the concentration of the DNA and RNA oligomers was typically 10^{-2} M. A sample of a 5–10 μm thickness was cast between two BaF_2 or Si_3N_4 windows.

The experiments at reduced hydration level were performed with thin-film DNA and RNA samples, prepared by exchanging the Na^+ counterions against cetyltrimethylammonium (CTMA), applying the procedure reported in [27]. The DNA and RNA concentration in the films was 10^{-2} M. Films of 10–25 μm thickness were prepared on BaF_2 or Si_3N_4 substrates and placed in a humidity cell [28]. This cell was connected to a reservoir containing a saturated aqueous $NaBrO_3$ solution (92% r.h., 20–30 water molecules per base pair) or P_5O_5 powder (0% r.h.). The hydration level was monitored via the spectral position of the asymmmetric PO_2^- stretching vibration of the DNA and RNA backbones [29].

Linear infrared spectra of DNA and RNA samples are summarized in Fig. 8.1. At high hydration levels, salmon testes DNA and the double-stranded DNA oligomers exist in a B-helix structure (top panel of Fig. 8.1) while double-stranded RNA forms an A-helix. In the frequency range from 900 to 1350 cm^{-1}, there are infrared absorption bands of seven characteristic backbone normal modes of B-DNA (Fig. 8.1) [18, 30, 31]. The asymmetric (P1) and the symmetric (P2) PO_2^- stretching band of the phosphate groups in the backbone is located around 1220 and 1090 cm^{-1}, respectively. The spectral position of P1 depends sensibly on the hydration level, displaying a red-shift with increasing water level. This behavior is evident from the absorption

spectra of the DNA oligomers at 92% r.h. (dash-dotted line) and for full hydration (black solid line). The phosphate stretching absorption bands are complemented by the absorption of the linker modes L1 to L3 and the ribose modes R1 and R2. A detailed analysis in terms of normal modes has been presented in [31]. It should be noted that, apart from minor changes of absorption strength and line shapes, the spectra of fully hydrated oligomers and salmon testes DNA display the same absorption pattern.

The additional OH group of the ribose unit in RNA compared to DNA gives rise to changes in the linear infrared spectrum. The spectrum of the fully hydrated RNA A-helices presented in Fig. 8.1b exhibits moderate spectral shifts of the phosphate and linker modes and a different pattern of the ribose modes R1 and R2 [32]. The P1 band of RNA is split into two subcomponents reflecting different local hydration patterns. The additional bands at 1120 and 1135 cm^{-1} are due to the $C_{2'}$-OH stretching mode of the additional OH group and to the $C_{1'}$-$O_{4'}$-$C_{4'}$ ribose stretching mode. The different RNA bands display a somewhat reduced linewidth compared to the corresponding bands in the DNA spectra, pointing to a reduced structural disorder of the hydrated A-helix.

8.2.2 Two-Dimensional Infrared Spectroscopy and Pump-Probe Methods

Two-dimensional infrared (2D-IR) and pump-probe spectroscopy are used for mapping the third-order nonlinear response of backbone vibrations of hydrated DNA, RNA, and model systems such as dimethyl phosphate. Heterodyne detected 3-pulse photon echoes are recorded in the standard folded-box-CARS geometry [33]. In this scheme, three femtosecond infrared pulses with wavevectors $\mathbf{k}_{1,2,3}$ interact sequentially with the sample. The first two pulses are separated by the coherence time τ while the third pulse follows after the population time T. The four-wave-mixing signal emitted in the direction $\mathbf{k}_s = -\mathbf{k}_1 + \mathbf{k}_2 + \mathbf{k}_3$ is heterodyned with a fourth local oscillator pulse traveling collinearly with the signal. The resulting interferogram is spectrally dispersed in a monochromator and detected by a 64-element array detector with a 2-cm^{-1} spectral resolution, thus giving the nonlinear signal as a function of detection frequency ν_3. Measurements of the signal as a function of coherence time and a subsequent Fourier transform along τ provide the nonlinear vibrational response as a function of the excitation frequency ν_1. In this scheme, two pairs of phase-locked pulses are generated with the help of diffractive optics, the pulses 1 and 2 as well as pulse 3 and the local oscillator. Throughout this chapter, we present absorptive 2D signals, given as the real part of the sum of the rephasing and nonrephasing third-order signals [34].

Femtosecond pulses tunable in wide spectral range from 900 to 4000 cm^{-1} were generated by two- or three-stage parametric frequency converters driven by sub-50 fs pulses from amplified Ti:sapphire lasers (repetition rate 1 kHz). The millijoule input

pulses are first converted into signal and idler pulses tunable in the near-infrared between 4000 and 8000 cm^{-1}, using BBO crystals. In a second step, difference frequency mixing of the near-infrared pulses in GaSe crystals of sub-millimeter thickness provides mid-infrared pulses of 80–150 fs duration (depending on the spectral position) and pulses energies up to 7 μJ. Details of the pulse generation and characterization have been given in [18]. All 2D-IR measurements were performed with pulses of parallel linear polarization.

The 2D-IR experiments were complemented by temporally and spectrally resolved pump-probe experiments. Independently tunable pump and probe pulses were generated in two optical parametric amplifiers, the intensity ratio between pump and probe pulses was 50:1 and the time resolution approximately 100 fs [23]. Pump and probe pulses were linearly polarized and interact with the sample in a non-collinear transmission geometry. The fraction of excited molecular oscillators was less than 1%. After interacting with the sample, both the probe and a reference beam for normalization were spectrally dispersed in a monochromator and detected by a double HgCdTe detector array with 64 elements each. The spectral resolution was 2 cm^{-1}. Normalization of the probe intensity to the reference pulse allows for the measurement of pump-induced absorbance changes ΔA down to some 5×10^{-5} OD.

8.2.3 Theoretical Description of Biomolecular Electrostatics

The modeling of biological systems at the molecular scale requires a description in terms of the atomic interactions. For solvation structures and dynamics around biomolecules the description of electrostatics is of particular importance due to the long-range nature and the pronounced polarity of water molecules that interact with, e.g., the charged phosphate groups of DNA and RNA. This molecular arrangement defines a highly complex many-body problem which is understood only in part. The structural dynamics in the first water layers impose electric field fluctuation amplitudes at the phosphate site on a multitude of time scales via, e.g., librational motions and the breaking and reformation of hydrogen bonds. In particular, fluctuation amplitudes and the effective spatial range of the electric fields at the surface of the biomolecule have remained highly controversial.

At the interface of the biomolecule with its aqueous surrounding the local static dielectric constant undergoes changes on molecular length scales. The arising dielectric discontinuity is an important quantity for electrostatic models rooted in Poisson–Boltzmann theory [35] and the results depend on the choice of the radial dielectric screening function $\epsilon(r)$ [36, 37]. For example, the choice of the static end-point of the discontinuity narrows the molecular contact region and affects the specificity of DNA-counterion interactions [38]. Moreover, Poisson–Boltzmann models do not account for a molecular description of the solvent and ion-ion correlations are absent. The simulation of solvation structures and dynamics aiming at the interpretation of multidimensional vibrational spectroscopic signals on a molecular level thus calls for atomistic descriptions. An excellent overview over theoretical methods employed for the description of biomolecular electrostatics can be found in [39, 40].

8.2.3.1 Molecular Dynamics Simulations of Solvation Structure and Dynamics

Atomistic molecular dynamics simulations mitigate crucial assumptions of Poisson–Boltzmann models and provide a molecular picture of the biomolecular interface via a representation of the molecular electrostatic potential in terms of atomic partial charges. The results crucially depend on quality and reliability of the employed force fields [41]. Observations of accumulating α/γ transitions [42] that corrupt DNA duplex structures on the tens-of-nanosecond time scale have spurred substantial effort towards a reparametrization of DNA force field parameters, in particular sugar puckering of the DNA sugar-phosphate backbone (e.g., the BSC0 [43] and BSC1 [44] variants of the AMBER force field and the CHARMM36 force field [45]). With such improved re-parametrization stability of DNA double strands has been demonstrated on the microsecond time scale [46] with excellent agreement to experimental reference structures [47, 48].

While the DNA force fields increasingly became reliable recently, the increased flexibility of RNA poses substantial difficulties and deficiencies have been identified in particular for noncanonical structures [49, 50]. Accordingly, force field refinement of RNA is a topic of ongoing research and the reliability of results should be carefully verified by comparison to experimental data. Similarly, counterion force field parameters are undergoing continuous reparametrization, in particular for multiple charged ions like Mg^{2+} and Ca^{2+} [51–54]. Further challenges arise due to large computational requirements on system size, required equilibration times of the ion atmosphere [55] and a lack of experimental benchmark data.

Due to recent progress in porting molecular dynamics algorithms to graphical processing unit (GPU) hardware [56, 57] atomistic force field simulations of the electrostatics of solvated biomolecules today provide routine access to the hundreds of nanoseconds to microsecond time scale for systems like oligomeric DNA/RNA double strands embedded in explicit water solvent.

8.2.3.2 Higher Order Multipoles, Many-Body Polarization Effects and Electrostatic Field-Frequency Mapping

Pairwise additive force-fields rely on a point-charge representation of the molecular charge density. Such a description provides access to the bulk polarization of water via a reorientation of individual water molecules subject to an imposed electric field, but is to be distinguished from a rearrangement of electronic structure within the individual molecules due to many-body polarization effects (induction). Further, higher order charge multipoles are commonly neglected. Major effort has been devoted to the development of polarizable force fields [58, 59] with first biomolecular applications approaching maturity [40, 60]. Many-body polarization is expected to be particularly important for the description of water at biological interfaces [61–63].

The Effective Fragment Potential (EFP) model [64–67] provides a description of intermolecular electrostatics that accounts for many-body polarization and higher order charge multipoles. Within the EFP model the intermolecular interaction potential U_{EFP} is partitioned into fundamental contributions that each have clear physical origin:

$$U_{\mathrm{EFP}} = U_{\mathrm{El}} + U_{\mathrm{Pol}} + U_{\mathrm{Disp}} + U_{\mathrm{Xr}} + U_{\mathrm{CT}}. \tag{8.1}$$

Here, $U_{\mathrm{El,\,Pol,\,Disp,\,Xr,\,CT}}$ denote electrostatic, polarization, dispersion, exchange repulsion and charge transfer contributions, respectively. In the following, we focus primarily on electrostatic and induced dipole interactions (polarization) which are expected to be the dominant contributions for long range field fluctuations at the charged phosphate-water interface due to their limiting $1/r$ and $1/r^3$ dependence.

Electrostatic Interactions

The electrostatic intermolecular interaction potential U_{El} is given by

$$\begin{aligned} U_k^{\mathrm{El}} = q_k\phi(r_x) - \sum_a^{x,y,z} \mu_k^a E_a(r_{kx}) \\ + \frac{1}{3}\sum_{a,b}^{x,y,z} \Theta_k^{ab} E_{ab}(r_{kx}) - \frac{1}{15}\sum_{a,b,c}^{x,y,z} \Omega_k^{abc} E_{abc}(r_{kx}) \end{aligned} \tag{8.2}$$

where $\phi(r_x)$ denotes the molecular electrostatic potential expanded up to octopoles, $E_a = -\nabla\phi(r_x)$ denotes the electric field, $E_{ab} = \nabla^2\phi(r_x)$ the electric field gradient and $E_{abc} = \nabla^2 E_a$ the electric field Hessian and q_k, μ_k^a, Θ_k^{ab} and Ω_k^{abc} are molecular electric quantities, i.e., charges, dipole, quadrupole and octopole moments, located at expansion points k.

Polarization Contribution

Many-body polarization forms a non-additive part of the total electrostatic interaction that is neglected in treatments with additive force fields. Within the EFP model polarization effects are considered self-consistently by mutual induction of dipoles at centroids of localized molecular orbitals due to an imposed electric field ($\mu_{i,\alpha}^{\mathrm{ind}} = \alpha \cdot E$). The electric field has components from static multipoles M_j as well as induced dipoles $\mu_{k,\alpha}^{\mathrm{ind}}$ at other sites k:

$$\mu_{i,\alpha}^{\mathrm{ind}} = \alpha_{i,\alpha,\beta}\left[\sum_j T_\alpha^{ij} M_j + \sum_k T_{\alpha\beta}^{ik}\mu_{k,\beta}^{\mathrm{ind}}\right], \quad \alpha,\beta = x,y,z. \tag{8.3}$$

Electric Field—Frequency Correlation

Focussing on the electric field E_a as the dominant contribution to the solvatochromic shift of phosphate stretch vibrations [68], the field is evaluated up to quadrupole interactions:

$$E_a(r_x) = \sum_k \Bigg[q_k T^a(r_{kx}) - \sum_{\alpha}^{x,y,z} \mu_k^{a,\mathrm{tot}} T^{ab}(r_{kx}) + \frac{1}{3} \sum_{b,a}^{x,y,z} \Theta_k^{ab} T^{abc}(r_{kx}) \Bigg]. \tag{8.4}$$

Here $\mu_k^{a,\mathrm{tot}}$ accounts for induced dipoles and permanent dipoles ($\mu_k^{a,\mathrm{tot}} = \mu_k^{a,ind} + \mu_k^{a,el}$) where the induced dipoles have been converged subject to mutual polarization (8.3) and T denotes the electrostatic tensors up to rank three. The electric field is evaluated as scalar quantity via a projection on the symmetry axis of the PO_2^- group (E^{C2}).

Assuming a linear relation, the solvent field induced solvatochromic shift is given by

$$\omega = \omega_0 + \delta\omega = \omega_0 + a \cdot E^{C2} \tag{8.5}$$

where a denotes the slope of the electric field - frequency correlation that can be compared to the experimental Stark tuning rate [69–71] and ω_0 denotes the field free frequency of, e.g., the asymmetric PO_2^- stretching vibration that is accessible from ab-initio simulations (cf. Sect. 8.2.3.3).

Parameters of the EFP model can be derived entirely from high level ab-intio simulations. The computational scaling is determined by self-consistent determination of induced dipoles (8.3) and allows to access fluctuation dynamics of nanosecond trajectories. For solvated DNA model systems like, e.g., dimethyl phosphate (DMP) converged field fluctuation correlation functions in the $\approx$10 ps range, the natural time scale of hydrogen-bond exchange were demonstrated [26].

8.2.3.3 Ab-Initio Simulations of DNA/RNA Backbone Vibrations

Ab-initio simulations of biomolecular systems interacting with a water environment are prohibitively expensive but provide most accurate insight into noncovalent intermolecular interactions. Due to the high computational costs, direct molecular dynamics simulations of biomolecules embedded in water are up-to-date not feasible on relevant time scales and carefully chosen model systems are required. As such ab-initio simulations primarily serve for the following purposes:

(1) Benchmark of electric field amplitudes: the magnitude of EFP simulated electric fields, imposed on the phosphate group by the solvent molecules, can be rigorously benchmarked in ab-initio simulations of solvated DNA model systems like DMP [26]. Such calculations (i) provide a benchmark on the accuracy of the EFP method and (ii) serve as indicator for dispersion, exchange repulsion and charge transfer contributions to the total intermolecular interaction, as the field evaluated with QM methods, like second order perturbation theory (MP2), naturally contains all contributions to the intermolecular interaction potential (cf. (8.1)).

(2) Microscopic picture of the molecular vibrational Hamiltonian: high level, ab-initio derived multidimensional vibrational model Hamiltonians provide insight into details of the molecular Hamiltonian and can be further employed to simulate linear IR and absorptive 2D-IR spectra of phosphate ion model systems in bulk H_2O [25]. The ab-initio derived model Hamiltonians reveal that inter-mode couplings and anharmonicities are generally small ($<15\,cm^{-1}$, see Sect. 8.3). Extensive quantum mechanical/molecular mechanical (QM/MM) simulations of backbone vibrations of an RNA $(AU)_{23}$ oligomer were further employed to provide a consistent microscopic mode assignments of the canonical A-RNA duplex sugar-phosphate backbone [32]. The simulations revealed the delicate impact of the $C_{2'}$-OH group on vibrational spectra. With such information a microscopic structural picture of mode couplings can be developed.

(3) Insight into solvatochromic shifts and noncovalent interactions: DNA model systems like DMP in aqueous solution show pronounced solvent imposed frequency shifts ($\approx$60–80 cm^{-1}) of the asymmetric PO_2^- stretching vibration (8.5) that closely resemble observed shifts of DNA phosphate stretching vibrations at different hydration levels. Ab-initio normal mode analysis and vibrational configuration interaction (VCI) simulations revealed how the phosphate stretch vibrational potential is decisively determined by the noncovalent interactions with the first few water shells [25, 26]. Such simulations provide a rationale how the phosphate vibrational modes serve as sensitive probes of hydration structure in DNA and RNA.

Ab-initio normal mode analysis further revealed that solvent induced frequency shifts of the asymmetric PO_2^- stretching vibration are primarily determined by the electrostatic phosphate-water interactions [24]. Due to the high polarizability, the rearrangement of the electronic structure within the phosphate group is the dominant mechanism via electrostatic interactions while charge transfer contributions are minor. Only upon formation of contact ion pairs (cf. Sect. 8.5) [72], exchange repulsion interactions become important and impose an $\approx 30\,cm^{-1}$ blue shift of the asymmetric PO_2^- stretching vibration.

8.2.3.4 Density Matrix Simulations for the Modeling of Two-Dimensional Infrared Spectra

The 2D spectra were analyzed by calculating the third-order response functions to the experimental photon-echo pulse sequence by a perturbative density matrix approach of light-matter interaction, including Kubo lineshape analysis and the lifetime broadening caused by population relaxation of the different vibrations. The treatment follows the perturbative approach developed in [19, 73], a detailed description of this treatment has been given in [18, 25]. The fluctuating forces originating from the aqueous environment and DNA/RNA structure fluctuations are included via the frequency fluctuation correlation function (FFCF). The FFCF is given by the Kubo ansatz

$$\langle \delta\nu_i(t)\delta\nu_i(0)\rangle = \Delta_{1,i}^2 \exp(-t/\tau_1) + \Delta_{2,i}^2 \exp(-t/\tau_2). \tag{8.6}$$

Here, $\delta\nu_i(t)$ denotes the frequency excursion of mode i at time t from its average transition frequency and $\Delta_{1,i}$ and $\Delta_{2,i}$ are fluctuation amplitudes of the frequency excursions, τ_1 and τ_2 are the fluctuation correlation times. To limit the number of free parameters in the modeling the values of $\tau_{1,2}$ are kept fixed in the simulations and the amplitudes $\Delta_{1,i}$ and $\Delta_{2,i}$ are adjusted to best reproduce the experimental line shapes. In the modeling of 2D spectra (see Sect. 8.3) a slow ($\tau_2 \approx 50$ ps) component is assumed that causes a quasi-static inhomogeneous broadening of the lineshapes and a fast component ($\tau_1 \approx 300$ fs) accounts for spectral diffusion. Microscopic simulations of the DMP model system provide similar time scales with slightly different values (50 fs, 1.2 ps) [26].

8.3 Two-Dimensional Infrared Spectra of DNA and RNA at Different Hydration Levels

The 2D-IR spectra presented in the following were recorded in two partly overlapping spectral ranges, the frequency interval between 1050 and 1300 cm^{-1} with the PO_2^- stretching modes P1 and P2, and the range from 900 to 1150 cm^{-1} in which the majority of the other backbone modes is located. The 2D-IR spectra of DNA and RNA oligomers shown in Fig. 8.2 display a series of peaks along the frequency diagonal $\nu_1 = \nu_3$, each consisting of a component due to absorption bleaching and stimulated emission on the fundamental $v = 0{-}1$ transition (yellow-red contours) and of a contribution caused by the $v = 1{-}2$ absorption (blue contours). The latter is

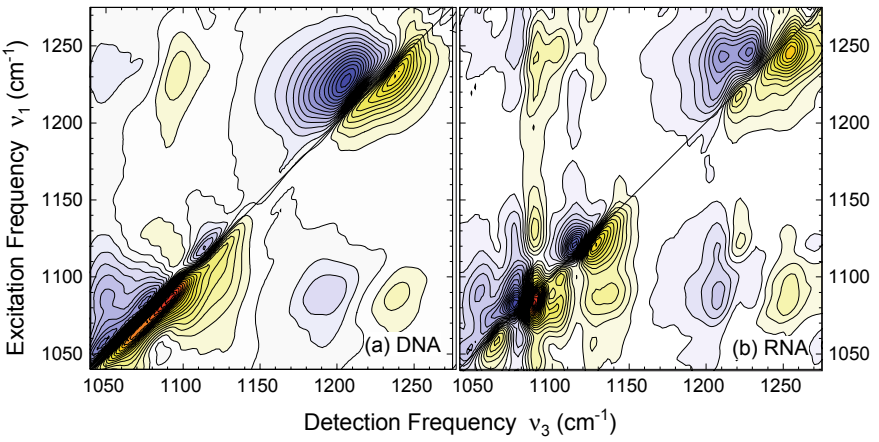

Fig. 8.2 Two-dimensional infrared (2D-IR) spectrum of **a** DNA oligomers containing 23 alternating adenine-thymine pairs at 92% r.h., and **b** fully hydrated RNA oligomers containing 23 adenine-uracil pairs. The absorptive 2D signal is plotted as a function of excitation and detection frequency. The spectra were recorded at a waiting time of T = 250 fs. The signal changes by 5% between neighboring contour lines

anharmonically red-shifted to lower detection frequencies. The uppermost diagonal peaks in the range $(\nu_1, \nu_3) > (1200, 1200)\,\mathrm{cm}^{-1}$ are due to the P1 modes. There is a single diagonal peak in the case of DNA (Fig. 8.2a) while the RNA spectrum in Fig. 8.2b displays two contributions, in agreement with the substructure observed in the linear infrared spectrum of Fig. 8.1b. Below $(1150, 1150)\,\mathrm{cm}^{-1}$, both the DNA and RNA 2D spectra show a pronounced diagonal peak due to the P2 mode around $(1090, 1090)\,\mathrm{cm}^{-1}$ which in the case of RNA is complemented by peaks from the $C_{2'}$-OH stretching and the $C_{1'}$-$O_{4'}$-$C_{4'}$ ribose stretching vibrations (Fig. 8.2b). The diagonal 2D peaks in the DNA spectrum of Fig. 8.2a are of elliptic shapes, thus revealing a substantial inhomogeneous broadening due to structural disorder of the hydrated helices. In contrast, inhomogeneous broadening is less present in the RNA 2D spectrum of Fig. 8.2b, pointing to a more homogeneous hydration structure. The vibrational lifetimes of the different backbone modes are on the order of 1 ps, with the exception of the P1 mode. The latter shows a substantially shorter lifetime between 300 and 360 fs in all phosphate systems in aqueous environment studied by femtosecond vibrational spectroscopy so far.

The pattern of cross peaks reflects the rich anharmonic coupling scheme between the backbone vibrations. First, the P1 and P2 modes of both DNA and RNA couple to each other, as is evident from the respective pairs of cross peaks. In RNA, there are no cross peaks between the two components of the P1 doublet, suggesting that the two contributions originate from different phosphate groups. The lower P1 component at $1220\,\mathrm{cm}^{-1}$ couples strongly to the $C_{2'}$-OH stretching vibration, giving rise to the cross peaks at (1220, 1120) and $(1120, 1220)\,\mathrm{cm}^{-1}$.

Figure 8.3 shows a more detailed comparison of 2D-IR spectra of fully hydrated RNA and DNA oligomers between 1030 and $1150\,\mathrm{cm}^{-1}$, corresponding to the lower frequency range of Fig. 8.2. The P2 diagonal peak of RNA (Fig. 8.3a) is oriented parallel to the ν_1 axis, revealing a predominant homogeneous broadening which is in contrast to the inhomogeneously broadened P2 peak of DNA (Fig. 8.3b). The presence of the additional $C_{2'}$-OH stretching and the $C_{1'}$-$O_{4'}$-$C_{4'}$ ribose stretching vibrations gives rise to the broad and asymmmetric diagonal peak at $(1130, 1130)\,\mathrm{cm}^{-1}$ and the complex cross peak pattern between the different modes. The reduced inhomogeneous broadening of RNA compared to DNA 2D peaks represents an important prerequisite for the observation of the fine details of vibrational coupling.

Figure 8.4 depicts solvation structures around double stranded RNA obtained from molecular dynamics simulations (cf. Sect. 8.2.3.1). The magnification (Fig. 8.4, right) highlights partially ordered water structures at the surface of RNA, i.e., water molecules bridging adjacent $PO_2^-\ldots PO_2^-$ units and a hydrogen bond network ring structure mediated by the $C_{2'}$-OH group. Such hydration structures are found in addition to the solvation of phosphate groups by three water molecules in an approximate tetrahedral geometry which is prototypical for DNA [10, 74]. Due to the A-helical geometry of RNA, the distances between neighboring phosphate groups are reduced compared to DNA in the B-form [7]. Accordingly, the phosphate groups can be bridged by single water molecules that form strong hydrogen bonds with the PO_2^- oxygen atoms. The additional OH group at the $C_{2'}$ position in RNA not only introduces additional vibrational modes but mediates hydrogen bonded rings of $\approx$3 water

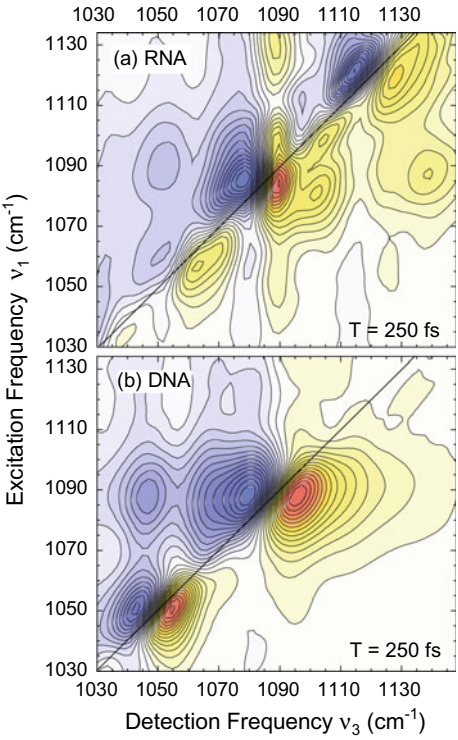

Fig. 8.3 Comparison of 2D-IR spectra of fully hydrated **a** RNA oligomers containing 23 adenine-uracil base pairs, and **b** DNA oligomers consisting of 23 alternating adenine-thymine base pairs. RNA displays a more complex mode and coupling pattern in the spectral range from 1030 to 1150 cm^{-1}

molecules to the PO_2^- oxygen atoms. Such ring structures lead to partially ordered water structure in the minor groove of RNA. Both, bridging water and ring structures observed in the molecular dynamics simulations are in line with reports from X-ray diffraction studies [11, 75] that suggest that the first hydration layer around RNA contains a larger number of water molecules in a more ordered arrangement.

Compared to DNA, the partly ordered hydration structure around the backbone of RNA imposes reduced heterogeneity of the first water layers around the helix. Such observations corroborate the reduced inhomogeneous width observed for the 2D lineshapes of RNA (cf. Figs. 8.2 and 8.3). For example, the P2 diagonal peak shows substantially reduced inhomogeneity and a pronounced coupling pattern to $C_{2'}$-OH stretching and the $C_{1'}$-$O_{4'}$-$C_{4'}$ ribose stretching vibrations where the limited inhomogeneous broadening of the diagonal peaks reflects the more ordered character of the hydration shell structure around RNA. The water molecules of the ring structures could be instrumental in inducing the pronounced intermode vibrational couplings between the phosphate group and the ribose unit. Further, the doublet structure of P1 peaks and the absence of cross peaks for this feature suggests distinct different phosphate group hydration sites along the A-helix. The reduced inhomogeneous broadening here is essential for separating the different P1 components and respective coupling patterns to the $C_{2'}$-OH stretching and $C_{1'}$-$O_{4'}$-$C_{4'}$ ribose stretching vibrations.

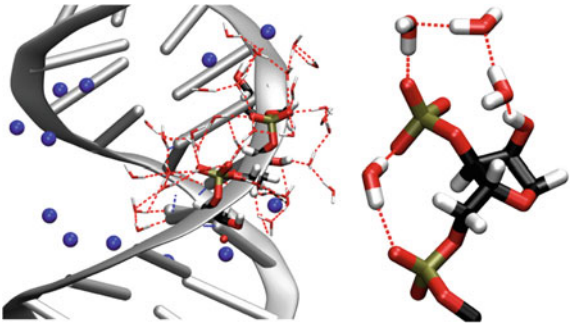

Fig. 8.4 Solvation structure of RNA oligomer backbone with counterions shown in blue. The magnification (right) highlights a $PO_2^-\ldots PO_2^-$ bridging water molecule and a hydrogen bond network ring structure mediated by the C2'-OH group

In the following, we focus on 2D-IR spectra of DNA oligomers with 23 alternating A-T pairs at a hydration level of 92% r.h. This water content of the sample corresponds to 20–30 water molecules per base pair which is sufficient to form two closed water layers around the B-helix of the oligomer. Figure 8.5a, b show absorptive 2D spectra in the spectral range from 900 to 1150 cm^{-1}, recorded at waiting times of 500 and 2000 fs. The arrows and the symbols on the right hand side of Fig. 8.5b give assignments of the diagonal peaks to the different backbone modes (cf. Fig. 8.1a). In addition to the diagonal peaks, the spectra display a complex pattern of cross peaks, appearing as stripe-like features of alternating sign in the upper triangle of the 2D frequency plane. The cross peaks indicate anharmonic couplings between essentially all backbone modes.

The complex arrangement of diagonal and cross peaks is preserved with unchanged spectral positions at longer waiting times. The relative intensities of the different peaks, however, undergo substantial changes. In particular, the relative strengths of the cross peaks at low detection frequencies ν_3 increases with waiting time. This behavior is a hallmark of inter-mode energy transfer, i.e., energy is transferred from the backbones modes at higher frequencies to those at low frequencies on a time scale of a few picoseconds. This process together with the vibrational relaxation of each individual mode determines the time evolution of the diagonal peaks as has been shown in more detail in [18].

The experimental 2D-IR spectra were analyzed with the help of the simulation approach outlined in Sect. 8.2.3.4. This treatment combines a density matrix approach for calculating the third-order nonlinear response to the photon-echo pulse sequence with a Kubo ansatz for the FFCF (cf. (8.6)). For reproducing the experimental results, the decay times in the Kubo FFCF were set as $\tau_1 = 300$ fs and $\tau_2 = 50$ ps, the latter leading to a quasi-static inhomogeneous broadening of the peaks in the 2D-IR spectrum. With such fixed correlation times, the fluctuation amplitudes $\Delta_{1,2}$ were adjusted for each of the seven modes to reproduce the observed lineshapes. The diagonal anharmonicities of the modes which determine the separation of the two components of the diagonal peaks along the detection frequency ν_3 were chosen for each mode individually while a global anharmonic intermode couplng of 10 cm^{-1} was chosen in order to calculate the cross peak pattern. The model includes inco-

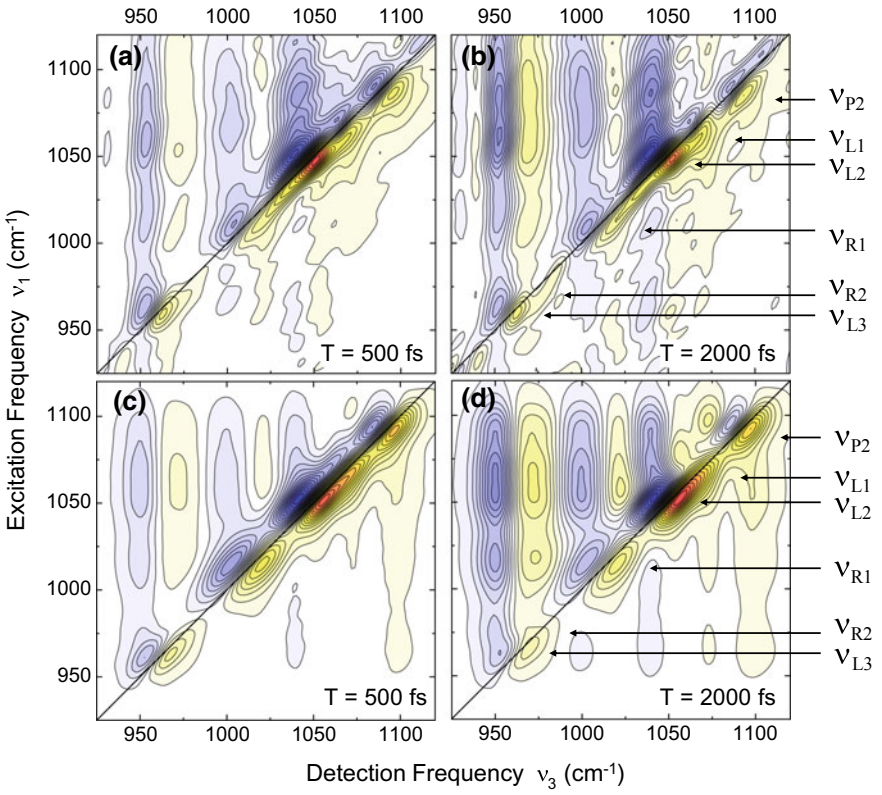

Fig. 8.5 Absorptive 2D-IR spectra of backbone modes of a double-stranded DNA oligomer containing 23 alternating adenine-thymine base pairs at a hydration level of 92% r.h. **a**, **b** Experimental spectra recorded at waiting times T = 500 and T = 2000 fs. **c**, **d** Simulated spectra. The symbols and arrows on the right-hand side mark the different backbone modes contributing to the spectra

herent down-hill energy transfer between the modes with a time constant of 2 ps and population relaxation of the $v = 1$ states of the vibrations with an average time constant of 1.7 ps. In parallel to the analysis of the 2D spectra, the linear infrared absorption spectrum of the DNA oligomers was fitted to benchmark the derived parameters entering in the Kubo FFCF.

The calculated spectra presented in Fig. 8.5c, d are in quantitative agreement with the experimental results in Fig. 8.5a, b. The diagonal anharmonicities are between 5 and 10 cm^{-1}, the fluctuation amplitudes in the Kubo function are $\Delta_1 = 6 - 8\,\text{cm}^{-1}$ and $\Delta_2 = 6 - 16\,\text{cm}^{-1}$. Selected FFCFs for the P1, L2, and R1 modes are plotted in Fig. 8.6 (blue lines), a detailed listing of the parameter values has been given in [18]. The initial 300 fs decay of the FFCF accounts for the antidiagonal width of the different 2D peaks which is determined by spectral diffusion of the vibrational transitions. Spectral diffusion mainly originates from the fluctuating Coulomb forces the first few water layers and, to lesser extent, solvated counterions exert on the back-

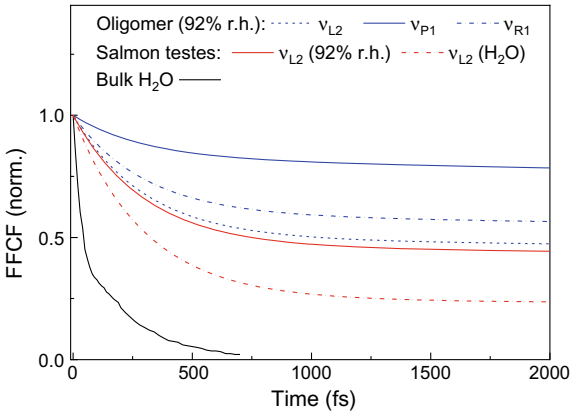

Fig. 8.6 Frequency fluctuation correlation functions (FFCFs) derived from the simulations of 2D-IR spectra of backbone modes of DNA oligomers and salmon testes DNA at different hydration levels. The FFCFs consist of a first term with a correlation decay time of 300 fs and a quasi-static contribution. The amplitudes of the two components are different for the different modes. Black solid line: FFCF of bulk water calculated in [76]

bone. Structural low-frequency fluctuations of the DNA backbone with its phosphate ions may contribute as well. The 300 fs decay is moderately slower than the initial sub-100 fs decay of the FFCF of bulk H_2O which is shown as a black solid line in Fig. 8.6 [76]. Water motions at the interface to a DNA helix, in particular librational degrees of freedom, are restricted by the steric boundary conditions the DNA surface sets in its major and minor grooves. This results in a somewhat slower FFCF decay compared to bulk water. However, the first few layers of the water shell are far from representing a rigid structure and, thus, the concepts of an 'iceberg-like' water structure and/or extremely slow biological water can be ruled out safely [3].

The second component of the FFCFs with a decay time beyond 10 ps results in quasi-static inhomogeneous broadening as manifested in the elliptic shape of the 2D diagonal peaks. This behavior reflects a comparably long-lived structural heterogeneity of hydration geometries, i.e., structural disorder along the DNA backbone. Hydrogen bonds between the water molecules in the first hydration layer and phosphate groups in the backbone are stronger than water-water hydrogen bonds and display, according to detailed molecular simulations of the interface [77], lifetimes on the order of 20 ps. As a result, the molecular pattern of the first water layer is preserved for this picosecond time range and differences in the local number of waters along the helix are expected to result in a quasi-static distribution of vibrational frequencies of the phosphate groups and the other interacting units of the backbone. It should be recalled that inhomogeneous broadening is less pronounced in the 2D-IR spectra of RNA oligomers (cf. Figs. 8.2 and 8.3), resulting in systematically smaller fluctuation amplitudes Δ_2 in the relevant FFCFs [32]. Here, the additional OH group of the ribose unit has a strong impact on the first-layer water structure and induces an overall more homogeneous hydration pattern.

8.4 Electric Fields at the DNA Surface and Energy Exchange Processes

The combination of 2D-IR spectroscopy with ab-initio based theory allows for an in-depth analysis of the electric interactions between a DNA helix and its water shell. Key issues are the strength and fluctuation amplitude of the interfacial electric fields, the relative contributions of water molecules, counterions, and phosphate groups to the local fields, and the spatial range of the electric forces in the dense water shell. Such issues have been addressed in a series of theoretical studies, starting with early polyelectrolyte theories and developing towards descriptions at the atomic level based on Poisson Boltzmann pictures for static geometries and/or classical molecular dynamics simulations. In the latter, the choice of the particular water model represents a major issue and most recent work has implemented flexible polarizable water molecules, e.g., on the SPC level. While early simulation work has been limited to a time range up to a few nanoseconds, current simulations have provided trajectories extending into the microsecond range.

The backbone modes of DNA and RNA are most sensitive and noninvasive probes of interfacial electric fields. In the following, we present recent results from 2D-IR experiments with native salmon testes DNA at different hydration levels. Salmon testes DNA with its approximately 2000 base pairs displays the same set of backbone normal modes as the much shorter oligomers discussed so far and a similar infrared absorption spectrum (cf. Fig. 8.1a). The experiments give insight into the fluctuation amplitudes of electric fields via the 2D line shapes and, in combination with theory, in the relevant strength and range of electric interactions.

Figure 8.7 summarizes absorptive 2D-IR spectra of salmon testes DNA at three different hydration levels and a population time of T = 500 fs. The spectra in Fig. 8.7a, b were recorded with thin-film samples containing CTMA instead of the genuine Na^+ counterions, while Fig. 8.7c shows a 2D-IR spectrum of fully hydrated DNA with Na^+ counterions. The basic pattern of diagonal and cross peaks is identical in all spectra and close to the 2D spectra of the much shorter DNA oligomers (cf. Fig. 8.5), with some minor spectral shifts and slight variations in the relative peak intensities. There are, however, systematic changes of the 2D line shapes with hydration which have been discussed in detail in [22]. The antidiagonal widths of the peaks on the frequency diagonal $\nu_1 = \nu_3$ are practically identical for 92% r.h. (20–30 water molecules per base pair) and full hydration (more than 150 water molecules per base pair). In contrast, the 2D spectrum for 0% r.h. (2 waters per base pair) shows narrower profiles along the antidiagonals. An opposite trend is found for the spectral widths along the diagonal which decrease with increasing hydration. As a result, the envelopes of the diagonal peaks in the spectrum of the fully hydrated samples appear tilted towards the vertical frequency axis ν_1, i.e., they appear more homogeneous. Additional measurements were performed with a fully hydrated sample in which the Na^+ counterions were exchanged against Mg^{2+} ions. Within the experimental accuracy, the 2D-IR spectrum was identical to the one shown in Fig. 8.7c.

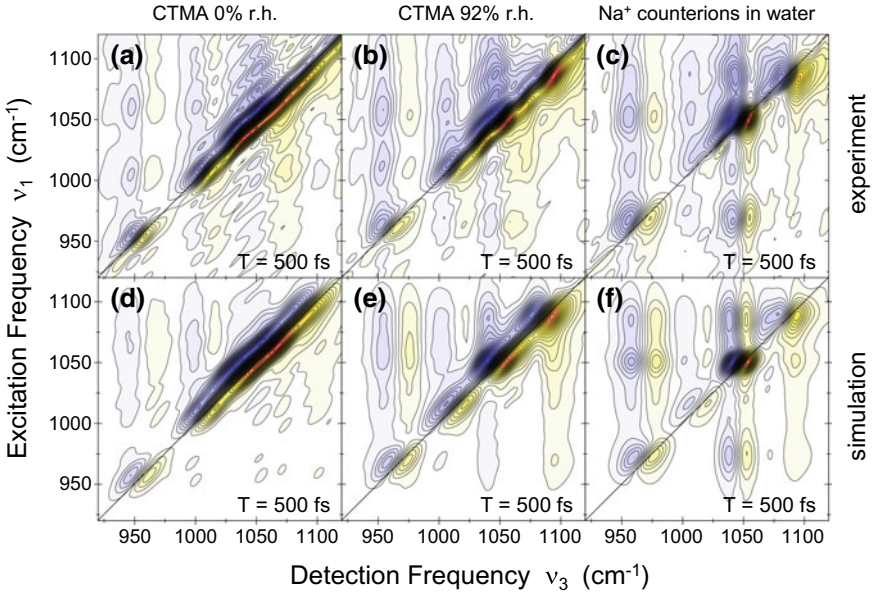

Fig. 8.7 2D-IR spectra of salmon testes DNA at different hydration levels. The spectra at 0 and 92% r.h. were measured with thin-film samples containing CTMA counterions. **a–c** Experimental spectra recorded at a waiting time T = 500 fs. **d–f** Simulated spectra

The salmon testes 2D-IR spectra were analyzed with the formalism described in Sects. 8.2.3.4 and 8.3, again using correlation times of 300 fs and 50 ps in the Kubo ansatz for the FFCF (8.6). The calculated spectra shown in Fig. 8.7d–f are in good agreement with the experiments. The FFCFs of the L2 mode of salmon testes DNA at 92% r.h. and full hydration are included in Fig. 8.6 (red lines). The FFCF for 92% r.h. agrees very well with the corresponding result for the DNA oligomers (blue dashed line) while the FFCF for full hydration exhibits a reduced amplitude of the quasi-static 50 ps component (red dash-dotted line), in line with the more homogeneous 2D lineshape of the L2 peak.

The fluctuation amplitudes for the 300 fs FFCF component for the different modes have values of $\Delta_1 = 6{-}11\,\mathrm{cm}^{-1}$ which are the same for full hydration and 92% r.h. In contrast, values up to $\Delta_1 = 5\,\mathrm{cm}^{-1}$ are found at 0% r.h. We conclude that (i) the water shell represents the predominant source of the fluctuating electric force giving rise to spectral diffusion, and (ii) that this force originates essentially from the first two water layers which are present at both 92% r.h. and for full hydration. In other words, the dipolar water molecules are the main source of short-range Coulomb forces which cause the fast frequency modulation of the vibrational transitions. The fluctuation amplitudes Δ_1 are proportional to the fluctuation amplitudes of the electric field from the two water layers, in the simplest linear approximation according to $\Delta_{1i} = a_i \cdot \Delta E_i$ where ΔE_i is the fluctuation amplitude projected on the vibrational coordinate of the respective backbone normal mode. The tuning rates a_i of the vibrational

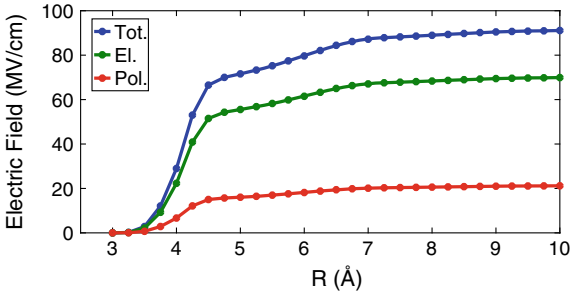

Fig. 8.8 Radial dependence of electric fields calculated for dimethyl phosphate (DMP) in bulk H_2O. The electric field strength projected on the C2 axis of the PO_2^- group is plotted as a function of radial distance R in angstroms. The total field consists of a predominant electrostatic component and a contribution arising from the mutual polarization of DMP and the solvent

transition frequencies can be estimated from molecular force fields for the different vibrations. Recent theoretical calculations for the symmetric (P2) and asymmetric (P1) PO_2^- stretching vibrations suggest a value of $a_i = 0.4-0.5$ cm^{-1}/(MV/cm). With such tuning rates, one derives a fluctuation amplitude $\Delta E_i = 20-25$ MV/cm with the help of the experimental $\Delta_{1,P2} = 10\,\text{cm}^{-1}$.

To benchmark the fluctuating electric forces relevant for spectral diffusion in the DNA 2D-IR spectra, theoretical calculations were performed for dimethyl phosphate [DMP, $(CH_3)_2PO_4^-$] in bulk H_2O. DMP has repeatedly been used as a model system for the phosphodiester moiety of the DNA and RNA backbones. The fluctuating electric forces on the phosphate group were calculated with the approach described in Sect. 8.2.3.2 which includes both electric fields from static multipoles and polarizations due to induced dipoles.

Figure 8.8 shows the dependence of the calculated time-averaged electric field from the water shell projected on the C2 axis of the PO_2^- entity and integrated over an increasing radial distance R from the phosphate group of DMP. The field reaches a maximum value on the order of 100 MV/cm. The total electric field generated by water molecules arises to a large extent from the first water layer. The second layer contributes some 18% with noticeable contributions from induction. Furthermore, the solvent electric field experienced by the phosphate group is the dominant contribution to the pronounced solvatochromism of the asymmetric PO_2^- stretching vibration. Accounting for a field expansion up to quadrupoles and polarization due to induced dipoles allows for simulating solvent induced frequency shifts and line shapes in almost quantitative agreement to experiment. The underlying field fluctuation amplitudes are found in the range $\Delta E \approx 25$ MV/cm, in excellent agreement with the experimental observations. The model strongly supports the picture of short-range electric forces that arise locally from the first and second hydration shell.

The electric forces the hydration shell exerts on the DNA backbone depend sensibly on the spatial arrangement of water molecules in the first and second water layer. Changes of this arrangement have a direct impact on the frequency positions,

absorption strengths, and lineshapes of the infrared absorption bands of backbone modes. In a recent pump-probe study [23], the water shell was heated by a femtosecond infrared pulse which was resonant to its OH stretching absorption band. The decay of the OH stretching excitation and subsequent energy redistribution generate a heated ground state of the water shell in which the water-water hydrogen bond strengths and arrangement of water molecules is modified. This structure change modifies the infrared absorption of the backbone modes as was directly monitored by a femtosecond probe pulse. The rise of such absorption changes follows in time the buildup of the hot water ground state, i.e., the change of electric interactions due to the rearrangement of water molecules. Energy transfer from the heated water shell into the initially unexcited DNA helix occurs on a substantially slower time scale of tens of picoseconds.

The impact of electric forces on transient line shapes of backbone modes is corroborated by simulations of electric fields for the DMP model system (cf. Sect. 8.2.3.2) in bulk H_2O at elevated temperatures [23]. While spatial rearrangements in the first and second solvation shell are moderate for increasing temperature, a resulting decrease of the electric field acting on the DMP phosphate group was found. The reduction of the field amplitudes induces a blue-shift of the symmetric and asymmetric PO_2^- stretching vibrations and is the origin of the observed modulation of line shapes. Such Coulomb-mediated coupling is predominantly mediated by the electric field the first few water layers exert on the backbone that changes upon formation of the hot water ground state. The limited reordering of water molecules in the first and second layer around the double helix demonstrates the pronounced sensitivity of the DNA backbone vibrations and their transient spectra to electric fields exerted by the aqueous environment.

8.5 Conclusions and Outlook

The results presented in this chapter demonstrate the important role of hydrogen bonds and Coulomb interactions for the structure and dynamics of biomolecules. Water molecules in the first hydration layer at the surface of DNA and RNA form hydrogen bonds with the phosphate groups in the backbone and with other polar groups of the backbone and the base pairs, resulting in a water structure different from the bulk liquid. The structure of the first hydration layer around RNA is affected by the additional OH group of the ribose units and less heterogeneous than around DNA. Local interactions at the hydrated interface and molecular dynamics connected with thermal excitations of low-frequency degrees of freedom are probed in a non-invasive way by backbone vibrations. The 2D-IR spectra of such modes display line shapes which are determined by spectral diffusion on a 300 fs time scale and by a quasi-static inhomogeneous broadening, reflecting the structural disorder along the helical DNA and RNA structures. Spectral diffusion is moderately slowed down compared to bulk water and originates mainly from fluctuating electric forces the water molecules in the first and second hydration layer exert on the different vibrational

oscillators. Experiments at different hydration levels demonstrate a short-range character of electric interactions, typically extending over 2 water layers. The electric field strength at the hydrated interface reaches values on the order of 100 MV/cm with fluctuation amplitudes of some 25 MV/cm. An in-depth theoretical analysis for the hydrated model system dimethyl phosphate suggests a predominant electrostatic (dipole) contribution to the total electric field while polarization forces account for approximately 20% of the field at the phosphate groups.

Counterions of the negatively charged DNA and RNA helices as well as positively charged excess ions are typically part of the native biomolecular environment. Their interaction with the backbone, in particular with the ionic phosphate groups, plays an important role for the stabilization and folding of macromolecular structures. In this context, magnesium ions (Mg^{2+}) are particularly relevant. Ions located close to the DNA and RNA surfaces are expected to contribute to the interfacial electric fields while the role of ions solvated in the hydration shell is less obvious. Ions in the first solvation shell around phosphate groups can form contact ion pairs whereas ions separated by at least one water layer from the backbone are partly mobile and part of the so-called diffuse ion atmosphere.

Electric interactions with the different types of ions have been the subject of extensive theoretical work, addressing the radial ion distributions around helices and the resulting field strength at the surfaces of DNA and RNA. In contrast, experimental work has remained limited. X-ray diffraction from crystallized samples has identified sites of essentially immobile ions in the vicinity of the DNA and RNA backbone but gives not much insight in the diffuse ion atmosphere [9, 11]. Small angle x-ray scattering has provided information on the thickness of the counterion layer and, to some extent, the radial concentration gradient [78].

Very recently, we have studied the interaction of Mg^{2+} ions with phosphate groups by 2D-IR spectroscopy of the model system dimethyl phosphate (DMP^-Na^+) in an H_2O environment where DMP^- and Na^+ are solvated separately [72]. The asymmetric PO_2^- stretching vibration of DMP^- serves as a probe. The 2D-IR spectrum in Fig. 8.9a measured with a DMP^- concentration of 0.2 M in absence of Mg^{2+} ions displays the diagonal peak of the P1 vibration around (1210, 1210) cm^{-1}, consisting of a component due to ground state bleaching and stimulated emission on the fundamental $v = 0{-}1$ transition (yellow-red contours) and the red-shifted peak of $v = 1{-}2$ absorption (blue contours). Upon addition of 2 M $Mg(H_2O)_6Cl_2$, i.e., a tenfold excess of Mg^{2+} ions, one observes a separate blue-shifted diagonal peak P1' around (1250, 1250) cm^{-1}. It is important to note that there are no cross peaks between P1 and P1', pointing to their origin from different DMP^- entities. Spectra recorded for different waiting times T and complementary pump-probe measurements give a decay time of 300 fs for P1 and of 400 fs for P1'. The two different species are also present in the linear infrared absorption spectra which were analyzed for different relative concentrations of DMP^- and Mg^{2+}.

An analysis of the relative concentrations of DMP^-, Mg^{2+}, their counterions Na^+ and Cl^-, and water shows that there is a significant fraction of DMP^-/Mg^{2+} contact ion pairs, i.e., DMP^- populates a site in the comparably rigid first hydration layer around Mg^{2+} which consists (in absence of DMP^-) of 6 water molecules

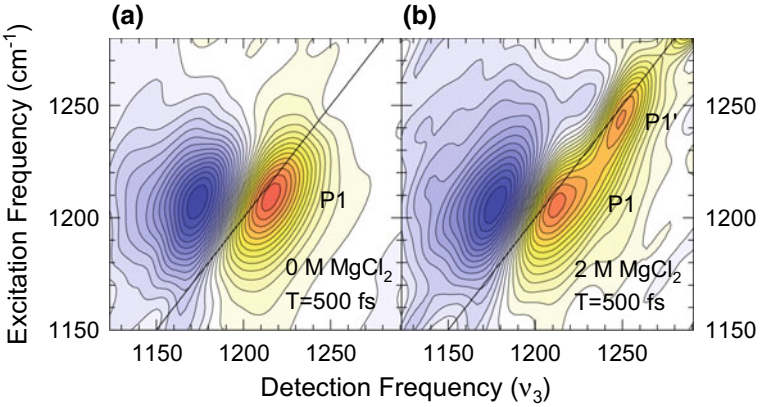

Fig. 8.9 Absorptive 2D-IR spectra of **a** dimethyl phosphate with sodium counterions (DMP-Na) in H_2O and **b** DMP-Na and 2 M $Mg(H_2O)_6Cl_2$ in H_2O. The spectra were recorded at a waiting time T = 500 fs. The 2D signal difference between neighboring contour lines is 7.5%

in an octahedral geometry. The strong interaction between the two ions in contact induces a blue-shift of the asymmetric PO_2^- stretching vibration of the phosphate group. The microscopic origin of this behavior was identified in ab-initio simulations (Sect. 8.2.3.3) on $DMP^-(H_2O)_xMg^{2+}$ clusters with $x = 19$ water molecules. For large distances, i.e., three water layers between Mg^{2+} and DMP^-, the frequency of the P1 mode is close to its value without any magnesium ions. Upon reducing the distance between the two ions, the P1 mode first displays a red-shift which is due to a spatial orientation of water molecules between the ions. The oriented water molecules exert a stronger electric field on the P1 oscillator, thus inducing the red-shift of its fundamental ($v = 0-1$) frequency. For even shorter distances with the DMP^- and Mg^{2+} ions in contact, the repulsive part of the ion-ion interaction prevails and induces a pronounced blue-shift of the P1 fundamental frequency. The calculated frequency shifts are in good agreement with the experimental results.

The application of phosphate vibrations as probes for contact ion pairs and, potentially, other ion configurations holds strong potential for analyzing the ion distribution around DNA and RNA on a multitude of time scales, ranging from hundreds of femtoseconds up to the micro- and millisecond time range of folding processes and other slower structure changes. Such work is presently underway.

References

1. H.J. Bakker, J.L. Skinner, Chem. Rev. **110**, 1498 (2010)
2. E.T.J. Nibbering, T. Elsaesser, Chem. Rev. **104**, 1887 (2004)
3. D. Laage, T. Elsaesser, J.T. Hynes, Chem. Rev. **117**, 10694 (2017)
4. P.L. Silvestrelli, M. Parrinello, Phys. Rev. Lett. **82**, 3308 (1999)
5. D. Laage, J.T. Hynes, Science **311**, 832 (2006)

6. S. Ashihara, N. Huse, A. Espagne, E.T.J. Nibbering, T. Elsaesser, J. Phys. Chem. A **111**, 743 (2007)
7. W. Saenger, W.N. Hunter, O. Kennard, Nature **324**, 385 (1986)
8. H.R. Drew, R.E. Dickerson, J. Mol. Biol. **151**, 535 (1981)
9. D. Vlieghe, J.P. Turkenburg, L. Van Meervelt, Acta Cryst. D Biol. Cryst. **55**, 1495 (1999)
10. B. Schneider, K. Patel, H.M. Berman, Biophys. J. **75**, 2422 (1998)
11. M. Egli, V. Tereshko, M. Teplova, G. Minasov, A. Joachimiak, R. Sanishvili, C.M. Weeks, R. Miller, M.A. Maier, H. An, P.D. Cook, M. Manoharan, Biopolymers **48**, 234 (1998)
12. S.K. Pal, A.H. Zewail, Chem. Rev. **104**, 2099 (2004)
13. D. Zhong, S.K. Pal, A.H. Zewail, Chem. Phys. Lett. **503**, 1 (2011)
14. D. Andreatta, J.L. Pérez Lustres, S.A. Kovalenko, N.P. Ernsting, C.J. Murphy, R.S. Coleman, M.A. Berg, J. Am. Chem. Soc. **127**, 7270 (2005)
15. B. Halle, L. Nilsson, J. Phys. Chem. B **113**, 8210 (2009)
16. K.E. Furse, S.A. Corcelli, J. Am. Chem. Soc. **130**, 13103 (2008)
17. M. Yang, Ł. Szyc, T. Elsaesser, J. Phys. Chem. B **115**, 13093 (2011)
18. T. Siebert, B. Guchhait, Y. Liu, R. Costard, T. Elsaesser, J. Phys. Chem. B **119**, 9670 (2015)
19. P. Hamm, M. Zanni, *Concepts and Methods of 2D Infrared Spectroscopy* (Cambridge University Press, Cambridge, 2011)
20. M. Cho, *Two-Dimensional Optical Spectroscopy* (CRC Press, Boca Raton, 2009)
21. B. Guchhait, Y. Liu, T. Siebert, T. Elsaesser, Struct. Dyn. **3**, 043202 (2016)
22. T. Siebert, B. Guchhait, Y. Liu, B.P. Fingerhut, T. Elsaesser, J. Phys. Chem. Lett. **7**, 3131 (2016)
23. Y. Liu, B. Guchhait, T. Siebert, B.F. Fingerhut, T. Elsaesser, Struct. Dyn. **4**, 044015 (2017)
24. R. Costard, T. Tyborski, B.P. Fingerhut, T. Elsaesser, J. Chem. Phys. **142**, 212406 (2015)
25. R. Costard, T. Tyborski, B.P. Fingerhut, Phys. Chem. Chem. Phys. **17**, 29906 (2015)
26. B.P. Fingerhut, R. Costard, T. Elsaesser, J. Chem. Phys. **145**, 115101 (2016)
27. K. Tanaka, Y. Okahata, J. Am. Chem. Soc. **118**, 10679 (1996)
28. J.R. Dwyer, Ł. Szyc, E.T.J. Nibbering, T. Elsaesser, Rev. Sci. Instrum. **84**, 036101 (2013)
29. M. Falk, K.A. Hartman, R.C. Lord, J. Am. Chem. Soc. **85**, 387 (1963)
30. M. Banyay, M. Sarkar, A. Gräslund, Biophys. Chem. **104**, 477 (2003)
31. Y. Guan, G.J. Thomas, Biopolymers **39**, 813 (1996)
32. E.M. Bruening, J. Schauss, T. Siebert, B.P. Fingerhut, T. Elsaesser, J. Phys. Chem. Lett. **9**, 583 (2018)
33. M.L. Cowan, B.D. Bruner, N. Huse, J.R. Dwyer, B. Chugh, E.T.J. Nibbering, T. Elsaesser, R.J.D. Miller, Nature **434**, 199 (2005)
34. M. Khalil, N. Demirdöven, A. Tokmakoff, J. Phys. Chem. A **107**, 5258 (2003)
35. S. Kirmizialtin, A.R.J. Silalahi, R. Elber, M.O. Fenley, Biophys. J. **102**, 829 (2012)
36. M.A. Young, B. Jayaram, D.L. Beveridge, J. Phys. Chem. B **102**, 7666 (1998)
37. B. Jayaram, K.A. Sharp, B. Honig, Biopolymers **28**, 975 (1989)
38. A. Cuervo, P.D. Dans, J.L. Carrascosa, M. Orozco, G. Gomila, L. Fumagalli, Proc. Natl. Acad. Sci. USA **111**, E3624 (2014)
39. P. Ren, J. Chun, D.G. Thomas, M.J. Schnieders, M. Marucho, J. Zhang, N.A. Baker, Quart. Rev. Biophys. **45**, 427 (2012)
40. G.A. Cisneros, M. Karttunen, P. Ren, C. Sagui, Chem. Rev. **114**, 779 (2014)
41. P.D. Dans, J. Walther, H. Gómez, M. Orozco, Curr. Opin. Struct. Biol. **37**, 29 (2016)
42. D.L. Beveridge, G. Barreiro, K.S. Byun, D.A. Case, T.E. Cheatham, S.B. Dixit, E. Giudice, F. Lankas, R. Lavery, J.H. Maddocks, R. Osman, E. Seibert, H. Sklenar, G. Stoll, K.M. Thayer, P. Varnai, M.A. Young, Biophys. J. **87**, 3799 (2004)
43. A. Pérez, I. Marchán, D. Svozil, J. Sponer, T.E. Cheatham, C.A. Laughton, M. Orozco, Biophys. J. **92**, 3817 (2007)
44. I. Ivani, P.D. Dans, A. Noy, A. Pérez, I. Faustino, A. Hospital, J. Walther, P. Andrio, R. Goñi, A. Balaceanu, G. Portella, F. Battistini, J.L. Gelpí, C. González, M. Vendruscolo, C.A. Laughton, S.A. Harris, D.A. Case, M. Orozco, Nat. Methods **13**, 55–58 (2016)
45. K. Hart, N. Foloppe, C.M. Baker, E.J. Denning, L. Nilsson, A.D. MacKerell, J. Chem. Theory Comput. **8**, 348 (2012)

46. R. Galindo-Murillo, D.R. Roe, T.E. Cheatham III, Nat. Commun. **5**, 5152 (2014)
47. R. Galindo-Murillo, J.C. Robertson, M. Zgarbová, J. Šponer, M. Otyepka, P. Jurečka, T.E. Cheatham, J. Chem. Theory Comp. **12**, 4114 (2016)
48. P.D. Dans, I. Ivani, A. Hospital, G. Portella, C. González, M. Orozco, Nucl. Acids Res. **45**, 4217 (2017)
49. J. Šponer, P. Banáš, P. Jurečka, M. Zgarbová, P. Kührová, M. Havrila, M. Krepl, P. Stadlbauer, M. Otyepka, J. Phys. Chem. Lett. **5**, 1771 (2014)
50. J. Šponer, G. Bussi, M. Krepl, P. Banáš, S. Bottaro, R.A. Cunha, A. Gil-Ley, G. Pinamonti, S. Poblete, P. Jurečka, N.G. Walter, M. Otyepka, Chem. Rev. **118**, 4177 (2018)
51. O. Allnér, L. Nilsson, A. Villa, J. Chem. Theory Comput. **8**, 1493 (2012)
52. J. Yoo, A. Aksimentiev, J. Phys. Chem. Lett. **3**, 45 (2012)
53. T. Martinek, E. Duboué-Dijon, Š. Timr, P.E. Mason, K. Baxová, H.E. Fischer, B. Schmidt, E. Pluhařová, P. Jungwirth, J. Chem. Phys. **148**, 222813 (2018)
54. P. Li, K.M. Merz, Chem. Rev. **117**, 1564 (2017)
55. R. Lavery, J.H. Maddocks, M. Pasi, K. Zakrzewska, Nucl. Acids Res. **42**, 8138 (2014)
56. R. Salomon-Ferrer, A.W. Götz, D. Poole, S. Le Grand, R.C. Walker, J. Chem. Theory Comput. **9**, 3878 (2013)
57. S. Páll, B. Hess, Comput. Phys. Commun. **184**, 2641 (2013)
58. P. Ren, J.W. Ponder, J. Phys. Chem. B **107**, 5933 (2003)
59. P. Tröster, K. Lorenzen, P. Tavan, J. Phys. Chem. B **118**, 1589 (2014)
60. J.W. Ponder, C. Wu, P. Ren, V.S. Pande, J.D. Chodera, M.J. Schnieders, I. Haque, D.L. Mobley, D.S. Lambrecht, J. Robert A. DiStasio, M. Head-Gordon, G.N.I. Clark, M.E. Johnson, T. Head-Gordon, J. Phys. Chem. B **114**, 2549 (2010)
61. I. Kuo, D.J. Tobias, J. Phys. Chem. B **105**, 5827 (2001)
62. E.A. Ploetz, A.S. Rustenburg, D.P. Geerke, P.E. Smith, J. Chem. Theory Comput. **12**, 2373 (2016)
63. G.A. Cisneros, K.T. Wikfeldt, L. Ojamäe, J. Lu, Y. Xu, H. Torabifard, A.P. Bartók, G. Csányi, V. Molinero, F. Paesani, Chem. Rev. **116**, 7501 (2016)
64. P.N. Day, J.H. Jensen, M.S. Gordon, S.P. Webb, W.J. Stevens, M. Krauss, D. Garmer, H. Basch, D. Cohen, J. Chem. Phys. **105**, 1968 (1996)
65. M.S. Gordon, M.A. Freitag, P. Bandyopadhyay, J.H. Jensen, V. Kairys, W.J. Stevens, J. Phys. Chem. A **105**, 293 (2001)
66. M.S. Gordon, D.G. Fedorov, S.R. Pruitt, L.V. Slipchenko, Chem. Rev. **112**, 632 (2012)
67. I.A. Kaliman, L.V. Slipchenko, J. Comput. Chem. **34**, 2284 (2013)
68. N.M. Levinson, E.E. Bolte, C.S. Miller, S.A. Corcelli, S.G. Boxer, J. Am. Chem. Soc. **133**, 13236 (2011)
69. S.D. Fried, S.G. Boxer, Acc. Chem. Res. **48**, 998 (2015)
70. H. Kim, M. Cho, Chem. Rev. **113**, 5817 (2013)
71. B. Błasiak, C.H. Londergan, L.J. Webb, M. Cho, Acc. Chem. Res. **50**, 968 (2017)
72. J. Schauss, F. Dahms, B.F. Fingerhut, T. Elsaesser, J. Phys. Chem. Lett. **10**, 238 (2019)
73. S. Mukamel, *Principles of Nonlinear Optical Spectroscopy*, 3rd edn., Oxford Series on Optical and Imaging Sciences (Oxford University Press, USA, 1999)
74. M.L. Kopka, A.V. Fratini, H.R. Drew, R.E. Dickerson, J. Mol. Biol. **163**, 129 (1983)
75. M. Egli, S. Portmann, N. Usman, Biochemistry **35**, 8489 (1996)
76. T.l.C. Jansen, B. Auer, M. Yang, J.L. Skinner, J. Chem. Phys. **132**, 224503 (2010)
77. E. Duboue-Dijon, A.C. Fogarty, J.T. Hynes, D. Laage, J. Am. Chem. Soc. **138**, 7610 (2016)
78. R. Das, T.T. Mills, L.W. Kwok, G.S. Maskel, I.S. Millett, S. Doniach, K.D. Finkelstein, D. Herschlag, L. Pollack, Phys. Rev. Lett. **90**, 188103 (2003)

Chapter 9
Two-Dimensional Terahertz-Infrared-Visible Spectroscopy Elucidates Coupling Between Low- and High-Frequency Modes

Laura Vietze, Mischa Bonn and Maksim Grechko

Abstract Elucidating the interaction between low-frequency modes and other degrees of freedom in soft and hard condensed matter is both scientifically intriguing, technologically important and experimentally challenging. Specifically, revealing the coupling between collective low-frequency and localized high-frequency vibrations in molecules and solids can advance models for energy relaxation and dissipation in such systems, as well as provide new insight into the physical nature of the low-frequency vibrations. The latter is particularly important, since low-frequency vibrations are thermally excited at room temperature and contribute significantly to the thermodynamic properties and functions, such as heat capacity and entropy. To measure the coupling between low- and high-frequency modes, we have developed two-dimensional terahertz-infrared-visible spectroscopy. In this chapter, we describe the experimental approach and theoretical formalism for this new spectroscopy technique and illustrate its application with two examples: liquid water and solid perovskite semiconductors.

9.1 Introduction

Molecular vibrational motions play a pivotal role in condensed phase chemical and biochemical reactions. Because of the quantum nature of molecules, their vibrations can usually occupy only discrete energy levels. The discreteness of the vibrational energy levels is crucial for the role that a given mode plays in molecular dynamics and thermodynamics. Vibrational modes with energy quanta (usually called frequency) comparable to or less than the thermal energy kT are excited at temperature T, in a manner defined by the Boltzmann distribution. Such vibrations constitute thermal fluctuations of a molecular system contributing significantly to its thermodynamic properties and functions, such as heat capacity and entropy [1]. On the microscopic

L. Vietze · M. Bonn (✉) · M. Grechko
Department of Molecular Spectroscopy, Max Planck Institute for Polymer Research, Ackermannweg 10, 55128 Mainz, Germany
e-mail: bonn@mpip-mainz.mpg.de

M. Cho (ed.), *Coherent Multidimensional Spectroscopy*,
Springer Series in Optical Sciences 226,
https://doi.org/10.1007/978-981-13-9753-0_9

scale, thermal fluctuations actuate the exchange between molecular conformations [2, 3] and can even break covalent bonds [4], promoting chemical reactions. In contrast, vibrational modes with energy quanta (frequency) significantly bigger than kT are usually not thermally excited, and their contribution to molecular thermodynamics is rather small. However, such modes can be populated transiently in a chemical reaction, facilitating energy relaxation and dissipation. In chemistry and biology, such modes are often used, due to their sensitivity, as probes of the molecular environment, conformation, and fluctuations. Thus, based on their energy quanta ω_i, we can classify molecular vibrations into two groups—low-frequency modes (LFMs, with low ω_i) and high-frequency modes (HFMs, with high ω_i).

Around room temperature ($T \approx 25\,^{\circ}\mathrm{C}$), which is typical for many chemical and biological systems, the thermal energy $kT \approx 200\,\mathrm{cm}^{-1}$. At this temperature the energy of $\sim$1000 cm^{-1} separates the states with a population of >1 and $<1\%$, and we can use this energy as a criterion for our classification of LFMs ($\omega_i < 1000\,\mathrm{cm}^{-1}$) and HFMs ($\omega_i > 1000\,\mathrm{cm}^{-1}$). With this classification, the frequencies of the LFMs are in the terahertz (far-infrared) frequency range, and those of HFMs are in the mid-infrared frequency range.

In the condensed phase, even as disordered as liquids, HFMs are typically sparse and characteristic for distinct chemical groups. The chemically-specific character of the HFMs stems from their localized nature—usually, these modes are associated with the motion of only a few atoms. For example, the O–H stretch, C–H stretch, C=O stretch vibrations mainly involve two to three atoms. In an absorption spectrum, these modes generate well-resolved peaks and are widely used to characterize the chemical and structural composition of a sample.

In contrast, the LFMs are often very broad and overlap even for chemically simple materials, such as water. These modes are typically collective and delocalized, i.e., they involve the motion of several to many atoms (for example phonons). On the one hand, the collective nature of the LFMs makes them attractive probes of material properties on the microscopic scale. In particular, intermolecular LFMs can provide information on the intermolecular forces and configurations [5]. On the other hand, analysis of the absorption spectra in the terahertz (far-infrared) spectral range is usually extremely challenging because of the spectral congestion, large anharmonicity and thermal population of the LFMs.

From 2D IR spectroscopy, we know that measuring correlations for molecular vibrations can greatly facilitate the analysis [6]. For instance, correlations measured by 2D IR spectroscopy for the same vibrational mode can distinguish homogeneous and inhomogeneous broadening of that vibrational mode. Correlations between different modes measured by cross-peaks in the 2D IR spectrum reflect the coupling between the corresponding motions, which reveals the otherwise hidden dynamics and can greatly assist in elucidating the molecular structure.

Inspired by the advances in the 2D IR spectroscopy, one can expect that resolving the correlations between LFMs can facilitate their analysis as well, and reveal their nature. To this end, measuring correlations between the LFMs and HFMs can be particularly beneficial. Such correlations can provide two types of information. On the one hand, from the HFM perspective, the coupling between the LFMs and HFMs

provides information on important HFM dynamics, including the energy relaxation and dephasing mechanisms and rates. On the other hand, from the LFM perspective, the coupling can provide insight into how LFMs are related to specific chemical groups inside a complex molecular material, thus enabling a "chemically-resolved" spectroscopy of the delocalized, and less chemically specific LFMs.

We note that the coupling between the LFMs and HFMs is indirectly measured by spectral diffusion in the 2D IR spectra. However, to clarify which LFM is affecting the HFM requires modeling and, typically, temperature dependent measurements. The direct measurement of the coupling between the HFMs and LFMs is therefore highly desirable.

To directly measure the coupling between the LFMs and HFMs, we have extended the approach of the 2D DOVE spectroscopy [7–9] by developing two-dimensional Terahertz-InfraRed-Visible (2D TIRV) spectroscopy. This nonlinear spectroscopy technique measures cross-peaks between the LFMs and HFMs (Fig. 9.1) and is based on the resonant enhancement of four-wave mixing of the terahertz (THz), infrared (IR) and visible (VIS) electromagnetic pulses in a sample. In the following sections, we discuss the experimental implementation and theoretical formalism for the 2D TIRV spectroscopy. We illustrate the utilization of the 2D TIRV spectroscopy by the studies of vibrational coupling in liquid water and hybrid organic-inorganic perovskite semiconductors.

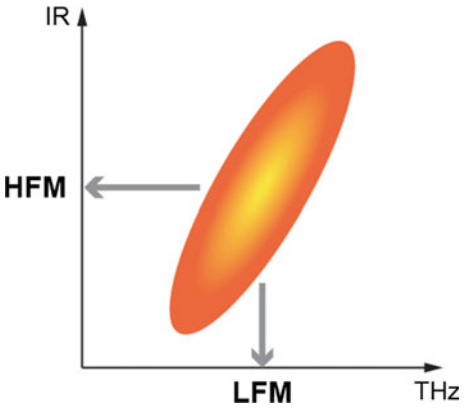

Fig. 9.1 Schematic diagram of a 2D TIRV spectrum. The abscissa axis represents the frequencies of the LFMs in the terahertz frequency range. The ordinate axis is associated with the frequencies of the HFMs in the mid-infrared frequency range. A cross-peak in this 2D plot reflects the coupling between the LFM and HFM. The center line slope of the cross-peak indicates a positive correlation between the frequencies of the HFM and LFM due to the inhomogeneity of the system

9.2 Experimental Implementation

To measure cross-peaks between the LFMs and HFMs, one needs to generate a signal which is enhanced by resonances with both LFM and HFM transitions. The lowest-order optical process that allows generating such signals, and is not forbidden in centrosymmetric materials, is four-wave mixing (FWM), with at least one beam at THz and one at IR frequencies. Although different excitation schemes can be employed for 2D TIRV spectroscopy, we use the excitation scheme shown in Fig. 9.2a. In this scheme, the interaction of a material with the THz, IR and VIS pulses (Fig. 9.2b)—each interacting once with the sample—generates a nonlinear polarization which emits the signal. The polarization and, thus, the signal, is enhanced by the resonances with the LFMs ($(|1\rangle)$) and HFMs ($(|2\rangle)$), given that there is coupling between these vibrational modes. The advantage of this excitation scheme is that it uses only one interaction between the sample and the usually weak THz pulse. This results in a more intense signal compared to the schemes which employ two interactions between the sample and the THz electromagnetic field. Also, using the VIS pulse produces a signal at visible frequencies (600–700 nm), where very sensitive detectors are available.

Our experimental 2D TIRV setup is shown schematically in Fig. 9.3. The output of an amplified femtosecond Ti:Sapphire laser with 1 kHz repetition rate and a central wavelength of 800 nm (60 nm full width at half maximum, FWHM) is split into *beam 1* (≈1 mJ/pulse), *2* (≈0.4 mJ/pulse) and *3* (≈1 mJ/pulse) to generate the IR, VIS and THz pulses, respectively.

Beam 1 pumps a TOPAS (traveling-wave optical parametric amplifier) system, which generates a broadband IR beam (∼400 cm^{-1} FWHM) with a tunable center frequency. The center frequency of the IR is tuned in resonance with the HFMs of the sample. To produce the VIS beam, we spectrally narrow *beam 2* to ∼30 cm^{-1} FWHM by passing it through a Fabry-Pérot interferometer (*FPI*). We combine the IR and the VIS beams using a beam combiner (*BC*) and focus them using a 20 cm CaF_2 lens (*L1*). For our measurements, we use an optical configuration in which the focus of the IR beam is at the sample, and the VIS beam is focused 1.5 cm in front of the sample. We use *beam 3* to generate the broadband THz pulse by two-color

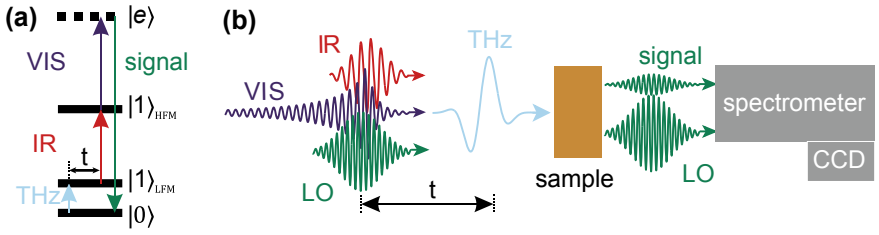

Fig. 9.2 **a** Energy level diagram for the four-wave mixing light-matter interactions used in 2D TIRV spectroscopy. **b** Scheme of 2D TIRV spectroscopy demonstrating the electromagnetic pulses used in the four-wave mixing and detection of the signal

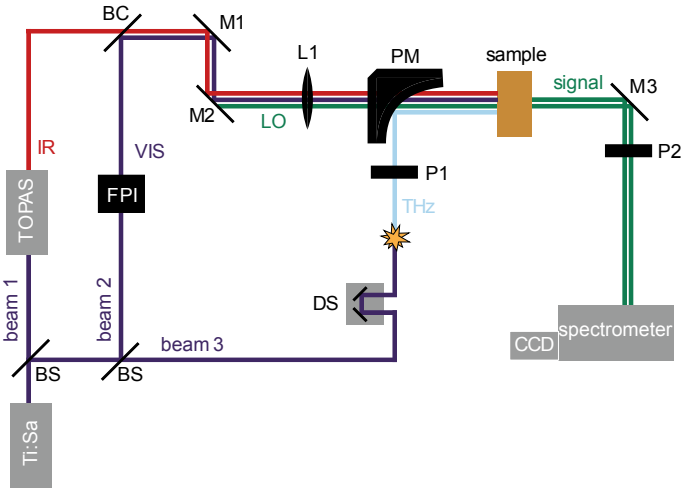

Fig. 9.3 Layout of the setup for 2D TIRV spectroscopy. The setup consists of the following optical and optomechanical components: beam combiner (*BC*); beam splitter (*BS*), protected gold-coated mirrors (*M1*, *M2,* and *M3*); lens (1); parabolic mirror (*PM*); delay stage (*DS*); THz polarizer (*P1*); optical polarizer (*P2*); Fabry-Pérot interferometer (*FPI*); spectrometer and detector (*CCD* camera)

femtosecond laser mixing in gas plasma [10–12]. To this end, we focus *beam 3* in air using a lens ($f = 20$ cm). The focused femtosecond pulse produces air plasma. About 5 cm before the focus we install a 100 μm thick beta barium borate (β-BBO) crystal on the beam pathway to generate the second harmonic of the *pulse 3*. Mixing of the ultrafast 800 nm and 400 nm electromagnetic fields in the air plasma results in the emission of a coherent and spectrally broad THz pulse ($20-450\ \mathrm{cm}^{-1}/0.6-13$ THz). The THz pulse is focused at the sample by the parabolic mirror (*PM*), and spatially overlapped with the IR and VIS beams. An optical delay stage (*DS*) allows to control the temporal delay between the terahertz pulse and the IR/VIS pulse pair.

Four-wave mixing (FWM) of the THz, IR and VIS electromagnetic fields in the sample generates a signal at visible frequencies ($\omega_{VIS} + \omega_{IR} \pm \omega_{THz}$). For 2D TIRV spectroscopy we measure the electric field of the signal, rather than its intensity. To this end, we use heterodyne detection by mixing the signal field with the local oscillator (*LO*) field. The latter is produced by sum-frequency generation of the IR and VIS pulses at the mirrors *M1* and *M2* (Fig. 9.3). The signal and the LO are aligned to the spectrometer, and a spectrally resolved interference of these two fields is measured by a CCD camera.

A 2D TIRV spectrum has the frequency axes ω_1 and ω_2. As explained in detail in the next section, the ω_2 frequencies are associated with the HFM resonances and the ω_1 frequencies reflect the LFM resonances in the sample. To derive the ω_2 axis we subtract the frequency of the VIS pulse from the frequency of the signal, which is given by the spectrometer. The ω_1 axis is obtained by the time-domain approach. For this, we measure the signal field (interference between the signal and LO) for different time delays t between the THz pulse and the IR/VIS pulse pair.

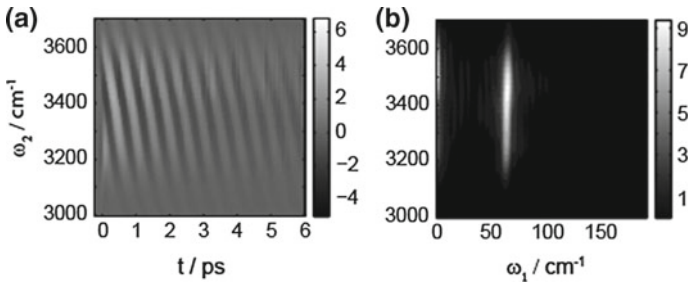

Fig. 9.4 2D TIRV data for the model sample—a CaF_2 crystal. **a** The time-domain 2D TIRV data is given by the interference between the signal and the local oscillator at different time delays t. **b** The absolute-value 2D TIRV spectrum is obtained by a Fourier transform of the time-domain data of (**a**)

The working principle underlying 2D TIRV spectroscopy can be nicely demonstrated by a CaF_2 model sample. In the CaF_2 crystal, the short THz pulse coherently excites phonon modes. The evolution of the excited phonon polarization is probed at varying time delays t by the IR/VIS pulse pair, as shown in Fig. 9.4a. The 2D TIRV spectrum can be derived from the time-domain data by Fourier transforming along the time axis t (for each ω_2 frequency), to obtain the ω_1 frequencies.

As shown in Fig. 9.4b, the absolute-value 2D TIRV spectrum of CaF_2 has one peak. Location and linewidth of this peak along the ω_1 axis are determined by, respectively, the frequency ($67\,cm^{-1}$) and lifetime ($\sim 3\,ps$) of the excited phonon coherence. Because the interaction with the IR field is non-resonant for CaF_2, the location and linewidth of the peak along the ω_2 axis are determined by the central frequency and bandwidth of the IR pulse, respectively.

9.3 Theoretical Formalism

In optical spectroscopies, molecular properties determine the linear and non-linear response functions $S^{(1)}$ and $S^{(n)}$, respectively. Deducing molecular properties from the experimental spectra requires, first of all, knowledge of the relationship between the signal measured by the detector and the corresponding response function of a sample. The same is true also for 2D TIRV spectroscopy, for which we need to determine how the signal at the detector relates to the third-order non-linear response function $S^{(3)}$ of the material. In the present section, we derive this relationship and illustrate it with a few theoretical model examples.

The electric field $E^{(3)}$ of the 2D TIRV signal is emitted by a sample after three interactions with the three relevant electromagnetic fields: one with the THz, one with the IR and one with the VIS pulse. The signal field is proportional to the third-order non-linear polarization generated by the material-light interactions. Thus, by employing the frequency domain formalism for the third-order nonlinear response

function ((5.32) in [13]) we obtain the signal field for a time delay τ of the THz pulse:

$$E^{(3)}(t,\tau) \propto \iiint d\omega_1 d\omega_2 d\omega_3 S^{(3)}(\omega_1+\omega_2+\omega_3,\omega_1 + \omega_2,\omega_1)\; E_{\mathrm{THz}}(\omega_1)e^{-i\omega_1\tau}E_{\mathrm{IR}}(\omega_2)E_{\mathrm{VIS}}(\omega_3)e^{-i\omega_s t}, \tag{9.1}$$

where t is the time; frequency $\omega_s = \omega_1+\omega_2+\omega_3$; $E_{\mathrm{THz}}(\omega_1)$, $E_{\mathrm{IR}}(\omega_2)$ and $E_{\mathrm{VIS}}(\omega_3)$ are electric fields of the THz, IR and VIS pulses at the frequencies ω_1, ω_2 and ω_3, respectively. We note that the integration in (9.1) is performed from $-\infty$ to $+\infty$, i.e. the frequencies take on both negative and positive values. In (9.1) the field $E^{(3)}$ changes with the time t and depends parametrically on the time delay τ: the time-dependent field is calculated for each delay time τ. In our experiment we use a local oscillator (LO) for the heterodyne detection of the signal. Thus, the total electromagnetic wave after the sample is:

$$E^{\mathrm{tot}}(t,\tau) = E_{\mathrm{LO}}(t) + E^{(3)}(t,\tau) \propto E_{\mathrm{LO}}(t) + \iiint d\omega_1 d\omega_2 d\omega_3 S^{(3)}(\omega_1+\omega_2+\omega_3,\omega_1+\omega_2,\omega_1) E_{\mathrm{THz}}(\omega_1)e^{-i\omega_1\tau}E_{\mathrm{IR}}(\omega_2)E_{\mathrm{VIS}}(\omega_3)e^{-i\omega_s t}, \tag{9.2}$$

where $E_{\mathrm{LO}}(t)$ is the electric field of the local oscillator. These combined fields are guided to the spectrometer, where they are dispersed by the grating. This dispersion is mathematically described by a Fourier transform of the field $E^{\mathrm{tot}}(t,\tau)$ over time t:

$$\begin{aligned} E^{\mathrm{tot}}\left(\Omega_3^{'},\tau\right) &= \mathrm{FT}\left[E_{\mathrm{LO}}(t)+E^{(3)}(t,\tau)\right] \propto E_{\mathrm{LO}}\left(\Omega_3^{'}\right)+E^{(3)}\left(\Omega_3^{'},\tau\right) \\ &= E_{\mathrm{LO}}\left(\Omega_3^{'}\right) \\ &\quad + \iiint d\omega_1 d\omega_2 d\omega_3 S^{(3)}(\omega_1+\omega_2+\omega_3,\omega_1+\omega_2,\omega_1) \\ &\quad E_{\mathrm{THz}}(\omega_1)e^{-i\omega_1\tau}E_{\mathrm{IR}}(\omega_2)E_{\mathrm{VIS}}(\omega_3)\delta\left(\Omega_3^{'}-\omega_s\right), \end{aligned} \tag{9.3}$$

where $E_{\mathrm{LO}}\left(\Omega_3^{'}\right)$ is the electric field of the LO at frequency $\Omega_3^{'}$ and δ is the Dirac delta function. The frequency $\Omega_3^{'}$ in (9.3) can have both positive and negative values. After the grating, spectral components of light at $+\Omega_3^{'}$ and $-\Omega_3^{'}$ travel in the same direction. This co-propagation of spectral components at frequencies with opposite sign ensures that the electromagnetic field is a real-valued function of space and time coordinates. The signal intensity A measured by the square-law detector (CCD camera) for the detection frequency $\Omega_3 \geq 0$ and integrated over accumulation time period T is given by:

$$A(\Omega_3,\tau) \propto \int_T \mathrm{d}t\left[E^{\mathrm{tot}}(\Omega_3,\tau)e^{-i\Omega_3 t} + E^{\mathrm{tot}}(-\Omega_3,\tau)e^{i\Omega_3 t}\right]^2$$

$$= \int_T \mathrm{d}t \Big[E^{(3)}(\Omega_3, \tau) e^{-i\Omega_3 t} + E^{(3)}(-\Omega_3, \tau) e^{i\Omega_3 t} + E_{\mathrm{LO}}(\Omega_3) e^{-i\Omega_3 t} + E_{\mathrm{LO}}(-\Omega_3) e^{i\Omega_3 t} \Big]^2. \tag{9.4}$$

By squaring the term under the integral, neglecting terms oscillating at very high frequency ($\sim 2\Omega_3$) and subtracting the homodyne terms of the form $E^{(3)}(\Omega_3, \tau) E^{(3)}(-\Omega_3, \tau)$ and $E_{\mathrm{LO}}(\Omega_3) E_{\mathrm{LO}}(-\Omega_3)$ we obtain the heterodyne-detected part B of the measured signal (B represents the interference between the signal field and the LO):

$$B(\Omega_3, \tau) \propto E^{(3)}(\Omega_3, \tau) E_{\mathrm{LO}}(-\Omega_3) + E^{(3)}(-\Omega_3, \tau) E_{\mathrm{LO}}(\Omega_3). \tag{9.5}$$

The heterodyne-detected signal depends parametrically on the time delay τ of the THz pulse. In the experiment, this dependence appears in the time-domain 2D TIRV data. In order to obtain the 2D TIRV spectrum $\Gamma(\Omega_3, \Omega_1)$ as a function of the detection frequency Ω_3 and the THz frequency Ω_1 we Fourier transform $B(\Omega_3, \tau)$ over τ:

$$\begin{aligned} \Gamma(\Omega_3, \Omega_1) &= \mathrm{FT}[B(\Omega_3, \tau)] \\ &\propto \mathrm{FT}[E^{(3)}(\Omega_3, \tau)] E_{\mathrm{LO}}(-\Omega_3) + \mathrm{FT}[E^{(3)}(-\Omega_3, \tau)] E_{\mathrm{LO}}(\Omega_3) \\ &= E^{(3)}(\Omega_3, \Omega_1) E_{\mathrm{LO}}(-\Omega_3) + E^{(3)}(-\Omega_3, \Omega_1) E_{\mathrm{LO}}(\Omega_3). \end{aligned} \tag{9.6}$$

Using (9.3) we obtain for $E^{(3)}(\Omega_3, \Omega_1)$:

$$\begin{aligned} E^{(3)}(\Omega_3, \Omega_1) &= \mathrm{FT}[E^{(3)}(\Omega_3, \tau)] \\ &\propto \iiint d\omega_1 d\omega_2 d\omega_3 S^{(3)}(\omega_1 + \omega_2 + \omega_3, \omega_1 + \omega_2, \omega_1) \\ &\quad E_{\mathrm{THz}}(\omega_1) \delta(\Omega_1 - \omega_1) E_{\mathrm{IR}}(\omega_2) E_{\mathrm{VIS}}(\omega_3) \delta(\Omega_3 - \omega_s). \end{aligned} \tag{9.7}$$

In the experiment, we use a narrowband VIS pulse with the frequency Ω_{VIS}. Note that Ω_{VIS} is a parameter rather than a variable, and we assume $\Omega_{\mathrm{VIS}} > 0$. Thus, we approximate the VIS spectrum by a delta function:

$$E_{\mathrm{VIS}}(\omega_3) = \delta(\Omega_{\mathrm{VIS}} - \omega_3) + \delta(\Omega_{\mathrm{VIS}} + \omega_3). \tag{9.8}$$

By substituting (9.8) into (9.7) and performing the integration, we obtain:

$$\begin{aligned} E^{(3)}(\Omega_3, \Omega_1) \propto\ & S^{(3)}(\Omega_3, \Omega_3 - \Omega_{\mathrm{VIS}}, \Omega_1) E_{\mathrm{THz}}(\Omega_1) E_{\mathrm{IR}}(\Omega_3 - \Omega_{\mathrm{VIS}} - \Omega_1) \\ &+ S^{(3)}(\Omega_3, \Omega_3 + \Omega_{\mathrm{VIS}}, \Omega_1) E_{\mathrm{THz}}(\Omega_1) E_{\mathrm{IR}}(\Omega_3 + \Omega_{\mathrm{VIS}} - \Omega_1). \end{aligned} \tag{9.9}$$

Because in our experiment the THz frequency $\Omega_1 \ll \Omega_3 + \Omega_{\mathrm{VIS}}$, the frequency $\Omega_3 + \Omega_{\mathrm{VIS}} - \Omega_1$ is beyond the bandwidth of the IR pulse. Thus, $E_{\mathrm{IR}}(\Omega_3 + \Omega_{\mathrm{VIS}} - \Omega_1) = 0$ and the second term in (9.9) vanishes. Similarly, for

$E^{(3)}(-\Omega_3, \Omega_1)$ we obtain:

$$E^{(3)}(-\Omega_3, \Omega_1) \propto S^{(3)}(-\Omega_3, -\Omega_3 + \Omega_{\mathrm{VIS}}, \Omega_1) E_{\mathrm{THz}}(\Omega_1) E_{\mathrm{IR}}(-\Omega_3 + \Omega_{\mathrm{VIS}} - \Omega_1). \tag{9.10}$$

By substituting (9.10) and (9.9) into (9.6) we obtain for the 2D TIRV spectrum:

$$\begin{aligned}\Gamma(\Omega_3, \Omega_1) \propto\ & S^{(3)}(\Omega_3, \Omega_3 - \Omega_{\mathrm{VIS}}, \Omega_1) E_{\mathrm{THz}}(\Omega_1) E_{\mathrm{IR}}(\Omega_3 - \Omega_{\mathrm{VIS}} - \Omega_1) E_{\mathrm{LO}}(-\Omega_3) \\ & + S^{(3)}(-\Omega_3, -\Omega_3 + \Omega_{\mathrm{VIS}}, \Omega_1) E_{\mathrm{THz}}(\Omega_1) E_{\mathrm{IR}}(-\Omega_3 + \Omega_{\mathrm{VIS}} - \Omega_1) E_{\mathrm{LO}}(\Omega_3).\end{aligned} \tag{9.11}$$

For the sake of convenience, we introduce the frequency $\Omega_2 = \Omega_3 - \Omega_{\mathrm{VIS}}$, which is in the IR frequency range, to write (9.11) in the alternative form:

$$\begin{aligned}\Gamma(\Omega_2 + \Omega_{\mathrm{VIS}}, \Omega_1) \propto\ & S^{(3)}(\Omega_2 + \Omega_{\mathrm{VIS}}, \Omega_2, \Omega_1) E_{\mathrm{THz}}(\Omega_1) E_{\mathrm{IR}}(\Omega_2 - \Omega_1) E_{\mathrm{LO}}(-\Omega_2 - \Omega_{\mathrm{VIS}}) \\ & + S^{(3)}(-\Omega_2 - \Omega_{\mathrm{VIS}}, -\Omega_2, \Omega_1) E_{\mathrm{THz}}(\Omega_1) E_{\mathrm{IR}}(-\Omega_2 - \Omega_1) E_{\mathrm{LO}}(\Omega_2 + \Omega_{\mathrm{VIS}}).\end{aligned} \tag{9.12}$$

Thus, in the experiment, the 2D TIRV spectrum is given by the product of the spectrum of the third-order nonlinear response function $S^{(3)}$ with the spectra E_{THz} and E_{IR} of the laser pulses. From (9.12) it follows that Ω_1 and Ω_2 are the frequencies of the coherences excited in the sample after interaction with the THz and the IR pulses, respectively. Because the VIS pulse is narrowband with frequency Ω_{VIS}, it is convenient and more informative to plot the 2D TIRV spectrum $\Gamma(\Omega_3, \Omega_1)$ as a function of the Ω_1 and Ω_2 frequencies, i.e., $\Gamma(\Omega_2, \Omega_1)$ by subtracting Ω_{VIS} from the detection frequency Ω_3. The advantage of doing so is that the Ω_2 frequencies reflect the HFMs resonances of the sample.

Equation 9.12 shows that the 2D TIRV spectra in our experiment are produced by the sum of the $S^{(3)}$ spectra in the two quadrants, (Ω_2, Ω_1) and $(-\Omega_2, \Omega_1)$. This is due to the utilization of the spectrometer to measure the second frequency axis and is analogous to the summation of the rephasing and non-rephasing spectra in the 2D IR spectroscopy employing the pump-probe geometry and a spectrometer.

Let us next consider the spectrum of the response function $S^{(3)}$ for a simple model of two coupled modes, one LFM and one HFM (Fig. 9.5). Figure 9.6 shows four different Liouville excitation pathways for this model. In diagrams **I** and **II**, the interactions with the THz, IR and VIS fields are all on the ket side of the density matrix. Thus, these diagrams represent the sum-frequency generation between all the three beams (first and second terms in (9.12) for $\Omega_1 > 0$ and $\Omega_1 < 0$, respectively). The first two diagrams are distinct in the following manner:

- In diagram **I**, the interactions with the THz and IR fields excite the LFM and HFM, respectively. These excitations are one-quantum transitions, i.e. they change only one vibrational quantum number of the sample at a time. In contrast, at either transition to the excited electronic state $|e\rangle$ induced by the VIS pulse or at the signal

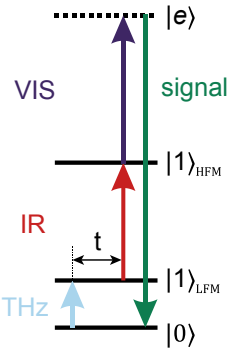

Fig. 9.5 Energy level diagram for the two interacting low-frequency ($|1\rangle_{LFM}$) and high-frequency ($|1\rangle_{HFM}$) vibrational states. Generally speaking, the transition to the electronically excited state $|e\rangle$ can be resonant or non-resonant. In the latter case, the state $|e\rangle$ is usually called a virtual state

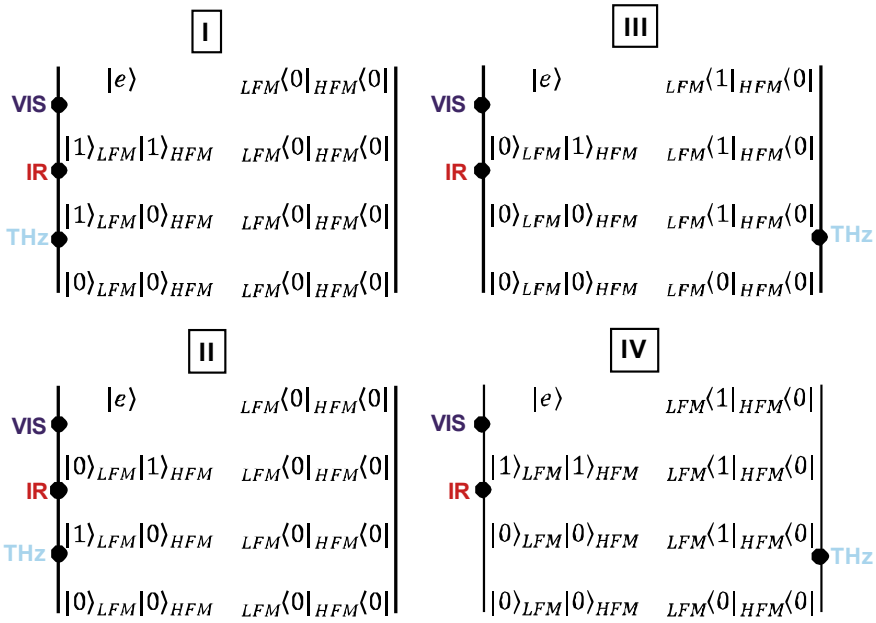

Fig. 9.6 Liouville excitation pathways for the 2D TIRV spectroscopy of the model in Fig. 9.5. Interactions with the laser fields are indicated by *black circles*. The diagrams **I** and **II** (**III** and **IV**) correspond to the $\omega_{\mathrm{VIS}} + \omega_{\mathrm{IR}} + \omega_{\mathrm{THz}}$ ($\omega_{\mathrm{VIS}} + \omega_{\mathrm{IR}} - \omega_{\mathrm{THz}}$) four-wave mixing

emission the sample undergoes a two-quantum transition [7]. This two-quantum transition changes both LFM and HFM quantum numbers simultaneously.
- In diagram **II**, the interaction with the THz pulse excites the LFM mode. The two-quantum transition takes place at the interaction with the IR pulse, which excites the HFM and simultaneously quenches the LFM. The subsequent interaction with the VIS pulse and the signal emission are both one-quantum transitions.

In diagrams **III** and **IV**, the interaction with the THz field occurs on the bra side of the density matrix, and the interactions with the IR and VIS fields are on the ket side. Thus, these diagrams represent signal generation at the sum frequency of the IR and VIS pulses minus frequency of the THz pulse.

- Similar to diagram **I**, in diagram **III**, the interactions with the THz and IR fields excite the LFM and HFM, and the two-quantum transition occurs at the interaction with the VIS pulse as well as for the emission of the signal field.
- Similar to diagram **II**, in diagram **IV**, the THz pulse excites the LFM and the IR pulse induces the two-quantum transition—it simultaneously excites the HFM and the LFM on the ket side of the density matrix. Both the interaction with the VIS pulse and the signal emission proceed via one-quantum transitions.

For all four diagrams in Fig. 9.6 there are complex-conjugate pathways, which can be obtained by changing all interactions from the ket to the bra side of the density matrix and vice versa. Because at least one of the transitions involves a simultaneous change of the vibrational quantum numbers for the HFM and LFM, the 2D TIRV signal requires a coupling between these modes [7, 8]. The coupling can originate from either the mechanical and/or electrical anharmonicity between the vibrations [14].

In our model, we assume the fast modulation (homogeneous) limit for the frequency fluctuation correlation function [6]. The temporal evolution of the LFM coherence $|\rho(t) \gg_{\mathrm{LFM}}$ with the initial conditions $|\rho(0) \gg_{\mathrm{LFM}} = |1\rangle_{\mathrm{LFM}}|0\rangle_{\mathrm{HFM}}{}_{\mathrm{LFM}}\langle 0|_{\mathrm{HFM}}\langle 0|$ is given by:

$$|\rho(t) \gg_{\mathrm{LFM}} = \exp\left(-i\frac{E_{\mathrm{LFM}}}{\hbar}t - \frac{1}{\mathrm{T}_{\mathrm{LFM}}}t\right)|\rho(0) \gg_{\mathrm{LFM}},$$

where $\mathrm{T}_{\mathrm{LFM}}$ is the LFM coherence lifetime and E_{LFM} is the energy of the LFM. Similarly, for the HFM coherence with the initial conditions $|\rho(0) \gg_{\mathrm{HFM}} = |0\rangle_{\mathrm{LFM}}|1\rangle_{\mathrm{HFM}}{}_{\mathrm{LFM}}\langle 0|_{\mathrm{HFM}}\langle 0|$:

$$|\rho(t) \gg_{\mathrm{HFM}} = \exp\left(-i\frac{E_{\mathrm{HFM}}}{\hbar}t - \frac{1}{\mathrm{T}_{\mathrm{HFM}}}t\right)|\rho(0) \gg_{\mathrm{HFM}},$$

where $\mathrm{T}_{\mathrm{HFM}}$ is the HFM coherence lifetime and E_{HFM} is the energy of the HFM. For the coherence $|\rho(t) \gg_e$ in the electronically excited state $|e\rangle$ we assume that the time dependence can be described by:

$$|\rho(t) \gg_e = \exp\left(-i\frac{E_e}{\hbar}t - \frac{1}{\mathrm{T}_e}t\right)|\rho(0) \gg_e,$$

where T_e is the electronic coherence lifetime, E_e is the energy of the excited electronic state $|e\rangle$ and $|\rho(0) \gg_e$ is the initial condition for the electronic coherence.

We assume that the two-quantum transition occurs at the interaction with the IR pulse. Thus the Liouville excitation pathways a given by the diagrams **II** and **IV** in Fig. 9.6. Using the equations above, we can write for the response function in diagram **II**:

$$S^{(3)}_{\mathbf{II}}(t_3, t_2, t_1) = \left(\frac{i}{\hbar}\right)^3 \mu_1\mu_2\mu_3\mu_4 \exp\left(-i\frac{E_e}{\hbar}t_3 - \frac{1}{\mathrm{T}_e}t_3\right) \exp\left(-i\frac{E_{\mathrm{HFM}}}{\hbar}t_2 - \frac{1}{\mathrm{T}_{\mathrm{HFM}}}t_2\right)\exp\left(-i\frac{E_{\mathrm{LFM}}}{\hbar}t_1 - \frac{1}{\mathrm{T}_{\mathrm{LFM}}}t_1\right) \quad (13)$$

where μ_1, μ_2, μ_3 and μ_4 are the transition dipole moments for the THz, IR, VIS excitations and the signal emission, respectively. Figure 9.7 shows the spectrum $S^{(3)}_{\mathrm{II}}(\Omega_2, \Omega_1)$. For this simulation, we have assumed non-resonant conditions for the electronic transition $\left(\frac{E_e}{\hbar} - \frac{1}{\mathrm{T}_e} \gg \Omega_3 = \Omega_2 + \Omega_{\mathrm{VIS}}\right)$ and use the following parameters: $\frac{E_{\mathrm{LFM}}}{\hbar} = 50\,\mathrm{cm}^{-1}$, $\mathrm{T}_{\mathrm{LFM}} = 300\mathrm{fs}$, $\frac{E_{\mathrm{HFM}}}{\hbar} = 3000\,\mathrm{cm}^{-1}$, $\mathrm{T}_{\mathrm{HFM}} = 150\,\mathrm{fs}$. The spectrum $S^{(3)}_{\mathbf{II}}(\Omega_2, \Omega_1)$ has a maximum in the first quadrant, i.e., when $\Omega_1 > 0$ and $\Omega_2 > 0$. Similarly, we can calculate the spectrum $S^{(3)}_{\mathbf{IV}}(\Omega_2, \Omega_1)$, which has a maximum in the second quadrant, i.e., for $\Omega_1 < 0$ and $\Omega_2 > 0$. The third and the fourth quadrants are dominated by the complex conjugate responses $\left(S^{(3)}_{\mathrm{II}}(\Omega_2, \Omega_1)\right)^*$ and $\left(S^{(3)}_{\mathrm{IV}}(\Omega_2, \Omega_1)\right)^*$, respectively.

By taking into account $S^{(3)}_{\mathrm{II}}(\Omega_2, \Omega_1)$, $S^{(3)}_{\mathrm{IV}}(\Omega_2, \Omega_1)$, $\left(S^{(3)}_{\mathrm{II}}(\Omega_2, \Omega_1)\right)^*$, $\left(S^{(3)}_{\mathrm{IV}}(\Omega_2, \Omega_1)\right)^*$ and assuming infinitely broad spectra for the THz, IR and

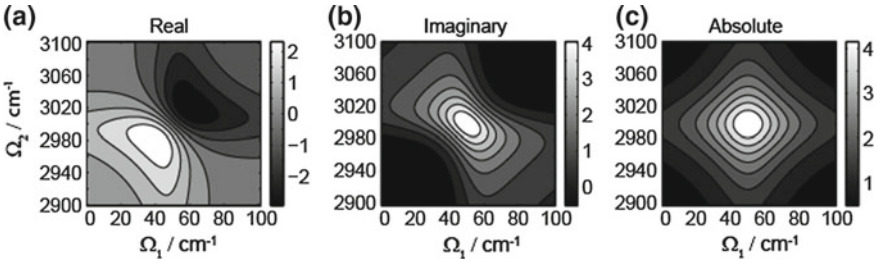

Fig. 9.7 Real- (**a**), imaginary- (**b**), and absolute-value (**c**) spectra for the third order non-linear response function $S^{(3)}_{\mathbf{II}}(\Omega_2,\ \Omega_1)$ for the model of two coupled LFM and HFM oscillators. The LFM oscillator has a frequency of $50\,\mathrm{cm}^{-1}$ and decay time of 300 fs. The HFM oscillator has a frequency of $3000\,\mathrm{cm}^{-1}$ and a decay time of 150 fs

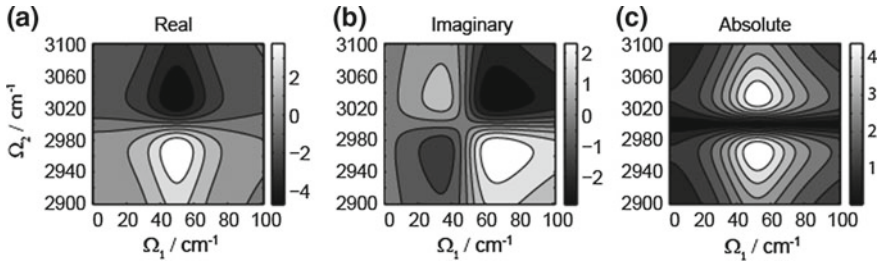

Fig. 9.8 Real- (**a**), imaginary (**b**) and absolute-value (**c**) spectra $\Gamma(\Omega_2,\ \Omega_1)$ for the model of two coupled LFM and HFM oscillators. The LFM and HFM oscillators have frequencies (lifetimes) of 50 cm^{-1}(300 fs) and 3000 cm^{-1} (150 fs), respectively

LO pulses, we can calculate $\Gamma(\Omega_2, \Omega_1)$ using (9.11) (Fig. 9.8). Note that in the spectrum $\Gamma(\Omega_2, \Omega_1)$ the responses in the first $\left(S_{\mathrm{II}}^{(3)}(\Omega_2, \Omega_1)\right)$ and fourth $\left(S_{\mathrm{IV}}^{(3)}(\Omega_2, \Omega_1)\right)^*$ quadrants add up destructively the central frequency of the HFM and produce a nodal line.

9.4 Application: Vibrational Coupling in Water

In liquid water, hydrogen bonding between the molecules arranges them into a short-lived (about 1 ps lifetime) local tetrahedral structure where each molecule donates and accepts, on average, about 3.6 hydrogen bonds [15, 16]. The intermolecular distances and relative orientations of the molecules in the local structure fluctuate on sub-picosecond time-scales [17–19]. These fluctuations constitute the low-frequency intermolecular vibrational modes of neat water. The fluctuations of the hydrogen bond network affect the high-frequency intramolecular vibrations of the water molecules. The intramolecular O–H stretch vibration is particularly sensitive to the configuration of the hydrogen bond network. The frequency and transition dipole moment of this HFM have, respectively, inverse and direct relationship with the strength of the electric field along the O–H bond, which is created by neighboring molecules [20, 21]. Thus, fluctuations of the hydrogen bond network caused by the LFMs perturb the O–H stretch vibration and give rise to the coupling between the LFMs and HFMs in liquid water. Recently, a growing number of studies point to a strong mixing between the LFMs and O–H stretch modes, implying an active role of such mixed states in the chemistry of water [22–24].

We use 2D TIRV spectroscopy to directly measure the coupling between the water LFMs and the O–H stretch vibration [25]. In this study, we focus on the 20−450 cm^{-1} spectral range for the intermolecular vibrations, which comprises mainly the hydrogen bond stretch (≈180 cm^{-1}) and bending (≈60 cm^{-1}) modes. Figure 9.9 shows the absolute-value 2D TIRV spectra for different isotope dilutions of H_2O in D_2O. The spectra for the 5% and 20% H/D ratio are similar and have one dominating

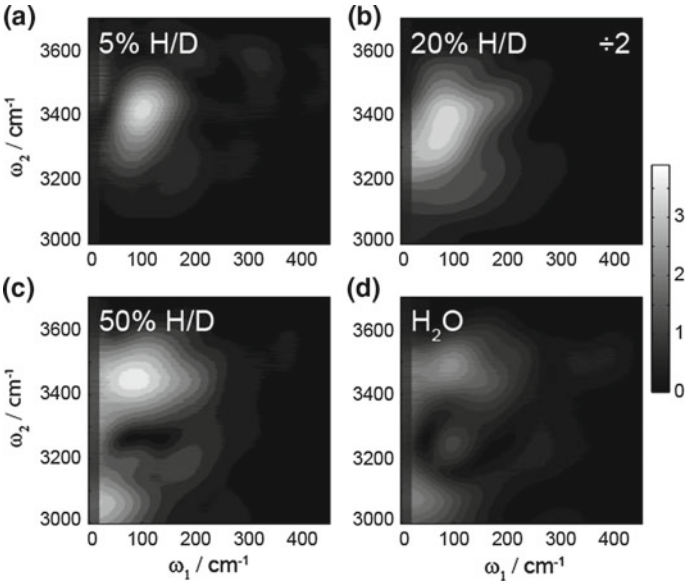

Fig. 9.9 Absolute-value 2D TIRV spectra for **a** 5% H/D, **b** 20% H/D, **c** 50% H/D and **d** 100% H_2O samples

peak. This peak is centered at $\omega_1 \approx 100\,\mathrm{cm}^{-1}$, $\omega_2 \approx 3415\,\mathrm{cm}^{-1}$ for the 5% sample and shifts to the slightly lower ω_2 ($\omega_2 \approx 3370\,\mathrm{cm}^{-1}$) with an increase of the proton concentration to 20%. But when the proton concentration increases further, to 50 and 100%, the line shape of the 2D TIRV spectrum changes substantially. This change is characterized by a significant broadening of the response to the lower ω_2 frequencies and the appearance of a nodal line at $\omega_2 \approx 3270\,\mathrm{cm}^{-1}$. Because the spectrum of the water LFMs in the $20-450\,\mathrm{cm}^{-1}$ frequency range changes only slightly with the change of the H/D ratio, the variation of the 2D TIRV spectrum is due to the new character of the O–H stretch vibration. This variation is caused by two different phenomena: (1) Fermi resonance between the O–H stretch and H–O–H bending modes; (2) excitonic intermolecular delocalization of the O–H stretch vibration. The excitonic delocalization stems from the increasing coupling between the O–H stretch oscillators with increasing proton concentration because of the higher concentration of the OH groups and the resulting smaller average distance between OH groups. The 5% H/D sample contains ~90% of D_2O molecules, 9.5% of HOD and 0.0025% of H_2O molecules. For this sample, the majority of the OH groups are separated and decoupled by D_2O molecules. Thus, the 2D TIRV spectrum for the 5% H/D sample reflects a vibrational coupling for the isolated O–H stretch oscillator. With increasing proton concentration, the average distance between the oscillators decreases—note that neighboring OH groups can be located in the same molecule (H_2O) or in the adjacent HOD/H_2O molecules. The shorter distances result in an increased coupling between the oscillators and an increased average intra- and intermolecular delocalization of the vibration. In addition to the coupling between the

O–H stretch oscillators, H_2O molecules have a Fermi resonance between the O–H stretch and the second excited H–O–H bending state. Increasing concentration of the H_2O species enhances the signal from the mixed stretch-bending states. As a result, the change of the 2D TIRV response can be linked to the appearance of the Fermi resonance and the formation of the vibrational exciton.

A comparison of the experimental 2D TIRV spectra and classical molecular dynamics simulations shows that the broadening of the spectrum to the lower ω_2 frequencies in H_2O is due to the stronger coupling between the LFMs and the red-shifted O–H stretch modes at $\sim 3250\,\mathrm{cm}^{-1}$. At the same time, the spectrum of the LFMs coupled with the O–H stretch oscillator is insensitive to the vibrational delocalization and Fermi resonance of the latter. Both isolated and delocalized O–H stretch are predominantly coupled with the broad spectrum of LFMs in the $50-250\,\mathrm{cm}^{-1}$ frequency range, which can be assigned to the hydrogen bond bending ($\approx 60\,\mathrm{cm}^{-1}$) and stretching ($\approx 180\,\mathrm{cm}^{-1}$) modes.

9.5 Application: Vibrational Coupling in Hybrid Perovskite

The outstanding photovoltaic performance of the perovskite semiconductors has attracted substantial attention, not only for improved devices, but also for the understanding of the fundamental physical properties of these promising materials. In particular, it is intriguing how different degrees of freedom, electronic and nuclear, interplay and influence diverse photophysical properties, such as charge transport, recombination, and hot-carrier relaxation [26]. In this regard, the loosely bound organic molecules inside the inorganic cage of hybrid perovskite are believed to play a substantial role. Although the main discussion in the literature has focused on the direct interaction of the molecular dipole moment with the charge carriers, the vibrational coupling between the organic and inorganic sub-lattices is expected to have an indirect influence on the electronic properties of perovskites.

The low-frequency vibrations in perovskites are the phonon modes of this crystalline material. Previous studies have identified a plethora of the perovskite phonon modes, with energies in the range of $0-150\,\mathrm{cm}^{-1}$ [27, 28]. In fact, the $0-60\,\mathrm{cm}^{-1}$ frequency range in the infrared absorption and Raman spectra of these materials is dominated by the phonons of the inorganic sub-lattice. Vibrations of the perovskite organic sub-lattice are those of the organic ions embedded into the inorganic cage. Some of these molecular motions are collective LFMs with relatively low frequencies, $\sim 60-150\,\mathrm{cm}^{-1}$. Alongside the collective LFMs, the organic ions have localized HFMs, which are specific to the chemical groups composing the ion. For example, methylammonium and formamidinium ions have N–H stretch modes with energies of $\sim 3100-3450\,\mathrm{cm}^{-1}$. A coupling between organic HFMs and inorganic phonons can generate mixed states with relatively high energy and low quantum numbers. Such mixed states can provide additional pathways for the electronic energy relaxation, via strong coupling between the phonon moiety and the excited electronic states [29].

2D TIRV spectroscopy enables a direct measurement of the coupling between the organic HFMs and inorganic LFMs in hybrid perovskites [30]. Figure 9.10 shows experimental spectra for the two prototypical samples, methylammonium lead triiodide ($MAPbI_3$) and mixed formamidinium methylammonium lead triiodide ($FA_{0.8}MA_{0.2}PbI_3$). The spectrum of $MAPbI_3$ has a single peak centered at $\omega_1 = 35\,\mathrm{cm}^{-1}$, $\omega_2 = 3135\,\mathrm{cm}^{-1}$, which reflects the coupling between the symmetric and asymmetric N–H stretch vibrations of the MA^+ on the one hand and the phonon mode on the other. Replacing MA^+ by the FA^+ results in a change of the 2D TIRV line shape along both the ω_1 and ω_2 axes. The change of the spectral profile along the ω_2 axis is in accordance with the difference of the N–H stretch absorption spectra for FA^+ and MA^+. However, the spectral change along the ω_1 axis is in sharp contrast to the almost identical phonon modes in the two types of perovskite. This indicates that the coupling between the N–H stretch mode and the phonons depend not only on the existing phonon vibrations, but also on the structure of the organic cation.

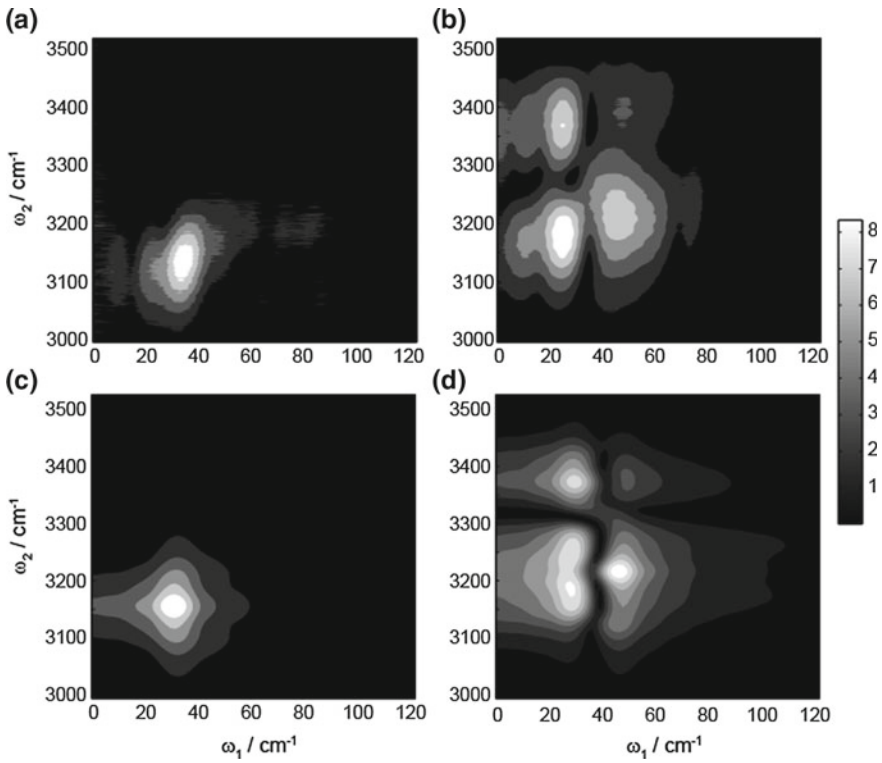

Fig. 9.10 Absolute-value measured 2D TIRV spectra for **a** $MAPbI_3$ and **b** $FA_{0.8}MA_{0.2}PbI_3$ perovskite semiconductors. Absolute-value simulated 2D TIRV spectra for **c** $MAPbI_3$ and **d** $FA_{0.8}MA_{0.2}PbI_3$

The comparison of the measured spectra with the simple model calculations based on (9.12) and (9.13) allows a better insight into the frequencies of the phonons coupled with the N–H stretch oscillator. The experimental data for MA^+ can be reproduced by assuming a coupling with the phonon mode centered at $32\,cm^{-1}$ (Fig. 9.10c). Reproducing the spectrum for FA^+ requires out-of-phase coupling with the two-phonon modes, at $32\,cm^{-1}$ and $45\,cm^{-1}$, respectively (Fig. 9.10d). This simple analysis indicates that for both MA^+ and FA^+ the phonons coupled with the N–H stretch vibration are the octahedral distortion modes of the inorganic PB-I cage.

9.6 Outlook

The development of the two-dimensional optical spectroscopy techniques in the infrared and visible spectral ranges has allowed an insight into the couplings and correlations for nuclear and electronic degrees of freedom with frequencies above $\sim 1000\,cm^{-1}$. This fresh and unique view proved to be highly fruitful and yielded improved models of structure and dynamics for a variety of systems in chemistry, biology and materials science. 2D TIRV spectroscopy enables the advantages of the 2D spectroscopy methods for the low-frequency, thermally particular relevant, energy range. The two systems considered in this chapter—water and perovskite semiconductor—demonstrate the use of this new tool in the research of materials as diverse as liquids and solids. The water study illustrates the application of 2D TIRV spectroscopy to investigate collective vibrations in complex samples which are composed of mixtures of distinct chemical substances—the problem that is particularly challenging to tackle using the far-infrared linear absorption spectroscopy. We believe that in the future, these unique capabilities will promote the use of 2D TIRV spectroscopy in a variety of research fields, enabling new exciting insights into the physical nature of the low-frequency molecular motions and their role in many types of physical and chemical phenomena.

References

1. M. Karplus, T. Ichiye, B.M. Pettitt, Biophys. J. **52**, 1083 (1987)
2. J. Guo, H.-X. Zhou, Chem. Rev. **116**, 6503 (2016)
3. H.N. Motlagh, J.O. Wrabl, J. Li, V.J. Hilser, Nature **508**, 331 (2014)
4. P.L. Geissler, C. Dellago, D. Chandler, J. Hutter, M. Parrinello, Science **291**, 2121 (2001)
5. D.F. Plusquellic, K. Siegrist, E.J. Heilweil, O. Esenturk, ChemPhysChem **8**, 2412 (2007)
6. P. Hamm, M. Zanni, *Concepts and Methods of 2D Infrared Spectroscopy* (Cambridge University Press, Cambridge, 2011)
7. W. Zhao, J. Wright, Phys. Rev. Lett. **83**, 1950 (1999)
8. W. Zhao, J.C. Wright, Phys. Rev. Lett. **84**, 1411 (2000)
9. K. Kwak, S. Cha, M. Cho, J.C. Wright, J. Chem. Phys. **117**, 5675 (2002)
10. F. D'Angelo, Z. Mics, M. Bonn, D. Turchinovich, Opt. Express **22**, 12475 (2014)
11. H.G. Roskos, M.D. Thomson, M. Kreß, T. Löffler, Laser Photonics Rev. **1**, 349 (2007)

12. J. Dai, J. Liu, X.-C. Zhang, IEEE J. Sel. Top. Quantum Electron **17**, 183 (2011)
13. S. Mukamel, *Principles of Nonlinear Optical Spectroscopy* (Oxford University Press, Oxford, 1995)
14. M. Cho, Phys. Rev. A **61**, 023406 (2000)
15. E.T.J. Nibbering, T. Elsaesser, Chem. Rev. **104**, 1887 (2004)
16. F. Perakis, L. De Marco, A. Shalit, F. Tang, Z.R. Kann, T.D. Kühne, R. Torre, M. Bonn, Y. Nagata, Chem. Rev. **116**, 7590 (2016)
17. S. Woutersen, U. Emmerichs, H.J. Bakker, Science **278**, 658 (1997)
18. C.J. Fecko, J.D. Eaves, J.J. Loparo, A. Tokmakoff, P.L. Geissler, Science **301**, 1698 (2003)
19. A. Luzar, D. Chandler, Nature **379**, 55 (1996)
20. B. Auer, R. Kumar, J.R. Schmidt, J.L. Skinner, Proc. Natl. Acad. Sci. **104**, 14215 (2007)
21. B.M. Auer, J.L. Skinner, J. Chem. Phys. **128**, 224511 (2008)
22. K. Ramasesha, L. De Marco, A. Mandal, A. Tokmakoff, Nat. Chem. **5**, 935 (2013)
23. S.M. Craig, F.S. Menges, C.H. Duong, J.K. Denton, L.R. Madison, A.B. McCoy, M.A. Johnson, Proc. Natl. Acad. Sci. **114**, E4706 (2017)
24. J.A. Fournier, W.B. Carpenter, N.H.C. Lewis, A. Tokmakoff, Nat. Chem. **10**, 932 (2018)
25. M. Grechko, T. Hasegawa, F. D'Angelo, H. Ito, D. Turchinovich, Y. Nagata, M. Bonn, Nat. Commun. **9**, 885 (2018)
26. L.M. Herz, J. Phys. Chem. Lett. **9**, 6853 (2018)
27. A.M.A. Leguy, A.R. Goñi, J.M. Frost, J. Skelton, F. Brivio, X. Rodríguez-Martínez, O.J. Weber, A. Pallipurath, M.I. Alonso, M. Campoy-Quiles, M.T. Weller, J. Nelson, A. Walsh, P.R.F. Barnes, Phys. Chem. Chem. Phys. **18**, 27051 (2016)
28. F. Brivio, J.M. Frost, J.M. Skelton, A.J. Jackson, O.J. Weber, M.T. Weller, A.R. Goñi, A.M.A. Leguy, P.R.F. Barnes, A. Walsh, Phys. Rev. B **92**, 144308 (2015)
29. H. Kim, J. Hunger, E. Cánovas, M. Karakus, Z. Mics, M. Grechko, D. Turchinovich, S.H. Parekh, M. Bonn, Nat. Commun. **8**, 687 (2017)
30. M. Grechko, S.A. Bretschneider, L. Vietze, H. Kim, M. Bonn, Angew. Chemie Int. Ed. **57**, 13657 (2018)

Chapter 10
Ultrafast Vibrational Dynamics at Aqueous Interfaces Studied by 2D Heterodyne-Detected Vibrational Sum Frequency Generation Spectroscopy

Ken-ichi Inoue, Satoshi Nihonyanagi and Tahei Tahara

Abstract In this article, we review our recent studies on the ultrafast vibrational dynamics at aqueous interfaces carried out with two-dimensional (2D) heterodyne-detected vibrational sum frequency generation (HD-VSFG) spectroscopy. Compared to the wealth of knowledge about bulk water, molecular-level understanding of interfacial water is still poor due to the technical difficulty in selectively observing molecules at the interfaces. HD-VSFG spectroscopy is based on the second-order optical process and thus intrinsically interface-selective. 2D HD-VSFG spectroscopy is its extension to the time-resolved measurement, and it is an interfacial analog of 2D IR spectroscopy which has been extensively utilized for bulk studies. This novel interface-selective ultrafast spectroscopy has enabled us to investigate ultrafast vibrational dynamics at aqueous interfaces at the high level equivalent to the bulk studies. We describe the principle and instrumentation of 2D HD-VSFG spectroscopy as well as several selected examples of 2D HD-VSFG studies that provided new insights into aqueous interfaces. At the air/neat water interface, 2D HD-VSFG indicated high similarity of hydrogen-bonded OH of interfacial water to that of bulk water while unique non-hydrogen bonded OH is present at the interface. At the charged surfactant/water interfaces, 2D HD-VSFG enabled us to clearly observe ultrafast spectral diffusion in the OH stretch band and demonstrated the importance of isotopic dilution for unambiguous observation of vibrational dynamics. At model membrane lipid/water interfaces, it was found that the hydrogen-bonded dynamics is greatly affected by the interaction between the interfacial water and the head group of the lipids and

K. Inoue · S. Nihonyanagi · T. Tahara (✉)
Molecular Spectroscopy Laboratory, RIKEN, 2-1 Hirosawa, Wako, Saitama 351-1098, Japan
e-mail: tahei@riken.jp

S. Nihonyanagi · T. Tahara
Ultrafast Spectroscopy Research Team, RIKEN Center for Advanced Photonics (RAP), 2-1 Hirosawa, Wako, Saitama 351-1098, Japan

Present Address:
K. Inoue
Department of Chemistry, Graduate School of Science,
Tohoku University, Sendai 980-8578, Japan

M. Cho (ed.), *Coherent Multidimensional Spectroscopy*,
Springer Series in Optical Sciences 226,
https://doi.org/10.1007/978-981-13-9753-0_10

that the effects of coexisting head groups cannot simply be summed up but they are highly cooperative.

10.1 Introduction

Water at interfaces plays essential roles in providing unique environments in life and many other fundamental processes. The unique properties of the water interfaces arise from the sudden truncation of the three-dimensional hydrogen-bond network that is formed among water molecules. Because the hydrogen-bond network is not static but highly dynamic [1], elucidation of the dynamic property of interfacial water is essential for understanding aqueous interfaces.

Although ultrafast vibrational dynamics of bulk water has been extensively studied using a variety of spectroscopic methods such as time-resolved (TR-) IR and two-dimensional (2D) IR spectroscopies, ultrafast vibrational dynamics of water at interfaces has not been well elucidated because of the technical difficulty in selectively observing dynamics at the liquid interfaces. Recently, interface-selective phase- and time-resolved spectroscopic methods have been developed by combining multiplex heterodyne-detected vibrational sum frequency generation (HD-VSFG) spectroscopy [2, 3] and the pump-probe technique. These novel ultrafast spectroscopies, which are called TR- and 2D HD-VSFG spectroscopies, are interfacial analogue of TR-IR and 2D IR spectroscopies, respectively. TR- and 2D HD-VSFG spectroscopies are very powerful tools to study ultrafast vibrational dynamics of interfaces. Application of these new ultrafast spectroscopies have begun for studying the hydrogen-bond dynamics of water at aqueous interfaces and revealed the unique property of interfacial water [4].

In this review, we describe the detail of 2D HD-VSFG spectroscopy (Sect. 10.2) and their applications to the ultrafast vibrational dynamics of aqueous interfaces (Sect. 10.3).

10.2 Principle and Instrumentation of 2D HD-VSFG Spectroscopy

10.2.1 Principle

Vibrational sum frequency generation (VSFG) spectroscopy is based on the second-order nonlinear optical process and hence is intrinsically interface-selective. In conventional VSFG spectroscopy, the intensity of the SFG light is detected, which is called homodyne detection [5]. In this homodyne measurement, the detected VSFG signal is proportional to the square of second-order nonlinear susceptibility ($|\chi^{(2)}|^2$) because the light intensity is proportional to the square of the electric field. Unfortu-

nately, the $|\chi^{(2)}|^2$ spectra are often heavily distorted due to the interference between resonant peak(s) and non-resonant background. Furthermore, the $|\chi^{(2)}|^2$ spectra lack the sign of $\chi^{(2)}$ which contains information about the up/down orientation of the interfacial molecule. Because of these problems, the true spectral response of the interfaces is obscured in the homodyne VSFG spectra, and it is difficult to properly interpret SFG spectra in many cases [6].

To overcome the drawbacks of conventional homodyne-detected VSFG spectroscopy, heterodyne-detected VSFG spectroscopy was developed, in which interference between the VSFG signal and a local oscillator (LO) is measured to obtain complex $\chi^{(2)}$ spectra [7, 8]. In particular, the obtained imaginary part of the $\chi^{(2)}$ ($\mathrm{Im}\chi^{(2)}$) spectra represent absorptive line shapes, in analogy with those in the linear absorption spectra which correspond to the imaginary part of linear susceptibility ($\mathrm{Im}\chi^{(1)}$). Furthermore, the sign of an $\mathrm{Im}\chi^{(2)}$ spectrum provides direct information of the up/down orientation of interfacial molecules. These marked advantages of HD-VSFG have enabled us to obtain various new insights into the steady-state (time-averaged) properties of water at the interfaces [2, 3].

Since VSFG measurements are performed with femtosecond and/or picosecond visible (ω_1) and IR (ω_2) pulses, they can be straightforwardly extended to time-resolved measurements by introducing an additional pump (ω_{pump}) pulse which excites the sample [9–11]. This TR-VSFG spectroscopy opens a door to investigate ultrafast dynamics at interfaces. However, TR-VSFG with homodyne detection measures the pump-induced intensity change of the VSFG signal which corresponds to the change of the square of second-order nonlinear susceptibility ($\Delta|\chi^{(2)}|^2$),

$$\begin{aligned}\Delta\left|\chi^{(2)}\right|^2 &= \left|\chi^{(2)}+\Delta\chi^{(2)}\right|^2-\left|\chi^{(2)}\right|^2 \\ &= \chi^{(2)}\Delta\chi^{(2)*}+\chi^{(2)*}\Delta\chi^{(2)}+\left|\Delta\chi^{(2)}\right|^2. \end{aligned} \tag{10.1}$$

Obviously, the observed time-resolved spectra have no straightforward physical meaning. In fact, the signal is dominated by the cross-terms between steady-state and transient components in usual cases of $\chi^{(2)} > \Delta\chi^{(2)}$. Thus, it is very difficult to derive relevant information from time-resolved VSFG spectra that are measured with homodyne detection.

In contrast, the pump-induced change in the $\mathrm{Im}\chi^{(2)}$ ($\Delta\mathrm{Im}\chi^{(2)}$) spectrum is directly obtained in TR-HD-VSFG measurements as the difference between the spectra measured with and without the pump pulse,

$$\Delta\mathrm{Im}\chi^{(2)} = \left(\mathrm{Im}\chi^{(2)}+\Delta\mathrm{Im}\chi^{(2)}\right)-\mathrm{Im}\chi^{(2)}. \tag{10.2}$$

$\Delta\mathrm{Im}\chi^{(2)}$ spectrum can be interpreted as we do for the bulk transient absorption spectra which correspond to $\Delta\mathrm{Im}\chi^{(1)}$ ($\chi^{(1)}$: linear susceptibility). Furthermore, the measurements of the ω_{pump} frequency dependence of the $\Delta\mathrm{Im}\chi^{(2)}$ spectra provide 2D HD-VSFG spectrum [12]. 2D HD-VSFG is interfacial analog of 2D IR spectroscopy which is considered one of the most advanced ultrafast spectroscopies in the bulk study [13].

10.2.2 Instrumentation

Figure 10.1 shows the schematic of one of the 2D HD-VSFG setups developed in our laboratory [14]. This setup is based on a combination of the narrowed IR pump and broadband HD-VSFG probe. (This is analogous to the early 2D IR spectroscopy developed by Hamm et al. [15]). The light source is a Ti:sapphire regenerative amplifier (pulse energy: 5.0 mJ, repetition rate: 1 kHz, pulse width: 80 fs, center wavelength: 795 nm, bandwidth: 22 nm) seeded by a femtosecond Ti:sapphire oscillator. The output from the regenerative amplifier is separated into three, and they are converted into narrow-band visible (ω_1), broadband IR (ω_2) and IR pump (ω_{pump}) pulses. The ω_1 pulse is centered at 795 nm, and the bandwidth is as narrow as 1.5 nm (24 cm^{-1}). The ω_2 pulse is generated by an optical parametric amplifier (OPA) with

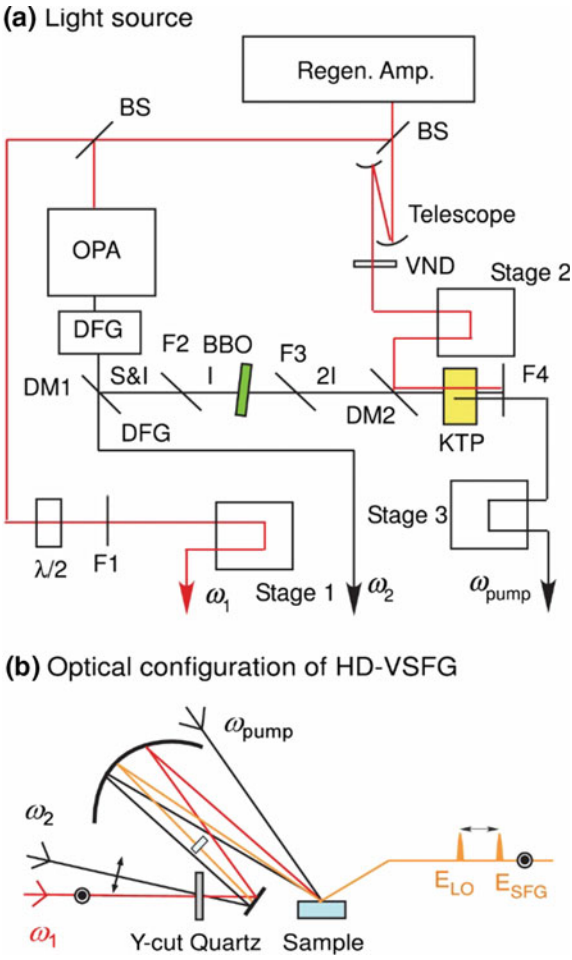

Fig. 10.1 Schematic of a setup for 2D HD-VSFG spectroscopy. **a** Light source. **b** Optical configuration for HD-VSFG. Reprinted with permission from [14]. Copyright 2015 American Institute of Physics

a collinear difference frequency generation (DFG). The broadband ω_2 (bandwidth: ~300 cm^{-1}) covers the whole OH stretch region without scanning the ω_2 frequency, and the multiplex HD-VSFG probe is achieved with the ω_1 and ω_2 pulses. The ω_{pump} pulse is generated by DFG between the frequency-doubled idler from OPA and the remaining fundamental output from Ti:sapphire regenerative amplifier. By using a 3-mm thick potassium titanyl phosphate (KTP) crystal for the DFG process, the ω_{pump} pulse having a relatively narrow bandwidth (~120 cm^{-1}) is generated with the pulse energy as high as 35 μJ. The center frequency of the ω_{pump} pulse is tuned by the rotation of the KTP crystal while the pulse energy is kept constant by adjusting the power of the fundamental beam with a variable neutral density filter.

In the heterodyne scheme adopted in this setup (Fig. 10.1b), LO is first generated from a thin y-cut quartz crystal (thickness: 10 μm) with a transmission geometry. After only the LO pulse passes through a 2-mm thick silica plate for generation of a time delay (~3.3 ps) from the other two pulses, the ω_1 and ω_2 and LO pulses are refocused by a concave mirror on the sample surface. Then, the VSFG signal generated from the sample and the LO pulse reflected at the sample surface collinearly propagate and are introduced to a polychromator in which they are dispersed and temporally stretched to produce interference fringes in the frequency domain. The interference fringes are finally recorded with a liquid-nitrogen-cooled CCD.

The procedure to obtain a complex $\chi^{(2)}$ spectrum from the raw data has been described in detail elsewhere [7, 16]. Briefly, the raw data measured with CCD corresponds to the intensity of the total electric field E_{total} ($= E_{SFG} + E_{LO}$), which is represented as,

$$|E_{total}|^2 = |E_{SFG}|^2 + |E_{LO}|^2 + E_{SFG}E_{LO}^* + E_{SFG}^* E_{LO}. \tag{10.3}$$

This frequency domain data is inversely Fourier transformed to the time domain, and the third term in the right-hand side of (10.3) is extracted by using a filter function. The extracted third term is then Fourier transformed back to the frequency domain. For calibrating the phase and amplitude of the data, a material with a known phase (such as z-cut quartz) is measured with the exactly the same condition, and the corresponding third term is obtained. Then, the third term of the sample is divided by that of the reference,

$$\frac{E_{SFG}E_{LO}^*}{E_{ref}E_{LO}^*} = \frac{\chi^{(2)}}{\chi_{ref}^{(2)}}. \tag{10.4}$$

Consequently, the normalized $\chi^{(2)}$ spectra, i.e. $\mathrm{Re}\chi^{(2)}$ and $\mathrm{Im}\chi^{(2)}$ spectra, of the sample are obtained.

For the time-resolved measurements, $\mathrm{Im}\chi^{(2)}$ spectra are measured with and without the ω_{pump} pulse, and their difference gives a $\Delta\mathrm{Im}\chi^{(2)}$ spectrum. The time resolution of the measurements is estimated by measuring the third-order nonlinear signal of $\omega_1 + \omega_2 + \omega_{pump}$ generated at the sample position by changing the ω_{pump} delay. The FWHM of the temporal response of the setup is ~200 fs (Fig. 10.2b). To obtain

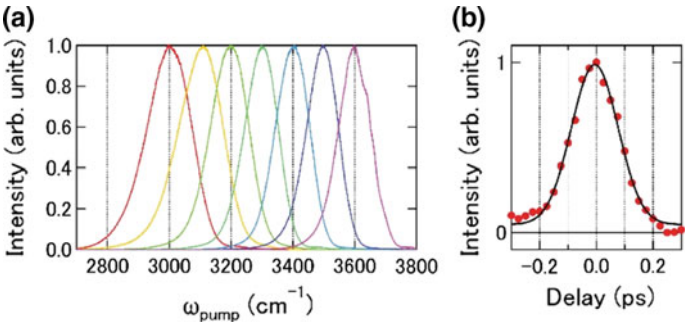

Fig. 10.2 **a** ω_{pump} spectra used for 2D HD-VSFG measurements. **b** Temporal trace of the third-order nonlinear signal of $\omega_1 + \omega_2 + \omega_{\text{pump}}$. (FWHM: ~200 fs). Reprinted with permission from [14]. Copyright 2015 American Institute of Physics

reliable $\text{Im}\chi^{(2)}$ and $\Delta\text{Im}\chi^{(2)}$ spectra, it is necessary to keep the height of the sample surface accurately. To achieve this, the height of the sample surface is monitored by a displacement sensor and is kept constant within the accuracy of 1 μm during the measurements. For a long time averaging (typically overnight), a drop of water is added by a programed syringe pump in every interval of the measurements to compensate the loss of water due to evaporation.

For obtaining a 2D HD-VSFG spectrum that corresponds to the ω_{pump} dependence of $\Delta\text{Im}\chi^{(2)}$ spectra, $\Delta\text{Im}\chi^{(2)}$ spectra are measured by changing ω_{pump} frequencies (Fig. 10.2a), and they are interpolated and combined. In our representation, the horizontal and vertical axes represent the ω_2 and ω_{pump} frequencies, respectively. (Note that the opposite representation is also used for 2D IR [17]). Therefore, the horizontal slice corresponds to the time-resolved $\Delta\text{Im}\chi^{(2)}$ spectrum measured with the ω_{pump} pulse whose frequency is given in the vertical axis. Up to now, all the 2D spectra of water at the aqueous interfaces have been measured with this scheme [4] although the interferometric excitation scheme has been employed in the measurements at solid interfaces [18–20].

10.3 Ultrafast Vibrational Dynamics at Aqueous Interfaces

10.3.1 Water at the Air/Neat Water Interface

In bulk water, the OH bonds of the water molecules participate in the three-dimensional hydrogen-bond network. In contrast, at the interface, a substantial number of OH bonds do not form hydrogen bonds because the hydrogen-bond network is truncated at the interface. Thus, it is of great interest to elucidate the effect of this truncation on the property of the water. The steady-state $\text{Im}\chi^{(2)}$ spectrum of the air/neat water (H_2O) interface exhibits a broad negative OH band around 3200–3600 cm^{-1}

and a sharp positive OH band at 3700 cm^{-1}. The former is assigned to the stretch vibration of hydrogen-bonded OH (HB OH) with H-down orientation, whereas the latter is attributed to non-hydrogen-bonded OH (free OH) that sticks out to the air with H-up orientation [21, 22]. The appearance of the free OH band clearly shows that the structure of water at the air/water interface is very different from that in bulk [23].

Figure 10.3 shows 2D HD-VSFG spectra at the air/neat water (H_2O) interface [24]. Negative, positive, and negative lobes appear at $\omega_2 = \sim 3250\ cm^{-1}$, $\omega_2 = \sim 3450\ cm^{-1}$, and $\omega_2 = \sim 3700\ cm^{-1}$, respectively, in the 2D spectrum at 0.0 ps. They are assignable to the $v = 1 \rightarrow 2$ hot band of HB OH, the bleach of HB OH, and the bleach of free OH, respectively. The hot band of free OH with a positive sign is overlapped with the bleach of HB OH. An important observation in the 2D spectrum at 0.0 ps is the cross-peaks between HB OH and free OH at $(\omega_{pump}, \omega_2) = (3450\ cm^{-1}, 3700\ cm^{-1})$ and $(3700\ cm^{-1}, 3450\ cm^{-1})$. In previous homodyne-detected 2D VSFG studies, it was claimed that the energy transfer between HB OH and free OH was the origin of the cross-peaks [25, 26]. However, the narrow bandwidth of the free OH band ($24\ cm^{-1}$) [22, 27] corresponds to the dephasing time of free OH as slow as ~0.4 ps

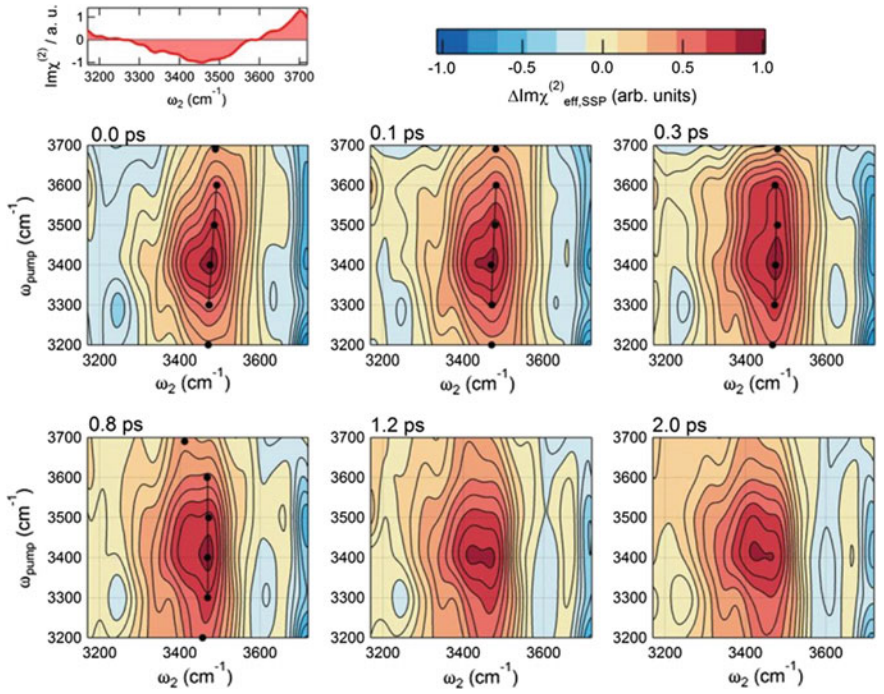

Fig. 10.3 2D HD-VSFG spectra of the air/neat water (H_2O) interface from 0.0 ps to 2.0 ps. (ω_{pump} bandwidth is ~200 cm^{-1}.) The vertical and horizontal axes are exchanged from the original paper. The steady-state Im$\chi^{(2)}$ spectrum is also shown in the top left panel. Reprinted with permission from [24]. Copyright 2013 American Institute of Physics

so that the cross-peaks should appear with a time constant equal to or larger than 0.4 ps if the energy transfer is the origin. In the 2D HD-VSFG spectra, the cross peaks are observed even at 0.0 ps, and therefore it is considered that they arise not from the energy transfer but from the frequency shift due to anharmonic coupling: When HB OH or free OH is excited, the frequency of the other free OH or HB OH of the same molecule exhibit a red-shift, giving rise to the cross peaks [28]. Another important observation is that the ω_{pump} dependence of the bleach of HB OH is recognized at 0.0 ps, which indicates the presence of spectral inhomogeneity in the HB OH band. This ω_{pump} dependence disappears in a few hundred femtoseconds due to efficient spectral diffusion at the interface.

This first 2D HD-VSFG experiment at the air/water interface was performed with the ω_{pump} pulse having a bandwidth as board as ~200 cm^{-1}, and hence the spectral diffusion of the HB OH band was not very clearly observed. The Bonn group performed the second 2D HD-VSFG experiments using much narrower ω_{pump} pulses (~100 cm^{-1}) and reported 2D spectra that exhibit a clearly tilted nodal line between the hot band and bleach lobes of HB OH at 0 fs [29]. This demonstrate the importance of the ω_{pump} pulses having an optimized bandwidth for clearly detecting the ω_{pump} dependence of the $\Delta\text{Im}\chi^{(2)}$ spectra. However, unlike the first 2D HD-VSFG study, they reported that the $\Delta\text{Im}\chi^{(2)}$ spectra obtained with the 3500 cm^{-1} ω_{pump} pulse was different from other $\Delta\text{Im}\chi^{(2)}$ spectra even at a very long delay time (1500 fs). This implies that the spectral diffusion following 3500 cm^{-1} excitation is surprisingly slow, and they claimed that HB OH around 3500 cm^{-1} was energetically isolated at the air/water interface. They also reported that the vibrational relaxation (T_1) time of HB OH at around 3500 cm^{-1} was as long as ~0.75 ps, which was more than twice longer than the T_1 time obtained with 3300 cm^{-1} excitation (~0.35 ps) [30].

To solve the discrepancy between the two 2D HD-VSFG studies, we re-examined ω_{pump} dependence of the vibrational dynamics of HB OH at the air/water interface by TR HD-VSFG, paying a special attention to the bandwidth (~120 cm^{-1}) and the energy (15 μJ) of the ω_{pump} pulse [31]. Figure 10.4a shows $\Delta\text{Im}\chi^{(2)}$ spectra obtained with the ω_{pump} pulse at 3300 and 3500 cm^{-1}. As readily seen, the difference in the $\Delta\text{Im}\chi^{(2)}$ spectra at 0.0 ps is very clearly observed owing to the narrow ω_{pump} pulses, which demonstrates inhomogeneity of the HB OH band. Nevertheless, this difference almost disappears at 0.5 ps, indicating ultrafast spectral diffusion occurring on the sub-picosecond time scale regardless of the difference in the ω_{pump} frequency. A complementary MD simulation well reproduced the observed efficient spectral diffusion and indicated that the memory of the initial vibrational frequency is lost within 0.6 ps [31]. Consequently, this TR-HD-VSFG measurement concluded that there is no extraordinary slow vibrational dynamics or energetically isolated HB OH species at the air/water interface. It was also found in this study that $\Delta\text{Im}\chi^{(2)}$ spectra measured with 3300 and 3500 cm^{-1} excitations at 1.5 ps became noticeably different from each other when the ω_{pump} energy was increased up to 35 μJ, reflecting the difference in the thermalization effect. Therefore, the spectral difference reported in the second 2D HD-VSFG study [29] was attributable to the difference in the local temperature increase at the air/water interface. Furthermore, the T_1 times of HB OH

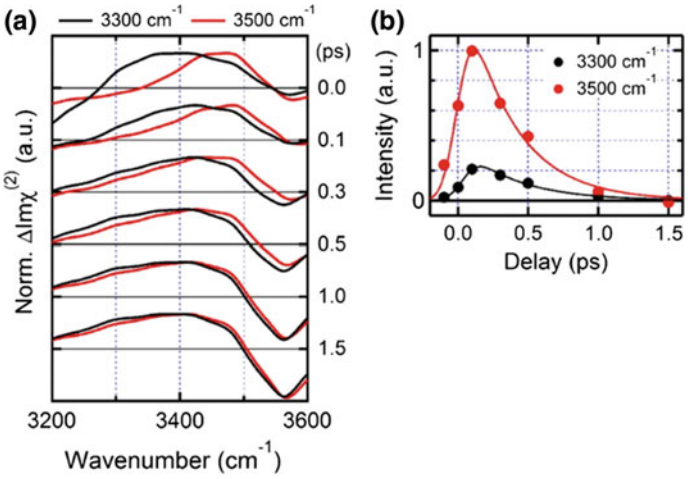

Fig. 10.4 **a** Normalized time-resolved $\Delta \mathrm{Im}\chi^{(2)}$ spectra obtained with 3300 cm^{-1} (black) and 3500 cm^{-1} (red) excitations. **b** The area intensity of the $\Delta \mathrm{Im}\chi^{(2)}$ spectra near 3500 cm^{-1} plotted as a function of delay, corresponding to the vibrational relaxation (T_1) time (0.39 ± 0.04 ps for 3300 cm^{-1} excitation and 0.35 ± 0.03 ps for 3500 cm^{-1} excitation.). Reprinted with permission from [31]. Copyright 2016 American Chemical Society

were evaluated to be 0.39 ± 0.04 ps and 0.35 ± 0.03 ps for 3300 cm^{-1} and 3500 cm^{-1} excitations, respectively, indicating that the ω_{pump} dependence of T_1 time is not significant (Fig. 10.4b).

In summary, at the air/water interface, spectral inhomogeneity of the HB OH band is clearly observed immediately after IR photoexcitaion but it quickly disappears in the femtosecond time region with ultrafast spectral diffusion. The T_1 time of HB OH deduced from TR-HD-VSFG measurements is ~0.4 ps for both 3300 and 3500-cm^{-1} excitations, and this T_1 value is comparable to or only slightly longer than the values reported for bulk water (0.26–0.35 ps) [30, 32, 33]. Furthermore, a significant anharmonic coupling is observed between HB OH and free OH, which gives rise to the cross-peaks in 2D spectra.

10.3.2 Water at the Charged Aqueous Interface

Charged interfaces are seen in many places in our world. For instance, they play important roles in bio-relevant science, colloid science and electrochemistry. Monolayers of charged surfactants on the water surface are good model systems for studying the fundamental properties of charged aqueous interfaces, and hence they have been intensively studied by VSFG [34–37] and HD-VSFG [7, 38–42]. Figure 10.5 shows the steady-state $\mathrm{Im}\chi^{(2)}$ spectrum in the OH stretch region of the interface between water and the monolayer of a prototypical cationic surfactant, cetyltrimethy-

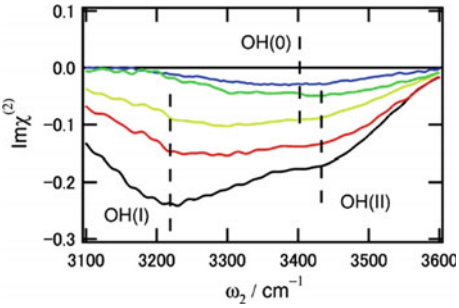

Fig. 10.5 Steady-state Im$\chi^{(2)}$ spectra of the cationic surfactant (CTAB)/water interfaces at various isotopic concentrations (black, H_2O; red, H_2O/HOD/D_2O = 9: 6: 1; yellow, 1: 2: 1; green, 1: 6: 9; blue, 1: 12: 33). Reprinted with permission from [43]. Copyright 2010 American Chemical Society

lammonium bromide (CTAB) (CTAB/water interface) [43]. The negative OH band indicates H-down orientation of interfacial water, which is induced by charge-dipole interaction between the cationic head group of CTAB and water dipole [7]. In the spectrum of the CTAB/H_2O interface (the black line), the broad OH band exhibits two peaks, as observed at various charged aqueous interfaces. In the past, this double-peaked feature was attributed to two different types of water species at the interface, namely, "*ice*-like" and "*liquid*-like" water [5, 44]. However, because they merge into one broad band when water is isotopically diluted as shown in Fig. 10.5, the double peaks in the H_2O spectrum is now attributed to the vibrational coupling, i.e., Fermi resonance between the symmetric OH stretch and the bend overtone [43, 45].

As clearly shown in Fig. 10.5, the isotopic dilution significantly affects the spectral feature of the OH stretch band of interfacial water. Actually, because a H_2O molecule has two equivalent OH bonds, the two OH stretch motions are coupled to each other and give rise to symmetric and antisymmetric OH stretch vibrations. Furthermore, the symmetric OH stretch vibration and the overtone of the bending vibration have close frequencies, which generates two bands due to Fermi resonance. In addition to these intramolecular vibrational couplings, the hydrogen-bond network of H_2O molecules causes the delocalization of the OH stretch motion over different H_2O molecules by intermolecular vibrational coupling. These couplings complicate the spectrum in the OH stretch region of H_2O. In contrast, in isotopically diluted water (HOD–D_2O), it can practically be considered that one single OH of HOD is isolated in D_2O and hence these vibrational couplings are eliminated. Figure 10.6a and b show 2D HD-VSFG spectra of the CTAB/H_2O and CTAB/HOD–D_2O interfaces at 0.0 ps, respectively. A positive lobe in the higher ω_2 region is assignable to the bleach of the OH stretch band while a negative lobe in the lower ω_2 region is attributed to the $v = 1 \rightarrow 2$ hot band (Note that the bleach and hot band appear with the positive and negative signs, respectively, because the OH stretch band has the negative sign.). In the 2D spectrum of the CTAB/H_2O interface, the bleach of the two characteristic peaks in the steady-state spectrum is observed along the diagonal at (ω_{pump}, ω_2) = (3200 cm^{-1}, 3200 cm^{-1}) and (ω_{pump}, ω_2) = (3400 cm^{-1}, 3400 cm^{-1}). Off-diagonal cross peaks are also clearly observed around (ω_{pump}, ω_2) = (3400 cm^{-1}, 3200 cm^{-1}) and (ω_{pump}, ω_2) = (3200 cm^{-1}, 3400 cm^{-1}). Because these cross-peaks are absent in the 2D spectrum of the CTAB/HOD–D_2O interface, the cross-peaks

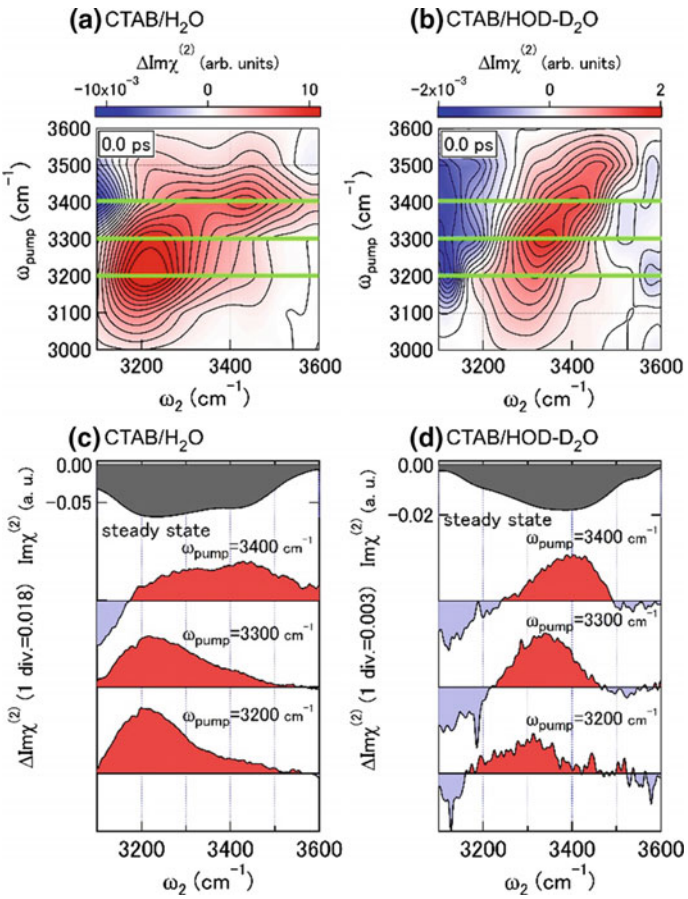

Fig. 10.6 2D HD-VSFG spectra of **a** CTAB/H_2O and **b** CTAB/HOD–D_2O (H_2O/HOD/D_2O = 1: 8: 16) interfaces at 0.0 ps. The horizontal slices indicated by green lines are shown in (**c**) and (**d**). Reprinted with permission from [14]. Copyright 2015 American Institute of Physics

of the CTAB/H_2O interface is undoubtedly attributable to the vibrational coupling. However, as seen in the horizontal slices of the 2D spectra shown in Fig. 10.6c, the relative intensity of the two bleach peaks significantly changes with the change of the ω_{pump} frequency. Such ω_{pump} dependence of the relative intensity is not explainable only by the vibrational coupling.

The horizontal slices of the 2D spectrum of the CTAB/HOD–D_2O interface only exhibit single-peaked bleach bands whose peak frequencies change according to the ω_{pump} frequencies (Fig. 10.6d). This clearly manifests the inhomogeneity of the OH stretch band. Because such inhomogeneous broadening should be also present in the OH stretch band of the CTAB/H_2O interface, the 2D spectra of the CTAB/H_2O interface need to be interpreted taking account of both of inhomogeneous broadening and Fermi resonance. In fact, the 2D spectrum simulated with a model function

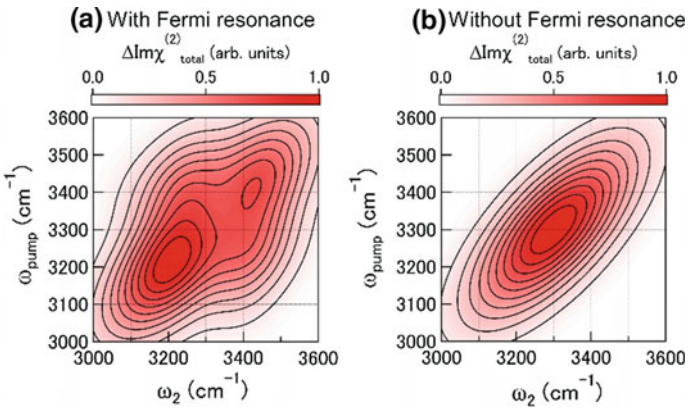

Fig. 10.7 Simulated bleach lobes in 2D HD-VSFG spectra **a** with Fermi resonance and **b** without Fermi resonance. Reprinted with permission from [14]. Copyright 2015 American Institute of Physics

that includes Fermi resonance as well as inhomogeneous broadening nicely reproduced essential features of the bleach lobe in the experimental 2D spectrum of the CTAB/H_2O interface (Fig. 10.7a). It is noteworthy that the simulated 2D spectrum becomes very similar to the experimental 2D spectrum of the CTAB/HOD–D_2O interface when the Fermi resonance is turned off (Fig. 10.7b).

The 2D HD-VSFG spectra of the CTAB/water interfaces demonstrated that the spectral response of the charged H_2O interfaces is heavily affected by the vibrational couplings and that isotopic dilution is essential for clearly observing the vibrational dynamics without their disturbance. Recently, it was proposed that two types of interfacial water exist at the anionic surfactant/H_2O interface in a 2D VSFG study carried out with homodyne detection [46]. However, the validity of this argument needs to be examined by HD-VSFG experiments using isotopic dilution, as described in this section.

10.3.3 Water at Biological Membrane Interfaces

10.3.3.1 Anionic and Cationic Lipid/Water Interfaces

As described in the previous section, early 2D HD-VSFG studies demonstrated that we can clearly capture the spectral diffusion of interfacial water using 2D HD-VSFG with isotopic dilution. This finding led us to apply 2D HD-VSFG to lipid monolayer interfaces which are a model of biological membranes. We investigated ultrafast dynamics of interfacial water at the lipid/water interfaces first for a cationic lipid (1,2-dipalmitoyl-3-trimethylammonium propane; DPTAP) and an anionic lipid

(1,2-dipalmitoyl-*sn*-glycero-3-phosphorylglycerol; DPPG), and clarified the effect of charged head groups on the dynamics of interfacial water [47].

The steady-state $\mathrm{Im}\chi^{(2)}$ spectra of the DPTAP/HOD–D_2O and DPPG/HOD–D_2O interfaces exhibit a broad OH stretch band with the opposite signs (Fig. 10.8). The opposite signs reflect the opposite orientation of interfacial water which is induced by the positive (DPTAP) and negative (DPPG) charges of the head groups [7]. Even though the sign is opposite, other spectral features such as the peak frequency and bandwidth are similar to each other, and the difference of these interfaces is not obvious in the steady-state spectra.

In spite of the similarity of the steady-state spectra, 2D HD-VSFG spectra of the DPTAP/HOD–D_2O and DPPG/HOD–D_2O interfaces are very different. Figure 10.9a shows 2D spectra at the DPTAP interface, in which the red and blue lobes are attributed to the bleach of the negative OH stretch band and the $v = 1 \rightarrow 2$ hot band, respectively. Figure 10.9b shows 2D spectra of the DPPG interface, and the sign of $\Delta\mathrm{Im}\chi^{(2)}$ signals is opposite to the DPTAP interface, reflecting the opposite sign of the OH stretch band in the steady-state spectra. The remarkable difference in these 2D spectra is the tilt angle of the bleach lobe at 0.0 ps: The tilt angle (from the vertical) is small for the DPTAP interface whereas that for the DPPG interface is as large as ~45°. These tilts of the bleach lobes were quantitatively analyzed using center line slope (CLS), which is the slope of the line that connects the peaks in the horizontal cuts at each ω_{pump} frequency [48]. CLS of the DPTAP and DPPG interfaces at 0.0 ps are 0.29 ± 0.04 (DPTAP) and 0.80 ± 0.03 (DPPG), respectively, and they decay with similar time constants of 750 ± 350 fs (Fig. 10.10).

Temporal change of CLS of the bleach lobes is considered equivalent to the frequency-frequency correlation function of the OH stretch vibration of interfacial water. It has been concluded by 2D IR studies that the frequency-frequency corre-

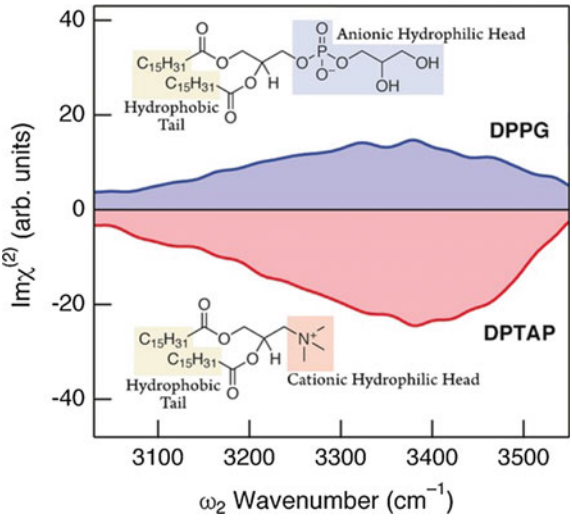

Fig. 10.8 Steady-state spectra of the cationic lipid DPTAP/HOD–D_2O interface (red) and the anionic lipid DPPG/HOD–D_2O (blue) interface. (H_2O/HOD/D_2O = 1: 8: 16) Chemical structures of DPTAP and DPPG are also shown. Reprinted with permission from [47]. Copyright 2016 Wiley-VCH

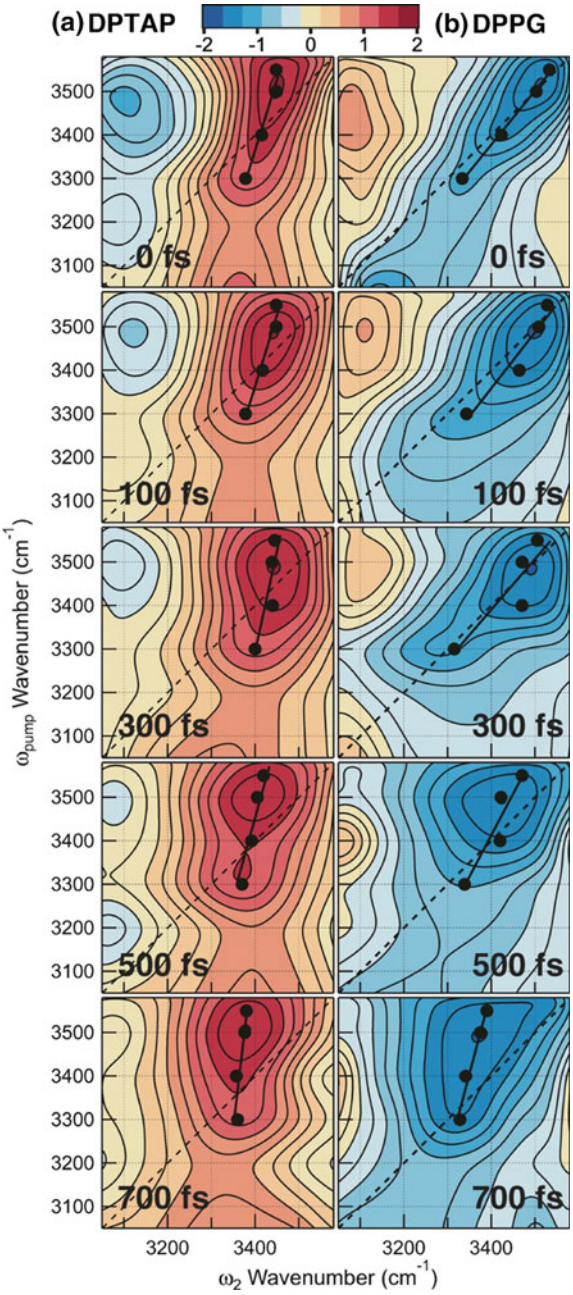

Fig. 10.9 2D HD-VSFG spectra of **a** DPTAP/HOD–D_2O interface and **b** DPPG/HOD–D_2O interface at delay times from 0 to 700 fs. The black straight line in the 2D spectra correspond to the center line slope (CLS). Reprinted with permission from [47]. Copyright 2016 Wiley-VCH

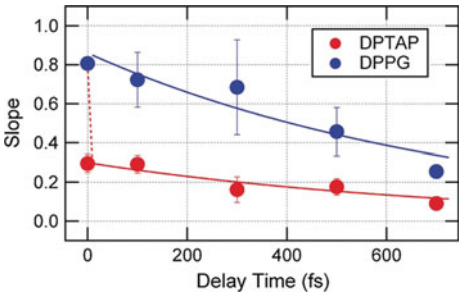

Fig. 10.10 Temporal change of the CLS of the DPTAP (red) and DPPG (blue) interfaces Reproduced with permission from [47]. Copyright 2016 Wiley-VCH

lation function of bulk HOD–D_2O exhibits a bimodal decay, and the ultrafast decay (~60 fs) is attributed to the ultrafast hydrogen-bond fluctuation whereas the slow decay (~1 ps) is assigned to the hydrogen-bond rearrangement [49]. Referring to this dynamics of bulk water, the small initial CLS value at the DPTAP interface can be rationalized with the "missing" component due to ultrafast hydrogen-bond fluctuation which is too fast to be detected with the limited time resolution (~200 fs) of the 2D HD-VSFG experiments. Then, the sub-picosecond decay (750 ± 350 fs) component of the CLS is attributable to the hydrogen-bond rearrangement. Consequently, it can be considered that the hydrogen-bond dynamics at the DPTAP interface is "bulk-like". At the DPPG interface, the initial CLS value is almost unity (which corresponds to the tilt angle of 45°), indicating that the ultrafast hydrogen-bond fluctuation is significantly suppressed at the DPPG interface. Obviously, hydrogen-bond dynamics at the DPPG interface is very different from the dynamics in bulk water.

This marked difference in the 2D spectra of the two lipid/HOD–D_2O interfaces is attributed to the difference in the hydrogen-bond ability of the head groups of the lipids. The phosphatidylglycerol head group of DPPG forms strong hydrogen bonds with interfacial water, while the choline group does not. The different spectral diffusion between the DPPG and DPTAP interfaces qualitatively agree with the prediction of a theoretical work by the Skinner group [50].

The 2D HD-VSFG study on the cationic and anionic lipid/water interfaces revealed the different spectral diffusion dynamics at these interfaces. This study explicitly demonstrated distinct hydrogen-bond dynamics at interfaces which reflects the different interaction between interfacial water and the head groups of the lipid. The effect of the hydrogen bonding with the head group of the monolayer was further studied for the interface of the octadecylammonium monolayer, which is cationic as DPTAP but forms hydrogen bonds with interfacial water [51]. It was found that the hydrogen-bond fluctuation is substantially affected even in the case that the monolayer has a cationic head group that acts as a hydrogen-bond donor to the interfacial water.

10.3.3.2 Zwitterionic Lipid/Water Interface

As described in the previous section, the 2D HD-VSFG study on the DPTAP and DPPG interfaces revealed that hydrogen-bond dynamics of interfacial water are markedly different between the cationic lipid/water and the anionic lipid/water interfaces [47]. A next question is the hydrogen-bond dynamics of the interfacial water when a lipid has both cationic and anionic head groups. This question was examined for the interface of zwitterionic phosphatidylcholine that has both of anionic phosphate and cationic choline in the head group (Fig. 10.11a). Phosphatidylcholine is a major constituent of cell membranes and is crucially important in bio-relevant sciences. As described below, this study revealed a cooperative effect of the head groups on the dynamics of interfacial water [52].

Figure 10.11b shows the $\mathrm{Im}\chi^{(2)}$ spectrum of the 1,2-dipalmitoyl-*sn*-glycero-3-phosphocholine (DPPC)/HOD–D_2O interface. This spectrum exhibits a single positive OH band peaked at around 3300 cm^{-1}. This indicates that the signal of the H-up water around the anionic phosphate site dominates the $\mathrm{Im}\chi^{(2)}$ spectrum in the OH stretch region [53].

In spite of the simple feature of the steady-state spectrum, 2D spectra provide very rich information about interfacial water (Fig. 10.11c). In the 2D spectrum at 0.0 ps, two positive lobes are observed in the low and high ω_2 regions (labelled with A and C, respectively) with a negative lobe (B) in between them. While the lobes B and A are readily assigned to the bleach and hot band of the positive OH stretch band, the appearance of the lobe C cannot be explained with a single positive band in the steady-state spectrum. This clearly indicates that there exists another OH stretch band having the opposite sign, which arises from another water species. Indeed, this positive lobe C is the key observation that reveals multiple water species at the zwitterionic lipid interface, and it is attributable to the bleach of a negative OH band of H-down water which is hidden by the signal of H-up water in the steady-state spectrum. In other words, the lobe C is the direct evidence that the cationic choline site is also hydrated by the H-down water. The individual hydration around the two sites in the head group of DPPC was first indicated by a steady-state HD-VSFG study [53] and was supported by several MD simulations [54, 55]. Nevertheless, there were several MD simulation studies that denied or did not recognize the H-down water around the choline site [56–58].

Another important observation in the 2D spectrum is that each lobe is almost vertically elongated even at 0.0 ps. This indicates ultrafast loss of the frequency-frequency correlation of the OH stretch vibration. As shown in Fig. 10.12, the initial CLS value of lobe B of the DPPC interface (0.15 ± 0.02) is much smaller than the value of the corresponding bleach lobe of the DPPG interface (0.80 ± 0.03), although both lobes represent the bleach of the OH stretch band of the water that hydrates the phosphate head group [47]. In fact, the initial CLS value of lobe B is close to the value of the bleach lobe of the DPTAP interface (0.29 ± 0.04) which exhibits bulk-like hydrogen-bond dynamics. This implies that the ultrafast hydrogen-bond fluctuation is not efficiently suppressed at the zwitterionic lipid interface even though the interfacial water forms hydrogen-bonds with the phosphate head group.

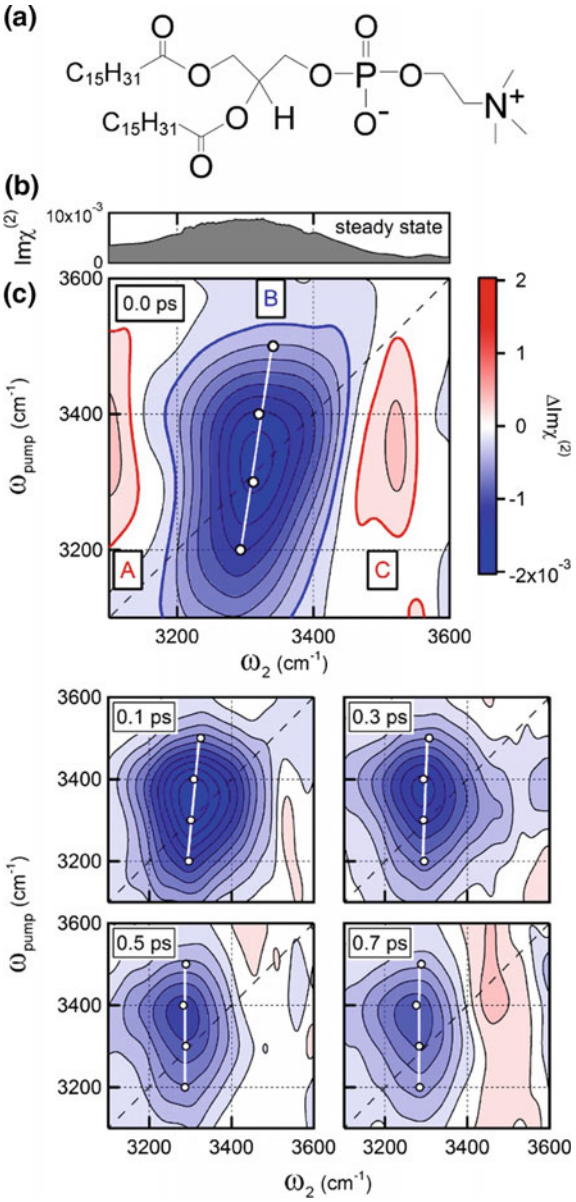

Fig. 10.11 **a** Chemical structure of DPPC. **b** The steady-state Im$\chi^{(2)}$ spectrum and **c** 2D HD-VSFG spectra at the delay time from 0.0 to 0.7 ps at the DPPC/HOD–D_2O (H_2O/HOD/D_2O = 1: 8: 16) interface. White solid lines in the 2D spectra represent the center line slope (CLS) of the lobe B. Reprinted with permission from [52]. Copyright 2017 American Chemical Society

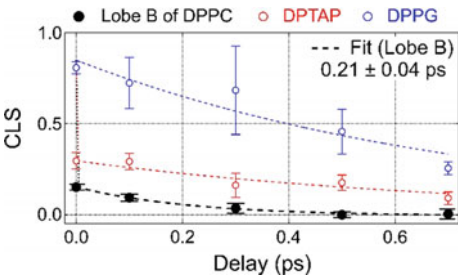

Fig. 10.12 Temporal change of CLS's of the bleach lobes in 2D spectra of the lipid/water interfaces, lobe B of DPPC (black), DPTAP (red) and DPPG (blue). Reprinted with permission from [52]. Copyright 2017 American Chemical Society

This 2D HD-VSFG study on the DPPC/HOD–D_2O interface shows that the hydrogen bond dynamics of water around the phosphate group is different between DPPC and DPPG interfaces. This difference is attributable to the presence of the nearby choline group in the head group of zwitterionic DPPC. As described in the previous section, the water around the choline site at the DPTAP interface exhibits bulk-like ultrafast hydrogen-bond fluctuation [47]. At the zwitterionic DPPC interface, however, because the phosphate and choline are closely located and form a mosaic structure of the H-up and H-down water [54], ultrafast hydrogen-bond fluctuation of the water around the choline is expected to perturb the hydrogen bond of the water around the phosphate site. It is considered that this disturbance gives rise to ultrafast fluctuation of the hydrogen bond of water also around the phosphate site at the DPPC interface (Fig. 10.13).

The 2D HD-VSFG study of the DPPC/water interface revealed that the hydrogen-bond dynamics of water at the zwitterionic lipid interface is not a simple sum of the dynamics of water around individual phosphate and choline sites, and provides a clear evidence of the cooperative effect of the two sites on the hydrogen-bond dynamics of interfacial water.

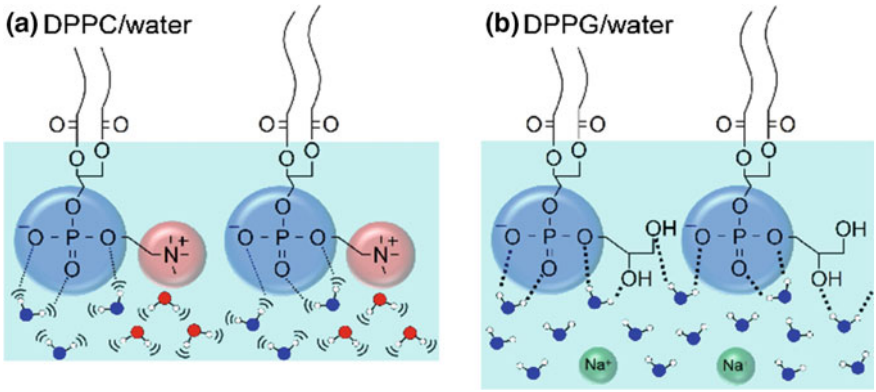

Fig. 10.13 Schematic of hydrogen-bond fluctuation at **a** the DPPC/water interface and **b** the DPPG/water interface. Reprinted with permission from [52]. Copyright 2017 American Chemical Society

10.4 Conclusion

In this review, we described our recent experimental studies of vibrational dynamics at aqueous interfaces carried out with 2D HD-VSFG spectroscopy. The 2D HD-VSFG study at the air/water interface clarified fundamental properties of interfacial water such as the anharmonic coupling between free OH and HB OH vibrations, inhomogeneity of the HB OH band and the T_1 time of HB OH vibration. The 2D HD-VSFG spectra of the CTAB/water interfaces demonstrated the importance of isotopic dilution for clear observation of spectral diffusion dynamics at aqueous interfaces. In the study of the model membrane lipid/water interfaces, 2D HD-VSFG clarified that the hydrogen-bond dynamics greatly depend on the interaction between the lipid head group and interfacial water. Furthermore, it was found that the effects of coexisting head groups on the dynamics of interfacial water is not a simple sum of the effect of individual head groups but they are highly cooperative.

2D HD-VSFG spectroscopy has just begun to unveil unique vibrational dynamics at liquid interfaces and clarify the difference between interface and bulk. This new interface-selective ultrafast nonlinear spectroscopy enables us to selectively and thoroughly investigate the vibrational dynamics at the liquid interfaces as we examine ultrafast dynamics in solution and to disclose the mechanism of unique properties of liquid interfaces.

References

1. E.T.J. Nibbering, T. Elsaesser, Ultrafast vibrational dynamics of hydrogen bonds in the condensed phase. Chem. Rev. **104**(4), 1887–1914 (2004)
2. S. Nihonyanagi, J.A. Mondal, S. Yamaguchi, T. Tahara, Structure and dynamics of interfacial water studied by heterodyne-detected vibrational sum-frequency generation. Annu. Rev. Phys. Chem. **64**(1), 579–603 (2013)
3. Y.R. Shen, Phase-sensitive sum-frequency spectroscopy. Annu. Rev. Phys. Chem. **64**(1), 129–150 (2013)
4. S. Nihonyanagi, S. Yamaguchi, T. Tahara, Ultrafast dynamics at water interfaces studied by vibrational sum frequency generation spectroscopy. Chem. Rev. **117**(16), 10665–10693 (2017)
5. Y.R. Shen, V. Ostroverkhov, Sum-frequency vibrational spectroscopy on water interfaces: polar orientation of water molecules at interfaces. Chem. Rev. **106**(4), 1140–1154 (2006)
6. C.S. Tian, Y.R. Shen, Sum-frequency vibrational spectroscopic studies of water/vapor interfaces. Chem. Phys. Lett. **470**(1), 1–6 (2009)
7. S. Nihonyanagi, S. Yamaguchi, T. Tahara, Direct evidence for orientational flip-flop of water molecules at charged interfaces: a heterodyne-detected vibrational sum frequency generation study. J. Chem. Phys. **130**(20), 204704 (2009)
8. R. Superfine, J.Y. Huang, Y.R. Shen, Phase measurement for surface infrared visible sum-frequency generation. Opt. Lett. **15**(22), 1276–1278 (1990)
9. J.A. McGuire, Y.R. Shen, Ultrafast vibrational dynamics at water interfaces. Science **313**(5795), 1945–1948 (2006)
10. M. Smits, A. Ghosh, M. Sterrer, M. Müller, M. Bonn, Ultrafast vibrational energy transfer between surface and bulk water at the air-water interface. Phys. Rev. Lett. **98**(9), 098302 (2007)

11. A. Ghosh, M. Smits, J. Bredenbeck, M. Bonn, membrane-bound water is energetically decoupled from nearby bulk water: an ultrafast surface-specific investigation. J. Am. Chem. Soc. **129**(31), 9608–9609 (2007)
12. P.C. Singh, S. Nihonyanagi, S. Yamaguchi, T. Tahara, Ultrafast vibrational dynamics of water at a charged interface revealed by two-dimensional heterodyne-detected vibrational sum frequency generation. J. Chem. Phys. **137**(9), 094706 (2012)
13. P. Hamm, M. Zanni, *Concepts and Methods of 2D Infrared Spectroscopy*. Cambridge University Press (2011)
14. K. Inoue, S. Nihonyanagi, P.C. Singh, S. Yamaguchi, T. Tahara, 2D heterodyne-detected sum frequency generation study on the ultrafast vibrational dynamics of H_2O and HOD water at charged interfaces. J. Chem. Phys. **142**(21), 212431 (2015)
15. P. Hamm, M. Lim, R.M. Hochstrasser, Structure of the amide I band of peptides measured by femtosecond nonlinear-infrared spectroscopy. J. Phys. Chem. B **102**(31), 6123–6138 (1998)
16. S. Yamaguchi, T. Tahara, Heterodyne-detected electronic sum frequency generation: "Up" versus "down" alignment of interfacial molecules. J. Chem. Phys. **129**(10), 101102 (2008)
17. M. Cho, Coherent two-dimensional optical spectroscopy. Chem. Rev. **108**(4), 1331–1418 (2008)
18. W. Xiong, J.E. Laaser, R.D. Mehlenbacher, M.T. Zanni, Adding a dimension to the infrared spectra of interfaces using heterodyne detected 2D sum-frequency generation (HD 2D SFG) spectroscopy. Proc. Natl. Acad. Sci. U.S.A. **108**(52), 20902–20907 (2011)
19. M. Schleeger, M. Grechko, M. Bonn, Background-free fourth-order sum frequency generation spectroscopy. J. Phys. Chem. Lett. **6**(11), 2114–2120 (2015)
20. H. Vanselous, A.M. Stingel, P.B. Petersen, Interferometric 2D sum frequency generation spectroscopy reveals structural heterogeneity of catalytic monolayers on transparent materials. J. Phys. Chem. Lett. **8**(4), 825–830 (2017)
21. S. Nihonyanagi, R. Kusaka, K. Inoue, A. Adhikari, S. Yamaguchi, T. Tahara, Accurate determination of complex $\chi^{(2)}$ spectrum of the air/water interface. J. Chem. Phys. **143**(12), 124707 (2015)
22. S. Yamaguchi, Development of single-channel heterodyne-detected sum frequency generation spectroscopy and its application to the water/vapor interface. J. Chem. Phys. **143**(3), 034202 (2015)
23. Q. Du, R. Superfine, E. Freysz, Y.R. Shen, Vibrational spectroscopy of water at the vapor/water interface. Phys. Rev. Lett. **70**(15), 2313–2316 (1993)
24. P.C. Singh, S. Nihonyanagi, S. Yamaguchi, T. Tahara, Communication: ultrafast vibrational dynamics of hydrogen bond network terminated at the air/water interface: a two-dimensional heterodyne-detected vibrational sum frequency generation study. J. Chem. Phys. **139**(16), 161101 (2013)
25. Z. Zhang, L. Piatkowski, H.J. Bakker, M. Bonn, Ultrafast vibrational energy transfer at the water/air interface revealed by two-dimensional surface vibrational spectroscopy. Nat. Chem. **3**(11), 888–893 (2011)
26. C.-S. Hsieh, R.K. Campen, M. Okuno, E.H.G. Backus, Y. Nagata, M. Bonn, Mechanism of vibrational energy dissipation of free OH groups at the air–water interface. Proc. Natl. Acad. Sci. USA **110**(47), 18780–18785 (2013)
27. X. Wei, Y.R. Shen, Motional effect in surface sum-frequency vibrational spectroscopy. Phys. Rev. Lett. **86**(21), 4799–4802 (2001)
28. T. Ishiyama, A. Morita, T. Tahara, Molecular dynamics study of two-dimensional sum frequency generation spectra at vapor/water interface. J. Chem. Phys. **142**(21), 212407 (2015)
29. C.-S. Hsieh, M. Okuno, J. Hunger, E.H.G. Backus, Y. Nagata, M. Bonn, Aqueous heterogeneity at the air/water interface revealed by 2D-HD-SFG spectroscopy. Angew. Chem. Int. Ed. **53**(31), 8146–8149 (2014)
30. S.T. van der Post, C.S. Hsieh, M. Okuno, Y. Nagata, H.J. Bakker, M. Bonn, J. Hunger, Strong frequency dependence of vibrational relaxation in bulk and surface water reveals sub-picosecond structural heterogeneity. Nat. Commun. **6**, 8384 (2015)

31. K. Inoue, T. Ishiyama, S. Nihonyanagi, S. Yamaguchi, A. Morita, T. Tahara, Efficient spectral diffusion at the air/water interface revealed by femtosecond time-resolved heterodyne-detected vibrational sum frequency generation spectroscopy. J. Phys. Chem. Lett. **7**(10), 1811–1815 (2016)
32. A.J. Lock, H.J. Bakker, Temperature dependence of vibrational relaxation in liquid H2O. J. Chem. Phys. **117**(4), 1708–1713 (2002)
33. K. Ramasesha, L. De Marco, A. Mandal, A. Tokmakoff, Water vibrations have strongly mixed intra- and intermolecular character. Nat. Chem. **5**(11), 935–940 (2013)
34. D.E. Gragson, G.L. Richmond, Investigations of the structure and hydrogen bonding of water molecules at liquid surfaces by vibrational sum frequency spectroscopy. J. Phys. Chem. B **102**(20), 3847–3861 (1998)
35. M.R. Watry, T.L. Tarbuck, G.L. Richmond, Vibrational sum-frequency studies of a series of phospholipid monolayers and the associated water structure at the vapor/water interface. J. Phys. Chem. B **107**(2), 512–518 (2003)
36. M.C. Gurau, S.-M. Lim, E.T. Castellana, F. Albertorio, S. Kataoka, P.S. Cremer, On the mechanism of the Hofmeister effect. J. Am. Chem. Soc. **126**(34), 10522–10523 (2004)
37. G. Ma, X. Chen, H.C. Allen, Dangling OD confined in a Langmuir monolayer. J. Am. Chem. Soc. **129**(45), 14053–14057 (2007)
38. X. Chen, W. Hua, Z. Huang, H.C. Allen, Interfacial water structure associated with phospholipid membranes studied by phase-sensitive vibrational sum frequency generation spectroscopy. J. Am. Chem. Soc. **132**(32), 11336–11342 (2010)
39. Y.-C. Wen, S. Zha, X. Liu, S. Yang, P. Guo, G. Shi, H. Fang, Y.R. Shen, C. Tian, Unveiling microscopic structures of charged water interfaces by surface-specific vibrational spectroscopy. Phys. Rev. Lett. **116**(1), 016101 (2016)
40. S. Strazdaite, K. Meister, H.J. Bakker, Orientation of polar molecules near charged protein interfaces. Phys. Chem. Chem. Phys. **18**(10), 7414–7418 (2016)
41. S. Devineau, K. Inoue, R. Kusaka, S.-H. Urashima, S. Nihonyanagi, D. Baigl, A. Tsuneshige, T. Tahara, Change of the isoelectric point of hemoglobin at the air/water interface probed by the orientational flip-flop of water molecules. Phys. Chem. Chem. Phys. **19**(16), 10292–10300 (2017)
42. N. Takeshita, M. Okuno, T.-A. Ishibashi, Molecular conformation of DPPC phospholipid Langmuir and Langmuir-Blodgett monolayers studied by heterodyne-detected vibrational sum frequency generation spectroscopy. Phys. Chem. Chem. Phys. **19**(3), 2060–2066 (2017)
43. S. Nihonyanagi, S. Yamaguchi, T. Tahara, Water hydrogen bond structure near highly charged interfaces is not like ice. J. Am. Chem. Soc. **132**(20), 6867–6869 (2010)
44. G.L. Richmond, Molecular bonding and interactions at aqueous surfaces as probed by vibrational sum frequency spectroscopy. Chem. Rev. **102**(8), 2693–2724 (2002)
45. M. Sovago, R.K. Campen, G.W.H. Wurpel, M. Müller, H.J. Bakker, M. Bonn, Vibrational response of hydrogen-bonded interfacial water is dominated by intramolecular coupling. Phys. Rev. Lett. **100**(17), 173901 (2008)
46. R.A. Livingstone, Y. Nagata, M. Bonn, E.H.G. Backus, Two types of water at the water—surfactant interface revealed by time resolved vibrational spectroscopy. J. Am. Chem. Soc. **137**(47), 14912–14919 (2015)
47. P.C. Singh, K. Inoue, S. Nihonyanagi, S. Yamaguchi, T. Tahara, Femtosecond hydrogen bond dynamics of bulk-like and bound water at positively and negatively charged lipid interfaces revealed by 2D HD-VSFG spectroscopy. Angew. Chem. Int. Ed. **55**(36), 10621–10625 (2016)
48. K. Kwak, S. Park, I.J. Finkelstein, M.D. Fayer, Frequency-frequency correlation functions and apodization in two-dimensional infrared vibrational echo spectroscopy: a new approach. J. Chem. Phys. **127**(12), 124503 (2007)
49. C.J. Fecko, J.D. Eaves, J.J. Loparo, A. Tokmakoff, P.L. Geissler, Ultrafast hydrogen-bond dynamics in the infrared spectroscopy of water. Science **301**(5640), 1698–1702 (2003)
50. S. Roy, S.M. Gruenbaum, J.L. Skinner, Theoretical vibrational sum-frequency generation spectroscopy of water near lipid and surfactant monolayer interfaces. II. Two-dimensional spectra. Two-dimensional spectra. J. Chem. Phys. **141**(22), 22D505 (2014)

51. K. Inoue, M. Ahmed, S. Nihonyanagi, T. Tahara, Effect of hydrogen-bond on ultrafast spectral diffusion dynamics of water at charged monolayer interfaces. J. Chem. Phys. **150**(5), 054705 (2019)
52. K. Inoue, P.C. Singh, S. Nihonyanagi, S. Yamaguchi, T. Tahara, Cooperative hydrogen-bond dynamics at a zwitterionic lipid/water interface revealed by 2D HD-VSFG spectroscopy. J. Phys. Chem. Lett. **8**(20), 5160–5165 (2017)
53. J.A. Mondal, S. Nihonyanagi, S. Yamaguchi, T. Tahara, Three distinct water structures at a zwitterionic lipid/water interface revealed by heterodyne-detected vibrational sum frequency generation. J. Am. Chem. Soc. **134**(18), 7842–7850 (2012)
54. S. Re, W. Nishima, T. Tahara, Y. Sugita, Mosaic of water orientation structures at a neutral zwitterionic lipid/water interface revealed by molecular dynamics simulations. J. Phys. Chem. Lett. **5**(24), 4343–4348 (2014)
55. T. Ishiyama, D. Terada, A. Morita, Hydrogen-bonding structure at zwitterionic lipid/water interface. J. Phys. Chem. Lett. **7**(2), 216–220 (2016)
56. Y. Nagata, S. Mukamel, Vibrational sum-frequency generation spectroscopy at the water/lipid interface: molecular dynamics simulation study. J. Am. Chem. Soc. **132**(18), 6434–6442 (2010)
57. S. Roy, S.M. Gruenbaum, J.L. Skinner, Theoretical vibrational sum-frequency generation spectroscopy of water near lipid and surfactant monolayer interfaces. J. Chem. Phys. **141**(18), 18C502 (2014)
58. T. Ohto, E.H.G. Backus, C.-S. Hsieh, M. Sulpizi, M. Bonn, Y. Nagata, Lipid carbonyl groups terminate the hydrogen bond network of membrane-bound water. J. Phys. Chem. Lett. **6**, 4499–4503 (2015)

Chapter 11
Ultrafast Spectroscopy of Hydrogenase Enzyme Models

Peter A. Eckert and Kevin J. Kubarych

Abstract Hydrogenase enzymes are nature's solution to using molecular hydrogen as an energy source. While the air-sensitivity of these biological catalysts make them impractical for industrial hydrogen generation, synthetic mimics show promise in acting as effective substitutes. Hydrogenase model compounds also enable detailed investigation of the ultrafast dynamics and chemical reaction mechanisms using ultrafast infrared spectroscopy. This chapter reviews the progress in applying ultrafast transient infrared absorption and multidimensional spectroscopy to a range of small molecule hydrogenase model compounds, as well as several macromolecular and larger constructs. The rich vibrational structure and straightforward chemical modularity of these diiron compounds represent an exciting class of molecules that are, at the same time, excellent model systems for fundamental chemical dynamics, and practical molecular catalytic components with direct application to next-generation hydrogen-based energy strategies.

11.1 Introduction

Metalloenzymes, ubiquitous in nature, perform a remarkable feat of chemistry: they catalyze complex redox reactions using base metal atoms in aqueous environments, under mild aqueous conditions. One example that forms the central focus of this chapter is the class of enzymes known as hydrogenases, which catalyze the equilibrium $H_2 \rightleftharpoons 2H^+ + 2e^-$, enabling microorganisms to use hydrogen as an energy source and maintaining cellular potential and pH [1]. Industrial production of hydrogen is

P. A. Eckert · K. J. Kubarych (✉)
Department of Chemistry, University of Michigan, 930 N. University Ave, Ann Arbor, MI 48109, USA
e-mail: kubarych@umich.edu

Present Address:
P. A. Eckert
Oak Ridge National Laboratory, Oak Ridge, TN, USA

M. Cho (ed.), *Coherent Multidimensional Spectroscopy*,
Springer Series in Optical Sciences 226,
https://doi.org/10.1007/978-981-13-9753-0_11

largely accomplished by steam reforming, an energy intensive process that not only consumes fossil fuels but also generates as much CO_2 as it does H_2, in addition to the CO_2 generated by heating [2]. There is a great effort underway to devise carbon-neutral means of hydrogen generation for use in fuel cells to enable a hydrogen-based energy economy [3]. One promising strategy would employ the same enzymes used by nature to generate hydrogen, but the natural enzymes are so acutely air-sensitive that they cannot be used in large-scale bioreactors. Nevertheless, the remarkable efficiency of hydrogenase enzymes provides inspiration to design chemical analogues that mimic the structure and function, while lacking the deleterious sensitivity to oxygen [4–6].

The two decades since the first x-ray structures of the diiron, bacterial [FeFe] hydrogenase have seen an explosive development of numerous examples of active site model compounds based on the diiron dithiolate core found in the enzyme [7]. This unusual active site poses many mysteries, not the least of which is its assembly, and a subfield of research is concerned with elucidating its biosynthetic pathway [1, 8]. Small molecule mimics of the organometallic enzyme active site enable detailed mechanistic studies to shed light on the enzymatic reaction, whereas abiological derivatives can lead to new chemical catalysis outside of the initial scope limited by natural conditions of pH and redox potentials.

The hydrogenase active site and its models (Fig. 11.1) present an ideal opportunity for new research in fundamental chemical reaction dynamics. Advances are greatly aided by the chemical modularity and relative ease of synthesis, coupled with the practical benefit of having very strong infrared transitions of the carbonyl and cyanide ligands that tune the structure and energetics of the diiron core. Unfortunately the extraordinary air sensitivity of the natural enzymes makes it quite a challenge to probe the structural dynamics, though we anticipate the rich information content will drive progress towards such investigations. Here we review the progress in using ultrafast spectroscopy, particularly two-dimensional infrared (2D-IR), to characterize equilibrium and non-equilibrium structural dynamics in a variety of active site models (Fig. 11.2).

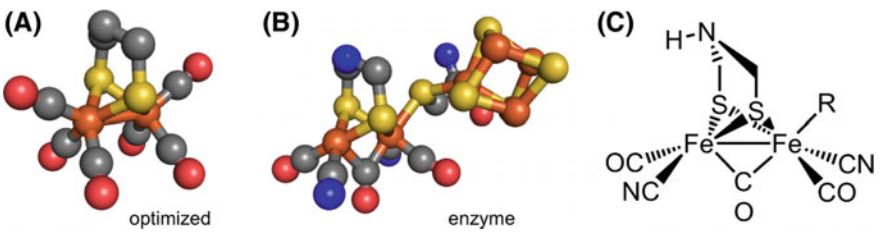

Fig. 11.1 Structures of **a** the basic diiron dithiolate model: μ-pdt-$[Fe(CO)_3]_2$, (pdt = propanedithiolate), **b** The FeFe hydrogenase H-cluster subsite, referred to here as the "active site", and **c** chemical structure showing the protonated nitrogen in the bridge, thought to participate in a proton shuttle mechanism to generate the Fe-H hydride. This figure is adapted from [15], Copyright the American Chemical Society (2017)

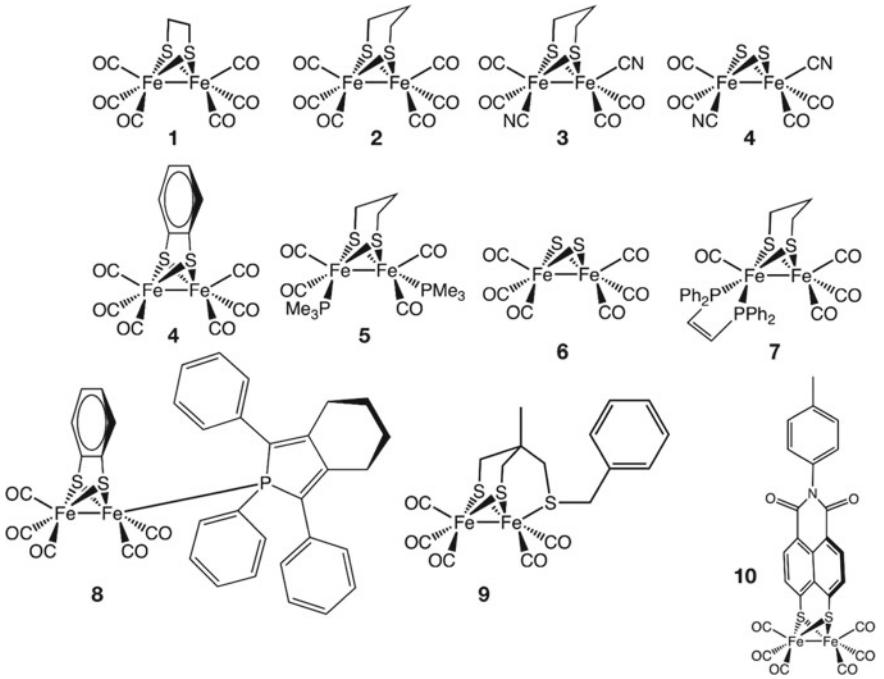

Fig. 11.2 Structures of hydrogenase models that are discussed in this chapter

Before embarking on the main subject of this chapter, it is worthwhile to review the main benefits of using ultrafast spectroscopic methods like 2D-IR to study enzymes and active site models. Chemical reactions generally occur, at least kinetically, on much slower time scales than those accessible to ultrafast infrared and electronic spectroscopy, so it may not be apparent that short time dynamics will be of much use in understanding enzyme catalysis. Indeed in many cases, the rate-limiting step of enzyme catalysis is product release, which is largely subject to diffusion control [9]. Diffusion within proteins has been established to be coupled to protein structural fluctuations, creating a direct link between ultrafast motions and the transport of molecules through the protein matrix [10]. At the active site, energetic factors can stabilize intermediates and transition states distinct from those in solution, thus greatly reducing reaction barriers, and likely altering the detailed mechanism. Catalytic activity is a central feature of enzymes, but in many cases, the more essential effect is the *differential* barrier reduction that endows selectivity of one reaction pathway over another. With a lowered barrier, the potential influence of dynamical fluctuations of the environment (i.e. solvent or local protein atoms) assumes more prominence than in the case of uncatalyzed solution-phase reactions. One limitation of applying ultrafast techniques to catalysis is the difficulty, or impossibility, of triggering the chemical reaction to synchronize an ensemble of molecules. Nevertheless, as has been shown to be especially useful in NMR spectroscopy, the ability to monitor

structural dynamics and fluctuations of untriggered processes has proven to be quite powerful in characterizing equilibrium dynamics of functional relevance [11].

Hydrogenase enzymes and their small-molecule mimics catalyze the reduction of protons to form molecular hydrogen (i.e. $2H^+ + 2\ e^- \rightarrow H_2$) and the oxidation of molecular hydrogen (i.e. $H_2 \rightarrow 2H^+ + 2\,e^-$). The hydrogenase active site and its models present an ideal opportunity for new research in fundamental chemical reaction dynamics because of a remarkable observation that appears to hold for a wide range of model compounds. Though many of the mimics cannot match the performance of the natural enzymes in terms of turnover number and frequency, encapsulation within some form of macromolecular scaffolding can greatly enhance the overall catalytic reactivity [12–14]. It is not surprising that the protein environment would be expected to confer high efficiency, given that millions of years of evolution have optimized the structural and electrostatic environment of the active site. It is perhaps less obvious that simply placing the active site in a container could have such a dramatic effect on the reactivity. A key aim of current research is to determine a minimal set of criteria needed to achieve performance resembling that of the protein, without requiring the full elaborate supramolecular scaffold of the natural enzyme.

11.2 2D-IR and Transient IR Spectroscopy of Small Molecule Active Site Mimics

The vibrational spectrum of diiron dithiolate hexacarbonyl complexes is characterized by five strongly IR active terminal CO vibrations, and a sixth mode that appears only in the Raman spectrum [15, 16]. As with all metal carbonyls, the normal modes are highly delocalized over all of the six CO ligands, with relatively weak coupling to other degrees of freedom, yielding narrow line width bands with quite long vibrational lifetimes (>30 ps) in a variety of organic solvents [17].

11.2.1 Intramolecular Vibrational Dynamics in the Diiron Core

The first 2D-IR spectra of any diiron carbonyl complexes were reported by Hunt et al., with the main goal of studying the fundamental vibrational dynamics of energy relaxation and intramolecular vibrational redistribution of **2** (Fig. 11.3) in a few representative solvents (heptane, hexadecane, and acetonitrile) [17]. Despite marked differences in the FT-IR line shapes, the vibrational population relaxation and energy transfer (i.e. IVR) are quite similar in all three solvents. Decays of most spectral features could be fit well with two or three exponentials, yielding characteristic timescales of 5–10 and 100–150 ps. As with many other studies of

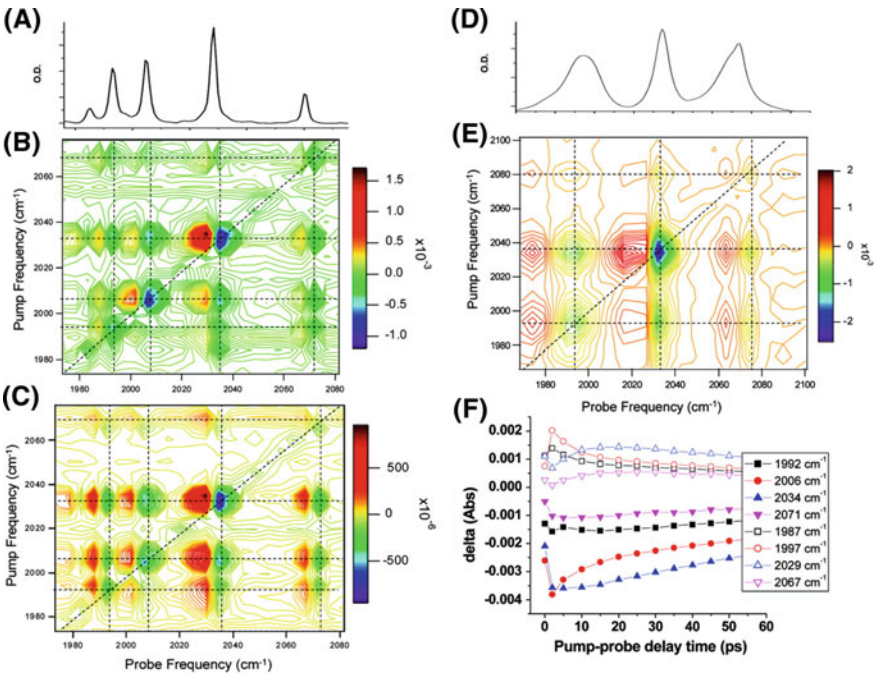

Fig. 11.3 μ-pdt-$[Fe(CO)_3]_2$ (**2**) studied with FT-IR and 2D-IR. **a** The FT-IR spectrum in heptane shows five well-resolved bands that are strongly coupled as revealed by the 4 2D-IR spectrum **b** recorded at a 5 ps waiting time. At later, 25-ps waiting time **c** intramolecular vibrational redistribution leads to the relative growth of the cross peaks. **f** Waiting time dependent slices of **2** in heptane show the vibrational population dynamics. For comparison, the more polar acetonitrile yields three resolvable bands in the FT-IR spectrum (**d**), and the 2D-IR spectra (**e**) appear to be homogeneously broadened on the 5 ps timescale. Spectral diffusion of metal carbonyls in acetonitrile is relatively rapid, as has been observed in other experiments. Figure is adapted from [17], Copyright the American Chemical Society (2008)

transition metal carbonyl complexes, the fast time scale is attributable to IVR and the slow time scale reflects vibrational energy relaxation to the ground state. Although anisotropy data were presented, rapid IVR, which randomizes vibrational energy among nearby excited modes with (generally) different transition dipole moment directions, prohibits isolation of the orientational motion from the IVR, which also produces a transient anisotropy decay. Nevertheless, isotropic relaxation (i.e. magic angle pump-probe transient absorption) showed only one dominant time scale in the case of the acetonitrile solvent. There are notable differences in the IVR time scales in heptane and hexadecane, which are similar to the solvent-dependent IVR recently reported elsewhere with a wider range of linear alkane solvents. The origin of alkane solvent dependent IVR is not yet understood.

In addition to the simplest diiron core model, Hunt et al. have studied several compounds with greater compositional similarity to the active site of the [FeFe]-hydrogenase enzyme [18]. Investigation of a complex with the air-sensitive and

biologically-favored $[Fe(CO)_2(CN)]_2$ core (**3**) revealed complex vibrational coupling between the distinct carbonyl and cyanide modes, where the IVR between the carbonyl and cyanide groups is much slower (~30 ps) than the intra-carbonyl IVR (<4 ps), and appears to be mediated through specific pathways of anharmonic vibrational coupling, including several low-frequency vibrational modes at ~500 cm^{-1} and a specific coupling between one cyanide and one carbonyl mode. The carbonyl vibrational modes of the $[Fe(CO)_2(CN)]_2$ core relax almost three times faster than the corresponding vibrational modes of the $[Fe(CO)_3]_2$ core, although the relative contributions of inter- and intra-molecular couplings to this acceleration of IVR remain uncertain.

In a different study, Hunt et al. investigated (Fig. 11.4) a complex (**9**) that has more structural similarity to the natural enzyme's active site, with a CO ligand exchanged for a third thiolate linkage through which a bulk aromatic group is attached [19]. The substitution leads to larger spacings between the CO modes, corresponding to enhanced coupling. Vibrational dynamics of (**9**) in heptane, acetonitrile, and 1,7-heptanediol reveals some degree of solvent and mode variation. The highest frequency band around 2050 cm^{-1} exhibits a bimodal bleach recovery (0–1 transition observed on the diagonal of the 2D spectrum), whereas the lower frequency band near 1990 cm^{-1} appears single-exponential except for the 1,7-heptanediol case. As would be expected for a more polar solvent, there is clear inhomogeneous broadening and spectral diffusion in the 1,7-heptanediol solution, but there is no clear indication of either in acetonitrile. Based on other reports of similar diiron carbonyls in acetonitrile, it is likely the spectral diffusion is too rapid to be observed with the double-resonance (i.e. narrow-band pump/broadband probe) method used by Hunt et al. Their earlier report of the basic diiron complex (**2**) in acetonitrile also did not resolve any transient inhomogeneity or dynamical spectral diffusion, likely for the same technical reason. The spectral diffusion in 1,7-heptanediol is characterized by a 3–4 ps time scale, which likely reflects primarily solvation dynamics, but there is also the possibility that flexibility of the whole complex, particularly with the bulky phenyl ring, leads to intramolecular frequency fluctuations that contribute to the spectral diffusion dynamics. The complex's flexibility may also be indicated by the long-time offset in the center-line slope measure of spectral correlation. Incomplete relaxation of spectral inhomogeneity would arise from pronounced structural variations that interconvert too slowly to be captured within the short-time portion of the spectral diffusion. Given the long vibrational lifetime of the CO modes, it should be possible to monitor much slower spectral diffusion should it in fact be present. Below we discuss more recent work to address this key issue of complex flexibility.

11.2.2 Ultrafast and Multi-timescale Photochemistry

In addition to the important seminal equilibrium 2D-IR spectroscopy, Hunt et al. have also investigated in detail the transient, non-equilibrium photochemistry of hydrogenase models in response to ligand dissociation [20–27]. Besides

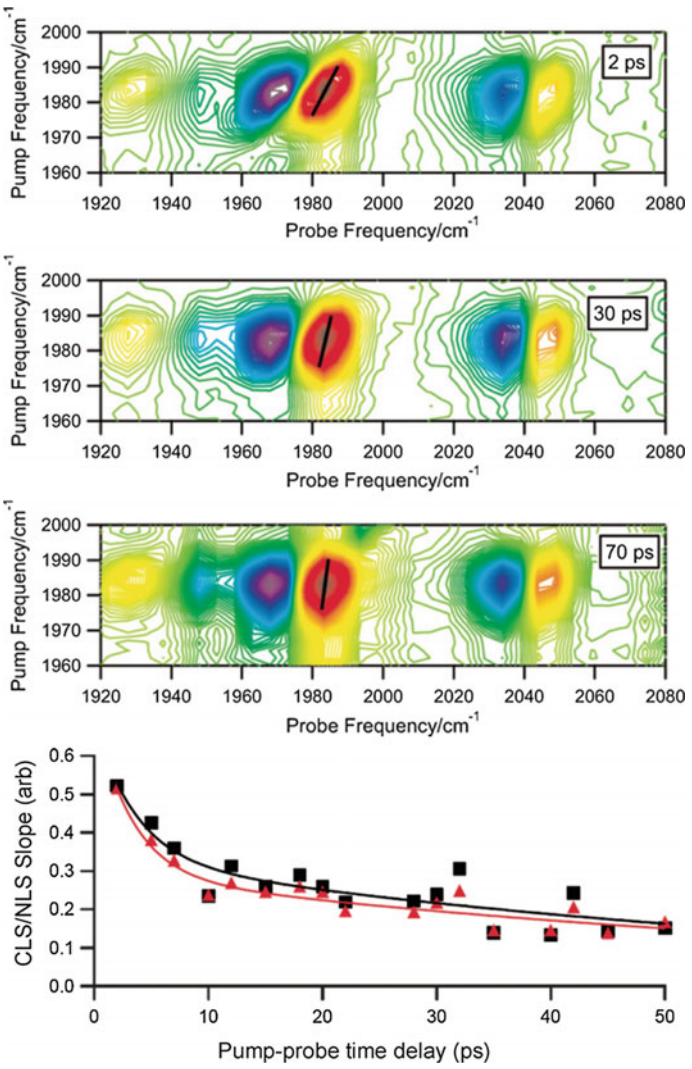

Fig. 11.4 Detail of 2D-IR spectra of **7** in 1,7-heptanediol. (top) The hydrogen bonded liquid induces slow spectral diffusion dynamics as evidenced by the correlation of the 2D-IR lineshape even at 70 ps. (bottom) Measuring the center line slope (CLS, squares) or the nodal line slope (NLS, triangles) results in essentially the same decay of spectral inhomogeneity, which persists for tens of picoseconds. A biexponential fit yields 3–4 and 70 ps time scales. Figure adapted from [19], Copyright the Royal Society of Chemistry (2010)

fundamental interest in ultrafast reaction dynamics, especially involving first solvation shell species, there is some interest in the loss of a ligand during the enzymatic reaction cycle. The evidence is largely due to observations that CO is an inhibitor of the enzyme [20]. Employing UV pump/IR probe transient absorption spectroscopy of (**2**), Hunt et al. initially found signatures for a pentacarbonyl species coordinated by a solvent molecule in a vacant site [20]. The spectral dynamics interestingly exhibited changes even on very long time scales, indicating slow equilibrium among transient species. Since transient absorption is still one-dimensional in the probing step, it is incapable of determining directly from transient spectra whether multiple spectral features correspond to different molecular species, or to coupled modes in a single species. 2D spectroscopy is ideally suited to this kind of spectral "separation," but in order to apply 2D-IR to non-equilibrium systems, one must perform fifth-order transient 2D-IR spectroscopy [28, 29]. Using transient 2D-IR, Hunt et al. were able to constrain the assignment of the photoproducts to a single pentacarbonyl species [22, 30]. Moreover, using transient IR/IR absorption anisotropy, where the transient IR pump-probe anisotropy is recorded for a fixed (200 ps) UV/IR delay, the authors concluded that the solvent occupies an axial coordination site, as opposed to an equatorial site. As mentioned above, transient IR absorption anisotropy is complicated to analyze when there are multiple modes that can exchange energy via IVR, and hence masquerade as motional reorientation. In this case, the time scale is clearly too fast to be attributable to orientational diffusion, and thus is indeed structural, providing access to the relative transition dipole moment directions among coupled modes.

A transient IR absorption study by Harris et al. compared long time spectral dynamics of (**4**) following UV excitation (inducing <10% CO photolysis) with the vibrational lifetimes estimated from IR-pump/IR-probe transient absorption [31]. The data clearly show that the long-time decay of the IR transient absorption is essentially identical whether excited in the UV or directly in the IR. The explanation for this result is that the UV excited electronic state dynamics relaxes on an ultrafast, ~10 ps timescale, with the energy being redistributed into intramolecular vibrations. Excitation at 400 nm provides 25,000 cm^{-1} of energy, so direct transfer to the CO modes would be unlikely since there are so many vibrations in the benzene dithiolate bridged diiron complex. Nevertheless, the authors do attribute some changes in their spectra to direct excitation of CO vibrations. One complication is that the model used for the data assumes IVR to occur faster than the other dynamical processes, but it has been directly observed subsequently in 2D-IR spectra that the IVR can be quite slow in alkane solvents (11 ps in hexane, and 27 ps in hexadecane) for two alkane dithiolate bridged complexes [15]. It is also not clear how to reconcile the claimed low 10% photolysis with many previous and subsequent reports of high photolysis rates in similar complexes using both 355 and 400 nm excitation [20–25, 30, 32]. Lacking a clear rationale for a non-statistical energy redistribution into the CO modes, the most likely scenario is that the 25,000 cm^{-1} populates numerous low-frequency modes which are themselves coupled to the CO vibrations, causing a transient absorption signal. It is interesting that the ultimate "cooling" (i.e. relaxation of those low-frequency modes) occurs on the same time scale as the CO vibrational relaxation monitored directly with IR/IR transient absorption. It remains an open

question as to how these intramolecular vibrational relaxation dynamics can be used to help inform or guide innovations in photo- or electrocatalysis in the family of diiron carbonyl complexes.

Photo-induced ligand dissociation has also been reported by Heilweil et al. in similar studies of cyanide- and phosphine-substituted hydrogenase models [30, 33, 34]. Phosphine (**5**) and cyanide (**3**) ligands electronically enrich the diiron molecular core and consequently red shift the carbonyl vibrational frequencies relative to the diiron hexacarbonyl moiety. They differ, however, with respect to their electronic charge; phosphines are neutral whereas cyanides are negatively charged. Phosphines have been widely employed in hydrogenase model compounds as air-stable and electronically donating ligands, but the air-sensitive cyanide ligands are more biologically relevant. The photochemistry of (μ-lig)[Fe(CO)$_2$(PMe$_3$)]$_2$ (lig = ethanedithiolate, propanedithiolate) in heptane and acetonitrile (Fig. 11.5) was studied by electronically exciting the sample with pump pulses at either 355 or 532 nm and monitoring carbonyl vibrational modes with TR-IR spectroscopy [30, 34]. The recovery of the ground state bleach occurs on a timescale of ~250 ps for both acetonitrile and heptane, while the photorproduct absorption typically persists several hundred picoseconds longer. In both solvents the bleaches and absorptions persist on the microsecond timescale after decaying to half of their initial intensity. The authors suggest, in agreement with previous studies, that photoexcitation initially induces a carbonyl dissociation. They attribute the several-hundred picosecond timescale to decay of the electronic excited state, vibrational cooling, and geminate rebinding of dissociated carbonyl ligands, and hypothesize that the long-lived transient spectral features represent a population of tricarbonyl species which do not undergo geminate recombination and compounds which geminately rebind carbonyl ligands in a non-thermal distribution.

Heilweil et al. subsequently employed the same experimental methodology to study (**3**, μ-lig)[Fe(CO)$_2$(CN)]$_2^{2-}$ (lig = ethanedithiolate, propanedithiolate), but used UV excitation frequencies of 266 and 400 nm [33]. As with the phosphine-substituted compounds, they observe a photo-induced dissociation of a carbonyl ligand and report the persistence of long-lived transient features which they ascribe to coordinatively unsaturated tricarbonyl species and a non-thermal distribution of ground-state isomers arising from geminate recombination of the dissociated carbonyl ligands. However, they note the absence of the several-hundred picosecond absorption and bleach recovery reported previously by Hunt and observed in their phosphine-substituted compounds. They note that a broad and weak spectral feature near 450 nm, present in the visible absorbance spectra of most hydrogenase models and assigned as a metal-to-metal charge transfer transition, is absent in the visible spectra of the dicyano-substituted compound. Heilweil et al. hypothesize that the presence of charged cyanide ligands alters the electronic structure of the entire complex and suppresses the excited electronic state which, in other model compounds, relaxes on a several-hundred picosecond timescale.

In contrast to previous analyses of photo-induced ligand dissociation in hydrogenase models, Heilweil et al. do not discuss the potential contribution of solvent complexation with the coordinately unsaturated solute. Acetonitrile is known to readily form solvent-solute complexes with unsaturated transition metal complexes through

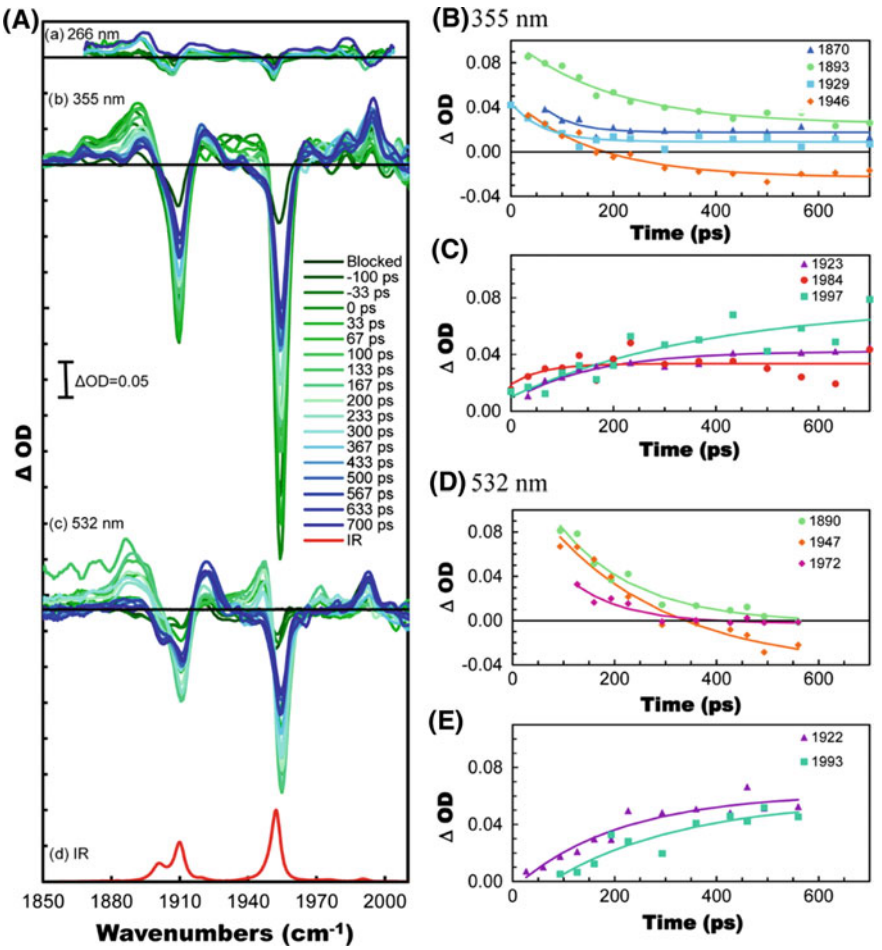

Fig. 11.5 **a** Transient IR absorption spectroscopy of **5** in *n*-heptane using **a** 20-ps 266 nm pulses, **b** 40-ps 355 nm pulses, and **c** 50-ps 532 nm pulses. The FT-IR is shown for reference in **d**. Transient spectral features following excitation at **b**–**c** 355 nm, and **d**–**e** 532 nm. Adapted from [34], Copyright the American Chemical Society (2013)

the terminal nitrogen, and previous work by Hunt et al. directly implicated transient interactions between the solvent and the unsaturated solute. However, we note that the presence or absence of solvent-solute complexes would not significantly impact their final evaluation of the transient and long-lived spectral features they report.

Transient IR absorption spectroscopy is particularly well suited to studying photoinduced charge transfer from a sensitizer to a diiron carbonyl catalytic site. In a first example of such a study, Woutersen et al. synthesized a diiron core with an extended aromatic dithiolate bridge (**10**), containing a pyridyl group that is able to interact favorably with a zinc tetraphenyl porphyrin (ZnTPP) sensitizer [35]. The

donor-acceptor complex forms spontaneously in CH_2Cl_2 solvent, and optical excitation of the ZnTPP donor leads to ultrafast photoinduced charge transfer to the diiron core. The charge separation occurs on a 40-ps time scale, followed by a slower charge recombination process that takes place in roughly 200 ps. Although the charge recombination is somewhat fast for a practical photocatalytic system in general, the work showed the promise of non-covalent coordination as a possible route for future development of sensitized hydrogenase models. Moreover, since the reaction mechanism in this case involves the reduction of protons, they can be made readily available in acidic solution, and their reduction can potentially beat the recombination process.

This work was followed up with a report of a new complex (**8**) containing a bound phosphole electron reservoir ligand, which replaces one of the carbonyls of a phenyl dithiolate bridged diiron core [36]. Although the main goal of that work was to characterize the electrochemistry and electrocataysis of the complex in aqueous solution, transient IR absorption was also used to study the photoinduced electron transfer from a ZnTPP sensitizer to the complex. For this system, the charge separation occurs with a 2.5 ps time constant and the charge separation has an 83 ps time constant. As in the previous case, the fast recombination is not deleterious when the protons can be made to be plentiful, or if they preferentially interact with the catalyst.

11.2.3 Molecular Flexibility: Motion Along the Reaction Coordinate

A key difference between the diiron hexacarbonyl dithiolate models and the natural [FeFe] hydrogenase is the enzyme's more open organometallic coordination sphere (Fig. 11.1). These differences have inspired a proposed mechanistic step that involves turnstile motion of the carbonyls to open a coordination site, implicating the flexibility of the complex in its reactivity [37]. Turnstile motion has been studied using 2D-IR in several tripodal transition metal complexes. In the limit of slow exchange among distinct dihedral angles, it should be possible to observe cross peaks whose kinetics gives the time scale for the equilibrium isomerization reaction. In practice, however, tripodal complexes typically do not exhibit large frequency shifts upon torsional distortion, making it essentially impossible to observe chemical exchange 2D-IR [38, 39]. Even few-cm^{-1} frequency variations, however, can manifest as spectral diffusion induced by the torsional angle fluctuations associated with full or partial rotation, depending on the barriers separating the conformers. Conformer-dependent vibrational frequencies are, therefore, a source of inhomogeneous broadening, that is practically only experimentally visible in the absence of strong solvation interactions that induce their own spectral broadening. Hence, the ability to monitor molecular flexibility is limited to nonpolar solvents where both inhomogeneous and homogeneous broadening are minimized.

Fluctuations within the structural ensemble will produce spectral diffusion that can be measured using 2D-IR spectroscopy. Before our work investigating hydrogenase models, we studied intramolecular conformational flexibility in a tripod, benzene chromium tricarbonyl (BCT), which is known to exchange rapidly on the NMR timescale [39]. The barrier to isomerization from one eclipsed conformer to another is roughly 0.3 k_BT, making this motion accessible on ultrafast timescales. Measurements of spectral diffusion shows a 3 ps time scale, which is notable in its lack of solvent viscosity dependence (in alkanes from hexane to hexadecane). Viscosity independent isomerization is known to occur in photoisomerization of constrained molecules when the overall volume change in small. Indeed, a torsionally isomerizing tripod has a negligible volume change, limiting the influence of the solvent fluctuations on the even very low barrier crossing.

In the context of the diiron hydrogenase model, two complexes (Fig. 11.6) differing in their dithiolate bridges (either ethanedithiolate or propanedithiolate) exhibit spectral diffusion on a 10 ps time scale in a range of alkane solvents (hexane to hexadecane) [15]. Similarly to the simple tripod case, the spectral diffusion in the

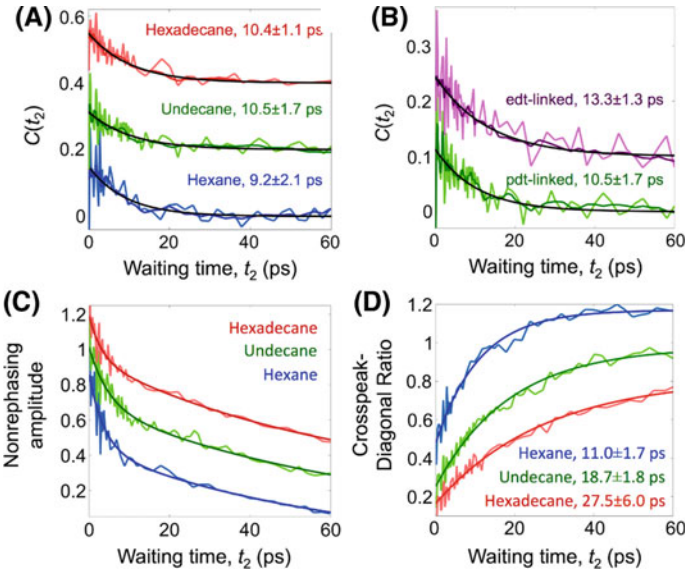

Fig. 11.6 Results of 2D-IR spectroscopy of basic diiron hexacarbonyls in *n*-alkane solvents. **a** Spectral diffusion dynamics (off-set for clarity) of pdt-linked (**2**) in hexadecane, undecane and hexane all exhibit essentially the same ~10 ps time scale. **b** Comparison with the edt-linked complex (**1**) in undecane shows a slightly slower timescale than for the pdt-linked complex. **c** Population dynamics measured using the non-rephasing spectral response shows identical long-time behavior, indicating solvent independent vibrational relaxation to the ground state. **d** Computing the cross-peak to diagonal peak ratio provides a direct measure of IVR, where there is a pronounced solvent chain length dependence. Remarkably, the dependence is well described as linear, with longer solvent molecules inducing slower IVR. This figure is adapted from [15], Copyright the American Chemical Society (2017)

diiron complexes is independent of alkane solvent viscosity. A potential energy surface based on density functional theory calculations constructed along the torsional coordinate (relaxing all other degrees of freedom) shows a rather broad range of accessible conformations at room temperature. Although the overall barrier to turnstile isomerization is too high to observe within the limited (~100 ps) vibrational lifetime of the CO modes, the spectral diffusion reflects equilibrium sampling and fluctuations within the torsional well. Besides the spectral diffusion, there is also a clear trend in the IVR timescales, which can be measured directly by computing the cross-peak to detected diagonal peak amplitude ratios in non-rephasing ($\mathbf{k}_s = +\mathbf{k}_1 - \mathbf{k}_2 + \mathbf{k}_3$) spectra [40, 41]. Non-rephasing spectra are preferable for population dynamics because the cross-peaks generally do not exhibit coherent oscillations caused by broadband excitation. The data exhibit a pronounced slowdown in IVR as the alkane chain length is increased, from ~11 ps in hexane to ~27 ps in hexadecane. More surprisingly, the IVR timescales can actually be fit well using a linear relationship: $\tau_{IVR} = n \times 1.65\ \text{ps} + 0.92\ \text{ps}$, where n is the number of carbon atoms in the solvent molecule. There is currently no explanation for this IVR trend. In a study of a different transition metal complex, $Mn_2(CO)_{10}$, in a series of alcohols, we found a strong chain-length dependence, but it was not monotonic [41]. Instead, we observed a surprising dependence of IVR time scales on the degree of hydrogen bonding determined using molecular dynamics simulations. Increased hydrogen bonding correlates with slower IVR, an effect we rationalized as being due to the energy shift caused by a hydrogen bond to a CO ligand. Similar to Anderson localization, an energetic defect can spatially trap an otherwise delocalized coupled (i.e. excitonic) state, slowing the rate of energy transfer among excited vibrations. Since the alkanes lack an obvious means of interaction with the complex, it is not clear how the chain length can influence the IVR time scale. Nevertheless, since energy randomization is an important aspect of chemical reaction dynamics, it is worth further investigations to ascertain whether there is any correlation between IVR and catalytic activity.

11.3 Larger Supramolecular Complexes and Constructs

11.3.1 FeFe Hydrogenase Complex Embedded Within Micelles, Hydrogels, and Metal-Organic Frameworks

One of the remarkable observations of hydrogenase models is that they can exhibit greatly enhanced catalytic activity under confinement [23, 26]. Both in terms of turnover number (i.e. the life span of the catalyst) and the turnover frequency (i.e. the rate of reaction), constraining the complex to an isolated environment, such as within a polymer [42], polypeptide [23], polysaccharide [43], protein [44], cyclodextrin [14, 45, 46], or a dendrimer [13], can improve catalyst performance. In the aqueous environment of living organisms, it is essential to be able to protect an enzyme's active site within the largely hydrophobic core, especially when the mechanism involves

charge transfer. Redox enzymes can avoid the very high reorganization energies in aqueous solution by cloistering the active site within the relatively low dielectric protein [47]. Structural fluctuations are also likely to be more constrained under confinement, which may reduce the likelihood of deleterious reaction products that limit the life of a catalyst molecule. Although there is no clear explanation for the success of confinement, it likely involves a combination of interplay of lowered reorganization energy, solvent shielding, and preferential solvation. There is, however, a straightforward set of dynamical observables that can be measured with multidimensional spectroscopy, and, ultimately, these should be useful in establishing links between structural dynamics and chemical reactivity.

Micelles are widely used models of biological components that allow tunable degrees of confinement and hydrophobicity. Normal phase micelles have a nonpolar core surrounded by polar head groups exposed to water. Naively, a nonpolar solute should become embedded within the hydrophobic core of the micelle, whereas amphiphilic or moderately polar solutes adopt a heterogeneous distribution of sites in the micelle. Hunt et al. studied the propanedithiolate bridged diiron carbonyl complex (**2**) in micelles of dodecyltrimethylammonium bromide (DTAB) in heptane/water solutions (Fig. 11.7) [26]. In the resulting microemulsions, analysis of FTIR and 2D-IR spectroscopy of carbonyl bands indicates that the diiron complex partitions between two different environments: one deep within the nonpolar core, and one closer to the head group region. The main rationale for this conclusion is the appearance of hydrogen bonded CO band shifts. Based on spectral diffusion results from 2D-IR, the authors conclude that the slower spectral dynamics attributed to the head group region results from the water molecules constrained near the head groups. Relatively slow spectral diffusion dynamics has been observed at surfactant interfaces by studying the head groups themselves [48], as well as by using thiocyanate probes that associate preferentially with cationic head groups of the same

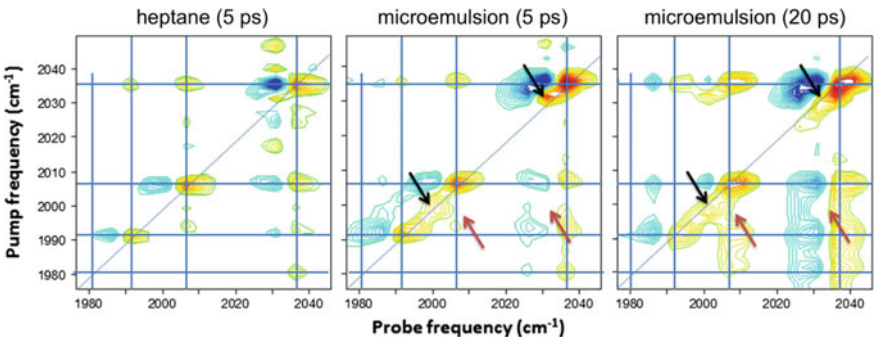

Fig. 11.7 2D-IR spectra of the pdt-linked diiron hexacarbonyl (**2**) in (left) heptane at a 5-ps waiting time, (middle, right) a micellar microemulsion at waiting times of 5 and 20 ps, respectively. Additional features appear in the 2D-IR spectrum in the micelle case, and based on the lack of cross peaks with the main bands, can be assign to distinct species. Diagonal elongation indicates some degree of inhomogeneous broadening, which is slightly relaxed by a waiting time of 20 ps. Figure adapted from [26], Copyright the American Chemical Society (2016)

DTAB surfactant studied here [49]. Since quantitative measures of the spectral diffusion time scales for molecules within the core and at the head groups were not reported, it remains unresolved the degree to which the conformational flexibility of the complex is altered by microsolvation in the micelle.

Within the theme of complex heterogeneous environments, Hunt et al. investigated the role of peptide hydrogels in mediating photophysics and photochemistry [23]. The short peptide Fmoc-Leu-Leu (Fmoc = 9-fluorenylmethoxycarbonyl) forms a hydrogel at low concentration (~10 mM), which is a large-scale network capable of confining solutes in protein-like environments. A propanedithiolate complex with two CO ligands replaced by trimethyl phospine (**5**) was incorporated into the Fmoc-Leu-Leu hydrogel and remained stable, in stark contrast to the low stability of the complex in ordinary aqueous solution. This stability suggests a microsolvation environment that is somewhat free of water. Although the IR-pump/IR-probe transient absorption was not reported, it is perhaps not entirely surprising that a complex with low water solubility would find itself in a relatively dehydrated peptide environment; leucine is, indeed, among the most non-polar side chains. Of course it is unknown the degree to which the solute perturbs the hydrogel structure itself, perhaps enhancing the hydrophobicity locally. Taking the slow phase of transient IR absorption to arise from CO geminate rebinding, it is clear that the confined space of the hydrogel leads to more complete and faster bimolecular recombination relative to a more simple solution environment. This study is particularly interesting because of the promise in using viscous solvents, such as ionic liquids and polyelectrolytes, in electrochemistry and electrocatalysis applications.

Metal-organic frameworks (MOFs) are supramolecular structures composed of repeating units of organometallic complexes. Although they are actually a form of organometallic polymer, they differ from classical polymers by frequently having a defined and quasi-fixed three-dimensional structure permeated by microscopic pores and cavities. Molecular catalysts sometimes show greater reactivity and stability when incorporated into cavities in a MOF than when freely dissolved in a reaction mixture, as exemplified by studies of the photocatalytically-driven reduction of H^+ to H_2 by a (bdt)$[Fe(CO)_3]_2$ (bdt = benzenedithiolate) reported by Pullen et al. [50]. Here, photoexcitation of a $[Ru(bpy)_3]^{2+}$ and subsequent reduction by an ascorbate electron donor precedes electron transfer from the $[Ru(bpy)_3]^{2+}$ to the (bdt)$[Fe(CO)_3]_2$ and formation of H_2 at the iron active site. Although the reaction mixture is not exceptional for hydrogen photocatalysis, incorporation of the (bdt)$[Fe(CO)_3]_2$ into a MOF significantly increases the reaction turnover number and the photostability of the (bdt)$[Fe(CO)_3]_2$ catalyst.

Nishida et al. studied the MOF-(bdt)$[Fe(CO)_3]_2$ using 2D-IR spectroscopy and found that the spectral diffusion of the carbonyl ligands occurs on timescales of 7 and ~670 ps, which the authors suggested reflected primarily dynamics of the (bdt)$[Fe(CO)_3]_2$ and macromolecular fluctuations of the MOF scaffold, respectively [51]. When the pores of the MOF are filled with N,N-dimethylformamide (DMF) the spectral diffusion timescales of the metal carbonyl groups slow to ~23 and >2000 ps. The four-fold increase of the slow timescale of spectral diffusion, previously linked to the fluctuations of the MOF scaffold, was attributed to the increased structural rigidity

of the solvent-filled MOF, and the three-fold slowdown of the 7 ps component of the spectral diffusion to ~23 ps was hypothesized to reflect the slow intermolecular dynamics of the constrained DMF solvent within the pores of the MOF. To date, this work remains the only 2D study of a MOF conducted with optical spectroscopy, and although the photochemical production of H_2 in this system was not directly studied, the addition of a slow timescale to the spectral diffusion of a vibrational probe upon incorporation into a sterically constrained environment underlines the importance of careful characterization of a complex macromolecular system before directly studying the system in a non-equilibrium state. Later studies of dendritic systems have demonstrated that comparable slow components of a probe's spectral diffusion dynamics may be induced even by relatively slight steric interactions.

11.3.2 Dendritic FeFe Hydrogenase Supramolecular Complexes

One promising supramolecular complex for photochemical hydrogen generation, synthesized by Li et al., contains a diiron hexacarbonyl core covalently bound to varying generations of poly(aryl ether) dendrimeric ogilomers [13]. Using a photocatalytic scheme employing common components, such as a $[Ir(ppy)_2(bpy)]^+$ photosensitizer and triethyl amine electron donor, the dendrimeric catalyst can be supplied with electrons energetically triggered by light absorption, ultimately reducing protons to generate H_2. Based on some optimization efforts, the authors identified a 9:1 (v/v) acetone/water solution as the best condition for this homogeneous photocatayltic process. The interesting solvent composition dependence hints at the potential for interplay between the dielectric properties, preferential solvation, and the dendrimer's conformational distribution.

Using the commercially available dendrimer, we synthesized the second generation diiron complex (Fig. 11.8), as well as a reference molecule which has two sulfur atoms bridging the irons, but no other bridging atoms between the sulfur atoms [52]. The basic approach of the work was to investigate the 2D-IR spectroscopy of the dendrimer and the reference complex (**6**) in a series of solvents. Unfortunately, due to the persistent microscale heterogeneity of water/acetone solutions, we could not sufficiently suppress scattering in our simple sample cell consisting of two 3-mm thick CaF_2 windows with a 50–100 μm Teflon spacer. Despite this technical limitation, we were able to examine both molecules in a wide range of solvents: toluene, chloroform, tetrahydrofuran, *N*-*N*-dimethyl formamide, acetone, and acetonitrile. From the perspective of the linear absorption spectrum, there are some similarities and systematic variations between the dendrimer and the small molecule reference in the solvent series. There are generally three distinct bands in all cases, though there are clearly visible shoulders which can be assigned to four-five transitions depending on the solvent. This collapse of the five bands is consistent with previous studies of diiron complexes in polar solvents. The dendrimer shows actually smaller variation

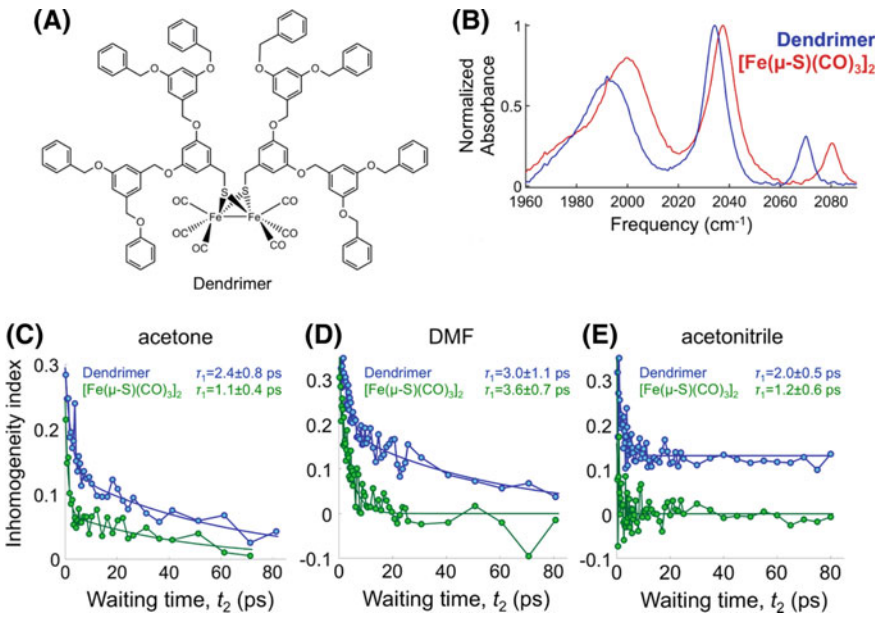

Fig. 11.8 **a** Second-generation poly(aryl ether) dendrimer with a diiron hexacarbonyl core. **b** FT-IR spectra of the dendrimer and the reference unbridged complex (**4**) in dimethylformamide (DMF) solution. Decays of the spectral inhomogeneity index, which is proportional to the frequency-fluctuation correlation function, exhibit solvent-dependent dynamics in **c** acetone, **d** DMF and **e** acetonitrile. In all cases, the dendrimer exhibits slower slow-phase spectral diffusion, or a larger constant offset, than does the core-only reference complex. Acetonitrile is a poor solvent for the dendrimer and exhibits only an offset, indicating a dynamical timescale for the dendrimer that is slower than our measurement window. Figure adapted from [52], Copyright the American Chemical Society (2018)

with solvent, likely reflecting the solvation environment presented by the dendrimer itself.

There are several aspects of the vibrational dynamics that are solvent and complex dependent. Both the fast intramolecular vibrational redistribution and the spectral diffusion time scales exhibit some differences, but the population relaxation is relatively insensitive, at least within the limited ~80 ps measurement window. For the spectral diffusion, as measured from the decay of the frequency-fluctuation correlation function, there are essentially three categories, and they all relate to the time scale of the slowest phase of dynamics. The data are fit to biexponentials in all cases, though for acetonitrile, the slow time constant is replaced by a static offset, which represents a slow phase that is fully beyond the accessible temporal dynamic range. Overall, the key observation from the analysis of spectral diffusion is that the slow phase correlates with the solvent "quality". Polymer solubility can be classified by the so-called solvent quality, which is a measure of the degree to which a macromolecular solute is fully solvated such that it can adopt extended conformations (i.e. a "good solvent"), as opposed to being soluble, but largely collapsed into a more compact conformational

ensemble (i.e. a "poor solvent"). The spectral diffusion results indicate that solvents that are poor (such as acetonitrile) for the dendrimer yield a quasi-static slow phase of spectral diffusion, whereas good solvents (such as acetone and DMF) induce a slow phase of dynamics that is faster than in the poor solvent case. The most likely interpretation is that the good solvents present a more heterogeneous and dynamic macromolecular solvation environment compared with the more homogeneous and rigid environment presented by the dendrimer in the poor solvent. Unfortunately it is not possible with 2D-IR spectroscopy to discern whether there is simply the weighted average of spectral diffusion dynamics for a static heterogeneous ensemble, or whether there are indeed dynamical fluctuations on the time scales reported by spectral diffusion. It is possible that 3D-IR spectroscopy would be able to disentangle the inhomogeneous distribution of spectral diffusion dynamics time scales, as has been done in the case of hydrogen bonded water [28, 29].

11.4 Future Directions

Rich chemistry and highly modular synthetic strategies enable the development of a wide range of hydrogenase models, many of which have already been shown to be promising photo- and electrocatalysts. Facile synthetic methodologies make this class of organometallic complex readily accessible in tailor-made forms and easily incorporated into a variety of macromolecular systems, including dendrimers, polymers, and MOFs. The small-molecule forms are readily soluble in a wide range of solvent systems, and the multiple bright, non-degenerate carbonyl stretching frequencies make the diiron hexacarbonyl motif an exceptionally promising probe for solvent dynamics, solvent-solute interactions, and intramolecular processes in organometallic compounds. Variations in intramolecular vibrational dynamics in hydrogenase model compounds have not been rigorously explained, but unique and puzzling solvent- and ligand-dependencies in the intra-carbonyl vibrational relaxation of hydrogenase models have been noted by several research groups. Steric bulk may be directly added to the diiron hexacarbonyl core in customized quantities, enabling direct interrogation of ultrafast solvation dynamics in crowded environments, and multiple studies have shown that the photochemistry of the diiron hexacarbonyl core may be carefully modified by a judicious choice of excitation frequency, bridging group, and terminal ligand. Even without considering its potential for photocatalysis of a primary source of renewable energy, the diiron hexacarbonyl moiety represents an almost optimal system for ultrafast vibrational and electronic research. However, the potential of the diiron hexacarbonyl moiety for catalysis cannot be ignored. Driven largely by the promise for low-energy production of molecular hydrogen, we can anticipate ever more innovation in engineering diiron active site motifs into purpose-built molecular scaffolds for distributed H_2 generation.

At the same time, notably absent from this chapter are reports of applying 2D-IR spectroscopy to the natural enzyme. At the moment, the air-sensitivity and low tolerance for concentration limits the ease with which the protein can be studied using

2D-IR. Nevertheless, especially as our knowledge of small molecule mimics increases, we expect that greater effort will be made to study the natural enzymes despite the practical challenges. Hydrogenases and their mimics should be ideal candidates to study using new spectroelectrochemistry techniques that use 2D-IR spectroscopy to probe electrochemistry and electrocatalysis in situ. Such methods are standard in the inorganic and bioinorganic communities, but are typically restricted to simple linear spectroscopy methods, rather than the more time-consuming and technically demanding multidimensional variants. The ability to study different oxidation states has the potential to unlock key missing information regarding catalytic intermediates needed to constrain proposed reaction mechanisms. Beyond the traditional chemical species information, we also anticipate new concepts in catalysis that directly address the role of dynamical fluctuations in the case of low barrier reactions. Perhaps by designing specific photoelectrochemical systems, it will be possible to phototrigger intermediate steps in an otherwise steady-state reaction mixture. In this way, we may be able to have the best of both worlds: mechanistic information about practical reaction schemes that have the potential to make a revolutionary transformation of the hydrogen sector of global economies.

Acknowledgements Our research on hydrogenase models is supported by the National Science Foundation (CHE–1300239 and CHE-1565795).

References

1. J.W. Peters, G.J. Schut, E.S. Boyd, D.W. Mulder, E.M. Shepard, J.B. Broderick, P.W. King, M.W.W. Adams, FeFe- and NiFe-hydrogenase diversity, mechanism, and maturation. Biochim. Biophys. Acta **2015**, 1350–1369 (1853)
2. T.D. Veras, T.S. Mozer, D. dos Santos, A.D. Cesar, Hydrogen: trends, production and characterization of the main process worldwide. Int. J. Hydrog. Energy **42**, 2018–2033 (2017)
3. G.J. Kubas, Fundamentals of H_2 binding and reactivity on transition metals underlying hydrogenase function and H_2 production and storage. Chem. Rev. **107**, 4152–4205 (2007)
4. D. Schilter, J.M. Camara, M.T. Huynh, S. Hammes-Schiffer, T.B. Rauchfuss, Hydrogenase enzymes and their synthetic models: the role of metal hydrides. Chem. Rev. **116**, 8693–8749 (2016)
5. J.M. Camara, T.B. Rauchfuss, Combining acid-base, redox and substrate binding functionalities to give a complete model for the FeFe-hydrogenase. Nat. Chem. **4**, 26–30 (2012)
6. I.P. Georgakaki, L.M. Thomson, E.J. Lyon, M.B. Hall, M.Y. Darensbourg, Fundamental properties of small molecule models of Fe-only hydrogenase: computations relative to the definition of an entatic state in the active site. Coord. Chem. Rev. **238**, 255–266 (2003)
7. J.W. Peters, W.N. Lanzilotta, B.J. Lemon, L.C. Seefeldt, X-ray crystal structure of the Fe-only hydrogenase (Cpl) from Clostridium pasteurianum to 1.8 angstrom resolution. Science **282**, 1853–1858 (1998)
8. D.L.M. Suess, R.D. Britt, Biosynthesis of the FeFe hydrogenase active site. FASEB J. **30** (2016)
9. A. Kohen, Role of dynamics in enzyme catalysis: substantial versus semantic controversies. Acc. Chem. Res. **48**, 466–473 (2015)
10. D. Beece, L. Eisenstein, H. Frauenfelder, D. Good, M.C. Marden, L. Reinisch, A.H. Reynolds, L.B. Sorensen, K.T. Yue, Solvent Viscosity and protein dynamics. Biochemistry **19**, 5147–5157 (1980)

11. E.Z. Eisenmesser, O. Millet, W. Labeikovsky, D.M. Korzhnev, M. Wolf-Watz, D.A. Bosco, J.J. Skalicky, L.E. Kay, D. Kern, Intrinsic dynamics of an enzyme underlies catalysis. Nature **438**, 117–121 (2005)
12. S. Hecht, J.M.J. Frechet, Dendritic encapsulation of function: applying nature's site isolation principle from biomimetics to materials science. Angew. Chem.-Int. Ed. **40**, 74–91 (2001)
13. T.J. Yu, Y. Zeng, J.P. Chen, Y.Y. Li, G.Q. Yang, Y. Li, Exceptional dendrimer-based mimics of diiron hydrogenase for the photochemical production of hydrogen. Angew. Chem.-Int. Ed. **52**, 5631–5635 (2013)
14. M.L. Singleton, J.H. Reibenspies, M.Y. Darensbourg, A cyclodextrin host/guest approach to a hydrogenase active site biomimetic cavity. J. Am. Chem. Soc. **132**, 8870–8871 (2010)
15. P.A. Eckert, K.J. Kubarych, Dynamic flexibility of hydrogenase active site models studied with 2D-IR spectroscopy. J. Phys. Chem. A **121**, 608–615 (2017)
16. M.G.I. Galinato, C.M. Whaley, N. Lehnert, Vibrational analysis of the model complex mu-edt $[Fe(CO)_3]_2$ and comparison to iron-only hydrogenase: the activation scale of hydrogenase model systems. Inorg. Chem. **49**, 3201–3215 (2010)
17. A.I. Stewart, I.P. Clark, M. Towrie, S.K. Ibrahim, A.W. Parker, C.J. Pickett, N.T. Hunt, Structure and vibrational dynamics of model compounds of the FeFe-hydrogenase enzyme system via ultrafast two-dimensional infrared spectroscopy. J. Phys. Chem. B **112**, 10023–10032 (2008)
18. S. Kaziannis, J.A. Wright, M. Candelaresi, R. Kania, G.M. Greetham, A.W. Parker, C.J. Pickett, N.T. Hunt, The role of CN and CO ligands in the vibrational relaxation dynamics of model compounds of the [FeFe]-hydrogenase enzyme. Phys. Chem. Chem. Phys. **13**, 10295–10305 (2011)
19. G.M. Bonner, A.R. Ridley, S.K. Ibrahim, C.J. Pickett, N.T. Hunt, Probing the effect of the solution environment on the vibrational dynamics of an enzyme model system with ultrafast 2D-IR spectroscopy. Faraday Discuss. **145**, 429–442 (2010)
20. A.R. Ridley, A.I. Stewart, K. Adamczyk, H.N. Ghosh, B. Kerkeni, Z.X. Guo, E.T.J. Nibbering, C.J. Pickett, N.T. Hunt, Multiple-timescale photoreactivity of a model compound related to the active site of FeFe-hydrogenase. Inorg. Chem. **47**, 7453–7455 (2008)
21. S. Kaziannis, S. Santabarbara, J.A. Wright, G.M. Greetham, M. Towrie, A.W. Parker, C.J. Pickett, N.T. Hunt, Femtosecond to microsecond photochemistry of a FeFe hydrogenase enzyme model compound. J. Phys. Chem. B **114**, 15370–15379 (2010)
22. A.I. Stewart, J.A. Wright, G.M. Greetham, S. Kaziannis, S. Santabarbara, M. Towrie, A.W. Parker, C.J. Pickett, N.T. Hunt, Determination of the photolysis products of FeFe hydrogenase enzyme model systems using ultrafast multidimensional infrared spectroscopy. Inorg. Chem. **49**, 9563–9573 (2010)
23. P.W.J.M. Frederix, R. Kania, J.A. Wright, D.A. Lamprou, R.V. Ulijn, C.J. Pickett, N.T. Hunt, Encapsulating [FeFe]-hydrogenase model compounds in peptide hydrogels dramatically modifies stability and photochemistry. Dalton Trans. **41**, 13112–13119 (2012)
24. R. Kania, P.W.J.M. Frederix, J.A. Wright, R.V. Ulijn, C.J. Pickett, N.T. Hunt, Solution-phase photochemistry of a [FeFe] hydrogenase model compound: evidence of photoinduced isomerisation. J. Chem. Phys. **136**, 044521 (2012)
25. P. Frederix, K. Adamczyk, J.A. Wright, T. Tuttle, R.V. Ulijn, C.J. Pickett, N.T. Hunt, Investigation of the ultrafast dynamics occurring during unsensitized photocatalytic H_2 evolution by an FeFe-hydrogenase subsite analogue. Organometallics **33**, 5888–5896 (2014)
26. R. Fritzsch, O. Brady, E. Adair, J.A. Wright, C.J. Pickett, N.T. Hunt, Encapsulating subsite analogues of the [FeFe]-hydrogenases in micelles enables direct water interactions. J. Phys. Chem. Lett. **7**, 2838–2843 (2016)
27. N.T. Hunt, J.A. Wright, C. Pickett, Detection of transient intermediates generated from subsite analogues of FeFe hydrogenases. Inorg. Chem. **55**, 399–410 (2016)
28. S. Garrett-Roe, F. Perakis, F. Rao, P. Hamm, Three-dimensional infrared spectroscopy of isotope-substituted liquid water reveals heterogeneous dynamics. J. Phys. Chem. B **115**, 6976–6984 (2011)
29. S. Garrett-Roe, P. Hamm, What can we learn from three-dimensional infrared spectroscopy? Acc. Chem. Res. **42**, 1412–1422 (2009)

30. R.L. Meyer, A.D. Zhandosova, T.M. Biser, E.J. Heilweil, C.J. Stromberg, Photochemical dynamics of a trimethyl-phosphine derivatized FeFe-hydrogenase model compound. Chem. Phys. **512**, 135–145 (2018)
31. B.W. Caplins, J.P. Lomont, S.C. Nguyen, C.B. Harris, Vibrational cooling dynamics of a FeFe-hydrogenase mimic probed by time-resolved infrared spectroscopy. J. Phys. Chem. A **118**, 11529–11540 (2014)
32. J.L. Bingaman, C.L. Kohnhorst, G.A. Van Meter, B.A. McElroy, E.A. Rakowski, B.W. Caplins, T.A. Gutowski, C.J. Stromberg, C.E. Webster, E.J. Heilweil, Time-resolved vibrational spectroscopy of FeFe-hydrogenase model compounds. J. Phys. Chem. A **116**, 7261–7271 (2012)
33. C.J. Stromberg, E.J. Heilweil, Ultrafast photodynamics of cyano-functionalized FeFe hydrogenase model compounds. J. Phys. Chem. A **122**, 4023–4030 (2018)
34. M. Johnson, J. Thuman, R.G. Letterman, C.J. Stromberg, C.E. Webster, E.J. Heilweil, Time-resolved infrared studies of a trimethylphosphine model derivative of FeFe-hydrogenase. J. Phys. Chem. B **117**, 15792–15803 (2013)
35. P. Li, S. Amirjalayer, F. Hartl, M. Lutz, B. de Bruin, R. Becker, S. Woutersen, J.N.H. Reek, Direct probing of photoinduced electron transfer in a self-assembled biomimetic 2Fe2S-hydrogenase complex using ultrafast vibrational spectroscopy. Inorg. Chem. **53**, 5373–5383 (2014)
36. R. Becker, S. Amirjalayer, P. Li, S. Woutersen, J.N.H. Reek, An iron-iron hydrogenase mimic with appended electron reservoir for efficient proton reduction in aqueous media. Sci. Adv. **2**, e1501014 (2016)
37. E.J. Lyon, I.P. Georgakaki, J.H. Reibenspies, M.Y. Darensbourg, Coordination sphere flexibility of active-site models for Fe-only hydrogenase: studies in intra- and intermolecular diatomic ligand exchange. J. Am. Chem. Soc. **123**, 3268–3278 (2001)
38. A.D. Hill, M.C. Zoerb, S.C. Nguyen, J.P. Lomont, M.A. Bowring, C.B. Harris, Determining equilibrium fluctuations using temperature-dependent 2D-IR. J. Phys. Chem. B **117**, 15346–15355 (2013)
39. I.A. Nilsen, D.G. Osborne, A.M. White, J.M. Anna, K.J. Kubarych, Monitoring equilibrium reaction dynamics of a nearly barrierless molecular rotor using ultrafast vibrational echoes. J. Chem. Phys. **141**, 134313 (2014)
40. J.M. Anna, J.T. King, K.J. Kubarych, Multiple structures and dynamics of $[CpRu(CO)_2]_2$ and $[CpFe(CO)_2]_2$ in solution revealed with two-dimensional infrared spectroscopy. Inorg. Chem. **50**, 9273–9283 (2011)
41. J.T. King, J.M. Anna, K.J. Kubarych, Solvent-hindered intramolecular vibrational redistribution. Phys. Chem. Chem. Phys. **13**, 5579–5583 (2011)
42. C.A. Tooley, S. Pazicni, E.B. Berda, Toward a tunable synthetic [FeFe] hydrogenase mimic: single-chain nanoparticles functionalized with a single diiron cluster. Polym. Chem. **6**, 7646–7651 (2015)
43. J.X. Jian, Q. Liu, Z.J. Li, F. Wang, X.B. Li, C.B. Li, B. Liu, Q.Y. Meng, B. Chen, K. Feng, C.H. Tung, L.Z. Wu, Chitosan confinement enhances hydrogen photogeneration from a mimic of the diiron subsite of [FeFe]-hydrogenase. Nat. Commun. **4**, 2695 (2013)
44. Y. Sano, A. Onoda, T. Hayashi, A hydrogenase model system based on the sequence of cytochrome c: photochemical hydrogen evolution in aqueous media. Chem. Commun. **47**, 8229–8231 (2011)
45. X.Q. Li, M. Wang, D.H. Zheng, K. Han, J.F. Dong, L.C. Sun, Photocatalytic H_2 production in aqueous solution with host-guest inclusions formed by insertion of an FeFe-hydrogenase mimic and an organic dye into cyclodextrins. Energy Environ. Sci. **5**, 8220–8224 (2012)
46. M. De Rosa, P. La Manna, C. Talotta, A. Soriente, C. Gaeta, P. Neri, Supramolecular organocatalysis in water mediated by macrocyclic compounds. Fronti. Chem. **6** (2018)
47. H.B. Gray, J.R. Winkler, Electron transfer in proteins. Annu. Rev. Biochem. **65**, 537–561 (1996)
48. D. Laage, T. Elsaesser, J.T. Hynes, Water dynamics in the hydration shells of biomolecules. Chem. Rev. **117**, 10694–10725 (2017)
49. V.P. Roy, K.J. Kubarych, Interfacial hydration dynamics in cationic micelles using 2D-IR and NMR. J. Phys. Chem. B **121**, 9621–9630 (2017)

50. S. Pullen, H.H. Fei, A. Orthaber, S.M. Cohen, S. Ott, Enhanced photochemical hydrogen production by a molecular diiron catalyst incorporated into a metal-organic framework. J. Am. Chem. Soc. **135**, 16997–17003 (2013)
51. J. Nishida, A. Tamimi, H.H. Fei, S. Pullen, S. Ott, S.M. Cohen, M.D. Fayer, Structural dynamics inside a functionalized metal-organic framework probed by ultrafast 2D IR spectroscopy. Proc. Natl. Acad. Sci. USA **111**, 18442–18447 (2014)
52. P.A. Eckert, K.J. Kubarych, Solvent quality controls macromolecular structural dynamics of a dendrimeric hydrogenase model. J. Phys. Chem. B **122**, 12154–12163 (2018)

Chapter 12
Vibrational Frequency Fluctuations of Ionic and Non-ionic Vibrational Probe Molecules in Aqueous Solutions

Masaki Okuda, Masahiro Higashi, Kaoru Ohta, Shinji Saito and Keisuke Tominaga

Abstract In this chapter we review our studies on vibrational frequency fluctuations in aqueous solutions. Experimentally, the frequency fluctuations were investigated by measuring frequency-frequency time-correlation function (FFTCF) by two-dimensional spectroscopy, and molecular dynamics simulations were carried to obtain molecular pictures for the frequency fluctuations in water. We here compare the two different types of vibrational probes; one is non-ionic, and the other is ionic. For the non-ionic probe, we chose 2-nitro-5-thiocyanate benzoic acid (NTBA), which possesses an electronically neutral vibrational probe (SCN group) and an aromatic ring. For the ionic probe, three atomic ions, SCN^- and N_3^-, were used. Although the charge distributions of the solutes and, consequently, hydration structures around the solutes are different for the ionic and non-ionic vibrational probes, both the ionic and non-ionic probes show similar decay time constants for FFTCF of about 1 ps. It is found that the frequency fluctuation for three atomic ions is almost determined by the electrostatic interaction from the water molecules in the first hydration shell. The collective dynamics of the water molecules in the first-hydration shell are found to be similar to those of bulk water, though the hydrogen bond between the ion and water molecule is very strong. In contrast to the hydration structure and water dynamics in

M. Okuda · K. Ohta · K. Tominaga (✉)
Molecular Photoscience Research Center, Kobe University, Rokkodai-cho 1-1, Nada, Kobe 657-8501, Japan
e-mail: tominaga@kobe-u.ac.jp

M. Higashi
Department of Chemistry, Biology and Marine Science, University of the Ryukyus, 1 Senbaru, Nishihara, Okinawa 903-0213, Japan

K. Ohta · K. Tominaga
Graduate School of Science, Kobe University, Rokkodai-cho 1-1, Nada, Kobe 657-8501, Japan

S. Saito
Department of Theoretical and Computational Molecular Science, Institute for Molecular Science, Myodaiji, Okazaki, Aichi 444-8585, Japan

Present Address:
M. Higashi
Department of Molecular Engineering, Kyoto University, Kyoto 615-8510, Japan

M. Cho (ed.), *Coherent Multidimensional Spectroscopy*,
Springer Series in Optical Sciences 226,
https://doi.org/10.1007/978-981-13-9753-0_12

these small ionic solutions, the hydration structure and water dynamics in the vicinity of the vibrational probe of NTBA are found to be similar to those in bulk. We consider that the electrostatic interactions with "bulk-like" water molecules around NTBA induce the slow decay component, i.e., 1-ps decay component, of the FFTCF of NTBA in H_2O.

12.1 Introduction

Various kinds of chemical and biological reactions take place in aqueous solutions. Detailed aspects of reaction, e.g., rates and pathways, are generally influenced by solvent molecules [1, 2]. Thus, it is essential to elucidate the solute-solvent interactions and dynamics around the solute molecules. In aqueous solutions, hydrogen bond (HB) network formed among water molecules constantly fluctuates and thus induced local and collective dynamics can affect solute molecules. It is well known that vibrational frequencies of the solute molecules are good reporters of their local environment [3–5]. Since the HB network changes occur in a wide range of spatiotemporal scales, the vibrational frequencies of solute molecules also fluctuate in a complicated manner. Therefore, detailed information of the hydration dynamics and solute-solvent interactions can be obtained by examining vibrational frequency fluctuations.

Femtosecond nonlinear infrared (IR) spectroscopy has been a powerful tool to address the underlying ultrafast molecular dynamics in solution, which are often obscured in linear spectroscopy [3–5]. Generally, vibrational dynamics are characterized by the following three relaxation processes: (i) vibrational energy relaxation (VER), (ii) rotational relaxation, and (iii) spectral diffusion. We can examine the first two vibrational dynamics, the VER and rotational relaxation, using IR pump-probe spectroscopy [6, 7]. We can investigate the third relaxation process, i.e., the spectral diffusion, using three-pulse IR photon echo (IR-3PE) method or two-dimensional IR (2D-IR) spectroscopy [8, 9]. As mentioned above, the solute-solvent interactions cause the vibrational frequency shift of a solute. Note that, the surrounding environment, i.e. solvation structure, of each solute is different. As a result, each solute has a slightly different vibrational frequency, so that there is the so-called an inhomogeneous distribution of vibrational frequencies. However, since the solvation structure is not static but dynamically fluctuates on sub-picosecond to picoseconds time scales, the vibrational frequency of the solute and the associated inhomogeneous distribution change with time. This process is called a spectral diffusion. Here, the vibrational frequency of a molecule at time T, $\omega(T)$, is defined as:

$$\omega(T) = \Delta\omega(T) + \langle\omega\rangle \tag{12.1}$$

where <…> denotes the ensemble average and $<\omega>$ and $\Delta\omega(T)$ are the time-averaged vibrational frequency and the deviation of frequency at time T from the average value,

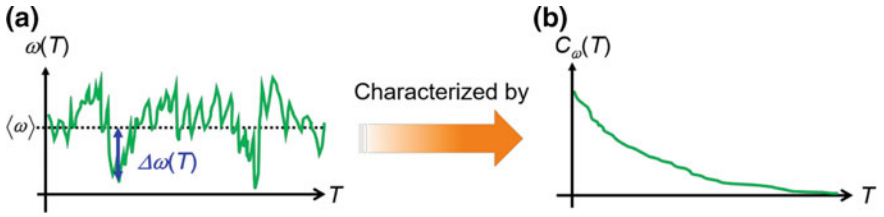

Fig. 12.1 Schematic illustration of **a** time-dependent frequency fluctuation and **b** its time correlation function

respectively (see Fig. 12.1a). Therefore, $\Delta\omega(T)$ reflects dynamical information on solute-solvent interaction and solvation structure in the vicinity of the solute [5, 10].

The time dependence of the frequency fluctuation is characterized by the time-correlation function of $\Delta\omega(T)$, i.e. frequency-frequency time-correlation function, FFTC F, $C_\omega(T)$ [5, 10]:

$$C_\omega(T) = \langle \Delta\omega(T)\Delta\omega(0)\rangle \tag{12.2}$$

Since the solvation structure around a solute does not change from its initial structure significantly at sufficiently short time T, a strong correlation exists between initial and final vibrational frequency shifts. On the other hand, at longer time T, the correlation is lost due to the change of the solvation structure. Therefore, $C_\omega(T)$ decays with T (see Fig. 12.1b), and the time scale of this decay reflects the solvation dynamics in the solution. IR-3PE method and 2D-IR spectroscopy can monitor the correlation function of vibrational frequency fluctuation, i.e., $C_\omega(T)$, for the investigated molecular systems. For instance, Fig. 12.2 gives an intuitive explanation for the time-dependence of 2D-IR spectra [8, 9]. For a molecular system with an inhomogeneous frequency distribution, at short time T, two vibrational frequencies (denoted as ω_1 and ω_3) are correlated and the 2D-IR lineshape is elongated along the diag-

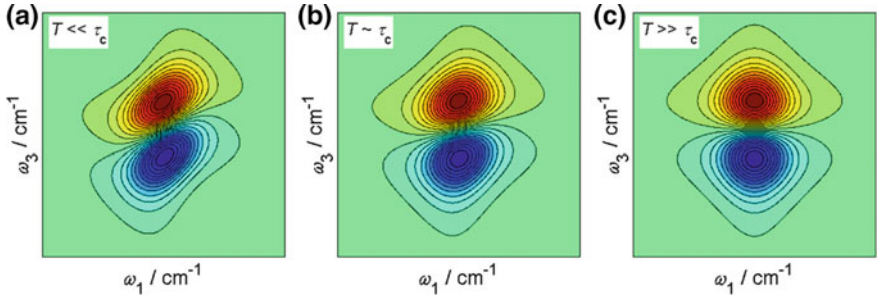

Fig. 12.2 Schematic illustration of a 2D-IR spectrum at three different times T: **a** $T \ll \tau_c$, **b** $T \sim \tau_c$, **c** $T \gg \tau_c$. The red and blue regions represent the positive and negative contributions of the 2D-IR spectrum, respectively. As time T increases, the lineshape of the 2D-IR spectrum changes from elliptic to round shapes, which reflects the loss of the correlation between the initial (ω_1) and final (ω_3) frequencies

onal line, i.e. line at $\omega_1 = \omega_3$, (see Fig. 12.2a). However, when time T becomes longer than a characteristic time (τ_C) for the solvation dynamics of the system, the correlation between the frequencies ω_1 and ω_3 is lost and the 2D-IR lineshape is gradually deformed roundly (see Fig. 12.2b). Finally, when the correlation between the frequencies ω_1 and ω_3 is completely lost, the 2D-IR lineshape becomes round (see Fig. 12.2c). Hence, we can determine the time scale of the solvation dynamics from the time dependence of the 2D-IR lineshape.

Molecular dynamics (MD) simulations are powerful tool to investigate relationship between the vibrational frequency fluctuations of a solute and its surrounding environment, e.g. solvation dynamics and solute-solvent interactions. By using appropriate methodologies, we can theoretically obtain the FFTCF of a solute in solution from MD simulations [8, 9, 11, 12]. Furthermore, since MD simulations can provide a microscopic picture of the temporal evolution of the solvation structure around a solute, which cannot be directly obtained from IR-3PE and 2D-IR experiments. Consequently, by combining experimental and theoretical studies, we can obtain deep understanding for microscopic mechanism of the vibrational frequency fluctuations of solutes in solutions.

So far, using these methods, several groups have experimentally investigated $C_\omega(T)$ of vibrational probes in water [13–31]. It has been shown that the FFTCF of ionic probes, such as SCN^- and $[Fe(CN)_6]^{4-}$, can be modeled by a double exponential function plus a quasi-static component:

$$C_\omega(T) = \Delta_0^2 + \Delta_1^2 \exp(-T/\tau_1) + \Delta_2^2 \exp(-T/\tau_2) \tag{12.3}$$

where Δ_i and τ_i are the amplitude and time constant of frequency fluctuations of component i, respectively. Since the component 1 is in the so-called "fast modulation limit" ($\Delta_1 \tau_1 < 1$), it is difficult to determine the parameters of Δ_1 and τ accurately. but only the value of $\Delta_1 \tau_1^2$ is evaluated from the IR-3PE and 2D-IR experiments, which corresponds to the dephasing time of the vibrational mode. The time constant τ_1 can be roughly estimated in the sub-100 fs time scale.

On the other hand, the component 2 is not in the fast modulation limit, and the parameters are estimated accurately. The decay time constant of the component 2 in the FFTCF is approximately 1 ps in aqueous solutions at room temperature regardless of the molecule [25]. The amplitude Δ_2 significantly depends on the solute molecule. A possible explanation for this observation is that the slow decay component is due to the making and breaking of the HBs between the ion and water molecules. If so, depending on the molecular properties, such as the charge distribution, of the vibrational probe molecule, the decay time constant should depend on the vibrational probe molecule as well. It should be noted that a similar time scales have been found in the frequency fluctuations in pure water; Fayer and Tokmakoff groups conducted the 2D-IR experiments for HOD in H_2O and in D_2O, respectively [32–34]. They revealed that the spectral diffusions of the OD stretching and OH stretching modes of HOD can be characterized by time constants of about 1.4 ps, which are similar to those of ions.

To date, several groups have performed theoretical investigation on the vibrational frequency fluctuations of water [35–51] and simple ionic vibrational probe molecules in water [52–56] by MD simulations. In the case of the frequency fluctuations of water, it was shown that the slow decaying component is originated from the structural evolution of HB network in water. By performing MD simulation for N_3^- in D_2O, Li et al. successfully reproduced the experimentally observed long-time decay of the FFTCF of the N_3 anti-symmetric stretching mode (>250 fs) [52]. They concluded that this slow decay of the FFTCF may result from the collective water dynamics around the solute due to long-range interactions. In other words, their result suggests that the dynamics of the HB network around the ions are similar to those in pure water, rather than depends on the ions [25].

However, it is still unclear whether this interpretation can be applied to the vibrational frequency fluctuations for non-ionic vibrational probes or not. Recently, the vibrational frequency fluctuations of biomolecules, which are labeled with non-ionic N_3 and CN groups as vibrational probes, in water have been investigated using 2D-IR spectroscopy [57–63]. Here, some of the FFTCFs for these molecules in water contain quasi-static components, which may be due to the long-lived inhomogeneous environment. Depending on the hydrophilic and hydrophobic groups around the vibrational probes, we can expect that the hydration structure and its dynamics around the non-ionic vibrational probes are different from those around the ionic ones. Furthermore, due to the high charge density of the ionic vibrational probes, they may possess stronger interactions with solvents than non-ionic ones. However, the molecular mechanism how the slower time constant of FFTCF of solutes in water is primarily determined by the solvent remains unclear.

In this chapter we describe the vibrational frequency fluctuations of the non-ionic and ionic vibrational probes in aqueous solutions. So far, several groups including us have experimentally found that the FFTCFs of aqueous solutions haves a component with approximately 1 ps, regardless of the probe molecule. Theoretically, MD simulations have reproduced this decay component of the FFTCF in aqueous solutions fairly well. However, the role of water molecules in each hydration shell in the vibrational frequency fluctuations is still unclear. Water molecules in the first solvation shell interact with the solute molecule strongly and the influence from the water molecule bound to the vibrational probe by HB should have a major effect on the vibrational frequency of the solute. However, the MD simulation studies have shown that the vibrational frequency fluctuations are affected by collective dynamics of water molecules near the solute molecule. It is interesting to reveal the role of water molecules in the vicinity of the vibrational probe in the frequency fluctuations.

The second point of this chapter is the comparison of the FFTCFs between the non-ionic and ionic probes. So far, many of the vibrational probes are ionic. Therefore, one may think what happens if the vibrational probe part is non-ionic since the charge distribution definitely affects the structure and dynamics of solvation. Furthermore, if the probe molecule possesses a hydrophobic group, water dynamics around the probe molecule may differ from those we have studied so far, because of the so-called hydrophobic effect.

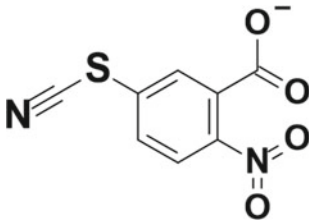

Fig. 12.3 Molecular structure of 2-nitro-5-thiocyanate benzoic acid (NTBA)

In this chapter we review the studies of the vibrational frequency fluctuations of non-ionic and ionic probes in aqueous solutions. First we describe the results for the SCN anti-symmetric stretching modes of 2-nitro-5-thiocyanate benzoic acid (abbreviated as NTBA, Fig. 12.3) and two three atomic ions, thiocyanate ion (SCN^-) and azide ion (N_3^-). The SCN group of NTBA forms a covalent bond with an aromatic ring, and the vibrational probe is electrically neutral and possesses different charge distribution from that of SCN^-. Therefore, the dependence of the frequency fluctuations on the electric properties of the vibrational probe can be investigated. Secondly, because there is an aromatic ring, which is considered to as a hydrophobic group, nearby the SCN group, the hydration structure around the vibrational probe of NTBA is expected to differ from that of SCN^-. Therefore, the dependence of the frequency fluctuations on the hydration structure of the vibrational probe can be examined.

Furthermore, in order to obtain microscopic information on water structure and its dynamics around the vibrational probe, we performed classical MD simulations and related theoretical analyses for the aqueous solutions with the three solutes. To obtain detailed information on local environment around NTBA, SCN^-, and N_3^- in H_2O, we investigated hydration structures around the vibrational probes, solute-solvent dynamics, and single/collective reorientational motion of hydrated water molecules. Moreover, based on the theoretical framework developed by Cho group [64], we calculated the SCN vibrational frequency fluctuations of NTBA and SCN^- in H_2O from the MD simulations. By calculating the radial-dependence of FFTCF and electrostatic potentials for the systems investigated, finally, we established microscopic pictures for the vibrational frequency fluctuations of NTBA and SCN^- in H_2O.

12.2 2D-IR Spectra of NTBA, SCN^-, and N_3^-

Figure 12.4 shows the IR absorption spectra of the three vibrational modes, the SCN anti-symmetric stretching modes of NTBA and SCN^- and the anti-symmetric stretching mode of N_3^- in H_2O. The normal mode analyses show that the SCN anti-symmetric stretching modes of NTBA and SCN^- are localized as the CN stretching motions. Note that the SCN anti-symmetric stretching modes of NTBA and SCN^- have different force constants. Because of the covalent bond between the SCN group

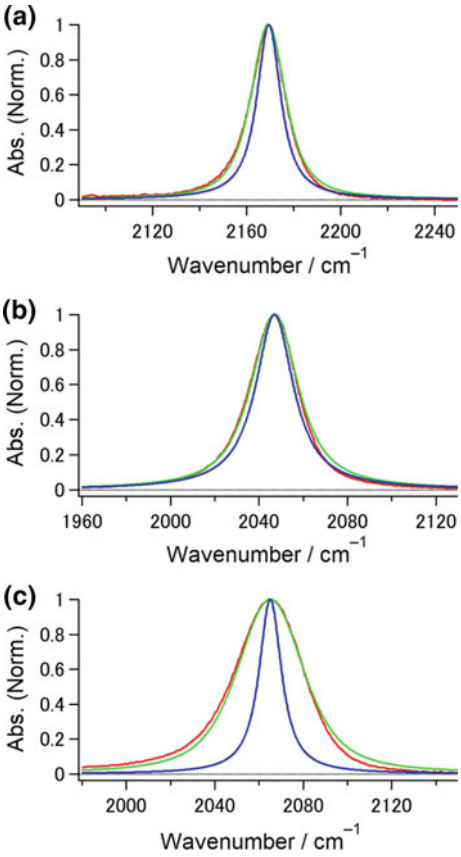

Fig. 12.4 Comparison of the experimental and simulated FT-IR spectra of **a** NTBA, **b** N_3^-, and **c** SCN^- in H_2O. The red lines represent the experimentally obtained FT-IR spectra of NTBA, N_3^-, and SCN^-. The green and blue lines are the numerically calculated FT-IR spectra with and without the slow decaying components in the FFTCF, respectively. The bandwidths of the inhomogeneous broadening of NTBA, N_3^-, and SCN^- were 5.1, 4.7, and 16.4 cm^{-1}, respectively

and the aromatic ring, the potential curve with respect to the SCN anti-stretching mode of NTBA is likely different from that of SCN^-. Therefore, the difference in the potential surface of the vibrational probe may provide the different peak wavenumbers of the SCN anti-symmetric stretching modes of NTBA and SCN^-.

The 2D-IR spectra of NTBA and SCN^- in H_2O were observed at different population times (t_2) ranging from 0 ps to 2 ps. Figure 12.5 shows the 2D-IR spectra of NTBA and SCN^- at $t_2 = 0.2$, 1, and 2 ps. Red and blue colors indicate the sum of the ground state bleach and stimulated emission signals and the transient absorption signal, respectively. The red lines represent the diagonal directions of the 2D-IR spectra ($\omega_1 = \omega_3$). At shorter population times, because of a correlation between two vibrational frequencies, i.e. ω_1 and ω_3, the 2D-IR spectrum elongates along the diagonal direction. As the population time increases, reflecting the loss of correlation between these frequencies owing to the change of the local environment around the vibrational probe, the shape of the 2D-IR spectrum becomes round. As seen in the change of the 2D-IR spectral shape, microscopic details of the frequency fluctuations of the solutes are obtained from the t_2-dependence of the 2D line shape.

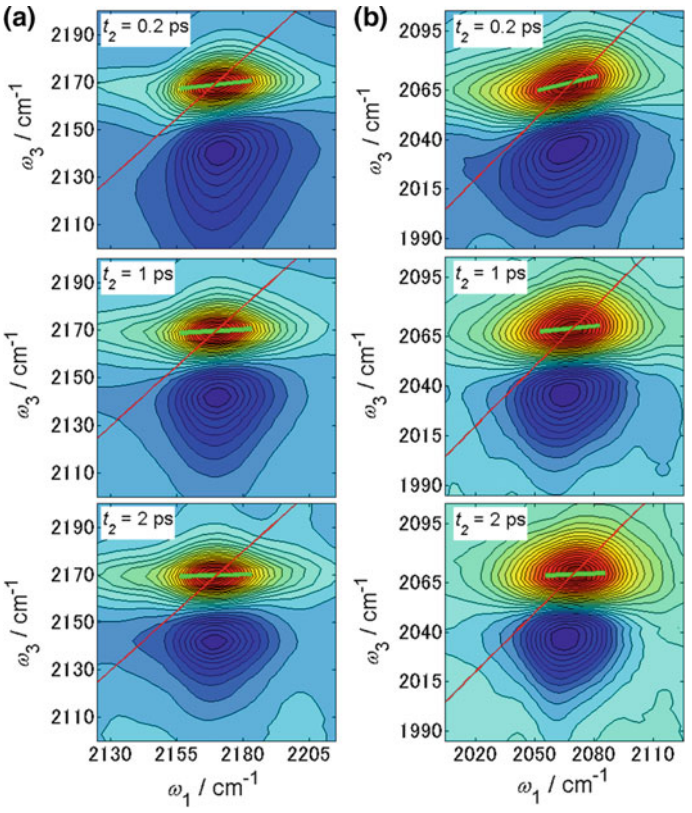

Fig. 12.5 2D-IR spectra of the SCN anti-stretching mode of **a** NTBA and **b** SCN^- in H_2O at population times of (top) 0.2 ps, (middle) 1 ps, and (bottom) 2 ps. The red lines indicate where $\omega_1 = \omega_3$. The green lines indicate the center lines of the 2D-IR signals that originate from the ground state bleach and stimulated emission

The time evolution of the spectral shape was analyzed using the center line slope (CLS) method developed by Kwak et al. [65, 66]. A fit to the decay of CLS as a function of the population time provides the decay time constant and its amplitude. The green lines in Fig. 12.5 are the center lines of the 2D-IR spectra, and the CLS was obtained from the slope of these lines with respect to the ω_1 axis. Figure 12.6 displays the CLSs of NTBA, SCN^-, and N_3^- as a function of the population time. When the IR spectrum contains homogeneous broadening to some extent, which originates from the frequency fluctuations in the fast modulation limit, the value of CLS at $t_2 = 0$ ps can be less than one. The initial CLS values of NTBA, SCN^- and N_3^- are approximately 0.16, 0.33, and 0.15, respectively. Moreover, as shown in Fig. 12.5, the CLSs possess decaying components, which originate from the slower frequency fluctuations. Note that a motionally narrowed component in the FFTCF can be expressed by a delta function. Moreover, a decay component in the FFTCF can be represented by a single exponential function. Therefore, the FFTCF of NTBA,

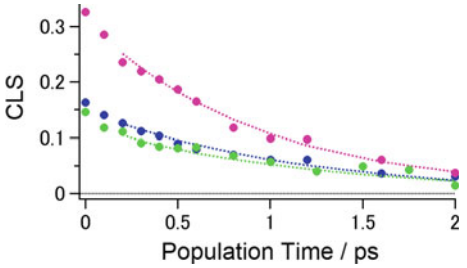

Fig. 12.6 CLS decay curves of NTBA (blue), N_3^- (green), and SCN^- (pink). The closed circles indicate experimentally obtained CLSs, and the dotted-lines are the numerically calculated ones using the optimized FFTCF parameters shown in Table 12.2

N_3^-, and SCN^- are modeled as:

$$C_\omega(t_2) = \delta(t_2)/T_2^* + \Delta_C^2 \exp(-t_2/\tau_C) + \Delta_0^2 \tag{12.4}$$

where T_2^* is the pure dephasing time constant, which characterizes the homogeneous component. Δ_C and τ_C are the amplitude and correlation time of the frequency fluctuations, respectively, which reflect the spectral diffusion process. The third term of (12.4) is a static inhomogeneous component, which expresses the decay slower than the observation time. The time constant τ_C is obtained from the fitting analysis for the CLS curve with a single exponential function. Furthermore, using the relationship of the linear IR and 2D-IR absorption spectra [5, 8, 9], the values of T_2^*, ${\Delta_C}^2$, and ${\Delta_0}^2$ of the FFTCF in (12.4) were determined by the numerical calculation to reproduce the experimentally obtained IR spectrum and the CLS [65, 66]. Here, the time constants of VER and orientational relaxation listed in Table 12.1 were used to calculate the vibrational and rotational line broadening functions. It is important to note that the non-Condon effect was not taken into account for the CLS analysis of SCN^-, and the CLS after $t_2 = 0.2$ ps was used to avoid the pulse overlapping effect.

The obtained FFTCF parameters are summarized in Table 12.1. Figure 12.4 displays the comparison between the experimental FT-IR spectra of NTBA and SCN^- in H_2O and the numerically calculated ones using the FFTCF parameters listed in Table 12.1. Previously, the 2D-IR experiments for trimethylamine-*N*-oxide (TMAO), tert-butyl-alcohol (TBA) and tetramethylurea (TMU) in water suggested that the hydration dynamics are slower than those of the bulk due to the hydrophobic effect of the methyl groups in these solutes [67, 68]. If such slow dynamics exist around the solutes, the FFTCF may contain a long-lived component. However, the CLS analysis reveals that no static component exists in the FFTCF of NTBA. On the other hand, although the FFTCFs of SCN^- and N_3^- have static components, its amplitude relative to the other components is quite small. Therefore, the frequency fluctuations of the SCN anti-symmetric stretching modes of NTBA and SCN^- in H_2O are controlled by the motionally narrowed homogeneous contribution and solvation dynamics, which are characterized by T_2^* and τ_C, respectively.

Table 12.1 Parameters that characterize the vibrational dynamics of the SCN anti-stretching mode of NTBA and SCN^- and N_3 anti-stretching mode of $N_3{}^-$ in H_2O

	Population relaxation[a]		Anisotropy decay[b]			Spectral diffusion[c]			
Solute	T_1/ps	Δ/cm^{-1}	A_∞	A_0	T_R/ps	T_2^*/ps	Δ_1/ps^{-1}	τ_C/ps	Δ_0/ps^{-1}
NTBA	0.8 ± 0.1	23.8 ± 0.5	0.1 ± 0.1	0.2 ± 0.1	1.3 ± 0.1	3.4	1.0	1.1	0
$N_3{}^-$	0.6 ± 0.1	27.0	0 ± 0.1	0.3 ± 0.1	2.8 ± 0.7	1.0	1.0	1.3	0.1
SCN^-	2.3 ± 0.1	32.7 ± 1.0	0 ± 0.1	0.3 ± 0.1	2.9 ± 0.3	0.7	2.2	0.9	0.2

[a] Δ: anharmonicity of the SCN anti-stretching mode

[b] A_∞: constant component in the fitting function; $A_\infty + A_0 \exp(-T/T_R)$

[c] The uncertainty of the time constant τ_C is estimated to be about $\pm 20\%$, and that of the other parameters is within a few percent

The 2D-IR experiments for NTBA and the three atomic ions in H_2O showed that the FFTCFs have a decay component of about 1 ps. Because the FFTCFs of NTBA and SCN^- in H_2O exhibited decay behaviors similar to those of HOD in H_2O and D_2O, the three vibrational modes investigated here are also sensitive to the structural fluctuations of the HB network around the vibrational probes.

However, it should be noted that the magnitudes of the frequency fluctuations depend on the solute. To determine the sensitivity of the vibrational modes to the solvation dynamics on the ~1 ps time scale, the numerically calculated IR spectra without the slow decaying components are shown in Fig. 12.4. Based on the spectra in Fig. 12.4, the ratios of the inhomogeneous bandwidth to the total bandwidth are approximately 0.29 and 0.46 for NTBA and SCN^-, respectively. Therefore, we found that the SCN anti-symmetric stretching mode of SCN^- is more sensitive to the solvation dynamics than that of NTBA, which is most likely due to stronger interaction between SCN^- and water molecules.

It is important to note that the molecular properties of a solute including charge distributions and molecular structure are expected to affect the network structure and dynamics of the water molecules surrounding the solute. Therefore, the structure and dynamics of water molecules around NTBA likely differ from those around SCN^- and $N_3{}^-$. Nevertheless, the 2D-IR measurements revealed that the FFTCF of NTBA in H_2O decayed with a time constant of 1.1 ps, which is similar to those of SCN^- and $N_3{}^-$. Therefore, why are the FFTCFs of NTBA and the three atomic ions characterized by the approximately same time constants? Because the two vibrational probe molecules differ in their charge distributions and molecular structures, when the solvent dynamics in the vicinity of the probe molecule dominates its vibrational frequency fluctuations, the FFTCFs of NTBA and the three atomic ions are expected to be different from each other.

12.3 Theoretical Analysis of the Frequency Fluctuations

We performed MD simulations for the three solutes, NTBA, SCN^- and $N_3{}^-$ in H_2O to investigate the hydration structures and dynamics of water molecules in the vicinity of the solutes. Furthermore, we calculated the vibrational frequency fluctuations for NTBA and SCN^- in H_2O using the trajectories obtained from the MD simulations. The relationship between the frequency fluctuations of the solute and its hydration structure and hydration dynamics is discussed from theoretical aspects here.

The Cho group showed that the multi-site electrostatic potential theory can be applied to the SCN frequency shifts induced by the interactions with surrounding water molecules [69, 70]. In their method, distributed interaction sites are placed at around solutes to calculate solute-solvent interactions. For a given solute-water configuration, by calculating the electrostatic potentials (ϕ) at all these interaction sites, the frequency shift ($\Delta\omega(\phi)$) is expressed as follows:

$$\Delta\omega(\phi) \equiv \omega(\phi) - \omega_0 = \sum_{i=1}^{N_{\mathrm{solu}}} (l_i + l_0) \sum_{j=1}^{N_{\mathrm{solv}}} \phi_{ij}, \ \text{with} \ \sum_{i=1}^{N_{\mathrm{solu}}} l_i = 0. \tag{12.5}$$

Here, N_{solu} and N_{solv} are the numbers of the interaction sites and water molecules in the system. In this study, 35 and 28 interaction sites are considered for NTBA and SCN^-, respectively, i.e. $N_{\mathrm{solu}} = 35$ for NTBA and $N_{\mathrm{solu}} = 28$ for SCN^-, (see Fig. 12.7), and the number of water molecules are 1841 and 1387 for NTBA and SCN^-, respectively. $\omega(\phi)$ and ω_0 are the SCN vibrational frequencies of the solute in a given cluster and the isolated one, respectively. ϕ_{ij} is the Coulomb electrostatic potential at the ith interaction site caused by the jth water molecule. The coefficient l_i is a measure of the sensitivity of the ith interaction site to the change in ϕ_{ij}. The value of l_0 is the additional parameter to represent the charge transfer effect due to the solute-solvent HB on the vibrational frequency shift [70]. Here, Choi et al. found that

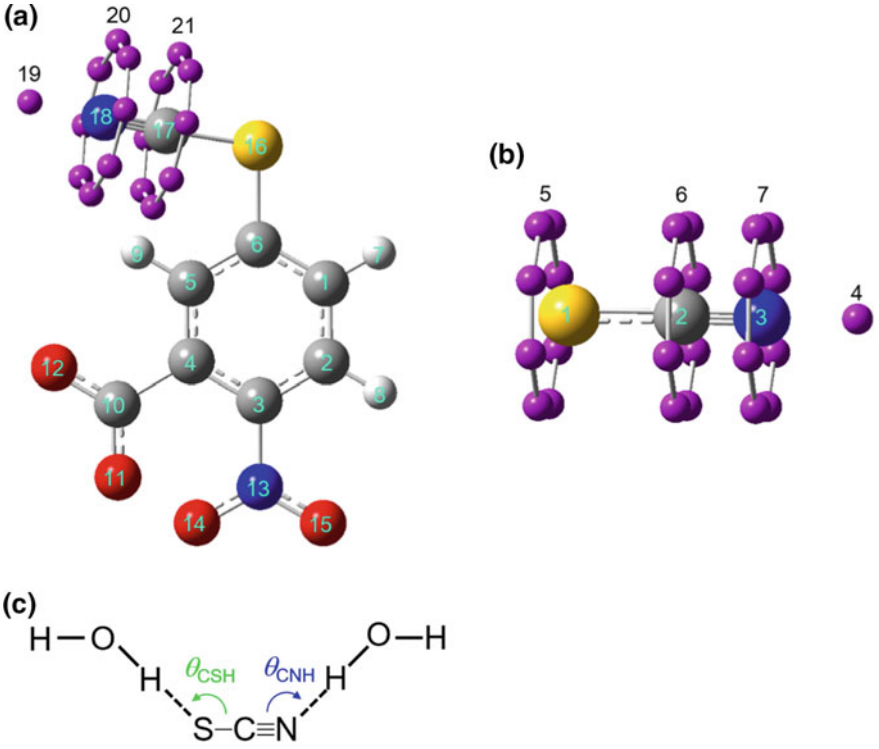

Fig. 12.7 Distributions of the interaction sites of **a** NTBA and **b** SCN^-. The number on each atom corresponds to the index i in (12.5). The 19th interaction site of NTBA and 4th interaction site of SCN^- are placed to represent the σ-type HB interaction. Moreover, the additional eight interaction sites placed on the circles around the S, C, and N atoms of the SCN group represent the π-type HB interaction. The geometrical definitions of these additional interaction sites of NTBA and SCN^- are given in [69] and [70], respectively. **c** Definition of the HB angles of θ_{CNH} (blue) and θ_{CSH} (green) between the SCN group and a single water molecule

the contribution of the charge transfer effect to the SCN frequency shift of MeSCN is negligibly small [69]. Therefore, in this study, the parameter l_0 for NTBA is set to zero as well.

In order to determine the parameters l_i for NTBA and SCN^-, we performed multivariate least-square fitting analysis with (12.5). Here, the following two constraint conditions are considered for the parameters l_i in (12.5) [69, 70]. The first condition is that a set of the parameters satisfies the charge neutrality. The second condition is that the corresponding parameters l_i for the additional eight interaction sites on the same circles are assumed to have the same values due to the approximately cylindrical symmetry of the π-orbitals. Therefore, to describe the solvent-induced frequency shift, 20 and 7 (including the additional parameter l_0) independent interaction sites are considered for NTBA and SCN^-, respectively. For the multivariate least-square fitting analyses, we randomly sampled 110 NTBA $-(H_2O)_n$ ($1 \leq n \leq 6$) and 100 SCN^-–$(H_2O)_n$ ($1 \leq n \leq 16$) clusters from the MD simulations and performed structural optimization and normal mode analysis for the solute in each cluster. Then, by taking the difference between the vibrational frequencies of the solute in the cluster and gas phase, we obtained the ab initio calculated SCN frequency shift [i.e. $\Delta\omega(\phi)$ in the left-hand side of (12.5)]. Regarding the right-hand side of (12.5), we obtained all the electrostatic potentials ($i = 1$–35 for NTBA and $i = 1$–7 SCN^-) from the NTBA/water and SCN^-/water clusters.

12.3.1 Hydration Structure Around Vibrational Probe

Hereafter, the results of the classical MD simulations for the three solute molecules, NTBA, SCN^-, and $N_3{}^-$ in H_2O and pure H_2O are discussed. First, we discuss the hydration structure around the three solutes. Figure 12.8 displays the pair radial distribution functions (RDFs) between the water H and O atoms and the N atoms of the SCN group of NTBA, SCN^-, and $N_3{}^-$ (denoted as $g_{NH}(r)$ and $g_{NO}(r)$, respectively). The first minimum and maximum of $g_{NH}(r)$ and $g_{NO}(r)$ are summarized in Table 12.2. As shown in the figures, $g_{NO}(r)$ of SCN^- and $N_3{}^-$ show sharper first peaks at around 3.0 Å and the amplitudes of the first peaks are larger than that of NTBA. This difference can be explained in terms of the charge density of the vibrational probe: due to the larger partial charges in the vibrational probe, the three atomic ions can attract the surrounding water molecules more strongly than the SCN group of NTBA. Therefore, we consider that the water molecules around SCN^- is more strongly interacts with SCN^- than that around the SCN group of NTBA. Moreover, based on the result of weak interaction between NTBA molecule and water compared with that with SCN^- and water, the hydration structure around the SCN group of NTBA can be expected to be similar to that of the pure water itself.

On the other hand, as shown in Fig. 12.8, the $g_{NH}(r)$ for NTBA, SCN^- and $N_3{}^-$ have the first sharp peaks at around 2 Å, which arises from the solute-solvent HBs. To define a HB between the vibrational probe and a water molecule (denoted as $-SCN\cdots H_2O$ for NTBA, $SCN^-\cdots H_2O$ for SCN^-, and $N_3{}^-\cdots H_2O$ for $N_3{}^-$), we

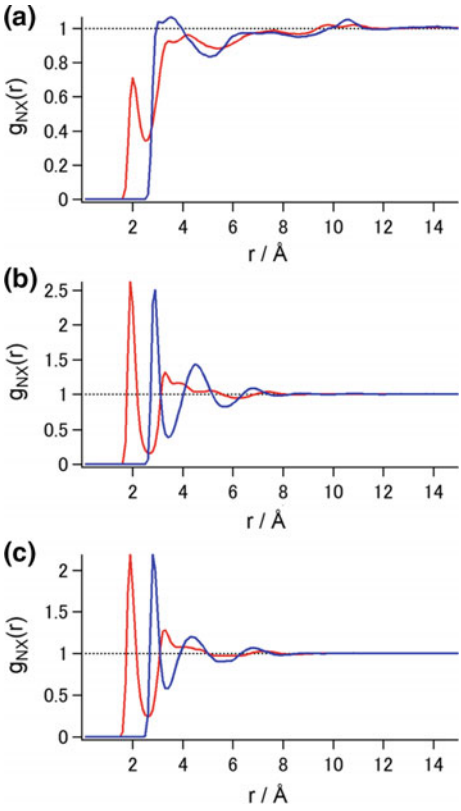

Fig. 12.8 Pair radial distribution function $g_{NX}(r)$ between SCN nitrogen and N_3 terminal nitrogen atoms and H_2O hydrogen (red, X = H) and oxygen (blue, X = O) atoms. **a** NTBA, **b** N_3^-, and **c** SCN^-

adopted geometrical criteria with respect to the length r_{NH} and the angle θ_{NOH} of the HB. Based on the angle-resolved RDFs for NTBA and SCN^-, we defined the HB criteria for $-SCN\cdots H_2O$ and $SCN^-\cdots H_2O$ as follows: $r_{NH} \leq 2.6$ Å and $\theta_{NOH} \leq 30°$. Here, it should be noted that NTBA and SCN^- possess the other HB sites, that is, the O atoms of the NO_2 and COO^- groups of NTBA and the S atom of SCN^-. Regarding to these HB sites, we also defined a HB in terms of geometrical criteria with respect to the length r_{XH} and the angle θ_{XOH} of the HB, where "X" represents a given HB site of NTBA and SCN^-. The value of r_{XH} is determined by the first minimum of the corresponding pair RDF $g_{XH}(r)$, and the θ_{XOH} is set to be 30°.

12.3.2 Water Dynamics Around the Vibrational Probes

As mentioned in the previous section, the interactions between water and SCN^- and N_3^- are much stronger than that between NTBA and water. Therefore, we can expect that the water dynamics around NTBA is different from that around SCN^- and N_3^-. First, we discuss HB dynamics between the solute and surrounding water

molecules. In order to evaluate the solute-solvent HB dynamics, we calculated the HB correlation functions (HBCFs) between the nitrogen atoms of the vibrational probes and water molecules as follows [71]:

$$C_{\mathrm{HB}}(T) \equiv \frac{\langle H(T)H(0)\rangle}{\langle H(0)H(0)\rangle} \tag{12.6}$$

where $H(T) = 1$ if a specific HB is formed at time T, and $H(T) = 0$ otherwise. Moreover, we calculated the HBCF for water-water HB (denoted as $H_2O\cdots H_2O$) from the MD simulations for pure H_2O system by using the geometrical definition given by Luzar and Chandler [71]. Figure 12.9 shows the HBCFs for $-SCN\cdots H_2O$, $N_3^-\cdots H_2O$, $SCN^-\cdots H_2O$, and $H_2O\cdots H_2O$. The HBCFs can be reproduced by a triple exponential function, and the corresponding time constants (τ_i) are listed in Table 12.2.

If a HBCF decays with a single time constant, the decay time constant can be interpreted as the HB lifetime. However, HBCFs typically show the multi-exponential decay due to the dynamics on different time scales, such as rotational motions and diffusion of water molecules [72–74]. Therefore, we characterized the HB lifetime by a single time constant $\tau_{1/e}$ defined as: $C_{\mathrm{HB}}(\tau_{1/e}) = e^{-1}C_{\mathrm{HB}}(0)$. The obtained time constants of $\tau_{1/e}$ for $-SCN\cdots H_2O$, $SCN^-\cdots H_2O$, and $N_3^-\cdots H_2O$ are 1.76 ps, 8.39 ps, and 16.13 ps, respectively. Regarding the HB dynamics between SCN^- and H_2O molecules, $\tau_{1/e}$ is consistent with the previous result for that between SCN^- and D_2O molecules reported by Czurlok et al. [28]. Moreover, $\tau_{1/e}$ for $H_2O\cdots H_2O$ is found to be 2.81 ps, which is also consistent with the result from the MD simulation for the TIP4P water system [75]. As the results that the $\tau_{1/e}$ for $SCN^-\cdots H_2O$ is longer than those of $-SCN\cdots H_2O$ and $H_2O\cdots H_2O$, we consider that SCN^- forms HBs with its neighboring water molecules more strongly than NTBA and H_2O. On the other hand, based on the results that the $\tau_{1/e}$ for $-SCN\cdots H_2O$ is close to that for $H_2O\cdots H_2O$, the HB between the SCN group of NTBA and a water molecule may not be significantly different from that between water molecules.

Next, we examined the reorientational relaxation of a single water molecule in the vicinity of NTBA, SCN^-, and N_3^-. In this study, we calculated the dipole moment

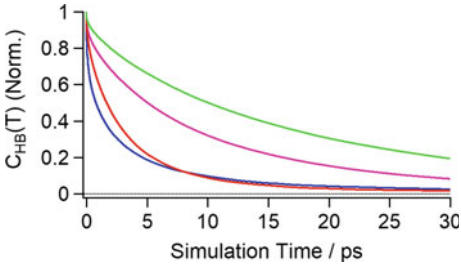

Fig. 12.9 HB correlation functions of $-SCN\cdots H_2O$ (blue), $N_3^-\cdots H_2O$ (green), $SCN^-\cdots H_2O$ (pink), and $H_2O\cdots H_2O$ (red). The characteristic time constants $\tau_{1/e}$ for these decay curves are as follows; $\tau_{1/e} = 1.76$ ps (NTBA), 16.1 ps (N_3^-), 8.39 ps (SCN^-), and 2.80 ps (bulk water)

Table 12.2 Obtained parameters of radial distribution functions, HBCFs, and FFTCFs for NTBA/water, SCN^-/water, and bulk water systems

Solute	Radial distribution function				Hydrogen bond lifetime[a, b]				Frequency fluctuation[a]	
	$r_{XH,min}$/Å	$r_{XH,max}$/Å	$r_{XO,min}$/Å	$r_{XO,max}$/Å	τ_1/ps	τ_2/ps	τ_3/ps	$\tau_{1/e}$ ps	τ_1/ps	τ_2/ps
NTBA (SCN group)	2.6	2.0	5.0	3.5	0.28 (0.30)	2.76 (0.51)	15.03 (0.19)	1.76	0.13 (0.64)	1.41 (0.36)
NTBA (COO^- group)	2.5	1.8	3.3	2.7	0.34 (0.09)	5.88 (0.31)	19.85 (0.60)	10.79		
NTBA (NO_2 group)	2.3	1.9	4.2	3.1	0.23 (0.40)	2.17 (0.46)	15.01 (0.14)	0.89		
N_3^-	2.6	1.9	3.4	2.9	0.48 (0.05)	6.11 (0.20)	22.65 (0.75)	16.13	–	–
Hydrated H_2O (N atom, N_3^-)	–	–	–	–	0.21 (0.16)	3.06 (0.63)	8.67 (0.21)	2.79	–	–
SCN^- (S atom)	2.8	2.1	3.6	3.0	0.41 (0.10)	5.96 (0.52)	18.93 (0.38)	7.70	0.13 (0.56)	1.44 (0.44)
SCN^- (N atom)	2.6	1.9	3.3	2.8	0.30 (0.09)	5.64 (0.44)	17.13 (0.47)	8.39		
Hydrated H_2O (S atom, SCN^-)	–	–	–	–	0.14 (0.20)	1.99 (0.47)	5.11 (0.33)	2.04	–	–
Hydrated H_2O (N atom, SCN^-)	–	–	–	–	0.15 (0.20)	2.31 (0.56)	5.98 (0.24)	2.05	–	–
Bulk H_2O	–	–	–	–	0.34 (0.15)	3.08 (0.70)	12.76 (0.15)	2.80	–	–

[a] τ_i: time constant of ith component in the fitting function; $\sum_{i=1}^{2 \text{ or } 3} A_i \exp(-T/\tau_i)$. The relative amplitude of ith component A_i is shown in the parentheses. Error bars for these parameters are approximately less than 5%

[b] $\tau_{1/e}$: time constant defined by $C_{HB}(\tau_{1/e}) = e^{-1} C_{HB}(0)$

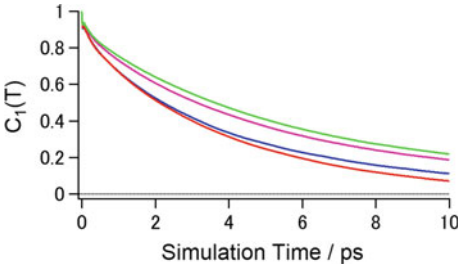

Fig. 12.10 Dipole moment reorientational correlation functions for water molecules around the SCN nitrogen atoms of NTBA (blue) and SCN^- (pink), N_3 nitrogen atom of $N_3{}^-$ (green), and those in bulk (red). The characteristic time constants $\tau_{1/e}$ for these decay curves are as follows; $\tau_{1/e}$ = 3.56 ps (NTBA), 5.72 ps ($N_3{}^-$), 5.04 ps (SCN^-), and 3.35 ps (bulk water)

reorientational correlation functions for a water molecule forming a HB with the solutes as follows:

$$C_{1,\mathrm{HB}}(T) = \left\langle P_1\left(\frac{\boldsymbol{\mu}(0)\cdot\boldsymbol{\mu}(T)}{|\boldsymbol{\mu}(0)||\boldsymbol{\mu}(T)|}\right)H(0)\right\rangle \tag{12.7}$$

and for bulk water as follows:

$$C_{1,\mathrm{bulk}}(T) = \left\langle P_1\left(\frac{\boldsymbol{\mu}(0)\cdot\boldsymbol{\mu}(T)}{|\boldsymbol{\mu}(0)||\boldsymbol{\mu}(T)|}\right)\right\rangle \tag{12.8}$$

where $\boldsymbol{\mu}(T)$ is the dipole moment vector of the water molecule, and $P_1(x)$ is the first-order Legendre polynomial. Figure 12.10 shows the obtained dipole moment reorientational correlation functions for water molecules neighboring to the vibrational probes and those in bulk. All the dipole moment reorientational correlation functions can be fitted well by a double exponential function and $\tau_{1/e}$ are 3.56 ps for NTBA, 5.04 ps for SCN^-, 5.72 ps for $N_3{}^-$, and 3.35 ps for bulk water. The result shows that the rotational relaxations of the water molecule which is hydrogen-bonded to SCN^- and $N_3{}^-$ are slower by approximately 50 and 70% than that of bulk water, respectively. On the other hand, the reorinetational motion of the water molecule nearby the SCN group of NTBA is found to be almost the same as that in bulk.

12.3.3 Theoretical Analysis for Vibrational Frequency Fluctuations

We calculated the solvent-induced frequency shifts of NTBA and SCN^- at a given time T ($\Delta\omega(T)$) based on (12.5) by using the time-dependent electrostatic potential $\phi_{ij}(T)$. We obtained the temporal evolution of the SCN frequency shifts of NTBA and SCN^- in H_2O from the trajectories of MD simulations up to 6 ns.

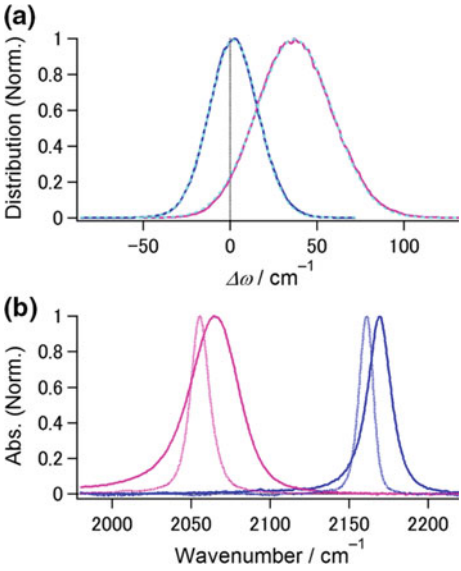

Fig. 12.11 **a** Distributions of the SCN frequency shifts of NTBA (blue) and SCN^- (pink) calculated by (12.5). The dotted light-blue lines indicate the results of Gauss fittings. **b** Comparison of experimental IR absorption spectra of NTBA (blue) and SCN^- (pink) in H_2O (solid) and DMSO (dotted). The peak wavenumbers of these IR bands in H_2O and DMSO are 2169.3 and 2161.1 cm^{-1} for NTBA, respectively, and, 2064.9 and 2055.5 cm^{-1} for SCN^-, respectively

First, we calculated the distributions of the SCN frequency fluctuations of NTBA and SCN^- in H_2O. Figure 12.11a shows the SCN frequency distributions of NTBA and SCN^-, which are well reproduced by Gaussian distributions with the peak frequencies of 2.0 and 36.9 cm^{-1}, respectively. Figure 12.11b displays the experimentally obtained IR absorption spectra of the SCN anti-symmetric stretching modes of NTBA and SCN^- in H_2O and dimethyl sulfoxide (DMSO). Here, DMSO was chosen as an aprotic solvent. Figure 12.11b indicates that, compared to the SCN frequencies of NTBA and SCN^- in DMSO, those in H_2O are shifted toward the higher frequency by 8.2 and 9.4 cm^{-1}, respectively. Therefore, based on the vibrational solvatochromism theory, we successfully reproduce the blue shift of the SCN frequencies of NTBA and SCN^- in H_2O.

Next, we calculated the FFTCFs of the SCN anti-symmetric stretching modes of NTBA and SCN^- in H_2O (Fig. 12.12 and Table 12.2). We found that the theoretically obtained FFTCFs of NTBA and SCN^- in H_2O can be fitted by a double exponential function. It should be noted that, from the theoretical analyses based on the multi-site electrostatic potential theory, we can reproduce the ~1-ps decay of the FFTCFs of the SCN anti-symmetric stretching modes of NTBA and SCN^- in H_2O. In the previous studies of the classical MD simulations for SPC/E water system, Fayer and Tokmakoff groups independently concluded that the decay of FFTCF of bulk water on approximately 1 ps time scale reflect the collective motion of water molecules accompanying the HB rearrangements [32–34]. Therefore, similarity of the time scale of τ_2 for NTBA and SCN^- to that of bulk water suggests that the slower SCN frequency fluctuations reflects the structural reorganization of the HB network around the solutes.

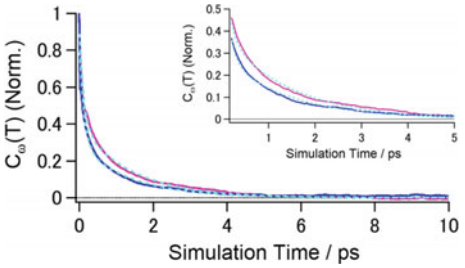

Fig. 12.12 Normalized FFTCFs of the SCN stretching modes of NTBA (blue) and SCN^- (pink) calculated by (12.5). The dotted light-blue lines are the fitting results to double-exponential functions. The inset highlights the FFTCF decay curves of NTBA (blue) and SCN^- (pink) at early simulation time

In order to extract more detailed information on the SCN frequency fluctuations of NTBA and SCN^- in H_2O, we examined the radial dependence of the FFTCFs of the solutes. Here, we defined the spatially-resolved SCN frequency fluctuation ($\Delta\omega_s(T)$) as:

$$\Delta\omega_S(T,r) \equiv \sum_{i=1}^{N_{solu}} (l_i + l_0) \sum_{j=1}^{N_{solv}} \phi_{ij}(T) f_j(T,r) \tag{12.9}$$

where $f_j(T, r)$ is the filtering function to characterize the radial-dependence of the $\Delta\omega_s(T)$ which is represented as:

$$f_j(T,r) \equiv \max_{1\le i\le N'_{solu}} \left\{ \frac{1}{2}\left(1 - \tanh\left[\gamma\left(r_{ij}(T) - r\right)\right]\right) \right\} \tag{12.10}$$

where N'_{solu} is the number of atoms in NTBA and SCN^-: $N'_{solu} = 18$ for NTBA and $N'_{solu} = 3$ for SCN^-. γ is the damping constant (set to 10 $Å^{-1}$). r_{ij} is the distance between the *i*th interaction site of the solutes and the O atom of the *j*th water molecule, and the r is the given cutoff distance, which characterizes the dependence of the FFTCF on solute-solvent distance. In this study, by varying r from 3.5 to 7.5 Å with a 1.0 Å step, we calculated the series of the spatially-resolved FFTCFs of NTBA and SCN^- in H_2O, as displayed in Fig. 12.13. As shown in Fig. 12.13a, the spatially-resolved FFTCF of NTBA gradually approaches to the total FFTCF with increasing the cutoff distance r, which indicates that the SCN frequency fluctuations of NTBA reflect the electrostatic interactions induced by water molecules existing far from the solute, i.e. bulk-like water molecules. On the other hand, Fig. 12.13c shows that the FFTCF of SCN^- is almost determined by the contribution form the water molecules within the distance of 3.5 Å from the solute, i.e. water molecules in the first hydration shell.

Here, we examined these results on the spatially-resolved FFTCFs of NTBA and SCN^- in H_2O from a different viewpoint. In order to evaluate the radial dependence

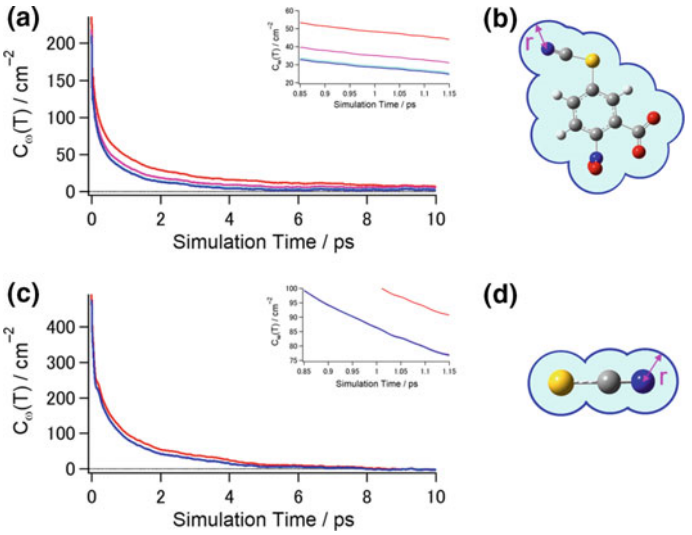

Fig. 12.13 Spatially-resolved FFTCFs of **a** NTBA and **c** SCN^- with the filtering function $f_j(T, r)$ defined by (12.10). The cutoff distance r for each profile is as follows: $r = 3.5$ Å (red), 5.5 Å (pink), 7.5 Å (light-blue), and no filtering (blue). The inset in (**a**) and (**c**) highlights the difference among the overlapping lines. (Inset) Schematic illustration of the filtering function $f_j(T, r)$ for **b** NTBA and **d** SCN^-. By considering sphere with a radius of r on each atoms of the solutes, the union of the spherical regions, i.e. light-blue region within closed blue line, characterizes the radial-dependence of the SCN frequency fluctuations

of the Coulomb interaction, we calculated the radial Coulomb electrostatic potentials for NTBA and SCN^- as follows [76]:

$$\phi(r) \equiv \left\langle \sum_{i=1}^{N_{\mathrm{solu}}} \sum_{j=1}^{N_{\mathrm{solv}}} \phi_{ij}(T) f_j(T, r) \right\rangle \tag{12.11}$$

where $f_j(T, r)$ is given in (12.10). Here, based on the parameter l_j for NTBA, we consider that the SCN frequency shift of the solute is approximately characterized by the electrostatic interactions between the SCN group and surrounding water molecules. Therefore, for the comparison between the non-ionic and ionic SCN groups in terms of the solute-solvent interactions, we calculated the Coulomb electrostatic potential only on the SCN group and its surrounding extra sites of NTBA is considered for NTBA. We also performed the same calculation for N_3^- in H_2O. Figure 12.14 clearly shows that the radial dependence of the electrostatic potentials on NTBA and the three atomic ions is different: while NTBA is influenced through the Coulomb interaction induced by water molecules approximately ~7 Å away from the solute (~90% of the converged value of the electrostatic potential), that on three atomic ions is almost determined by the water molecules in the first and second hydration shells (<5.0 Å, ~90% of the converged electrostatic potential) and the contribution from

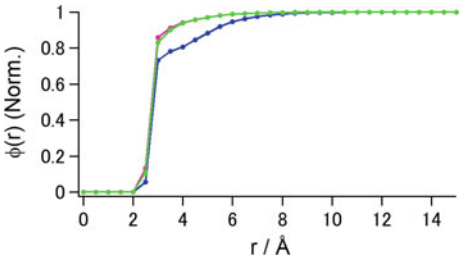

Fig. 12.14 Normalized radial Coulomb electrostatic potential for NTBA (blue), N_3^- (green), and SCN^- (pink)

water molecules beyond the second hydration shell is negligibly small. Based on the results above, in the case of NTBA/water system, we consider that, since NTBA feels the electrostatic interactions from water molecules existing far from the solute, which are expected to behave as bulk water, the fluctuations of the HB network system in bulk can induce the SCN frequency fluctuations on the 1 ps time scale.

On the other hand, in the case of SCN^-/water and N_3^-/water systems, we found that the electrostatic interaction further beyond the second hydration shell is "screened out", which is in good agreement with the theoretical work on dimethylphosphate $(CH_3O)_2PO_2^-$) in H_2O reported by Fingerhut et al. [76]. Here, with respect to the water dynamics around SCN^- and N_3^-, it should be noted that the HB dynamics between the ions and water molecules are significantly slower than that between water molecules in bulk. Moreover, the reorientational motions of the water molecule forming the HB with SCN^- and N_3^- is about 50 and 70% slower than that of the bulk water, respectively. These results suggest that the vibrational frequency fluctuations of the ions in H_2O are mainly dominated by the collective water dynamics in the first hydration shell, not the HB dynamics between water molecules and the ions. Consequently, in order to investigate the collective water dynamics around SCN^- and N_3^-, we calculated the normalized total dipole moment time correlation function for water molecules in the first and second hydration shells of the ions as follows:

$$C_{\mathrm{TDP,solv}}(T) \equiv \frac{\left\langle \left(\sum_{i=1}^{N_{\mathrm{solv}}} \boldsymbol{\mu}_i(T) f_i(T,r) \right) \cdot \left(\sum_{j=1}^{N_{\mathrm{solv}}} \boldsymbol{\mu}_j(0) f_j(0,r) \right) \right\rangle}{\left\langle \left| \sum_{i=1}^{N_{\mathrm{solv}}} \boldsymbol{\mu}_i(0) f_i(0,r) \right|^2 \right\rangle} \tag{12.12}$$

where the cutoff distance r is set to 5.0 Å. Moreover, for comparison, we calculated the corresponding time correlation function for the bulk water system without SCN^- and N_3^- as follows:

$$C_{\mathrm{TDP,water}}(T) \equiv \frac{\left\langle \left(\sum_{i=1}^{N_{\mathrm{solv}}} \boldsymbol{\mu}_i(T) f_i'(T,r) \right) \cdot \left(\sum_{j=1}^{N_{\mathrm{solv}}} \boldsymbol{\mu}_j(0) f_j'(0,r) \right) \right\rangle}{\left\langle \left| \sum_{i=1}^{N_{\mathrm{solv}}} \boldsymbol{\mu}_i(0) f_i'(0,r) \right|^2 \right\rangle} \tag{12.13}$$

Here, in order to define the filtering function $f_i'(T, r)$, we considered a "hypothetical hydration shell" as shown in Fig. 12.15. Inside a "hypothetical hydration shell", $f_i'(T, r)$ is set to 0. Outside a shell, $f_i'(T, r)$ is the same as that in (12.10). Figure 12.16 shows $C_{\mathrm{TDP,solv}}(T)$ and $C_{\mathrm{TDP,water}}(T)$ for the SCN^-/water, N_3^-/water, and bulk water systems, respectively. These decays can be characterized by characteristic time constants of $\tau_{1/e}$ of 3.77 ps and 5.12 ps for SCN^-/water and N_3^-/water systems, respectively. On the other hand, the $C_{\mathrm{TDP,water}}(T)$ for the hypothetical hydration shell of SCN^- and N_3^- decay with characteristic time constants of 3.33 and 4.35 ps, respectively. The differences between the ion/water system and the bulk water system are only 13 and 17% for SCN^- and N_3^-, respectively. This result indicates that the collective water dynamics in the first and second hydration shells of SCN^- and N_3^- are "more similar" to that of bulk water than the single molecule dynamics of a water molecule forming the HB with the ions.

Here, as mentioned above, it should be noted that HBs between SCN^- and N_3^- and neighboring water molecules are very strong compared with that between bulk-

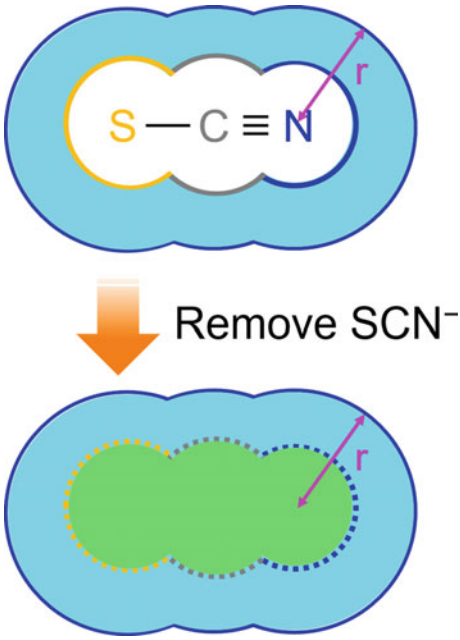

Fig. 12.15 Schematic illustration of a "hypothetical hydration shell of SCN^-" in bulk water system. In order to define this hydration shell in the bulk water system, SCN^- molecule is simply removed from the hydration shell of SCN^-/water system. Here, the molecular structure of SCN^- (i.e. bond lengths and bond angle) is the same as that for SCN^-/water system. Regarding the size of each atom of this hypothetical SCN^- in bulk water system, radius r is defined as the shortest length in which the corresponding RDF $g_{\mathrm{XO}}(r)$ (X = S, C, or N) has non-zero value. For the light-blue region (i.e. hydration shell of SCN^-), the filtering function $f_i'(T, r)$ is the same as that in (12.10). On the other hand, for the green region (i.e. inside of the hypothetical SCN^-), the filtering function $f_i'(T, r)$ is set to 0

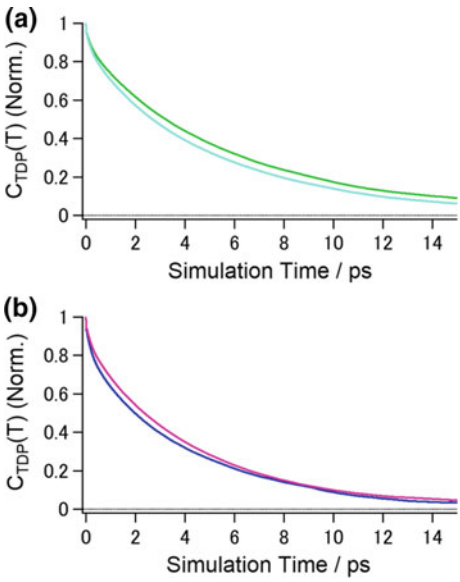

Fig. 12.16 Total dipole moment time correlation functions for water molecules in **a** N_3^-/water and **b** SCN^-/water systems. The green and pink lines correspond to the results for N_3^-/water and SCN^-/water given by (12.12) with cut-off length $r = 5.0$ Å, respectively. The light-blue and blue lines are the result for the hypothetical hydration shell of N_3^- and SCN^- in bulk water systems given by (12.13) with cut-off length $r = 5.0$ Å, respectively. The characteristic time constants $\tau_{1/e}$ for these decay curves are as follows; $\tau_{1/e} = 5.12$ ps (N_3^-/water system), 3.77 ps (SCN^-/water system), 4.35 ps (hypothetical hydration shell of N_3^-), and 3.33 ps (hypothetical hydration shell of SCN^-)

water molecules. In order to clarify the fluctuation of the water molecules in the first hydration shell of SCN^- and N_3^-, we investigated the HBCF for water molecules in the first hydration shell of the ions by defining the following time correlation function:

$$C_{\mathrm{HB,Hyd}}(T) \equiv \frac{\langle H'(T)H'(0)R(T)\rangle}{\langle H'(0)H'(0)R(0)\rangle} \tag{12.14}$$

where $H'(T) = 1$ if the water molecule in the first-hydration shell forms HB with another water molecule at time T and $H'(T) = 0$ otherwise. $R(T)$ defines the region of the first-hydration shell of SCN^- and N_3^-: $R(T) = 1$ if the distance between the O atom of a specific water molecule and the terminal N atoms of SCN^- and N_3^- are less than a cutoff distance ($R_{\mathrm{cut,N}}$) at time T and $R(T) = 0$ otherwise. In this study, based on the first minima of $g_{\mathrm{NO}}(r)$ for the SCN^-/water and N_3^-/water systems, the $R_{\mathrm{cut,N}}$ are set to 3.3 Å and 3.4 Å, respectively. Figure 12.17 displays the comparison between the HBCFs of water pairs in the first hydration shells of the terminal N atoms of SCN^- and N_3^- (denoted as $H_2O_{\mathrm{HW,SCN-}}\cdots H_2O$ and $H_2O_{\mathrm{HW,N_3^-}}\cdots H_2O$, respectively) and those in bulk. The HBCFs for $H_2O_{\mathrm{HW,SCN-}}\cdots H_2O$ and $H_2O_{\mathrm{HW,N_3^-}}\cdots H_2O$ can be

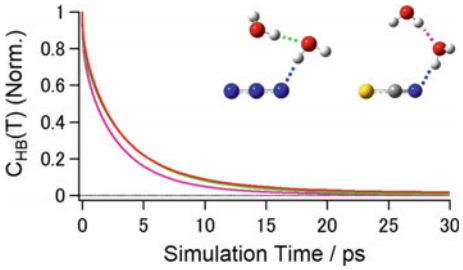

Fig. 12.17 Comparison of the HBCFs among $H_2O_{HW,N3-}\cdots H_2O$ (green), $H_2O_{HW,SCN-}\cdots H_2O$ (pink), and bulk $H_2O\cdots H_2O$ (red, same result as the red line in Fig. 12.9). (Inset) Snapshots of the MD simulations for water pairs in the first hydration shell of the terminal N atoms of N_3^- and SCN^-. The characteristic time constants $\tau_{1/e}$ for these decay curves are as follows; $\tau_{1/e} = 2.79$ ps ($H_2O_{HW,N3-}\cdots H_2O$) and 2.05 ps ($H_2O_{HW,SCN-}\cdots H_2O$)

characterized by characteristic time constants $\tau_{1/e}$ of 2.05 and 2.79 ps, respectively. We found that the HB dynamics between water molecules in the vicinity of SCN^- and N_3^- are faster than those between the ions and water molecules, and are almost the same as those in bulk. Consequently, since SCN^- and N_3^- form relatively strong HBs with surrounding water molecules, the motion of these water molecules, e.g. translational and rotational motions, can be controlled by the collective rearrangement of the HB network without breaking the HBs with the solute. In other words, the antisymmetric stretching modes of SCN^- and N_3^- are perturbed by the structural fluctuations of the HB network through the water molecules directly hydrogen-bonded to the solute, which results in the experimentally observed vibrational frequency fluctuations of SCN^- and N_3^- in water on the 1 ps time scale.

12.4 Conclusion

In this chapter, in order to establish molecular pictures for the vibrational frequency fluctuations of the non-ionic and ionic vibrational probes, the three solute molecules, NTBA, SCN^-, and N_3^-, were investigated experimentally and theoretically. By two-dimensional IR spectroscopy, the FFTCF of the vibrational frequency fluctuations were obtained, and the decay time constants of the FFTCF were found to be approximately 1 ps. We aimed to answer to the following questions on the vibrational frequency fluctuations; what kind intermolecular interaction between the solute and solvent molecules determine the frequency fluctuations and what kind of solvent dynamics affects that. We theoretically investigated the structural fluctuations of the local environment around the solute for the three systems. By calculating the solute-solvent pair radial-distribution functions, the hydrogen-bond correlation function, and the single-water dipole moment correlation function, we found that the hydration structure and water dynamics in the vicinity of the SCN group of NTBA are almost similar to those in bulk. Moreover, by calculating the spatially-resolved FFTCF and

the electrostatic potential on the vibrational probe, we revealed that longer-range solute-solvent interaction is important for the SCN vibrational frequency fluctuations of NTBA, which is a different result from the SCN^-/water and N_3^-/water systems. Therefore, we consider that the electrostatic interactions with such "bulk-like" water molecules are responsible for the slow decay component, i.e. 1-ps decay component, of the FFTCF of NTBA in H_2O. This is in a sharp contrast with the molecular mechanism for the FFTCFs of SCN^- and N_3^- in H_2O, where the SCN and N_3 vibrational frequency fluctuations are controlled by the water molecules tightly hydrogen bonding to the ions. From the comparison between our current and previous studies, it is revealed that the molecular origin of vibrational frequency fluctuations can be significantly different between ionic and non-ionic vibrational probe molecules in terms of the solute-solvent interactions and solvation dynamics, even if we observe similar time scales of decay components in their FFTCFs by 2D-IR spectroscopy.

Acknowledgements We performed quantum chemical calculations and classical MD simulations using the Research Center for Computational Science, Okazaki, Japan. This work was partially supported by a Grant-in-Aid for Scientific Research on the 16J05643 from the Ministry of Education, Culture, Sports, Science, and Technology (MEXT) of Japan and the Joint Studies Program (2015–2016) of the Institute for Molecular Science.

References

1. I. Ohmine, H. Tanaka, Chem. Rev. **93**, 2545 (1993)
2. B. Bagchi, *Water in Biological and Chemical Processes* (Cambridge University Press, New York, 2013)
3. D.W. Oxtoby, Annu. Rev. Phys. Chem. **32**, 77 (1981)
4. M.D. Fayer (ed.), *Ultrafast Infrared Vibrational Spectroscopy* (CRC Press, New York, 2013)
5. S. Mukamel, *Principles of Nonlinear Optical Spectroscopy* (Oxford University Press, Oxford, 1995)
6. J.C. Owrutsky, D. Raftery, R.M. Hochstrasser, Annu. Rev. Phys. Chem. **45**, 519 (1994)
7. M. Banno, K. Ohta, S. Yamaguchi, S. Hirai, K. Tominaga, Acc. Chem. Res. **42**, 1259 (2009)
8. M. Cho, *Two-Dimensional Optical Spectroscopy* (CRC Press, Boca Raton, 2009)
9. P. Hamm, M. Zanni, *Concepts and Methods of 2D Infrared Spectroscopy* (Cambridge University Press, New York, 2011)
10. R. Kubo, M. Toda, N. Hashitsume, *Statistical Physics II, Nonequilibrium Statistical Mechanics* (Springer, Berlin, 1991)
11. H. Kim, M. Cho, Chem. Rev. **113**, 5817 (2013)
12. T. Yagasaki, S. Saito, Annu. Rev. Phys. Chem. **64**, 55 (2013)
13. P. Hamm, M. Lim, R.M. Hochstrasser, Phys. Rev. Lett. **81**, 5326 (1998)
14. P. Hamm, M. Lim, W.F. De Grado, R.M. Hochstrasser, J. Phys. Chem. A **103**, 10049 (1999)
15. M.T. Zanni, M.C. Asplund, R.M. Hochstrasser, J. Chem. Phys **114**, 5479 (2001)
16. S. Woutersen, R. Pfister, P. Hamm, Y. Mu, D.S. Kosov, G. Stock, J. Chem. Phys. **117**, 6833 (2002)
17. N.–H. Ge, M.T. Zanni, R.M. Hochstrasser, J. Phys. Chem. A **106**, 962 (2002)
18. M. Kozinski, S. Garrett-Roe, P. Hamm, Chem. Phys. **341**, 5 (2007)
19. K. Ohta, H. Maekawa, S. Saito, K. Tominaga, J. Phys. Chem. A **107**, 5645 (2003)
20. K. Ohta, H. Maekawa, K. Tominaga, J. Phys. Chem. A **108**, 1333 (2004)

21. K. Ohta, H. Maekawa, K. Tominaga, Chem. Phys. Lett. **386**, 32 (2004)
22. J. Tayama, A. Ishihara, M. Banno, K. Ohta, S. Saito, K. Tominaga, J. Chem. Phys. **133**, 014505 (2010)
23. K. Ohta, J. Tayama, K. Tominaga, Phys. Chem. Chem. Phys. **14**, 10455 (2012)
24. J. Tayama, K. Ohta, K. Tominaga, Chem. Lett. **41**, 366 (2012)
25. K. Ohta, J. Tayama, S. Saito, K. Tominaga, Acc. Chem. Res. **45**, 1982 (2012)
26. M. Okuda, K. Ohta, K. Tominaga, J. Chem. Phys. **142**, 212418 (2015)
27. M. Okuda, K. Ohta, K. Tominaga, J. Chem. Phys. **145**, 114503 (2016)
28. D. Czurlok, M. von Domaros, M. Thomas, J. Gleim, J. Lindner, B. Kirchner, P. Vöhringer, Phys. Chem. Chem. Phys. **17**, 29776 (2015)
29. R. Yuan, C. Yan, A. Tamimi, M.D. Fayer, J. Phys. Chem B **119**, 13407 (2015)
30. S. Dutta, Z. Ren, T. Brinzer, S. Garrett-Roe, Phys. Chem. Chem. Phys. **17**, 26575 (2015)
31. K.M. Slenkamp, M.S. Lynch, J.F. Brookes, C.C. Bannan, S.L. Daifuku, M. Khalil, Struct. Dyn. **3**, 023609 (2016)
32. J.B. Asbury, T. Steinel, K. Kwak, S.A. Corcelli, C.P. Lawrence, J.L. Skinner, M.D. Fayer, J. Chem. Phys. **121**, 12431 (2004)
33. C.J. Fecko, J.J. Loparo, S.T. Loberts, A. Tokmakoff, J. Chem. Phys. **122**, 054506 (2005)
34. J.J. Loparo, S.T. Roberts, A. Tokmakoff, J. Chem Phys. **125**, 194521 (2006)
35. K.F. Everitt, E. Geva, J.L. Skinner, J. Chem. Phys. **114**, 1326 (2001)
36. A. Piryatinski, J.L. Skinner, J. Phys. Chem B **106**, 8055 (2002)
37. K. Kwac, M. Cho, J. Chem. Phys. **119**, 2247 (2003)
38. C.P. Lawrence, J.L. Skinner, J. Chem. Phys. **118**, 164 (2003)
39. K. Kwac, H. Lee, M. Cho, J. Chem. Phys. **120**, 1477 (2004)
40. S.A. Corcelli, C.P. Lawrence, J.B. Asbury, T. Steinel, M.D. Fayer, J.L. Skinner, J. Chem. Phys. **121**, 8897 (2004)
41. S.A. Corcelli, C.P. Lawrence, J.L. Skinner, J. Chem. Phys. **120**, 8107 (2004)
42. J.D. Eaves, A. Tokmakoff, P.L. Geissler, J. Phys. Chem. A **109**, 9424 (2005)
43. B. Auer, R. Kumar, R. Schmidt, J.L. Skinner, Proc. Natl. Acad. Sci. U. S. A. **104**, 14215 (2007)
44. J.–H. Choi, K.–I. Oh, M. Cho, J. Chem. Phys. **129**, 174512 (2012)
45. J. Jeon, M. Cho, J. Phys. Chem. B **118**, 8148 (2014)
46. G. Prampolini, P. Yu, S. Pizzanelli, I. Cacelli, F. Yang, J. Zhao, J. Wang, J. Phys. Chem. B **118**, 14899 (2014)
47. J.R. Schmidt, S.T. Roberts, J.J. Loparo, A. Tokmakoff, M.D. Fayer, J.L. Skinner, Chem. Phys. **341**, 143 (2007)
48. B.S. Mallik, A. Semparithi, A. Chandra, J. Phys. Chem. A **112**, 5104 (2008)
49. T. Yagasaki, S. Saito, J. Chem. Phys. **128**, 154521 (2008)
50. T. Yagasaki, S. Saito, Acc. Chem. Res. **42**, 1250 (2009)
51. S. Imoto, S.S. Xantheas, S. Saito, J. Chem. Phys. **139**, 044503 (2013)
52. S. Li, J.R. Schmidt, A. Piryatinski, C.P. Lawrence, J.L. Skinner, J. Phys. Chem. B **110**, 18933 (2006)
53. M.W. Lee, J.K. Carr, M. Göllner, P. Hamm, M. Meuwly, J. Chem. Phys. **139**, 054506 (2013)
54. A. Karmakar, A. Chandra, J. Chem. Phys. **142**, 164505 (2015)
55. M. Okuda, M. Higashi, K. Ohta, S. Saito, K. Tominaga, Chem. Phys. Lett. **683**, 547 (2017)
56. M. Okuda, M. Higashi, K. Ohta, S. Saito, K. Tominaga, Chem. Phys. **512**, 82 (2018)
57. R. Bloem, K. Koziol, S.A. Waldauer, B. Buchli, R. Walser, B. Samatanga, I. Jesarov, P. Hamm, J. Phys. Chem. B **116**, 13705 (2012)
58. J.K. Chung, M.C. Thielges, M.D. Fayer, Proc. Natl. Acad. Sci. U. S. A. **108**, 3578 (2011)
59. M.C. Thielges, J.Y. Axup, D. Wong, H.S. Lee, J.K. Chung, P.G. Schultz, M.D. Fayer, J. Phys. Chem. B **115**, 11294 (2011)
60. S. Dutta, W. Rock, R.J. Cook, A. Kohen, C.M. Cheatum, J. Phys. Chem. **135**, 055106 (2011)
61. S. Dutta, Y.-L. Li, W. Rock, J.C.D. Houtman, A. Kohen, C.M. Cheatum, J. Phys. Chem. B **116**, 542 (2012)
62. D.C. Urbanek, D.Y. Vorobyev, A.L. Serrano, F. Gai, R.M. Hochstrasser, J. Phys. Chem. Lett. **1**, 3311 (2010)

63. M.J. Tucker, X.S. Gai, E.E. Fenlon, S.H. Brewer, R.M. Hochstrasser, Phys. Chem. Chem. Phys. **13**, 2237 (2011)
64. K.-K. Lee, K.-H. Park, C. Joo, H.-J. Kwon, H. Han, J.-H. Ha, S. Park, M. Cho, Chem. Phys. **396**, 23 (2012)
65. K. Kwak, S. Park, I.J. Finkelstein, M.D. Fayer, J. Chem. Phys. **127**, 124503 (2007)
66. K. Kwak, D.E. Rosenfeld, M.D. Fayer, J. Chem. Phys. **128**, 204505 (2008)
67. A. Bakulin, C. Liang, T.L. Jansen, D.A. Wiersma, H.J. Bakker, M.S. Pshenichnikv, Acc. Chem. Res. **42**, 1229 (2009)
68. A. Bakulin, M.S. Pshenichnikv, H.J. Bakker, C. Petersen, J. Phys. Chem. A **115**, 1821 (2011)
69. J.-H. Choi, K.-I. Oh, H. Lee, C. Lee, M. Cho, J. Chem. Phys. **128**, 134506 (2008)
70. H. Lee, J.-H. Choi, M. Cho, Phys. Chem. Chem. Phys. **12**, 12658 (2010)
71. A. Luzar, D. Chandler, Nature **379**, 55 (1996)
72. A. Chandra, Phys. Rev. Lett. **85**, 768 (2000)
73. M. Higashi, S. Hirai, M. Banno, K. Ohta, S. Saito, K. Tominaga, J. Phys. Chem. B **117**, 4723 (2013)
74. P.-A. Cazade, T. Bereau, M. Meuwly, J. Phys. Chem. B, **118**, 8135 (2014)
75. H. Xu, H.A. Stern, B.J. Berne, J. Phys. CHem. B **106**, 2054 (2002)
76. B.P. Fingerhut, R. Costard, T. Elsaesser, J. Chem. Phys. **145**, 115101 (2016)

Chapter 13
Surface-Enhanced 2DIR Spectroscopy of nm-Thick Films Using Plasmonic Nano-arrays

Robert T. Mackin, Bar Cohn, Lev Chuntonov and Igor V. Rubtsov

Abstract The ability to interrogate structure and dynamics of molecules at interfaces is crucial for many fields of science and technology. In this chapter, we discuss the implementation of surface-enhanced two-dimensional infrared (SE 2DIR) vibrational spectroscopy to examine molecules in thin films down to a monolayer, enabled by lithographically-fabricated plasmonic nano-antenna arrays. A variety of nonlinear IR measurements are presented for sample films of different thicknesses, ranging from a monolayer to ca. 100 nm, including diagonal and cross peak 3rd-order SE 2DIR measurements and diagonal 5th-order SE IR measurements. High raw-signal enhancement factors reaching 5.1×10^4 were obtained for diagonal peaks of a carbonyl stretching mode in a 1.5 nm thick sample via the 3rd-order SE 2DIR measurements. A similar enhancement factor of 4.3×10^4 was observed for cross peaks among the modes, frequency separated by ca. 350 cm^{-1} and distance separated by over 12 Å, in nanometer-thick films. The mechanism of the enhancement was examined, using classical coupled oscillators approach. It revealed that for thicker samples the signal is dominated by a radiation damping mechanism, whereas the near-field enhancement is dominant for thinner samples of less than 3 nm thick. An application of SE 2DIR method to study sample monolayers and cross and diagonal peak waiting time dependences makes a wide arsenal of 2DIR techniques applicable for interrogating molecules at interfaces.

R. T. Mackin · I. V. Rubtsov (✉)
Department of Chemistry, Tulane University, New Orleans, USA
e-mail: irubtsov@tulane.edu

R. T. Mackin
e-mail: rmackin@tulane.edu

B. Cohn · L. Chuntonov
Technion – Israel Institute of Technology, Haifa, Israel
e-mail: crcohn58@gmail.com

L. Chuntonov
e-mail: chunt@technion.ac.il

M. Cho (ed.), *Coherent Multidimensional Spectroscopy*,
Springer Series in Optical Sciences 226,
https://doi.org/10.1007/978-981-13-9753-0_13

13.1 Introduction

Plasmonic enhancement of spectroscopic signals is based on the ability of free electrons to locally enhance electric field in the vicinity of metal surfaces, thus allowing to perform spectroscopic measurements with higher sensitivity [1–4]. The highest signal enhancements are obtained when molecular transitions are in resonance with the collective excitations of the conduction electrons, known as localized plasmon resonances. Extensive research in the field of nano-plasmonics during the last decade demonstrated that such resonance conditions can be achieved by tuning the optical properties of localized plasmons via the rational design of the size, shape, and material of metallic structures [5]. For example, nanostructures which are tens of nanometers in size made from noble metals (mainly from gold and silver) were shown to generate enhancement of the local field reaching factors of several hundreds and even a thousand, when the corresponding plasmon resonance are excited in the visible and near-IR spectral regions. These enhancements are exploited in surface-enhanced Raman scattering (SERS) spectroscopy [6, 7]. The SERS method has even shown single molecule detection as the result of incredibly high signal enhancements (10^{14}) [8, 9]. In the mid-IR, plasmon-enhanced vibrational spectroscopy measurements began on solid metal surfaces and metal-island films [1, 10–12], however, recent lithographic techniques have allowed for the fabrication of metal nano-antennas which generate stronger localized plasmonic fields and their excitations can be tuned in-resonance with the molecular transitions [13–17]. Resonant enhancement in the mid-IR region, though, requires larger-scale half-wavelength nanostructures, reaching several micron is size [13, 15, 16, 18], which provide smaller, yet very significant, signal enhancements for surface-enhanced infrared absorption (SEIRA) measurements [13, 14]. SEIRA has been developing actively for decades, involving studies of proteins [13, 14, 19], DNA [20], small molecules [1, 21–23], etc., deposited over or chemisorbed to the surface of the nano-structures.

Recent development of two-dimensional IR (2DIR) spectroscopy [24–26] enabled characterization of structural features and dynamics of molecules in condensed phase in the bulk via recording interactions of vibrational modes. Using the plasmonic nanostructures, which include nanoparticles [3, 27], rough metal surfaces [28–31], and nano-arrays [13, 15–17, 32–36], the 2DIR diagonal-peak measurements were extended to thin sample films and even to monolayers [28–30, 37]. Note that it is advantageous to use a 3rd-order nonlinear technique, such as 2DIR, as well as higher-order methods, as the signal enhancement increases with the order of the technique in the electric field [16].

Here we report on the evaluation of enhancements provided by lithographically manufactured nano-arrays via linear absorption, third order pump-probe (PP), three-beam dual-frequency 2DIR, and 5th-order IR spectroscopies. We report SE cross peak measurements from a 1-nm-thick sample, as well as a range of nonlinear IR measurements for films ranging from 1 to 80 nm in thickness. Analysis of the line-shapes in SE 2DIR measurements is given. We discuss the mechanism of the signal enhancement, which was found to change between very thin films of less than 3–5 nm

to the films exceeding 5 nm. Fifth-order spectra and 2DIR spectra of a monolayer are also discussed. The strong signal enhancements, reaching a factor of 10^5 in the 3rd-order 2DIR measurements, show a strong potential of the SE 2DIR spectroscopy for interrogating molecules at interfaces.

13.2 Sample Preparation and Experimental Methods

13.2.1 Fabrication of Nano-antenna Arrays

The gold antenna arrays were fabricated on CaF_2 substrates using standard methods of electron beam lithography on a RAITH EBPG 5200 machine. The high uniformity of nanostructure size and shape across the sample of few millimeters in size were confirmed by both optical spectroscopy and electron microscopy. The large sample size of 5 mm × 5 mm facilitated spectroscopic measurements. The unit cell dimensions of the array were chosen to optimize its plasmonic optical properties, where the plasmon resonance was tuned to match molecular excitations. The array dimensions are shown in Fig. 13.1. The period of the array was always below the critical grating radiation period [13].

13.2.2 Sample Preparation

Two compounds were interrogated in this study, 4-azidobutyrate-N-hydroxysuccinimide ester (azNHS) and mercapto acetic acid (mAA). azNHS was mixed with polystyrene (PS) in toluene and spin-coated onto the gold nano-arrays. The thickness of this sample was varied by controlling the amount of toluene and the speed during spin-coating. mAA was chemisorbed onto the surface of the gold nano-array via the thiol end group. This process was performed by submerging

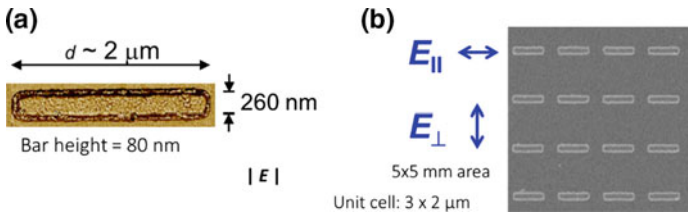

Fig. 13.1 Dimensions of the antenna array. **a** Atomic force microscopy phase image of a single nano-antenna measured in tapping mode. Each bar has length 2 μm, width 260 nm, and height 80 nm. **b** Scanning electron microscopy of the array collected with normal electron beam incidence. The array was patterned over a 5 × 5 mm^2 area

the arrays in a dilute solution of mAA (10 mM) in ethanol overnight followed by rinsing with ethanol and drying under a stream of dry air [38].

13.2.3 Linear Spectroscopy

The surface-enhanced infrared absorption (SEIRA) and reference measurements were performed with a Vertex 80 spectrometer (Bruker) in transmission mode. A wire-grid polarizer, placed before the sample, was used for measuring IR spectra polarized along and perpendicular to the gold bars of the nano-array. Additionally, an aperture of ca. 1.5 mm was placed before the sample to limit the beam size to the region of the nano-array.

13.2.4 Non-linear Spectroscopy

The 2DIR and pump-probe (PP) measurements were performed using a fully-automated dual-frequency three-beam 2DIR instrument with heterodyned detection [39, 40]. Three m-IR laser beams featuring k_1, k_2, and k_3 wavevectors overlap in the sample (Fig. 13.2) and the 3rd-order signal is detected by heterodyning with a local oscillator (LO) in the direction that satisfies the phase-matching conditions. To avoid light-induced degradation of the nano-array during the measurements, a large neutral density (ND) filter (OD = 1) was placed on all three beams at the same time; for the measurements of the reference sample off the array the filter was removed to increase the signal. Additional ND filters were used to tune the pulse energies to 40 nJ and 8 nJ for the pump (k_1 and k_2) and probe (k_3) beams, respectively (Fig. 13.2). For the power dependence measurements, the large filter was replaced by a half waveplate and polarizer placed on the pump beams to allow for greater control of the k_1, k_2 pulse energy (Fig. 13.2).

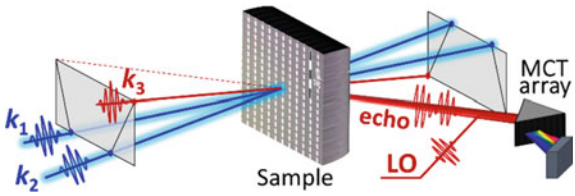

Fig. 13.2 Schematics of SE 2DIR spectroscopy. The sample is deposited onto the plasmonic nano-array

13.2.5 FDTD Simulations

Optical properties of the gold antenna arrays and linear surface-enhanced molecular signals were modeled based on the numerical solutions of the Maxwell equations with the Finite Difference Time Domain propagation method (FDTD) using Lumerical software. The geometry of the nano-array used in the simulations was identified by scanning electron microscopy imaging of the fabricated samples, which included imaging of the antenna arrays at titled angles and imaging of the antenna's cross-sections that were milled by a focused ion beam [17].

All the FDTD simulations were performed with an effective refractive index of the environment of $n = 1.21$, which represented a combined effect of the CaF_2 substrate and thin Cr adhesion layer under the gold structures. Standard dielectric constants of gold were used [41], while the vibrational transitions were modeled by a collection of Lorentz oscillators with the permittivity function $\varepsilon(\omega) = n_0^2 + \sum_k \frac{f_k \omega_0^2}{\omega_{0,k}^2 - \omega^2 - i\omega\gamma_k}$, where n_0 represents the refractive index of the polymer matrix, assumed to be constant across the relevant frequency range, and the summation is over the molecular vibrational transitions; $\omega_{0,k}$ is the corresponding transition frequency, f_k is the oscillator strength, and γ_k is the associated line width. The values of these parameters were obtained by modeling a series of linear absorption spectra of thick polymer layers [16].

13.3 Surface-Enhanced Infrared Absorption

The FTIR transmission spectrum of the bare nano-array has a full-width at half maximum (*fwhm*) of ca. 200 cm^{-1} and the extinction at the maximum of 1.9–2.1 in optical density, when detected with radiation polarized along the bars (Fig. 13.3, green line). The peak is associated with a plasmon resonance, while the peak frequency depends on the bar length. Upon sample deposition onto the nano-array, the plasmon

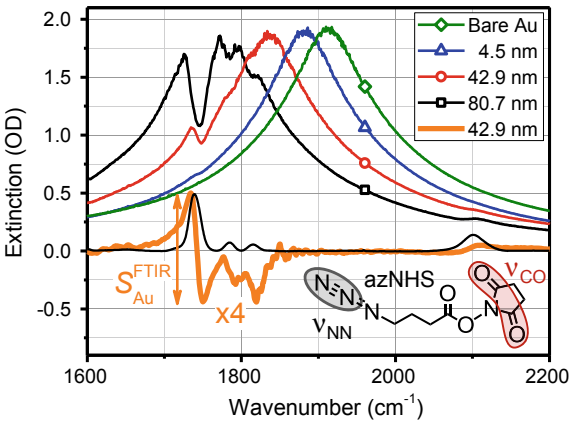

Fig. 13.3 Linear FTIR extinction spectra of bare and azNHS/PS coated nano-arrays. The isolated molecular features for the 42.9 nm thick sample (thick orange line; ×4), show Fano-shaped peaks of azNHS. Normalized absorption spectrum of the reference sample is shown with thin black line

spectrum is red shifted due to the changes of the dielectric medium around the antennas [32], as shown for the azNHS/PS films of different thicknesses in Fig. 13.3. The amount of the red shift allows for the determination of the sample thickness [16]. If the sample has a molecular transition in the vicinity of the plasmon transition, the former is enhanced significantly by the plasmon, as apparent for the CO transitions at 1740, 1780, 1820 cm^{-1} and the N_3 transition at 2100 cm^{-1} of the azNHS (Fig. 13.3). The lineshape of the molecular transition is, in general, dispersive, taking a so-called Fano shape [42].

The Fano lineshape arises from interference of two (or more) fields in the far-field at the detector. One contribution consists of a scattering of the nano-array itself, responsible for the broad plasmon spectrum for a given dielectric environment. Another contribution is associated with resonant excitation of the molecular transitions by the plasmonic field. The excited molecular states feature relatively long lifetime (~1 ps) and re-excite the plasmon after a delay. The plasmon emits and the second field, which interferes with the first field, is measured at the detector in the far-field. The phase lag between these two fields leads to the typical dispersive character of the Fano lines. The accumulated phase is dependent on the molecular excited state lifetime and on the frequency mismatch between the plasmon and molecular transitions as different phases are accumulated for different mismatches.

The molecular spectral signature can be isolated by subtracting the spectrum of the plasmon, numerically shifted to match the dielectric environment of the sample, from the spectrum of the nano-array with the sample film (Fig. 13.3, thick orange line). The Fano amplitude, S_{Au}^{FTIR} (Fig. 13.3 vertical arrow), is proportional to the strength of the molecular transition and the enhanced plasmonic field acting upon it. The ratio of S_{Au}^{FTIR} and the optical density of the molecular transition of the reference sample of the same thickness without the nano-array, S_{ref}^{FTIR}, represents raw signal enhancement, which in turn is equal to the square of the effective field enhancement by the nano-array, ξ^2. Because the plasmon field decreases away from the nano-antenna surface, the raw enhancement, as well as the effective field enhancement, ξ, is expected to depend on the sample thickness. Indeed, a drastic dependence of the enhancement on the sample thickness was observed experimentally for the CO and NN transitions of azNHS/PS thin film samples (Fig. 13.4a). Note that the ordinate in Fig. 13.4a shows ξ values, while the raw enhancement values, given by ξ^2, are shown in parentheses.

A sharp increase of ξ is observed for thicknesses shorter than 5 nm reaching $\xi = 22$ for a 1.4-nm-thick film, as the signal is dominated by the molecules located in the region with the strongest plasmonic field near the gold surface. The enhancement decreases for larger sample thicknesses. In addition, at larger sample thicknesses the plasmon maximum is red shifted, resulting in a better resonance with the CO mode and poorer resonance with the NN mode of azNHS. As a result of this detuning, the enhancement for NN, ξ_{NN}^{lin}, decreases at large thicknesses more than the enhancement for CO, ξ_{CO}^{lin}, which even shows a plateau between 10 and 30 nm thicknesses. Numerical FDTD calculations of the field enhancements for both CO and NN transitions as a function of sample thickness were performed, showing an impressive agreement with the experiment (Fig. 13.4a, solid lines).

13.4 Surface-Enhanced Third-Order Spectroscopy

The linear SEIRA experiments showed a sharp increase of the enhancement for thinner films (Fig. 13.4a). In order to determine how the signal enhancement depends on the film thickness in third-order spectroscopies, mid-IR pump-probe (PP) and three-pulse heterodyned photon echo (HPE) measurements were performed for diagonal and cross peaks on the nano-array. Before discussing the enhancement, we describe the shape of the plasmon enhanced IR spectra.

13.4.1 Shape of Transient Surface-Enhanced IR Spectra

Transient IR spectra of the CO modes of azNHS on (blue) and off (green) the nano-array are shown in Fig. 13.5. These peaks are diagonal peaks obtained using IR excitation and probing pulses centered at ca. 1740 cm^{-1}. The spectrum off the array shows two typical contributions, a ground state bleach (GSB) and stimulated emission (SE) centered at 1746 cm^{-1} and an excited state absorption (ESA) anharmonically red-shifted by ca. 15 cm^{-1}. The PP spectrum on the nano-array shows different phasing of the two contributions. As explained above, such spectral shape, the Fano shape, is caused by the interference of several contributions, all involving the plasmon scattering.

Notice that while the SE PP signals are observed via plasmon scattering, their peaks reflect mostly the properties of the molecular transition. They have a similar width to those off the array and their waiting time dynamics match that for the reference samples (Fig. 13.6). The transient evolution of the signal of the CO diagonal mode at 1746 cm^{-1} is found to be the same, within the noise level, for the sample on (blue line) and off (green line) the nano-array (Fig. 13.6). Similar observations

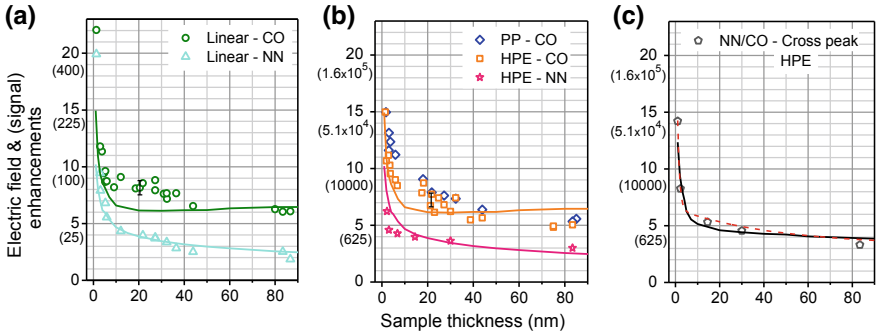

Fig. 13.4 Thickness dependence of the effective electric field (raw signal) enhancement for **a** linear, **b** pump-probe (PP), and diagonal 2DIR (HPE) and **c** cross-peak HPE measurements. The dashed line (**c**) shows cross-peak enhancement evaluated as $\xi_{NN/CO}^{cross} = (\xi_{NN}^{HPE}\xi_{CO}^{HPE})^{0.5}$. Modeling is given by the solid lines. Adapted with permission from [16]. Copyright (2018) American Chemical Society

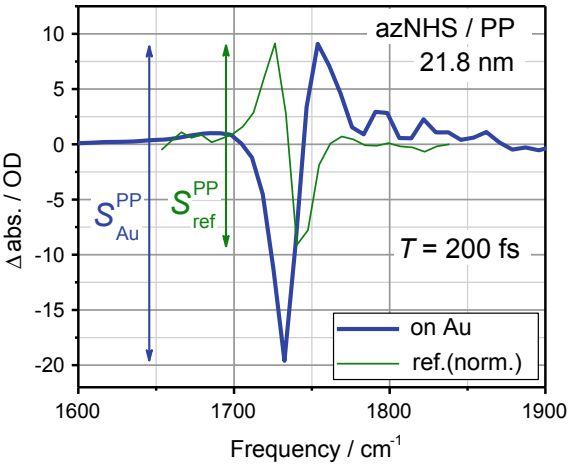

Fig. 13.5 IR PP spectra of 21.8 nm thick azNHS/PP sample on nano-array (blue, bold) and off the array (green, normalized) measured at $T = 200$ fs. The pump and probe pulses were centered at 1740 cm^{-1}. The way the peak amplitudes were measured is indicated with arrows

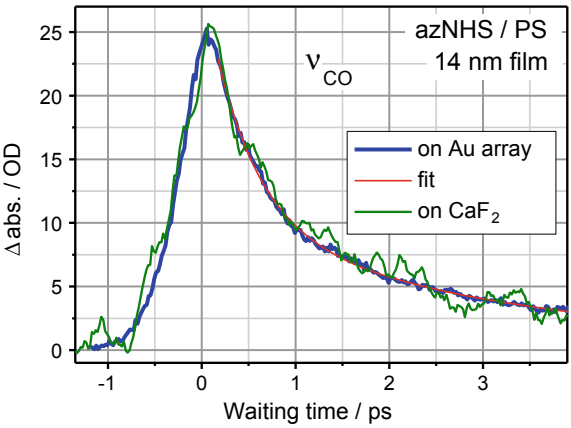

Fig. 13.6 IR PP kinetics of the ν_{CO} diagonal peak of 14 nm thick azNHS/PS sample on nano-array (blue, bold) and off the array (green, normalized). The pump and probe pulses were centered at 1740 cm^{-1}. Double exponential fit is shown with red line

were made also by Rezus and co-workers for PMMA [15]. Analogous observation of similarity of coherent oscillations with and without a plasmonic nano-array was made for a Rhodium dicarbonyl complex [36, 43]. These observations and the results of calculations [35] indicate that the interaction between the plasmon and the molecular transitions is in the weak coupling limit.

13.4.1.1 The Fano Line Shapes of Vibrational Transitions

A suitable model for describing the asymmetric lines of the enhanced signals is essential as the vibrational line shapes play important roles in the studies of molecular structure and dynamics [23, 44, 45]. A popular approach to understanding the line shapes in surface-enhanced linear spectroscopy experiments is based on the model of

coupled mechanical oscillators representing the antenna and molecular excitations, respectively. The corresponding equations of motion are given by

$$\begin{aligned} \ddot{x}_{\mathrm{pl}} + \gamma_{\mathrm{pl}}\dot{x}_{\mathrm{pl}} + \omega_{\mathrm{pl}}^2 x_{\mathrm{pl}} + g_{\mathrm{eff}}^2 x_{\mathrm{mol}} &= \alpha_{\mathrm{pl}} E(t) \\ \ddot{x}_{\mathrm{mol}} + \gamma_{\mathrm{mol}}\dot{x}_{\mathrm{mol}} + \omega_{\mathrm{mol}}^2 x_{\mathrm{mol}} + g_{\mathrm{eff}}^2 x_{\mathrm{pl}} &= 0 \,, \end{aligned} \tag{13.1}$$

where x_{pl} stands for the coordinate of the bright oscillator of the plasmonic antenna with eigen frequency ω_{pl} and polarizability α_{pl} driven by the electric field of light $E(t)$ and damped at the intrinsic rate γ_{pl} dominated by the electron-electron scattering [45–48]. Molecular transitions are described by a dark oscillator with coordinate x_{mol}, with the corresponding parameters ω_{mol} and γ_{mol}, that cannot be excited by $E(t)$ directly, but couples to the bright oscillator via the near-field interaction, represented by the oscillators being coupled via the coordinate with the coupling strength g_{eff}. The general harmonic solutions to (13.1) are given by the complex amplitudes $x_{\mathrm{pl}} = \left|c_{\mathrm{pl}}(\omega)\right| e^{i\varphi_{\mathrm{pl}}(\omega)}$ and $x_{\mathrm{mol}} = |c_{\mathrm{mol}}(\omega)| e^{i\varphi_{\mathrm{mol}}(\omega)}$, and the linear spectrum can be readily obtained by evaluating the extinction of the system

$$S^{(1)}(\omega) = -\mathrm{Im}\left\{c_{\mathrm{pl}}(\omega)\right\} . \tag{13.2}$$

Indeed, the amplitude of the bright oscillator of the plasmonic antenna is modified by its coupling to the dark molecular excitation, while the corresponding line shape depends on the detuning between the molecular and plasmon excitations. The linear spectra obtained with the model fully reproduced the asymmetric line shapes measured experimentally [17, 35]. The effect of the coupling strength can be illustrated at the resonance frequency $\omega = \omega_{\mathrm{mol}} = \omega_{\mathrm{pl}}$, where we obtain

$$S^{(1)} = \frac{\alpha_{\mathrm{pl}} E_0^2 \gamma_{\mathrm{mol}} \omega_{\mathrm{mol}}}{\gamma_{\mathrm{mol}}\gamma_{\mathrm{pl}}\omega_{\mathrm{mol}}^2 + g_{\mathrm{eff}}^4}, \tag{13.3}$$

such that the magnitude of the enhanced molecular signal depends on g_{eff}^4.

In order to facilitate description of the asymmetric line shapes, assuming that the detected signal originates from the bright plasmonic mode, we focus on the phase of the signal electric field $\varphi_{\mathrm{sig}}(\omega) = \varphi_{\mathrm{pl}}(\omega)$. As mentioned above, $\varphi_{\mathrm{sig}}(\omega)$ can be intuitively understood through the decomposition of the signal generation process into two steps: excitation of the dark molecular mode via its coupling to the bright plasmon mode and a consequent secondary excitation of the plasmon by the molecules from the near-field [49–51]. Therefore,

$$\varphi_{\mathrm{sig}}(\omega) = \varphi_{\mathrm{mol}}(\omega) + \varphi_{\mathrm{exc}}(\omega) \tag{13.4}$$

where the first term is associated with the near-field excitation of the molecule, and the second term—with the off-resonant driving the plasmonic antenna by the excited molecules with the phase lag of $\varphi_{\mathrm{exc}}(\omega) = \tan^{-1}\left(\frac{\gamma_{\mathrm{pl}}\omega}{\omega^2 - \omega_{\mathrm{pl}}^2}\right)$. For the cases of weak

coupling, the linear signal can be rewritten as the interference of two light pathways

$$S^{(1)}(\omega) \propto -\mathrm{Im}\left\{ R^{(1)}_{\mathrm{pl}}(\omega) + R^{(1)}_{\mathrm{mol}}(\omega) \right\}, \tag{13.5}$$

where $R^{(1)}(\omega) = \mu_\alpha^2 I_\alpha(\omega)$ and $I_\alpha(\omega) = (\omega - \omega_\alpha + i\gamma_\alpha)^{-1}$ is the homogeneous Liouville space Green function associated with the excitation at the transition frequency ω_α and μ_α are the corresponding transition dipole moments [52]. $R^{(1)}_{\mathrm{pl}} = \mu^2_{\mathrm{pl}} I_{\mathrm{pl}}(\omega)$ represents the pathway where the light is scattered by the plasmonic antenna directly into the detector; $R^{(1)}_{\mathrm{mol}}(\omega) = \mu^2_{\mathrm{mol}} \xi^2 |I_{\mathrm{mol}}(\omega)| e^{i\varphi_{\mathrm{sig}}(\omega)}$ represents the pathway involving secondary plasmon excitation by the molecules, and ξ is the near-field enhancement factor associated with the molecular excitation. As expected, evaluation of the linear signals by formulas (13.2) and (13.5) results in identical line shapes [17].

Similar principles were used to describe the line shapes of the third-order 2DIR signals measured with heterodyned detection,

$$S^{(3)}(\omega_1, T_w, \omega_3) = \sum_n R^{(3)}_n(\omega_1, T_w, \omega_3) e^{i\varphi_{\mathrm{sig},n}(\omega_1, \omega_3)} \tag{13.6}$$

Here, the third-order excitations pathways in the molecular system are described by the corresponding response functions, $R^{(3)}_n$, involving both stimulated emission and excited state absorption signals, which generally appear with opposite phases and at different frequencies. Thus, their line shape asymmetries, which strongly depend on the detuning between the molecular and plasmonic excitations are also different. The phase, $\varphi_{\mathrm{sig},n}(\omega_1, \omega_3)$, associated with the pathway $R^{(3)}_n$, originates from the indirect excitation of the molecular transitions by the three laser pulses via molecular coupling to the plasmon mode as well as from the signal emission process involving secondary excitation of the plasmon mode by the excited molecules. Phase-matching conditions in the 2DIR experiment conducted in the BOXCARS configuration imply that $\varphi_{\mathrm{sig},n}(\omega_1, \omega_3) = \mp\varphi_{\mathrm{mol}}(\omega_\alpha) \pm \varphi_{\mathrm{mol}}(\omega_\beta) + \varphi_{\mathrm{mol}}(\omega_\gamma) + \varphi_{\mathrm{exc}}(\omega_\delta)$ for the rephasing (upper signs) and non-rephasing (lower signs) signals, respectively, where $\alpha - \delta$ enumerate molecular transitions involved in the corresponding pathway, $R^{(3)}_n$. The phase-modified response functions (13.6) were used to simulate 2DIR line shapes and were found to be in a satisfactory qualitative agreement with the experimental results for various detuning between the plasmonic and molecular excitations. The tested cases involved samples with vibrational excitations giving rise to individual diagonal peaks of PMMA and azNHS (Fig. 13.7), as well as cases with the coupled vibrational excitations featuring cross-peaks (RDC) [17, 35, 36, 43].

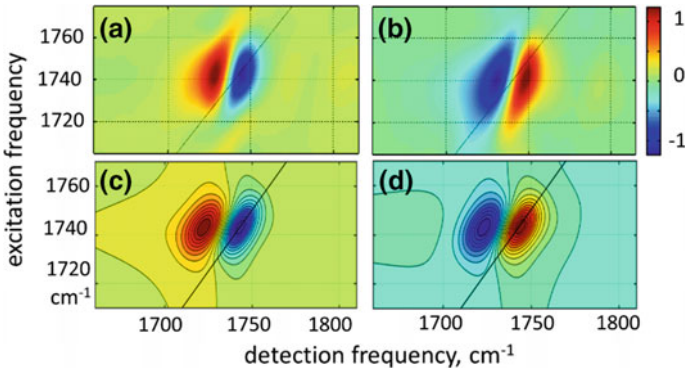

Fig. 13.7 Modeling of the SE-2DIR spectra with phase-modified response functions. Panels **a** and **b** show experimental spectra of azNHS molecules embedded in a thick PS film and in a thin PS film spin deposited on the array of plasmonic antennas, respectively. Panels **c** and **d** show simulations of the corresponding spectra based on the model of (13.1) and (13.6)

13.4.2 Signal Enhancement Provided by the Nano-arrays via 3rd-Order Spectroscopies

The dependence of signal enhancement provided by the nano-array in PP and HPE experiments on the film thickness was measured for ν_{CO} and ν_{NN} diagonal peaks of azNHS. To obtain a raw enhancement value for the sample of specific thickness, the 3rd-order signals with the array (S^{PP}_{Au} or S^{HPE}_{Au}) were divided by those for the reference sample (S^{PP}_{ref} or S^{HPE}_{ref}) of the same thickness (S^{PP}_{Au}/S^{PP}_{ref} or $S^{HPE}_{Au}/S^{HPE}_{ref}$).

An example of mid-IR PP spectra of 21.8 nm thick azNHS/PP sample on and off nano-array is shown in Fig. 13.5. The S^{PP}_{Au} values were determined by the overall amplitude of the Fano-shaped transient peaks, as shown in Fig. 13.5 with an arrow; the S^{PP}_{ref} values were determined similarly (Fig. 13.5). An example of magnitude SE HPE diagonal spectra of ν_{CO} and ν_{NN}, measured on and off the nano-array, are shown in Fig. 13.8. As expected, the magnitude SE HPE spectra show a single peak, rather than a Fano lineshape observed in PP; the amplitude of this peak, S^{HPE}_{Au}, was used in the enhancement evaluation.

The effective electric-field enhancements, calculated as fourth root of the raw enhancements, $\xi^{PP} = (S^{PP}_{Au}/S^{PP}_{ref})^{1/4}$ and $\xi^{HPE} = (S^{HPE}_{Au}/S^{HPE}_{ref})^{1/4}$, are shown in Fig. 13.4b. The corresponding values of the raw enhancement are shown in parentheses along the Y-axis. These results show that the values of the effective field enhancements, ξ^{PP} and ξ^{HPE}, are similar to each other and similar to those obtained in the linear measurements, ξ^{lin}, for the same sample thickness, whereas the raw 3rd-order signal enhancements are much larger, reaching 5.1×10^4 for the 1.5 nm thick sample. This similarity between the enhancements in the linear and 3rd-order experiments suggests that the regions of the highest electric field dominate the linear and nonlinear measurements, resulting in a simple scaling of the raw enhancement

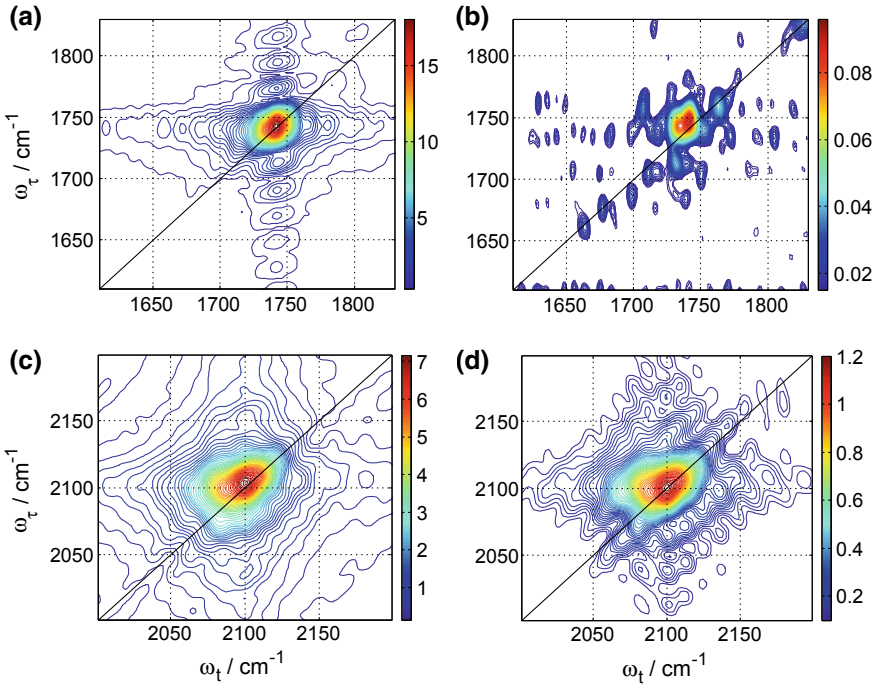

Fig. 13.8 Examples of SE 2DIR HPE diagonal spectra for ν_{CO} (**a**, **b**) and ν_{NN} (**c**, **d**) of azNHS measured on (**a**, **c**) and off (**b**, **d**) the nano-array. The spectra were collected at a waiting time, T, of 0.1 ps; the reference spectra (**b**, **d**) were measured at a spot on the CaF_2 adjacent to the nano-array. The azNHS/PS sample thickness was 5.9 nm (**a**, **c**) and 14.5 nm (**b**, **d**). Adapted with permission from [16]. Copyright (2018) American Chemical Society

as the electric field in the $(n + 1)$th power, where n is the order of the technique in the electric field.

13.4.3 Surface-Enhanced Cross-Peak Measurements

Cross peaks in 2DIR spectroscopy provide crucial information on mode coupling, which, using modeling can be linked to the distance and mutual orientation of the interacting groups (modes) [26]. Therefore gaining the ability of detecting cross peaks in thin samples is of utmost interest. Here we demonstrate that, due to plasmon enhancement, the cross peak among ν_{NN} and ν_{CO} can be measured for thicknesses as small as 1 nm (Fig. 13.9). The amplitude of this cross peak is governed by the anharmonic coupling of the two modes, manifested in the shift $\Delta_{NN/CO}$ of the combination band frequency, ν_{NN+CO}, from the sum of the fundamental frequencies, $\nu_{NN} + \nu_{CO}$. Because the CO and NN groups in azNHS are separated by over 12 Å, the NN/CO anharmonicity $\Delta_{NN/CO}$ is small, at ca. 0.03 cm^{-1} [53]. As a result, the cross

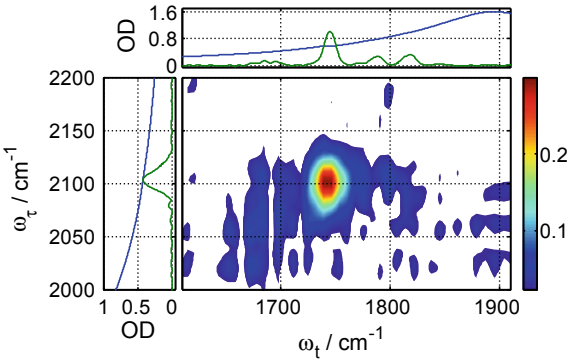

Fig. 13.9 SE HPE 2DIR spectrum focusing on the cross peak among ν_{NN} and ν_{CO}, measured for the 1.0 nm thick azNHS/PS sample at $T = 3.8$ ps. The first two laser pulses were centered at 2100 cm^{-1} to excite ν_{NN}, while the third pulse and LO were centered at ca. 1750 cm^{-1} to excite ν_{CO}. The plasmon spectrum (blue) and the spectrum of the reference sample (green, ×3000) are shown in the attached panels. Adapted with permission from [16]. Copyright (2018) American Chemical Society

peak of the reference sample was detectable only for the thicker samples, exceeding 30 nm. Nevertheless, using the nano-array, the NN/CO cross peak was measurable for thicknesses down to 1 nm (Fig. 13.9). Notice that the azNHS concentration in the azNHS/PS sample of 1.0 nm was less than 0.03 M, corresponding to the surface density of only 0.06 molecules/nm^2.

The raw signal enhancements were determined for various sample thicknesses, similarly to the diagonal enhancements. The effective electric-field enhancement, calculated as $\xi^{HPE}_{NN/CO} = (S^{HPE}_{Au}/S^{HPE}_{ref})^{1/4}$, is shown in Fig. 13.4c as a function of sample thickness. The data show a similar trend with a sharp increase of $\xi^{HPE}_{NN/CO}$ at smaller thicknesses. The raw enhancement of 4.3×10^4 ($\xi = 14.4$) was obtained for the thinnest samples of 1 nm. Note that the enhancement values are affected by the frequency mismatch between the plasmon and the two molecular transitions separated by ca. 350 cm^{-1}, as the two transitions cannot be both optimally enhanced. The raw signal enhancement is expected to be a combination of the enhancements for the two involved transitions such that $\xi^{HPE}_{NN/CO} = (\xi^{HPE}_{NN}\xi^{HPE}_{CO})^{1/2}$. Dashed line in Fig. 13.4c, calculated using the fitted experimental data for ξ^{HPE}_{NN} and ξ^{HPE}_{CO}, matches the experimental data well.

13.4.4 Modeling the Signal Enhancement

FDTD calculations were used to describe linear extinction spectra of the bare nano-array and the array coated with the azNHS/PS film [17]. Figure 13.10 shows the extinction spectra of the same nano-array when uncoated (left axis, black line), coated with 30 nm thick PS film (blue), and coated with 30 nm azNHS/PS film (red).

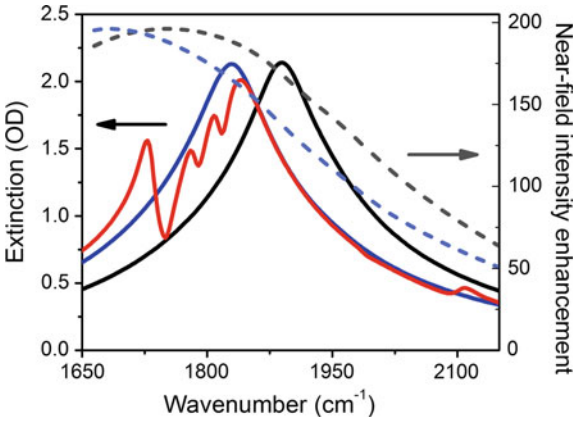

Fig. 13.10 FDTD computed extinction spectra of a bare nano-array (black solid line), the array coated with 30 nm thick PS film (blue solid line), and coated with 30 nm azNHS/PS film (red line). The signal enhancement spectra are shown for the bare (grey dashed line) and PS coated (blue dashed line) nano-arrays. Adapted with permission from [16]. Copyright (2018) American Chemical Society

To determine the enhancement, the spectrum of the PS-coated sample was subtracted from that of the azNHS/PS-coated sample. To evaluate the signal enhancement, the overall Fano amplitude of the resulting molecular line shape was compared to the amplitude of the unenhanced signal, similar to that in Fig. 13.3.

The simulated signal enhancements for CO and NN transitions of azNHS are in a good agreement with the experimental results (Fig. 13.4a, solid lines). The signal enhancement spectra for the bare and PS coated nano-arrays (Fig. 13.10, dashed lines), calculated at 20 nm above the substrate on a line passing through the center of the antenna and 1 nm from the antenna edge, are shown in Fig. 13.10 (dashed lines). It has been shown that the enhancement of the signal from molecules located close to the antenna surface scales linearly with the intensity of the enhanced near field [33, 54]. The near-field spectra are red-shifted with respect to their far-field extinction counterpart. The CO transition has a smaller detuning from the resonance of the red-shifted near-field spectrum of the array for thin samples and a smaller detuning from the resonance of the far-field spectrum of the array for thicker samples, as compared to the NN transition. Thus, it is expected that the CO transition would be enhanced more than the NN transition, as indeed is seen experimentally.

13.5 Radiation Damping

13.5.1 Estimation of the Near-Field Coupling Strength

The linear coupling between the plasmonic and molecular excitations in (13.1) through the coordinate assumes that it occurs via the enhanced near-field of the antenna [55]. The effective coupling strength, g_{eff}, which accounts for the interaction of all molecules in the polymer film surrounding the antenna with the plasmon near field, is given by

$$g_{\text{eff}}^2 = \sum_i (\mu_\alpha \cdot E(r_i))^2 \tag{13.7}$$

where $E(r_i)$ is the amplitude of the locally-enhanced near-field at the location r_i. In order to evaluate the magnitude of g_{eff}, we have used typical transition dipole moments of vibrational transitions, $\mu_\alpha = 0.2$–0.5 D, while the absolute value of the local field was obtained invoking the considerations from quantum electrodynamics (QED).

Within the QED approach, the unit cell of the antenna array is treated as a photonic cavity represented by the harmonic potential. The spectrum of the cavity is given by the expectation value of the energy operator $\left\langle n|\hat{H}|n\right\rangle = \hbar\omega_{\text{pl}}\left(n + \frac{1}{2}\right)$, where $|n\rangle$ is the corresponding mode of the field in the cavity. At low excitation light intensities, the molecules are coupled to the vacuum mode of the cavity, $|0\rangle$, which stores electromagnetic energy amount of $U = \hbar\omega_{\text{pl}}/2$, where ω_{pl} is the resonance frequency of the plasmonic antenna. On the other hand, the stored energy is given by the integral of the energy density over the volume of the array unit cell, $U = \int \bar{W} \mathrm{d}V$, where $\bar{W} = \varepsilon_0\left(\varepsilon' + 2\omega\varepsilon''/\gamma_e\right)|E|^2/4$ is the energy density corrected for the dispersive material with Lorentz dielectric function $\varepsilon = \varepsilon' + i\varepsilon''$ and intrinsic damping rate γ_e [56–59]. Here, the spatial distribution of the electromagnetic field associated with the vacuum mode $|0\rangle$ is described by the local field obtained from the FDTD simulations $E(r)$. These relations between the field amplitude and the vacuum energy have been used to find the absolute magnitude of the field, and to evaluate g_{eff} according to (13.7). For example, for a 80 nm-thick PS film, doped with azNHS molecules ($\mu_\alpha = 0.5$ D), we found $g_{\text{eff}} = 3$ cm^{-1}. Note, however, this value of g_{eff}, when used with the model of (13.1), appeared to be two orders of magnitude lower than that needed to reproduce the magnitude of the enhanced molecular signals in Fig. 13.4. The same results were obtained for all polymer films thicker than a few nanometers.

The estimation of such a weak near-field coupling strength was further supported by 2DIR measurements of ultrafast quantum dynamics. These experiments focused on measurements of the rates of the excited population relaxation and of the rates of the dephasing of coherent superposition of coupled vibrational modes excited in molecules, which were embedded in polymer films of a few tens of nanometer thickness, spin-coated on the plasmonic nano-array. The interaction between the molecular and plasmonic excitations was manifested both in the 10^4 signal enhancement and in the expected line shape asymmetry, however, the life times of the excited molecular population (Fig. 13.6) and the coherence dephasing rates were not affected by this interaction. For example, the damping rate of quantum beating associated with the excitation of superposition of the carbonyl stretching modes in Rhodium acetylacetonato dicarbonyl was found to be 20 cm^{-1}, as measured in experiments with both enhanced and non-enhanced signals [36, 43]. This dephasing rate can be used to estimate the upper limit for the coupling strength between the molecular and plasmonic excitation, which should be an order of magnitude lower, suggesting the g_{eff} to be on the order of few wavenumber in agreement with the result obtained based on (13.7).

Thus, g_{eff} along cannot account for the magnitude of the enhanced signals obtained for the samples with polymer films thicker than a few nanometers [35].

13.5.2 Coupling via Radiation Damping

It was recently observed that the effect of radiation damping can play an important role in plasmonic systems with large scattering cross-section [60]. Because the optical properties of the arrays of infrared antenna used in our experiments are dominated by scattering, we generalize (13.1) to account for the effect of radiation damping [47]. The modified oscillator's equation of motion reads

$$\begin{aligned} \ddot{x}_{\text{pl}} + \gamma_{\text{pl}}\dot{x}_{\text{pl}} + \omega_{\text{pl}}^2 x_{\text{pl}} + g_{\text{eff}}^2 x_{\text{mol}} &= \dddot{P}_{\text{tot}} + \alpha_{\text{pl}} E_0 \\ \ddot{x}_{\text{mol}} + \gamma_{\text{mol}}\dot{x}_{\text{mol}} + \omega_{\text{mol}}^2 x_{\text{mol}} + g_{\text{eff}}^2 x_{\text{pl}} &= \dddot{P}_{\text{tot}} \end{aligned} \tag{13.8}$$

where the radiation reaction (Abraham-Lorentz) force is applied by the total dipole moment of the system $P_{\text{tot}} = \alpha_{\text{pl}} x_{\text{pl}} + \alpha_{\text{mol}} x_{\text{mol}}$, where α_{pl} and α_{mol} are molecular and plasmonic polarizabilities. Here, we assumed again that molecular transitions are not excited by light directly, such that $\alpha_{\text{pl}} \gg \alpha_{\text{mol}}$. The enhanced linear signal calculated from the complex amplitude solution for the bright mode at the resonance frequency $\omega = \omega_{\text{pl}} = \omega_{\text{mol}}$ now reads

$$S^{(1)} = \frac{\alpha_{\text{pl}} E_0^2 \tilde{\gamma}_{\text{mol}} \omega_{\text{mol}}}{\tilde{\gamma}_{\text{mol}} \tilde{\gamma}_{\text{pl}} \omega_{\text{mol}}^2 + \left(g_{\text{eff}}^2 + i\alpha_{\text{pl}}\omega_{\text{mol}}^3\right)\left(g_{\text{eff}}^2 + i\alpha_{\text{mol}}\omega_{\text{mol}}^3\right)}, \tag{13.9}$$

where $\tilde{\gamma}$ represents the total damping rate of the plasmonic and molecular excitations that does not include their mutual interaction via the radiation force, i.e. $\tilde{\gamma}_{\text{pl}} = \gamma_{\text{pl}} + \alpha_{\text{pl}}\omega^3 \approx \alpha_{\text{pl}}\omega^3$, and $\tilde{\gamma}_{\text{mol}} \approx \gamma_{\text{mol}}$. Here, in addition to the near-field coupling manifested in (13.3) and (13.9) by g_{eff}^4, the radiative coupling term $\alpha_{\text{mol}}\alpha_{\text{pl}}\omega_{\text{mol}}^6$ appears. This term, which leads to the same line shape asymmetry as coupling via the near-field, describes the amplitude contributed to the total magnitude of the enhanced signal by molecules located outside the reach of the enhanced near-fields at the antenna surface. A good agreement between the magnitude of the enhanced experimental signal and the signal strength evaluated based on the model of (13.8) was obtained (Fig. 13.4a).

It would be useful to estimate the range over which the action of the radiation reaction force can be observed in our plasmonic system. First, using FDTD simulations, we evaluated the contribution to the overall signal by molecules that are located within the regions of the strongest near-field. To this end, the oscillator strength of the molecular dielectric function was set to zero in the region around the antenna, extending to a distance of 20 nm from the antenna surface, where the enhanced near-field drops by a factor of $1/e$. Consistently with the expectation based on the estimation of the near-field coupling strength g_{eff}, exclusion of the molecules located

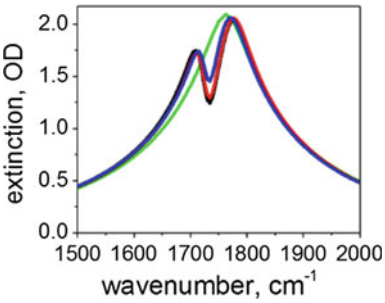

Fig. 13.11 Electromagnetic simulations of the linear spectrum of plasmonic nano-array covered by the 80 nm polymer layer with dispersed molecules with a transition at 1740 cm^{-1} (black line) and without such molecules (green line). Red line shows the spectrum obtained after removal of molecules from a 20 nm (red line) and 70 nm (blue line) shell around the antenna are shown. Adapted with permission from [35]. Copyright (2018) American Chemical Society

in this region did not lead to a significant reduction in the enhanced signal amplitude (Fig. 13.11). Thus, we concluded that the enhanced signal in samples with thicker polymer films is contributed by the molecules located at distances larger than 20 nm from the antenna surface.

13.6 Other Applications of Nonlinear IR Spectroscopy

13.6.1 Surface Enhanced 5th-Order IR Spectra

The signal enhancement in 3rd-order measurements can be approximately computed as a square of the signal enhancement in the linear measurements. Much higher raw enhancements are expected in the 5th-order IR measurements as the signal is proportional to the ξ^6. 5th-order IR spectra were previously measured for bulk samples [61–63], reporting on three-point correlation functions [64], identifying complex coupling patterns [63], and, together with the 3rd-order 2DIR spectra, providing means to identify the energy receiving modes in the vibrational energy transport [42]. Here we show that, with the help of plasmonic nano-arrays, the 5th-order IR spectra of nm-thick samples can be accessed. Using the fully-automated dual-frequency three-pulse 2DIR spectrometer with heterodyned detection the 3rd- and 5th-order signals are separated naturally into different directions [63, 65]. Moreover, the instrument permits rapid switching between the 3rd- and 5th-order spectra [39]. The diagonal 5th-order spectra propagating in the k_{5th} direction were measured, involving two-quanta sequential excitation of an overtone state by each of the two first pulses, k_1 and k_2, which was probed by the k_3 pulse: $\vec{k}_{5th} = 2\left(\vec{k}_1 - \vec{k}_2\right) + \vec{k}_3$. Diagonal 5rd-order spectrum of the ν_{CO} mode of azNHS was recorded (Fig. 13.12), involving molecular transitions between $0 \leftrightarrow 1$, $1 \leftrightarrow 2$ and $2 \leftrightarrow 3$ quantum states of CO.

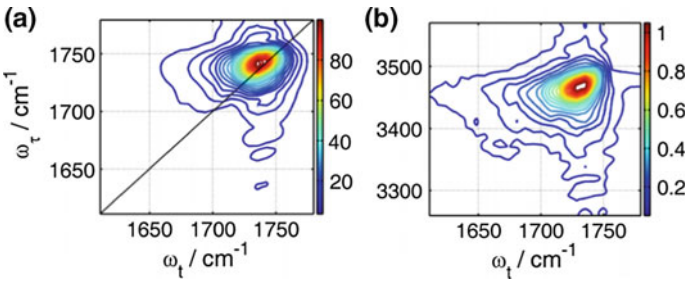

Fig. 13.12 3rd- (**a**) and 5th- (**b**) order SE IR spectra of 20-nm-thick azNHS/PS sample

The raw enhancement measured from the 5th-order signals were ca. 6.3×10^4 for the 20 nm thick sample and 1.3×10^6 for the 3.5-nm-thick sample. The resulting effective field enhancement factors of 6.3 and 10.4 for 20 and 3.5 nm thick samples respectively are close to the values measured from the SE 3rd-order experiments of 7.3 and 10.0, respectively (Fig. 13.4b).

13.6.2 Studies on a Monolayer Sample

Measurements on gold nano-antenna arrays can be extended down to a single monolayer to examine interactions of molecules at interfaces. A monolayer of mercaptoacetic acid (mAA) chemisorbed on the gold surface of the nano-array was prepared by standard methods [38]. Figure 13.13 shows a SE 2DIR diagonal spectrum for $\nu_{C=O}$ of mAA of the monolayer. A large inhomogeneous linewidth of the spectrum (diagonal width) indicates the presence of a variety of structural motifs featuring different interactions. The spectrum illustrates the power of the SE 2DIR technique to detect spectra of very small amounts of analyte on the arrays.

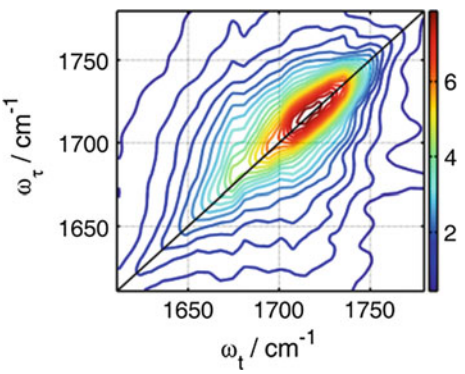

Fig. 13.13 $\nu_{C=O}$ diagonal SE 2DIR spectrum of a mAA monolayer chemisorbed to the gold antenna array

13.6.3 Surface-Enhanced Relaxation-Assisted 2DIR

Waiting time evolution for peaks in 2DIR spectra contain valuable information on various processes in the sample, including spectral diffusion, chemical exchange, and vibrational energy transport. The waiting time dependence of a cross peak among vibrational modes localized at spatially remote groups, for instance located at different ends of a large molecule, reports on the energy transport between the groups [66]. It is advantageous to perform such measurements in thin films as it will help in characterizing the interface and the molecules at the interface. Plasmonic enhancement of the nano-array permits performing such measurements. The waiting time dependences of the NN/CO cross peak amplitude of two azNHS/PS films of 39.5 and 2.4 nm thick are shown in Fig. 13.14. The relaxation-assisted 2DIR approach (RA 2DIR) permits measuring the energy transport time between the groups. Here the ν_{NN} mode, excited by the first two m-IR pulses, relaxes to other modes, initiating a cascade of IVR steps by which the energy propagates in the direction of the ν_{CO} reporter. The NN/CO cross peak increases when the excess energy arrives to the reporter site, as the low frequency modes coupled to the reporter become excited. The cross-peak maximum, T_{max}, is associated with the energy transport time between the involved sites (NN and CO). Moreover, a plateau is observed at large waiting times due to residual heating of the sample through the tag excitation.

The T_{max} for the waiting time kinetics are similar for both film samples, while the relative level of the plateau is different, reflecting a higher azNHS concentration in the thicker film [67]. Note that the narrow cross peak observed (Fig. 13.9) reports specifically on the energy transport between the modes of azNHS, although the gold bars are also heated up by the excitation pulses. It is conceivable that the observed difference (Fig. 13.14, insert) in the T_{max} values between the films and solution is associated with the difference in the environment as well in the effective temperature during the transport. The decay dynamics after 100 ps reflects the cooling of the sample layer into the gold bars, thus helping studying energy transport across the interface.

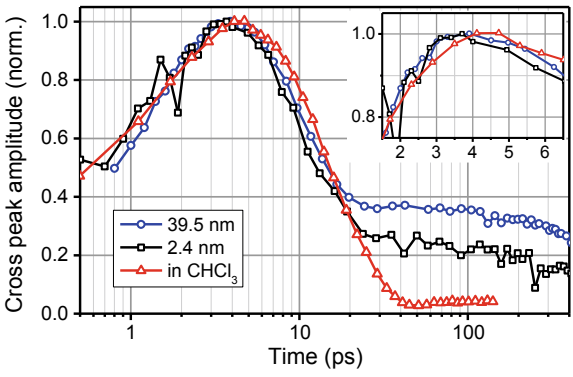

Fig. 13.14 Waiting time dependences of the surface enhanced NN/CO cross peak amplitude for azNHS/PS films of 39.5 nm (circles) and 2.4 nm (squares) thickness and for the NN/CO cross peak for azNHS dissolved in $CHCl_3$ without the nano-array (triangles)

13.7 Conclusions

In this chapter, we have shown a range of nonlinear IR experiments for studying nanometer-thick films, which became available through the application of plasmonic nano-arrays. The raw signal enhancement of 5.1×10^4 was obtained for a 1.5 nm thick sample in the 3rd-order SE 2DIR measurements. A strong thickness dependence of the effective electric field enhancement observed in the linear FTIR measurements, was also found in the SE 2DIR measurements, permitting simple evaluation of the latter via the linear measurements. The results of a numerical modeling of the field enhancement using FDTD method are in a good agreement with the experiment. Analysis of the enhancement mechanisms, using classical coupled oscillators approach, revealed that, for the thinnest samples of less than 3–5 nm, the near-field strength of the plasmon is the source of the enhancement, whereas the signal from the thicker samples is dominated by a radiation damping mechanism while the region within the near field contributes little.

We also showed that, despite a rather narrow bandwidth of the plasmonic enhancement spectrum, a cross peak among modes, frequency separated by ca. 350 cm^{-1} and distance separated by over 12 Å, is accessible in thin films via SE 2DIR. A simple way of evaluating the cross-peak effective field enhancement is revealed by taking a square root of the product of the field enhancements for the two interacting modes. A raw-signal enhancement of 4.3×10^4 was achieved for the NN/CO cross-peak in 1 nm thick film of azNHS in PS. So large enhancement enables high-quality measurements of the cross-peak waiting time dynamics, which makes applicable a range of 2DIR techniques, including relaxation-assisted, spectral diffusion, and chemical exchange 2DIR spectroscopies.

The high plasmonic enhancement provided by nano-arrays enables performing higher order multidimensional spectroscopy measurements for thin samples. Raw signal enhancements of ca. 1.3×10^6 were obtained for the 5th-order IR experiments with a 3.5-nm-thick azNHS/PS sample. The measurements were extended to interrogate monolayers of samples chemisorbed on a gold surface of nano-bars via thiol groups. There are no apparent limitations to extend the measurements on monolayers for recording cross peaks and to performing higher order spectroscopies, as even higher enhancements are expected at the vicinity of the nano-rod surface. Further extensions may include generating stronger electric near fields using nano-gaps, trimers, and other nano structures [13, 18, 36].

Acknowledgements This work is supported by the United States-Israel Binational Science Foundation (grant 2016167), United States National Science Foundation (CHE-1462075), and by Israel Science Foundation (1118/15). Plasmonic arrays were prepared at the Micro- and Nano-Fabrication Unit, Technion, with support from the Russell Berrie Nanotechnology Institute.

References

1. M. Osawa, M. Ikeda, Surface-enhanced infrared absorption of P-nitrobenzoic acid deposited on silver island films: contributions of electromagnetic and chemical mechanisms. J. Phys. Chem. **95**, 9914–9919 (1991). https://doi.org/10.1021/j100177a056
2. T.R. Jensen, R.P. Van Duyne, S.A. Johnson, V.A. Maroni, Surface-enhanced infrared spectroscopy: a comparison of metal island films with discrete and nondiscrete surface plasmons. Appl. Spectrosc. **54**, 371–377 (2000). https://doi.org/10.1366/0003702001949654
3. R.F. Aroca, D.J. Ross, C. Domingo, Surface-enhanced infrared spectroscopy. Appl. Spectrosc. **58**, 324A–338A (2004). https://doi.org/10.1366/0003702042475420
4. D. Enders, A. Pucci, Surface enhanced infrared absorption of octadecanethiol on wet-chemically prepared Au nanoparticle films. Appl. Phys. Lett. **88**, 184104 (2006). https://doi.org/10.1063/1.2201880
5. G. Haran, L. Chuntonov, Artificial plasmonic molecules and their interaction with real molecules. Chem. Rev. **118**, 5539–5580 (2018). https://doi.org/10.1021/acs.chemrev.7b00647
6. P.L. Stiles, J.A. Dieringer, N.C. Shah, R.P.V. Duyne, Surface-enhanced raman spectroscopy. Annu. Rev. Anal. Chem. **1**, 338–346 (2008). https://doi.org/10.1146/annurev.anchem.1.031207.112814
7. J.D. Caldwell, O. Glembocki, F.J. Bezares, N.D. Bassim, R.W. Rendell, M. Feygelson, M. Ukaegbu, R. Kasica, L. Shirey, C. Hosten, Plasmonic nanopillar arrays for large-area, high-enhancement surface-enhanced raman scattering sensors. ACS Nano **5**, 4046–4055 (2011). https://doi.org/10.1021/nn200636t
8. K. Kneipp, Y. Wang, H. Kneipp, L.T. Perelman, I. Itzkan, R.R. Dasari, M.S. Feld, Single molecule detection using surface-enhanced Raman scattering (SERS). Phys. Rev. Lett. **78**, 1667–1670 (1997). https://doi.org/10.1103/PhysRevLett.78.1667
9. H. Xu, E.J. Bjerneld, M. Käll, L. Börjesson, Spectroscopy of single hemoglobin molecules by surface enhanced Raman scattering. Phys. Rev. Lett. **83**, 4357–4360 (1999). https://doi.org/10.1103/PhysRevLett.83.4357
10. M. Osawa, Dynamic processes in electrochemical reactions studied by surface-enhanced infrared absorption spectroscopy (SEIRAS). Bull. Chem. Soc. Jpn. **70**, 2861–2880 (1997). https://doi.org/10.1246/bcsj.70.2861
11. F.M. Hoffmann, Infrared reflection-absorption spectroscopy of adsorbed molecules. Surf. Sci. Rep. **3**, 109–192 (1983). https://doi.org/10.1016/0167-5729(83)90001-8
12. Y. Zhong, S.D. Malagari, T. Hamilton, D.M. Wasserman, Review of mid-infrared plasmonic materials. J. Nanophotonics **9**, 093791 (2015). https://doi.org/10.1117/1.JNP.9.093791
13. R. Adato, A.A. Yanik, J.J. Amsden, D.L. Kaplan, F.G. Omenetto, M.K. Honge, S. Erramilli, H. Altug, Ultra-sensitive vibrational spectroscopy of protein monolayers with plasmonic nanoantenna arrays. Proc. Natl. Acad. Sci. U.S.A. **106**, 19227–19232 (2009). https://doi.org/10.1073/pnas.0907459106
14. R. Adato, H. Altug, In-situ ultra-sensitive infrared absorption spectroscopy of biomolecule interactions in real time with plasmonic nanoantennas. Nat. Commun. **4**, 1–10 (2013). https://doi.org/10.1038/ncomms3154
15. O. Selig, R. Siffels, Y.L.A. Rezus, Ultrasensitive ultrafast vibrational spectroscopy employing the near field of gold nanoantennas. Phys. Rev. Lett. **114**, 233004 (2015). https://doi.org/10.1103/PhysRevLett.114.233004
16. R.T. Mackin, B. Cohn, A. Gandman, J.D. Leger, L. Chuntonov, I.V. Rubtsov, Surface-enhanced dual-frequency two-dimensional vibrational spectroscopy of thin layers at an interface. J. Phys. Chem. C **122**, 11015–11023 (2018). https://doi.org/10.1021/acs.jpcc.8b02436
17. A. Gandman, R. Mackin, B. Cohn, I.V. Rubtsov, L. Chuntonov, Two-dimensional Fano lineshapes in ultrafast vibrational spectroscopy of thin molecular layers on plasmonic arrays. J. Phys. Chem. Lett. **8**, 3341–3346 (2017). https://doi.org/10.1021/acs.jpclett.7b01490
18. B.S. Simpkins, J.P. Long, O.J. Glembocki, J. Guo, J.D. Caldwell, J.C. Owrutsky, Pitch-dependent resonances and near-field coupling in infrared nanoantenna arrays. Opt. Express **20**, 27725–27739 (2012). https://doi.org/10.1364/OE.20.027725

19. K. Ataka, S.T. Stripp, J. Heberle, Surface-enhanced infrared absorption spectroscopy (SEIRAS) to probe monolayers of membrane proteins. Biochim. Biophys. Acta **1828**, 2283–2293 (2013). https://doi.org/10.1016/j.bbamem.2013.04.026
20. K. Ataka, J. Heberle, Biochemical applications of surface-enhanced infrared absorption spectroscopy. Anal. Bioanal. Chem. **388**, 47–54 (2007). https://doi.org/10.1007/s00216-006-1071-4
21. A. Hatta, T. Ohshima, W. Suëtaka, Observation of the enhanced infrared absorption of P-nitrobenzoate on Ag island films with an ATR technique. Appl. Phys. A **29**, 71–75 (1982). https://doi.org/10.1007/BF00632429
22. F. Neubrech, C. Huck, K. Weber, A. Pucci, H. Giessen, Surface-enhanced infrared spectroscopy using resonant nanoantennas. Chem. Rev. **117**, 5110–5145 (2017). https://doi.org/10.1021/acs.chemrev.6b00743
23. F. Neubrech, A. Pucci, T.W. Cornelius, S. Karim, A. Garcia-Etxarri, J. Aizpurua, Resonant plasmonic and vibrational coupling in a tailored nanoantenna for infrared detection. Phys. Rev. Lett. **101**, 157403 (2008). https://doi.org/10.1103/PhysRevLett.101.157403
24. M.C. Asplund, M.T. Zanni, R.M. Hochstrasser, Two-dimensional infrared spectroscopy of peptides by phase-controlled femtosecond vibrational photon echoes. Proc. Natl. Acad. Sci. U.S.A. **97**, 8219–8224 (2000)
25. I.V. Rubtsov, J. Wang, R.M. Hochstrasser, Dual frequency 2D-IR heterodyned photon-echo of the peptide bond. Proc. Natl. Acad. Sci. U.S.A. **100**, 5601–5606 (2003)
26. P. Hamm, M.T. Zanni, *Concepts and Methods of 2D Infrared Spectroscopy*, 1st edn. (Cambridge University Press, Cambridge, New York, 2011)
27. F. Neubrech, A. Pucci, Plasmonic enhancement of vibrational excitations in the infrared. IEEE J. Sel. Top. Quantum Electron. **19**, 4600809 (2013). https://doi.org/10.1109/JSTQE.2012.2227302
28. C. Yan, R. Yuan, W.C. Pfalzgraff, J. Nishida, L. Wang, T.E. Markland, M.D. Fayer, Unraveling the dynamics and structure of functionalized self-assembled monolayers on gold using 2D IR spectroscopy and MD simulations. Proc. Natl. Acad. Sci. U.S.A. **113**, 4929–4934 (2016). https://doi.org/10.1073/pnas.1603080113
29. J.P. Kraack, A. Kaech, P. Hamm, Surface enhancement in ultrafast 2D ATR IR spectroscopy at the metal-liquid interface. J. Phys. Chem. C **120**, 3350–3359 (2016). https://doi.org/10.1021/acs.jpcc.5b11051
30. J.P. Kraack, P. Hamm, Vibrational ladder-climbing in surface-enhanced, ultrafast infrared spectroscopy. Phys. Chem. Chem. Phys. **18**, 16088–16093 (2016). https://doi.org/10.1039/c6cp02589g
31. N. Goutev, M. Futamata, Attenuated total reflection surface-enhanced infrared absorption spectroscopy of carboxyl terminated self-assembled monolayers on gold. Appl. Spectrosc. **57**, 506–513 (2003). https://doi.org/10.1366/000370203321666506
32. D. Dregely, F. Neubrech, H. Duan, R. Vogelgesang, H. Giessen, Vibrational near-field mapping of planar and buried three-dimensional plasmonic nanostructures. Nat. Commun. **4**, 3237 (2013). https://doi.org/10.1038/ncomms3237
33. F. Neubrech, S. Beck, T. Glaser, M. Hentschel, H. Giessen, A. Pucci, Spatial extent of plasmonic enhancement of vibrational signals in the infrared. ACS Nano **8**, 6250–6258 (2014). https://doi.org/10.1021/nn5017204
34. X. Han, X. Ji, H. Wen, J. Zhang, H-shaped resonant optical antennas with slot coupling. Plasmonics **7**, 7–11 (2012). https://doi.org/10.1007/s11468-011-9268-6
35. A. Gandman, R.T. Mackin, B. Cohn, I.V. Rubtsov, L. Chuntonov, Radiative enhancement of linear and third-order vibrational excitations by array of infrared plasmonic antennas. ACS Nano **12**, 4521–4528 (2018). https://doi.org/10.1021/acsnano.8b00845
36. B. Cohn, B. Engelman, A. Goldner, L. Chuntonov, Two-dimensional infrared spectroscopy with local plasmonic fields of a trimer gap-antenna array. J. Phys. Chem. Lett. **9**, 4596–4601 (2018). https://doi.org/10.1021/acs.jpclett.8b01937
37. J.P. Kraack, P. Hamm, Surface-sensitive and surface-specific ultrafast two-dimensional vibrational spectroscopy. Chem. Rev. **117**, 10623–10664 (2017). https://doi.org/10.1021/acs.chemrev.6b00437

38. C.D. Bain, E.B. Troughton, Y.-T. Tao, J. Evall, G.M. Whitesides, R.G. Nuzzo, Formation of monolayer films by the spontaneous assembly of organic thiols from solution onto gold. J. Am. Chem. Soc. **111**, 321–335 (1989). https://doi.org/10.1021/ja00183a049
39. J.D. Leger, C.M. Nyby, C. Varner, J. Tang, N.I. Rubtsova, Y. Yue, V.V. Kireev, V.D. Burtsev, L.N. Qasim, G.I. Rubtsov, I.V. Rubtsov, Fully automated dual-frequency three-pulse-echo 2DIR spectrometer accessing spectral range from 800 to 4000 wavenumbers. Rev. Sci. Instrum. **85**, 083109 (2014). https://doi.org/10.1063/1.4892480
40. C.M. Nyby, J.D. Leger, J. Tang, C. Varner, V.V. Kireev, I.V. Rubtsov, Mid-IR beam direction stabilization scheme for vibrational spectroscopy, including dual-frequency 2DIR. Opt. Express **22**, 6801–6809 (2014). https://doi.org/10.1364/OE.22.006801
41. P.B. Johnson, R.W. Christy, Optical constants of the noble metals. Phys. Rev. B **6**, 4370–4379 (1972). https://doi.org/10.1103/PhysRevB.6.4370
42. U. Fano, Effects of configuration interaction on intensities and phase shifts. Phys. Rev. **124**, 1866–1878 (1961). https://doi.org/10.1103/PhysRev.124.1866
43. B. Cohn, A.K. Prasad, L. Chuntonov, Communication: probing the interaction of infrared antenna arrays and molecular films with ultrafast quantum dynamics. J. Chem. Phys. **148**, 131101 (2018). https://doi.org/10.1063/1.5025600
44. D. Finkelstein-Shapiro, A. Keller, Ubiquity of Beutler-Fano profiles: from scattering to dissipative processes. Phys. Rev. A **97**, 1–12 (2018). https://doi.org/10.1103/PhysRevA.97.023411
45. B. Gallinet, O.J.F. Martin, Ab initio theory of Fano resonances in plasmonic nanostructures and metamaterials. Phys. Rev. B **83**, 1–6 (2011). https://doi.org/10.1103/PhysRevB.83.235427
46. Y.S. Joe, A.M. Satanin, C.S. Kim, Classical analogy of Fano resonances. Phys. Scr. **74**, 259–266 (2006). https://doi.org/10.1088/0031-8949/74/2/020
47. A. Lovera, B. Gallinet, P. Nordlander, O.J.F. Martin, Mechanisms of Fano resonances in coupled plasmonic systems. ACS Nano **7**, 4527–4536 (2013). https://doi.org/10.1021/nn401175j
48. X. Wu, S.K. Gray, M. Pelton, Quantum-dot-induced transparency in a nanoscale plasmonic resonator. Opt. Express **18**, 23633–23645 (2010). https://doi.org/10.1364/OE.18.023633
49. M. Kerker, D.-S. Wang, H. Chew, Surface enhanced Raman scattering (SERS) by molecules adsorbed at spherical particles: errata. Appl. Opt. **19**, 4159–4174 (1980). https://doi.org/10.1364/AO.19.004159
50. L. Chuntonov, G. Haran, Optical activity in single-molecule surface-enhanced Raman scattering: role of symmetry. MRS Bull. **38**, 642–647 (2013). https://doi.org/10.1557/mrs.2013.159
51. L. Chuntonov, G. Haran, Maximal Raman optical activity in hybrid single molecule-plasmonic nanostructures with multiple dipolar resonances. Nano Lett. **13**, 1285–1290 (2013). https://doi.org/10.1021/nl400046z
52. S. Mukamel, *Principles of Nonlinear Optical Spectroscopy*. (Oxford University Press, New York, 1995)
53. Z. Lin, P. Keiffer, I.V. Rubtsov, A method for determining small anharmonicity values from 2DIR spectra using thermally induced shifts of frequencies of high-frequency modes. J. Phys. Chem. B **115**, 5347–5353 (2011). https://doi.org/10.1021/jp1094189
54. T. Neuman, C. Huck, J. Vogt, F. Neubrech, R. Hillenbrand, J. Aizpurua, A. Pucci, Importance of plasmonic scattering for an optimal enhancement of vibrational absorption in SEIRA with linear metallic antennas. J. Phys. Chem. C **119**, 26652–26662 (2015). https://doi.org/10.1021/acs.jpcc.5b08344
55. J. Zuloaga, P. Nordlander, On the energy shift between near-field and far-field peak Intensities in localized plasmon systems. Nano Lett. **11**, 1280–1283 (2011). https://doi.org/10.1021/nl1043242
56. A.F. Koenderink, On the use of Purcell factors for plasmon antennas. Opt. Lett. **35**, 4208–4210 (2010). https://doi.org/10.1364/OL.35.004208
57. R. Esteban, J. Aizpurua, G.W. Bryant, Strong coupling of single emitters interacting with phononic infrared antennae. New J. Phys. **16**, 1–17 (2014). https://doi.org/10.1088/1367-2630/16/1/013052

58. R. Ruppin, Electromagnetic energy density in a dispersive and absorptive material. Phys. Lett. A **299**, 309–312 (2002). https://doi.org/10.1016/S0375-9601(01)00838-6
59. K. Santhosh, O. Bitton, L. Chuntonov, G. Haran, Vacuum Rabi splitting in a plasmonic cavity at the single quantum emitter limit. Nat. Commun. **7** (2016). https://doi.org/10.1038/ncomms11823
60. M.A. Kats, N. Yu, P. Genevet, Z. Gaburro, F. Capasso, Effect of radiation damping on the spectral response of plasmonic components. Opt. Express **19**, 21748–21753 (2011). https://doi.org/10.1364/OE.19.021748
61. F. Ding, E.C. Fulmer, M.T. Zanni, Heterodyned fifth-order two-dimensional IR spectroscopy: third-quantum states and polarization selectivity. J. Chem. Phys. **123**, 94502 (2005). https://doi.org/10.1063/1.1998829
62. F. Ding, M.T. Zanni, Heterodyned 3D IR spectroscopy. Chem. Phys. **341**, 95–105 (2007). https://doi.org/10.1016/j.chemphys.2007.06.010
63. J.D. Leger, C. Varner, G.I. Rubtsov, Multi-mode heterodyned 5th-order infrared spectroscopy. J. Chem. Phys. **145**, 154201 (2016). https://doi.org/10.1063/1.4963815
64. S. Garrett-Roe, P. Hamm, What can we learn from three-dimensional infrared spectroscopy? Acc. Chem. Res. **42**, 1412–1422 (2009). https://doi.org/10.1021/ar900028k
65. S.S. Mukherjee, D.R. Skoff, C.T. Middleton, M.T. Zanni, Fully absorptive 3D IR spectroscopy using a dual mid-infrared pulse shaper. J. Chem. Phys. **139**, 144205 (2013). https://doi.org/10.1063/1.4824638
66. N.I. Rubtsova, L.N. Qasim, A.A. Kurnosov, A.L. Burin, I.V. Rubtsov, Ballistic energy transport in oligomers. Acc. Chem. Res. **48**, 2547–2555 (2015). https://doi.org/10.1021/acs.accounts.5b00299
67. N.I. Rubtsova, I.V. Rubtsov, Vibrational energy transport in molecules studied by relaxation-assisted two-dimensional infrared spectroscopy. Ann. Rev. Phys. Chem. **66**, 717–738 (2015)

Chapter 14
The Development of Coherent Multidimensional Microspectroscopy

Clara A. Tibbetts, Bradley M. Luther and Amber T. Krummel

Abstract The development of coherent multidimensional microspectroscopy (CMDMS) is driven by a desire to investigate heterogenous samples and spatially resolve details about molecular structure and dynamics that are available using coherent multidimensional techniques (CMDS). However, incorporating traditional CMDS techniques into imaging modalities requires tackling obstacles including acquisition time, spatial resolution, and detection methods. Thus, this chapter reviews these challenges, the basics of microscopy and spatial resolution, and how different experimental setups implemented by the five research groups that have executed CMDMS approach these obstacles. In addition to a brief review of experimental set-ups, the main findings of each group are reviewed. Most of the current research is shown to be proof of concept, however with additional improvements valuable information could be gained about different biological and materials samples. In looking towards the future of the field, this chapter also reviews other methods for data reduction and detection methods that have been applied in CMDS experiments such as compressive sensing and fluorescence detection or fluorescence encoding methods to combat long acquisition times, IR detection limitations, and the diffraction limited spatial resolution inherent to the mid-IR.

14.1 Introduction

Humans have been working to magnify their surroundings since the first century AD when the Romans invented the lens. They discovered that objects could be made larger and light could be focused using glass pieces that were thick in the center and thinner at the edges. Centuries later in 1590 the first compound microscope was built by two Dutchmen, Zacharias and Han Jansen [1]. Optical microscopies along with many other imaging modalities continue to advance in spatial resolution, acquisition

C. A. Tibbetts · B. M. Luther · A. T. Krummel (✉)
Department of Chemistry, Colorado State University, Colorado, USA
e-mail: Amber.Krummel@colostate.edu

M. Cho (ed.), *Coherent Multidimensional Spectroscopy*,
Springer Series in Optical Sciences 226,
https://doi.org/10.1007/978-981-13-9753-0_14

rates, and chemical selectivity. Ultimately experimental tools will be developed to image chemistry on molecular length and time scales.

Chemical imaging can be accomplished by spatially resolving absorption processes, emission processes, and scattering processes. For example, images from Fourier transform infrared (FTIR) microscopy are produced by monitoring the absorption of light by molecular vibrations, whereas an image produced by Raman microscopy is produced by monitoring the scattering of light to report molecular vibrations. Chemical imaging techniques utilize wavelengths across the electromagnetic spectrum including long wavelengths in magnetic resonance imaging (MRI), to infrared, visible, extreme ultraviolet, and x-ray in different optical imaging modalities. Each of these different wavelengths will utilize their own chromophores and have their own advantages. For example, fluorescence imaging has been a work horse in biological imaging applications due to its inherent sensitivity and spatial resolution. The need for fluorescent labels can be limiting, but our knowledge of cellular structures has increased dramatically since the inception of fluorescence microscopy. FTIR microspectroscopy has made impactful contributions [2–4] to the study of disease states in biology due to having narrow spectral features as compared to fluorescence microspectroscopy. However, FTIR imaging is limited in spatial resolution due to the 5 to 8 μm wavelengths associated with the vibrational modes of biological molecules including proteins and nucleic acids. Hence, FTIR imaging has generated important insights into chemistry of disease states at the tissue level. The advent of lasers with ultrashort pulses provided a path to access nonlinear optical processes more routinely and thus, offer improved imaging.

Nonlinear optical processes have been exploited to produce better imaging contrasts as well as improve spatial resolution. For example, two-photon excitation fluorescence (TPEF) microscopy and third harmonic generation (THG) microscopy are both based on third-order nonlinear processes produced in a sample [5–7]. TPEF and THG imaging are widely used as contrasts in biological imaging, in part due to drastic reduction in fluorescence background. In particular THG requires three ultrafast pulses to be overlapped in space and time; as such the THG signal is irradiated from femtoliter focal volumes. If one is interested in high contrast imaging of interfaces, second harmonic generation (SHG) becomes the imaging modality of choice [8, 9]. In each of these cases background signals irradiated through the entire thickness of the sample are eliminated. Similarly, other nonlinear optical contrast mechanisms have been developed including coherent anti-Stokes Raman scattering (CARS) [10–12] microscopy or sum frequency generation (SFG) microscopy for interfaces [13–15]. Each of the above-mentioned imaging modalities can be utilized in a microspectroscopy fashion in which the nonlinear optical spectrum is collected at each image voxel. In each spectrum collected, the nonlinear signal intensity is plotted as a function of wavelength, Raman shift, or the vibrational excitation frequency as is the case for vibrational SFG (VSFG). Thus, the resulting spectrum is effectively a linear spectrum. A linear spectrum can be very useful to determine chemical constituents present in a sample, however, quantitative details of molecular structures and chemical dynamics can remain hidden in linear spectra.

Coherent multidimensional spectroscopy (CMDS) techniques have been developed to reveal quantitative details of molecular structures and dynamics—this book is a testament to these investigative efforts. Coherent multidimensional spectroscopy experiments are being performed with wavelengths spanning nearly the entire electromagnetic spectrum. The CMDS suite of tools allow researchers to capture details of chemistry and biology at the length scales and time scales upon which they occur. For example, using 2D IR spectroscopy molecular motions occurring at sub-100 fs time scales can be captured and subsequent spectroscopic snapshots can be collected of molecular folding or aggregation occurring at millisecond timescales and longer. Each chapter of this book provides examples of the power in each CMDS tool and the multitude of observables captured by each coherent multidimensional spectroscopy technique developed over the past two decades. In this chapter, we discuss recent efforts to spatially resolve these observables in a suite of coherent multidimensional microspectroscopy (CMDMS) experiments. Herein, the reader is provided with details of spatial resolution in nonlinear microscopes, experimental implementations, practical approaches to signal isolation, approaches to data reduction, and then an overview of the CMDMS experiments in the literature to date.

14.2 Introductory Concepts of Microscopy

14.2.1 Spatial Resolution of Ultrafast Nonlinear Microscopes

A diffraction limited linear microscope has spatial resolution dependent on the incident wavelength of light, and the microscope objective in use. Numerical aperture (NA) is a value that measures the ability of a microscope objective or lens to focus incoming light to resolve spatial detail of a sample at a certain object distance. NA is defined as $n \sin\theta$ with n being the refractive index of the material between the lens and sample and θ the aperture angle. The lateral (x and y-directions) resolving power of a microscope can be defined with the Abbe diffraction limit (14.1). The axial (z-direction) resolution is worse than that in the lateral direction (14.2).

$$\text{Abbe Resolution}_{x,y} = \lambda/2\text{NA} \tag{14.1}$$

$$\text{Abbe Resolution}_{z} = 2\lambda/\text{NA}^2 \tag{14.2}$$

As described by (14.1) and (14.2), increasing NA or decreasing the excitation wavelength will decrease the distance between two points in a sample that can be spatially resolved. A point-spread function (PSF) is a three-dimensional function describing the diffraction pattern of a point source in both the lateral and axial directions. An image is formed by convolution of the PSF and the object being imaged. In addition to using the Abbe diffraction limit to report spatial resolution several other definitions are used. These other means of reporting resolution include

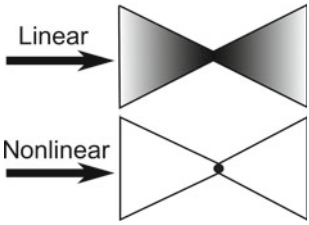

Fig. 14.1 Volume of interaction for a linear spectroscopic technique relative to a nonlinear technique with the black representing the volume of interaction

using the Rayleigh criterion, the full width of a point spread function measured at half its maximum intensity (FWHM), or the Sparrow limit [16]. These three resolution definitions rely on properties of the PSF, unlike the Abbe diffraction limit that is solely determined from the optics in use. The Rayleigh criterion states that two points can be resolved when the minimum diffraction for one point coincides with the maximum of diffraction for the second source (14.3).

$$\text{Rayleigh Resolution}_{x,y} = 0.61\lambda/\text{NA} \tag{14.3}$$

Taken together, (14.1)–(14.3) provide a picture as to how spatial resolution will change in different types of coherent multidimensional microspectroscopy (CMDMS) experiments. Due to the diffraction limit being wavelength dependent the spatial resolution achieved by 2D infrared (IR) versus 2D electronic microscopy (2D ES) are different orders of magnitude due to the dependence on IR and visible wavelengths, respectively. Thus, the diffraction limit would suggest the best achievable 2D IR microspectroscopy resolution is in the range of ~2–4 μm versus ~0.1–0.3 μm for 2D E microspectroscopy.

For nonlinear imaging techniques specifically, the order of nonlinear interaction will also play a role in defining the resolving power of the microscope. For example, this is shown with two–photon absorption experiments [17]. It can be approximated that the PSF for an *N*th order nonlinear process would be the corresponding linear PSF raised to the *N*th power, thus resulting in a decrease in the interaction volume that contributes to the majority of the nonlinear signal. Figure 14.1 depicts the relative area contributing to collected signal for a linear and nonlinear spectroscopic technique [5].

14.3 Implementations of Coherent Multidimensional Microspectroscopy

At present, five groups have implemented a form of microscopy based on coherent multidimensional spectroscopy techniques. The following sections of this chapter will provide brief descriptions of the experimental approaches making these mea-

surements possible, as well as the main findings from each study. These experiments are paving the way for a new field that can give access to an untapped well of information regarding femtosecond chemical dynamics in spatially heterogenous systems.

14.3.1 Optical Geometries and Pulse Sequences

2D IR and 2D ES are four wave mixing processes which depend on the interaction of three fields in time and space and the generation of a fourth signal field. In general, the electric fields involved in these experiments are two pump pulses and a probe pulse. The first pump pulse creates a superposition between the first excited state and the ground state. The second pump pulse can drive a population into the ground or first excited state, the probe pulse can then generate a superposition between the second excited state and the first excited state or the ground and first excited state followed by the generation of the signal field. An example pulse sequence is shown in Fig. 14.2. 2D experiments are often done in a boxcar geometry, in which the two pump beams and the probe beam each have a unique wave vector, $\vec{k}$, allowing the signal to be collected in its own background free direction. Equation (14.4) shows the direction of the rephasing, R, signal, and (14.5) the non-rephasing, NR [18, 19].

$$\vec{k}_{\mathrm{sig},R} = -\vec{k}_1 + \vec{k}_2 + \vec{k}_3 \tag{14.4}$$

$$\vec{k}_{\mathrm{sig},NR} = +\vec{k}_1 - \vec{k}_2 + \vec{k}_3 \tag{14.5}$$

A second beam geometry often used is the pump-probe geometry in which two pump pulses share a wave vector direction, $\vec{k}_1$, and the probe beam has a different wave vector, $\vec{k}_2$. In the pump-probe geometry the probe beam also serves to heterodyne detect the signal field that is emitted along the same direction as the probe. The boxcar and pump-probe geometries offer access to spatial phase matching. Spa-

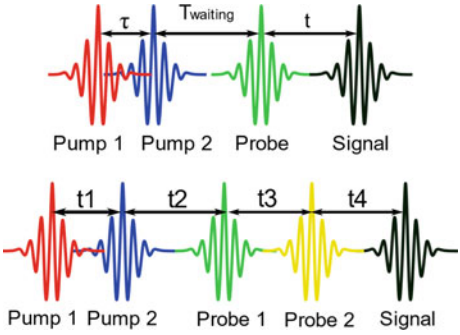

Fig. 14.2 (**Top**) Example pulse sequence for a 2D IR experiment. The first coherence time, between pump 1 and pump 2, represented by τ and the waiting time T_{waiting}. (**Bottom**) Example fluorescence detected 2D ES pulse sequence

tial phase matching is advantageous for decreasing background noise, but it is not desirable when it is necessary to interface with a microscope objective. A collinear geometry is preferred when interfacing with a microscope objective. In a collinear geometry it is necessary to use phase cycling or phase modulation [20] to remove the unwanted signals and reveal the nonlinear signal of interest. The necessity for collinear geometry comes at the cost of collecting data sets for each phase cycle resulting in 4, 8,16, or 27 sets of data for each delay [20–23]. The collinear geometry poses an advantage relative to a non-collinear geometry such as a boxcar or pump-probe geometry. In a non-collinear geometry, a requirement for signal production in a phase-matched direction is the generation a grating of oscillating dipoles. To write this grating an excitation volume of at least λ^3 is required, with λ as the excitation wavelength. This requirement no longer exists in a collinear geometry, thus reducing the size of the excitation volume needed [24] CMDMS experiments require many laser pulses and can be time intensive. However, if the proper balance is chosen with regard to beam geometry, phase-cycling schemes, and polarization conditions, the CMDMS experiments can yield vast amounts of information within a reasonable amount of time. One example of this balance is the consideration of collecting an absorptive spectrum using a collinear beam geometry in a cross polarization condition. In this type of experiment, it is possible to isolate the signal of interest with only a 4 or 8-frame phase cycling scheme. In contrast, if one requires the absorptive signal to be collected in a collinear beam geometry and under a co-polarization condition, the number of frames in the phase-cycling scheme must be increased and a greater number of pulses are required. A second example of balancing use of laser pulses with image contrast is the use of fluorescence detection of the third order signal. Fluorescence detection involves the addition of a fourth field interaction [24]. The fourth field interaction is necessary to change the coherence that was generated by the third field interaction to a population. The additional field interaction can be done by adding a fourth pulse or by using two interactions from the third pulse. In the case of a four pulse sequence, as shown in Fig. 14.2, t_1 and t_2 are stepped in time and Fourier transformed to create the pump and probe frequency axes, respectively. The fluorescence is proportional to the population of the excited state or states. To remove unwanted signals phase cycling of 16–27 frames are used. The details of which will be discussed below. However, fluorescence detection of the third order signal is advantageous because it can be collected off axis, thus increasing signal to noise and giving the potential to improve image contrast. It is possible that the improved signal-to-noise ratio using fluorescence detection is worth the additional phase cycles required. Below details are provided to help the reader determine how best to balance the requirements for their own CMDMS experiments with their laser pulse budget.

Table 14.1 Phase added to each pump pulse in a four-frame phase cycling scheme, with A–D being the four frames

Frame	Pump 1 phase	Pump 2 phase
A	0	0
B	0	π
C	π	π
D	π	0

14.3.2 Methods for Signal Isolation

14.3.2.1 Phase Cycling

As mentioned above the use of fluorescence detection or non-boxcar beam geometries necessitates the use of phase cycling or phase modulation to remove unwanted signals. Phase cycling is dependent on the fact that the third order nonlinear signal can be written as a function of the difference in phase between the two pump pulses, $\Delta\varphi_{12}$, whereas unwanted signals such as transient absorption or scatter are not [25]. This method is commonly used in both collinear and pump-probe geometries. For example, with a two-frame phase cycling scheme, the signal is collected at $\Delta\varphi_{12}$ equals 0 and $\Delta\varphi_{12}$ equals π. The difference between these two signals is taken, resulting in the third order signal doubling and the unwanted signals not dependent on $\Delta\varphi_{12}$ cancelling. Thus, the signal to noise ratio in the data collected is increased. This can be further improved with four frame phase cycling. Table 14.1 includes the relative phase added to each pump pulse in a four-frame phase cycling scheme. In a four-frame scheme the signal plotted is then Signal(A–B) + Signal(C–D), which then quadruples the signal to noise ratio [18]. While four-frame phase cycling is sufficient in a pump probe geometry in a completely collinear geometry it is necessary to increase the phase cycles or use cross polarized pump and probe beams. If the pump beams can be sufficiently eliminated with crossed polarizers four phase cycles can be used. If however the pump beam reduction is not sufficient it is necessary to add a chopper and collect eight frame phase cycles in which the probe beam is chopped as shown in Table 14.2 [22]. Fluorescence detection results in multiple pathways contributing to the collected signal and an increased number of phase cycles to remove unwanted contributions. This results in up to 27 frames being collected for each nonlinear spectrum [26, 27].

14.3.2.2 Phase Modulation

Phase modulation is another method used to achieve back-ground free detection. Phase modulation was developed by Tekavec et al. in 2007 for fluorescence detected 2D ES [20]. Four acousto-optic modulators (AOMs) are used write an independent radio frequency onto the four pulses, Ω_i ($i = 1$–4). These AOMs are each in an arm of a Mach Zehnder interferometer. The first two pulses are recombined and are con-

Table 14.2 8-frame phase cycling scheme implemented by Baiz et al. [22]

Frame	Phase						
	Input fields			Detected			
	Φ_1	Φ_2	Φ_3	E_1E_2	E_1E_3	E_2E_3	S_{2DIR}
A	0	0	0	0	0	0	0
B	0	π	0	0	π	π	π[a]
C	π	0	0	π	π	0	π[a]
D	π	π	0	π	0	π	0
E	0	0	–	0	–	–	–
F	0	π	–	π	–	–	–
G	π	0	–	π	–	–	–
H	π	π	–	0	–	–	–

A dash refers to the probe field being chopped. The 0 and π represent the phase of carrier field
Signal I: $(B + C) - (A + D) = 4S_{2DIR} + 4E_1E_2$
Signal II: $(F + G) - (E + H) = 4E_1E_2$
Signal I − Signal II = $4S_{2DIR}$
[a]Phase being ± π depending on the response functions

sequently modulated at the difference frequency of $\Omega_{21} = \Omega_2 - \Omega_1$. Thus, at some coherence time between pulses 1 and 2 any given wavelength that corresponds to a transition will oscillate between being pumped or not at the difference frequency between the pulses, Ω_{21}. Similarly, the other pulse pair is modulated at the frequency $\Omega_{43} = \Omega_4 - \Omega_3$. Signal at the sum, $\Omega_{43} + \Omega_{21}$, and difference, $\Omega_{43} - \Omega_{21}$, frequencies will give rise to the nonrephasing and rephasing signals, respectively [20]. The fluorescence signal is collected using lock in detection at the sum and difference frequencies generated by the independent AOMs. The detection process involves replacing the relative phases between the laser pulses with those of reference phases which are determined by monochromator settings. The reference frequencies can be downshifted by the monochromators to allow for systematic undersampling, similar to rotating frame used in 2D IR spectroscopy which is discussed below [28].

14.3.3 Techniques for Data Reduction

14.3.3.1 Rotating Frame

Of the research groups already using multidimensional microscopy techniques, many already utilize approaches to reduce the number of data points required during spectral acquisition including sampling below the Nyquist frequency or the application of a rotating frame. The Nyquist criterion sets the required sampling frequency of a waveform to allow the signal to be reconstructed without the loss of information. Typically, one tries to avoid aliasing of the signal due to infrequent sampling, how-

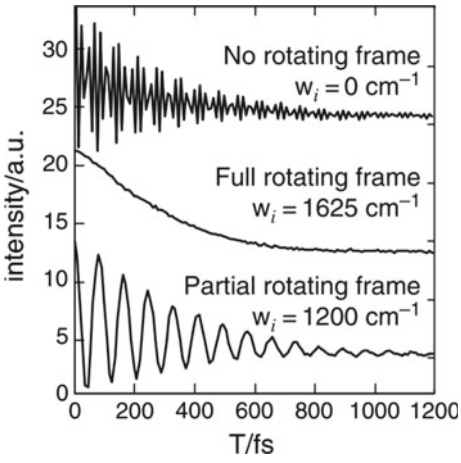

Fig. 14.3 (Top) No rotating frame (Middle) Full rotating frame (Bottom) Partial rotating frame. Reprinted from [18]

ever, aliasing by a known factor can be one path to reducing the number of points needed to maintain the information contained within a signal. For example, under sampling a signal by a known factor allows one to operate below the Nyquist criterion for sampling frequency, meaning fewer points must be collected, however the factor by which the signal is under sampled must be taken into account during post processing of the data. Alternatively, the number of points can be reduced using approaches such as the rotating frame. Rotating frame works by shifting the phase between the two pump pulses while τ is changed to decrease the period of the emitted signal field (14.6). In (14.6), ω_i is a constant and is the frequency by which the fundamental frequency is shifted. An example of the results of rotating frame is depicted in Fig. 14.3 [18, 25].

$$\Delta\varphi_{12} = -\omega_i \tau \tag{14.6}$$

14.3.3.2 Compressive Sensing

Another approach to tackling experimental limitations imposed by data acquisition time is implementing a type of data reduction algorithm. An example of this is the compressive sensing (CS) approach. The application of compressive sensing to multidimensional spectroscopy has been demonstrated by Almeida et al. [29], Sanders et al. [30] and Dunbar et al. [31]. The goal of CS is to reduce the number of points required to specify a particular dimension and maintain the fidelity of the signal in that dimension. In the application of CS to multidimensional spectroscopy investigators have used CS to reduce the number of time domain delays needed to generate the frequency axes of a 2D spectrum. Often one of the frequency axes is generated with a Fourier transform carried out optically by implementing a detection scheme that includes a monochromator and array detector. Assuming the experiment is car-

ried out in the time domain, the second frequency axis is generated from the Fourier Transform (FT) of the time delay axis with the total time delay. These conditions determine the spectral resolution and the step size is chosen to satisfy the Nyquist frequency. Typically, reduction of the number of time delays leads to a reduction in the temporal window and poor resolution in the frequency domain. However, CS allows a small portion of the coherence window near a node in the free induction decay to be sampled and the frequency domain to be reconstructed with higher resolution than using a Fourier Transform. This is accomplished using CS algorithms that replace the Fourier Transform and apply the condition of sparseness to find a solution. Since the frequency axis is underdetermined in the CS approach there are multiple solutions. The sparsity requirement seeks the solution that maximizes the number of zero coefficients in the frequency domain. This allows the determination of peak positions but does not accurately reproduce the line shapes.

Dunbar et al. [31] compared the use of CS and Fourier Transform analysis on dicarbonyl-acetylacetonato-rhodium(I) (RDC). The FT 2D IR spectra were collected using a full 10 ps coherence time scan as well as a 500 fs coherence time scan and compared to results from a 500 fs coherence time scan using CS (Fig. 14.4). While the 500 fs FT analysis suffers from poor resolution due to the narrow time window, the 520 fs CS analysis can reproduce the peak positions and amplitudes with over an order of magnitude reduction in collection time. Sanders et al. [30] demonstrated the use of CS on the 2D electronic spectra of ^{87}Rb vapor. Both the pump and probe axes were collected in the time domain using a four pulse sequence from a Ti:Sapphire laser. FT and CS algorithms were used to analyze the data with the CS analysis giving over an order of magnitude improvement in the resolution. Results for FT and CS analysis are shown in Fig. 14.5. It was also shown that using a random sampling with CS allows for even greater reduction of the time domain sampling.

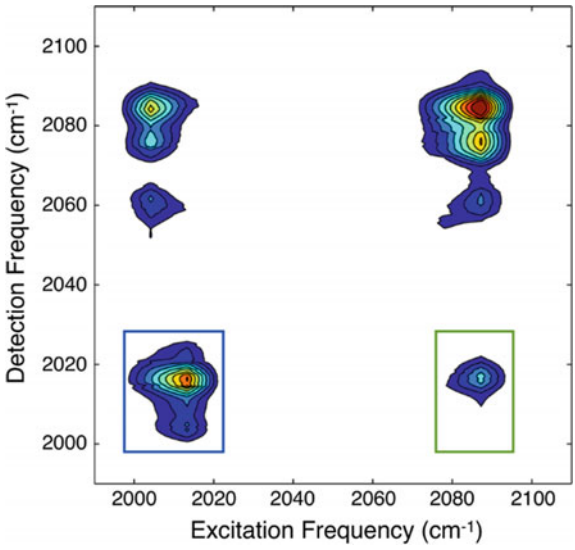

Fig. 14.4 2D IR spectrum analyzed using compressed sensing. Reprinted from [31]

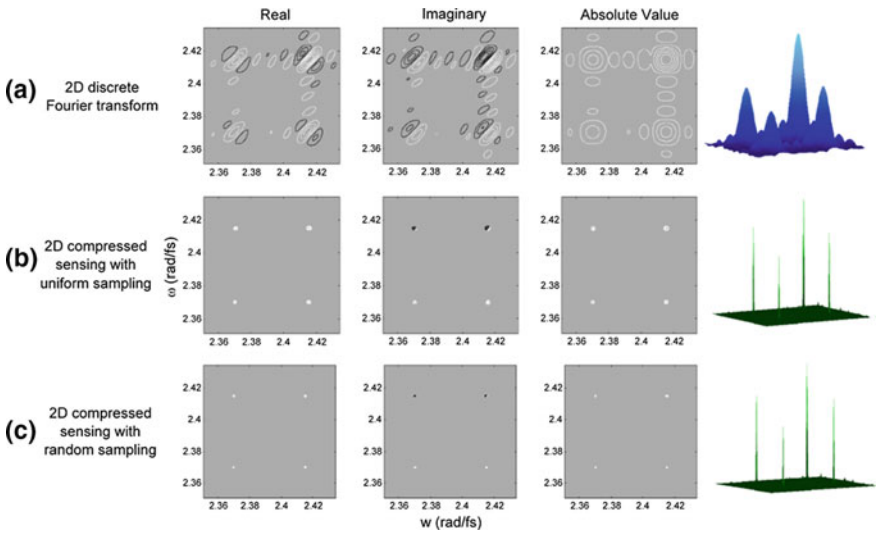

Fig. 14.5 Comparison of data collected using CS approaches to data collected using Fourier transform approaches. Reprinted from [30]

While CS can lead to over an order of magnitude reduction in collection times, care must be taken to avoid under sampling which can result in peak position error and splitting between peak positions. The tradeoff between collection time and line shape accuracy must be determined and while CS is not applicable to extracting frequency-frequency correlation functions using peak slopes it is applicable to determining spectral diffusion using the inhomogeneity index [32].

14.4 2D IR Microscopy: Point Scanning Collection

The first implementation of a 2D IR microscopy was accomplished by Baiz et al. [22]. In this experiment, a point scanning method was used to collect spectra of polystyrene beads swelled with a solution of metal-carbonyl molecules. They defined their spatial resolution by the FWHM of the beam spot size at the focus, giving resolution close to the theoretical diffraction limit of 4.4 μm (Fig. 14.6). The optical set up used in the experiment is shown in Fig. 14.7. In this experiment the collinear geometry allowed for the incorporation of a mid-IR microscope (Hyperion 2000, Bruker Optics). These experiments were performed in a crossed polarization scheme, in which a combination of polarizers block the pump and reduce the residual probe light that reaches the mercury cadmium telluride detector (MCT). In addition, an eight-frame phase cycling scheme was employed to reduce unwanted background interference with the desired third order 2D IR signal (Table 14.2).

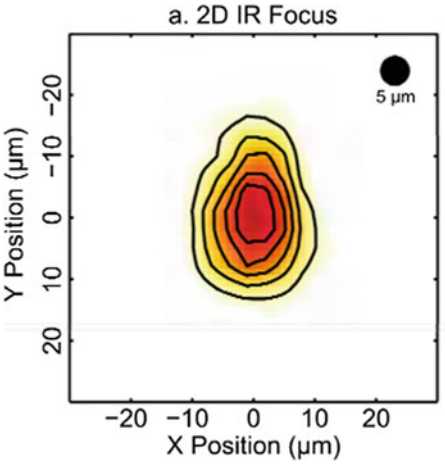

Fig. 14.6 2D IR focus in experiments performed by Baiz et al. Reprinted from [22]

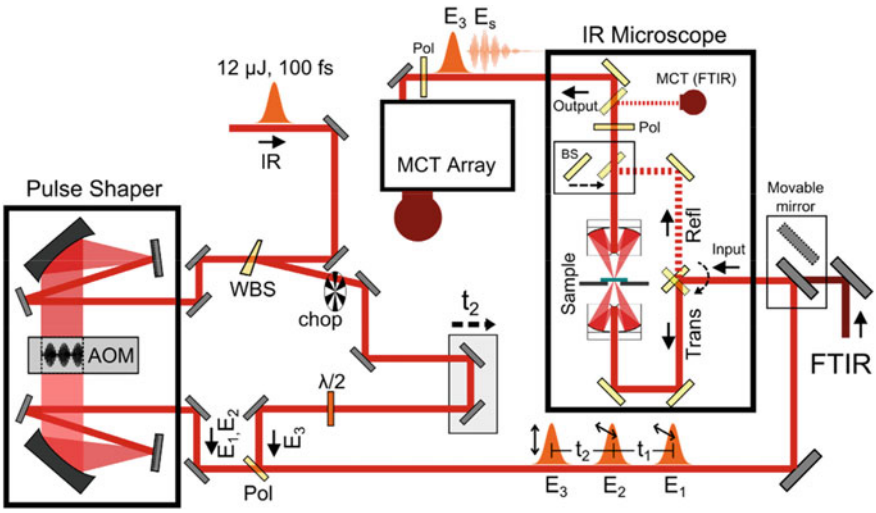

Fig. 14.7 Experimental set-up used by Baiz et al. [22]

This work was a proof of concept investigation looking at a sample of polystyrene beads swelled with a solution of metal-carbonyl molecules, $Mn_2(CO)_{10}$ (dimanganese decacarbonyl, DMDC). A brightfield image of the polystyrene bead overlaid with points representing the 2D IR spectra collected and the intensity of the vibrational mode at 2008 cm^{-1} is shown in Fig. 14.8a. This study was able to distinguish between different environments experienced by the metal carbonyl vibrational probe. The difference in local environment surrounding the probe molecule was investigated using Stimulated-emission Lifetime IR Microscopy (SLIM). Shorter vibrational life-

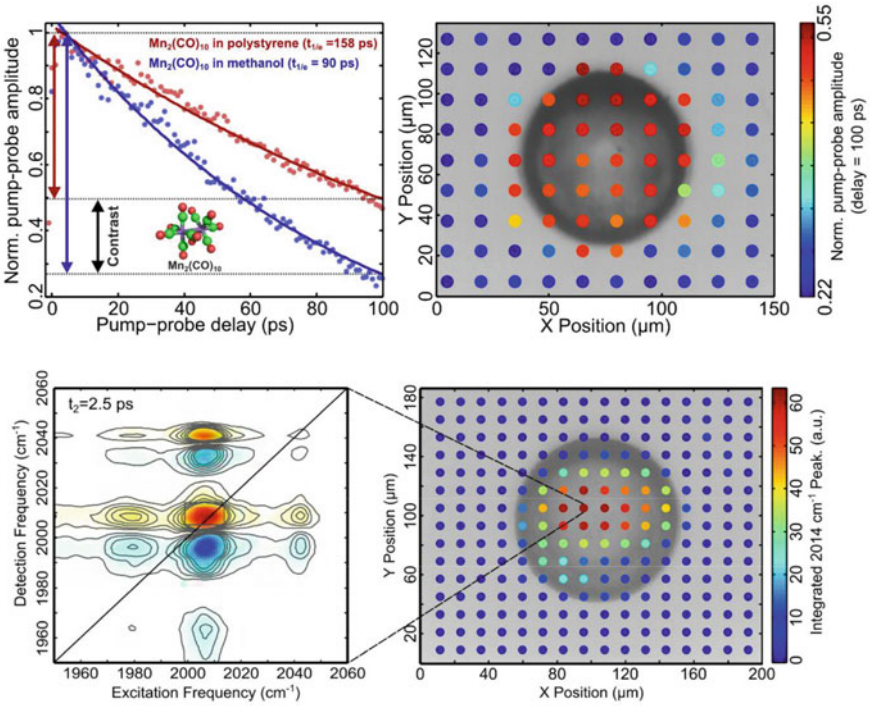

Fig. 14.8 (**a—top right**) Bright field image of polystyrene bead overlaid with points for each 2D IR spectrum taken, with the color representing the signal intensity for the on diagonal 2008 cm^{-1} transition. (**b—top left**) An example 2D IR spectrum corresponding to the indicated point in the center of the bead (**c—bottom left**) vibrational lifetime as a function of waiting time (pump – probe delay) (**d—bottom right**) vibrational lifetimes plotted for each 2D IR spectrum. Reproduced from [22]

times were observed in the bulk methanol solution versus the longer lifetimes of the probe absorbed in the polystyrene, as depicted in the blue and red curves in Fig. 14.8b, respectively. Further information distinguishing the chemical dynamics of these two distinct environments could be gained by performing waiting time experiments to look at the spectral diffusion overtime. Currently the acquisition time of this type of data is a limiting factor with a single 2D IR spectrum taking approximately 30 s to acquire in this experimental system.

14.5 2D IR Microscopy: Wide-Field Collection

The second implementation of 2D IR microscopy was by Ostrander et al. [33]. In this experimental setup a wide-field approach, in contrast to the raster scanning technique utilized by Baiz et al. [22] was employed to improve upon spatial resolution and

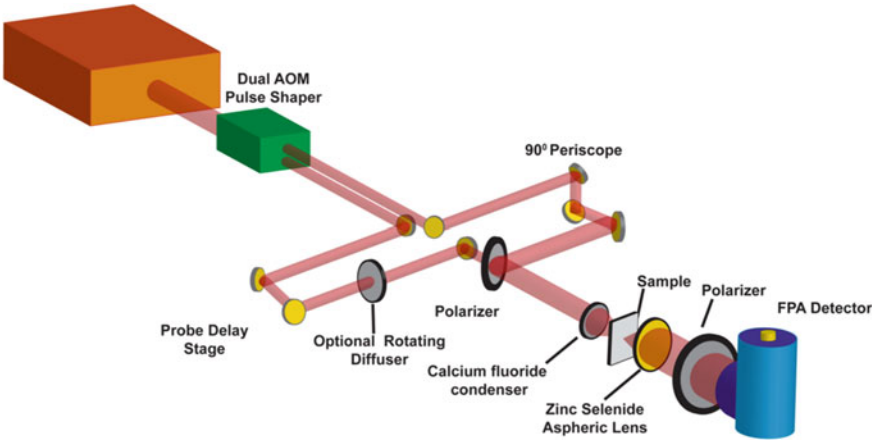

Fig. 14.9 Experimental set-up used by Ostrander et al. Reprinted from [33]

acquisition times. In a wide-field approach the need to scan through the focal plane point by point is eliminated. The experimental setup consisted of a dual acousto optic modulator (AOM) to generate the pump and probe pulses from a single optical parametric amplifier (OPA) (Fig. 14.9). The pulses are centered at 5 μm. The probe pulse is delayed in time relative to the pump pulses. The pump pulses are rotated 90° relative to the probe pulse to allow for the filtering of the desired third order 2D IR signal from background interference. Rotating frame, shifting the observed frequency by 1900 cm^{-1}, is used to reduce the number of data points required. In addition, an eight-frame phase cycling scheme eliminates unwanted background interference with the 2D IR signal. Moreover, in this experimental set-up, unlike point scanning (Fig. 14.10b) where a full 2D IR spectrum is collected at one point, the detector records an image on a 128 × 128-pixel MCT focal plane array detector (FPA), independently for each τ step (Fig. 14.10a). After all values of τ are collected and Fourier transformed a full 2D IR spectral image is generated. Thus, the advantage of this technique is the ability to collect 128 × 128 points simultaneously. The disadvantage being the loss of the ability to collect one axis in the frequency domain via a spectrometer. Instead t_1 and t_3 are stepped from 0 to 3.28 ps, for the purely time domain method of acquisition.

The study by Ostrander et al. [33] was also a proof of concept investigation of polystyrene beads swollen with two different metal carbonyl solutions, DMDC and tungsten hexacarbonyl ($W(CO)_6$). Figure 14.11a is an image of a group of six polystyrene beads with distinct absorption features corresponding to the different metal carbonyl solutions. The beads highlighted in blue indicate the $W(CO)_6$ solution and those in red the DMDC solution. Figure 14.11b exhibits the ability to spatially resolve cross-peaks, showing, in orange the cross peaks attributed to DMDC. Figure 14.11c, d include the corresponding 2D IR spectra collected at a single pixel, for $W(CO)_6$ and DMDC respectively. The orange dotted line in Fig. 14.11d corresponds to the DMDC cross peaks, shown spatially in Fig. 14.11b.

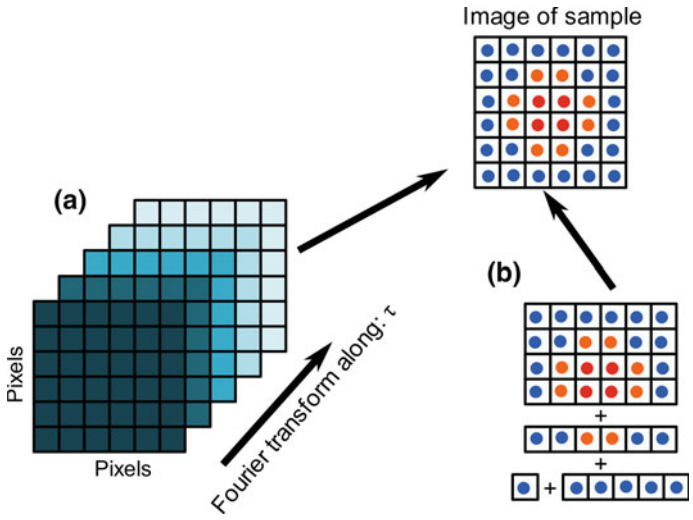

Fig. 14.10 **a** Taking a full image, and then stepping in time to get full 2D IR spectra. **b** Adding full spectra collected separately to get an image

The wide-field technique improves collection time relative to the point scanning method at 1 kHz and allows approximately 16,384 2D IR spectra to be captured in approximately 50 s. The spatial resolution of this system was determined to be between 3.11 and 3.48 μm. This was determined by measuring a series of equally spaced bars on CaF_2 plates. This resolution is better than the predicted Rayleigh criterion of 4.3 μm. This improvement was attributed to the increased resolution gained from nonlinear techniques versus linear techniques (Fig. 14.1).

14.6 2D IR Microscopy at 100 kHz Repetition Rate

A shift from Ti:sapphire laser sources to diode pumped ytterbium oscillators and amplifiers allows for increased repetition rate. This has been demonstrated by Luther et al. [21] and Donaldson et al. [34]. Work by Donaldson and coworkers established that the root mean square noise in mid-IR intensity is approximately 0.15% and there is approximately a 10 μOD peak-to-peak noise in the probe spectrum over 5000 laser shots for a 100 kHz mid-IR laser. This level of noise is similar to values from Ti:sapphire systems. The distinguishing factor being that the collection of these 5000 shots is one-hundredth or one-tenth of the time in a 100 kHz system opposed to 1 or 10 kHz systems. Thus, it is established that Ytterbium based sources can provide higher stability and better signal to noise relative to traditional Ti:sapphire systems. Figure 14.12b shows a comparison of both Ti:sapphire and Ytterbium systems operating at 1 kHz. The estimated laser correlation, r_k, drops more rapidly for the Ti:sapphire system, the red curve. In addition, Kearns et al. [35] have demon-

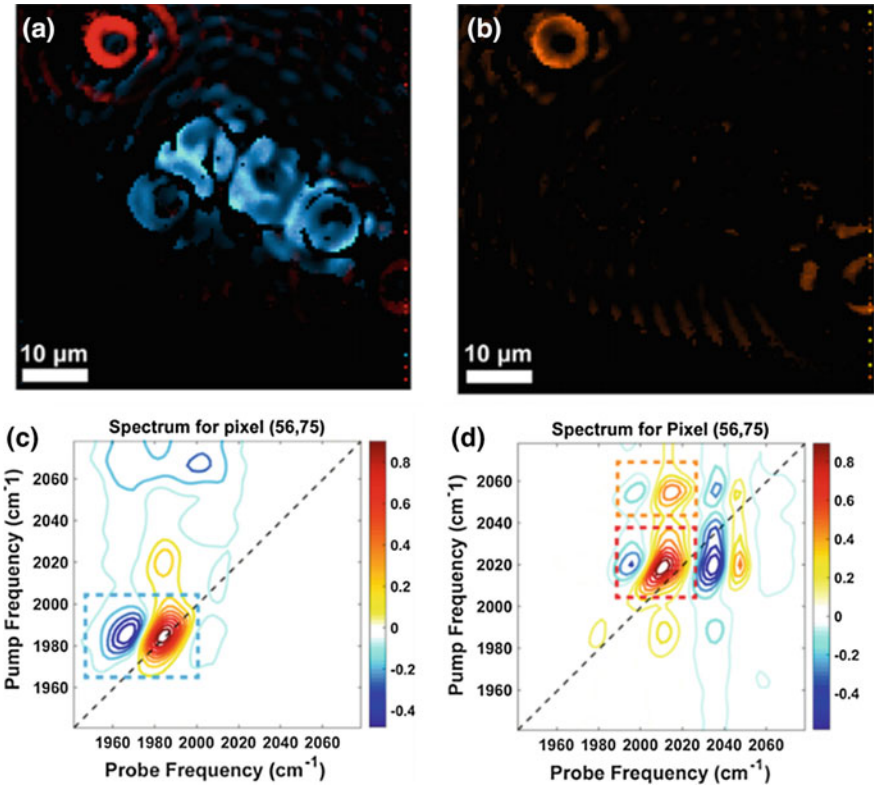

Fig. 14.11 **a** Image of six polystyrene beads, blue representing those swollen with $W(CO)_6$ solution and red those swollen with DMDC. **b** Spatial location of cross peaks for DMDC. **c** Single 2D IR for pixel 56, 75 showing frequency ranges including $W(CO)_6$ absorption features. **d** Single 2D IR for pixel 56, 75 showing frequency ranges including DMDC absorption features. Figure from [33]

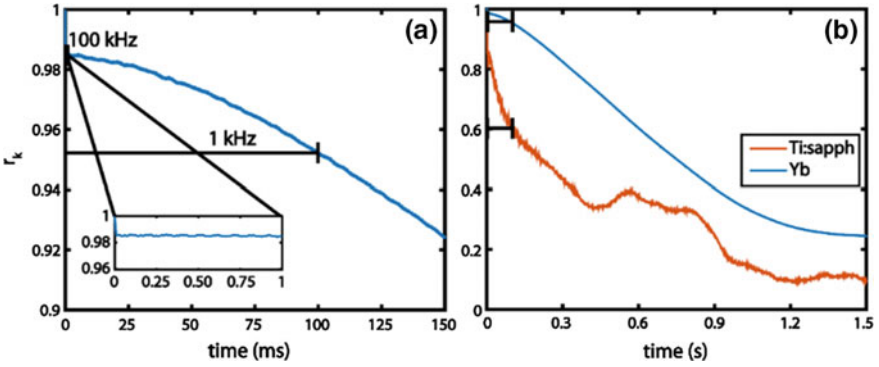

Fig. 14.12 **a** Ytterbium laser, time required for both a 1 kHz and 100 kHz laser. **b** Time required for a Ytterbium laser, blue curve, relative to Ti:sapphire system, red curve. From [34]

strated the advantage of a 100 kHz system by showing that the pulses required are better correlated. This correlation is depicted in Fig. 14.12a [35].

In efforts to combat the limitation of acquisition time in 2D IR microscopy, a 100 kHz 2D IR microscope was developed by Tracy et al. [36] using the 100 kHz mid-IR source setup implemented by Luther et al. [21]. This mid-IR source uses parametric chirped-pulse amplification (OPCPA) in magnesium doped periodically poled lithium niobate (MgO:PPLN) and difference frequency generation (DFG) in zinc germanium diphosphide (ZGP) to generate mid-IR light centered at 4.65 μm [21]. The 2D IR microscopy data are collected in a collinear geometry with a cross polarization configuration. A germanium silicon (Ge/Si) achromatic lens is used to focus the pump and probe pulses onto a sample cell (Fig. 14.13). Transmission through a 10 μm pinhole was used to determine the PSF for the pump and probe beams. Then spatial resolution was determined by the convolution of the point spread function for the pump and probe beams giving a FWHM of ~12 μm.

Isolation of the 2D IR signal was done using 2000 cm^{-1} rotating frame and a four-frame phase cycling scheme. This system allows for the collection of 1984 spectral points per minute, allowing for 2D IR spectra to be collected as a function of waiting time (T_w) across spatially heterogenous samples. A single 2D spectrum can be collected in 0.5 ms.

In the first 100 kHz 2D IR microscopy experiment by Tracy et al. room temperature ionic liquid (RTIL) microdroplet chemistry was investigated [36]. Specifically, a droplet of 1:500 by volume 1-ethyl-3-methylimidazolium tricyanomethanide (Emim TCM) in 1-ethyl-3-methylimidazolium tetrafluoroborate ($EmimBF_4$) was studied, with the TCM^- acting as the vibrational probe. Figure 14.14a is a bright field microscope image of a RTIL microdroplet. Each point on the droplet represents a 2D IR spectrum collected in 25 μm steps across the 450 μm × 600 μm wide image.

Chemical dynamics were investigated by collecting T_w-dependent 2D IR spectra in region of interest (ROI). Nodal line slope (NLS) analysis was used to analyze spectral diffusion at points reporting on the interfacial region versus the bulk region.

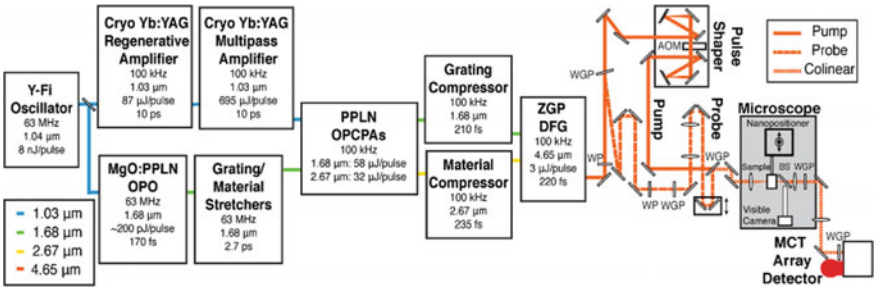

Fig. 14.13 Experimental set-up from Tracy et al. Y–Fi = ytterbium fiber. Cryo Yb:YAG = cryogenically cooled ytterbium doped gain medium, specifically yttrium aluminum garnet. PPLN = periodically poled lithium niobite. OPO = optical parametric oscillator. OPCPA = optical parametrically chirped pulse amplification. ZPG = zinc germanium diphosphide. DFG = difference frequency generation. Reproduced from [21]

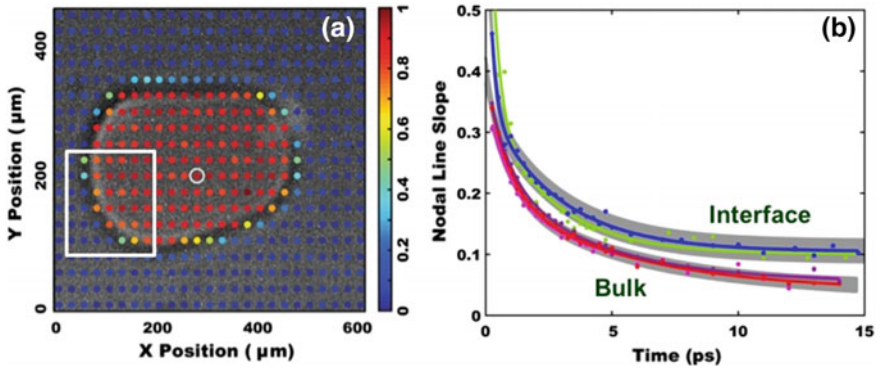

Fig. 14.14 **a** Bright field image IL microdroplet and chemical map generated by integrating over the diagonal peak of TCM^- in the 2D IR spectra collected at each point. The white box indicates the specified region of interest in which waiting time experiments were performed. **b** NLS decay curves for several points within the ROI [36]

Nodal line slope decays in Fig. 14.14b provide evidence that there are distinct spatial regions of the RTIL microdroplet which can be characterized by spectral diffusion measurements.

14.7 2D Fluorescence Detected Microspectroscopy

Fluorescence detected 2D ES was first executed by Wagner et al. in 2005 [24]. One reason for the use of fluorescence detection is increased sensitivity relative to conventional absorption measurements [24]. Wagner et al. investigated rubidium vapor. This first demonstration of fluorescence detection 2D ES used a four interaction, three pulse set-up, with a 16-frame phase cycling scheme to isolate the relevant signals (the phase cycling scheme was proposed and discussed in detail in earlier work) [23].

The first demonstration of fluorescence detected 2D electronic microscopy was by Goetz et al. [27]. This work was a proof of concept study probing the nonlinear response of a laterally heterogenous nanostructured array of F_{16}ZnPc pillars.

As in prior demonstrations of fluorescence-detected 2D ES, [20, 26, 37], a four-interaction excitation sequence is needed. In this case a four-pulse sequence is used (Fig. 14.2).

The measurements were made using a NA of 1.4 giving approximately 260 nm lateral spatial resolution determined by the Abbe diffraction limit. Similar to the 2D IR microscopes discussed previously the optical geometry in this microscope is collinear. Thus, a pulse shaper was utilized to generate a 27-step phase cycling scheme to distinguish and retrieve all relevant nonlinear contributions to the signal. This

phase cycling scheme also tracks photobleaching for each time step and allows for a correction to the signal intensity. The experimental system is shown in Fig. 14.15.

This study chose fluorinated zinc phthalocyanine (F_{16}ZnPc) for a demonstration of 2D ES microscopy, imaging a diffraction-limited hotspot on the film of F_{16}ZnPc. Figure 14.16 is a fluorescence map of the pillar array, with the higher areas of fluorescence considered hotspots. The 2D absorptive spectrum of a hotspot in the F_{16}ZnPc pillar array is shown in Fig. 14.17. This experiment acted as a proof of concept and

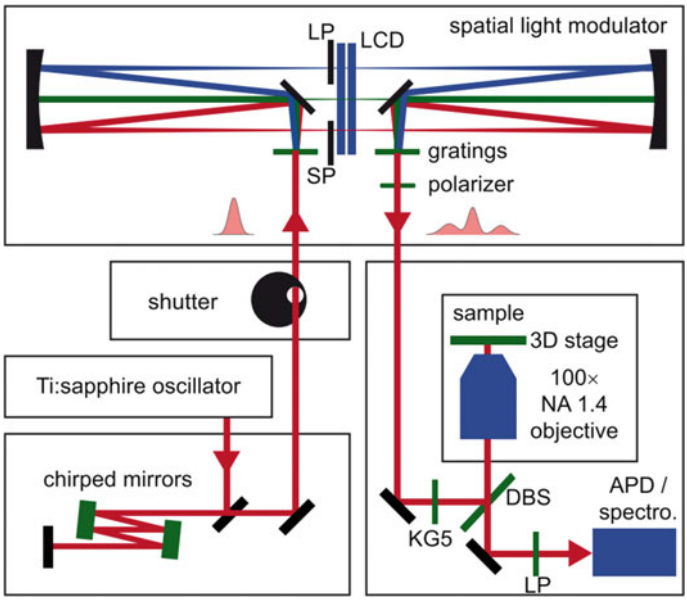

Fig. 14.15 Experimental set-up for Goetz et al. LCD = liquid crystal display, SP = short pass, LP = long pass, APD = Avalanche photodiode. From [27]

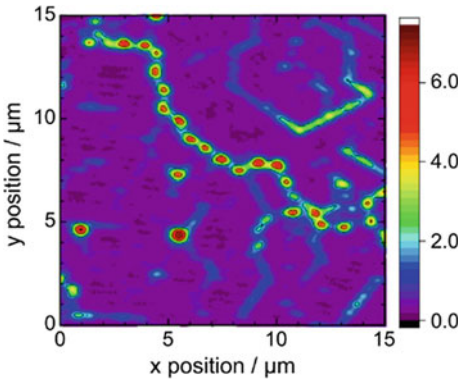

Fig. 14.16 Fluorescence map of the nanostructured array of F_{16}ZnPc pillars. From [27]

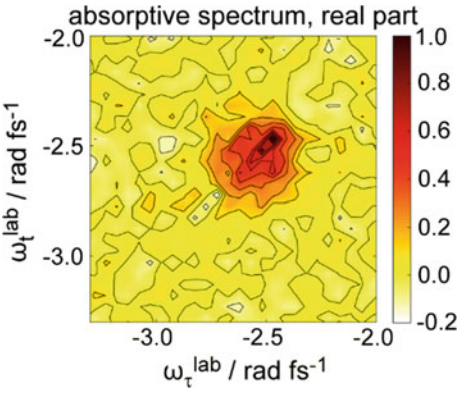

Fig. 14.17 2D absorptive spectrum of a hotspot in the F_{16}ZnPc pillar array with ω_τ being the coherence time between pulses one and two and ω_t between pulses 3 and 4. From [27]

further information about chemical dynamics in this system could be gained with T_w-dependent experiments.

14.8 Spatially Resolved Fluorescence Detected 2D ES

The second display of spatially resolved fluorescence detected 2D electronic spectroscopy (SF 2D ES) was by Tiwari et al. [28]. In this case phase modulation is used, to allow for phase-cycling in 'real-time' as opposed to implementing a combination of multiple phase scans. This is important in fluorescence detection to avoid photo-bleaching and is generally useful to avoid laser fluctuations which decrease the signal to noise. Phase-modulation for fluorescence detected 2D ES was initially implemented by Tekavec et al. [20]. In brief, a four-pulse sequence is generated using a pair of Mach-Zehnder interferometers and four acousto-optic modulators (AOMs) or Bragg cells to tag each pulse with a unique radio-frequency (Fig. 14.18). Each pulse with a specific optical frequency entering the AOM is tagged with a sound wave frequency. This sound wave frequency is generated by a piezoelectric transducer attached to the AOM crystal. Consequently, the nonlinear signals of interest are contained in a population modulated at frequencies that are linear combinations of the radio frequencies coded to the four pulses. The nonlinear signals are then detected using lock-in amplifiers. Moreover, the signal is under sampled by detecting relative to a reference wavelength. This causes the signal to be less sensitive to phase noise.

SF 2D ES is applied, in vivo, to the investigation of purple photosynthetic bacteria grown with varied lighting conditions. SF 2D ES can distinguish differences in the structure of purple bacteria colonies grown under high (HL) or low light (LL) exposure. Spatial resolution is limited, meaning single bacterium cannot be individually investigated. However, excitonic structure across colonies was investigated. Two peaks on the diagonal of the 2D spectra (Fig. 14.19) allow tracking of a monomeric ring of bacteriochlorophyll a (absorbing at ~800 nm therefore referred to as the B800 ring) and a dimeric ring of bacteriochlorophyll a (B850 ring, absorbing at ~850 nm).

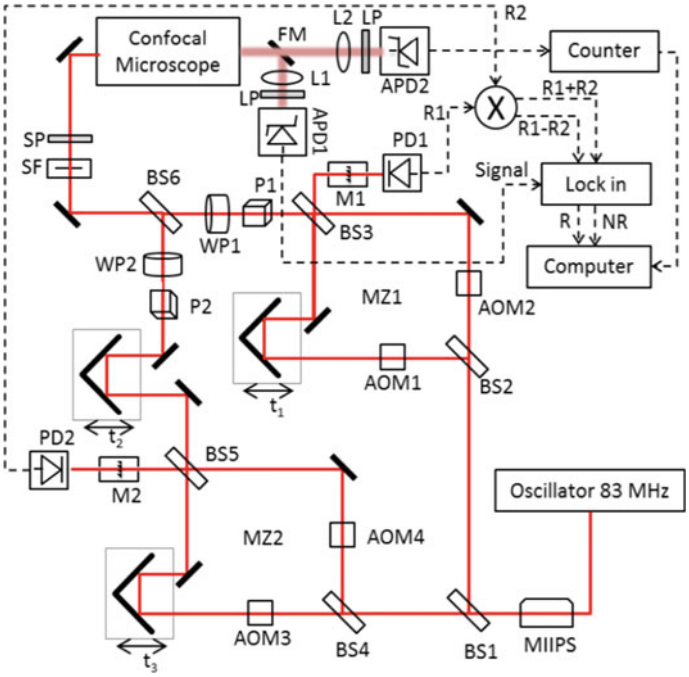

Fig. 14.18 Experimental set-up used by Tiwari et al. SP = Short pass, BS = beam splitter, M = monochromater, WP = waveplate, PD = photodiode, LP = long pass, MZ = Mach Zehnder, AOM = acousto-optic modulator. From [28]

Cross peaks suggest that the B800 and B850 states are coupled, sharing a common ground state. Cross peak signs and amplitudes have previously been shown to be different in conventional 2D ES and fluorescence detected 2D ES [38]. Cross peaks were clearly visible when the waiting time was zero. However, the sample seemed to suffer from the effects of photobleaching at longer times. Thus, to gain more information about system dynamics different sample preparations, and experimental set-up changes could be made to decrease photobleaching.

To demonstrate the ability of SF 2D ES to characterize spatially heterogenous samples, a mixture of HL and LL bacteria was investigated. Spectra for HL and LL grown colonies were used to form a basis to then fit a mixed sample. Different locations on a mixed sample were fit with ratio of the purely HL and LL. Thus, Tiwari et al. [28] show that SF 2D ES can be used to successfully resolve variation in excitonic structure which impacts peak shape and amplitude.

In studying spatially heterogenous systems it is important to consider the volume of the sample that is contributing to the collected signal. In this SF 2D ES experiment the volume of excitation is estimated to be approximately six orders of magnitude below what is estimated for conventional 2D ES (in a non-microscopy system). This is due to the optical sectioning that is enabled by the point spread function of the four-wave mixing (FWM). The sensitivity of this system was estimated by analyzing

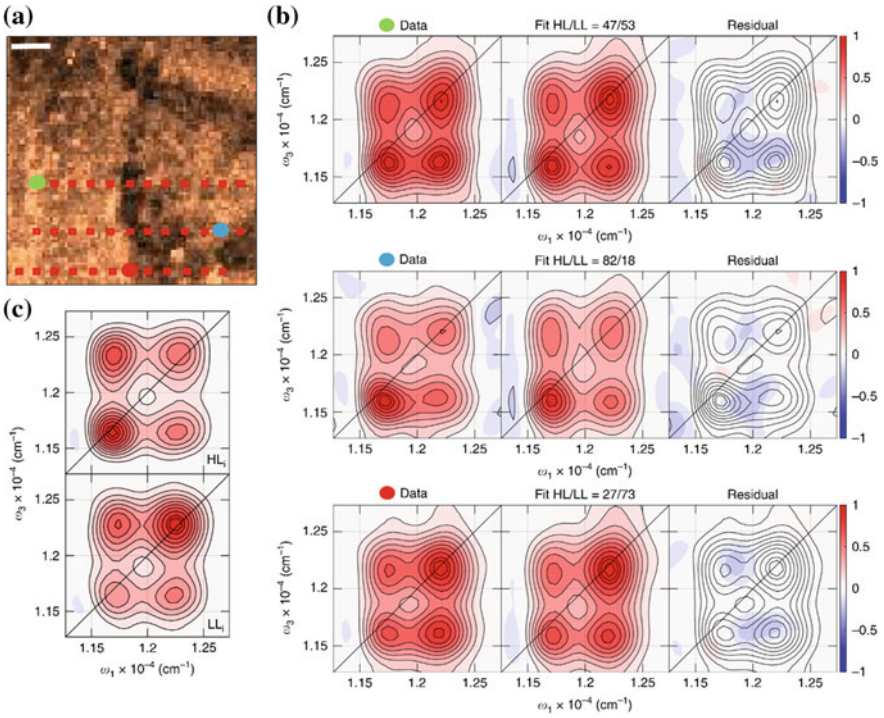

Fig. 14.19 **a** Confocal fluorescence image of a sample of purple photosynthetic bacteria, include HL and LL. Red squares indicate location of 2D ES measurements. Circles correspond to data shown in (**b**). Scale bar is 10 μm. **b** Spectra on left being raw data, middle being a fit, and right the fit residuals. **c** Spectra corresponding to the HH and HL samples of photosynthetic bacteria. From [28]

a 0.5 μm bead. A confocal fluorescence image was collected. The resulting fit to the image gave an average lateral FWHM of 0.83 μm, the theoretically calculated ideal lateral FWHM would have been 0.52 μm, giving a 1.6× deviation from ideal to experimental. This is for the linear case, the FWM non-ideal PSF is estimated as the linear PSF squared. This is shown in the right panel of Fig. 14.20. In this PSF, the volume from which 90% of the FWM signal is generated is then within the 10% contour. Thus, resulting in a ~0.55 μm^3 volume of excitation.

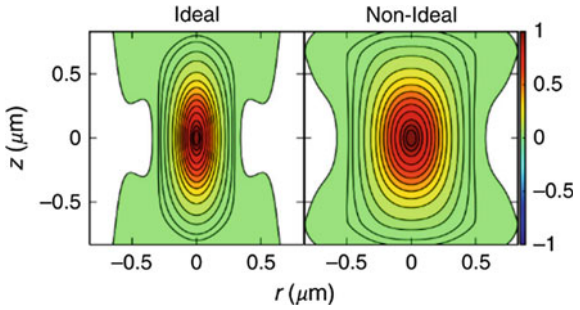

Fig. 14.20 (left) PSF for the ideal diffraction limited case (right) Experimental PSF. From [28]

14.9 Future Directions for Coherent Multidimensional Microspectroscopy

The field of coherent multidimensional spectroscopy has produced high impact results across a wide array of chemical and biological problems. It is expected that spatially resolving the many observables available in a coherent multidimensional spectroscopy experiment will produced another generation of high impact results. However, we are at a crucial point in developing the field of coherent multidimensional microspectroscopy because there are important technical issues that need to be overcome to fully realize the utility of CMDMS techniques. A summary of the successfully implemented approaches to coherent multidimensional microspectroscopy has been compiled into Table 14.3.

14.9.1 Challenges with Mid-IR Detection

The technical issues to overcome are somewhat exacerbated in the mid IR frequency range specifically. The use of Ytterbium based amplifiers and sources in contrast to Ti:sapphire systems will allow access to repetition rates up to the MHz range. However, currently, detection in the mid-IR at repetition rates higher than 100 kHz poses a limitation when attempting to achieve even higher repetition rates. This limitation is caused by the response rates of MCT detectors in the Mid-IR. In addition, signals detected in the mid-IR limit spatial resolution based on the wavelength dependence in the Abbe diffraction limit.

Consequently, future work needs to focus on improvement of mid-IR detection. There are also possibilities of circumventing the need to detect in the mid-IR region, and retrieving similar information about chemical dynamics, using methods such as fluorescence encoding.

Table 14.3 Summary of the current state of CMDMS

	Group Using CMDMS Techniques				
	Tokmakoff [22]	Zanni [33]	Krummel [36]	Brixner [27]	Ogilvie [28]
Year of Publication	2014	2016	*Submitted*	2018	2018
Laser Source	Ti:sapphire	Ti:sapphire	Yttirbium	Ti:sapphire	Ti:sapphire
Type of Spectroscopy	2D IR	2D IR	2D IR	2D ES	2D ES
Repetition Rate	1 kHz	1 kHz	100 kHz	80 MHz	83 MHz
Method of Detection	MCT detection in the Mid-IR	MCT detection in the Mid-IR	MCT detection in the Mid-IR	Fluorescence detection in the visible	Fluorescence detection in the visible
Acquisition time/single 2D spectrum	30 s	~16,384 spectra/50 s	0.5 ms	~ 8 h[a]	12 s[a]
Method of Signal Isolation	8 frame phase cycling	8 frame phase cycling	4 frame phase cycling	27 frame phase cycling	Phase modulation
Sample of Investigation	Metal carbonyl swelled polystyrene beads	Metal carbonyl swelled polystyrene beads	RTIL microdroplet	$F_{16}ZnPc$ nanostructured pillars	Purple photosynthetic bacteria
Reported spatial resolution	4.4 μm	3.48 μm	12.5 μm FWHM of experimental PSF	0.26 μm based on Abbe diffraction limit	0.25 μm × 0.69 μm FWHM of experimental PSF

[a]Referring to the optimal collection time of the system

14.9.1.1 Fluorescence Encoded Infrared Spectroscopy (FT FEIR)

A major factor contributing to high acquisition times is the limit of infrared detector response times. Mastron et al. [39] demonstrated that Fourier Transform Fluorescence-Encoded Infrared Spectroscopy (FT FEIR) can achieve high levels of sensitivity in solution-phase IR spectroscopy (sensitivity as low as pM concentrations). This work exhibits the ability to detect qualitatively similar information about coupled vibrational modes to 2D IR spectroscopy. The samples used to demonstrate FT FEIR were 7-(diethylamino) coumarin (Coumarin 466, C466) in cyclohexane. Certain vibrational modes give rise to similar cross peaks in 2D IR and 2D FEIR despite arising from different physical processes. This technology in conjunction with the successful implementation of fluorescence detected 2D ES microscopy [27, 28] suggests the possibility for expanding the field of multidimensional infrared

microscopy by incorporation of fluorescence encoding. Fluorescence encoding is a promising avenue to improve spatial resolution, allow use of increased repetition rate laser systems, and improve sensitivity of measurements. However, there are still unanswered questions to the impact that spectral diffusion and inhomogeneous broadening may have on 2D FEIR line shapes [39].

In closing, it is clear that the field of CMDMS is in its infancy. However, the recent experimental accomplishments demonstrate the potential of CMDMS experiments to reveal the spatial dependence of chemical structure, chemical dynamics, and energy transport in heterogeneous systems.

References

1. D. Bardell, The biologists' forum: the invention of the microscope. bios **75**, 78–84 (2004). https://doi.org/10.1893/0005-3155(2004)75%3c78:TIOTM%3e2.0.CO;2 (2004)
2. J.A. Kimber, S.G. Kazarian, Spectroscopic imaging of biomaterials and biological systems with FTIR microscopy or with quantum cascade lasers. Anal. Bioanal. Chem. **409**, 5813–5820 (2017). https://doi.org/10.1007/s00216-017-0574-5
3. S. Prati, E. Joseph, G. Sciutto, R. Mazzeo, New advances in the application of FTIR microscopy and spectroscopy for the characterization of artistic materials. Acc. Chem. Res. **43**, 792–801 (2010). https://doi.org/10.1021/ar900274f
4. L.M. Miller, M.W. Bourassa, R.J. Smith, FTIR spectroscopic imaging of protein aggregation in living cells. Biochimica et Biophysica Acta (BBA) - Biomembranes **1828**, 2339–2346 (2013). https://doi.org/10.1016/j.bbamem.2013.01.014 (2013)
5. F. Helmchen, W, Denk, Deep tissue two-photon microscopy. Nat. Methods **2**, 932–940 (2005). https://doi.org/10.1038/NMETH818
6. J. Squier, M. Müller, High resolution nonlinear microscopy: a review of sources and methods for achieving optimal imaging. Rev. Sci. Instrum. **72**, 2855–2867 (2001). https://doi.org/10.1063/1.1379598
7. R. Carriles, D.N. Schafer, K.E. Sheetz, et al., Invited review article: imaging techniques for harmonic and multiphoton absorption fluorescence microscopy. Rev. Sci. Instrum. **80**, 081101 (2009). https://doi.org/10.1063/1.3184828
8. D.J. Kissick, D. Wanapun, G.J. Simpson, Second-order nonlinear optical imaging of chiral crystals. Annu. Rev. Anal. Chem. **4**, 419–437 (2011). https://doi.org/10.1146/annurev.anchem.111808.073722
9. R.J. Tran, K.L. Sly, J.C. Conboy, Applications of surface second harmonic generation in biological sensing. Annu. Rev. Anal. Chem. **10**, 387–414 (2017). https://doi.org/10.1146/annurev-anchem-071015-041453
10. J.P.R. Day, K.F. Domke, G. Rago et al., Quantitative Coherent Anti-Stokes Raman Scattering (CARS) Microscopy. J. Phys. Chem. B **115**, 7713–7725 (2011). https://doi.org/10.1021/jp200606e
11. C.L. Evans, X.S. Xie, Coherent Anti-Stokes Raman scattering microscopy: chemical imaging for biology and medicine. Annu. Rev. Anal. Chem. **1**, 883–909 (2008). https://doi.org/10.1146/annurev.anchem.1.031207.112754
12. D. Polli, V. Kumar, C.M. Valensise et al., Broadband coherent Raman Scattering Microscopy. Laser Photonics Rev. **12**, 1800020 (2018). https://doi.org/10.1002/lpor.201800020
13. A. Hanninen, M.W. Shu, E.O. Potma, Hyperspectral imaging with laser-scanning sum-frequency generation microscopy. Biomed Opt. Express **8**, 4230–4242 (2017). https://doi.org/10.1364/BOE.8.004230

14. C.M. Lee, K. Kafle, S. Huang, S.H. Kim, Multimodal broadband vibrational sum frequency generation (MM-BB-V-SFG) spectrometer and microscope. J. Phys. Chem. B. **120**, 102–116 (2016). https://doi.org/10.1021/acs.jpcb.5b10290
15. Y. Li, D. Chen, H. Niu, A method for achieving super resolution vibrational sum-frequency generation microscopy by structured illumination. IEEE Photonics J. **9**, 1–8 (2017). https://doi.org/10.1109/JPHOT.2017.2705124
16. R. Heintzmann, G. Ficz, Breaking the resolution limit in light microscopy. Brief. Func. Genomics **5**, 289–301 (2006). https://doi.org/10.1093/bfgp/ell036
17. J. Squier, M. Müller, High resolution nonlinear microscopy: a review of sources and methods for achieving optimal imaging High resolution nonlinear microscopy: a review of sources and methods for achieving optimal imaging. Rev. Sci. Instrum. **2855**, 2855–2867 (2001). https://doi.org/10.1063/1.1379598
18. P. Hamm, M. Zanni, *Concepts and Methods of 2D Infrared Spectroscopy*. (Cambridge University Press, 2011)
19. S. Mukamel, *Principles of Nonlinear Optical Spectroscopy* (Oxford University Press, New York, 1999)
20. P.F. Tekavec, G.A. Lott, A.H. Marcus, Fluorescence-detected two-dimensional electronic coherence spectroscopy by acousto-optic phase modulation Fluorescence-detected two-dimensional electronic coherence spectroscopy by acousto-optic phase modulation. J. Chem. Phys. **127**, 214307 (2007). https://doi.org/10.1063/1.2800560
21. B.M. Luther, K.M. Tracy, M. Gerrity et al., 2D IR spectroscopy at 100 kHz utilizing a Mid-IR OPCPA laser source. Opt. Express **24**, 10095–10100 (2016). https://doi.org/10.1364/OE.24.004117
22. C.R. Baiz, D. Schach, A. Tokmakoff, Ultrafast 2D IR microscopy. Opt. Express **22**, 875–885 (2014). https://doi.org/10.1364/OE.22.018724
23. D. Keusters, H. Tan, W.S. Warren, Role of Pulse Phase and Direction in Two-Dimensional Optical Spectroscopy. J. Phys. Chem. A **103**, 10369–10380 (1999). https://doi.org/10.1021/jp992325b
24. W. Wagner, C. Li, J. Semmlow, W. Warren, Rapid phase-cycled two-dimensional optical spectroscopy in fluorescence and transmission mode. Opt. Express **13**, 3697–3706 (2005). https://doi.org/10.1364/OPEX.13.003697
25. S. Shim, M.T. Zanni, How to turn your pump—probe instrument into a multidimensional spectrometer: 2D IR and vis spectroscopies via pulse shaping. Phys. Chem. Chem. Phys. **11**, 748–761 (2009). https://doi.org/10.1039/b813817f
26. S. Draeger, S. Roeding, T. Brixner, Rapid-scan coherent 2D fluorescence spectroscopy. Opt. Express **25**, 3259 (2017). https://doi.org/10.1364/OE.25.003259
27. S. Goetz, D. Li, V. Kolb et al., Coherent two-dimensional fluorescence micro-spectroscopy. Opt. Express **26**, 3915 (2018). https://doi.org/10.1364/OE.26.003915
28. V. Tiwari, Y.A. Matutes, A.T. Gardiner, et al., Spatially-resolved fluorescence-detected two-dimensional electronic spectroscopy probes varying excitonic structure in photosynthetic bacteria. Nat. Commun. **9**, 4219 (2018) https://doi.org/10.1038/s41467-018-06619-x
29. J. Almeida, J. Prior, M.B. Plenio, Computation of two-dimensional spectra assisted by compressed sampling. J. Phys. Chem. Lett. **3**, 2692–2696 (2012). https://doi.org/10.1021/jz3009369
30. J.N. Sanders, S.K. Saikin, S. Mostame, et al., Compressed sensing for multidimensional spectroscopy experiments. J. Phys. Chem. Lett. **3**, 2697–2702 (2012). https://doi.org/10.1021/jz300988p
31. J.A. Dunbar, D.G. Osborne, J.M. Anna, K.J. Kubarych, Accelerated 2D-IR using compressed sensing. J. Phys. Chem. Lett. **4**, 2489–2492 (2013). https://doi.org/10.1021/jz401281r
32. S.T. Roberts, J.J. Loparo, A. Tokmakoff, Characterization of spectral diffusion from two-dimensional line shapes. J. Chem. Phys. **125**, 084502 (2006). https://doi.org/10.1063/1.2232271
33. J.S. Ostrander, A.L. Serrano, A. Ghosh, M.T. Zanni, Spatially resolved two-dimensional infrared spectroscopy via wide- field microscopy. ACS Photonics **3**, 1315–1323 (2016). https://doi.org/10.1021/acsphotonics.6b00297

34. P.M. Donaldson, G.M. Greetham, D.J. Shaw et al., A 100 kHz pulse shaping 2D-IR spectrometer based on dual Yb:KGW amplifiers. J. Phys. Chem. A **122**, 780–787 (2018). https://doi.org/10.1021/acs.jpca.7b10259
35. N.M. Kearns, R.D. Mehlenbacher, A.C. Jones, M.T. Zanni, Broadband 2D electronic spectrometer using white light and pulse shaping: noise and signal evaluation at 1 and 100 kHz. Opt. Express **25**, 7869 (2017). https://doi.org/10.1364/OE.25.007869
36. K.M. Tracy, B. Guchhait, C.A. Tibbetts, et al., Visualizing chemical dynamics in an ionic liquid microdroplet using ultrafast 2DIR microscopy. In preparation (2019)
37. A.K. De, D. Monahan, J.M. Dawlaty, G.R. Fleming, Two-dimensional fluorescence-detected coherent spectroscopy with absolute phasing by confocal imaging of a dynamic grating and 27-step phase-cycling. J. Chem. Phys. **140**, 194201 (2014). https://doi.org/10.1063/1.4874697
38. G.A. Lott, A. Perdomo-ortiz, J.K. Utterback, et al., Conformation of self-assembled porphyrin dimers in liposome vesicles by phase-modulation 2D fluorescence spectroscopy. Proc. Natl. Acad. Sci. USA, **108**, 16521–16526 (2011). https://doi.org/10.1073/pnas.1017308108
39. J.N. Mastron, A. Tokmako, Fourier transform fluorescence-encoded infrared spectroscopy. J. Phys. Chem. A **122**, 554–562 (2018). https://doi.org/10.1021/acs.jpca.7b10305

Chapter 15
Frequency Comb-Based Multidimensional Coherent Spectroscopy

Bachana Lomsadze and Steven T. Cundiff

Abstract We present a novel approach to multidimensional coherent spectroscopy that utilizes optical frequency combs. This approach enables the measurement of a multidimensional coherent spectrum rapidly and with unprecedented frequency resolution. To demonstrate the improvements in resolution and data acquisition speed we apply this method to Doppler broadened Rb atoms whose energy level splittings are of the order of hundreds of MHz and measure a rephasing 2D spectrum. We also show how this method can probe and give insight about extremely weak dipole-dipole interactions in an atomic vapor. This novel method has the potential to become a field deployable device for chemical sensing applications.

15.1 Introduction

Optical multidimensional coherent spectroscopy (MDCS) [1] is a very powerful technique that has been developed over the last two decades for studying structure, properties and ultrafast dynamics of a wide range of materials [2–6]. MDCS is an optical analog of multidimensional Nuclear Magnetic Resonances (NMR) spectroscopy [7], which enabled the determination of molecular structure. Optical MDCS uses a sequence of pulses (typically three, denoted A, B, C) incident on the sample of interest and detects a four-wave-mixing (FWM) signal emitted by the sample as a function of the time delay(s) between the excitation pulses. A multidimensional spectrum is then generated by taking Fourier transforms of the FWM signal with respect to the time delays between the pulses.

B. Lomsadze (✉) · S. T. Cundiff
Department of Physics, University of Michigan, Ann Arbor, MI 48109, USA
e-mail: blomsadze@scu.edu

S. T. Cundiff
e-mail: cundiff@umich.edu

B. Lomsadze
Department of Physics, Santa Clara University, Santa Clara, CA 90503, USA

M. Cho (ed.), *Coherent Multidimensional Spectroscopy*,
Springer Series in Optical Sciences 226,
https://doi.org/10.1007/978-981-13-9753-0_15

A multidimensional spectrum contains rich spectroscopic information compared to a linear spectrum. Depending on the time ordering of the excitation pulses it can give insight into different physical properties/phenomena. For instance, if the photon-echo [8] excitation scheme is used where the first pulse is complex phase conjugated (A*, B, C), a multidimensional spectrum, referred to as a single-quantum 2D spectrum, shows the coupling between the excited states. A single-quantum 2D spectrum can also differentiate the homogenous and inhomogeneous linewidths and track the energy redistribution in complex systems in real time. This information cannot be simultaneously obtained by any other known linear or nonlinear optical methods. On the other hand, if the complex phase-conjugated pulse arrives last (B, C, A*) then the corresponding 2D spectrum, referred to as a double-quantum 2D spectrum, can identify weak many-body interactions [9, 10]. For example, a double-quantum 2D spectrum can probe long range dipole-dipole interactions in atomic and molecular systems. This capability is very important as these interactions govern the physical mechanisms of many phenomena (e.g. photosynthesis and formation of complex molecules) [11–13].

Over the years, several MDCS methods have been developed both in the visible and IR regions that utilize either a collinear or box geometry configuration. However, these techniques require long acquisition time (when implemented using mechanical stages) and/or provide low spectral resolution (limited by spectrometer resolution, pulse shaper resolution or the time delays achievable by various techniques) [3, 14–23]. Due to these limitations, these methods have only been used so far to probe systems that have broad resonances or dephasing dynamics. They have not been able to probe atomic systems (both cold and Doppler broadened) where the dephasing times are measured in nanoseconds and energy level splittings are of the order of tens to hundreds of MHz [24–28]. In addition, currently available methods struggle to distinguish very congested ro-vibrational levels in complex molecules and identify the energy transfer between these states.

We note that previously multidimensional coherent spectroscopy has been used to measure single and double-quantum spectra of atomic systems [4, 29] (rubidium, Rb, and potassium, K) with the goal to investigate long-range dipole-dipole interactions in dilute atomic vapors. However, due to spectrometer resolution limitations, an argon (Ar) buffer gas was introduced into the vapor cell to artificially broaden the resonances and match them to the spectrometer resolution. The experiments were able to give insight about basic properties and underlying physics of dipole-dipole interactions. However, the broadening led to the modification of the resonance lineshapes [30] and hence the measurements did not provide a complete picture of the interactions and dynamics in an atomic vapor. In addition, the measurements could not differentiate the interactions between the same and different isotope atoms, which is critical for understating the formation of homo and hetero-nuclear molecules.

To overcome the resolution and acquisition speed limitations we recently developed a novel approach to performing MDCS that utilizes a dual-comb spectroscopy (DCS) detection technique [31, 32]. In DCS one frequency comb (typically a mode-locked laser) is used to excite the sample and the response is sampled in time with another comb (Local Oscillator LO) that has a slightly different repetition rate.

The resulting interferogram is captured by a single photodetector. In the frequency domain, the DCS arrangement produces a Radio Frequency (RF) comb spectrum that results from these two optical combs beating against each other on a photodetector [33]. The RF spectrum directly maps to the optical absorption spectrum of the sample. DCS is similar to Fourier-transform infrared (FTIR) [34] spectroscopy but contains no moving elements and hence enables the measurement of a broad absorption spectrum rapidly and with high spectral resolution. In addition, dual-comb spectroscopy is becoming compact with the development of mirco-resonators [35–39] for the applications outside the laboratory (LIDAR, chemical detection, etc.) [31, 40, 41].

In the next section, we describe the marriage of DCS and MDCS methods [42, 43] that we call M-DCS^2. This combination enables the measurement of a multidimensional coherent spectrum rapidly and with high resolution. These improvements now make MDCS relevant for systems with long dephasing rates particularly for atomic and molecular systems. To show the improved resolution and acquisition speed we apply the novel method to Doppler broadened Rb atoms and measure a single-quantum two-dimensional spectrum. In the following section, we will also show how M-DCS^2 can be used to measure a double-quantum two-dimensional spectrum that probes extremely weak many-body interactions (dipole-dipole interactions) in Rb atomic vapor and gives insight about the effects of thermal motion on dipole-dipole interactions [44]. In the last section, we introduce a novel approach to comb-based multidimensional coherent spectroscopy, Tri-comb spectroscopy (TCS) [45] that contains no mechanical moving parts and enables the measurement of a comb-resolution two-dimensional spectrum in under half a second. This approach has the potential to become a field deployable device for chemical sensing applications.

15.2 Frequency Comb-Based Single-Quantum Multidimensional Coherent Spectroscopy

A schematic diagram of frequency comb-based single-quantum multidimensional coherent spectroscopy is shown in Fig. 15.1a. We briefly describe the experiment here, please see Ref. [42] for details. We used two-home built Kerr-lens mode-locked Ti:Sapphire lasers with locked repetition frequencies. The comb offset frequencies were not stabilized but the phase fluctuations due to the relative repetition frequency (between two combs), offset frequencies and path length fluctuations were measured and corrected [46]. The output of the signal comb was split into two parts. One part was frequency shifted using an accousto-optical modulator (AOM) and then combined with the other part whose delay was controlled using a retro-reflector mounted on a mechanical stage. The combined beams were then focused to a 5 μm spot in a 0.5 mm thin vapor cell. The cell contained ^{87}Rb and ^{85}Rb atoms at 100 °C. The beams were optically filtered to excite only the D_1 lines of both Rb isotopes.

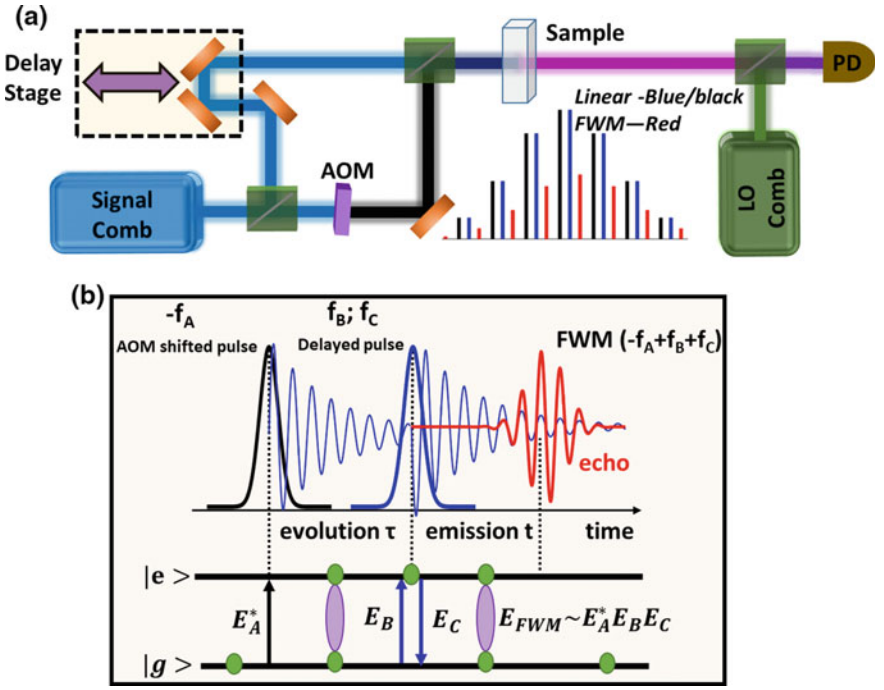

Fig. 15.1 **a** Experimental setup for M-DCS[2]. Two combs with different offset frequencies are generated using a signal comb and an acousto-optical modulator. These combs then interact with the sample and generate a FWM signal at a different time delay between combs. The FWM signal is sampled using a LO comb. **b** Photon echo excitation scheme (please see the text for details), |g>-ground state, |e>-excited state

For this experiment we used a photon echo excitation scheme to generate a four-wave-mixing (FWM) signal (shown in Fig. 15.1b). In this scheme the first pulse is a complex phase-conjugated pulse (E_A*) and excites a coherence between the ground state and the excited state. The second pulse (E_B) then converts this coherence into a population of the excited (or ground) state and then it (E_C) converts this population into the third-order coherence that radiates the FWM signal (photon echo shown in red). The FWM signal is then interfered with the LO comb (that has a slightly different repetition frequency) on a photodetector and isolated from the linear signals in the RF domain (please see below for details). To generate the second axis for the two-dimensional spectrum the delay between the excitation pulses was varied from 0 to 3.3 ns with 10 ps steps. A two-dimensional coherent spectrum was generated by calculating Fourier transforms of the FWM signal with respect to the emission and evolution times.

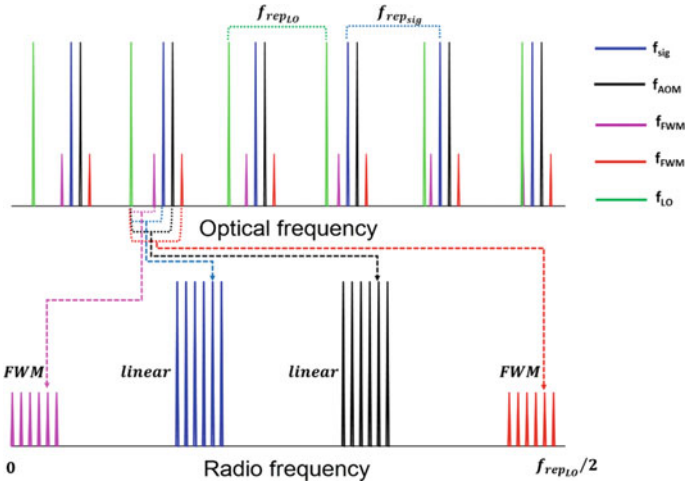

Fig. 15.2 Schematic diagram showing how the linear and FWM comb lines are separated after down converting them from the optical to RF domain

15.2.1 Separation of Linear and FWM Signals

Figure 15.2 shows the generation and separation of the FWM signal in the frequency domain. The black lines correspond to the AOM shifted comb lines, blue lines correspond to the original (signal) comb lines and the red and magenta lines correspond to the generated FWM signals. The green lines correspond to the LO comb teeth. The detector in Fig. 15.1a measures the interference between all of these lines which produces multi-heterodyne beat signals in the RF domain where the linear and FWM signals are spectrally separated (Fig. 15.2, bottom plot). We note that both FWM combs are present only at a zero delay between the excitation pulses but only one is generated for a finite time delay due to causality.

15.2.2 Results

Figure 15.3a, b show the energy level diagram and the measured linear absorption spectrum of the D_1 lines of ^{87}Rb and ^{85}Rb atoms, respectively. The absorption axis is plotted with respect to an arbitrary reference, $f_{\text{ref}} = 377.103258084$ THz. The natural linewidths of the hyperfine lines (a–h) for Rb atoms are about 6 MHz, however the absorption profile at 100C is Doppler broadened up to ~600 MHz and hence the hyperfine lines are overlapped. In Fig. 15.4a, b we show two-dimensional spectra measured using cross-linearly (HVV-H) and co-linearly (HHH-H) polarized excitation pulses, respectively. The negative values on the absorption/evolution axis reflect

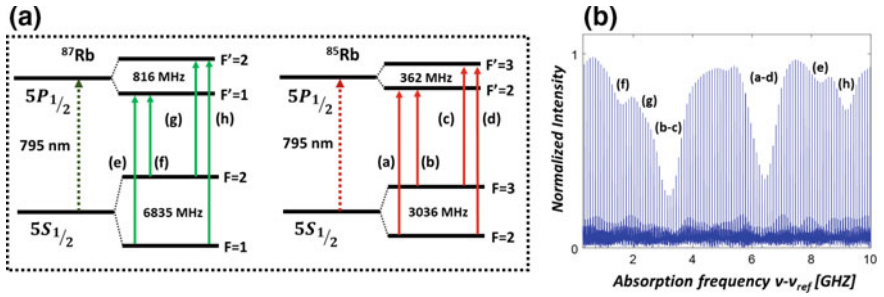

Fig. 15.3 **a** Energy level diagram of ^{87}Rb and ^{85}Rb atoms D1 hyperfine lines. **b** Measured transmission spectrum for ^{87}Rb and ^{85}Rb. $\nu_{\text{ref}} = 377.103258084$ THz

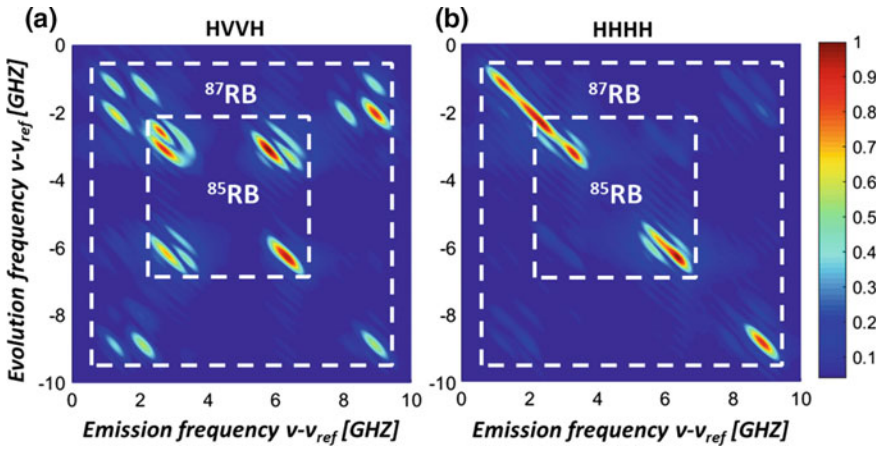

Fig. 15.4 Measured two-dimensional spectra generated by **a** cross-linearly (HVVH) and **b** co-linearly (HHHH) polarized excitations pulses. H-Horizontal, V-Vertical. $\nu_{\text{ref}} = 377.103258084$ THz. The color scale shows the normalized signal magnitude

the negative phase evolution during the evolution period in the photon echo excitation sequence (Please see Fig. 15.1b).

The diagonal peaks (along the (0, 0) and (10, –10) line) correspond to absorption/evolution and emission at the same (a–h) resonance frequencies. The elongation in the diagonal direction is due to Doppler broadening. Along the cross-diagonal direction the inhomogeneity is removed and the line shapes reflect the homogeneous linewidth. Although the resolution in this direction is limited by the scan range achievable with the mechanical stage, we are able to see the hyperfine structure and all possible couplings between the resonances that appear at unique locations [42]. It is also clear that the two-dimensional energy spectra do not show the coupling peaks between ^{87}Rb and ^{85}Rb isotopes indicating that they behave as two independent atoms. This is valuable information for chemical sensing applications especially when detecting a mixture without prior knowledge of its constituent species.

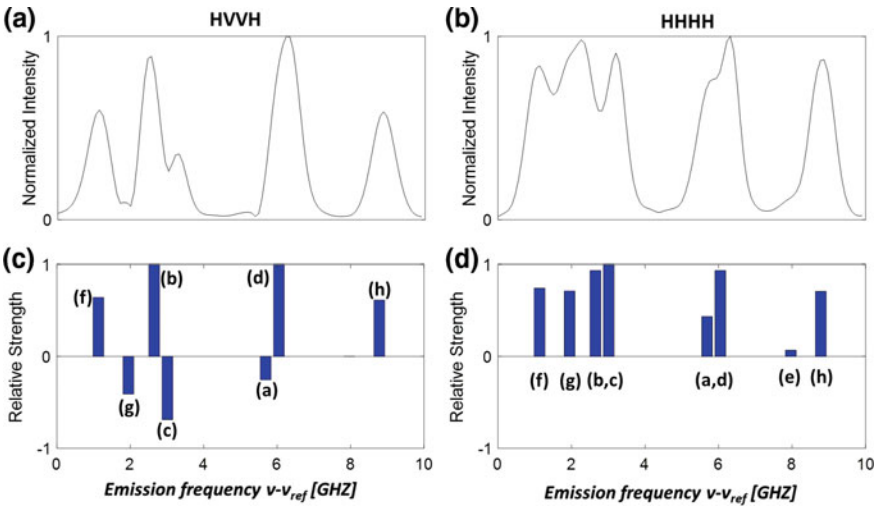

Fig. 15.5 Diagonal slices of Fig. 15.4a, b respectively. **c** and **d** Theoretical simulations showing the strength of the FWM signal at each hyperfine resonance (**a**–**h**) for HVVH and HHHH cases

Some of the diagonal peaks are suppressed for HVVH case compared to HHHH case. In Fig. 15.5a, b the diagonal slices of Fig. 15.4a, b are plotted. The slices show that peaks at (g, c, a) frequencies are suppressed and the peak at (e) frequency is absent for HVVH case. We explained this behavior by calculating all possible double-sided Feynman diagrams [47] for each state (including the magnetic sub-levels) in HHHH and HVVH cases respectively. Our simulations showed that for the HVVH case the FWM signals for F to F'= F transitions had the opposite sign compared to the F to F'= F $\pm$ 1 transitions, which caused the closely spaced neighboring peaks to be partially canceled. The simulation also showed that the FWM signal is zero for F = 1 to F' = 1 transition for ^{87}Rb. For the HHHH case, all of the Feynman diagrams have the same sign and hence the peaks do not cancel each other. The results of our calculation shown in Fig. 15.5c, d are in good agreement with the experimental results. The slight mismatch between theory and experiment we attribute to laser pulse propagation effects.

Lastly, the two-dimensional plots in Fig. 15.4 show additional interesting behavior. The strengths of the off-diagonal peaks are not the geometric mean of its corresponding diagonal peaks strengths that is expected for a 3-level system. Furthermore, some of the peaks are even weaker than their corresponding diagonal peaks. For instance the peak around (3, –6.5) GHz on Fig. 15.4b is much weaker compared to peaks at (3, –3) GHz and (6.5, –6.5) GHz that correspond to the F = 3 to F' = 3 and F = 2 to F' = 3 transitions in ^{85}Rb, respectively. This can be explained with the fact that F = 2 state has 5 magnetic sub-levels whereas F = F' = 3 has 7 sub-levels. In the linear polarization bases (π) all the sublevels of the F = 2 and F = 3 states contribute for the diagonal peaks (except $m_F = 0$ for the F = 3 to F' = 3 transitions whose Clebsh–Gordan coefficient is zero). However only (m_F = –2, –1, 1, 2) sub-levels

of the F = 2 and F = 3 hyperfine states contribute for the off-diagonal peak. Our theoretical calculation showed good agreement with the experimental results for this and other off-diagonal peaks as well.

We also would like to note that the two-dimensional spectra shown in Fig. 15.4a, b were generated in under 4 min. Similar resolution either is not achievable or requires several hours or even days of acquisition time with currently available methods.

15.3 Frequency Comb-Based Double-Quantum Multidimensional Coherent Spectroscopy

As shown above, frequency comb-based single-quantum multidimensional coherent spectroscopy is a very powerful method however it cannot provide complete information about the sample. Particularly it cannot access information such as many-body interactions (dipole-dipole interactions) and collective effects in an atomic vapor. These interactions are extremely weak and single-quantum two-dimensional spectroscopy is not sensitive enough to isolate the FWM signal that is due to interactions from the signal that is produced by an individual atom. This can clearly be seen from the Fig. 15.4a, b above. The FWM signal due to the couplings of two different atoms via dipole-dipole interactions is nonzero however its strength is very weak and it is not noticeable in the graph. To probe these processes the measurement of a double-quantum two-dimensional spectrum is required.

Frequency comb based double-quantum multidimensional coherent spectroscopy [44] is an extension of a single-quantum multidimensional coherent spectroscopy. Experimentally its spectrum can be generated with the same experimental apparatus shown above (Fig. 15.1a) but swapping the time order of the excitation pulses such that the AOM shifted pulse arrives last.

The generation of a double-quantum FWM signal in the time domain is shown in Fig. 15.6a. The first pulse excites the coherence between the ground and excited states and then it converts into the coherence between the ground and doubly excited states. The doubly excited coherence evolves with the frequency that corresponds to the energy difference between the ground and doubly excited states. The second pulse then converts this coherence either back to the single coherence between the ground and excited states or to the coherence between the excited and doubly excited states. This coherence emits the FWM signal that is detected as a function of the emission time and the evolution time between the excitation pulses. However, in the experiment, the laser spectrum was filtered such that it could not excite any doubly excited states in Rb atoms (Fig. 15.6b). In this case the generation of a double-quantum FWM signal can be explained by introducing a combined atom picture shown in Fig. 15.6c where the doubly-excited state indicates that both atoms are in the excited state. But it is critical to note that the combined picture itself (shown in Fig. 15.6c) cannot produce any FWM signal as the contributions shown in Fig. 15.6d (described using Double-sided Feynman diagrams) have opposite signs and equal

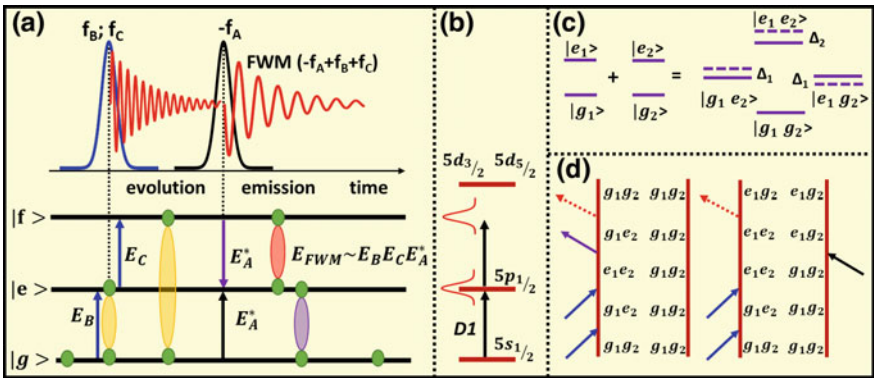

Fig. 15.6 **a** The generation of a FWM signal in the double-quantum excitation scheme. |g>-ground state, |e>-excited state, |f> doubly excited state. **b** Energy level diagram of Rb showing no energy level at 2 × D1 frequency. **c** Energy level diagram of two combined atoms without interaction (solid lines) and with interaction (dashed lines). **d** Double-sided Feynman diagrams of the double-quantum FWM signals

strengths. However, in the presence of interactions (even very weak interactions such as dipole-dipole interactions) singly and doubly excited states experience slight energy shifts (dashed lines shown in Fig. 15.6c) or changes in their linewidth. These changes lead to only partial cancelation in the contributions described above and hence the generation of a FWM signal.

Figures 15.7a, b show a two-dimensional double-quantum spectrum measured by the cross-linearly (HVV-H) and co-linearly (HHH-H) polarized excitation pulses, respectively. The diagonal peaks (along the (0, 0) and (10, 20) GHz line) correspond to coupling between the same hyperfine energy levels (a–h lines shown in Fig. 15.3a) of two atoms whereas the off-diagonal peaks show coupling between different hyperfine

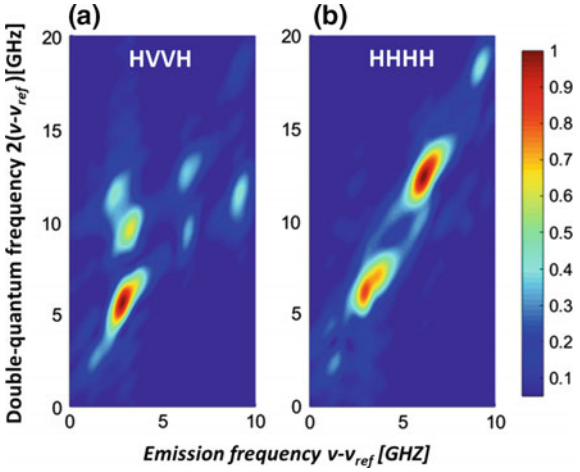

Fig. 15.7 **a** and **b** Double-quantum spectrum generated by cross-linearly and co-linearly polarized excitation pulses. ν_{ref} = 377.103258084 THz. The color scale shows the normalized signal magnitude

energy levels of two atoms of the same and different isotopes (please see [44] for details). It is important to emphasize that the signal in this experiment is only due to interactions between two independent atoms and contains no information about the signal that is due to an individual atom. Hence frequency comb-based double-quantum MDCS excels in isolating and identifying many-body interactions with extremely high precision.

In Fig. 15.7a, b it is clear that the peaks are diagonally elongated which suggests that the emission and double-quantum frequencies are correlated. The elongation has never been observed for Doppler broadened atomic systems (due to resolution limitations of current MDCS methods). The correlation indicates that the FWM signal is predominantly from those two atoms that have near zero relative velocity.

To show this point we solved optical Bloch-equations for a two coupled two-level system and included the inhomogeneous broadening using a generalized two-dimensional Gaussian function [48]:

$$f(x,y)=\frac{1}{2\pi\sigma_x\sigma_y\sqrt{1-\rho^2}}e^{-\left\{[(x-\mu_x)/\sigma_x]^2-2\rho[\frac{x-\mu_x}{\sigma_x}][\frac{y-\mu_y}{\sigma_y}]+\left[(y-\mu_y)/\sigma_y\right]^2\right\}/2(1-\rho^2)}$$

where: μ_x, μ_y, σ_x, and σ_y, are the centers and widths of two interacting Doppler-broadened resonances and ρ is a correlation parameter. For Doppler broadened systems $\rho = 1$ (perfect correlation) indicates that only those two atoms that have zero relative velocity are coupled where as $\rho = 0$ corresponds to coupling of two atoms with any relative velocity.

The simulated double-quantum 2D spectra for $\rho = 0$ and $\rho = 0.75$ are shown in Fig. 15.8a, b, respectively. It is clear that the peaks in both spectra are diagonally elongated. To compare the experimental and theoretical results we used the elipticity as a metric to describe the peak elongation. The elipticity is defined as

$$E=\frac{a^2-b^2}{a^2+b^2}$$

where a and b are the sizes of the ellipse along the major and minor axes (Fig. 15.8a). The ellipticity for Fig. 15.8a is 0.5 whereas for Fig. 15.8b it is 0.85 which is in good agreement with the ellipticity of the experimental results (Fig. 15.7a, b). $E = 0.85$ corresponds to $\rho = 0.75$ which indicates that the FWM signal is due to atoms that have near zero relative velocity.

In summary, frequency-comb based double-quantum multidimensional spectra identified the collective hyperfine resonances in atomic vapor (containing two different isotopes) that were induced by dipole-dipole interactions. In addition the measured spectra gave insight of the effects of thermal motion on dipole-dipole interactions. Until now, these information were not accessible with currently available MDCS methods.

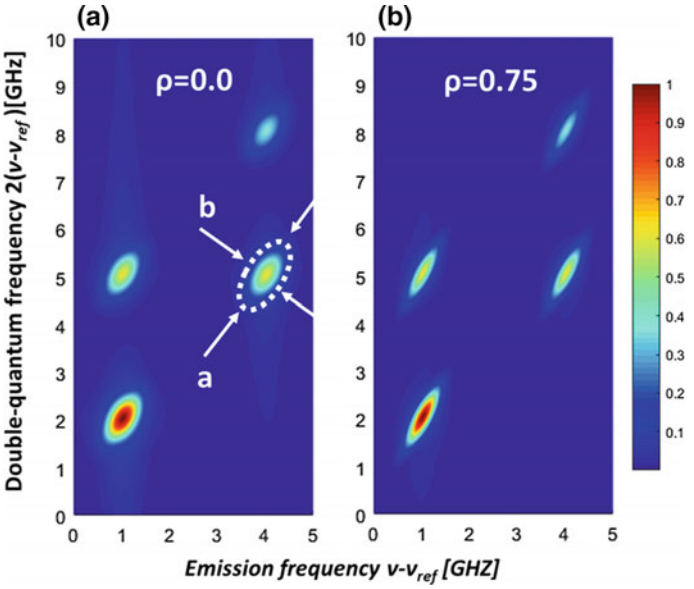

Fig. 15.8 Theoretical simulation. **a** $\rho = 0.0$, **b** $\rho = 0.75$. The color scale shows the normalized signal magnitude. ν_{ref}—arbitrary reference

15.4 Tri-comb Spectroscopy

Frequency comb-based single and double-quantum spectroscopy (M-DCS[2] described above) enables the measurement of multidimensional coherent spectra rapidly and with high-resolution. However, the experimental setup contains a mechanical stage, which still limits both the resolution and acquisition speed. To fully leverage the advantages provided by frequency combs recently we proposed and demonstrated a novel approach to multidimensional coherent spectroscopy that utilizes three frequency combs. This novel approach, which we call tri-comb spectroscopy (TCS) [45], contains no mechanical moving elements and can measure comb-resolution multidimensional coherent spectra in under half a second.

The experimental setup for tri-comb spectroscopy is pictorially shown in Fig. 15.9a. We used three frequency combs (Comb 1, Comb 2 and LO Comb) with slightly different repetition rates and locked the phases of the repetition frequencies to a four-channel direct-digital synthesizer (DDS). Path length and offset frequency fluctuations for each comb were measured and corrected.

Pulses from Comb 1 and Comb 2 were used for the generation of a photon echo (Fig. 15.9b). The emitted FWM signal was then sampled and spectrally isolated in the RF domain after interfering with the LO Comb on a photodetector [45]. The output of the detector was digitized using a fast data acquisition board. Figure 15.9c is a cartoon and shows a magnitude of a photon echo FWM signal as a function of the evolution and emission times. The signal is non-zero only near the diagonal

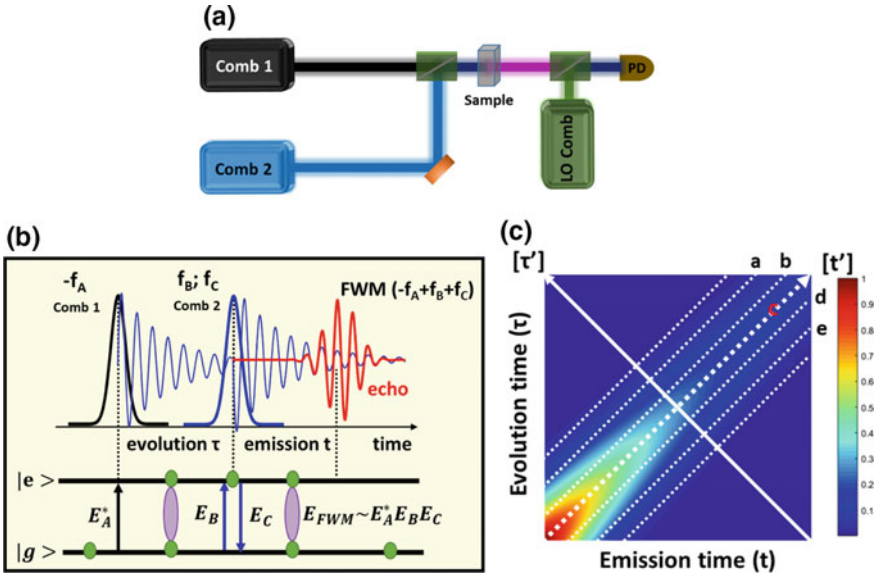

Fig. 15.9 **a** Schematic diagram of tri-comb spectroscopy. Comb 1 and Comb 2 are used for the generation of a photon echo FWM signal which is then sampled using a LO comb. **b** Photon echo excitation scheme (please see the text for details). **c** Cartoon showing the magnitude of a FWM signal as a function of emission and evolution times. The color scale shows the normalized signal magnitude

line, hence to optimize the acquisition speed we set the relative repetition frequencies between Comb 2 and LO comb to be exactly equal to the relative repetition frequency between Comb 1 and Comb 2. This arraignment enabled the signal to be sampled along the echo (along the diagonal line) and not in the region where the signal is zero. In order to sample points off the diagonal we stepped the phase of the DDS serving as the reference for the LO comb (which time shifts the LO pulses but without using a delay line), and measured the FWM signal along the lines parallel to the diagonal (dashed white lines (a, b, c, d, e) shown in Fig. 15.9c). After digitizing the FWM signal, a multidimensional spectrum was generated by calculating a two-dimensional Fourier transform with respect to t' and τ'.

To demonstrate the resolution and acquisition speed improvement that can be achieved with TCS we repeated the measurement shown in Fig. 15.4a. The results are shown in Fig. 15.10a. The two-dimensional spectrum is tilted by 45° to show the spectrum in the ν_t and ν_τ coordinate system. Comparing Figs. 15.4a and 15.10a shows that we have reproduced the same results but improved the cross-diagonal resolution by a factor 4. The spectrum shown in Fig. 15.10a was generated by 365 ms of data, which is 600 times improvement compare to Fig. 15.4a. Figure 15.10b shows the same spectrum with the acquisition time of 2 s which clearly shows an improvement in signal to noise, however all the Rb resonances can be identified in the 365 ms data.

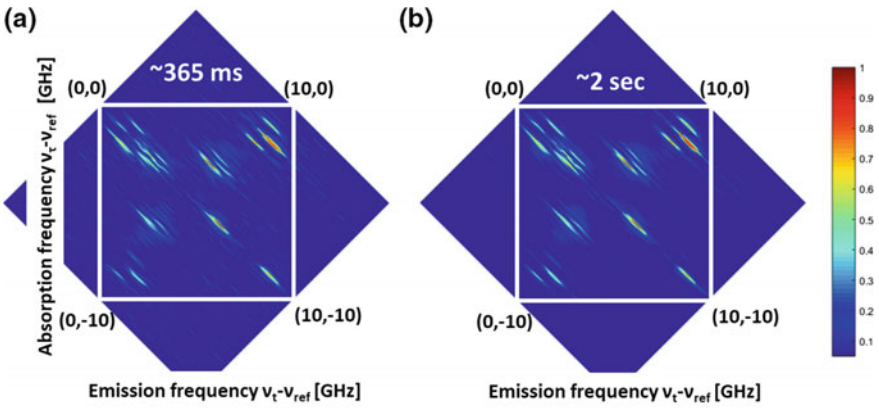

Fig. 15.10 Two-dimensional spectra generated using **a** 365 ms **b** 2 s data records. The color scale shows the normalized signal magnitude

15.5 Conclusion

We have demonstrated frequency comb-based multidimensional coherent spectroscopy (MDCS). We showed that this novel approach offers much higher spectral resolution and acquisition speed than traditional two-dimensional spectroscopy techniques, making MDCS relevant for systems with long dephasing rates. We also showed how this technique can be used to probe extremely weak many-body interactions in an atomic vapor and can be extended to cold atomic and molecular systems as well as color centers. In addition, we presented a novel approach to comb-based multidimensional spectroscopy, Tri-comb spectroscopy (TCS), that contains no mechanical moving parts and enables the measurement of comb resolution multidimensional spectra in under half a second. With the development of micro-resonators, TCS will become a field deployable devices for chemical sensing and other applications outside the laboratory. TCS also has excellent potential to be used for real-time medical imaging applications.

Acknowledgements The research is based on work supported by the Office of the Director of National Intelligence (ODNI), Intelligence Advanced Research Projects Activity (IARPA), via contract 2018-18020600001. The views and conclusions contained herein are those of the authors and should not be interpreted as necessarily representing the official policies or endorsements, either expressed or implied, of the ODNI, IARPA, or the U.S. government. The U.S. government is authorized to reproduce and distribute reprints for governmental purposes notwithstanding any copyright annotation thereon.

References

1. S.T. Cundiff, S. Mukamel, Optical multidimensional coherent. Spectroscopy **66**, 44–49 (2013). https://doi.org/10.1063/pt.3.2047
2. C.L. Smallwood, S.T. Cundiff, Coherent spectroscopy: multidimensional coherent spectroscopy of semiconductors. Laser Photon. Rev. **12**, 1870052 (2018). https://doi.org/10.1002/lpor.201870052
3. M. Thämer, L. De Marco, K. Ramasesha, A. Mandal, A. Tokmakoff, Ultrafast 2D IR spectroscopy of the excess proton in liquid water. Science **350**, 78–82 (2015). https://doi.org/10.1126/science.aab3908
4. X. Dai et al., Two-dimensional double-quantum spectra reveal collective resonances in an atomic vapor. Phys. Rev. Lett. **108**, 193201 (2012). https://doi.org/10.1103/PhysRevLett.108.193201
5. P. Tian, D. Keusters, Y. Suzaki, W.S. Warren, Femtosecond phase-coherent two-dimensional spectroscopy. Science **300**, 1553 (2003). https://doi.org/10.1126/science.1083433
6. P. Hamm, M. Zanni, *Concepts and Methods of 2D Infrared Spectroscopy* (Cambridge University Press, Cambridge, 2011)
7. R.R. Ernst, G. Bodenhausen, and A. Wokaun. *Principles of Nuclear Magnetic Resonance in One and Two Dimensions*. (Oxford University Press, London, 1987)
8. N.A. Kurnit, I.D. Abella, S.R. Hartmann, Observation of a photon echo. Phys. Rev. Lett. **13**, 567–568 (1964). https://doi.org/10.1103/PhysRevLett.13.567
9. L. Yang, S. Mukamel, Two-dimensional correlation spectroscopy of two-exciton resonances in semiconductor quantum wells. Phys. Rev. Lett. **100**, 057402 (2008). https://doi.org/10.1103/PhysRevLett.100.057402
10. L. Yang, S. Mukamel, Revealing exciton-exciton couplings in semiconductors using multidimensional four-wave mixing signals. Phys. Rev. B **77**, 075335 (2008). https://doi.org/10.1103/PhysRevB.77.075335
11. S. Ravets et al., Coherent dipole–dipole coupling between two single Rydberg atoms at an electrically-tuned Förster resonance. Nat. Phys. **10**, 914 (2014). https://doi.org/10.1038/nphys3119
12. E. Collini et al., Coherently wired light-harvesting in photosynthetic marine algae at ambient temperature. Nature **463**, 644 (2010). https://doi.org/10.1038/nature08811, https://www.nature.com/articles/nature08811#supplementary-information
13. V. Bendkowsky et al., Observation of ultralong-range Rydberg molecules. Nature **458**, 1005 (2009). https://doi.org/10.1038/nature07945
14. S. Draeger, S. Roeding, T. Brixner, Rapid-scan coherent 2D fluorescence spectroscopy. Opt. Express **25**, 3259–3267 (2017). https://doi.org/10.1364/OE.25.003259
15. H. Frostig, T. Bayer, N. Dudovich, Y.C. Eldar, Y. Silberberg, Single-beam spectrally controlled two-dimensional Raman spectroscopy. Nat. Photonics **9**, 339–343 (2015). https://doi.org/10.1038/nphoton.2015.64
16. F.D. Fuller, D.E. Wilcox, J.P. Ogilvie, Pulse shaping based two-dimensional electronic spectroscopy in a background free geometry. Opt. Express **22**, 1018–1027 (2014). https://doi.org/10.1364/OE.22.001018
17. G. Nardin et al., Coherent excitonic coupling in an asymmetric double InGaAs quantum well arises from many-body effects. Phys. Rev. Lett. **112**, 046402 (2014). https://doi.org/10.1103/PhysRevLett.112.046402
18. J.P. Ogilvie, K.J. Kubarych, *Advances in Atomic, Molecular, and Optical Physics*, vol. 57 (Academic, New York, 2009), pp. 249–321
19. G.S. Schlau-Cohen, J.M. Dawlaty, G.R. Fleming, Ultrafast multidimensional spectroscopy: principles and applications to photosynthetic systems. IEEE J. Sel. Top. Quantum Electron. **18**, 283–295 (2012). https://doi.org/10.1109/JSTQE.2011.2112640
20. P.F. Tekavec, G.A. Lott, A.H. Marcus, Fluorescence-detected two-dimensional electronic coherence spectroscopy by acousto-optic phase modulation. J. Chem. Phys. **127**, 214307 (2007). https://doi.org/10.1063/1.2800560

21. D.B. Turner, K.A. Nelson, Coherent measurements of high-order electronic correlations in quantum wells. Nature **466**, 1089–1092 (2010). http://www.nature.com/nature/journal/v466/n7310/abs/nature09286.html#supplementary-information
22. A.D. Bristow et al., A versatile ultrastable platform for optical multidimensional Fourier-transform spectroscopy. Rev. Sci. Instrum. **80**, 073108 (2009). https://doi.org/10.1063/1.3184103
23. E. Harel, A.F. Fidler, G.S. Engel, Real-time mapping of electronic structure with single-shot two-dimensional electronic spectroscopy. Proc. Natl. Acad. Sci. **107**, 16444 (2010). https://doi.org/10.1073/pnas.1007579107
24. B. Lomsadze, C.W. Fehrenbach, B.D. DePaola, Calculation of ionization in direct-frequency comb spectroscopy. Phys. Rev. A **85**, 043403 (2012). https://doi.org/10.1103/PhysRevA.85.043403
25. B. Lomsadze, C.W. Fehrenbach, B.D. DePaola, Measurement of ionization in direct frequency comb spectroscopy. J. Appl. Phys. **113**, 103105 (2013). https://doi.org/10.1063/1.4794813
26. A. Marian, M.C. Stowe, J.R. Lawall, D. Felinto, J. Ye, United time-frequency spectroscopy for dynamics and global structure. Science **306**, 2063–2068 (2004). https://doi.org/10.1126/science.1105660
27. B. Lomsadze, *Encyclopedia of Modern Optics*, ed. by B.D. Guenther, D.G. Steel, 2nd ed. (Elsevier, Amsterdam, 2018), pp. 227–232
28. H.U. Jang et al., Interaction of a finite train of short pulses with an atomic ladder system. Phys. Rev. A **82**, 043424 (2010). https://doi.org/10.1103/PhysRevA.82.043424
29. F. Gao, S.T. Cundiff, H. Li, Probing dipole–dipole interaction in a rubidium gas via double-quantum 2D spectroscopy. Opt. Lett. **41**, 2954–2957 (2016). https://doi.org/10.1364/OL.41.002954
30. M.E. Siemens, G. Moody, H. Li, A.D. Bristow, S.T. Cundiff, Resonance lineshapes in two-dimensional Fourier transform spectroscopy. Opt. Express **18**, 17699–17708 (2010). https://doi.org/10.1364/OE.18.017699
31. I. Coddington, N. Newbury, W. Swann, Dual-comb spectroscopy. Optica **3**, 414–426 (2016). https://doi.org/10.1364/OPTICA.3.000414
32. I. Coddington, W.C. Swann, N.R. Newbury, Coherent multiheterodyne spectroscopy using stabilized optical frequency combs. Phys. Rev. Lett. **100**, 013902 (2008). https://doi.org/10.1103/PhysRevLett.100.013902
33. B.C. Smith, B. Lomsadze, S.T. Cundiff, Optimum repetition rates for dual-comb spectroscopy. Opt. Express **26**, 12049–12056 (2018). https://doi.org/10.1364/OE.26.012049
34. B.C. Smith, *Fourier Transform Infrared Spectroscopy* (CRC Press, Boca Raton, 1996)
35. M.-G. Suh, K.J. Vahala, Soliton microcomb range measurement. Science **359**, 884–887 (2018). https://doi.org/10.1126/science.aao1968
36. M.-G. Suh, Q.-F. Yang, K.Y. Yang, X. Yi, K.J. Vahala, Microresonator soliton dual-comb spectroscopy. Science **354**, 600–603 (2016). https://doi.org/10.1126/science.aah6516
37. P. Trocha et al., Ultrafast optical ranging using microresonator soliton frequency combs. Science **359**, 887–891 (2018). https://doi.org/10.1126/science.aao3924
38. E. Lucas et al., Spatial multiplexing of soliton microcombs. Nat. Photonics **12**, 699–705 (2018). https://doi.org/10.1038/s41566-018-0256-7
39. T.J. Kippenberg, R. Holzwarth, S.A. Diddams, Microresonator-based optical frequency combs. Science **332**, 555–559 (2011). https://doi.org/10.1126/science.1193968
40. S. Boudreau, S. Levasseur, C. Perilla, S. Roy, J. Genest, Chemical detection with hyperspectral lidar using dual frequency combs. Opt. Express **21**, 7411–7418 (2013). https://doi.org/10.1364/OE.21.007411
41. M. Godbout, J.-D. Deschênes, J. Genest, Spectrally resolved laser ranging with frequency combs. Opt. Express **18**, 15981–15989 (2010). https://doi.org/10.1364/OE.18.015981
42. B. Lomsadze, S.T. Cundiff, Frequency combs enable rapid and high-resolution multidimensional coherent spectroscopy. Science **357**, 1389–1391 (2017). https://doi.org/10.1126/science.aao1090

43. B. Lomsadze, S.T. Cundiff, Multi-heterodyne two dimensional coherent spectroscopy using frequency combs. Sci. Rep. **7**, 14018 (2017). https://doi.org/10.1038/s41598-017-14537-z
44. B. Lomsadze, S.T. Cundiff, Frequency-comb based double-quantum two-dimensional spectrum identifies collective hyperfine resonances in atomic vapor induced by dipole-dipole interactions. Phys. Rev. Lett. **120**, 233401 (2018). https://doi.org/10.1103/PhysRevLett.120.233401
45. B. Lomsadze, B.C. Smith, S.T. Cundiff, Tri-comb spectroscopy. Nat. Photonics **12**, 676–680 (2018). https://doi.org/10.1038/s41566-018-0267-4
46. B. Lomsadze, S.T. Cundiff, Frequency comb-based four-wave-mixing spectroscopy. Opt. Lett. **42**, 2346–2349 (2017). https://doi.org/10.1364/OL.42.002346
47. S. Mukamel. *Principles of Nonlinear Optical Spectroscopy*. (Oxford University Press, New York, 1995)
48. S.T. Cundiff, Effects of correlation between inhomogeneously broadened transitions on quantum beats in transient four-wave mixing. Phys. Rev. A **49**, 3114–3118 (1994). https://doi.org/10.1103/PhysRevA.49.3114

Chapter 16
Nonlinear Spectroscopy of Chromophores in Condensed Phases with Multiple Frequency Combs

JunWoo Kim and Minhaeng Cho

Abstract Coherent multidimensional spectroscopy involves more than one pulsed field-matter interaction, which creates nonlinear polarization in an optical sample and generates phase-matched coherently emitted electromagnetic fields under detection. To maintain the coherence of the involved electromagnetic fields, each single laser pulse is split into multiple pulses that remain in a fixed relative phase within their coherence lengths. However, multi-comb nonlinear spectroscopy breaks this conventional paradigm in that two or more frequency-comb lasers, which are phase stabilized and locked with one another, are used to create nonlinear polarization in the optical sample. In this chapter, nonlinear spectroscopic research utilizing two frequency combs is summarized and explained in terms of the nonlinear response function. In addition to a review of linear and nonlinear dual frequency-comb spectroscopy theory and applications, we discuss the future possibilities for the development of multi-comb nonlinear spectroscopy.

16.1 Introduction

Molecular spectroscopy is used to study the distribution, energetic fluctuation, state-to-state correlation, energy exchange, and thermal relaxation of molecular eigenstates as determined by the associated Hamiltonian. These observables provide direct information on molecular structures and intermolecular interactions. Thus, this technique has been considered one of the central research tools for studying chemical and biological reactions in condensed phases and living organisms [1–3].

To extract information on the molecular dynamics of a system beyond its thermal equilibrium ensemble properties, time-resolved spectroscopy has long been used to

J. Kim · M. Cho (✉)
Center for Molecular Spectroscopy and Dynamics, Institute for Basic Science (IBS), Seoul 02841, Republic of Korea
e-mail: mcho@korea.ac.kr

M. Cho
Department of Chemistry, Korea University, Seoul 02841, Republic of Korea

M. Cho (ed.), *Coherent Multidimensional Spectroscopy*,
Springer Series in Optical Sciences 226,
https://doi.org/10.1007/978-981-13-9753-0_16

monitor the responses of a molecular system to external electromagnetic perturbations. The recent development of femtosecond nonlinear spectroscopy has enabled the investigation of various forms of molecular dynamics in nature, such as photochemical and photophysical processes [4], light-harvesting processes in photosynthetic systems [1, 5], molecular reaction dynamics [6], solvation dynamics [7], and biomolecular and cellular dynamics [2, 3]. In the linear response regime, the molecules under investigation interact with an electronically or vibrationally resonant field and affect the net photon number and the speed of incoming light in accordance with their absorptive and dispersive properties, respectively. However, linear spectroscopic techniques cannot be used to study molecular dynamic changes in the time domain.

One of the most popular time-resolved spectroscopic techniques is the two-pulse pump-probe method, where a pump pulse perturbs the molecular system so that it is almost instantaneously put into a non-equilibrium, non-stationary state in which the experimental observables change over time. Time-dependent changes in molecular properties due to chromophore system-bath interactions, inter-chromophore interactions, and intramolecular relaxation processes can thus be monitored using a time-delayed interrogating probe pulse. Pump-probe measurement involves the time-dependent monitoring of population changes in the ground and excited states. Consequently, the phase of the pump electromagnetic field, i.e., the oscillating electric field amplitude, does not have to be fixed in relation to that of the probe field because second-order (in the electric field) pump photon annihilation and probe photon creation (or annihilation) during each pump-probe interaction event erases information about the optical phase of the incoming electromagnetic field.

However, coherent multidimensional spectroscopy involves multiple interactions with more than one light pulse and the signal becomes a function of more than one coherence between two or more system eigenstates. For example, let us consider three-pulse two-dimensional spectroscopy with two collinearly propagating pump pulses with wave vector $\mathbf{k}_{\mathrm{pu}}$ and a probe pulse with wave vector $\mathbf{k}_{\mathrm{pr}}$ ($\neq \mathbf{k}_{\mathrm{pu}}$). Suppose that the third-order signal field satisfying the corresponding phase-matching condition, i.e., $\mathbf{k}_{\mathrm{sig}} = -\mathbf{k}_{\mathrm{pu}} + \mathbf{k}_{\mathrm{pu}} + \mathbf{k}_{\mathrm{pr}} = \mathbf{k}_{\mathrm{pr}}$, is detected by allowing it to interfere with the probe field. Here, the relative phase between the first and second pulsed electric fields is very important and should be stabilized during three-pulse pump-probe-type 2D spectroscopy experiments, otherwise the average signal would vanish. Here, mode-locked lasers have been used as a pivotal tool to generate a train of femtosecond optical pulses with a broad spectral bandwidth, which allows nonlinear susceptibility measurement and offers a high time resolution due to the high peak power and femtosecond pulse duration, respectively. However, because there is no phase relationship between the oscillating electric fields under a pair of neighboring pulses separated by 1 ms for an amplified Ti:Sapphire laser with a repetition rate of 1 kHz, each individual pulse is used to produce time-delayed coherent pulses using beam splitters.

Over the past two decades, an interesting technological advance in precision measurement has been the use of optical frequency combs, which are a specialized mode-locked laser [8]. One of the intrinsic properties of mode-locked lasers is their discrete

spectral lines, which show a comb-like structure in that they are evenly spaced and the frequency spacing between a pair of neighboring lines is determined by the repetition frequency. The comb structure is generated by the coupling between the broad optical gain spectrum and the multiple spectral modes of the laser oscillator, which are given by the geometrical boundary conditions of the oscillator. Once the two frequency degrees of freedom of mode-locked lasers, i.e., the repetition rate and the carrier-envelope-offset (CEO) frequency, are stabilized, the system becomes an ideal frequency-comb laser, producing individual spectral lines with a narrow linewidth and exactly the same line spacing, thus becoming a precise frequency ruler that offers a high spectral resolution in the frequency domain.

Mode-locked laser-based frequency combs can be utilized to achieve both high frequency-resolution and ultrafast time-resolution spectroscopy. Nevertheless, until recently, frequency-comb technology was not actively employed for the study of condensed-phase molecular systems because the transition linewidth of the system is incomparably broader than the spectral resolution of frequency combs. However, the use of two optical frequency combs (OFCs) together in femtosecond dual frequency-comb (DFC) spectroscopy has been shown to be of great assistance in studying molecules in gas [9] and condensed phases [10]. Two notable features of the DFC system are (i) the automatic time-delay scan originating from the slightly detuned repetition rates of the two OFCs, which is known as asynchronous optical sampling (ASOPS), and (ii) the fixed carrier-envelope phase (CEP) for each pulse. Due to these characteristic properties, DFC linear spectroscopy (DFC-LS) can record linear molecular responses in a down-converted manner. DFC-LS was first introduced as a form of gas-phase molecular spectroscopy to measure Doppler-broadened molecular spectra with a fast scan rate [9]. Recently, DFC-LS has been employed to study molecular dynamics and intermolecular interactions [11] and to develop DFC-based microscopy [12, 13]. For molecular spectroscopy targeting electronic or vibrational chromophores in condensed phases, it is necessary for the spectral bandwidth of the pulses to be broader than the molecular transition linewidth. Thus, ultrashort pulses whose bandwidths are on the order of tens to hundreds of THz are necessary for chromophores with a vibrational or electronic dephasing time of a few picoseconds or tens of femtoseconds, respectively. We have recently demonstrated that it is experimentally feasible to apply DFC-LS [10] and DFC-based nonlinear time-resolved spectroscopy [14, 15] to the study of dye molecules in solution. We also showed that broadband dual frequency combs allow the measurement of a wide dynamic range of two-dimensional electronic coherences in condensed phases.

In this chapter, we present a theoretical description of OFC, DFC-LS, and DFC-based nonlinear spectroscopy and the diverse range of applications that employ two OFCs. Recently, we published a review article showing that various nonlinear spectroscopic techniques, such as transient absorption (TA), transient grating, two- and three-pulse photon echoes, two-dimensional spectroscopy, and stimulated Raman scattering, can be theoretically described using our DFC nonlinear spectroscopy theory [16]. In that article, it was clearly shown that the combination of the time-dependent perturbation theory and the OFC field expression explains previously proposed and/or demonstrated experiments quite well and elucidates how molecu-

lar responses are reflected in DFC spectroscopy signals. Here, we shall present the details of a few representative DFC nonlinear spectroscopic techniques and then end with an overview of multi-comb nonlinear spectroscopy and a few concluding remarks.

16.2 Frequency Combs: Temporal and Spectral Properties

OFC lasers generate an infinite train of pulses with a pulse interval determined by the repetition frequency f_{r}. The other frequency variable that is critical for specifying the absolute frequency distribution of spectral comb lines is the carrier-envelop-offset (CEO) frequency (Fig. 16.1). This CEO frequency is related to the pulse-to-pulse (or carrier-envelop-offset) phase slip $\Delta\phi$ using $f_{\mathrm{ceo}} = f_{\mathrm{r}} \cdot (\Delta\phi/2\pi)$. The spectral bandwidth of each pulse is related to the pulse width Δt_ω as $\Delta\omega = 1/\Delta t_\omega$.

In general, the electric field of an OFC, denoted as $\mathcal{E}_k(\mathbf{r}, t)$ for the kth comb laser can be expressed in terms of the repetition frequency ($f_{\mathrm{r},k}$) and the CEO frequency ($f_{\mathrm{ceo},k}$), where the linewidth of a single comb line is assumed to be a Dirac delta function:

$$\mathcal{E}_k(\mathbf{r}, t) = E_k(\mathbf{r}, t) + c.c. \tag{16.1}$$

Here, the positive frequency component is

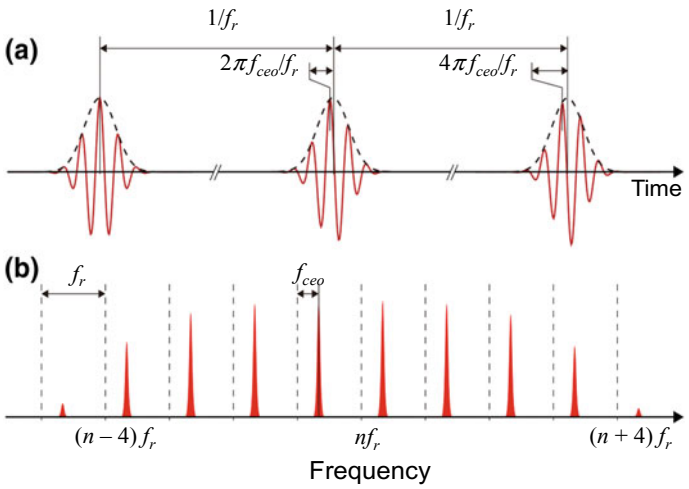

Fig. 16.1 Optical frequency comb (OFC). **a** Time profile of an OFC electric field and pulse envelop. **b** Power spectrum of the OFC electric field

$$E_k(\mathbf{r}, t) = \frac{1}{2} e^{i\mathbf{k}(\omega_{c,k})\cdot\mathbf{r}} \sum_{n=0}^{\infty} c_{k,n} e^{-i\,(\omega_{ceo,k}+n\omega_{r,k})t}, \tag{16.2}$$

where the angular frequency (ω) is related to frequency (f) by $\omega = 2\pi f$ and $c_{k,n}$ is the Fourier coefficient of the pulse envelope function, which represents the spectral amplitude of each comb line at $\omega_{ceo,k} + n\omega_{r,k}$. Although the mode-expansion form for the electric field of an OFC in (16.2) is exact, it is often convenient to introduce the carrier frequency $f_{c,k}$ of the OFC so that there are approximately an equal number of frequency comb modes in the lower and higher regions of the OFC spectrum around $f_{c,k}$. The carrier angular frequency is related to the carrier frequency as $\omega_{c,k} = 2\pi f_{c,k}$, which is defined as

$$\omega_{c,k} = N_c \omega_{r,k} + \omega_{ceo,k}, \tag{16.3}$$

where N_c is the mode number associated with the carrier frequency. Equation (16.2) can then be written in a very useful and familiar form as

$$E_k(\mathrm{r}, t) = e^{i[\mathbf{k}(\omega_{c,k})\cdot\mathbf{r} - \omega_{c,k}t]} \sum_{n=-\infty}^{\infty} A_{k,n} e^{-in\omega_{r,k}t}, \tag{16.4}$$

where $A_{k,n} = c_{k,n+N_c}$. Note that the summation in (16.4) runs symmetrically across the carrier frequency and each comb component has an equal frequency spacing given by the repetition frequency $f_{r,k}$. Thus, the frequency of the nth comb line is given as

$$\omega_{n,k} = \omega_{c,k} + n\omega_{r,k} = N_c\omega_{r,k} + n\omega_{r,k} + \omega_{ceo,k}. \tag{16.5}$$

It is possible to stabilize $f_{ceo,k}$ and even to make it zero. In this case, the optical frequency of the nth mode is given strictly by the integer multiple of the repetition frequency, i.e., $(N_c + n) f_{r,k}$ (Fig. 16.1), resulting in every pulse having the same carrier-envelop-offset phase (CEP). If the CEO frequency is not zero, i.e., $f_{ceo,k} \neq 0$, the frequencies of the comb modes are all simultaneously translated by $f_{ceo,k}$ in the frequency domain (see 16.5), while it linearly increases the CEP slip by increments of $2\pi f_{ceo,k}/f_{r,k}$ in the time domain, resulting in repetitive phase synchronization after $f_{r,k}/f_{ceo,k}$ pulses. To stabilize both $f_{r,k}$ and $f_{ceo,k}$ of the kth comb, the phase-locking technique in the radio frequency (RF) domain should be used. Typically, external stable reference frequencies such as those from a GPS-disciplined Rb atomic clock can be employed for the phase-locking of f_r and f_{ceo}.

Although the OFC has been of great use in precision measurement and metrology, its spectroscopic applications are limited due to its weak energy per comb line and lack of a fast-response (i.e., hundreds of MHz) array detector. However, because a variety of DFC-based spectroscopic applications require just one fast photodetector in the RF domain, dual frequency comb technology could eventually revolutionize linear and nonlinear spectroscopy and imaging research.

16.3 Dual Frequency Comb Spectroscopy: General Overview

Dual frequency-comb linear spectroscopy (DFC-LS) was first proposed in early 2000 [17, 18] and was successfully applied to Doppler limited gas-phase spectroscopy [9]. Although similar tasks can be handled with single-comb spectroscopy, DFC-LS is able to simultaneously measure the absorption and dispersion spectra related to the imaginary and real parts of complex susceptibility, respectively, because it measures the spectral information interferometrically in the time domain. Note that, for interferometric spectroscopy with two frequency combs, the spectral response is more sensitive than for spectrally (spatially) resolved spectroscopy. To understand the key differences between DFC and conventional spectroscopy when a single radiation source and a spectrometer are employed, the frequency down-conversion achieved using the DFC technique needs to be explained first.

Consider two OFCs with slightly different repetition rates, $f_r \equiv f_{r,1} = f_{r,2} - \Delta f_r$, where Δf_r is the experimentally controllable detuning frequency. Note that the integer N_c specifying the carrier frequency (see 16.3) is the same for the two OFCs, because in general $N_c \Delta\omega_r$ is chosen not to exceed $\omega_r/2$ to avoid the aliasing caused by improper under-sampling. The slightly detuned repetition rates of the two OFCs combined generate a linearly increasing time delay with the increment Δt between the two OFCs given by

$$\Delta t = \frac{\Delta f_r}{f_r(f_r + \Delta f_r)} \simeq \frac{\Delta f_r}{f_r^2} = \frac{f_D}{f_r}, \tag{16.6}$$

where the down-conversion factor f_D is defined as

$$f_D \equiv \frac{\Delta f_r}{f_r}. \tag{16.7}$$

As mentioned in the Introduction, the automatic time delay generated by two mode-locked lasers with slightly different repetition rates is known as asynchronous optical sampling (ASOPS). Typically, an atomic clock provides a highly accurate pulse interval (Δt) for ASOPS. On the other hand, in conventional interferometry or time-resolved spectroscopy, the time delay between two pulses is mechanically controlled by differentiating their optical path lengths with a translational stage. As a result, the mechanical time-delay scan rate and accuracy are limited by the maximum speed of the stage and the servo bandwidth of the position-encoding system. In contrast, in DFC spectroscopy, a scan speed with equal pulse intervals and its timing accuracy are simultaneously controlled at atomic clock accuracy because the scan rate and Δt are essentially determined by Δf_r. Because the repetition frequency is related to the cavity length (L) by $f_r = c/2L$, where c is the speed of light, both Δf_r and f_r can be precisely stabilized by controlling the cavity length using the well-developed RF phase-locking technique.

In summary, the three key time-domain parameters—the pulse-to-pulse time interval $T = 1/f_r$, its jittering $\delta T = \delta f_r/f_r^2$, where δf_r is the fluctuating component of the repetition frequency, and the pump-to-probe (OFC1-to-OFC2) delay timestep $\Delta t = \Delta f_r/f_r^2$—are all directly connected to their frequency domain conjugate parameters under stabilization when employing RF technology. To ensure that the DFC spectrometer developed by us recently was capable of sub-optical cycle sampling, we were able to stabilize the f_r and f_{ceo} of both OFCs with the relative frequency stabilities $\delta f_r/f_r < 10^{-11}$ and $\delta f_{ceo} < 0.01$ Hz, respectively. Therefore, $\delta T < 1.5$ as is within reach in our DFC spectroscopy, resulting in a less than femtosecond pulse-to-pulse timing jitter, optical triggering for DFC interferogram acquisition with sub-femtosecond precision (an optical cycle of 2.7 fs), and a pump-to-probe OFC delay time Δt with a sub-cycle sampling time.

Note that, in typical DFC spectroscopy experiments, optical time t is effectively down-converted into effective time by the frequency down-conversion factor, i.e., $t_{eff} = t \times f_D$. Usually, f_r is in the order of 100 MHz and Δf can be controlled to fall within the Hz to kHz range, meaning that the frequency down-conversion factor f_D is within the range of 10^{-5} to 10^{-8}. Thus, any molecular dynamics occurring on the time scale of a picosecond can be measured with a microsecond to millisecond time-scale detector. This is one of the most important features of DFC spectroscopy. In the frequency domain, the DFC technique can shift and the down-convert optical frequency signals (spectra) associated with linear and nonlinear molecular responses to signals in the RF frequency domain.

Another practical advantage of DFC spectroscopy is that it provides a uniform spatial beam quality during each time-delay scan. Therefore, the beam overlapping conditions at the sample and at the detector remain unchanged regardless of the time delay, which is believed to be an important factor for the high-frequency resolvability of DFC spectroscopy.

In the following sections, we address linear and nonlinear DFC spectroscopy theories, taking into account the experimental availability of two phase-stabilized OFC sources, including linear and nonlinear DFC spectroscopy schemes previously reported by us and other research groups and newly proposed nonlinear DFC spectroscopy techniques.

16.4 Linear Spectroscopy with Dual Frequency Combs

DFC-based linear spectroscopy (DFC-LS), which utilizes two OFCs with slightly different repetition frequencies and stabilized CEO frequencies, is capable of an extremely high frequency resolution because of the exceptionally stabilized spectral positions of the two OFC lines. Naturally, early uses of DFC-LS involved the measurement of the Doppler-broadened linewidths (a few GHz) of atoms and molecules in the gas phase [9]. Note that the typical frequency spacing between neighboring comb lines is in the order of 100 MHz, which is significantly smaller than the rovibrational spectral linewidth of polyatomic molecules in the gas phase. Additionally,

by stabilizing one of the comb modes using an ultra-narrow continuous-wave laser (instead of stabilizing the CEO frequency using a self-reference interferometer), the entire comb linewidth can be made to approach the sub-Hz level, thus allowing high precision measurement in such applications as cold-atom spectroscopy [19].

When conducting DFC-LS on chromophores in condensed phases, the optical frequency domain response is down-converted to the RF domain. Thus, it is possible to use a detection frequency window in the relatively noise-free region by adjusting the frequency down-conversion factor f_{D} or f_{ceo}. Furthermore, the use of a suitable apodization scheme or a band-pass filter can improve the signal-to-noise ratio. One of the important advantages of DFC-LS is that there is no frequency-dependent power loss when the absorption or refractive index spectra are measured by using dispersive optics for achieving spectral resolution. This is because DFC-LS extracts frequency-domain information by taking the Fourier transform of the time-domain interferogram measured with a photodetector, not with diffractive optics such as a grating and a spectrometer. It should be noted that the bandwidth of the detector should be larger than half of the repetition frequency of the OFC used.

For DFC-LS, let us assume that OFC1 interacts with the sample. The transmitted pulses from OFC1 are then combined with those from OFC2 at a beam splitter, which produces a time-domain interferogram on the single-point photodetector (Fig. 16.2). The linear polarization induced by the interaction of the OFC1 field, $E_1(\mathbf{r}, t)$, with the chromophores can be described by the convolution of the linear response function, $R^{(1)}(t_1)$, and $E_1(\mathbf{r}, t)$:

$$P^{(1)}(\mathbf{r}, t) = \int_0^\infty \mathrm{d}t_1 R^{(1)}(t_1) E_1(\mathbf{r}, t - t_1), \tag{16.8}$$

where $\mathbf{r}$ is the position vector. After inserting the mode expansion form of the OFC1 field given in (16.4) into (16.8), we have [16, 20]

$$\begin{aligned} P^{(1)}(\mathbf{r}, t) &= \mathrm{e}^{i\mathbf{k}(\omega_{\mathrm{c}})\cdot\mathbf{r}} \sum_{n=-\infty}^{\infty} \int_0^\infty \mathrm{d}t_1 R^{(1)}(t_1) A_{1,n} \mathrm{e}^{-i(\omega_{\mathrm{c},1}+n\omega_{\mathrm{r}})(t-t_1)} \\ &= \mathrm{e}^{i\mathbf{k}(\omega_{\mathrm{c}})\cdot\mathbf{r}} \sum_{n=-\infty}^{\infty} \tilde{R}^{(1)}(\omega_{\mathrm{c},1} + n\omega_{\mathrm{r}}) A_{1,n} \mathrm{e}^{-i(\omega_{\mathrm{c},1}+n\omega_{\mathrm{r}})t} \end{aligned} \tag{16.9}$$

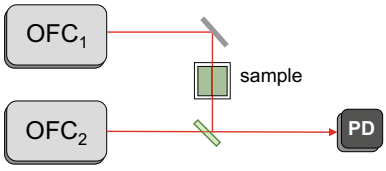

Fig. 16.2 Dual frequency comb linear spectroscopy (DFC-LS). Schematic representation of the DFC-LS experimental setup. PD = photodetector

Here, $\tilde{R}^{(1)}(\omega)$ is the one-sided Fourier transform of the linear response function, which is defined as

$$\tilde{R}^{(1)}(\omega) = \int_0^\infty \mathrm{d}t\, R^{(1)}(t)\mathrm{e}^{i\omega t}. \tag{16.10}$$

As can be seen in (16.9), the material polarization is a Fourier expansion with respect to the frequency comb components, where the weighting factor or Fourier coefficient is determined by the spectrum of the linear response function, i.e., complex susceptibility, and the Fourier coefficient of the pulse envelope function.

The measured intensity on the photodetector is proportional to the modulus square of the superposed electric field, i.e.,

$$\begin{aligned} I(t) &\propto \left|E_2(\mathrm{r},t) + E^{(1)}(\mathrm{r},t)\right|^2 \\ &= |E_2(\mathrm{r},t)|^2 + \left|E^{(1)}(\mathbf{r},t)\right|^2 + 2\mathrm{Re}\left[E_2^*(\mathrm{r},t)E^{(1)}(\mathbf{r},t)\right], \end{aligned} \tag{16.11}$$

where $E^{(1)}(\mathbf{r},t)$ is the electric field induced by $P^{(1)}(\mathbf{r},t)$. In the limit of weak absorption and dispersion, the oscillating component in the time-domain interferogram, which corresponds to the last term in (16.11), is proportional to the imaginary part of $E_2^*(\mathbf{r},t)P^{(1)}(\mathbf{r},t)$:

$$\begin{aligned} S_{\mathrm{DFC-LS}}(t) &\equiv \mathrm{Im}\left[E_2^*(\mathbf{r},t)P^{(1)}(\mathbf{r},t)\right] \\ &= \mathrm{Im}\left[\sum_{m,n=-\infty}^{\infty} \tilde{R}^{(1)}(\omega_{\mathrm{c},1}+n\omega_{\mathrm{r}})A_{2,m}^* A_{1,n}\mathrm{e}^{i((m-n)\omega_{\mathrm{r}}+m\Delta\omega_{\mathrm{r}}+\Delta\omega_{\mathrm{c}})t}\right] \end{aligned} \tag{16.12}$$

Note that the oscillating pattern in the time-domain interferogram is determined by the frequency-dependent linear susceptibility, pulse spectrum, and discrete comb mode frequency. It should be emphasized that the summations over m and n in (16.12) can be rewritten as a series of $m-n$, i.e.,

$$\begin{aligned} S_{\mathrm{DFC-LS}}(t) = S_0(t; m-n=0) + S_{+1}(t; m-n=1) \\ + S_{-1}(t; m-n=-1) + \cdots \end{aligned} \tag{16.13}$$

where

$$S_0(t; m-n=0) = \mathrm{Im}\left[\sum_{m=-\infty}^{\infty} \tilde{R}^{(1)}(\omega_{\mathrm{c},1}+m\omega_{\mathrm{r}})A_{2,m}^* A_{1,m}\mathrm{e}^{i(m\Delta\omega_{\mathrm{r}}+\Delta\omega_{\mathrm{c}})t}\right]$$

$$S_{+1}(t; m-n=1) = \mathrm{Im}\left[\sum_{m=-\infty}^{\infty} \tilde{R}^{(1)}(\omega_{\mathrm{c},1}+(m-1)\omega_{\mathrm{r}})A_{2,m}^* A_{1,m-1}\mathrm{e}^{i(\omega_{\mathrm{r}}+m\Delta\omega_{\mathrm{r}}+\Delta\omega_{\mathrm{c}})t}\right]$$

$$S_{-1}(t; m-n=-1) = \mathrm{Im}\left[\sum_{m=-\infty}^{\infty} \tilde{R}^{(1)}(\omega_{c,1} + (m+1)\omega_r) A_{2,m}^* A_{1,m+1} e^{i(-\omega_r + m\Delta\omega_r + \Delta\omega_c)t}\right]. \quad (16.14)$$

If these terms in (16.12) are Fourier-transformed, the corresponding spectra appear repeatedly in groups separated by the angular repetition frequency ω_r. Interestingly, they have essentially the same information about the complex linear susceptibility of chromophores in condensed phases and the two comb spectra. The advantage of the DFC technique is that a slow-response detector whose bandwidth is lower than the repetition rate of the OFCs can be used to selectively remove all of the highly oscillating terms with $|m - n| \geq 1$. Of course, a band-pass filter can be used to selectively measure the spectral contributions from comb modes whose frequencies range from $\omega_r + \Delta\omega_c$ to $2\omega_r + \Delta\omega_c$. Here, let us consider the zeroth term, i.e., $m - n = 0$. By truncating all of the highly oscillating terms, (16.13) reduces to and can be rewritten as

$$S_{\mathrm{DFC-LS}}(t) = \mathrm{Im}\left[\sum_{m=-\infty}^{\infty} \tilde{R}^{(1)}(\omega_{c,1} + m\omega_r) A_{2,m}^* A_{1,m} e^{i((\omega_{c,1} + m\omega_r) f_D + \Delta\omega_{ceo})t}\right]. \quad (16.15)$$

Here, we use the following approximate equality to rewrite the zeroth term in (16.14) with (16.15):

$$\Delta\omega_c = \omega_{c,2} - \omega_{c,1} = N_c \Delta\omega_r + \Delta\omega_{ceo} \cong \omega_{c,1} f_D + \Delta\omega_{ceo}. \quad (16.16)$$

To understand the frequency down-conversion component of DFC spectroscopy, let us consider the frequency factor in the exponent in (16.15). The optical response at $\omega_{c,1} + n\omega_r$, which is manifest in the weighting factor, $\tilde{R}^{(1)}(\omega_{c,1} + m\omega_r)$, of the mth comb component, is down-converted to $(\omega_{c,1} + n\omega_r) f_D + \Delta\omega_{ceo}$ without changing the amplitude or the phase of the optical response. Note that the down-converted frequency in (16.15), $(\omega_{c,1} + n\omega_r) f_D + \Delta\omega_{ceo}$, is the same as the down-converted frequency estimated from (16.6) except for $\Delta\omega_{ceo}$. The presence of $\Delta\omega_{ceo}$ in (16.15) indicates that the *detection* frequency can be shifted by controlling the difference in f_{ceo} between the two OFCs without varying Δf_r. This is easily achievable by controlling f_{ceo} with an acousto-optic modulator (AOM). This additional controllability is a critical and practical advantage of the DFC technique because the detection frequency window can be moved to a noise-free region by employing frequency modulation and the aliasing caused by improper sampling conditions can also be prevented.

The scan rate and frequency resolution of a conventional interferometer is limited by the control bandwidth of the moving stage and the frequency-reference laser. However, DFC-LS has an intrinsically high scan rate, which is equivalent to Δf_r, and its frequency resolution is as accurate as the frequency reference used to stabilize the f_r and f_{ceo} for the two OFCs.

To complete an overview of the theory behind DFC-LS, it is necessary to provide a theoretical expression for the linear response susceptibility $\tilde{R}^{(1)}(\omega_{c,1} + m\omega_r)$. However, because the main focus of this chapter is to discuss how linear and nonlinear DFC spectroscopy differs from conventional methods and because the theory behind linear and nonlinear response functions and associated susceptibilities has been presented and discussed in previous review articles [21] and books [22, 23], further details will not be discussed here.

Over the past decade, DFC-LS has been actively applied to gas-phase analyses due to its high frequency resolution capability. For example, DFC-LS has been used to measure the complete rovibrational spectrum of gas-phase molecules [9]. However, to employ condensed-phase molecular spectroscopy, a significantly broad comb spectrum with a bandwidth in the order of tens to hundreds of THz is required because the electronic and vibrational transitions of molecules in condensed phases have a broad bandwidth in the visible and IR frequency regions.

Only recently, femtosecond Ti:Sapphire mode-locked lasers and OFCs have become available [24]. Using the broadband OFCs, we for the first time demonstrated broadband DFC-LS for measuring the complex linear susceptibility of dye molecules in solution [10]. To stabilize the CEO frequency, we used a feed-forward loop to achieve minimal fluctuation using an AOM. This AOM is driven by the mixed signal of the measured f_r and f_{ceo} so that each frequency component, $f_n = nf_r + f_{ceo}$, becomes $f_n = (n-1)f_r$ at its -1st order diffracted beam [24]. Because the measured f_r and f_{ceo} fluctuate, f_{ceo} can be maintained at zero within the bandwidth of the servo control. We showed that a single time-domain interferogram is sufficient to obtain the broad absorption spectrum of the dye solution. Based on its scan-less mechanism and rapid spectrum recovery using a single-point detector, the application of DFC-LS could be extended to optical chirality and ellipsometry measurement for chiral molecules in condensed phases [25].

16.5 Nonlinear Spectroscopy with Dual Frequency Combs

Mode-locked lasers revolutionized time-domain nonlinear spectroscopy due to their high peak power and short pulse duration. A number of different nonlinear spectroscopic techniques have been developed based on these lasers, and they have been critical to the study of various molecular systems in isotropic solutions, on anisotropic surfaces, and at anisotropic interfaces. Of these, third-order (four-wave-mixing) spectroscopy is the lowest odd-order nonlinear spectroscopic technique used for solution samples, and it can be conveniently described with the corresponding third-order response functions. Recently, dual frequency comb nonlinear spectroscopy (DFC-NS) with pulses of a sub-10-fs duration has been demonstrated [14, 15]. DFC-NS has unique and advantageous properties: (i) by adjusting the two repetition rates to be slightly different from each other, automatic pulse-to-pulse time delay scans can be achieved; (ii) the spatial overlap of laser pulses can be maintained during pulse scanning; and (iii) the third-order signal field can be frequency-shifted to the radio

frequency domain. These characteristic features of DFC-NS allow the wide dynamic range (i.e., six decades) measurement of population relaxation, excitation migration, local heating, and thermal diffusion processes.

16.5.1 Third-Order Polarization

To calculate a DFC-NS signal, it is necessary to build a theory for the calculation of the third-order polarization created by the three field-matter interactions with comb lasers. In general, the third-order polarization can always be expressed in terms of the convoluted form of the third-order response function, $R^{(3)}(t_3, t_2, t_1)$, and three electric fields as [21, 23]

$$P^{(3)}(\mathbf{r}, t) = \int_0^\infty \mathrm{d}t_3 \int_0^\infty \mathrm{d}t_2 \int_0^\infty \mathrm{d}t_1 R^{(3)}(t_3, t_2, t_1)\mathcal{E}(\mathbf{r}, t - t_3)\mathcal{E}(\mathbf{r}, t - t_3 - t_2)\mathcal{E}(\mathbf{r}, t - t_3 - t_2 - t_1). \tag{16.17}$$

Here, $\mathcal{E}(\mathbf{r}, t)$ is the superposition of all incident electric fields at time t and $R^{(3)}(t_3, t_2, t_1)$ is a fourth-rank tensor representing the response of the molecular system to the three interactions with the electric field. $R^{(3)}(t_3, t_2, t_1)$ contains three commutators, which describes the time evolution in Liouville space, so that there are four interaction pathways and their corresponding complex conjugates. The electric field of a given OFC is then expanded in terms of the Fourier components determined by the comb-line numbers. The triple product of the electric field in the integrand of (16.17) becomes a sum over three comb-line numbers. Thus, unlike conventional time-resolved spectroscopy, where the pulsed electric field is treated as a continuous function with respect to frequency, multiple frequency comb spectroscopy can be described as a discrete sum of distinctively different oscillating components and the molecular responses to them. The expression for the time-domain DFC-LS interferogram in (16.15) is a representative example showing the discreteness of the spectral distribution of oscillating terms contributing to the time-domain interferogram or to the corresponding comb-structured linear spectrum.

16.5.2 DFC Pump-Probe Spectroscopy

One of the simplest approaches and still the most common time-resolved technique is pump-probe spectroscopy. Two or more pulses with variable time delays are used to investigate ultrafast photo-induced chemical, biological, or physical processes in condensed phases. The pump initiates the photo-induced process, followed by the probe pulse, which is used to interrogate the process in real time. The probe absorption changes due to various relaxations, energy transfers, and chemical reactions, thus providing critical information on the associated kinetics.

For DFC pump-probe (PP) spectroscopy, the DFC interferometric approach utilizing optical interference between two OFC fields may not be of great use for studying the ultrafast electronic dephasing processes of chromophores in condensed phases, which are on the order of tens of femtoseconds. For example, the automatic scan range of a DFC system that employs an OFC with a repetition rate of 100 MHz is 10 ns. If this OFC is used to measure electronic dephasing processes occurring on a time scale of ~100 fs, 99.999% of the OFC pulse energy will be wasted. In other words, the high spectral resolution capability of a DFC system is not required for molecular spectroscopic analysis of chromophores in condensed phases. On the other hand, the relaxation times of the incoherent population changes of chromophores in solution occur on a time scale of picoseconds to nanoseconds under ambient conditions. In this case, DFC-PP spectroscopy can provide high spectral resolution data. ASOPS with a DFC setup is thus an excellent choice for the long-term monitoring of the population relaxation processes of chromophores in condensed phases. In fact, incoherent relaxation measurement does not require phase-locked dual comb lasers because the absolute phase relationship between the pulses from the two lasers is not important. However, to achieve coherent averaging over multiple sets of time-domain interferograms, highly phase-stabilized comb lasers are useful for developing and applying DFC-PP spectroscopy for use with molecules under thermal fluctuation [14].

The time scales associated with femtosecond pulse-induced vibrational coherence evolution and relaxation, intramolecular vibration relaxation, internal conversion processes, intermolecular energy transfers, and conformational transitions range from a few femtoseconds to nanoseconds. They can be investigated using the PP measurement method. As mentioned earlier, the first ASOPS-based transient absorption (TA) study was reported in 1987, in which two repetition-rate-stabilized mode-locked lasers without CEO frequency stabilization were used [26]. Recently, we experimentally demonstrated DFC-PP-based spectroscopy of chromophores in solution, which fully utilized the phase coherent nature of OFCs. It should be noted that both the repetition rates and CEO frequencies of our OFCs were stabilized [14]. In addition to the advantage of our DFC-PP spectroscopy with fully phase-stabilized OFCs in terms of coherent averaging, it could also be used for ultrashort interferometric triggering, specifically for initiating data collection. It was found that the timing jitter in our measurements does not exceed the half-period of the carrier frequency.

In DFC-PP spectroscopy, two non-collinearly propagating trains of femtosecond pulses from the two OFCs are focused onto an optical sample (Fig. 16.3). The change in intensity of the probe beam, which interacts resonantly with the chromophores, is induced by the presence of the pump beam. Simultaneously, small portions of the two comb laser beams are separated by beam splitters and are allowed to interfere with each other in a nonlinear crystal to produce a second-harmonic-generation (SHG) field. It is only when the two pulses from OFCs temporally overlap that the SHG field is produced. If the intensity of the SHG field is higher than a given threshold value, it is used as an optical trigger for data collection. This triggering approach minimizes the time jitter, which is needed for coherent averaging and for setting time zero for pump-probe measurements.

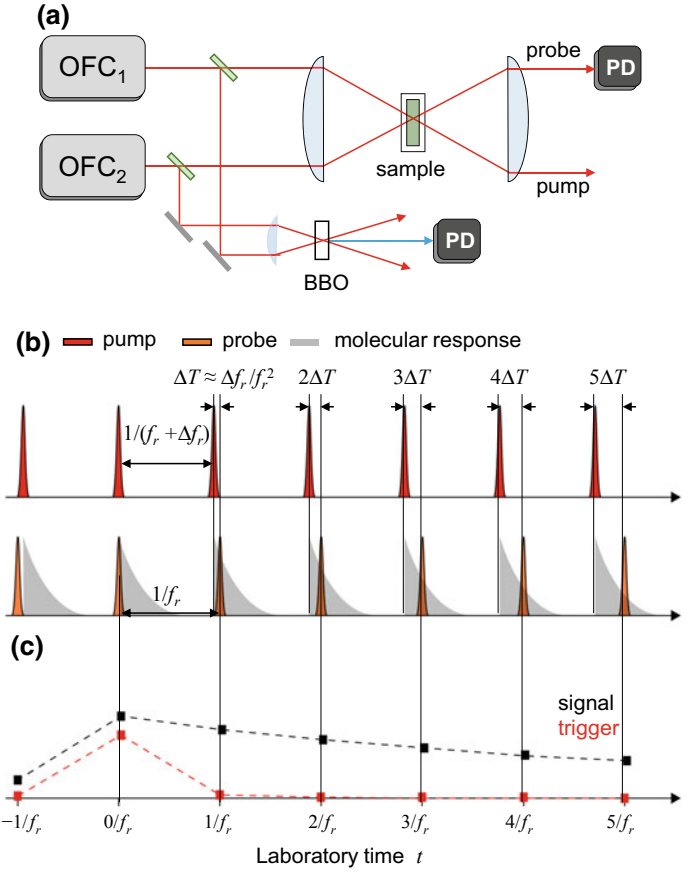

Fig. 16.3 Dual frequency comb pump-probe (DFC-PP). **a** Schematic representation of DFC-PP experimental setup. BBO, beta barium borate crystal; PD, photodetector. **b** Pulse sequences of the two OFCs in DFC-PP in laboratory time. **c** Discretely recorded DFC-PP (black) signal and trigger (red) signal at the corresponding detectors

In our DFC-PP study, we showed that four different Liouville space pathways contribute to the PP signal, where the corresponding third-order polarization that satisfies the phase-matching geometry, i.e., $\mathbf{k}_{\mathrm{PP}} = \mathbf{k}_{\mathrm{pr}}$, is given by [14]

$$
\begin{aligned}
P^{(3)}_{\mathrm{PP}}(\mathbf{k}_{\mathrm{pr}}, t) = \int_0^\infty \mathrm{d}t_3 \int_0^\infty \mathrm{d}t_2 \int_0^\infty \mathrm{d}t_1 R^{(3)}(t_3, t_2, t_1)[E_2(\mathbf{k}_{\mathrm{pr}}, t - t_3) E_1 \\
(\mathbf{k}_{\mathrm{pu}}, t - t_3 - t_2) E_1^*(\mathbf{k}_{\mathrm{pu}}, t - t_3 - t_2 - t_1) \\
+ E_1(\mathbf{k}_{\mathrm{pu}}, t - t_3) E_2(\mathbf{k}_{\mathrm{pr}}, t - t_3 - t_2) E_1^*(\mathbf{k}_{\mathrm{pu}}, t - t_3 - t_2 - t_1) \\
+ E_2(\mathbf{k}_{\mathrm{pr}}, t - t_3) E_1^*(\mathbf{k}_{\mathrm{pu}}, t - t_3 - t_2) E_1(\mathbf{k}_{\mathrm{pu}}, t - t_3 - t_2 - t_1)
\end{aligned}
$$

$$+E_1(\mathbf{k}_{\mathrm{pu}}, t-t_3)E_1^*(\mathbf{k}_{\mathrm{pu}}, t-t_3-t_2)E_2(\mathbf{k}_{\mathrm{pr}}, t-t_3-t_2-t_1)\Big] \tag{16.18}$$

Inserting the comb expressions for the two OFCs into (16.18), the third-order DFC-PP polarization, which is expressed as the sum over three comb line numbers, can be obtained. This polarization produces the corresponding third-order electric field, which is then allowed to interfere with the probe beam from OFC2. It then becomes possible to measure the time-domain interferogram, which is determined by the corresponding interference term between the DFC-PP signal field and the probe field. Similar to the time-domain interferogram for linear spectroscopic measurement (see 16.13), some terms oscillate strongly over detection time t with frequencies larger than ω_{r}. Using a slow-response detector and a low pass filter, only the contributions that oscillate with frequencies less than the repetition frequency can be selectively measured at a single-element photodetector.

After carrying out the triple integration with respect to t_1, t_2 and t_3 in (16.18), we obtained the DFC-PP interferogram in the time domain, which can be recast in the following form:

$$\begin{aligned} S_{\mathrm{DFC-PP}}(t) &\propto \mathrm{Im}\Big[E_2^*(\mathbf{k}_{\mathrm{pr}}, t)P_{\mathrm{PP}}^{(3)}(\mathbf{k}_{\mathrm{pr}}, t)\Big] \\ &\propto \mathrm{Im}\Bigg[\sum_{q,m,n=-\infty}^{\infty}\Big\{A_{q+m-n,2}^*A_{q,2}A_{m,1}A_{n,1}^*\tilde{R}_{\mathrm{RE}}^{(3)}\Big(\omega_{q,m,n}^{\mathrm{RE}}, \omega_{m,n}^{\mathrm{RE}}, \omega_n^{\mathrm{RE}}\Big)\Big(\mathrm{e}^{i\omega_{m,n}^{\mathrm{RE}}f_{\mathrm{D}}t}+\mathrm{e}^{i\omega_{q,n}^{\mathrm{RE}}f_{\mathrm{D}}t}\Big) \\ &+A_{q-m+n,2}^*A_{q,2}A_{m,1}^*A_{n,1}\tilde{R}_{\mathrm{NR}}^{(3)}\Big(\omega_{q,m,n}^{\mathrm{NR}}, \omega_{m,n}^{\mathrm{NR}}, \omega_n^{\mathrm{NR}}\Big)\Big(\mathrm{e}^{i\omega_{m,n}^{\mathrm{NR}}f_Dt}+\mathrm{e}^{i\omega_{m,q}^{\mathrm{NR}}f_{\mathrm{D}}t}\Big)\Big\}\Bigg] \end{aligned} \tag{16.19}$$

In the above equation, *RE* and *NR* represent the rephasing and non-rephasing response spectra, respectively, where the corresponding response functions can be found in the book by Cho (see [22]), and the comb line number-dependent frequencies are defined as

$$\begin{aligned} &\omega_n^{\mathrm{RE}} = -\omega_n^{\mathrm{NR}} = -\omega_{c,1} - n\omega_{\mathrm{r}},\ \omega_{m,n}^{\mathrm{RE}} = -\omega_{m,n}^{\mathrm{NR}} = (m-n)\omega_{\mathrm{r}} \\ &\omega_{q,m,n}^{\mathrm{RE}} = \omega_{\mathrm{c},1} + (q+m-n)\omega_{\mathrm{r}} \text{ and } \omega_{q,m,n}^{\mathrm{NR}} = \omega_{\mathrm{c},1} + (q-m+n)\omega_{\mathrm{r}}. \end{aligned} \tag{16.20}$$

Although the resulting (16.19) appears to be complicated, the pre-exponential terms are the products of the OFC pulse spectra and triple one-sided Fourier transform of the third-order response function that corresponds to the third-order susceptibility, $\tilde{R}^{(3)}(\omega_3, \omega_2, \omega_1)$. $\tilde{R}^{(3)}(\omega_3, \omega_2, \omega_1)$ is more intuitive to understand the experimental data and the embedded nonlinear interactions than the corresponding time-domain nonlinear response function $R^{(3)}(t_3, t_2, t_1)$. In, ω_1 (ω_3) corresponds to the frequency conjugate of the first (second) coherence oscillating with the electronic transition frequency, and it is related to the absorptive (emissive) frequency of the electronic chromophore. On the other hand, ω_2 is the frequency representing the spectral density associated with the photo-induced vibrational coherence decay, population relaxation, and solvation dynamics of the excited molecules [22, 23].

Here, the population relaxation (pump-probe delay) time scale is down-converted to a laboratory-measurement time scale by the down-conversion factor f_{D} as $f_{\mathrm{D}}t$ in (16.19). Experimentally, to determine time zero for pump-probe measurement, it is necessary to adjust the actual recording time in reference to the SHG optical trigger. One of the important aspects of the theoretical result in (16.19) is that the DFC-PP interferogram does not depend on the CEO angular frequency ω_{ceo} so that, in principle, DFC-PP spectroscopy does not require CEO frequency stabilization because it probes the incoherent population changes of excited molecules.

16.5.3 Interferometric Pump-Probe Spectroscopy with Dual Frequency Combs

Although DFC-PP spectroscopy with a photodetector provides time-dependent signals over a wide dynamic range of time scales, the spectrum of a PP signal at a given waiting time cannot be measured unless diffractive optics and an array detector are used. Unfortunately, an array detector that can follow an OFC repetition rate of a few hundred MHz is not available. Therefore, to obtain the spectrum of the PP signal, we proposed DFC-based interferometric pump-probe (DFC-IPP) spectroscopy and successfully demonstrated that it was feasible for dye molecules in solution [15]. DFC-IPP spectroscopy shares the same beam configuration as DFC-PP spectroscopy, but due to the additional interferometric detection scheme implemented in the DFC-IPP system, it is possible to use it to measure the complex transient spectrum whose real and imaginary parts are associated with the transient refraction and absorption spectra of dye molecules in condensed phases.

The experimental layout of DFC-IPP spectroscopy is schematically presented in Fig. 16.4. The pump OFC1 and probe OFC2 are used for the ASOPS of the pump-probe response. The generated third-order PP field then needs to be interferometrically detected. A small fraction of the OFC2 beam is separated before the sample and combined with the probe beam carrying the PP signal immediately after the sample. The time delay (τ) between the probe and local oscillator (LO) pulses is scanned using a translational stage. At a fixed τ, the time-resolved response of the sample interfered with by the LO is recorded by a photodetector. Using the comb expression for the pump, probe, and LO fields, we found that the theoretical expression of the DFC-IPP interferogram is given as

$$
\begin{aligned}
&S_{\mathrm{DFC-IPP}}(t,\tau) \propto \mathrm{Im}[E_2^*(\mathbf{k}_{pr},t)P^{(3)}(\mathbf{k}_{\mathrm{pr}},t,\tau)] \\
&\propto \mathrm{Im}\Bigg[\sum_{q,m,n=-\infty}^{\infty}\Big\{A^*_{q+m-n,2}A_{q,2}A_{m,1}A^*_{n,1}\tilde{R}^{(3)}_{\mathrm{RE}}\left(\omega^{\mathrm{RE}}_{q,m,n},\omega^{\mathrm{RE}}_{m,n},\omega^{\mathrm{RE}}_{n}\right)\mathrm{e}^{i\omega^{\mathrm{RE}}_{q,m,n}\tau}\left(\mathrm{e}^{i\omega^{\mathrm{RE}}_{m,n}f_D t}+\mathrm{e}^{i\omega^{\mathrm{RE}}_{q,n}f_D t}\right). \\
&+A^*_{q-m+n,2}A_{q,2}A^*_{m,1}A_{n,1}\tilde{R}^{(3)}_{\mathrm{NR}}\left(\omega^{\mathrm{NR}}_{q,m,n},\omega^{\mathrm{NR}}_{m,n},\omega^{\mathrm{NR}}_{n}\right)\mathrm{e}^{i\omega^{\mathrm{NR}}_{q,m,n}\tau}\left(\mathrm{e}^{i\omega^{\mathrm{NR}}_{m,n}f_{\mathrm{D}}t}+\mathrm{e}^{i\omega^{\mathrm{NR}}_{m,q}f_{\mathrm{D}}t}\right)\Big\}\Bigg]
\end{aligned}
\tag{16.21}
$$

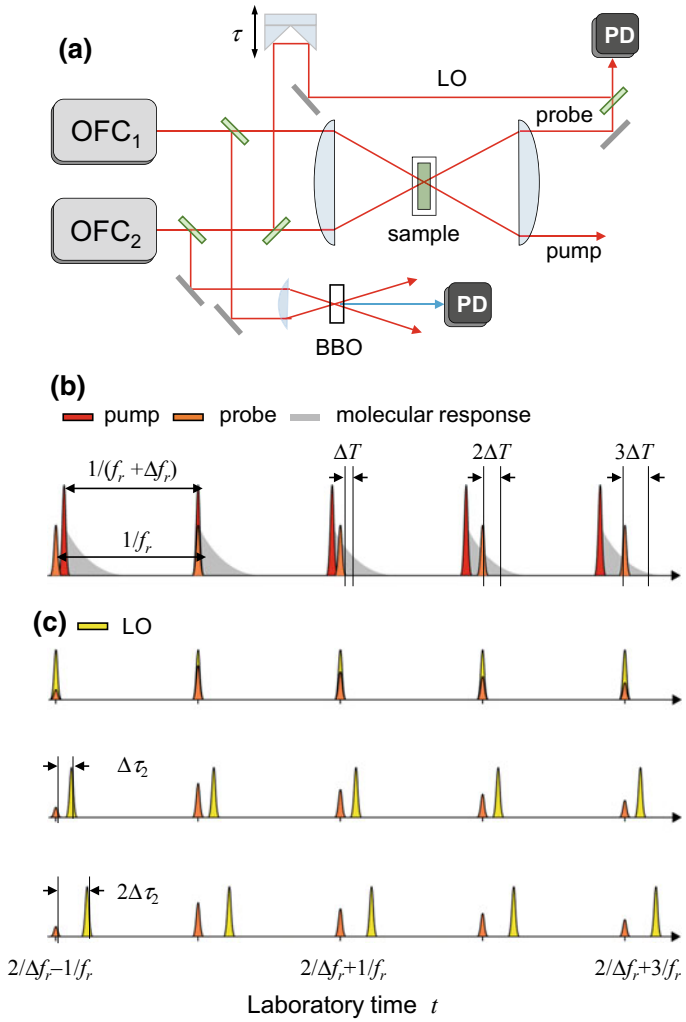

Fig. 16.4 Dual frequency comb interferometric pump-probe (DFC-IPP). **a** Schematic representation of DFC-IPP experimental setup. **b** Pulse sequence of the pump and probe OFCs at the optical sample in laboratory time. **c** Pulse sequences of the probe and local oscillator (LO) OFCs at the detector in DFC-IPP

Equation (16.21) shows that the DFC-IPP signal carries information on the complex nonlinear response in a two-dimensional time-resolved manner. First, the t-dependent interferogram provides information about the vibrational coherence evolution, population relaxation, and rotational dynamics of the chromophores with respect to waiting time. The τ-dependence of the DFC-IPP signal is determined by electronic dephasing, inhomogeneous line broadening, and vibronic progression because the chromophore dynamics determine the electronic decoherence during τ. To obtain

the waiting time-dependent and probe frequency-resolved transient absorption and refraction spectra, the measured τ-dependent time(t)-domain interferogram needs to be Fourier-transformed with respect to τ.

Although the theoretical expression for the DFC-IPP interferogram appears to be similar to that of the DFC-PP interferogram, it is quite different experimentally. Due to its additional probe frequency resolvability, DFC-IPP spectroscopy is better suited for studying changes in molecular structures and state-to-state energy transfer processes induced by femtosecond photo-excitation because they affect the transient absorption and refraction properties of chromophores in condensed phases. For typical electronic chromophores in solution, it should be noted that DFC-IPP spectroscopy does not require a long τ-scan because of the subpicosecond electronic dephasing processes. As a result, DFC-IPP spectroscopy, with its wide dynamic range measurement capability (6 decades) enables rapid data acquisition compared to the conventional pump-probe method with a translation stage for waiting time scanning.

Recently, we were able to measure a complete time- and frequency-resolved DFC-IPP signal from a dye solution, with the pulse frequency covering a broad window from 325 THz to 450 THz and the waiting time scanning from 10 fs up to 1.5 ns [15]. The data collection took just a few seconds. Furthermore, with the controllability of the repetition frequency detuning factor Δf_r and the long-term phase stability, DFC-IPP's femtosecond time-resolution makes it possible to investigate vibrational coherence dynamics even for averaged DFC-IPP data.

ASOPS schemes, which fully utilize an automatic time-delay scan by two different mode-locked lasers with different repetition rates, allow a significantly fast waiting time scan to be achieved compared to conventional mechanical time-delay-based PP measurement methods. This would thus be useful for monitoring the change in quantum state populations induced by excitation transfers or local environmental changes. Furthermore, when it combined with our interferometric optical trigger technique, DFC-PP and DFC-IPP are advantageous for samples that are vulnerable to photochemical damage during spectroscopic measurement. In fact, a number of chemical and biological systems of great interest are easily damaged by the high peak power or high average power of incident radiation from amplified femtosecond lasers. For example, the high peak power of an incident beam causes undesirable high-order multi-photon processes that result in unwanted irreversible chemical reactions such as ionization or bond breaking. Secondly, the high average power of the light source increases the local temperature at a focal spot through non-radiative relaxation (i.e., heat dissipation) of the excited molecules. These two forms of photo-induced degradation can be dramatically suppressed by employing DFC-PP and DFC-IPP spectroscopy. This is because the peak power or a single pulse energy of each OFC used in DFC spectroscopy does not have to be high because of its fast and efficient data acquisition scheme. Secondly, it should be emphasized that the local thermal heating effect can be reduced by introducing a gated measurement when employing the interferometric optical triggering scheme, as we have demonstrated in the past [14, 15]. These technical advances make DFC-PP and DFC-IPP spectroscopy suitable for the study of various chemical and biological systems that have not been able to be investigated before.

16.5.4 Interferometric Photon-Echo Spectroscopy with Dual Frequency Combs

In Sects. 16.5.2 and 16.5.3, we described the theory and experimental outcomes of the time-resolved PP and time- and frequency-resolved interferometric PP measurement methods. A natural extension of DFC-based nonlinear spectroscopy is the development of coherent two-dimensional spectroscopy by employing non-collinear beam geometry and using the corresponding phase-matching condition to separate the nonlinear optical signal field from the other injected beams. Recently, we theoretically considered DFC photon echo spectroscopy (PES) [20]. In this non-collinear geometry consisting of two OFC beams with wave vectors $\mathbf{k}_1$ and $\mathbf{k}_2$, only the signal propagating along the rephasing direction, i.e., $\mathrm{k_{sig}} = -\mathrm{k}_1 + 2\mathrm{k}_2$, is assumed to be measured (Fig. 16.5). The third-order polarization for the two-pulse DFC-PES signal can then be written as

$$P^{(3)}_{\mathrm{2P-PE}}(\mathbf{r},t) = \int_0^\infty \mathrm{d}t_3 \int_0^\infty \mathrm{d}t_2 \int_0^\infty \mathrm{d}t_1\, R^{(3)}(t_3,t_2,t_1) \times \left[E_2(\mathbf{k}_2, t-t_3)E_2(\mathbf{k}_2, t-t_3-t_2)E_1^*(\mathbf{k}_1, t-t_3-t_2-t_1) + E_2(\mathbf{k}_2, t-t_3)E_1^*(\mathbf{k}_1, t-t_3-t_2)E_2(\mathbf{k}_2, t-t_3-t_2-t_1)\right]. \tag{16.22}$$

We proceed in the same way as in DFC-IPP spectroscopy by substituting the comb field expressions into (16.22) and multiplying the LO field, $E_2(\mathbf{k}_{\mathrm{sig}}, t)$, which is delayed by τ_2, to obtain the final expression for the two-pulse DFC-PES signal (i.e., the time-domain interferogram) as follows:

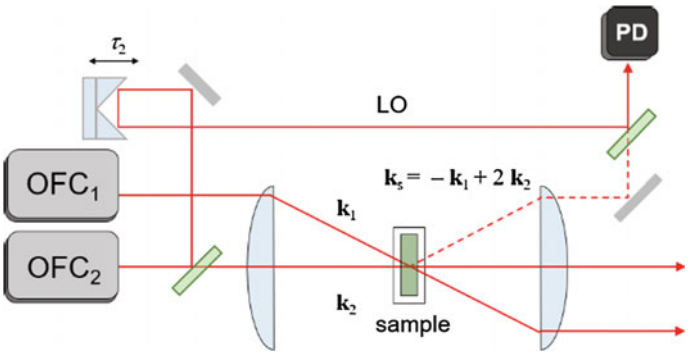

Fig. 16.5 Two-pulse dual frequency comb photon-echo spectroscopy (2P-DFC-PE). Simplified schematic representation of 2P-DFC-PE experimental setup is shown in this figure. The two non-collinearly propagating fields with wave vectors k1 and k2 interact with an optical sample and the generated third-order signal is detected by making it interfere with OFC2 field

$$S_{\mathrm{2P-DFC-PES}}(t,\tau_2) \propto \mathrm{Im}\Big[E_2^*(\mathbf{k}_{\mathrm{sig}},t-\tau_2)P^{(3)}_{\mathrm{2P-PE}}(\mathbf{k}_{\mathrm{sig}},t)\Big]$$
$$\propto \mathrm{Im}\Bigg[\sum_{q,m,n=-\infty}^{\infty}\Big\{A^*_{q+m-n,2}A_{q,2}A_{m,2}A^*_{n,1}\tilde{R}^{(3)}_{\mathrm{RE}}\Big(\omega^{\mathrm{RE}}_{q,m,n},\omega^{\mathrm{RE}}_{m,n},\omega^{\mathrm{RE}}_{n}\Big)\mathrm{e}^{i\,\omega^{\mathrm{RE}}_{q,m,n}\tau_2+i(\omega^{\mathrm{RE}}_n f_{\mathrm{D}}+\Delta\omega_{\mathrm{ceo}})t}$$
$$+A^*_{q-m+n,2}A_{q,2}A^*_{m,1}A_{n,2}\tilde{R}^{(3)}_{\mathrm{NR}}\Big(\omega^{\mathrm{NR}}_{q,m,n},\omega^{\mathrm{NR}}_{m,n},\omega^{\mathrm{NR}}_{n}\Big)\mathrm{e}^{i\,\omega^{\mathrm{NR}}_{q,m,n}\tau_2+i(\omega^{\mathrm{NR}}_n f_{\mathrm{D}}+\Delta\omega_{\mathrm{ceo}})t}\Big\}\Bigg]. \tag{16.23}$$

The frequencies of the oscillating components contributing to the t-dependent interferogram measured at the photodetector are down-converted by the factor f_{D}. Note that the frequency ω^{RE}_n ($=-\omega^{\mathrm{NR}}_n$) is determined by the center frequency of the OFC1, which should be close to the electronic transition frequency. However, due to the multiplied down-conversion factor f_{D}, which is typically 10^{-6}–10^{-8}, the actual frequency detected at the single-point photodetector is in the RF domain. However, the oscillating frequency during the τ_2 scan that is achieved when employing a mechanical translational stage or a pair of sliding glass wedges is in the optical (electronic transition) frequency domain. Therefore, the double Fourier transformations of the t- and τ_2-resolved interferograms over the two time arguments provide a 2D electronic or vibrational spectrum, depending on the nature of the molecular quantum states involved in the two-pulse photon echo experiment. More specifically, the 2D two-pulse DFC-PES spectrum is given as

$$\tilde{S}_{\text{2P-DFC-PES}}(\omega_2,\omega_1) = \int_{-\infty}^{\infty}\mathrm{d}\tau_2\int_{-\infty}^{\infty}\mathrm{d}t\,S_{\text{2P - DFC - PES}}(t,\tau_2)\mathrm{e}^{-i\omega_2\tau_2-i\omega_1 t}$$
$$\propto \mathrm{Im}\Bigg[\sum_{q,m,n=-\infty}^{\infty}\Big\{A^*_{q+m-n,2}A_{q,2}A_{m,2}A^*_{n,1}\tilde{R}^{(3)}_{\mathrm{RE}}\Big(\omega^{\mathrm{RE}}_{q,m,n},\omega^{\mathrm{RE}}_{m,n},\omega^{\mathrm{RE}}_{n}\Big)\delta\Big(\omega_2-\omega^{\mathrm{RE}}_{q,m,n}\Big)\delta\big(\omega_1-\omega^{\mathrm{RE}}_n f_{\mathrm{D}}-\Delta\omega_{\mathrm{ceo}}\big)$$
$$+A^*_{q-m+n,2}A_{q,2}A^*_{m,1}A_{n,2}\tilde{R}^{(3)}_{\mathrm{NR}}\Big(\omega^{\mathrm{NR}}_{q,m,n},\omega^{\mathrm{NR}}_{m,n},\omega^{\mathrm{NR}}_{n}\Big)\delta\Big(\omega_2-\omega^{\mathrm{NR}}_{q,m,n}\Big)\delta\big(\omega_1-\omega^{\mathrm{NR}}_n f_{\mathrm{D}}-\Delta\omega_{\mathrm{ceo}}\big)\Big\}\Bigg] \tag{16.24}$$

When the carrier frequencies of the two OFCs are tuned to be identical to the transition frequency ω_{eg} of a model two-level system with ground state $|g\rangle$ and excited state $|e\rangle$, the peak position of the corresponding rephasing 2D spectroscopic signal appears at ω_{eg} along the ω_2 axis. On the other hand, the corresponding peak position along the ω_1 axis is at $\omega_{\mathrm{eg}} f_{\mathrm{D}}+\Delta\omega_{\mathrm{ceo}}$. Note that the transition frequency ω_{eg} is down-converted by the factor f_{D}. Therefore, to convert the experimentally measured frequency $\omega_{\mathrm{eg}} f_{\mathrm{D}}+\Delta\omega_{\mathrm{ceo}}$ from the 2D spectrum to the molecular transition frequency, experimentally measured $\Delta\omega_{\mathrm{ceo}}$ and f_{D} should be used.

Usually, conventional photon echo spectroscopy or three-pulse scattering spectroscopy adopts a non-collinear geometry, where the incident *pu1*, *pu2*, and *pr* pulses propagate in different directions, and these directions are also different from that of the generated third-order signal field satisfying the corresponding phase-matching condition. However, Lomsadze et al. recently demonstrated DFC photon echo spectroscopy that employed a frequency modulation technique with a collinear geometry, where the incident *pu1*, *pu2*, and *pr* pulses and generated signal fields all propagate in the same direction [27, 28]. To selectively measure the third-order signal field, its frequencies were shifted to a specific and different frequency window by shifting the frequency of the *pu2* beams by ω_{m} (in the order of tens of MHz) with an AOM.

Therefore, only those frequency components in the measured time-domain interferogram that oscillate with frequencies shifted by $2\omega_m$ could be selectively detected in the radio frequency domain, even though all the incident and four-wave-mixing fields propagated collinearly. The 2D spectrum constructed from the selected radio frequency region was obtained for Rb atomic vapor.

Collinear DFC-PES has certain advantages. Unlike non-collinear DFC-PES, it does not require careful alignment for the spatial overlap of the two OFC beams at the sample. Note that, due to the weakness of photon echo signals, it is difficult to spatially overlap this signal with the local oscillator beam. In addition, in a non-collinear geometry, the signal appears along a specific direction, satisfying the phase-matching angle of the experiment. Thus, the direction of the signal field depends on the wavelength of the incident fields, which causes the spatial dispersion of the signal beam. In particular, when broadband incident and local oscillator fields are used, a reduction in measurement sensitivity due to this spatial dispersion problem cannot be easily avoided. In this regard, a collinear geometry, which is free from this effect, may be more practical. However, it should be emphasized that the use of an AOM to shift all of the comb lines in collinear DFC-PES makes it difficult to extend and further develop this technique for femtosecond time-resolved and broadband photon echo spectroscopy because of the intrinsically large temporal dispersion of AOMs. Therefore, we have recently carried out noncollinear DFC-based two-dimensional electronic spectroscopy of chromophores in solution by combining ASOPS scheme for monitoring population relaxation taking place on the timescale ranging from sub-picosecond to nanosecond with heterodyne-detection method for measuring the phase and amplitude of generated third-order signal.

16.5.5 Time-Resolved Photon-Echo Spectroscopy with Dual Frequency Combs

Two-pulse DFC-PES, as outlined in (16.24) and demonstrated in ref. 20 via numerical simulations, enable the two-dimensional spectrum of chromophores in condensed phases to be measured. However, due to a lack of additional time variables associated with the population or waiting time, it does not generate waiting time-resolved 2D spectra. To achieve completely time-resolved DFC-PES, we have added one more translational stage to control the time delay between the generated third-order signal field and the local oscillator field. More specifically, OFC1 pulses are split into two trains of pulses with a beam splitter and the time delay (τ_1) between the *pu1* (wave vector $\mathbf{k}_1$) and *pu2* (wave vector $\mathbf{k}_2$) pulses is scanned with a delay stage. A waiting time (T) scan is then achieved by employing ASOPS because the third *pr* (wave vector $\mathbf{k}_3$) pulse is from the OFC2, whose repetition rate is slightly lower than that of the OFC1. Finally, the generated photon echo field with the wave vector $\mathbf{k}_{sig} = -\mathbf{k}_1 + \mathbf{k}_2 + \mathbf{k}_3$ is allowed to interfere with the local oscillator field that is taken from the same OFC2 (Fig. 16.6). The delay time τ_2 between the *pr* pulse and the

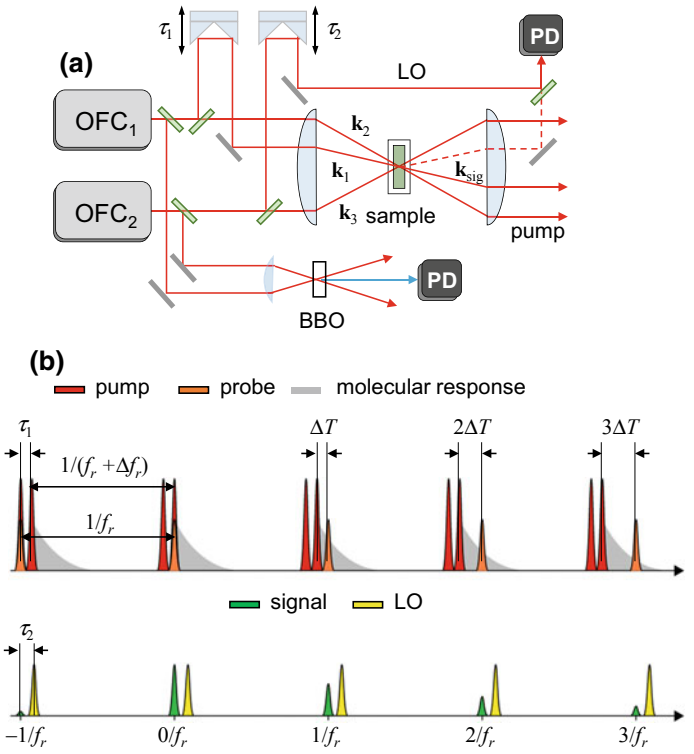

Fig. 16.6 Dual frequency comb photon-echo spectroscopy (DFC-PES). **a** Schematic representation of DFC-PES experimental setup. **b** Pulse sequence of the pump and probe OFCs at the sample position (top) and that of the PES signal field and LO pulse arriving at the detector (bottom)

local oscillator pulse is scanned with another delay stage. Therefore, the measured time-domain interferogram is a function of τ_1 and τ_2. Including the measurement time t, we find that the genuine three-pulse DFC-PES interferogram is given as

$$
\begin{aligned}
&S_{\text{DFC-PES}}(\tau_2, t, \tau_1) \propto \text{Im}\left[E_2^*(\mathbf{k}_{\text{sig}}, t-\tau_2) P_{\text{PE}}^{(3)}(\mathbf{k}_{\text{sig}}, t, \tau_1)\right] \\
&\propto \text{Im}\left[\sum_{q,m,n=-\infty}^{\infty} \left\{ A_{q+m-n,2}^* A_{q,2} A_{m,1} A_{n,1}^* \tilde{R}_{\text{RE}}^{(3)}\left(\omega_{q,m,n}^{\text{RE}}, \omega_{m,n}^{\text{RE}}, \omega_n^{\text{RE}}\right) e^{i\,\omega_{q,m,n}^{\text{RE}}\tau_2 + i\omega_{m,n}^{\text{RE}} f_{\text{D}} t + i\,\omega_n^{\text{RE}}\tau_1} \right.\right. \\
&\left.\left. + A_{q-m+n,2}^* A_{q,2} A_{m,1}^* A_{n,1} \tilde{R}_{\text{NR}}^{(3)}\left(\omega_{q,m,n}^{\text{NR}}, \omega_{m,n}^{\text{NR}}, \omega_n^{\text{NR}}\right) e^{i\,\omega_{q,m,n}^{\text{NR}}\tau_2 + i\omega_{m,n}^{\text{NR}} f_{\text{D}} t + i\omega_n^{\text{NR}}\tau_1} \right\}\right]
\end{aligned}
\tag{16.25}
$$

where $\Delta\omega_{\text{ceo}}$ was canceled out much like DFC-PP and DFC-IPP. Again, due to the use of ASOPS for the waiting time scan with respect to t, the oscillating frequencies with respect to the measurement time t are down-converted by the factor f_{D}.

The t-dependent decay of $S_{\text{DFC}-PES}(\tau_2, t, \tau_1)$ provides information about the population relaxation processes during the waiting time in laboratory time, which is slower than the molecular relaxation time by a factor of $1/f_D$. To obtain

the time(t)-resolved 2D spectrum from (16.25), the double Fourier transform of $S_{\mathrm{DFC-PES}}(\tau_2, t, \tau_1)$ with respect to τ_1 and τ_2 should be taken to find

$$\begin{aligned}\tilde{S}_{\mathrm{DFC\,-\,PES}}(\omega_2, t, \omega_1) &= \int_{-\infty}^{\infty} \mathrm{d}\tau_2 \int_{-\infty}^{\infty} \mathrm{d}\tau_1 S_{\mathrm{DFC\,-\,PES}}(\tau_2, t, \tau_1) \mathrm{e}^{-i\omega_2\tau_2 - i\omega_1\tau_1} \\ &\propto \mathrm{Im}\Bigg[\sum_{q,m,n=-\infty}^{\infty} \{A^*_{q+m-n,2} A_{q,2} A_{m,1} A^*_{n,1} \tilde{R}^{(3)}_{\mathrm{RE}}\left(\omega^{\mathrm{RE}}_{q,m,n}, \omega^{\mathrm{RE}}_{m,n}, \omega^{\mathrm{RE}}_{n}\right) \mathrm{e}^{i\omega^{\mathrm{RE}}_n f_{\mathrm{D}} t} \delta\left(\omega_2 - \omega^{\mathrm{RE}}_{q,m,n}\right) \delta\left(\omega_1 - \omega^{\mathrm{RE}}_{n}\right) \\ &+ A^*_{q-m+n,2} A_{q,2} A^*_{m,1} A_{n,1} \tilde{R}^{(3)}_{\mathrm{NR}}\left(\omega^{\mathrm{NR}}_{q,m,n}, \omega^{\mathrm{NR}}_{m,n}, \omega^{\mathrm{NR}}_{n}\right) \mathrm{e}^{i\omega^{\mathrm{NR}}_n f_{\mathrm{D}} t} \delta\left(\omega_2 - \omega^{\mathrm{NR}}_{q,m,n}\right) \delta\left(\omega_1 - \omega^{\mathrm{NR}}_{n}\right)\}\Bigg] \end{aligned} \quad (16.26)$$

DFC-PES experiments were conducted for dye solutions. We demonstrated that dual frequency combs enable the measurement of the 2D electronic coherences of chromophores in condensed phases over a wide dynamic range (6 decades).

16.6 Overview and a Few Concluding Remarks

OFC is a special type of mode-locked laser. Due to the stabilized repetition and CEO frequencies, the corresponding spectrum has spectral lines that are equally spaced at fixed frequencies. Although OFC lasers have been used in a variety of research fields including precision measurement [19] and metrology [29], only recently have they become used for spectroscopic applications [15, 27]. In particular, when two independent OFCs are set to have slightly different repetition rates, precise time-delay scanning in the time domain is achievable, guaranteeing DFC spectroscopy with a high spectral resolution. In the various spectroscopic applications of DFC spectroscopy based on interferometric detection with a single photodetector, the measured time-domain interferogram provides information on the holographic (phase and amplitude) responses of the molecules under investigation. Most of the earlier uses of DFC spectroscopy aimed to obtain the rovibrational spectra of gas-phase molecules not only because the high-frequency resolvability of the OFC technique is suited for gas-phase molecular spectroscopy but also because truly broadband OFC lasers whose bandwidth covers the entire absorption spectrum of chromophores in condensed phases have not been available until recently.

We have, using the unique and characteristic advantages of broadband OFC techniques, recently developed DFC-based time-resolved nonlinear spectroscopy. In this chapter, we reviewed our experimental techniques and the underlying theory. The three most popular time-domain nonlinear spectroscopic methods—DFC-PP [14], DFC-IPP [15], and DFC-PES—have all been experimentally demonstrated. As emphasized in this chapter, the optical molecular response in the optical or vibrational frequency domain (on femtosecond and picosecond time scales) can be measured with a single detector working in the down-converted frequency RF domain.

Currently, we are developing DFC-based sum-frequency-generation, difference-frequency-generation, and other four-wave-mixing spectroscopic techniques. We also plan to use triple comb lasers to carry out high-order nonlinear spectroscopy and

coherent multidimensional spectroscopy. Of course, the phase stabilization of each OFC laser is important for the coherent averaging of the measured signals, but the phase locking of three or more comb lasers is a prerequisite for successful interferometric studies of the electronic or vibrational coherences induced by field-matter interactions with these multiple comb lasers.

The extremely high frequency resolution of OFC may not be needed for condensed-phase molecular spectroscopy. However, when two or more phase-locked OFCs are combined to develop multiple frequency comb spectroscopic techniques with coherent averaging, time- or space-to-frequency conversion, frequency modulation, and asymmetric optical sampling, they will be of critical use for studying population relaxation and coherence evolution in separate time windows for coupled chromophores in condensed phases.

Acknowledgements This work was supported by IBS-R023-D1.

References

1. T. Brixner et al., Two-dimensional spectroscopy of electronic couplings in photosynthesis. Nature **434**, 625–628 (2005)
2. V.I. Prokhorenko et al., Coherent control of retinal isomerization in bacteriorhodopsin. Science **313**, 1257–1261 (2006)
3. C.-C. Hsieh et al., Comprehensive studies on an overall proton transfer cycle of the ortho-green fluorescent protein chromophore. J. Am. Chem. Soc. **133**, 2932–2943 (2011)
4. Y.I. Suzuki, T. Fuji, T. Horio, T. Suzuki, Time-resolved photoelectron imaging of ultrafast S_2 -> S_1 internal conversion through conical intersection in pyrazine. J. Chem. Phys. **132**, 174302 (2010)
5. T. Mirkovic et al., Light absorption and energy transfer in the antenna complexes of photosynthetic organisms. Chem. Rev. **117**, 249–293 (2017)
6. J. Kim, D.E. Kim, T. Joo, Excited-state dynamics of Thioflavin T: planar stable intermediate revealed by nuclear wave packet spectroscopies. J. Phys. Chem. A **122**, 1283–1290 (2018)
7. T. Joo, Y. Jia, J.Y. Yu, M.J. Lang, G.R. Fleming, Third-order nonlinear time domain probes of solvation dynamics. J. Chem. Phys. **104**, 6089–6108 (1996)
8. D.J. Jones et al., Carrier-envelope phase control of femtosecond mode-locked lasers and direct optical frequency synthesis. Science **288**, 635–639 (2000)
9. B. Bernhardt et al., Cavity-enhanced dual-comb spectroscopy. Nat. Photon. **4**, 55–57 (2009)
10. B. Cho, T.H. Yoon, M. Cho, Dual-comb spectroscopy of molecular electronic transitions in condensed phases. Phys. Rev. A **97**, 033831 (2018)
11. D.I. Herman et al., Real-time liquid-phase organic reaction monitoring with mid-infrared attenuated total reflectance dual frequency comb spectroscopy. J. Mol. Spectrosc. **356**, 39–45 (2019)
12. E. Hase et al., Scan-less confocal phase imaging based on dual-comb microscopy. Optica **5**, 634–643 (2018)
13. H. Mikami et al., Ultrafast confocal fluorescence microscopy beyond the fluorescence lifetime limit. Optica **5**, 117–126 (2018)
14. J. Kim, B. Cho, T.H. Yoon, M. Cho, Dual-frequency comb transient absorption: broad dynamic range measurement of femtosecond to nanosecond relaxation processes. J. Phys. Chem. Lett. 1866–1871 (2018)
15. J. Kim, T.H. Yoon, M. Cho, Interferometric measurement of transient absorption and refraction spectra with dual frequency comb. J. Phys. Chem. B **122**, 9775–9785 (2018)

16. J. Kim, J. Jeon, T.H. Yoon, M. Cho, Dual frequency-comb spectroscopy of chromophores in condensed phases. Chem. Phys. 520, 122-137 (2019)
17. S.-J. Lee, W. Bambang, K. Motonobu, O. Motoichi, Ultra high scanning speed optical coherence tomography using optical frequency comb generators. Jpn. J. Appl. Phys. **40**, L878 (2001)
18. S. Schiller, Spectrometry with frequency combs. Opt. Lett. **27**, 766–768 (2002)
19. T.M. Fortier et al., Kilohertz-resolution spectroscopy of cold atoms with an optical frequency comb. Phys. Rev. Lett. **97**, 163905 (2006)
20. J. Jeon, J. Kim, T.H. Yoon, M. Cho, Dual frequency comb photon echo spectroscopy. J. Opt. Soc. Am. B **36**, 223–234 (2019)
21. M. Cho, Coherent two-dimensional optical spectroscopy. Chem. Rev. **108**, 1331–1418 (2008)
22. M. Cho, *Two-dimensional Optical Spectroscopy* (CRC Press, Boca Raton, 2009)
23. S. Mukamel, *Principles of Nonlinear Optical Spectroscopy* (Oxford University Press, Oxford, 1995)
24. S. Koke et al., Direct frequency comb synthesis with arbitrary offset and shot-noise-limited phase noise. Nat. Photon. **4**, 462 (2010)
25. T. Minamikawa et al., Dual-comb spectroscopic ellipsometry. Nat. Commun. **8**, 610 (2017)
26. P.A. Elzinga, F.E. Lytle, Y. Jian, G.B. King, N.M. Laurendeau, Pump/probe spectroscopy by asynchronous optical sampling. Appl. Spectr. **41**, 2–4 (1987)
27. B. Lomsadze, S.T. Cundiff, Frequency combs enable rapid and high-resolution multidimensional coherent spectroscopy. Science **357**, 1389–1391 (2017)
28. B. Lomsadze, S.T. Cundiff, Frequency comb-based four-wave-mixing spectroscopy. Opt. Lett. **42**, 2346–2349 (2017)
29. M. Lezius et al., Space-borne frequency comb metrology. Optica **3**, 1381–1387 (2016)

Index

M. Cho (ed.), *Coherent Multidimensional Spectroscopy*,
Springer Series in Optical Sciences 226,
https://doi.org/10.1007/978-981-13-9753-0

Q